UNICA

UNIVERSITÀ
DEGLI STUDI
DI CAGLIARI

Ph.D. DEGREE IN
PHYSICS

Cycle XXXVI

TITLE OF THE Ph.D. THESIS

Standard model physics and beyond in low energy neutrino scattering and parity violating electron interactions with nuclei

Scientific Disciplinary Sector(s)

FIS/04 and FIS/02

Ph.D. Student: Nicola Cargioli

Supervisor Dott. Matteo Cadeddu

Final exam. Academic Year 2022/2023
Thesis defence: January 2024 Session

UNIVERSITÀ DEGLI STUDI DI CAGLIARI

Faculty of Science

Department of Physics

PHD school of physics

Cycle: XXXVI

THESIS FOR THE DEGREE OF DOCTOR OF PHILOSOPHY

Standard model physics and beyond in low energy neutrino scattering and parity violating electron interactions with nuclei

Nicola Cargioli

matr: 200/1053/65054

Academic Advisor:

Dott. Matteo Cadeddu

Submitted 2022/2023

Contents

List of Publications

List of the publications in which I was involved that are discussed in this thesis work

[1] M. Cadeddu, **N. Cargioli**, F. Dordei, C. Giunti, Y.F. Li, E. Picciau, Y.Y. Zhang, "*Constraints on light vector mediators through coherent elastic neutrino nucleus scattering data from COHERENT*", Published in Journal of High Energy Physics 01 (2021) 116

[2] M. Cadeddu, **N. Cargioli**, F. Dordei, C. Giunti, Y.F. Li, E. Picciau, Y.Y. Zhang, "*New insights into nuclear physics and weak mixing angle using electroweak probes*", Published in Physical Review C 104 (2021) 6, 065502

[3] M. Cadeddu, **N. Cargioli**, F. Dordei, C. Giunti, E. Picciau, "*Muon and electron g-2 and proton and cesium weak charges implications on dark Z_d models*", Published in Physical Review D 104 (2021) 1, 011701

[4] M. Atzori Corona, M. Cadeddu, **N. Cargioli**, P. Finelli, M. Vorabbi, "*Incorporating the weak mixing angle dependence to reconcile the neutron skin measurement on ^{208}Pb by PREX-II*", Published in Physical Review C 105 (2022) 5, 055503

[5] M. Atzori Corona, M. Cadeddu, **N. Cargioli**, F. Dordei, C. Giunti, Y.F. Li, E. Picciau, C.A. Ternes, Y.Y. Zhang, "*Probing light mediators and (g-2)$_\mu$ through detection of coherent elastic neutrino nucleus scattering at COHERENT*", Published in Journal of High Energy Physics 05 (2022) 109

[6] M. Atzori Corona, M. Cadeddu, **N. Cargioli**, F. Dordei, C. Giunti, Y.F. Li, C.A. Ternes, Y.Y. Zhang, "*Impact of the Dresden-II and COHERENT neutrino scattering data on neutrino electromagnetic properties and electroweak physics*", Published in Journal of High Energy Physics 09 (2022) 164

[7] M. Atzori Corona, W.M. Bonivento, M. Cadeddu, **N. Cargioli**, F. Dordei, "*New constraint on neutrino magnetic moment and neutrino millicharge from LUX-ZEPLIN dark matter search results*", Published in Physical Review D 107 (2023) 5, 053001

[8] M. Atzori Corona, M. Cadeddu, **N. Cargioli**, F. Dordei, C. Giunti, G. Masia, "*Nuclear neutron radius and weak mixing angle measurements from latest COHERENT CsI and atomic parity violation Cs data*", Published in European Physical Journal C 83 (2023) 7, 683

[9] DarkSide-50 Collaboration, "*A study of events with photoelectric emission in the DarkSide-50 liquid argon Time Projection Chamber*", Published in Astroparticle Physics Journal 140 (2022) 102704

Additional publications in which I was involved, also in the context of DarkSide-50, DarkSide-20k and Global Argon Dark Matter Collaborations, can be found in Refs. [10–21].

Introduction

The standard model of particle physics has been proved to be a solid theory to describe the interactions among particles. Many tests have been performed in the last decades, mainly corroborating the current theory. However, some small fractures motivate the study of beyond the standard model scenarios which would open particle physics towards a completely new phenomenology. In this framework, neutrinos may play a leading role.
While neutrinos have been widely studied during the past decades, some special processes have been observed just in recent years, allowing one to perform further tests of the standard model theory and thus, providing a novel way of probing new physics effects. In this thesis, we will study two low energy processes involving neutrinos, namely the coherent elastic neutrino nucleus scattering (CEνNS) and the elastic scattering of neutrinos off electrons (νES). The latter process is well known, both theoretically and experimentally, as it has been widely exploited for example in the context of solar neutrino physics. Whereas, CEνNS has been observed for the first time only in 2017 by the COHERENT Collaboration, despite having been predicted in 1974. CEνNS is a purely weak-neutral current process in which the neutrinos interact coherently with the target nucleus, which thus, responds as a whole. The coherent response of the nucleons in the target determines an enhancement in the cross section, which results to be rather large compared to the ones of other concurrent neutrino processes at low energies. The first observation of such a process confirmed the standard model prediction of neutrino interactions and paved the way for a large number of experimental programs worldwide, with the aim of precisely characterizing the interaction mechanism exploiting different detection systems and neutrino sources, such as solar neutrinos, reactor neutrinos and neutrinos from either pion or kaon decay-at-rest processes.
The current picture counts two CEνNS measurements from the COHERENT Collaboration, namely on a cesium-iodide crystal detector and a liquid argon one, achieved by exploiting neutrinos produced by the pion-decay-at-rest at the spallation neutron source at the Oak Ridge Laboratory, in Tennessee. The COHERENT Collaboration has proved to be a pioneer of CEνNS searches and is still leading the program, planning for many upgrades in upcoming years. Moreover, recently the observation of CEνNS was reported also by the NCC-1701 detector which exploits neutrinos from the Dresden-II reactor power plant in Illinois.
By exploiting the available data, it is possible to perform various analyses in order to extract standard model quantities, such as the weak mixing angle, which describes the couplings in the electroweak theory, and the nuclear neutron radius,

which describes the neutron distribution inside the target nucleus. Furthermore, many beyond the standard model scenarios can be studied, looking for a hint of new physics inside the data. For example, one can search for the presence of extra particles, in particular of a new mediator similar to the standard model Z boson, but lighter in mass, which may represent a portal for dark matter. One can look for signatures of non standard neutrino properties, such as a neutrino magnetic moment or a neutrino electric charge, but also measure the so-called neutrino charge radius, which is the neutrino electromagnetic property predicted within the standard model. This property is usually included among the radiative corrections, which are vertex corrections due to higher order diagrams contributing to the process.
To provide a complete vision of the status of searches in the low energy electroweak sector, we will discuss the complementary between CEνNS and νES searches with the parity violating electron scattering (PVES) experiments. Effectively, the electrons scattering off a nucleus behave similarly to neutrinos scattering off a nucleus, so it is possible to combine the different experimental probes. Likewise, the atomic parity violation process can provide complementary information, since it involves parity violating transitions of atomic electrons interacting with the nucleus.
Additionally, we will discuss the importance of CEνNS and νES in the context of direct dark matter searches. Indeed, the advanced technologies developed in the dark matter community are fruitful also for measuring CEνNS, as the interaction mechanism is not very different. In this sense, we will show that direct dark matter detectors may provide very competitive results in testing beyond the standard model scenarios considered in CEνNS and νES searches.

This thesis is organized into two different parts. The first part is made of three chapters, Chapter 1 focuses on introducing the standard model electroweak theory, with special attention on the weak mixing angle. Chapter 2 deals with low energy neutrino interactions, namely the CEνNS and νES processes, with a description of the neutrino sources and the experimental programs considered in this work. Chapter 3 instead considers low energy electron interactions, so the parity violation electron scattering and the atomic parity violation process, together with a discussion of the available measurements.
In the second part of the thesis, we present all the analysis performed exploiting the different available data via the developments of numerical codes, so that each of the four chapters describes a different physics outcome. In Chapter 4 we discuss the nuclear structure information that can be extracted mainly from PVES measurements, while in Chapter 5 the one that can be extracted from CEνNS measurements. In both chapters also the results on the weak mixing angle will be presented. Chapter 6 focuses on extensions of the standard model via an additional boson mediator, which can arise from a new gauge group. We will discuss a variety of different models for the latter new particle. In the last chapter, Chapter 7, we will instead discuss the status of searches for neutrino electromagnetic properties, such as the neutrino charge radius, the neutrino magnetic moment and the neutrino electric charge.

Part I

Low energy electroweak interactions

Chapter 1

Introduction to the Standard Model and the Electroweak theory

Particles represent the fundamental elements that constitute nature. Particle physics studies the properties of particles and the way they interact among them, through the so-called forces. Physicists have worked for years to build a complete theory to describe all the fundamental forces and the entire particle "zoo". Our current knowledge led us to develop the Standard Model (SM) of particle physics, which provides a global description of the interaction between particles as happening through the exchange of another particle. We currently have many tests of the success of the SM theory coming from a variety of different experiments. However, we are currently aware of the existence of some open points, yet to be explained, that require an extension of the SM theory.

Particles are divided into two main categories, depending on whether their intrinsic angular moment, spin, has an integer value, whose case we speak about bosons, or half-integer value, correspondent to the so-called fermions. Fermions are the constituents of matter, while the particles that are exchanged during the interactions are bosons, in which case, they are referred to as force carriers.

The standard model describes all matter as made of compounds of three different kinds of elementary particles: leptons, quarks and mediators. Both leptons and quarks are fermions. The standard model accounts for six leptons, classified according to the values of their quantum numbers, in particular, the value of the electric charge Q (normalized to the absolute value of the charge of the electron, e_0) and the leptonic number (L_α, with α the so-called flavor).

There is evidence of three different flavor types: electronic, L_e, muonic, L_μ, and tauonic, L_τ, therefore, the leptons are organized in three *generations*, made of pairs of a charged lepton and a neutral lepton which share the same leptonic quantum number. As it is shown in Fig. 1.1, the three charged leptons are the so-called electron, the muon and tau, and the corresponding neutral particles are called neutrinos, in particular the electron neutrino, the muon neutrino and the tau neutrino.

In reality, also six antileptons are described by the SM and are shown in the same figure. They can be easily described by reversing the signs of all the quantum numbers, so that the positron, for example, has a unitary positive charge and elec-

tron lepton number -1 as opposed to the positive charge of the electron and the $+1$ value of its electron lepton number.
The neutrinos are a peculiar type of leptons, and more in general elementary particles, as they are predicted to be massless in the standard model, also after the introduction of the Higgs mechanism [22], which instead gives mass to the other fermions, and are the only elementary chargeless fermions in the standard model. Being neutrinos still particles to be fully understood, they represent a very fascinating object to be studied, so that a great part of this thesis work will deal with them. Among the open issues about their nature, one popular one is known as the neutrino mass problem, although this specific issue will not be discussed in the context of this work.
In a very similar fashion, there are six types of quarks, classified by quantum numbers (electric charge, strangeness, charm, beauty, truth for example). The six quarks are also organized in three generations, where the first one is made of the up, u, and down, d, quarks, the second one of the charm, c, and the strange, s, quarks, while the third of the top, t, and bottom, b, quarks. Quarks are all charged leptons, but with a fractional electric charge, namely $+2/3e_0$ for the u, c and t quarks and $-1/3e_0$ for the d, s and b quarks. By reversing the sign of the quantum numbers, the corresponding antiquarks can be easily defined. The quark sector however has another complication, in fact, each of them can have a "color" between the red (r), green (g) and blue (b) colors, so that to be formally correct, the total amount of quarks is not 6, but 18 (36 counting the antiquarks).

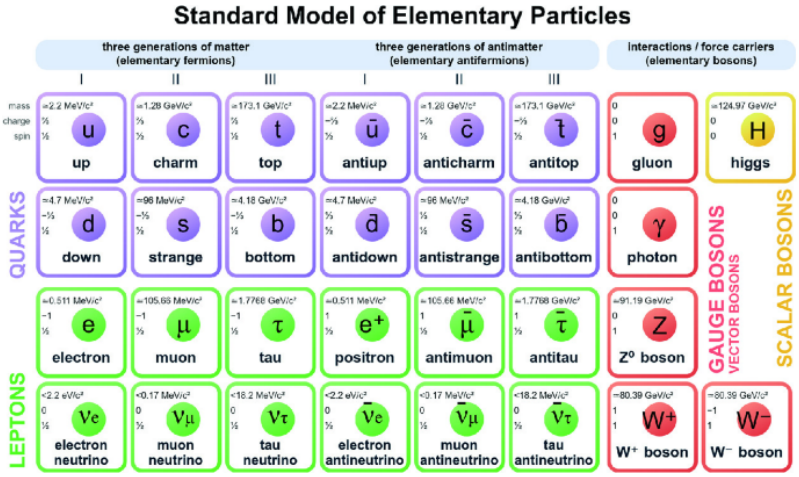

Figure 1.1: Picture collecting the elementary particles (and antiparticles) described by the standard model of particle physics. The quark, leptonic and bosonic sectors are identified by different colors [23].

The third particle type present in the standard model is made of the so-called mediators, or force carriers, and differently from quarks and leptons which are all fermions (spin 1/2), are all bosons (integer spin quantum number).
The photon, γ, is a massless boson responsible for the electromagnetic interactions while the W's and the Z bosons are massive bosons, carriers of the weak interaction. The last fundamental force is the strong force, whose mediators are represented by the gluons, g. The SM predicts 8 different gluons characterised by

the color, similarly to the quarks. The existence of the color is of key importance in the impossibility of observing both gluons and quarks as isolated particles, because matter is colorless. The theory of quarks and gluons, together with the color quantum number, is very complicated and still undergoing a serious investigation by particle physics theorists, representing the development of the so-called Quantum Chromo-Dynamics (QCD) theory, which is far beyond the scope of this thesis work.
In summary, we can count 12 leptons, 12 quarks and 12 mediators (considering antiparticles) as the elementary particles described by the standard model of particle physics, where the graviton, i.e. the putative carrier of the gravitational force, was not counted still being a postulation. The Higgs boson has then to be added to the theory to provide a mass term for the quarks and massive leptons.

As already introduced, among the large number of elementary particles included in the standard model, neutrinos are very peculiar and certainly deserve particular attention and consideration.
Neutrinos have been introduced in the context of nuclear physics around the 1930s, when studying the radioactive transformation of a heavy nucleus into a lighter one, the process that today we know as β-decay [24]. Being the process thought to be a decay of one nucleus in two objects, the lighter nucleus and the electron, the conservation of energy and momentum imposes a monoenergetic spectrum for the outgoing electron. However, experimentally this was not observed, as the electron shows a continuous spectrum of energies covering a wide energy range, up to an endpoint represented by the expected energy value calculated from the kinematics of the two body decay.
Pauli suggested the presence of an additional particle in the process, so that being the decay a three-body decay, the spectrum was not expected anymore to be a monoenergetic line. Such conjecture requires the additional particle to be electrically neutral in order to prevent from violating the conservation of the electric charge, so that Pauli called it neutron. This led to some confusion when few years later the particle that we know as neutron was discovered. Enrico Fermi tried to develop a theory of beta decay based on Pauli's suggestion, but since the new particle had to be lighter than the just discovered neutron, he changed the name to neutrino (light neutron) even if it turned out that neutron and neutrinos have very few things in common, mainly the fact that they are both neutral particles.
Neutrino physics has done many steps forward since the conjectures of Pauli and Fermi's first attempts of building a theory of beta decay. Neutrinos have been detected for the first time in the '50s and still today represent one of the most challenging particles to detect given the very small interaction cross section, as they interact only through weak interaction, without any electromagnetic or strong interaction contributions.
While the electromagnetic interaction is "easy" to understand as the interaction happening between charged particles and the strong force as the interaction between particles with a color (so that leptons do not undergo strong interactions), the weak interaction is more complicated. Hence, all quarks and all leptons undergo weak interaction, but only neutrinos are characterised by interaction only

through the weak force, as they are neutral particles (no electromagnetic interactions) and are colorless particles (no strong interactions). Thus, they represent the ideal candidate to fully understand weak interactions.
In general, we can distinguish two different types of weak interactions: charged current interactions, mediated by the W's bosons, and neutral current interactions, mediated by the Z boson.
The weak interactions are different from the electromagnetic and strong interactions, and in particular, it was observed that they violate parity. This property of weak interactions has impacts on neutrinos, so that in the standard model neutrinos are only left-handed and antineutrinos are right-handed.
Another fundamental difference between the weak interaction and the electromagnetic and strong ones is related to the properties of the mediators. The W's and Z bosons are heavy particles, while the photon and the gluons are massless. The masses of the weak mediators are pretty well measured, in particular, the latest measurements report [25]

$$m_W = 80.377 \pm 0.012 \text{ GeV}/c^2, \quad m_Z = 91.1876 \pm 0.0021 \text{GeV}/c^2 \,, \tag{1.1}$$

where c is the speed of light. Being massive particles with spin 1, the weak interaction mediators have three allowed polarization states, whereas a massless spin 1 particle only has two, so that the propagator of the interaction becomes more complex than in the case of the electromagnetic interaction, namely the weak interaction propagator is

$$\frac{-i(g_{\mu\nu} - q_\mu q_\nu / M^2 c^2)}{q^2 - M^2 c^2}, \tag{1.2}$$

where $g_{\mu\nu}$ is the metric tensor, M the mediator mass, and q the four-momentum transfer in the interaction. In most cases, in particular, in the processes that will be considered in this thesis work, the momentum transfer is significantly smaller than the mediator mass, so that the propagator can be safely approximated to the form

$$\frac{i\, g_{\mu\nu}}{M^2 c^2}. \tag{1.3}$$

It is clear that being the mediator a heavy particle the propagator is suppressed by the mass, making the weak interaction "weaker" than the electromagnetic interaction for instance.

—— Electroweak unification ——

The gauge structure of the weak interaction is SU$(2)_L$. The neutral current process, happening through the third gauge boson, $W^{(3)}$ would happen only coupling to left-handed and right-handed particles, due to the specific chirality structure of the theory. However, experiments were showing that the physical gauge boson responsible for the neutral weak currents couples to both left- and right-handed states, even if not in an equal way.
Glashow, Salam and Weinberg (GSW) had the intuition the third (neutral) gauge

boson of the SU$(2)_L$ group, could be not the physical mediator of the interaction, but instead a quantum state that could mix with another neutral gauge field, that before had been identified with the photon, coming from the electromagnetic gauge group symmetry U(1). In the GSW model, the electromagnetic and weak interactions are not distinct interactions, but part of a unique gauge group SU$(2)_L \times$U$(1)_Y$, from which four physical mediators arise, namely the W's, the Z and the photon, γ.
In this mechanism, the gauge boson associated with the U$(1)_Y$ group, usually referred to as B_μ, doesn't couple to the electric charge, but to a novel kind of charge, called weak hypercharge, Y.
The physical mediators, the Z boson and the photon, are then obtained as a linear combination of the two gauge bosons, B_μ of the U$(1)_Y$ group and $W^{(3)}$ of the SU$(2)_L$ group according to

$$A_\mu = +B_\mu \cos\theta_W + W_\mu^{(3)} \sin\theta_W \ , \tag{1.4}$$

$$Z_\mu = -B_\mu \sin\theta_W + W_\mu^{(3)} \cos\theta_W \ , \tag{1.5}$$

where the angle θ_W, known as the weak mixing angle, describes the mixing between the two gauge fields. The weak mixing angle is also referred to as the Weinberg angle and it describes the mixing between the neutral fields in the electroweak theory. A schematic representation of such mixing is shown in Fig. 1.2.

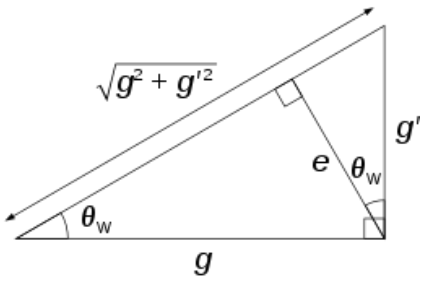

Figure 1.2: Scheme of the mixing between the weak and electromagnetic couplings [26].

The GSW model of electroweak unification directly implies that the two interactions are intimately related, thus, the couplings of weak and electromagnetic interactions are interconnected.
The weak hypercharge associated with a fermion can be defined as a linear combination of the electric charge and the third component of the weak isospin $I_W^{(3)}$, namely

$$Y = 2Q - 2I_W^{(3)}. \tag{1.6}$$

From the equivalence between the hypercharge of a left-handed electron and a left-handed neutrino, it is easy to extract the relation between the electromagnetic and weak coupling, and as it could be expected, it depends on the weak mixing angle, in particular through the relation

$$e_0 = g \sin\theta_W, \tag{1.7}$$

where e_0 is the electric charge and g the coupling of the weak interaction.
However, we can relate the coupling of the electromagnetic current to the electric charge as well, finding

$$e_0 = g' \cos\theta_W, \tag{1.8}$$

and hence, combining the two latter equations we find that

$$e_0 = g \sin\theta_W = g' \cos\theta_W \ . \tag{1.9}$$

It is easy to rewrite Eq. 1.9 to obtain a definition of the weak mixing angle in terms of the couplings, by squaring the equations, and after some manipulations, we obtain that

$$\sin^2\theta_W = \frac{g'^2}{g^2 + g'^2}. \tag{1.10}$$

1.1 The weak mixing angle

As the weak mixing angle describes the coupling in the electroweak theory, the capability of precisely predicting its value is fundamental.
The couplings in Eq. 1.10 are proportional to the masses of the gauge bosons mediating the interaction according to the electroweak symmetry breaking. Therefore, it is possible to redefine the weak mixing angle in terms of the masses of the W and Z bosons, through the simple relation [25]

$$\sin^2\theta_W \equiv 1 - \frac{m_W^2}{m_Z^2} \ . \tag{1.11}$$

Let us notice that such a powerful relation provides a way to obtain the weak mixing angle from the measurements W and Z masses, although the relation is valid only at the tree-level. In reality, the value of the weak mixing angle is not constant, reason why people often speak about the *running* of the weak mixing angle, or in other words, the dependence of the weak mixing angle on the energy scale.
As radiative corrections are necessary to correctly calculate the weak mixing angle to be compared with experimental measurements, one has to fix the renormalization scheme. One popular renormalization scheme, often adopted, is the so-called on-shell scheme [25], where the relation in Eq. 1.11 is promoted to a definition of the weak mixing angle to all orders in the perturbation theory.
The most popular scheme, that will be also adopted in this thesis work, is known as *modified minimal subtraction* ($\overline{\rm MS}$) scheme [25], where the weak mixing angle is defined through

$$\sin^2\hat{\theta}_W(\mu) \equiv \frac{\hat{g}'^2(\mu)}{\hat{g}^2(\mu) + \hat{g}'^2(\mu)} \, , \tag{1.12}$$

where the couplings $\hat{g}$ and $\hat{g}'$ are defined by the modified minimal subtraction and μ represents an energy scale, often set to be the mass of the Z boson.
The adoption of such a scheme for the weak mixing angle is convenient because the value at the Z boson mass $\hat{s}_Z^2 \equiv \sin^2\hat{\theta}_W(m_Z)$ extracted from m_Z is less sensitive to most new physics effects, unlike the on-shell scheme [25].

In most of the processes of our interest, the useful quantity is the value of the weak mixing angle in the low energy regime (below about 300 MeV), which can be related to the value evaluated at the Z boson mass scale, according to [27]

$$\sin^2\hat{\theta}_W(0) \equiv \hat{k}(0)\sin^2\hat{\theta}_W(m_Z) \equiv [1+\Delta\hat{k}(0)]\hat{s}_Z^2\,. \tag{1.13}$$

$\Delta\hat{k}(0)$ is a flavor-independent radiative correction that allows one to retrieve the low energy value of the weak mixing angle from its value at the Z mass energy scale.
The first significant contribution to be taken into account when calculating the running of the weak mixing angle is the so-called leading order RGE (renormalization group equation) term, which are logarithmic terms of the form [27]

$$\frac{\alpha}{\pi\sin^2\hat{\theta}_W}\ln\frac{m_Z^2}{m_i^2}, \tag{1.14}$$

with the i-index referring to all the involved particles, m_i being the particle mass and α the fine structure constant. Such logarithmic terms arise from scale dependent self-energy mixing diagrams between the photon and the Z boson. Within these conventions the RGE is

$$\mu^2\frac{d\hat{v}_f}{d\mu^2} = \frac{\hat{\alpha}}{24\pi}Q_f\sum_i N_i^c\gamma_i\hat{v}_iQ_i, \tag{1.15}$$

where N_i^c is the color factor (3 for quarks and 1 for leptons), $\hat{\alpha}$ is the running of the fine structure constant in the RGE scheme, μ is the energy scale, Q_i is the electric charge and $\hat{v}$ is defined as a flavor dependent effective mixing angle appearing in the coupling to the Z vector currents, namely $\hat{v}_f = T_f - 2Q_f\sin^2\theta_f^{\text{eff}}$. T_f is the third component of the isospin of the fermion f. In Eq. 1.15, the γ_i term has been introduced in order to build a unique formalism for different spin species. γ_i is the spin factor which weights the contribution of the particles inside the radiative diagram. In particular, $\gamma_i = 1$ for real scalar, 2 for complex scalars, 4 for chiral fermions and Majorana fermions, 8 for Dirac fermions and -22 for massless gauge bosons.
In this formalism, the RGE equation is solved by [27]

$$\sin^2\hat{\theta}_W(\mu) = \frac{\hat{\alpha}(\mu)}{\hat{\alpha}(\mu_0)}\sin^2\hat{\theta}_W(\mu_0) + \frac{\sum_i N_i^c\gamma_iQ_iT_i}{\sum_i N_i^c\gamma_iQ_i^2}\Big[1-\frac{\hat{\alpha}(\mu)}{\hat{\alpha}(\mu_0)}\Big], \tag{1.16}$$

where the reference scale μ_0 has been introduced. The same result can be equivalently written in the form

$$\sin^2\hat{\theta}_W(\mu) = \sin^2\hat{\theta}_W(\mu_0)\Big[1+\frac{\hat{\alpha}(\mu)}{24\pi\sin^2\hat{\theta}_W(\mu_0)}\sum_i N_i^c\gamma_iQ_i[T_i-Q_i\sin^2\hat{\theta}_W(\mu_0)]\ln\frac{\mu_0^2}{\mu^2}\Big]. \tag{1.17}$$

The formula in Eq. 1.17 re-sums all logarithmic terms of $\mathcal{O}(\alpha^n\ln^n\frac{\mu_0}{\mu})$, however, it works only when no particle production threshold is present between the energy scales μ and μ_0. So in practice, this solution has to be applied successively from one

particle threshold to the next, as crossing a threshold the corresponding particle is integrated out, and one continues to work in an effective theory without that particular particle.
We can use the result in Eq. 1.17 to obtain a definition of the $\Delta\hat{k}(0)$ introduced in Eq. 1.13

$$\Delta\hat{k}(0) = \frac{\alpha}{\pi s_Z^2}\Big[\frac{1}{6}\sum_f N_f^c Q_f (T_f - 2Q_f s_Z^2)\ln\frac{m_Z^2}{m_f^2} - \Big(\frac{43}{24} - \frac{7}{4}s_Z^2\Big)\ln\frac{m_Z^2}{m_W^2}\Big], \quad (1.18)$$

where the sum is over all the standard model fermions, but the top quark. In Eq. 1.18, the second term in the brackets is obtained by explicitly isolating the contribution of the $W^\pm$ bosons in the loops of the radiative diagrams.
To correctly calculate the weak mixing angle running, it is necessary to go beyond the leading order. Thus, it is possible to generalize the procedure just described to re-sum also next-to-leading logarithms of $\mathcal{O}(\alpha^{n+1}\ln^n\frac{\mu_0}{\mu})$ and $\mathcal{O}(\alpha\alpha_s^n\ln^n\frac{\mu_0}{\mu})$, as well as next-to-next-to-leading order logarithms of $\mathcal{O}(\alpha\alpha_s^{n+1}\ln^n\frac{\mu_0}{\mu})$ and the next-to-next-to-next-to-leading order contributions of $\mathcal{O}(\alpha\alpha_s^{n+2}\ln^n\frac{\mu_0}{\mu})$. Including such contributions the relation in Eq. 1.15 becomes [27, 28]

$$\mu^2\frac{d\hat{v}_f}{d\mu^2} = \frac{\hat{\alpha}}{24\pi}Q_f\Big[\sum_i K_i\gamma_i\hat{v}_i Q_i + 12\sigma\Big(\sum_q \hat{v}_q\Big)\Big(\sum_q Q_q\Big)\Big], \quad (1.19)$$

where in the case of quarks [28]

$$\begin{aligned}
K_i &= N_i^c\Big\{1 + \frac{3}{4}Q_i^2\frac{\hat{\alpha}}{\pi} + \frac{\hat{\alpha}_s}{\pi} + \frac{\hat{\alpha}_s^2}{\pi^2}\Big(\frac{125}{48} - \frac{11}{72}n_q\Big) + & (1.20)\\
&+ \frac{\hat{\alpha}_s^3}{\pi^3}\Big[\frac{10487}{1728} + \frac{55}{18}\zeta(3) - \Big(\frac{707}{864} + \frac{55}{54}\zeta(3)\Big)n_q - \frac{77}{3888}n_q^2\Big] + & (1.21)\\
&+ \frac{\hat{\alpha}_s^4}{4\pi^4}\Big[\frac{2665349}{41472} + \frac{182335}{864}\zeta(3) - \frac{605}{16}\zeta(4) - \frac{31375}{288}\zeta(5) +\\
&- n_q\Big(\frac{11785}{648} + \frac{58625}{864}\zeta(3) - \frac{715}{48}\zeta(4) - \frac{13325}{432}\zeta(5)\Big) +\\
&- n_q^2\Big(\frac{4729}{31104} - \frac{3163}{1296}\zeta(3) + \frac{55}{72}\zeta(4)\Big) + n_q^3\Big(\frac{107}{15552} + \frac{1}{108}\zeta(3)\Big)\Big]\Big\},
\end{aligned}$$

with n_q being the effective number of quarks, ζ the Riemann function and $\hat{\alpha}_s$ the strong coupling constant. K_i, for quarks, contains QED and QCD corrections to the lowest order vacuum polarization diagrams [28]. In the case of leptons only the term involving $\hat{\alpha}$ remains, while for bosons only the lowest order is considered so that $K_{W^\pm} = 1$. In Eq. 1.19, the second term contains a sum over quark fields only with [28]

$$\begin{aligned}
\sigma = \frac{\hat{\alpha}_s^3}{\pi^3}\Big[\frac{55}{216} - \frac{5}{9}\zeta(3)\Big] &+ \frac{\hat{\alpha}_s^4}{\pi^4}\Big[\frac{11065}{3456} - \frac{34775}{3456}\zeta(3) + \frac{55}{32}\zeta(4) + \frac{3875}{864}\zeta(5) +\\
&- n_q\Big(\frac{275}{1728} - \frac{205}{576}\zeta(3) + \frac{5}{48}\zeta(4) + \frac{25}{144}\zeta(5)\Big)\Big], \quad (1.22)
\end{aligned}$$

accounting for the QCD singlet contribution.
In a similar fashion to what was done for the leading RGE, it is possible to obtain an expression for the weak mixing angle as a function of the energy scale, namely

$$\hat{s}^2(\mu) = \frac{\hat{\alpha}(\mu)}{\hat{\alpha}(\mu_0)}\hat{s}^2(\mu_0) + \lambda_1\Big[1 - \frac{\hat{\alpha}(\mu)}{\hat{\alpha}(\mu_0)}\Big] + \frac{\hat{\alpha}(\mu)}{\pi}\Big[\frac{\lambda_2}{3}\ln\frac{\mu^2}{\mu_0^2} + \frac{3\lambda_3}{4}\ln\frac{\hat{\alpha}(\mu)}{\hat{\alpha}(\mu_0)} + \tilde{\sigma}(\mu_0) - \tilde{\sigma}(\mu)\Big] \tag{1.23}$$

where we have used the notation $\hat{s}^2(\mu) = \sin^2\hat{\theta}_W(\mu)$. In Eq. 1.23, the dependence of the running of the weak mixing angle on the running of the fine structure constant is made explicit, which introduces hadronic uncertainties mainly due to the values of the light quark threshold masses [27, 28]. The coefficients λ_i inside the equation depend on the energy scale, as they account for the contributions of the particles involved at that certain energy scale, and are defined as [28]

$$\lambda_1 = \frac{\sum_q T_q Q_q}{2\sum_q Q_q^2}\,, \tag{1.24}$$

$$\lambda_2 = \frac{1}{8}\sum_{i\neq q}\gamma_i(\lambda_1 Q_i^2 - T_i Q_i) = \frac{1}{8}\sum_i N_i^c\gamma_i(\lambda_1 Q_i^2 - T_i Q_i)\,, \tag{1.25}$$

$$\lambda_3 = \frac{\sum_i N_i^c\gamma_i[\lambda_1 Q_i^4 - T_i Q_i^3]}{\sum_i N_i^c\gamma_i Q_i^2}\,, \tag{1.26}$$

$$\lambda_4 = \Big[\lambda_1\Big(\sum_q Q_q\Big)^2 - \frac{1}{2}\Big(\sum_q T_q\Big)\Big(\sum_q Q_q\Big)\Big]\,. \tag{1.27}$$

The λ_4 contributes to the factors $\tilde{\sigma}$ inside Eq. 1.23 [28]

$$\tilde{\sigma}(\mu) = \frac{\lambda_4}{33 - 2n_q}\frac{5}{36}\Big[(11 - 24\zeta(3))\frac{\hat{\alpha}_s^2(\mu)}{\pi^2} + b\frac{\hat{\alpha}_s^3(\mu)}{\pi^3}\Big]\,, \tag{1.28}$$

where also the strong constant $\hat{\alpha}_s$ contributes at the appropriate scale and the b coefficient is

$$b = \frac{2213}{24} - \frac{6955}{24}\zeta(3) + \frac{99}{2}\zeta(4) + \frac{775}{6}\zeta(5) - n_q\Big(\frac{55}{12} - \frac{41}{4}\zeta(3) + 3\zeta(4) + 5\zeta(5)\Big) + - \frac{(153 - 19n_q)(11 - 24\zeta(3))}{99 - 6n_q}\,. \tag{1.29}$$

A table summarising the values of the factors λ_i evaluated between the particle thresholds, is shown in Tab. 1.1.
As already discussed, this description is based on a sub-sequence of the effective threshold between particle production thresholds. However, when the energy scale crosses a particle threshold, we are introducing a discontinuity in the weak mixing angle running. This effect is not strictly physical and can be cured by introducing some matching conditions at the particle threshold crossing.
In particular, when the threshold is relative to the production of a fermion *f*, we need to impose [27, 28]

$$\sin^2\hat{\theta}_W(m_i)^- = \frac{\hat{\alpha}(m_i)^-}{\hat{\alpha}(m_i)^+}\sin^2\hat{\theta}_W(m_i)^+ + \frac{Q_i T_i}{2Q_i^2}\Big[1 - \frac{\hat{\alpha}(m_i)^-}{\hat{\alpha}(m_i)^+}\Big]\,, \tag{1.30}$$

where the superscript "+" or "-" indicates the effective theory when the fermion f has been included or excluded.

energy range	λ_1	λ_2	λ_3	λ_4
$\overline{m}_t \leq \mu$	9/20	289/80	14/55	9/20
$m_W \leq \mu < \overline{m}_t$	21/44	625/176	6/11	3/22
$\overline{m}_b \leq \mu < m_W$	21/44	15/22	51/440	3/22
$m_\tau \leq \mu < \overline{m}_b$	9/20	3/5	2/19	1/5
$\overline{m}_c \leq \mu < m_\tau$	9/20	2/5	7/80	1/5
$\overline{m}_s \leq \mu < \overline{m}_c$	1/2	1/2	5/36	0
$\overline{m}_d \leq \mu < \overline{m}_s$	9/20	2/5	13/110	1/20
$\overline{m}_u \leq \mu < \overline{m}_d$	3/8	1/4	3/40	0
$m_\mu \leq \mu < \overline{m}_u$	1/4	0	0	0
$m_e \leq \mu < m_\mu$	1/4	0	0	0
$\mu < m_e$	0	0	0	0

Table 1.1: Table of the values of the λ_i factors entering the running of the weak mixing angle, evaluated between all the energy thresholds [27, 28].

Also, the RGE matching conditions for the fine structure constant have to be included at the threshold, so that [27]

$$\frac{1}{\hat{\alpha}(m_f)^+} = \frac{1}{\hat{\alpha}(m_f)^-} - \frac{Q_f^2}{\pi}\Big\{\frac{15}{16}N_f^c Q_f^2\frac{\hat{\alpha}(m_f)}{\pi} + \tag{1.31}$$
$$+ \quad \frac{(N_f^c-1)}{2}\frac{\hat{\alpha}_s(m_f)}{\pi}\Big[\frac{13}{12} + \frac{\hat{\alpha}_s(m_f)}{\pi}\Big(\frac{655}{144}\zeta(3) - \frac{3847}{864} + \frac{361}{1296}n_q + \frac{295}{1296}\frac{\sum_{q\neq f}Q_q^2}{Q_f^2}\Big)\Big]\Big\}\,.$$

The matching condition which accounts for corrections of order $\hat{\alpha}_s^3$ can be found in Eq. (2.8) of Ref. [28] Inside the latter relation the value for n_q has to be considered by counting the number of quarks including the threshold quark [28].
In the case of the W bosons, the shift in the fine structure constant is slightly different with respect to the one defined for the fermions, namely

$$\frac{1}{\hat{\alpha}(m_W)^+} = \frac{1}{\hat{\alpha}(m_W)^-} + \frac{1}{6\pi}\,, \tag{1.32}$$

so that at the W mass threshold, the matching condition for the weak mixing angle becomes

$$\sin^2\hat{\theta}_W(m_W)^+ = 1 - \frac{\hat{\alpha}(m_W)+}{\hat{\alpha}(m_W)^-}\cos^2\hat{\theta}_W(m_W)^-\,. \tag{1.33}$$

This RGE description of the running of the weak mixing angle represents the current state-of-the-art of theoretical calculation of such quantities, and has improved the previous approximated description reported in Refs. [29, 30].
In the precedent approach, the running of the weak mixing angle was evaluated accounting only for 1-loop level contribution, resulting in an approximated approach which however represents a good description of the general behaviour of

the weak mixing angle and highlights the need for standard model tests through the measurement of the weak mixing angle at different energy scales.

	u	d	s	c	b	t
m_q [GeV/c^2]	0.246	0.246	0.342	1.185	3.99	172.74

Table 1.2: Table reporting the values adopted for the quark masses used inside the calculation of the running of the weak mixing angle, taken from Ref. [28].

In order to reproduce the weak mixing angle running in the RGE formalism, just described, we have set the quark masses to the values reported in table 1.2, following the choices reported in Ref. [28].

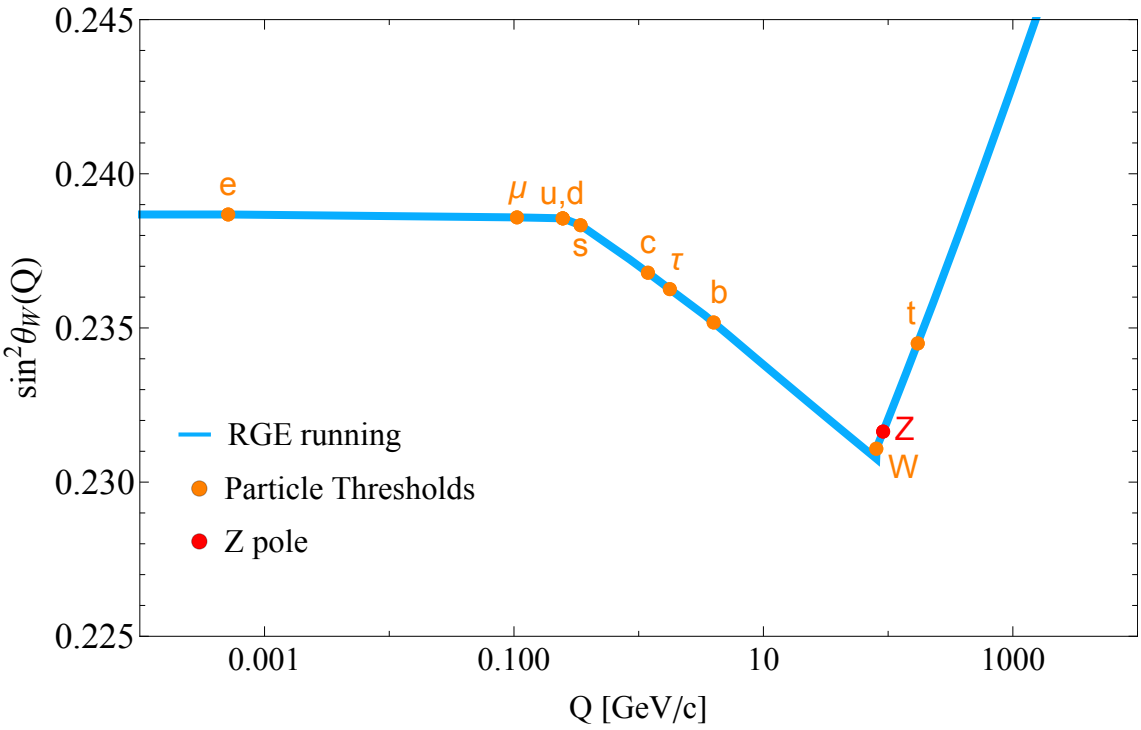

Figure 1.3: Running of the sine squared of the weak mixing angle with the energy scale evaluated in the RGE formalism. The orange dots represent the particle production thresholds and the red dot the Z boson mass energy scale, known as Z pole.

In Fig. 1.3, the result of the running of the weak mixing angle[1] in the RGE formalism is presented as a function of the momentum transfer[2] in the process Q. The blue line represents the calculated value of the weak mixing angle at a certain energy scale, the orange dots indicate the particle thresholds, while the red

[1]From now on we will drop the notation $\sin^2\hat{\theta}_W(Q)$ replacing it with $\sin^2\theta_W(Q)$.

[2]We have replaced the energy scale μ used in the formula for the RGE formalism with the symbol Q, as the energy scale of the experiments it is set by the momentum transfer in the process.

dot identifies the Z boson mass energy scale, known as the Z pole. The plot is a reproduction of the running reported in Ref. [25].
In Ref. [28], the authors have carried out also a careful error budget estimate for the theoretical calculation of the running of the weak mixing angle, obtaining an uncertainty of $1.8 \cdot 10^{-5}$, on top of which a parametric uncertainty of $5 \cdot 10^{-5}$ has to be added. So, it is clear that it is possible to precisely calculate the value of the weak mixing angle at zero momentum transfer, having as an input the experimental measurement of the weak mixing angle at the Z pole. Using the global fit to the SM for $\sin^2\theta_W(m_Z)$, namely $\sin^2\theta_W(m_Z) \equiv s_Z^2 = 0.23122(4)$ [25], one can precisely predict $\sin^2\theta_W(0)$ to be [25]

$$\sin^2\theta_W(0) \equiv s_0^2 = 0.23863 \pm 0.00005 \pm 0.00002\,. \tag{1.34}$$

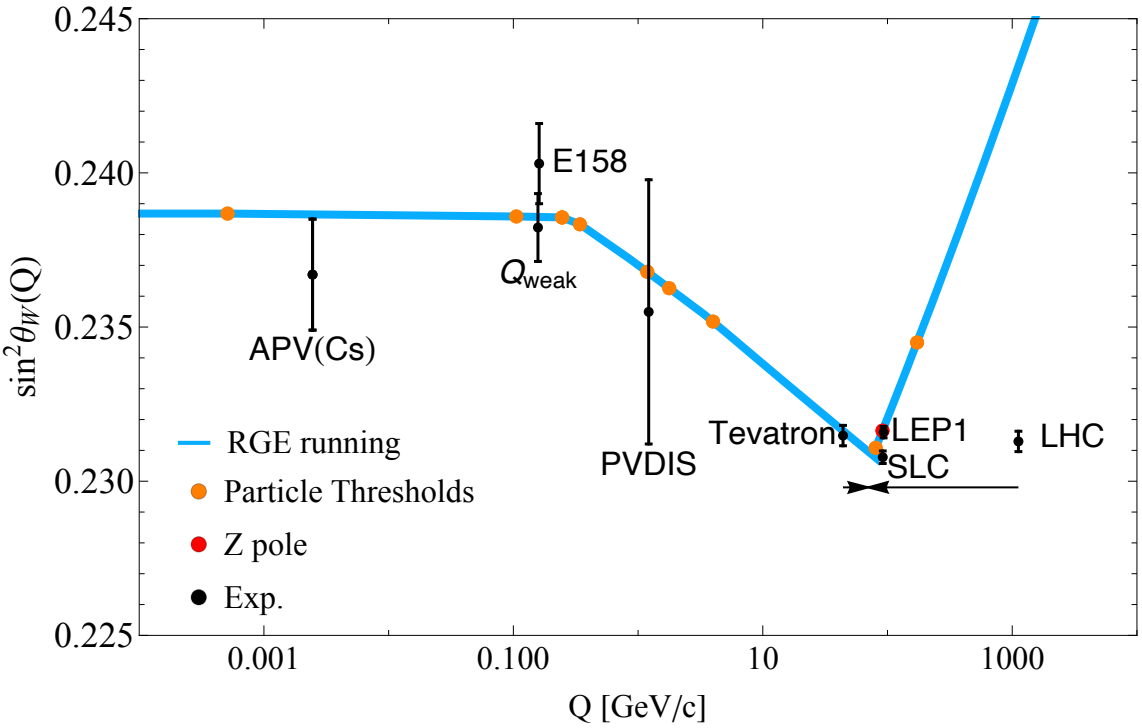

Figure 1.4: Running of the sine squared of the weak mixing angle with the energy scale evaluated in the RGE formalism. The orange dots represent the particle production thresholds and the red dot the Z pole. The black points show the currently available experimental measurements, as reported by the Particle Data Group in Ref. [25]. In particular, the measurements reported come from atomic parity violation on cesium (APV(Cs)) [31, 32], weak charge of the proton (Q_{weak}) [33] and electron (E158) [34] measurements, deep inelastic scattering experiments (PVDIS) [35], and high energy scattering experiments [25]. The Tevatron and LHC data points are measured at the Z pole and displayed at different energy scales just for graphical purposes.

The prediction of the weak mixing angle at low energy is of crucial interest in the context of this thesis work. In fact, despite the fact that its value is very precisely

predicted in the standard model, the experimental status is much different.
In Fig. 1.4, we show the current status of measurement of the weak mixing angle at different energy scales as reported in the latest review by the Particle Data Group (PDG) [25]. From the figure, it is clear that the weak mixing angle has been tested very precisely around the Z pole by accelerator based experiments, such as Tevatron and LHC [25], resulting in a great agreement between the experiments. The situation at low energy ($Q \lesssim 200$ MeV$/c$) is very different, as only a few measurements have been performed, and where the current experimental precision is still to be improved.
Testing the running of the weak mixing angle at low energy is of crucial interest as it represents a fundamental test of the SM theory. In case of deviation from its SM prediction, such a measurement would indicate the necessity of an extension of the SM theory, paving the way for plenty beyond the standard model (BSM) scenarios, which are widely studied and searched for by the community.
In particular, the available measurements come from the electron and proton weak charge measurements performed by the E158 experiment [34] and by the Q_{weak} Collaboration, respectively, and from the parity violating deep inelastic scattering (PVDIS) experiments [35].
The measurement performed at the lowest energy scale so far, is the measurement of atomic parity violation on cesium [31, 32], which will be discussed in more detail in Sec. 3.2.2. This represents an electroweak measurement that, as we will discuss, is complementary to other electroweak probes, such as neutrino or polarized electron scattering processes.

In this thesis work, the weak mixing angle will represent a starting point for studying electroweak low energy processes, such as those just mentioned above. We will present new measurements of the weak mixing angle and possible beyond the standard model scenarios hints of whom can be looked for in the available experimental data. Together with the weak mixing angle and related beyond the standard model effects, we will discuss other standard and non-standard neutrino processes, together with nuclear effects, that as we will carefully discuss, are almost always present in this kind of measurements[3].

[3]From now on we will adopt natural units, so that the speed of light will be set to unity, $c = 1$.

Chapter 2

Low energy Neutrino interactions

Short introduction

In this chapter, we will discuss the details of neutrino interactions at low energies, below E_ν ∼100 MeV. The two main concurrent processes of our interest are the scattering off nuclei and off atomic electrons. We will give an insight on the cross section calculations and discuss the main characteristics of such processes.
The discussion will continue by introducing the sources of neutrinos employed in the two scattering processes together with the main experimental measurements available at the time of this thesis work and the analysis procedures.

2.1 νES: the Neutrino-Electron Elastic Scattering process

A well known neutrino process which occurs at low energy is the elastic interaction of neutrinos with electrons, namely the atomic electrons. If the neutrino has low energy, it would have a certain probability of scattering off the electron cloud surrounding the target nuclei. In this sense, we will talk about the elastic scattering of neutrinos with electrons, νES, mainly in the context of direct dark matter searches.
The neutrino-electron scattering process has a much "older" origin in particle physics with respect to the experiment we will be dealing with in this thesis work. Such process has been fundamental for example in the context of water Cherenkov solar neutrino detectors [24], representing one of the mechanisms used for looking for signals of neutrinos produced by the Sun. Indeed, it represents a very simple interaction, as it is a fully leptonic process, which allowed us to observe for the first time the weak neutral currents in 1973 by the Gargamelle experiment [36].
The νES scattering is an elastic process, therefore the particles in the initial and final states are the same so that we can write the interaction as

$$\overset{(-)}{\nu}_{e,\mu,\tau} + e^- \rightarrow \overset{(-)}{\nu}_{e,\mu,\tau} + e^- \,. \tag{2.1}$$

Being an elastic process, the neutrino makes the target electron recoil, so that in the interaction there is a momentum transfer between the involved particles.
Depending on the flavor of the incoming neutrinos, the total cross section will count on different contributions.

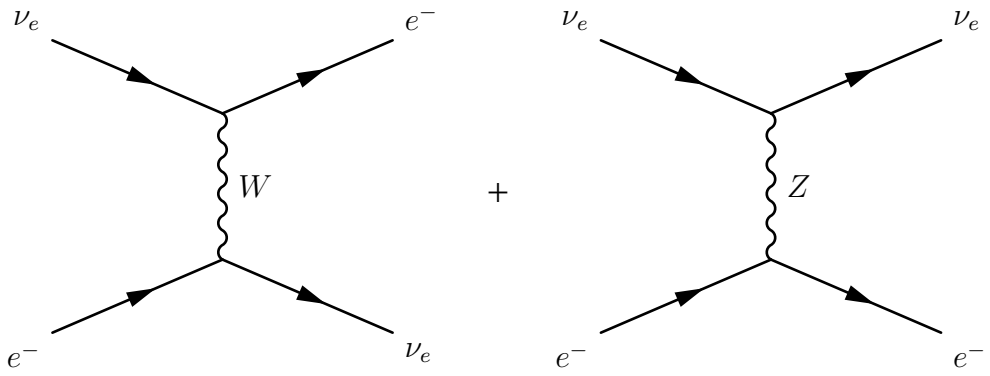

Figure 2.1: Tree-level Feynman diagrams for the charge (left) and neutral (right) currents contributions to the ν_e-e elastic scattering process.

In the case of electron neutrino scattering off electrons, the interaction can happen both via charge current (CC) and neutral current (NC) diagrams, as schematized in Fig. 2.1 [24]. In the figure, the left diagram shows the charge current interaction, mediated by the W boson, while the right diagram shows the neutral current one, mediated by the Z boson. The total cross section is obtained by summing the two amplitudes.

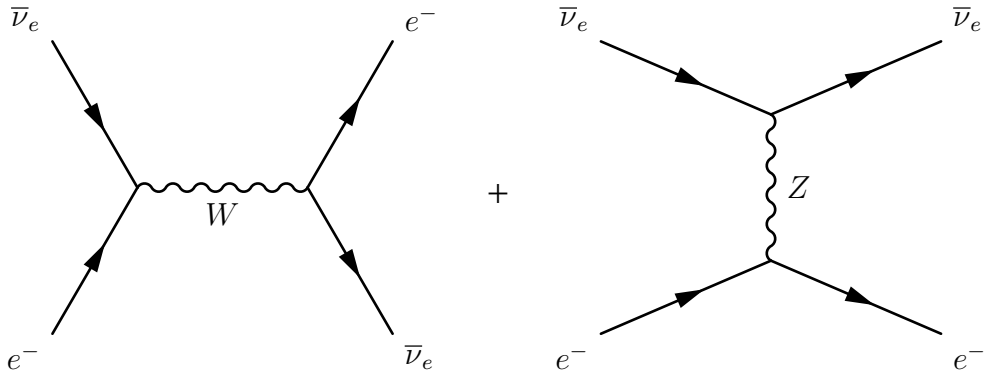

Figure 2.2: Tree-level Feynman diagrams for the charge (left) and neutral (right) currents contributions to the $\overline{\nu}_e$-e elastic scattering process.

In the case of electron antineutrinos, there are still two contributions, one coming from the CC and one from the NC diagrams, however, the CC diagram is in the *s-channel* instead of the *t-channel* (left diagram in Fig. 2.1), as shown in the left

diagrams in Fig. 2.2 [24]. The NC diagram, shown in the right plot in the same figure, is the same considered for the electron neutrino case.
The interaction between neutrinos or antineutrinos of muon and tau flavor with electrons can happen only via the NC interaction, represented in the diagram in Fig. 2.3, so that the cross section corresponds to the NC cross section only [24].

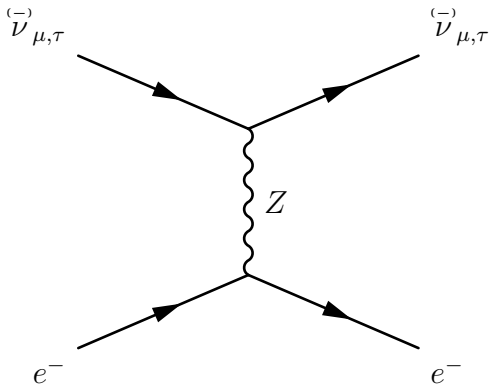

Figure 2.3: Tree-level Feynman neutral current diagram for the elastic interaction between neutrinos (or antineutrinos) of μ or τ flavor with electrons.

For neutrino scattering processes at low energies, the effects of the W and Z propagators can be safely neglected, so that the aforementioned processes are described through effective CC and NC Lagrangians. Taking as an example the elastic scattering process of electron (anti-)neutrinos on electrons, the Lagrangian takes the form [24]

$$\begin{aligned}\mathcal{L}_{\text{eff}}(\overset{(-)}{\nu}_e e^- \to \overset{(-)}{\nu}_e e^-) &= -\frac{G_F}{\sqrt{2}}\{[\overline{\nu_e}\gamma^\rho(1-\gamma^5)e][\overline{e}\gamma_\rho(1-\gamma^5)\nu_e] + \\ &+ [\overline{\nu_e}\gamma^\rho(1-\gamma^5)\nu_e][\overline{e}\gamma_\rho(g_V^\ell - g_A^\ell\gamma^5)e]\}\,,\end{aligned} \tag{2.2}$$

where ν_e and e are the neutrino and electron fields, respectively. γ^ρ and γ^5 are the usual *Dirac γ matrices* and g_V^ℓ and g_A^ℓ represent the neutral current coupling of the neutrino with the massive lepton ℓ. For $\ell = e$, the couplings in the SM are $g_V^e = -1/2 + 2\sin^2\theta_W$ and $g_A^e = -1/2$ [24]. G_F is the Fermi constant, which in some sense represents the strength of the weak interaction, and whose value is $G_F = 1.1663788(6)\cdot 10^{-5}\ \text{GeV}^{-2}$ [25].
The first term in Eq. 2.2 arises from the CC contribution, while the second term is the NC one. Through some manipulation, we can rewrite the Lagrangian so that it takes a more compact form

$$\mathcal{L}_{\text{eff}}(\overset{(-)}{\nu}_e e^- \to \overset{(-)}{\nu}_e e^-) = -\frac{G_F}{\sqrt{2}}[\overline{\nu_e}\gamma^\rho(1-\gamma^5)\nu_e][\overline{e}\gamma_\rho((1+g_V^\ell) - (1+g_A^\ell)\gamma^5)e]\,, \tag{2.3}$$

which reminds of a simple NC Lagrangian but for the unit factors added to the couplings in the second square brackets.
In the case of scattering of muon or tau flavor (anti-)neutrinos, only the NC contribution is present, so that the Lagrangian is

$$\mathcal{L}_{\text{eff}}(\overset{(-)}{\nu}_\alpha e^- \to \overset{(-)}{\nu}_\alpha e^-) = -\frac{G_F}{\sqrt{2}}[\overline{\nu_\alpha}\gamma^\rho(1-\gamma^5)\nu_\alpha][\overline{e}\gamma_\rho(g_V^\ell - g_A^\ell)\gamma^5)e]\,, \tag{2.4}$$

where $\alpha = \mu, \tau$ [24]. Starting from the Lagrangians in Eq. 2.3 and Eq. 2.4, it is possible to obtain the cross-section for the elastic neutrino-electron scattering process. In particular, after integrating over the scattering angle, the differential cross section as a function of the electron recoil energy, T_e, results to be [37]

$$\frac{d\sigma^{\rm ES}_{\nu_\ell - e}}{dT_e}(E_\nu, T_e) = \frac{G_F^2 m_e}{2\pi}\left[(g_V^{\nu_\ell e}+g_A^{\nu_\ell e})^2+(g_V^{\nu_\ell e}-g_A^{\nu_\ell e})^2\left(1-\frac{T_e}{E_\nu}\right)^2-((g_V^{\nu_\ell e})^2-(g_A^{\nu_\ell e})^2)\frac{m_e T_e}{E_\nu^2}\right], \tag{2.5}$$

where m_e is the electron mass.
In the latter equation, the couplings $g_V^{\nu_\ell e}$ and $g_A^{\nu_\ell e}$ represent the vector and axial coupling between a neutrino ν_ℓ and an electron respectively. At tree-level, the SM values of these couplings are

$$g_V^{\nu_e e} = 2\sin^2\theta_W + 1/2\,, \qquad g_A^{\nu_e e} = 1/2\,, \tag{2.6}$$
$$g_V^{\nu_{\mu,\tau} e} = 2\sin^2\theta_W - 1/2\,, \qquad g_A^{\nu_{\mu,\tau} e} = -1/2\,. \tag{2.7}$$

For antineutrinos one must substitute $g_A^{\nu_\ell e} \to g_A^{\overline{\nu}_\ell e} = -g_A^{\nu_\ell e}$ inside the cross section in Eq. 2.5. Let us note, that in the couplings in Eq. 2.6 we have already included inside the couplings contribution coming from the CC diagram contributing the cross section for scattering of electron neutrinos off electrons, so that the cross section takes the same form for all neutrino flavors.
The definitions of the couplings in Eq. 2.6 and Eq. 2.7 are valid only at the tree-level, so to perform more precise calculations for the cross sections, the radiative correction contributions have to be accounted for. A detailed discussion and calculation of the neutrino-electron couplings can be found in Appendix A.
The values, accounting for radiative corrections, are

$$g_V^{\nu_e e} = 0.9521, \qquad g_A^{\nu_e e} = 0.4938, \tag{2.8}$$
$$g_V^{\nu_\mu e} = -0.0397, \qquad g_A^{\nu_\mu e} = -0.5062, \tag{2.9}$$
$$g_V^{\nu_\tau e} = -0.0353, \qquad g_A^{\nu_\tau e} = -0.5062, \tag{2.10}$$

from whose values we notice that the couplings have acquired a flavor dependence, due to the so-called neutrino charge radius radiative correction, which will be discussed in more detail in Sec. 7.1.
In Fig. 2.4, we show the integrated cross section for the (anti-)neutrino elastic scattering off electrons, $\sigma_{\nu-e^-}$, considering both electron and muon flavors, calculated including radiative corrections. The integrated cross section reads

$$\sigma_{\nu-e^-}(E_\nu) = \int_0^{T_e^{\rm max}(E_\nu)} \frac{d\sigma^{\rm ES}_{\nu_\ell - e}}{dT_e}(E_\nu, T_e)\, dT_e, \tag{2.11}$$

where the integral goes from zero recoil energy up to the maximum recoil energy kinetically achievable given a certain neutrino energy, namely [24]

$$T_e^{\rm max}(E_\nu) \simeq \frac{2E_\nu^2}{m_e + 2E_\nu}\,. \tag{2.12}$$

From the latter formula, it is easy to understand that a MeV neutrino will produce a recoiling electron with a maximum energy of about 800 keV, while a neutrino

with $E_\nu = 30$ MeV will produce a maximum recoil energy of about 30 MeV.
From the comparison between electron and muon neutrino scattering, it is clear that due to the contribution of the CC process, the cross section for the scattering of electron neutrinos is significantly larger than the one for muon neutrinos.
In the lower panel of Fig. 2.4, we have assessed the impact of the radiative corrections in the cross section calculation. We defined the variation $\Delta\sigma_{\nu-e^-}$ due to the radiative corrections as the difference between the tree-level cross section, $\sigma^{\text{T.L.}}_{\nu-e^-}$ and the one with radiative corrections, $\sigma_{\nu-e^-}$, normalized to the latter one, i.e.

$$\Delta\sigma_{\nu-e^-}(E_\nu) = \frac{\sigma^{\text{T.L.}}_{\nu-e^-}(E_\nu) - \sigma_{\nu-e^-}(E_\nu)}{\sigma_{\nu-e^-}(E_\nu)}\,. \tag{2.13}$$

What was observed, is that the variation of the total cross section due to the introduction of the radiative correction is up to the order of 5% and is roughly independent of the neutrino energy. The smallest impact corresponds to the case of muon anti-neutrinos, for which the cross section is practically unaffected by the effect of radiative corrections from neutrino energies above 1 MeV.

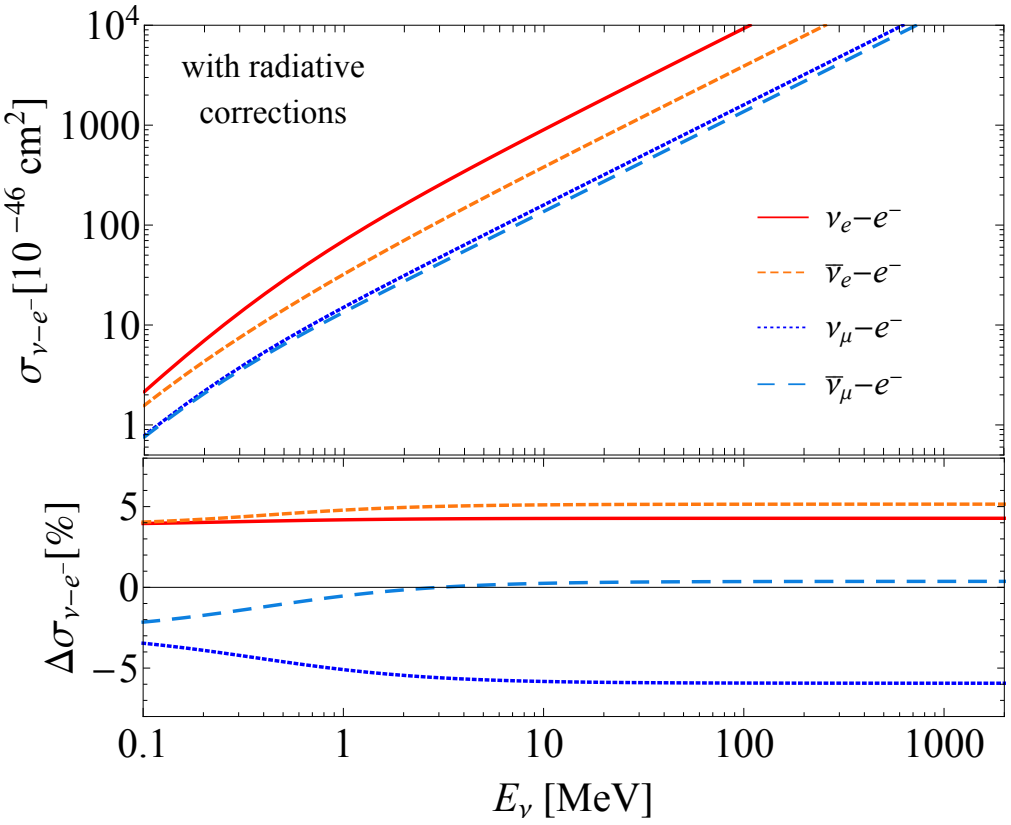

Figure 2.4: Integrated cross section for the (anti-)neutrino-electron elastic scattering process including radiative corrections to the couplings. In the lower panel, the impact of the radiative correction is shown, in terms of the percentage variation as a function of the neutrino energy.

In the following of this thesis work, the cross section that will be used inside the calculations and analysis will not be the integrated cross section, but the differ-

ential one obtained accounting for the radiative corrections, which is shown in Eq. 2.5. Moreover, we have so far discussed the interaction of a neutrino with one isolated and free electron, which does not represent the reality of experiments, where one should consider that the electrons are bound to the atoms constituting the detector material. In this sense, the cross section has to be generalised to the case of Z electrons, where Z is the atomic number of the target atom, $\mathcal{A}$. This can be easily accomplished by multiplying the cross section for the interaction with the single electron in Eq. 2.5, by the number of atomic electron Z, thus obtaining a cross section that will be called $\sigma^{\rm ES}_{\nu_\ell-\mathcal{A}}$, to make its dependence on the target atom $\mathcal{A}$ explicit. Therefore, the cross section becomes

$$\frac{d\sigma^{\rm ES}_{\nu_\ell-\mathcal{A}}}{dT_e}(E_\nu,T_e) = Z\frac{G_F^2 m_e}{2\pi}\Big[(g_V^{\nu_\ell e}+g_A^{\nu_\ell e})^2+(g_V^{\nu_\ell e}-g_A^{\nu_\ell e})^2\Big(1-\frac{T_e}{E_\nu}\Big)^2+ \tag{2.14}$$

$$-\Big((g_V^{\nu_\ell e})^2-(g_A^{\nu_\ell e})^2\Big)\frac{m_e T_e}{E_\nu^2}\Big]\,. \tag{2.15}$$

This cross section effectively describes an atomic system with Z electrons, which are treated as free electrons, reason why it is often referred to as Free Electron Approximation (FEA). Thus, it neglects any effect due to the binding energy of the electrons to the atomic nucleus and to the electron-electron interaction.
A clear theory of how to treat the interaction with bound electrons has not been developed and agreed on by the community, even if some attempts have been developed by many research groups [38–41], especially trying to develop an *ab-initio* calculation applied to the many body problem of atomic electrons.
An easy approach, that is often adopted in the community, is based on correcting the FEA approximation using a step function, instead of a constant factor Z, which depends on the energy deposit (recoil energy) [42–45]. In this effective approach, a factor $Z^{\mathcal{A}}_{\rm eff}(T_e)$ is introduced in place of the atomic number, so that the cross section in Eq. 2.15 becomes

$$\begin{aligned}\frac{d\sigma^{\rm ES}_{\nu_\ell-\mathcal{A}}}{dT_e}(E_\nu,T_e) &= Z^{\mathcal{A}}_{\rm eff}(T_e)\frac{G_F^2 m_e}{2\pi}\Big[(g_V^{\nu_\ell e}+g_A^{\nu_\ell e})^2+(g_V^{\nu_\ell e}-g_A^{\nu_\ell e})^2\Big(1-\frac{T_e}{E_\nu}\Big)^2+\\ &- \Big((g_V^{\nu_\ell e})^2-(g_A^{\nu_\ell e})^2\Big)\frac{m_e T_e}{E_\nu^2}\Big]\,.\end{aligned} \tag{2.16}$$

The introduction of such effective energy dependent factor quantifies the number of electrons that can be ionized by a certain energy deposit T_e [46, 47], and can be obtained by using the so-called edge energies, i.e. the binding energies of the various atomic shells, extracted from photo-absorption data [48, 49].
In Appendix C, we report the values adopted for the $Z^{\mathcal{A}}_{\rm eff}(T_e)$ terms in this thesis work, so namely the ones for Cesium, Iodine, Argon, Germanium and Xenon atoms.
As the cross section scales roughly with the atomic number Z, the scattering cross section is greater for heavy atoms like Xenon. This can be seen in Fig. 2.5, where the cross sections in green/cyan are the largest ones, and correspond to the Xenon case, while the case for a lighter atom, like Argon, is pictured in red/orange.
We compare the cross section for the FEA approximation (see Eq. 2.15) with the

ones with the effective factor $Z^{\mathcal{A}}_{\text{eff}}(T_e)$ (see Eq. 2.16), by showing both in the figure. The FEA cross section is represented by the dashed lines, while the modified FEA by the solid lines, for the case of Argon (red/orange), Germanium (blue/azure) and Xenon (green/cyan).

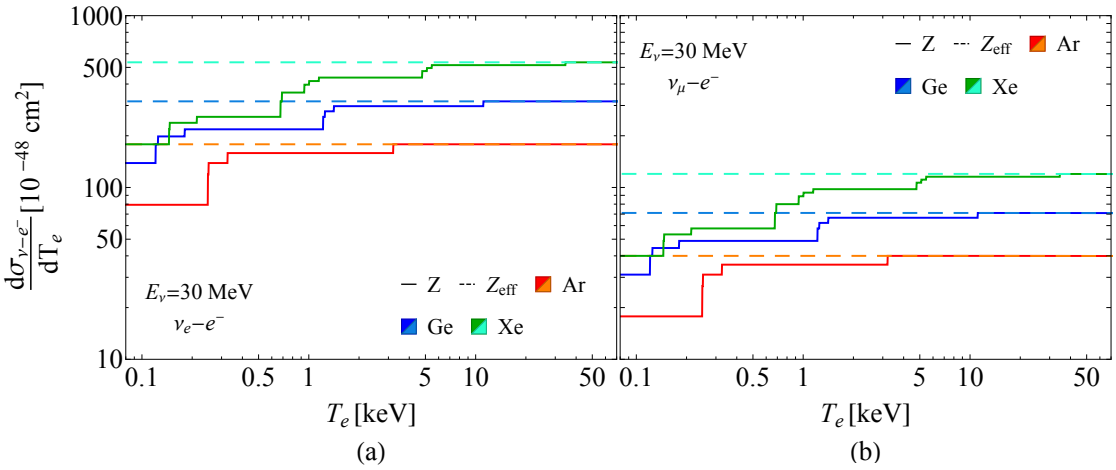

Figure 2.5: Differential cross section for the elastic scattering of neutrinos off atomic electrons as a function of the recoil energy, calculated for a neutrino energy of $E_\nu = 30$ MeV. The (a) panel shows the cross section of electron neutrinos scattering, while the (b) panel the muon neutrino scattering. In the plot, we compare the results obtained for the free electron approximation (dashed) with the ones using the effective step function $Z^{\mathcal{A}}_{\text{eff}}(T_e)$ (solid).

From Fig. 2.5, it can be observed how the impact of using the effective $Z^{\mathcal{A}}_{\text{eff}}(T_e)$ instead of Z is more important for heavy atoms, as the binding effects are stronger there. Indeed, the structure for heavier atoms is much more complicated, so that $Z^{\mathcal{A}}_{\text{eff}}(T_e)$ has more steps with respect to the case of lighter atoms. The same effect is reflected on the recoil energy at which the free electron approximation and the modified treatment become equivalent. In general, for recoil energies greater than ~ 50 keV, the step function becomes flat at the value of the corresponding atomic number Z, as for those recoil energies, all the energy levels are actually available. Thus, the importance of a sophisticated treatment of such effects is clearly fundamental when dealing with low recoil regimes, even if it has been shown that this treatment works quite well even at lower energies within the SM [41]. In addition, for lighter atoms, like Argon, the free electron approximation becomes a good approximation already at $T_e \simeq 3 - 4$ keV, so at energies significantly smaller than the ones for heavier atoms.
Fig. 2.5 has been obtained by fixing the neutrino energy to 30 MeV, but according to Eq. 2.12, given the typical edge energies of atoms, it is clear that already for less energetic neutrinos, it is still possible to produce recoils energetic enough to be above $T_e \simeq 50$ keV.
Also from this figure, it is possible to observe that the cross section for electron neutrinos scattering off electrons is significantly larger than the one of muon neutrinos, due to the CC contribution present only for electron flavor neutrinos.

2.2 CEνNS: the Coherent Elastic Neutrino-Nucleus Scattering process

The coherent elastic neutrino nucleus scattering, known as CEνNS, is a weak neutral current process happening when a low energy neutrino hits a nucleus, producing a small nuclear recoil, and it was first predicted by Freedman in 1974 [50].
When a low energy neutrino scatters off a nucleus, the momentum transfer is rather small, and more precisely the de Broglie wavelength of the exchanged Z boson mediator is of the order of the radius of the target nucleus, so that the nucleus responds *coherently* (recoils as a whole). The coherence of the interaction makes such elastic neutrino scattering process of particular interest, as it results in a rather large cross section if compared to the other low energy neutrino interactions.
Indeed, the coherency phenomenon happens when a projectile particle (i.e. the neutrino) scatters elastically off a complex object (i.e. the nucleus), assumed to be composed of A individual constituents (i.e. the nucleons) identified by some defined positions $\mathbf{x}_i$, $i = 1, ...,$A. Applying the superposition principle, one can define the scattering amplitude $\mathcal{A}(\mathbf{q})$, where $\mathbf{q}$ is the momentum transfer vector, as the sum over the single amplitudes, $a_i(\mathbf{q})$, weighted by a phase factor,

$$\mathcal{A}(\mathbf{q}) = \sum_{j=1}^{A} a_j(\mathbf{q}) \exp^{i\mathbf{q}\mathbf{x}_j} . \tag{2.17}$$

When the momentum transfer multiplied for the dimension of the target R results to be very small, $qR \ll 1$, the phase factors are negligible, so that the amplitude becomes the single constituent amplitude multiplied by the constituent number A, so that the cross section scales with the constituent number to the second power. Hence, it is easy to understand that this approximated $\propto \mathrm{A}^2$ dependence leads to a significant enhancement for heavy nuclei.
Given that the typical nuclear dimensions run between few $\sim$ fm up to ~ 5 fm, in order to be in the coherency regime, the momentum transfer has to be smaller than[1]

$$q \sim \frac{200 \text{ MeV fm}}{R} \sim \frac{200 \text{ MeV fm}}{5 \text{ fm}} \sim 40 \text{ MeV}. \tag{2.18}$$

The CEνNS process has been theoretically predicted more than 40 years ago, however, it has been experimentally proved only in recent years with its first measurement in 2017 by the COHERENT Collaboration [51], despite having rather a large cross section. This is due to the challenging recoil energies of the target nucleus that need to be observed by the detectors. We can use the estimate of the typical momentum transfer to have coherence, to understand the typical recoil energies, T_{nr}, that need to be measured,

$$T_{\mathrm{nr}} \simeq \frac{q^2}{2m_N} , \tag{2.19}$$

[1] Reintroducing the constants the relation becomes $q \sim (\hbar c)/R$, where $\hbar$ is the reduced Plank's constant, c the speed of light and we have used $\hbar c \sim 200$ MeV fm.

where m_N represents the mass of the target nucleus, and it is usually of the order of $10 - 100$ GeV. In the case of an argon target $m_N \sim 40$ GeV, considering a momentum transfer $q \sim 40$ MeV, the recoil energy turns out to be $T_{\rm nr} \sim$ few keV.
Being an elastic scattering process, the particles in the initial and final states remain unvaried, so that we can write the process as

$$\overset{(-)}{\nu}_\ell + \mathcal{N} \to \overset{(-)}{\nu}_\ell + \mathcal{N}\,. \tag{2.20}$$

We can also define an effective Lagrangian for the process as

$$\mathcal{L}_{\rm eff}(\overset{(-)}{\nu}_\ell \mathcal{N} \to \overset{(-)}{\nu}_\ell \mathcal{N}) = \frac{G_F}{\sqrt{2}} \sum_q [\overline{\nu}\gamma^\mu (g_V^{\nu_\ell} - g_A^{\nu_\ell}\gamma^5)\nu][\overline{q}\gamma_\mu (g_V^q + g_A^q \gamma^5) q]\,, \tag{2.21}$$

where ν and q are the neutrino and quark fields, respectively.
The Lagrangian was defined as a sum of the interaction on the quarks inside the nucleons, and the second term in Eq. 2.21 represents the spin dependent contribution.

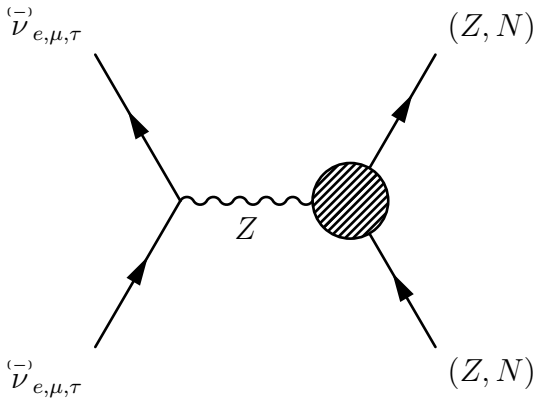

Figure 2.6: Diagram of the CEνNS process, where the blob indicates the interaction vertex between the nucleus and the Z boson which mediates the interaction.

The vector and axial coupling of the neutrino are predicted to be $g_{V,A}^\nu = 1/2$ in the SM at the tree-level, while the vector couplings of the quarks carry a dependence on the weak mixing angle, so that

$$g_V^q = \frac{1}{2} - \frac{4}{3}\sin^2\theta_W\,, \qquad q = u, c, t\,, \tag{2.22}$$

$$g_V^q = -\frac{1}{2} + \frac{2}{3}\sin^2\theta_W\,, \qquad q = d, s, b\,, \tag{2.23}$$

where $u,\ c,\ t,\ d,\ s,\ b$ indicates the quark type.
Moreover, in the case of a spin-0 nucleus, the axial contribution from quark currents is zero. When the nucleus has a non-zero spin, the axial contribution from quarks should be considered. However, it roughly scales as $\propto 1/\mathrm{A}$, therefore, it is subdominant with respect to the vector contribution ($\propto \mathrm{A}^2$), so it is usually neglected, and the same will be done in this thesis work.
The Lagrangian in Eq. 2.21 is not properly correct to describe the CEνNS process,

as it actually describes the scattering of a neutrino with quarks, and not the coherent response of the nucleons inside the nucleus, as it is pictured instead in the diagram in Fig. 2.6. In the diagram, the interaction vertex with the nucleus is represented with a "blob" to account for the fact that the scattering is on a non-fundamental object. In order to account for this, we can elevate the quark operator $\hat{O}_q$ to a nucleon operator $\hat{O}_\eta$, where $\eta = n,\ p$ indicates the two possible nucleons. In principle, the sum in the Lagrangian in Eq. 2.21 runs over all the quark types, but since both protons and neutrons are mainly made of u and d quarks, the other contributions will be neglected.
In this way, if we project the quark current on the initial and final nucleon states, we obtain

$$\langle \eta(p_f)|\overline{q}\gamma^\mu q|\eta(p_i)\rangle = N_\eta^q \overline{\eta}\gamma^\mu \eta\,, \tag{2.24}$$

where $p_{i,f}$ are the initial and final quadrimomenta of the nucleons inside the nucleus respectively, η represents the nucleon field and N_η^q is the quark number operator that quantifies the number of quarks q inside the nucleon η. Thus, we can now define the quark vector currents

$$\begin{aligned} & g_V^u \langle n|\overline{u}\gamma^\mu u|n\rangle + g_V^d \langle n|\overline{d}\gamma^\mu d|n\rangle + g_V^u \langle p|\overline{u}\gamma^\mu u|p\rangle + g_V^d \langle p|\overline{d}\gamma^\mu d|p\rangle = & (2.25)\\ = \;& g_V^u N_n^u \overline{n}\gamma^\mu n + g_V^d N_n^d \overline{n}\gamma^\mu n + g_V^u N_p^u \overline{p}\gamma^\mu p + g_V^d N_p^d \overline{p}\gamma^\mu p = \\ = \;& (g_V^u + 2g_V^d)\,\overline{n}\gamma^\mu n + (2g_V^u + g_V^d)\,\overline{p}\gamma^\mu p = \\ = \;& g_V^n\,\overline{n}\gamma^\mu n + g_V^p\,\overline{p}\gamma^\mu p\,, & (2.26)\end{aligned}$$

where we have used the fact that the neutron is $n = [udd]$ and the proton $p = [uud]$, and we have defined the vector coupling to neutron, g_V^n, and proton, g_V^p, as

$$g_V^n = g_V^u + 2g_V^d\,, \qquad g_V^p = 2g_V^u + g_V^d\,. \tag{2.27}$$

The couplings, in the SM at tree-level, are defined as

$$g_V^n = -1/2\,, \qquad g_V^p = 1/2 - 2\sin^2\theta_W\,, \tag{2.28}$$

from which it is easy to notice that only the vector coupling to the proton depends on the weak mixing angle.
Again, also the latter results are not the definitive description of the interaction, as we need to go from interaction with nucleons to interaction with the nucleus. We can follow a similar approach by defining the nucleus operator

$$\langle \mathcal{N}(k_f)|\overline{\eta}\gamma^\mu \eta|\mathcal{N}(k_i)\rangle\,, \tag{2.29}$$

where $k_{i,f}$ are the initial and final momenta of the nucleus. Such operator provides the number of a certain nucleon inside a nucleus.
From the Lorentz structure, one can obtain that the nucleus current becomes

$$N_\eta \overline{\mathcal{N}}[\gamma^\mu F_V^\eta(q^2)]\mathcal{N}\,. \tag{2.30}$$

In the latter equation, N_η is the number of a certain nucleon type inside the nucleus, while F_V^η is the vector form factor and q^2 corresponds to the momentum

transfer in the scattering process. Let us note that in the current we have neglected the contribution of the magnetic form factor, associated with a different Lorentz structure, because it results to be subdominant to the vector contribution. If we now apply this relation to protons and neutrons, we obtain

$$[Zg_V^p F_V^p(q^2) + Ng_V^n F_V^n(q^2)]\overline{\mathcal{N}}\gamma^\mu\mathcal{N}\,, \tag{2.31}$$

where Z and N are the proton and neutron numbers of the target nucleus respectively and $F_V^{p,n}(q^2)$ are the proton/neutron form factors and account for the proton/neutron spatial distributions inside the nucleus, and they will be discussed in more details in Chapter 3, Chapter 4 and Chapter 5.
The quantity in the square brackets in Eq. 2.31 has the form of a form factor, that will be called the weak form factor. In fact, we can state that the Z boson couples to the protons and the neutrons because those nucleons have a weak charge, in this sense, the weak form factor is defined as

$$\tilde{F}_W(q^2) = Zg_V^p F_V^p(q^2) + Ng_V^n F_V^n(q^2)\,. \tag{2.32}$$

However, the form factor has to be a normalized quantity, and the normalization is defined by the nuclear weak charge $Q_W = Zg_V^p + Ng_V^n$, which is the weak "coupling" to the nucleus[2]. Thus, we obtain the normalized weak form factor

$$F_W(q^2) = \frac{1}{Q_W}\tilde{F}_W(q^2)\,. \tag{2.33}$$

We can now go back to the effective Lagrangian in Eq. 2.21, and after some manipulations and using the above definition, we obtain

$$\mathcal{L}_{\text{eff}}({}^{(-)}_{\nu}{}_\ell\mathcal{N} \to {}^{(-)}_{\nu}{}_\ell\mathcal{N}) = \frac{G_F}{\sqrt{2}}\Big[\overline{\nu}\gamma_\mu\Big(\frac{1-\gamma^5}{2}\Big)\nu\Big]\Big[Q_W F_W\overline{\mathcal{N}}\gamma^\mu\mathcal{N}\Big]\,. \tag{2.34}$$

In this Lagrangian, it is easy to identify a lepton current L_μ and a hadron one W^μ, so that it can often be written in the form

$$\mathcal{L}_{\text{eff}}({}^{(-)}_{\nu}{}_\ell\mathcal{N} \to {}^{(-)}_{\nu}{}_\ell\mathcal{N}) = \frac{G_F}{\sqrt{2}}Q_W F_W L_\mu W^\mu\,. \tag{2.35}$$

Now we need to calculate the matrix element, $M^{ss'rr'}$, for the process, following also the diagram in Fig. 2.6, so that, in the rest frame is given by

$$M^{ss'rr'} = \frac{G_F}{\sqrt{2}}Q_W F_W[\overline{u}^{s'}(p')\gamma^\mu P_L u(p)^s][\overline{u}^{r'}(k')\gamma_\mu u^r(k)]\,, \tag{2.36}$$

where $s, p(s', p')$ are the initial (final) spin and momentum of the neutrino, while $r, k(r', k')$ the corresponding ones of the nucleus. P_L is the left projector operator, which is defined as $P_L = (1-\gamma^5)/2$.

[2]Let us note that this is retrieved using the normalization condition of the vector proton and neutron form factor, which at $q^2 \to 0$ are normalized to unity.

The cross section will be obtained by the module squared of the sum over the spin states of the matrix element,

$$|M|^2 = \sum_{s,s'} \sum_{r,r'} |M^{ss'rr'}|^2 \,. \tag{2.37}$$

Actually, a factor of $1/2$ appears from averaging over the nuclear spin states. We are making the calculations treating the nucleus as if it were a fermion, but there is no reason to assume it to be left or right-handed.
We thus obtain,

$$|M|^2 = \frac{G_F^2}{2} Q_W^2 F_W^2 L^{\mu\nu} W_{\mu\nu} \,, \tag{2.38}$$

where now we obtain a lepton and a hadron tensor (two indices) from the squaring procedure, of the form

$$L^{\mu\nu} = \sum_{s,s'} [\overline{u}^{s'}(p')\gamma^\mu P_L u(p)^s][\overline{u}^s(p)\gamma^\nu P_L u(p')^{s'}] \,, \tag{2.39}$$

to which we can apply the fact that $\sum_s u^s(p)\overline{u}^s(p) = \not{p} + m$, where $\not{p} = \gamma^\mu p_\mu$. Being the neutrino massless (or at least having a mass term negligible with respect to the momentum), the lepton tensor becomes

$$L^{\mu\nu} = Tr[\not{p}'\gamma^\mu P_L \not{p}\gamma^\nu P_L] \,, \tag{2.40}$$

where Tr stands for the trace operation. The mass term in the hadron tensor, m_N, instead cannot be neglected, so

$$W_{\mu\nu} = \frac{1}{4} Tr[(\not{k}' + m_N)\gamma_\mu(\not{k} + m_N)\gamma_\nu] \,. \tag{2.41}$$

We will only use the t channel (as shown in the diagram in Fig. 2.6).
The cross section differential in the Mandelstam variable t is

$$\frac{d\sigma_{\nu_\ell - \mathcal{N}}}{dt} = \frac{1}{16\pi} \frac{1}{(s - m_N^2)^2} |M|^2 \,. \tag{2.42}$$

The s Mandelstam variable is given by $s = (p + k)^2 = m_N^2 + 2E_\nu m_N$, while the t variable is given by $t = (k - k') = 2m_N^2 - 2E_N m_N$, where E_N has to be redefined in terms of the observable quantity known has nuclear recoil energy $T_{\rm nr}$. Namely, $E_N = m_N + T_{\rm nr}$. Then, $t = -2m_N T_{\rm nr}$.
Manipulating Eq. 2.42, we can obtain the differential cross section in the nuclear recoil energy,

$$\frac{d\sigma_{\nu_\ell - \mathcal{N}}}{dT_{\rm nr}} = \frac{G_F^2}{128\pi} \frac{Q_W^2}{E_\nu^2 m_N} F_W^2 L^{\mu\nu} W_{\mu\nu} \,. \tag{2.43}$$

From the traces calculations, one obtains

$$L^{\mu\nu} W_{\mu\nu} \simeq 128 E_\nu^2 m_N^2 \Big(1 - \frac{T_{\rm nr}}{E_\nu} - \frac{m_N T_{\rm nr}}{2E_\nu^2}\Big) \,, \tag{2.44}$$

so that the differential cross section becomes

$$\frac{d\sigma_{\nu_\ell-\mathcal{N}}}{dT_{\rm nr}} = \frac{G_F^2}{\pi} m_N \Big(1 - \frac{T_{\rm nr}}{E_\nu} - \frac{m_N T_{\rm nr}}{2E_\nu^2}\Big) Q_W^2 F_W^2 \,, \tag{2.45}$$

or similarly

$$\frac{d\sigma_{\nu_\ell-\mathcal{N}}}{dT_{\rm nr}} = \frac{G_F^2}{\pi} m_N \Big(1 - \frac{T_{\rm nr}}{E_\nu} - \frac{m_N T_{\rm nr}}{2E_\nu^2}\Big) \Big[Z g_V^p F_V^p(q^2) + N g_V^n F_V^n(q^2)\Big]^2 , \tag{2.46}$$

where we have used the explicit definition of $\tilde{F}_W$ in Eq. 2.32. Often, the nuclear weak charge is effectively identified with $\tilde{F}_W$, in order to define a coupling to the nucleus which includes the nuclear dependence, so that

$$Q_W = Z g_V^p F_V^p(q^2) + N g_V^n F_V^n(q^2) \,. \tag{2.47}$$

We have defined the proton and neutron vector coupling in Eq. 2.28 by giving their tree-level definition. A detailed discussion of the radiative corrections for CEνNS can be found in Appendix A, from which we obtain that the couplings become

$$g_V^p(\nu_e) = 0.0382 \,, \qquad g_V^n(\nu_e) = -0.5117 \,, \tag{2.48}$$
$$g_V^p(\nu_\mu) = 0.0300 \,, \qquad g_V^n(\nu_\mu) = -0.5117 \,, \tag{2.49}$$
$$g_V^p(\nu_\tau) = 0.0255 \,, \qquad g_V^n(\nu_\tau) = -0.5117 \,, \tag{2.50}$$

from which we can observe that the CEνNS cross section is flavor independent only at the tree-level, as due to the neutrino charge radius radiative correction, the neutrino-proton vector coupling becomes flavor dependent. However, we can also notice that the neutrino-proton vector coupling, which by chance is the coupling which incorporates the dependence of the cross section on the weak mixing angle, is significantly suppressed with respect to the coupling to neutrons. Effectively, we can say that the neutrinos couple mainly to the neutrons and that the CEνNS cross section roughly scales as the number of neutrons to the second power, rather than the number of nucleons [22].
We can define the flux averaged integrated cross section by integrating the differential cross section multiplied by the neutrino flux, $\phi_{\rm SNS}$ (we have considered the SNS neutrino flux as an example, see Sec. 2.3.4), over the neutrino energy and the nuclear recoil energy

$$\langle\sigma\rangle = \int_0^{E_\nu^{\rm max}} \int_0^{T_{\rm nr}^{\rm max}(E_\nu)} \frac{d\sigma_{\nu_\ell-\mathcal{N}}}{dT_{\rm nr}}(E_\nu, T_{\rm nr}) \phi_{\rm SNS}(E_\nu)\, dT_{\rm nr} dE_\nu, \tag{2.51}$$

where $E_\nu^{\rm max}$ is the maximum neutrino energy allowed for the considered neutrino flux, and $T_{\rm nr}^{\rm max}(E_\nu)$ is the corresponding maximum nuclear recoil energy allowed by the kinematics, namely

$$T_{\rm nr}^{\rm max}(E_\nu) \simeq \frac{2E_\nu^2}{m_N + 2E_\nu} \sim \frac{2E_\nu^2}{m_N} \,, \tag{2.52}$$

where we can neglect the neutrino energy in the denominator as the typical neutrino energies required to maintain the coherency condition are much smaller than

the mass of nuclei. From the latter relation, we can estimate the typical nuclear recoil energies: for instance a $E_\nu \sim 30\,\mathrm{MeV}$ neutrino will produce a maximum recoil energy of $T_{\mathrm{nr}} \sim 50\ \mathrm{keV}$, considering argon nuclei. This estimate gives an idea of the very tiny recoils produced in the interaction.
In Fig. 2.7, the dependence of $\langle\sigma\rangle$ on the number of neutrons, N, is shown. We can see that if we consider the point-like nucleus limit, in which the form factors are set to unity, we can see that the cross section for $N \sim 20$ is about $\sigma \sim 20 \cdot 10^{-40}\,\mathrm{cm}^2$. If we double the neutron number, so $N \sim 40$, the cross section is roughly $\sigma \sim 80 \cdot 10^{-40}\,\mathrm{cm}^2$, a factor 4 larger, so that the approximated dependence on N^2 is confirmed, and consistent also with currently available experimental measurements. Of course, it is worth mentioning, that the form factors effect in some sense "spoils" this N^2 dependence, as the nuclear structure effects get more complicated for heavier nuclei.

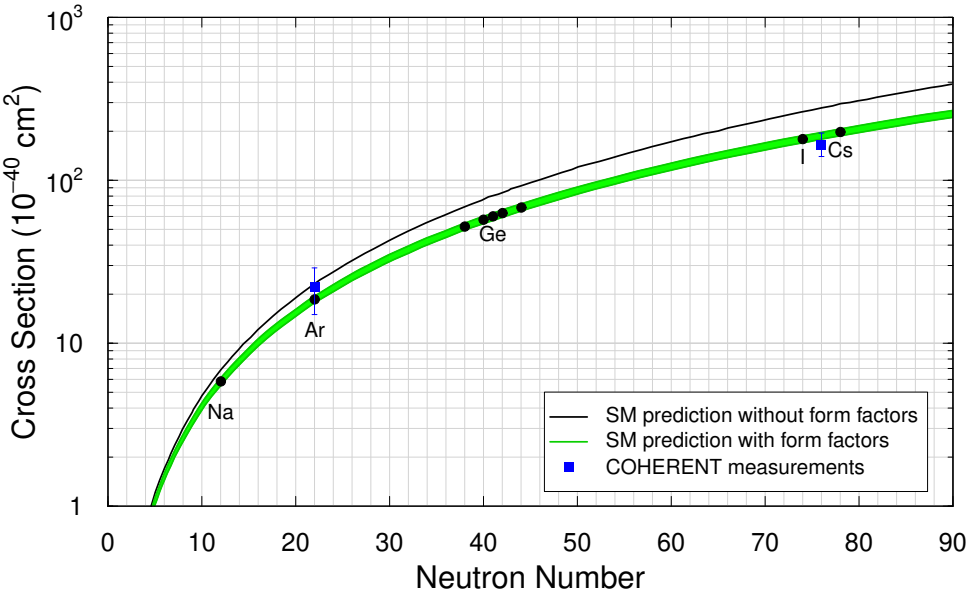

Figure 2.7: Integrated CEνNS cross section averaged over the SNS neutrino flux (see Sec. 2.3.4) as a function of the number of neutrons of the target nucleus taken from Ref. [52]. The black line shows the expected cross section in the point-like nucleus approximation, so for $F_V^p(q^2), F_V^n(q^2) \to 1$. The green band represents the prediction considering the form factors. The black dots are the expected prediction for some selected nuclear targets, like sodium, argon, germanium, cesium and iodine, while the blue data points show the current measurements from the COHERENT Collaboration using a liquid argon and cesium iodine crystal targets [51, 53, 54].

In Fig. 2.8, we show the CEνNS integrated cross section as a function of the neutrino energy, $\sigma_{\nu-\mathcal{N}}(E_\nu)$, which is defined by

$$\sigma_{\nu-\mathcal{N}}(E_\nu) = \int_0^{T_{\mathrm{nr}}^{\max}(E_\nu)} \frac{d\sigma_{\nu_\ell-\mathcal{N}}}{dT_{\mathrm{nr}}}(E_\nu, T_{\mathrm{nr}})\, dT_{\mathrm{nr}}. \tag{2.53}$$

In particular, in the upper panel of Fig. 2.8, we show the comparison between the electron and muon neutrino flavors considering two different nuclear targets,

namely cesium (red/orange lines) and argon (blu/turquoise lines).
In a similar way to what was done for νES in Fig. 2.4, in the lower panel we evaluated the impact of the radiative corrections on the cross section, $\Delta\sigma_{\nu-\mathcal{N}}$,

$$\Delta\sigma_{\nu-\mathcal{N}}(E_\nu) = \frac{\sigma^{\text{T.L.}}_{\nu-\mathcal{N}}(E_\nu) - \sigma_{\nu-\mathcal{N}}(E_\nu)}{\sigma_{\nu-\mathcal{N}}(E_\nu)} \,. \tag{2.54}$$

We notice that the impact is always within a few percent, and it is generally larger for muon neutrinos (as they have a larger charge radius contribution as we will see in Sec. 7.1).

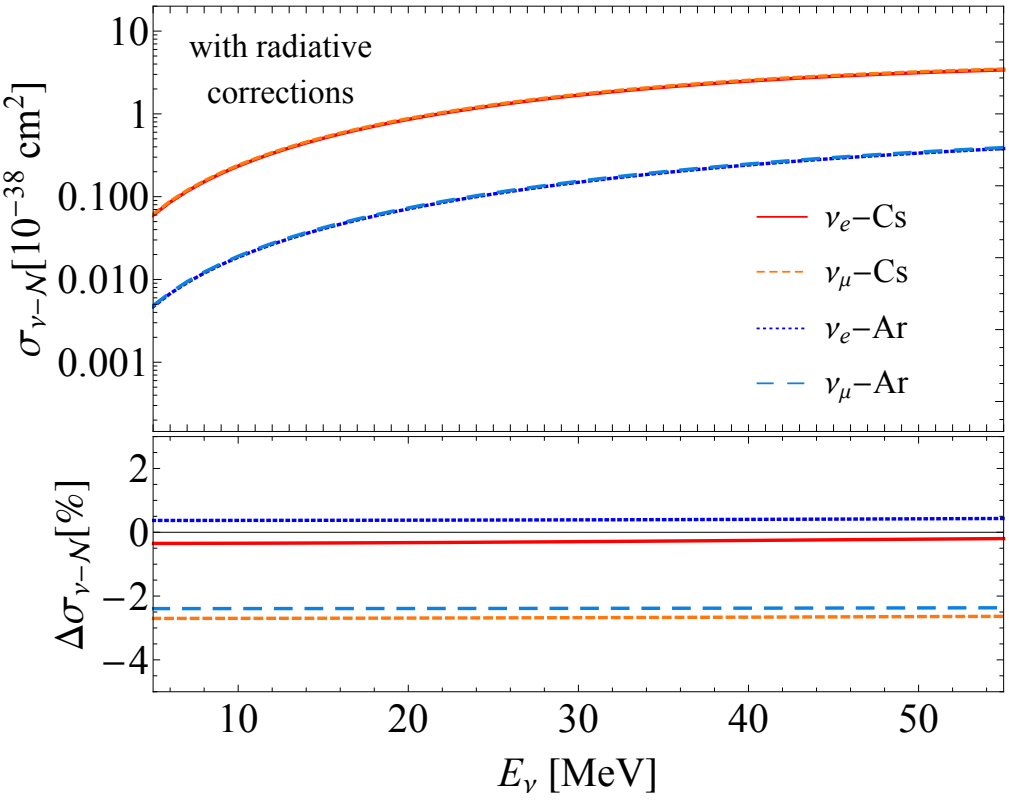

Figure 2.8: In the upper panel, integrated cross section for the electron and muon neutrino-nucleus coherent scattering process (including radiative corrections to the couplings) as a function of the neutrino energy. In the lower panel, the impact of the radiative correction is shown, in terms of the percentage variation with respect to the tree-level cross section as a function of the neutrino energy.

The impact of the radiative correction depends also on the target nucleus, as the overall effect is driven by the nuclear weak charge in Eq. 2.47, which is made of the combination of proton and neutron vector couplings weighted by the Z, N numbers and form factors, which depend on the target. Indeed, this produces the effect of a positive value of $\Delta\sigma_{\nu-\mathcal{N}}$ for an electron neutrino impinging on an argon nucleus, while it is negative when the target is cesium, as it is shown in Fig. 2.8.
To further stress the relative largeness of the CEνNS cross section, due to coherency, it is useful to compare the integrated CEνNS cross section shown in

Fig. 2.8 to other concurrent neutrino processes, such as the νES (discussed in Sec. 2.1), the inverse beta decay (IBD) [51, 55] and the neutrino-induced neutron (NIN) generation following the CC process on lead $^{208}\mathrm{Pb}$ [51, 56]. Therefore, in Fig. 2.9 we show such comparison considering CEνNS and νES from electron neutrinos on different target materials, namely cesium, argon, germanium and iodine. In particular, the NIN process is worth to be considered as many detectors employ a lead shielding system, so that the process may produce a signal in the data acquisition, representing a background for the experiments.
From the comparison clearly emerges that the CEνNS cross section is orders of magnitude greater than the νES and IBD ones even for relatively light nuclei such as argon, while the NIN cross section is comparable to the CEνNS cross section on germanium for neutrino energies above $\sim 30\,\mathrm{MeV}$. This is important, especially in the design of the detectors, so that the number of events produced by the interaction of neutrinos on the shielding lead has to be kept small enough not to spoil the measurement.

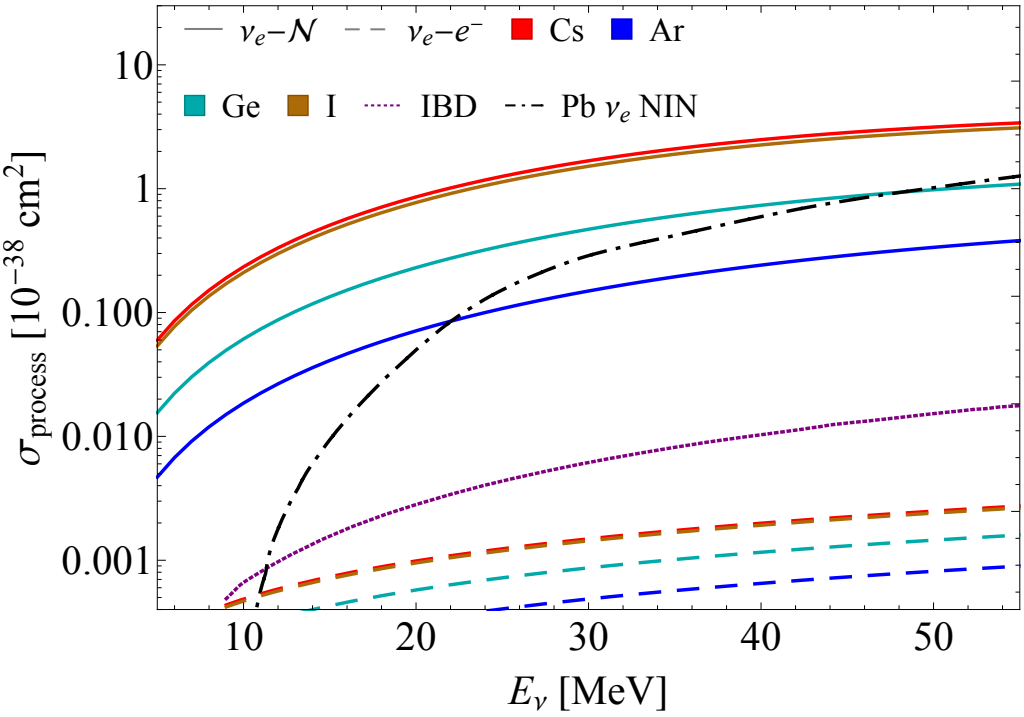

Figure 2.9: Integrated cross section for CEνNS by electron neutrinos on cesium (solid red), argon (solid blue), germanium (solid darker cyan) and iodine (solid brown) nuclei as a function of the neutrino energy. The CEνNS cross sections are compared to the neutrino-electron cross section for the corresponding atoms (dashed and same color code) and to other concurrent neutrino processes, namely the Inverse Beta Decay, IBD (purple dotted), and the Neutrino-Induced Neutron, NIN (black dot-dashed), on lead [51].

In Fig. 2.10, we compare the differential cross section as a function of the nuclear recoil energy, T_{nr}, for different nuclear targets at different neutrino energies. In particular, the neutrino energy has been fixed to some reference values: $E_\nu = 3\ \mathrm{MeV}$, typical energy for reactor neutrinos, $E_\nu = 30\ \mathrm{MeV}$, average energy of

neutrinos from pion decay at rest, $E_\nu = 50$ MeV, basically endpoint energy of the neutrinos from pion decay at rest, and $E_\nu = 150$ MeV, higher energy value, accessible via kaon decay at rest in future facilities.

	$T_{\rm nr}^{\rm end}$[keV]			
	$E_\nu = 3$ MeV	$E_\nu = 30$ MeV	$E_\nu = 50$ MeV	$E_\nu = 150$ MeV
Ar	0.45	45	125	1125
Ge	0.26	26	71	643
Cs	0.14	14	38	346

Table 2.1: Table reporting the value at which the kinematic factor in the CEνNS cross section vanishes, for different nuclear targets and neutrino energies.

From the figure it is possible to notice again that the cross section is generally higher for heavier nuclei, however, this is true at low recoil energies. Indeed, at higher recoil energies the cross section drops due to the combined effect of the kinematic factor in Eq. 2.46 and the form factor (larger recoil energies means also higher momentum transfer, so decoherence).

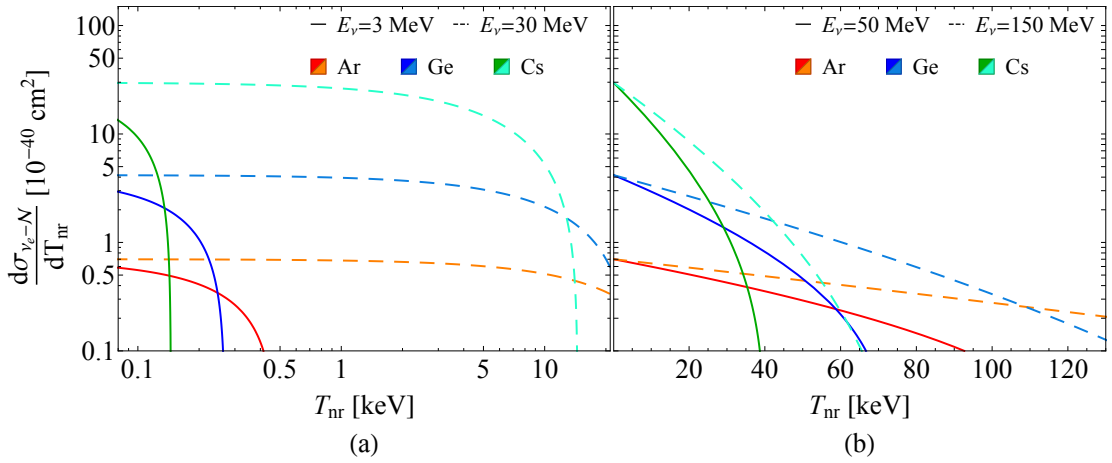

Figure 2.10: Differential cross section for electron neutrino scattering off different target nuclei, as a function of the nuclear recoil energy at different neutrino energies.

Using the kinematic factor in Eq. 2.46, we can calculate the recoil energies at which we have the drop, namely

$$1 - \frac{T_{\rm nr}}{E_\nu} - \frac{m_N T_{\rm nr}}{2E_\nu^2} = 0\,, \tag{2.55}$$

where we can neglect for second term, as $T_{\rm nr}/E_\nu \ll 1$, so that we obtain

$$T_{\rm nr}^{\rm end} \simeq \frac{2E_\nu^2}{m_N}\,. \tag{2.56}$$

Substituting the nuclear mass of argon ($\sim 40\,\mathrm{GeV}$), germanium ($\sim 70\,\mathrm{GeV}$), and cesium ($\sim 130\,\mathrm{GeV}$) and considering the different neutrino energies we obtain the results in Tab. 2.1.
We can notice that the values in the table match the "endpoints" of the cross section in Fig. 2.10, so that the closure of the cross section that we see is mainly given by the kinematic of the interaction. However, this is not fully correct. In fact, we can see that the endpoint matches the values in the table only for low energy neutrinos. When we consider $E_\nu = 50\,\mathrm{MeV}$, we already see a closure at slightly lower recoil energies, and this becomes more evident at even higher energies, and this is due to the effect of the decoherence, accounted for through the form factors.
To further show such an effect, we produce a new plot based on Fig. 2.10, but setting the form factor to unity (so neglecting their effect), and the results are shown in Fig. 2.11.

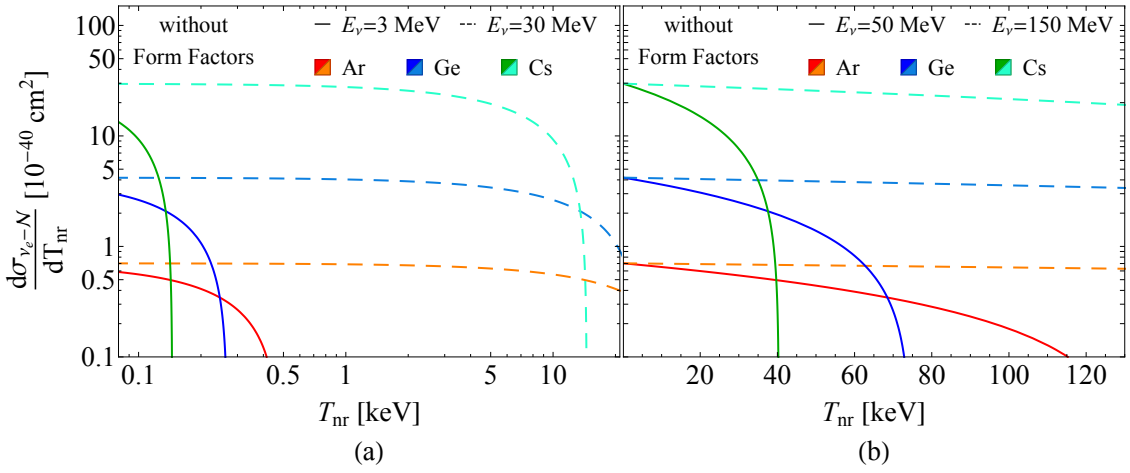

Figure 2.11: Differential cross section for electron neutrino scattering off different target nuclei, as a function of the nuclear recoil energy at different neutrino energies, neglecting the effects of the form factors in the cross section.

By comparing the results in the two figures, it is clear that the form factors have a small impact on the results in the left panels (panels a), so when the neutrino energy is below 30 MeV. Instead, the results for 50 MeV and 150 MeV are significantly affected by the form factors contribution. We observe that the endpoint recoil energy is driven by the kinematic factor, but the sharpness at which the drop happens is due to the form factors. In fact, at low neutrino energy the drop is practically vertical because the form factors do not produce a significant effect, differently from what is observed for higher neutrino energies, where the form factors make the drop less sharp, but cause a significant lowering in the cross section for recoil energies of the order of tens of keV, so in the "intermediate" recoil energy range, which reversing Eq. 2.19 translate to momentum transfer $q \sim 50-100\,\mathrm{MeV}$.
Nevertheless, the effect of form factors and the underlying nuclear properties on CEνNS experiments will be discussed in more detail in the next chapters of this thesis, namely in Chapter 5.
As a reference, we leave in the closure of this section a table (Tab. 2.2) reporting

the values for the nuclear masses, the proton and neutron numbers, and the radii for the proton (R_p), neutron (R_n) and charge[3] ($R_{\rm ch}$) density distribution (necessary for the form factor definitions) used as reference values in all the figures and calculations involving the CEνNS cross section. Whenever such values are taken to be different from the one reported in the latter table, it will be specified [57–60]. In particular, the charge radii have been taken from the tables in Refs. [58, 59], the neutron radii come from the shell model calculations in Ref. [60], while the proton radii have been derived from the tabulated charge radii values.

	m_N [GeV]	Z	N	R_p [fm]	R_n [fm]	$R_{\rm ch}$ [fm]
Ar	37.216	18	22	3.447	3.55	3.4266
Ge	66.995	32	40	4.073	4.22	4.0547
I	118.211	53	74	4.766	5.03	4.7492
Xe	122.296	54	77	4.799	5.07	4.7812
Cs	123.801	55	78	4.821	5.09	4.8043

Table 2.2: Values of the nuclear constant for the nuclei of interest of this thesis work. In particular, the columns report the nuclear mass, the proton and neutron numbers, the proton, neutron and charge nuclear root-mean-square radii [57–60].

2.3 Neutrino sources

In this section, we will give a brief introduction to the neutrino sources that will be considered in the rest of this thesis work to calculate the rate of events for both CEνNS and νES processes. The aim of this section is thus to provide the neutrino flux spectra for the different neutrino sources considered.

2.3.1 —— Solar neutrinos ——

With solar neutrinos, we refer to the neutrinos emitted from the Sun as a product of the thermonuclear fusion reactions taking place in the core of the star.
Indeed, the Sun represents a very productive factory of electron neutrinos of energies around 1 MeV. Such neutrinos, thanks to their feeble interactions, travel practically undisturbed out of the stellar matter. Thus, part of these neutrinos can reach the Earth's surface with an extremely large flux, about $6 \cdot 10^{10}\,\mathrm{cm^{-2}s^{-1}}$ [24], and produce a signal in the huge terrestrial neutrino detectors.
The first experimental proof of the emission of neutrinos by the Sun dates back to 1970 in the Homestake experiment [61, 62], through the observation of the neutrino capture on chlorine [22, 24],

$$\nu_e + {}^{37}\mathrm{Cl} \rightarrow {}^{37}\mathrm{Ar} + e^- \,, \tag{2.57}$$

[3]Let us note that $R_p \neq R_{\rm ch}$, as it will be discussed in more detail in Chapter 3.

which provided a confirmation of the hidden processes happening in the interior of the Sun. The Homestake experiment ran for about 24 years. Meanwhile, starting from the '80s other experimental apparatus have been developed to provide a further measurement of solar neutrinos, such as Kamiokande, Gallex, and Sage, to be followed by the precision era with Super-Kamiokand and SNO experiments from the late '90s [24]. At the date of this thesis work, the latest measurements of solar neutrinos come from the Borexino experiment, which has been the leader of solar neutrino measurements in the last decade [63–65].

According to the standard solar model [66], the Sun is powered by two groups of thermonuclear reactions, known as the pp chain and the CNO cycle [22, 24]. Both processes result in the conversion of four protons and two electrons into a ^{4}He nucleus accompanied by two electron neutrinos,

$$4p + 2e^- \rightarrow {}^4\mathrm{He} + 2\nu_e + \mathcal{Q}\,, \tag{2.58}$$

where $\mathcal{Q}$ is known as the $\mathcal{Q}$-value of the reaction, which corresponds to the energy released, whose values is $\mathcal{Q} \simeq 26.731\,\mathrm{MeV}$ [24]. Hence, it is clear that the neutrinos produced by the Sun are all of electron flavor. This is worth remarking, as in the first years of solar neutrino observation, experiments were observing a deficit in the number of expected electron neutrinos reaching the detectors with respect to the one predicted by the standard solar model. This phenomenon is known as the *solar neutrino problem* and found its solution in the neutrino oscillation mechanism [22, 24, 67].

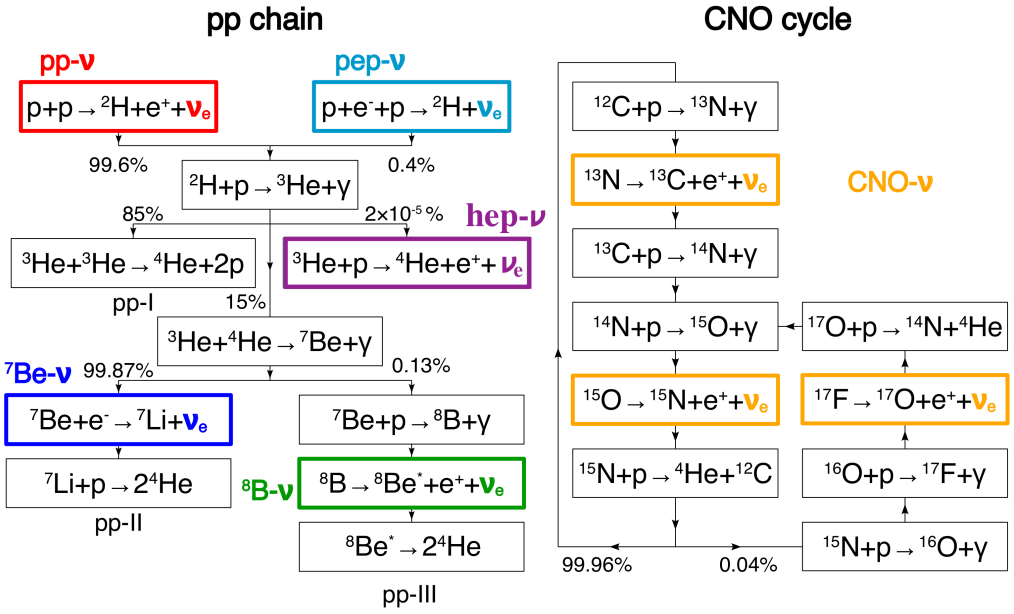

Figure 2.12: Schematic representation of the pp chain (left) and CNO cycle (right) nuclear fusion sequences, taken from Ref. [68]. The colored boxes indicate the processes during the sequence where neutrinos are produced.

Neutrinos, propagating through space, undergo an oscillation phenomenon, which converts electron neutrinos into muon and tau neutrinos. This is explained by the

fact that the interaction states and the mass states do not coincide in the case of neutrinos, so that the interaction (i.e. flavor) states are made of a mixture of mass states. During the propagation, the electron neutrino has a certain probability of being converted into a muonic or a tau flavor neutrino. The neutrino oscillation mechanism is very relevant in solar neutrino experiments as well as many other experiments, however, it will not be discussed in detail in this thesis work. For further details, a complete discussion can be found in Refs. [22, 24].
The nuclear fusion chain is complicated and made of many intermediate steps, both in the case of the pp chain and the CNO cycle. A scheme of the nuclear fusion sequence can be found in Fig. 2.12, taken from Ref. [68], where the colored boxes highlight the chain steps where electron neutrinos are produced. It is possible to observe that the neutrino fluxes produced in the sequence are made of some continuous contributions and some monochromatic lines (originated by processes with only two objects in the final state, i.e. in which the kinematic is fixed).

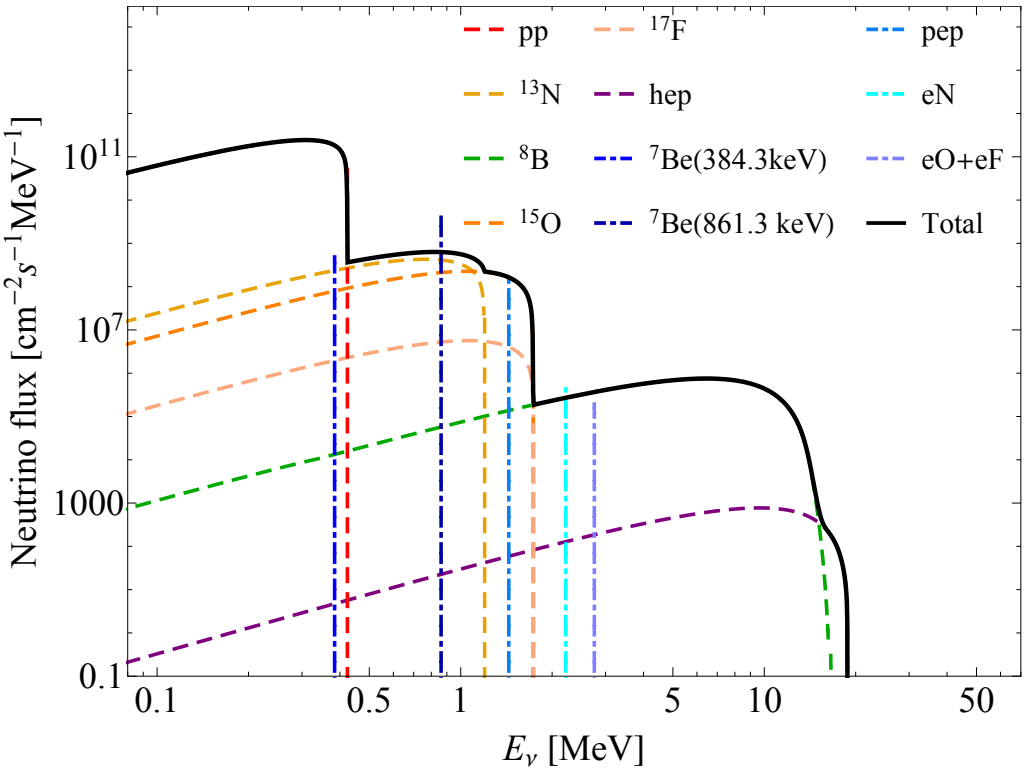

Figure 2.13: Solar neutrino flux as a function of the neutrino energy [69]. The different colors indicate the single flux components produced in the various steps of the pp chain and CNO cycle. The dashed lines represent the continuous spectra components, while the dot-dashed ones the monochromatic line contributions. The black solid line indicates the sum of the various continuous components.

The contributions are not all picked at the same neutrino energy so the neutrino flux presents many peaks. Each process has also a maximum neutrino energy given by the kinematics of the specific interaction.
The solar neutrino flux can be seen in Fig. 2.13, where all the different components can be appreciated through the dashed lines, while the monochromatic lines

contributing are shown through the dot-dashed vertical lines. The black solid line shows the total neutrino flux (without the line contributions). From the figure, it can be observed that the contribution from the lines is generally sub-dominant with respect to the one of the continuous spectra, but for the $^{7}\mathrm{Be}$(861.3 keV) line. In the low energy part of the spectra in Fig. 2.13, the pp process from the pp chain dominates, generating the highest flux, followed by the three different decay processes of the CNO cycle ($^{13}\mathrm{N}$, $^{15}\mathrm{O}$, $^{17}\mathrm{F}$). At higher neutrino energies the $^{8}\mathrm{B}$ contribution becomes the dominating one (above $E_\nu \sim 2\,\mathrm{MeV}$), while at even higher E_ν, namely above $E_\nu \sim 10 - 11\,\mathrm{MeV}$, also the hep contribution plays a role, although with a significantly lower neutrino flux value. The monochromatic lines come from $^{7}\mathrm{Be}$, the pep and electron capture lines on nitrogen, oxygen and fluorine [69].
In Tab. 2.3, we collect the current status of solar neutrino fluxes measurements. The table is adapted from the one in Ref. [69], and we have added the latest Borexino measurement of CNO cycle neutrinos [65, 70]. The observed fluxes are compared to the one predicted by the standard solar model GS98 [66]. In the table, we report also the average neutrino energy for each flux component and the corresponding maximum energy.

Channel	Flux	E_{av} [MeV]	E_{max} [MeV]	Flux at Earth			
				GS98		Observed	Units
pp Chains	Φ_{pp}	0.267	0.423	5.98	$\pm 0.6\%$	$5.971^{+0.62\%}_{-0.55\%}$	$10^{10}\mathrm{cm}^{-2}\mathrm{s}^{-1}$
	Φ_{B}	6.735 ± 0.036	~ 15	5.46	$\pm 12\%$	$5.16^{+2.5\%}_{-1.7\%}$	$10^{6}\mathrm{cm}^{-2}\mathrm{s}^{-1}$
(β^+)	Φ_{hep}	9.628	18.778	0.80	$\pm 30\%$	$1.9^{+63\%}_{-47\%}$	$10^{4}\mathrm{cm}^{-2}\mathrm{s}^{-1}$
pp Chains	Φ_{Be}	0.863 (89.7%) 0.386 (10.3%)		4.93	$\pm 6\%$	$4.80^{+5.9\%}_{-4.6\%}$	$10^{9}\mathrm{cm}^{-2}\mathrm{s}^{-1}$
(EC)	Φ_{pep}	1.445		1.44	$\pm 1\%$	$1.448^{+0.90\%}_{-0.90\%}$	$10^{8}\mathrm{cm}^{-2}\mathrm{s}^{-1}$
CNO Cycle	Φ_{N}	0.706	1.198	2.78	$\pm 15\%$	$6.6^{+2.0}_{-0.9}$	$10^{8}\mathrm{cm}^{-2}\mathrm{s}^{-1}$
	Φ_{O}	0.996	1.732	2.05	$\pm 17\%$		
(β^+)	Φ_{F}	0.998	1.736	5.29	$\pm 20\%$	—	$10^{6}\mathrm{cm}^{-2}\mathrm{s}^{-1}$
CNO Cycle	Φ_{eN}	2.220		2.20	$\pm 15\%$	—	$10^{5}\ \mathrm{cm}^{-2}\ \mathrm{s}^{-1}$
	Φ_{eO}	2.754		0.81	$\pm 17\%$	—	$10^{5}\ \mathrm{cm}^{-2}\ \mathrm{s}^{-1}$
(EC)	Φ_{eF}	2.758		3.11	$\pm 20\%$	—	$10^{3}\ \mathrm{cm}^{-2}\ \mathrm{s}^{-1}$

Table 2.3: Table collecting the status of the flux prediction and measurements of solar neutrinos, adapted from Ref. [69]. The table shows also the average energy of the neutrino flux component, E_{av}, and the maximum energy of the latter, E_{max}. The theoretical solar neutrino model is the standard solar model GS98 [66]. The observed fluxes from the pp chain come from the global analysis in Ref. [71], while the CNO cycle neutrino flux from the latest Borexino measurement in Ref. [65, 70].

It can be noticed that solar neutrinos have energies around the hundreds of keVs up to 20 MeV, so a very suitable energy range for CEνNS and νES scattering processes, representing a possible neutrino source of such processes. As we will see later in this thesis, solar neutrino CEνNS, but also νES, play a fundamental role in direct dark matter searches, representing a non negligible background component, as well as a possible signal to look for beyond the standard model neutrino

properties.
One further aspect to be mentioned in dealing with solar neutrinos is that, as already anticipated, solar neutrinos unveiled the neutrino oscillation mechanism [22, 24]. Solar neutrino flux measurements also allowed us to understand that the standard oscillation mechanism in vacuum had to be improved, as neutrinos passing through matter oscillate in a different way. The so-called Mikheyev-Smirnov-Wolfenstein (MSW) effect [67] describes the oscillation mechanism in matter, and it was crucial to solve the famous solar neutrino problem.
In Fig. 2.14, we show the survival probability of electron neutrinos, i.e. the probability that a neutrino produced in the Sun as an electron neutrinos arrives at the Earth's surface as an electron neutrino, as a function of the neutrino energy in the three-flavor scenarios [64]. The pink band represents the MSW prediction, while the gray band the standard oscillation in vacuum prediction. The experimental points are all in agreement with the MSW prediction [64]. Let us note that the survival probability depends on the neutrino energy according to the MSW effect, while for oscillation in vacuum the value is constant.

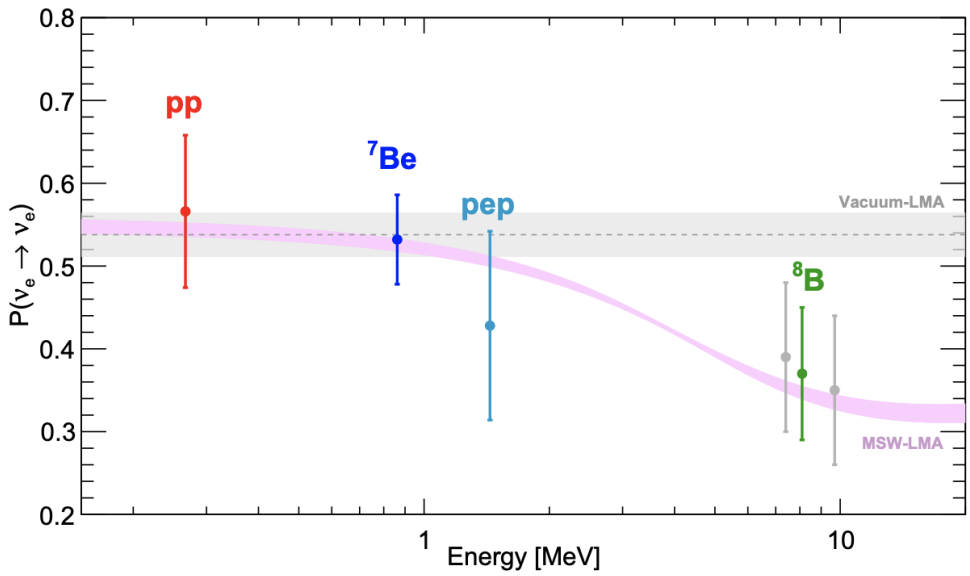

Figure 2.14: Survival probability for solar neutrinos at the Earth surface in the three-flavor scenario as a function of the neutrino energy [64]. The pink band shows the MSW prediction, while the gray band the standard vacuum oscillation mechanism. The data points represent the current status of experimental observations [64].

Using the latest values for the mixing angles reported in Ref. [25], for pp neutrinos the survival probability is ~ 0.54, with around 21% neutrinos converting into muonic neutrinos and 25% to tau ones, while for boron neutrinos, which have higher energies, the survival probability gets as low as ~ 0.33, with $\sim 30\%$ of the electron neutrinos becoming muonic neutrinos and $\sim 36\%$ tau ones.
As already shown in Chapter 2.1 and 2.2, the cross sections gain a flavor dependence due to radiative corrections when one goes beyond the tree-level, so

knowing the neutrino flavor is of crucial importance when studying solar neutrino CEνNS and νES rates in terrestrial detectors and when investigating beyond the standard model flavor dependent neutrino properties.

2.3.2 —— Atmospheric neutrinos ——

The interaction of primary cosmic rays with the nuclei in the higher layers of the atmosphere may produce a flux of neutrinos, commonly known as atmospheric neutrinos. In fact, primary cosmic rays, which are mainly made of energetic ($\sim$GeV) protons and a small component of nuclei, can interact with the nuclei present in the atmosphere generating the so-called secondary cosmic rays. Secondary cosmic rays are therefore made of hadrons and their decay products.
Neutrinos are mainly produced by the decay of charged pions, which are efficiently produced as a part of the secondary cosmic rays. The charged pions, subsequently, decay mainly into muons and muon neutrinos, followed by the decay of the decay in flight of muons into electrons, electron neutrinos and muon neutrinos, before hitting the ground. A schematic of this neutrino production process is shown in Fig. 2.15.

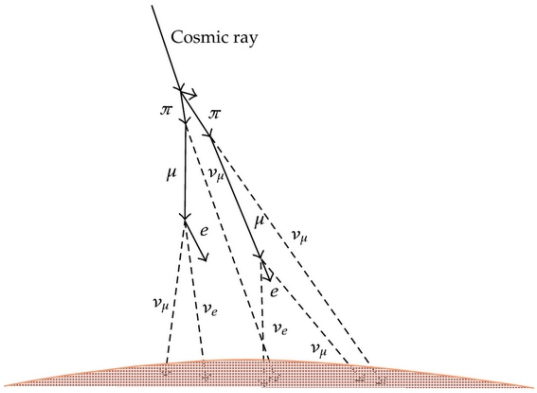

Figure 2.15: Schematic representation of the production of neutrinos from the interaction of primary cosmic rays with nuclei in the atmosphere through the decay of pions and muons during the flight toward the Earth's surface, taken from Ref. [72].

To summarize, atmospheric neutrinos are produced through the following decay processes [24]

$$\pi^+ \to \mu^+ + \nu_\mu\,, \qquad \pi^- \to \mu^- + \overline{\nu}_\mu\,, \tag{2.59}$$

$$\mu^+ \to e^+ + \nu_e + \overline{\nu}_\mu\,, \qquad \mu^- \to e^- + \overline{\nu}_e + \nu_\mu\,. \tag{2.60}$$

Let us notice that high energy primary cosmic rays can also produce kaons, which contribute to the production mechanism by decaying into muons (anti-muon) and muon anti-neutrinos (neutrinos). Indeed, the kaon can also directly decay, through a three-body decay, into a neutral pion, a positron (electron) and an electron neutrino (anti-neutrino), or into a charged pion and a negative pion [24, 69].

From the subsequent charged pion decay, other neutrinos are produced.
These neutrinos, called atmospheric neutrinos, have energies ranging from ~ 100 MeV up to ~ 100 GeV. Thus, it is possible to observe that atmospheric neutrinos are in some sense complementary to solar neutrinos, as they extend the neutrino flux reaching the Earth's surface toward higher neutrino energies. It can also be observed, as we will see later in this work, that also atmospheric neutrinos can produce CEνNS (mainly the less energetic ones) and νES signals in terrestrial experiments, such as direct dark matter detectors.
For low energy cosmic rays ($\lesssim 1$ GeV), most of the muons produced in the process in Eq. 2.59 decay before reaching the ground, so that the neutrino fluxes, Φ, satisfy the following ratios [24]

$$\frac{\Phi_{\nu_\mu} + \Phi_{\overline{\nu}_\mu}}{\Phi_{\nu_e} + \Phi_{\overline{\nu}_e}} \simeq 2\,, \qquad \frac{\Phi_{\nu_\mu}}{\Phi_{\overline{\nu}_\mu}} \simeq 1\,, \qquad \frac{\Phi_{\nu_e}}{\Phi_{\overline{\nu}_e}} \simeq \frac{\Phi_{\mu^+}}{\Phi_{\mu^-}}\,, \tag{2.61}$$

which means that the muon flavor neutrinos are roughly twice as much as electron flavor neutrinos.
However, for higher energy cosmic rays, the fraction of muons that reach the ground without undergoing a decay process increases, increasing the ratio $(\Phi_{\nu_\mu} + \Phi_{\overline{\nu}_\mu})/(\Phi_{\nu_e} + \Phi_{\overline{\nu}_e})$, since muon neutrinos are produced also by the $\pi^\pm$ decays, while electrons only from $\mu^\pm$ decays.
For the purpose of this thesis, only the lower part ($E_\nu \lesssim 100$ MeV) of the atmospheric neutrino flux is relevant. At those energies, the estimated uncertainty on the neutrino flux is approximately $\sim 20\%$ [73].

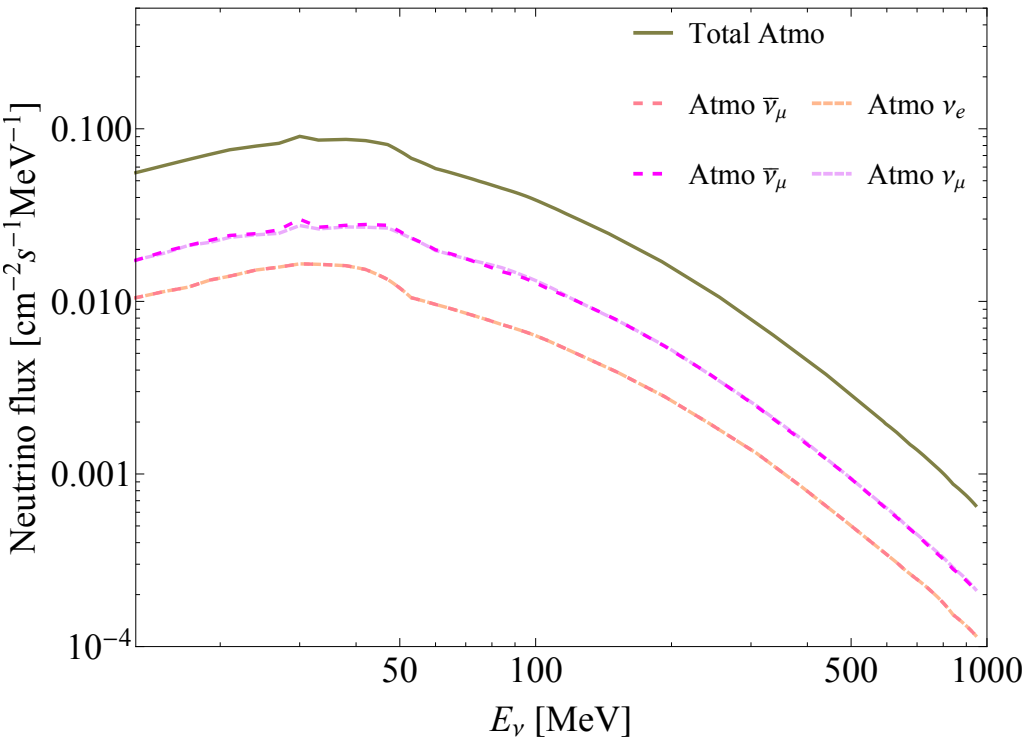

Figure 2.16: Atmospheric neutrino flux as a function of the neutrino energy. The solid line shows the total neutrino flux, while the dashed lines show the different flavor components [74].

We took as a reference for atmospheric neutrino fluxes calculations the results of the FLUKA simulation reported in Ref. [74], which provides the different flavor components. The resulting atmospheric neutrino flux is shown in Fig. 2.16, where the solid line shows the total flux, while the different dashed lines indicate the electron and muon neutrino and anti-neutrino components for energies below ~ 1 GeV.
It is interesting to notice that the flux is much lower with respect to the solar neutrino one shown in Fig. 2.13, but it covers energies higher than the $\sim 20\,\mathrm{MeV}$ endpoint of the solar neutrino flux.
To further compare the solar and the atmospheric neutrino fluxes, in Fig. 2.17 we show them together. The gray shaded region corresponds to the total solar neutrino flux, while the brown one to the atmospheric neutrinos one. We also show the relevant components for neutrino energies $1\,\mathrm{MeV} \lesssim E_\nu \lesssim 1\,\mathrm{GeV}$. Clearly, the atmospheric neutrino flux is about 7 orders of magnitude lower than the ^{8}B flux, but as it covers an energy range uncovered by solar neutrinos, it can not be neglected.

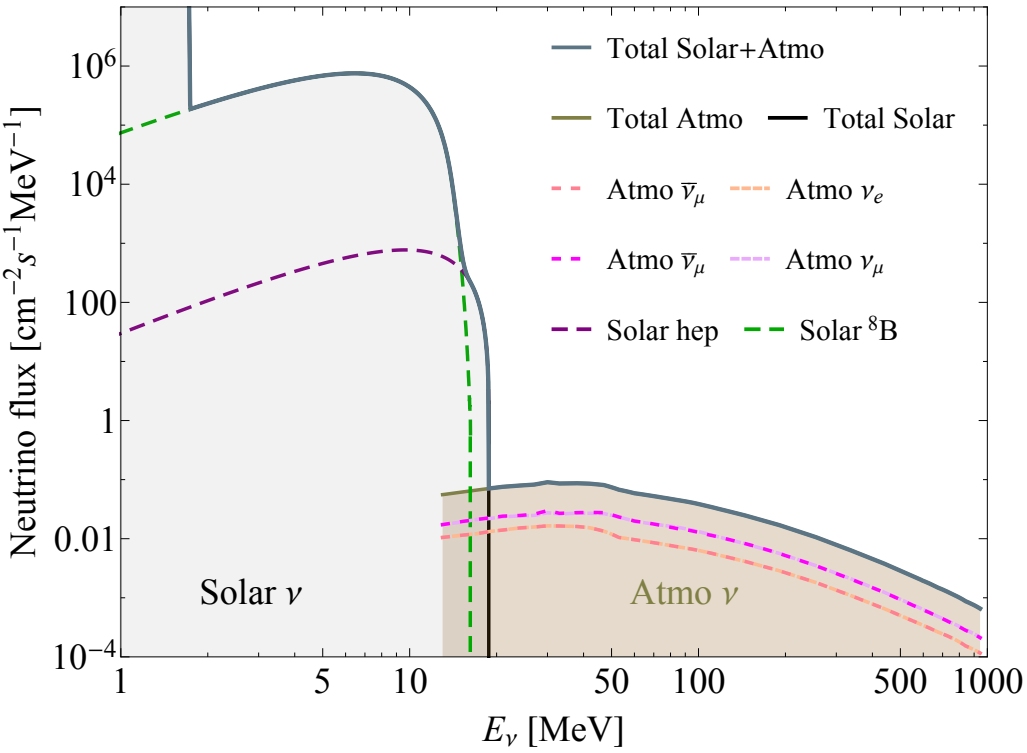

Figure 2.17: Higher energy solar neutrino flux and atmospheric neutrino flux as a function of the neutrino energy [69, 74]. The green dashed line refers to boron solar neutrinos, and the purple one to the solar hep component. The pinkish dashed lines refer to the different atmospheric neutrino components [74]. The gray shaded area shows the part of the total flux coming from solar neutrinos, while the brown one the region relative to atmospheric neutrinos.

As we will see later in this thesis work, atmospheric neutrinos, as well as solar neutrinos, represent a suitable neutrino source to produce CEνNS and νES signals in terrestrial detectors, especially in the case of direct dark matter detectors. In

this sense, solar and atmospheric neutrinos represent the two main sources of natural origin to look for CEνNS signals.

2.3.3 —— Reactor neutrinos ——

Differently from solar and atmospheric neutrinos, reactor neutrinos have an "artificial" origin, as they are the product of nuclear power plants.
Indeed, nuclear power plants employ the nuclear fission process with the aim of producing an enormous amount of energy, part of which (around $\sim 5\%$) is released in the form of electron antineutrinos, arising from the β-decay of fission products [24, 69].
Nuclear power plants produce a diffuse and rather high neutrino flux, that has been employed during the years to discover fundamental neutrino properties, including the first actual detection of the neutrino by Reines and Cowan [69].
The main contribution of neutrinos comes from the fission of four isotopes: $^{235}\mathrm{U}(\sim 56\%)$, $^{239}\mathrm{Pu}(\sim 30\%)$, $^{238}\mathrm{U}(\sim 8\%)$ and $^{241}\mathrm{Pu}(\sim 6\%)$, where the percentage of each isotope varies over time and may depend also on the specific power plant considered [24].

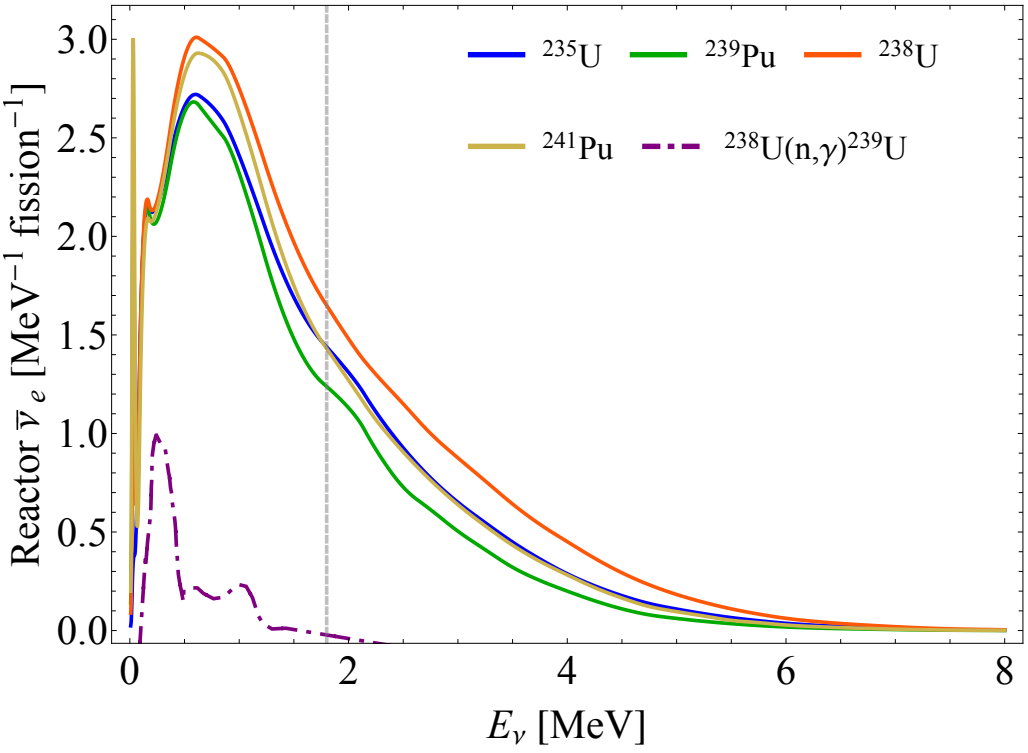

Figure 2.18: $\bar{\nu}_e$ energy spectra for $^{235}\mathrm{U}$, $^{239}\mathrm{Pu}$, $^{238}\mathrm{U}$ and $^{241}\mathrm{Pu}$ fissions. The low energy spectra ($E_\nu < 2\,\mathrm{MeV}$) are taken from Ref. [75], while the high energy part from Ref. [76]. The gray dashed vertical line represents the inverse beta decay (IBD) threshold. The purple dot-dashed spectrum is due to the neutron capture process $^{238}\mathrm{U}(n,\gamma)^{239}\mathrm{U}$, and is rescaled by a factor 1/20.

The fission process presents a chain of β-decays, in which electron anti-neutrinos are produced. As each fission produces ~ 200 MeV on average, and in each fission

about six $\overline{\nu}_e$ are emitted, the electron antineutrino yield is around $2 \cdot 10^{20}\,\mathrm{s}^{-1}$ for each $\mathrm{GW_{th}}$ of thermal power, giving an idea of the enormous number of anti-neutrinos coming out of a nuclear power plant, constituting a huge neutrino flux if one gets close enough to the core of the reactor. Below $E_\nu \simeq 1.8\,\mathrm{MeV}$, $\overline{\nu}_e$ can also be produced through neutron capture processes. The main part of this contribution is given by the decay of $^{239}\mathrm{U}$, produced by the neutron capture on $^{238}\mathrm{U}$ [24], and usually referred to as $^{238}\mathrm{U}(n,\gamma)^{239}\mathrm{U}$.
$E_\nu = 1.8\,\mathrm{MeV}$ represents the threshold of the inverse β decay process, which is usually used to measure reactor neutrino fluxes. As the detection process has such a threshold, it is easy to comprehend that the lowest part of the reactor neutrino spectra is not yet fully understood, while for energies $\gtrsim 2\,\mathrm{MeV}$ is relatively well measured. This is of great importance, as the lowest energy part of the spectrum is dominated by neutron capture contribution [69].

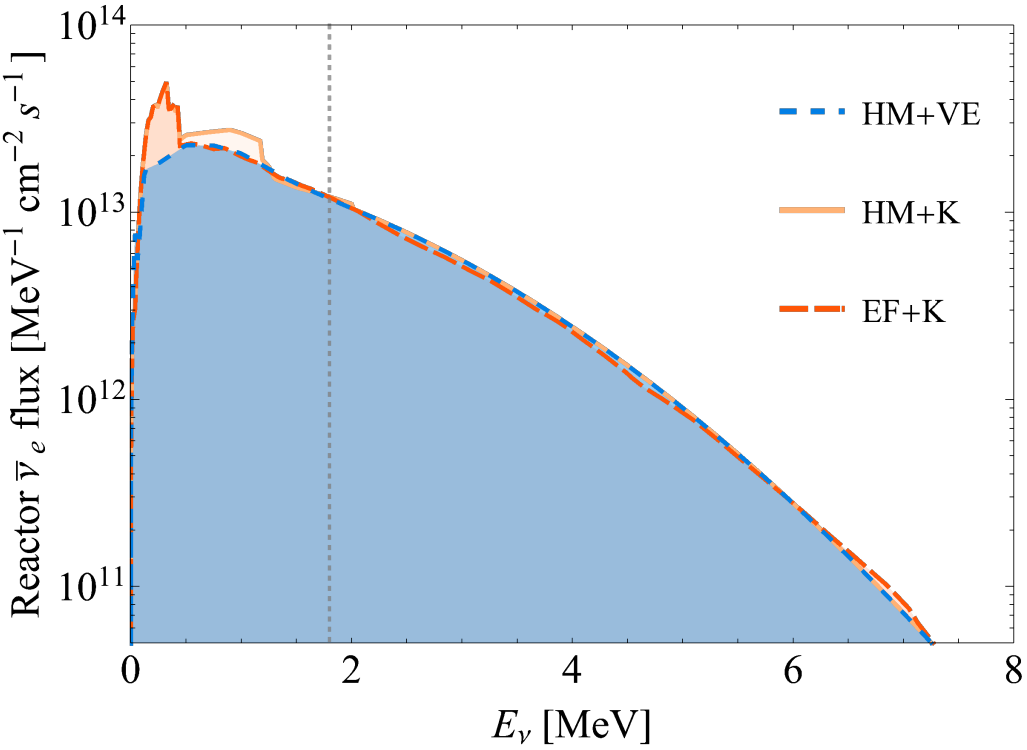

Figure 2.19: Reactor electron anti-neutrino flux normalized to $\Phi_{\overline{\nu}_e} = 4.8 \cdot 10^{13}\,\mathrm{cm}^{-2}\mathrm{s}^{-1}$ (typical value for a power of $\sim 3\,\mathrm{GW_{th}}$ and a reactor-detector distance of $L \sim 10$ m) as a function of the neutrino energy for different predictions. HM describes the high energy regime according to Refs. [76, 77], while EF refers to the same regime but predicted from Ref. [78]. VE represents the classical prediction for the low energy spectrum which accounts only for the fission processes [75], while K refers to the description where the neutron capture process is calculated [79, 80]. The gray dashed vertical line indicates the IBD threshold.

In Fig. 2.18, the reactor electron anti-neutrino spectra for the different fission chains are shown together with the neutron capture one from the $^{238}\mathrm{U}(n,\gamma)^{239}\mathrm{U}$ process. For graphical purposes, the neutron capture spectra have been rescaled by a factor 1/20, so that is clear that it is the dominant contribution at low energies

(below the IBD threshold). The spectra in the figure have been obtained by using the predictions in Ref. [75] for $E_\nu < 2\,\mathrm{MeV}$ and from Ref. [76] for $E_\nu > 2\,\mathrm{MeV}$, as these are typical references for reactor neutrino spectra.
To obtain the actual flux, one has to sum the different contributions weighted by the mean energy per fission characteristic of the specific chain, which can be found in Ref. [81], and multiply them for the percentage of a certain isotope in the specific reactor that is being considered. The spectra have to be multiplied by the reactor power of the considered power plant, and then one has to consider the geometric factor which depends on the distance from the reactor at which one wants to evaluate the $\overline{\nu}_e$ flux.
In Fig. 2.19, we show an example of reactor neutrino flux, obtained considering a flux normalization of $\Phi_{\overline{\nu}_e} = 4.8 \cdot 10^{13}\,\mathrm{cm^{-2}s^{-1}}$, which is a typical value for a detector placed at ~ 10 m from the core of a $\sim 3\,\mathrm{GW_{th}}$ reactor power plant, and we compare different parametrization of the flux. Indeed, we consider three different scenarios, built on the combination of different predictions for the low energy spectra and for the high energy spectra [6]. In particular, we chose to follow the predictions for the high energy part of the spectra from Hubert and Mueller (HM) in Refs. [76, 77] and from Estienne and Fallot (EF) in Ref. [78], while for the low energy part, the description from Vogel and Engel (VE) in Ref. [75] and from Kopeikin (K) from Refs. [79, 80]. Let us notice that the description from Kopeikin is the only one where the neutron capture term is calculated, so that at low energy the flux is higher. The VE parametrization is instead the classical calculation of the fission components only, so in some sense, it represents a sort of "benchmark" prediction for the reactor anti-neutrino spectra at low energy. For the high energy regime instead, HM and EF are very similar, so the choice of one or another parametrization doesn't affect significantly the flux definition.
By looking at Fig. 2.19, we can notice that, independently of the specific parametrization, nuclear power plants can deliver an enormous number of neutrinos, resulting in a very intense flux. Another interesting aspect is that the flux is picked around $E_\nu \sim 1-2$ MeV, and extends up to $E_\nu \sim 8-10$ MeV, so covering basically the same energy range of solar neutrinos from boron (green dashed curve in Fig. 2.13) and CNO neutrinos from oxygen (orange dashed curve in the same figure). Hence, it is clear that reactor anti-neutrinos are a suitable neutrino source to study CEνNS and νES, especially with a detector installed at distances around ~ 10 m from the reactor core.

2.3.4 —— Neutrinos from $\pi(K)$ decay-at-rest ——

Decay-at-rest neutrinos are neutrinos produced by the decay process of some heavier particles, such as charged pions $\pi^\pm$ and kaons $K^\pm$, in their rest reference frame. These decay processes have been already discussed as the responsible of atmospheric neutrinos, see Eq. 2.59, however in this context we speak about decay-at-rest (DAR) neutrinos referring to laboratory neutrino sources. In this sense, usually, neutrinos from $\pi^\pm$ decay-at-rest are said to be produced in the so-called π-DAR, while the ones from $K^\pm$ at the K-DAR.
Thus, the first step for such a neutrino source is to produce charged pions (kaons).

In order to produce pions, one can employ the collision between high energy protons (hundreds of MeV up to GeV scale) on a target, that produces a significant amount of hadrons, of which, a rather large number are pions, if the proton energy $E_p \geq 300$ MeV [82].
If the proton beam is at higher energies (GeV scale), the pions will not decay at rest, producing high energy neutrinos (which carry some of the pion momentum). Instead, by selecting a dense material for the target, for example, mercury target, the pions will lose energy in the material until the stop and decay-at-rest.
Protons impinging on the dense target material produce charged pion pairs. However, practically all ($\sim 99\%$) the negative pions get captured by the target material shortly after their production, so that only the positive pions travel in the material until their DAR. So, π-DAR neutrinos are mainly due to the π^+ decay, see the process in the left column of Eq. 2.59, and the subsequent μ^+ decay, see the left column in Eq. 2.60.
Spallation neutron source (SNS) facilities turn out to be the perfect place to have a production of π-DAR neutrinos as a side product. A virtuous example of this neutrino source is the Oak Ridge Laboratory SNS [82], where a pulsed ~ 1 GeV proton beam operating at a power of 1.4 MW is delivered on a liquid mercury target. Let us notice that for $E_p > 1.1$ GeV, also kaons would be produced, complicating the overall description and leading to the production of a higher energy flux component, but the K-DAR contribution will not be considered in this thesis work.

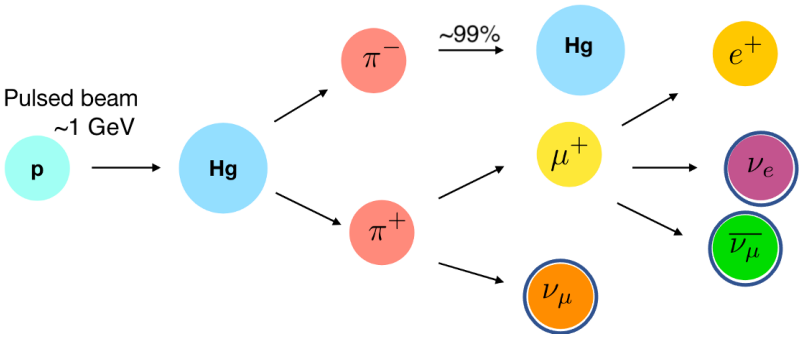

Figure 2.20: Schematic representation of a spallation neutron source, in which the π-DAR neutrino production mechanism is shown [83].

In Fig. 2.20, a scheme of the processes that produce neutrinos at the SNS through the π-DAR is shown. The decay process of the π^+ is a very fast process, with a decay constant $\tau_{\pi^+} = 26.033$ ns, whereas the subsequent μ^+ decay happens on a much slower time scale, $\tau_{\mu^+} = 2.197\,\mu$s, so that the neutrino components are usually divided in two groups: the prompt neutrinos and the delayed neutrinos. This particular time structure is very useful from the experimental point of view, as it allows one to exploit a timing information in the data analysis. In Fig. 2.21, we show the arrival time distribution $P_\nu(t)$ for the prompt and delayed flux components, according to the information provided in Ref. [54] for the SNS.
The time information can be used not only because of the very different decay time constants, but also because the SNS employs a pulsed proton beam. In this

way, neutrinos will in some sense be produced in coincidence or with a specific delay with respect to the proton beam time. We can say that the proton beam time gives in practice the "zero" time of the arrival time distribution of the neutrinos. Moreover, having a pulsed beam, allows one to disentangle beam correlated and beam uncorrelated backgrounds to have a better background rejection. This will be discussed in more detail in Sec. 2.4.1.
The prompt flux is constituted of a monochromatic ν_μ component with energy $E_{\nu_\mu} = 29.792$ MeV, obtained by the kinematic of the two body decay process. The delayed flux component is made of two contributions, one of $\overline{\nu}_\mu$ and one of ν_e, that have continuous spectrum up to the maximum energy available, $E_{\text{end}} = m_\mu/2 = 52.8$ MeV, where $m_\mu = 105.66$ MeV is the muon mass.

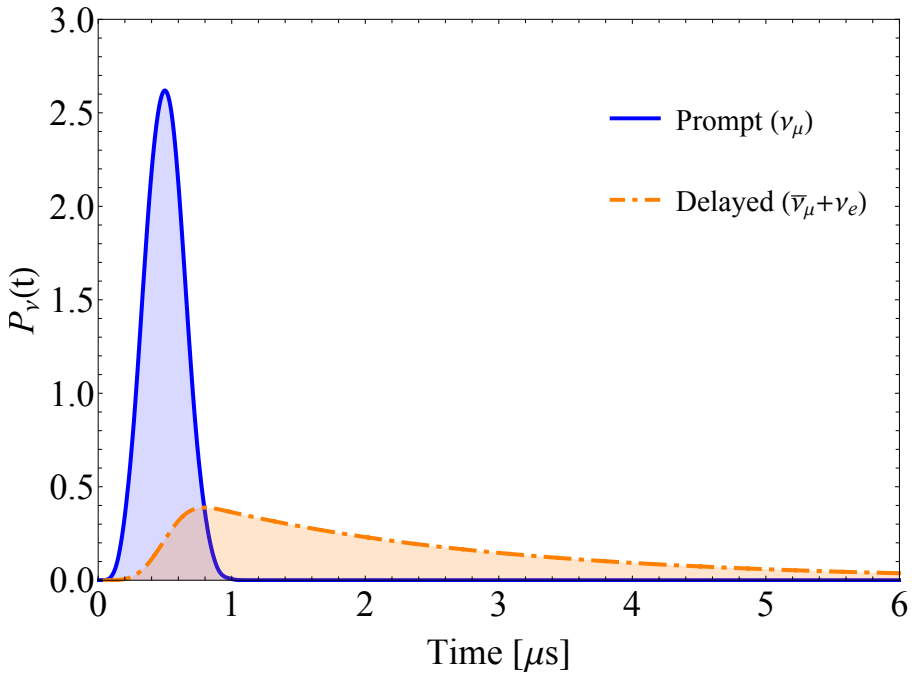

Figure 2.21: Arrival time distribution of the prompt (blue) and delayed (orange) neutrino flux components as a function of the time extracted from the information provided in Ref. [54] for the SNS during the COHERENT CsI data taking.

The three different neutrino fluxes can be described by the following distributions [1, 5]

$$\frac{dN_{\nu_\mu}}{dE_\nu} = \frac{rN_{POT}}{4\pi L^2}\delta\Big(E_\nu - \frac{m_\pi^2 - m_\mu^2}{2m_\pi}\Big), \tag{2.62}$$

$$\frac{dN_{\overline{\nu}_\mu}}{dE_\nu} = \frac{rN_{POT}}{4\pi L^2}\frac{64E_\nu^2}{m_\mu^3}\Big(\frac{3}{4} - \frac{E_\nu}{m_\mu}\Big), \quad (E_\nu \leq m_\mu/2) \tag{2.63}$$

$$\frac{dN_{\nu_e}}{dE_\nu} = \frac{rN_{POT}}{4\pi L^2}\frac{192E_\nu^2}{m_\mu^3}\Big(\frac{1}{2} - \frac{E_\nu}{m_\mu}\Big), \quad (E_\nu \leq m_\mu/2), \tag{2.64}$$

where $m_\pi = 139.57$ MeV is the charged pion mass, N_{POT} the number of protons-on-target (POT), r indicates the number of π^+ produced for each POT, hence the

number of neutrinos for each flavor, $\delta(x)$ is the Dirac delta function and L the distance at which the flux is evaluated at.
In Fig. 2.22, we show a typical SNS neutrino flux, divide into the three different flavor components, normalised according to the setup of the COHERENT CsI detector [54] that will be described in the next chapter (Sec. 2.4.1), so considering a number of POT $N_{POT} = 3.198 \cdot 10^{23}$, with a fraction of pions $r = 0.0848$ and a detector set at a distance of $L = 19.3$ m from the mercury target. The fluxes are presented in units of one SNS-year, in the sense that N_{POT} is the total number of POT in one year of operations at the SNS (~ 5000 hours). By comparing the SNS flux and the reactor neutrino flux in Fig. 2.19, it is clear that the latter one is much more intense with respect to the SNS one, although we consider a comparable distance between the neutrino source and the detector.

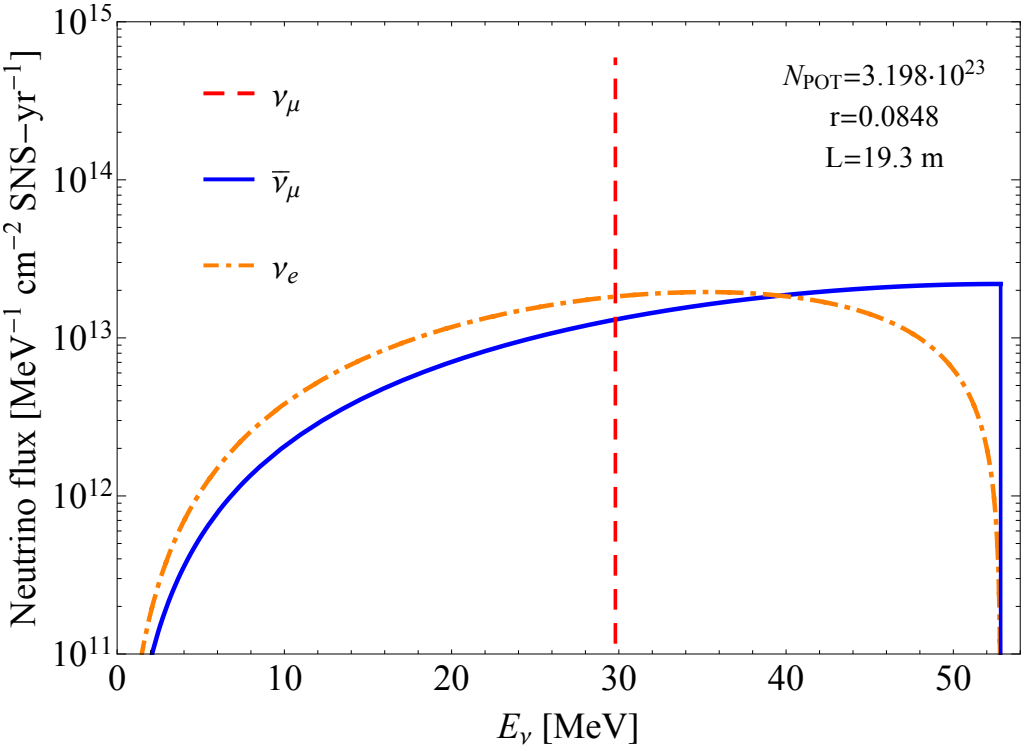

Figure 2.22: Neutrino flux at the SNS in Oak Ridge [82] as a function of the neutrino energy divided in the three different components. The vertical red dashed line corresponds to the monochromatic ν_μ line, while the other curves refer to the $\overline{\nu}_\mu$ (blue) and ν_e (orange) components. The fluxes are normalized considering the beam energy and power of the SNS, and $N_{POT} = 3.198 \cdot 10^{23}$, $r = 0.0848$ and $L = 19.3$ m, values relative to the COHERENT CsI detector configuration in Ref. [54].

From Fig. 2.22, it is also clear that the SNS provides neutrinos of energy up to ~ 50 MeV, so significantly above the reactor neutrino energies, and this is important in order to be sensitive to the nuclear form factors, and thus, to study nuclear structure. At K-DAR facility even higher neutrino energies are produced, so that they can complete the energy range of interest for CEνNS and νES measurements.

2.4 Experimental measurements

In this section, we will present the latest and most relevant experimental Collaborations, measurements and detectors in the field of CEνNS and νES research. In particular, the past and current COHERENT experimental program, which leads the CEνNS searches on a worldwide basis, will be discussed, together with the first observation of reactor CEνNS from the NCC-1701 germanium detector at the Dresden-II nuclear power plant[4]. Then, we will discuss the CEνNS and νES importance in direct dark matter searches in the context of noble liquid dual-phase TPC (time projection chamber) detectors, both using liquid xenon (LXe) and liquid argon (LAr) technologies, namely discussing the Lux-Zeplin measurement and the DarkSide-20k program. In this section, we will discuss also the statistical procedures adopted to analyse available data.

2.4.1 —— COHERENT ——

The COHERENT Collaboration is responsible for the first experimental observation of CEνNS [51], and it is still leading the field on a worldwide basis. The COHERENT detectors are all installed in the so-called "neutrino alley" at the Oak Ridge National Laboratory (ORNL) in Tennessee, in a corridor behind the interaction vertex of the SNS, shielded by a thick concrete wall [84].
The SNS provides high quality neutrinos from π-DAR (see Sec. 2.3.4) and working with a pulsed proton beam, allows experiments to have an efficient background rejection.

Nuclear target	target mass [kg]	Distance from source [m]	NR Energy threshold [keV]	Deployment period
CsI[Na]	14.57	19.3	5	2015-2019
Ar	24.4	27.5	20	2016-2021
Ge	18	22	<5	2022
NaI[Tl]	3500	22	13	2022
Ar	750	29	20	2025
Ge	50	22	<5	2025
CsI	10∼15	20	1.4	2025

Table 2.4: Summary of the different targets participating in the COHERENT experimental program together with their properties (such as target mass, distance, energy threshold and operation period) adapted from Ref. [84]. The gray background indicates the two detectors that have been operating and are now terminated. The green background indicates the detectors currently in operation or under development.

[4]For convenience, we will refer to this measurement as the Dresden-II measurement, and to the authors as Dresden-II Collaboration.

The COHERENT experimental program is made of a number of detectors with diverse nuclear targets, technologies and purposes. Some detectors have been developed to characterise the background levels around the neutrino alley, other represent the one to actually make the CEνNS measurements. The program is in continuous development, with some already dismissed detectors, some taking data, and some still being developed and installed. The situation of detectors installed at the neutrino alley is shown in Fig. 2.23, where the status updated to 2018 (upper) and to 2022 (lower) is shown.
In this thesis, we will discuss only the two detectors exploited for the two currently available CEνNS measurements, namely a cesium-iodine crystal, CsI, and a liquid argon single-phase detector, LAr. Other details about the background monitoring detector system and the undergoing experimental detectors which will lead next year's searches can be found in Ref. [84].

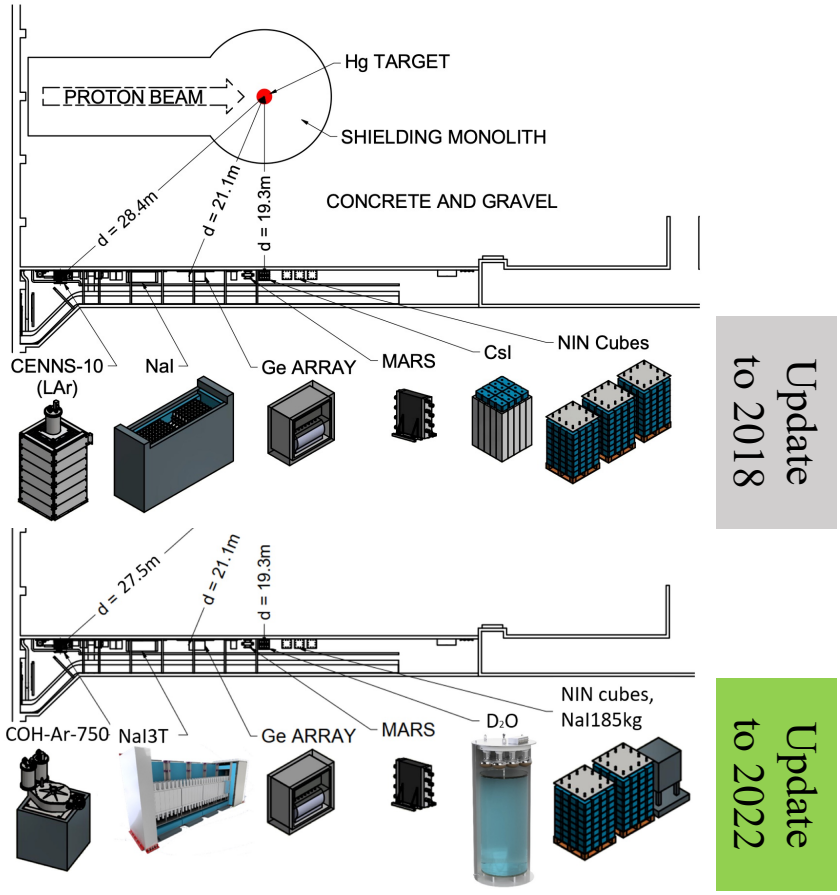

Figure 2.23: Schematic of the neutrino alley at ORNL showing the SNS proton beam and target, together with the COHERENT Collaboration detectors updated to 2018 (see Ref. [84]) and to 2022 (see Ref. [85]).

The COHERENT CsI experimental program has been particularly relevant as it has provided the first experimental proof of the CEνNS process in 2017 [51, 83], whose results have been updated in 2021 [54]. The detector is made of 14.57 kg of CsI[Na] crystal located at 19.3 m from the SNS mercury target, and it has observed around 130 CEνNS events in the first campaign, and up to 300 events in

the second campaign [51, 54, 83]. The first measurement led to a 6.7σ confidence level (C.L.) evidence of CEνNS over the background, improved to 11.6σ evidence with the second measurement. A schematic of the detector and its shielding system is shown in Fig. 2.24 (left).
In 2020 the COHERENT Collaboration reported the first measurement of CEνNS on a liquid argon target, thanks to the CENNS-10 detector: a single-phase liquid argon detector with a 24.4 kg active mass at 27.5 m from the SNS target. A schematic of the CENNS-10 detector and its shielding system is shown in Fig. 2.24 (right).

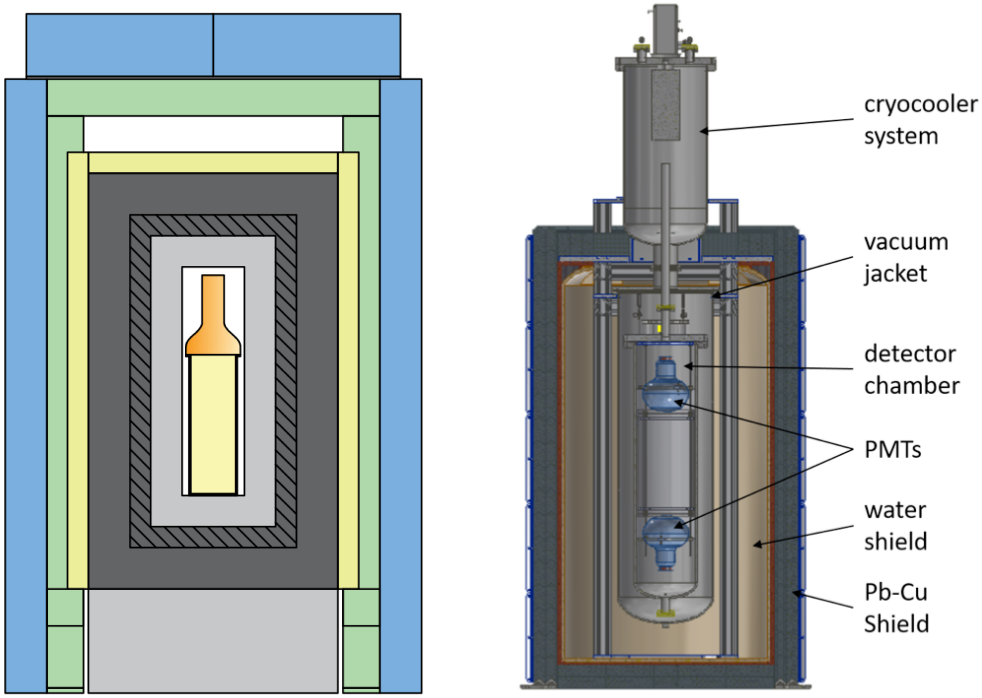

Figure 2.24: (Left) Schematic of the CsI[Na] shielding and detector at the SNS, taken from Ref. [83]. (Right) Schematic of the LAr (CENNS-10) detector with shielding taken from Ref. [85].

The first measurement campaign with the CENNS-10 detector led to the observation of around 160 CEνNS events, resulting in an observation at $\sim$3 σ. The second campaign finished in 2021, but the data are not yet available to the community, but are expected to improve the previous measurement.

COHERENT CsI measurements and Data analysis procedure

Thanks to the time information given by the π-DAR process, already discussed in Sec. 2.3, the data for the COHERENT CsI experimental program are given as a function of the number of extracted photo-electrons and as a function of the arrival time, as it is shown for the 2017 data set in Fig. 2.25. Indeed, the experimental variable is not the recoil energy, but the number of photo-electrons extracted as a consequence of a recoil in the target material.

The number of photo-electron $N_{\rm PE}$ is related to the recoil energy through the electron-equivalent recoil energy (or simply electron recoil energy), T_e, and the light yield, L_Y. The electron recoil (ER) energy, is obtained from the nuclear recoil (NR) energy, through the so-called quenching factor, f_Q, through

$$T_e = f_Q \times T_{\rm nr}\,, \tag{2.65}$$

where the quenching factor f_Q depends on the material and it is also a function of the recoil energy. Hence, f_Q is the ratio between the scintillation light produced by electron and nuclear recoils, respectively, and in practice, it determines the relation between the number of detected photo-electrons and the kinetic energy of the recoiling nucleus. However, the quenching factor is still quite an unknown quantity, as only a few measurements are available, and on a relatively limited energy range.

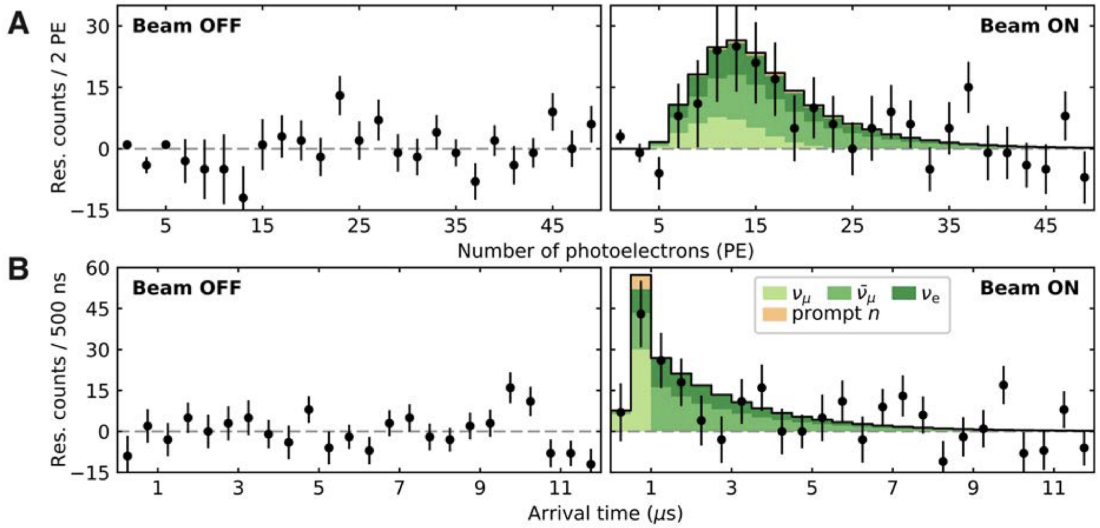

Figure 2.25: Residual counts for beam OFF and beam ON period as a function of the number of photo-electrons (upper panel) and of the arrival time (lower panel) for the COHERENT CsI 2017 measurement [51].

The light yield, instead, quantifies the response of the material to an electron recoil in terms of the number of photo-electrons extracted for a keV of ER energy deposited in the detector, so that

$$N_{\rm PE} = L_Y \times T_e = L_Y \times f_Q \times T_{\rm nr}\,. \tag{2.66}$$

At the time of Ref. [51], it was measured that a for a nuclear recoil energy[5] of $\sim \mathrm{keV_{nr}}$ approximately 1.17 photo-electrons are extracted.
The quenching factor for CsI was measured by the COHERENT Collaboration in 2017 and can be found in Ref. [51], together with the signal acceptance function as a function of the number of photo-electrons for the COHERENT CsI 2017 measurement.

[5]We have explicitly used the under-script "nr" to stress that we refer to a nuclear recoil energy. For electron recoils we will use the under-script "ee" (electron-equivalent).

In 2021 the COHERENT Collaboration released a new data set with the CsI detector [54], therefore, in this thesis, we will present the results from the analysis of the latest results. The new data set is shown in Fig. 2.26, always in the form of a function of the number of photo-electrons and time.
The number of protons of target for the latest measurement is $N_{\mathrm{POT}} = 3.198 \cdot 10^{23}$, with the fraction of produced pions $r = 0.0848$ and a light yield measured to be $L_Y = 13.35\,\mathrm{PE/keV}_{ee}$ [54].

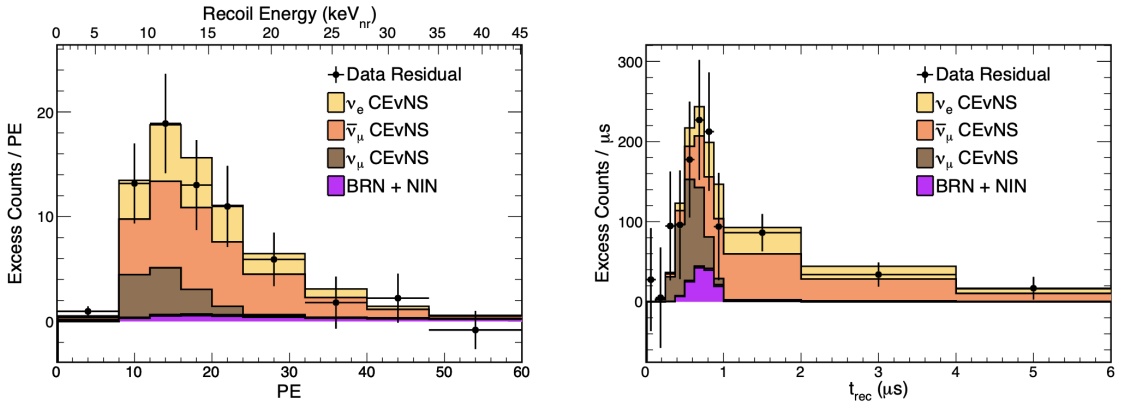

Figure 2.26: Excess counts as a function of the number of photo-electrons (left) and arrival time (right). The figure shows the data residuals, and the contribution from the three different neutrino flux components, together with two beam-related background components (BRN and NIN) [54].

In Fig. 2.26, together with the data residual, the histograms show the contribution of the different neutrino flux components, as described in Sec. 2.3.4. In the figure also two "beam-related" background components are shown, namely the BRN (beam related neutrons), which consists of neutrons produced by the SNS that produce a signal in the detector, and NIN (neutrino induced neutrons), a process already briefly introduced in Sec. 2.2.
The 2021 CsI measurement is not only characterised by a larger amount of collected data, but also by a redefined quenching factor, obtained by a larger amount of dedicated measurements, as described in Ref. [86], which is shown in Fig. 2.27 (left). The new quenching factor model for the CsI[Na] crystal, is built upon a polynomial function

$$f_Q^{\mathrm{CsI}}(T_{\mathrm{nr}}) = 0.0554628 + 4.30681\frac{T_{\mathrm{nr}}}{\mathrm{MeV}} - 111.707\left(\frac{T_{\mathrm{nr}}}{\mathrm{MeV}}\right)^2 + 840.384\left(\frac{T_{\mathrm{nr}}}{\mathrm{MeV}}\right)^3 . \quad (2.67)$$

Instead, in Fig. 2.27 (right) we show the signal acceptance, $A(N_{\mathrm{PE}})$, as a function of N_{PE} (and also nuclear recoil energy). In the supplemental of Ref. [54], also the time acceptance, ϵ_T, is presented, and has the form

$$\epsilon_T(t) = \begin{cases} 1 & t < a\,, \\ e^{-b(t-a)} & t \geq a\,, \end{cases} \quad (2.68)$$

with $a = 0.52\,\mu\mathrm{s}$ and $b = 0.0494/\mu\mathrm{s}$.
In that document, also the detector energy resolution, $R(N_{\mathrm{PE}}, N'_{\mathrm{PE}})$, is provided

and has the form of a Gamma distribution

$$R(N_{\rm PE}, N'_{\rm PE}) = \frac{[a_R(1+b_R)^{1+b_R}]}{\Gamma(1+b_R)} N_{\rm PE}^{b_R} e^{-a_R(1+b_R)N_{\rm PE}} , \tag{2.69}$$

with $a_R = 1/N'_{\rm PE}$ and $b_R = 0.716 N'_{\rm PE}$, $N_{\rm PE}$ being the number of detected photo-electrons and $N'_{\rm PE}$ the true number of photo-electrons.

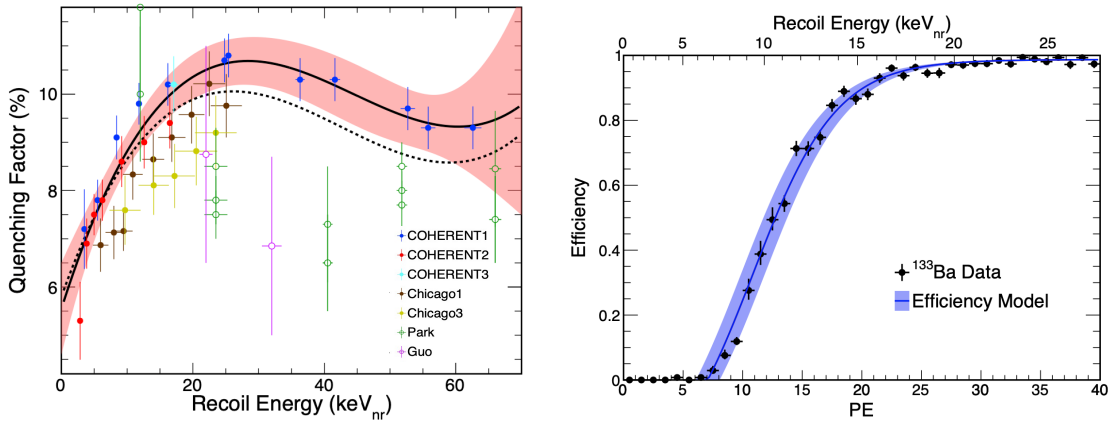

Figure 2.27: (Left) Quenching factor campaign measurement for CsI crystal as a function of the nuclear recoil energy adapted from Ref. [86]. The pink band shows the quenching model and its corresponding uncertainty. (Right) Signal acceptance as a function of $N_{\rm PE}$ (and nuclear recoil energy) taken from Ref. [54].

The first step to compare theory and experiment, is to compute the expected rate of CEνNS events for the COHERENT CsI detector. In order to do so, we need to fold the CEνNS cross section in Eq. 2.46 with the neutrino flux of the SNS, described in Eq. 2.62, Eq. 2.63, Eq. 2.64 and shown in Fig. 2.22, properly normalized to the location of the detector and data taking period. Thus, we can define the differential CEνNS rate as[6]

$$\frac{dR_{\nu_\ell}}{dT_{\rm nr}} = N(\mathcal{N}) \int_{E_\nu^{\rm min}}^{E_\nu^{\rm max}} \frac{dN_{\nu_\ell}}{dE_\nu} \times \frac{d\sigma_{\nu_\ell - \mathcal{N}}}{dT_{\rm nr}} dE_\nu , \tag{2.70}$$

where $N(\mathcal{N})$ is the number of target atoms in a kg of detector. One remark is that to obtain the rate on a CsI crystal, one has to sum together the cross section on cesium and iodine. To properly calculate the CEνNS cross section, one has to fix a parametrization for the nuclear form factors in Eq. 2.46 and use the appropriate nuclear radii reported in Tab. 2.2. A possible choice is known as the symmetrized two-parameter Fermi model [87], SF, which provides an analytic expression for the form factor, namely

$$F_Z^{\rm SF}(q^2) = \frac{3}{qc\,[(qc)^2 + (\pi qa)^2]} \left[\frac{\pi qa}{\sinh(\pi qa)}\right] \left[\frac{\pi qa \sin(qc)}{\tanh(\pi qa)} - qc\cos(qc)\right] . \tag{2.71}$$

[6]Let us note that the calculation of the νES rate is practically identical, even if it is a function of the electron recoil energy and not nuclear recoil energy. However, since as shown in Fig. 2.9 we showed the SM prediction of νES cross section to be much smaller than the CEνNS one, we will now concentrate only on CEνNS rates, and discuss νES ones only in beyond the standard model theories for which it produces a non-negligible impact.

The SF parametrization of the form factor depends on two model parameters, c and a. c is the half-density radius and a is the diffuseness parameter, which describes the drop of the density in the periphery of the nucleus. a is related to the surface thickness t through $t = 4\ a\ \ln(3)$ and is commonly fixed to the value $t = 2.30$ fm both for the neutron and proton form factor, as most of the theoretical nuclear models predict roughly the same density drop between proton and neutron distributions. The *root-mean-square* (rms) radius is related to a through $R^2 = 3/5\, c^2 + 7/5\, (\pi a)^2$ and, for the proton distribution inside the nucleus, we use the proton rms radii obtained from the muonic atom spectroscopy data [58, 59].

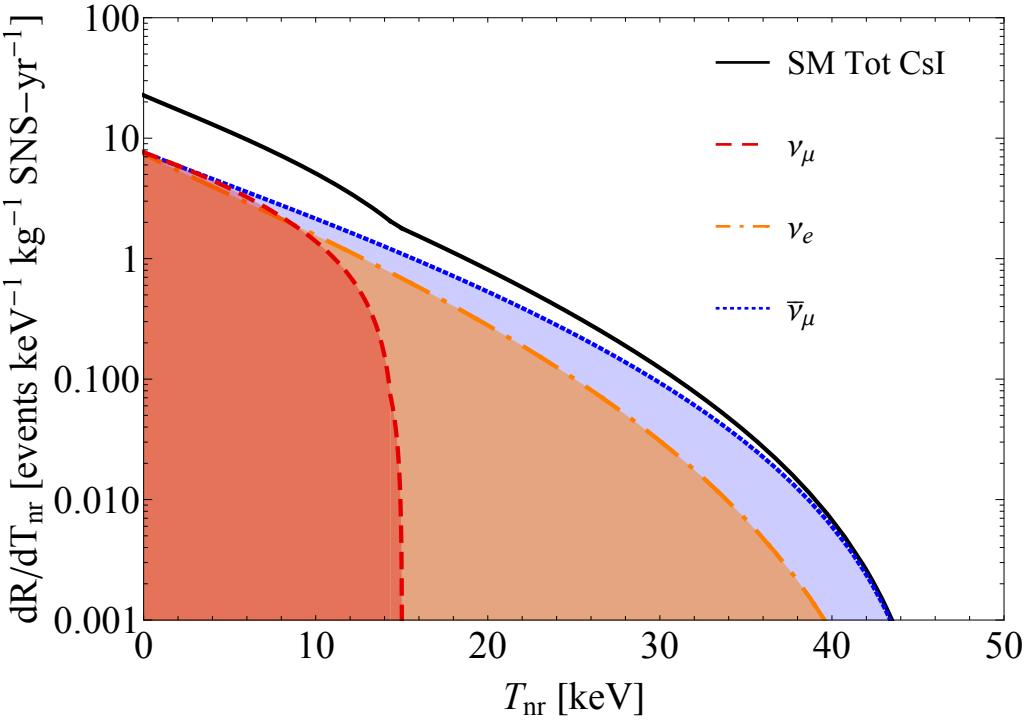

Figure 2.28: Standard model CEνNS event rate as a function of the nuclear recoil energy considering a CsI target. The different colored regions indicate the three different neutrino flux components, while the black curve is the total expected event rate.

For the neutron form factor, we have used a different description, known as Helm parametrization [88], given by

$$F^{\text{Helm}}\left(|\vec{q}|^2\right) = 3\frac{j_1(qR_0)}{qR_0}e^{-|\vec{q}|^2 s^2/2}, \tag{2.72}$$

where $j_1(x) = \sin(x)/x^2 - \cos(x)$ is the order-one spherical Bessel function, while R_0 is the box (or diffraction) radius. The rms radius of the corresponding nucleon distribution is given by $R^2 = 3/5R_0^2 + 3s^2$, where the parameter s quantifies the so-called surface thickness. We consider a value of $s = 0.9$ fm, which is the typical value determined for the proton form factor for this type of nuclei [89]. A detailed discussion of form factor descriptions and models will be presented in Sec. 3.1, also because the choice of using Helm or SF in the context of COHERENT

data leads to practically identical results.
In Fig. 2.28, we show the standard model rate of CEνNS events for the COHERENT CsI detector as a function of the nuclear recoil energy. The black line shows the total rate, while the colored curves indicate the three different neutrino components' contribution to the rate. Let us note that the rate decreases significantly around $T_{\rm nr}$ ∼40-50 keV due to the effect of the nuclear form factors.
Such rate needs to be converted into an integrated number of events for each of the experimental energy (and time) bins. The number of events in the i energy bin can be obtained by

$$N_i^{\rm CE\nu NS}(\mathcal{N}) = M_{\rm det} \int_{T_{\rm nr}^i}^{T_{\rm nr}^{i+1}} dT_{\rm nr} A(T_{\rm nr}) \times \\ \times \int_0^{T'^{\rm max}_{\rm nr}} dT'_{\rm nr} R(T_{\rm nr}, T'_{\rm nr}) \sum_{\nu_\ell = \nu_e, \nu_\mu, \overline{\nu}_\mu} \frac{dR_{\nu_\ell}}{dT'_{\rm nr}}, \tag{2.73}$$

where we recognise the acceptance $A(T_{\rm nr})$ and the energy resolution $R(T_{\rm nr}, T'_{\rm nr})$ already discussed before. $M_{\rm det}$ is the detector mass. To account for the time distribution, one has to calculate the number of theoretical CEνNS events not only in the i energy bin, but also in the j time interval

$$N_{ij}^{\rm CE\nu NS} = (N_i^{\rm CE\nu NS})_{\nu_\mu} P_j^{(\nu_\mu)} + (N_i^{\rm CE\nu NS})_{\nu_e, \overline{\nu}_\mu} P_j^{(\nu_e, \overline{\nu}_\mu)}, \tag{2.74}$$

where we use the fact that the ν_μ constitutes a prompt neutrino flux. $P_j^{\nu_\mu}$ and $P_j^{(\nu_e, \overline{\nu}_\mu)}$ are obtained by integrating the time arrival distributions, shown in Fig. 2.21, with the time efficiency in the corresponding time interval j.
$N_{ij}^{\rm CE\nu NS}$ can now be compared with the experimental number of events in the correspondent i-th energy bin and j-th time bin.
To statistically compare the theoretical rate with the data, we can build a chi-square function. Since the COHERENT CsI present several bins with a significantly low number of events, we build a Poissonian chi-square function [25, 90], instead of the typical Gaussian one,

$$\chi^2_{\rm CsI} = 2 \sum_{i=1}^{9} \sum_{j=1}^{11} \left[\sum_{z=1}^{4} (1+\eta_z) N_{ij}^z - N_{ij}^{\rm exp} + N_{ij}^{\rm exp} \ln \left(\frac{N_{ij}^{\rm exp}}{\sum_{z=1}^{4} (1+\eta_z) N_{ij}^z} \right) \right] + \\ + \sum_{z=1}^{4} \left(\frac{\eta_z}{\sigma_z} \right)^2, \tag{2.75}$$

where the indices i, j represent the nuclear-recoil energy and arrival time bin, respectively, while the indices $z = 1, 2, 3, 4$ for N_{ij}^z stand, respectively, for CEνNS, ($N_{ij}^1 = N_{ij}^{\rm CE\nu NS}$), beam-related neutron ($N_{ij}^2 = N_{ij}^{\rm BRN}$), neutrino-induced neutron ($N_{ij}^3 = N_{ij}^{\rm NIN}$) and steady-state ($N_{ij}^4 = N_{ij}^{\rm SS}$) backgrounds obtained from the anti-coincidence data provided by the COHERENT Collaboration. In our notation, $N_{ij}^{\rm exp}$ is the experimental event number obtained from coincidence data and $N_{ij}^{\rm CE\nu NS}$ is the predicted number of CEνNS events that depends on the physics model under consideration, so here the SM prediction.

We take into account the systematic uncertainties with the nuisance parameters η_z, which allows the components to fluctuate in the fit, and the corresponding uncertainties $\sigma_{\text{CE}\nu\text{NS}} = 0.12$, $\sigma_{\text{BRN}} = 0.25$, $\sigma_{\text{NIN}} = 0.35$ and $\sigma_{\text{SS}} = 0.021$ as explained in Refs. [5, 54].
Let us conclude by saying that the procedure just described is rather general and will be followed in all the BSM scenarios studied in this thesis work. When considering BSM effects, the number of theoretical events, $N_{ij}^{1} = N_{ij}^{\text{CE}\nu\text{NS}}$, will be modified and in some scenarios also the corresponding nuisance parameter uncertainty will be modified, to avoid double counting.
In the case in which also νES contribution is included in the fit, the chi-square function has to be modified to incorporate such contribution. A description of such a modified chi-square function and the discussion on the nuisance parameters to be considered can be found in Ref. [6].

COHERENT LAr measurement and Data analysis procedure

The COHERENT LAr measurement will be discussed in a similar way to what was done for the CsI measurement, but with the difference that the LAr data set is provided directly as a function of the electron-equivalent recoil energy T_e, instead of than number of photo-electrons. The data are shown in Fig 2.29 as a function of the arrival time (left) and the recoil energy (right) together with the residual background components. In principle, in the data release file in Ref. [91], the data are provided in terms of a third variable, known as F_{90}, which quantifies the light fraction emitted in the first 90 ns after the recoil with respect to the total light collected. In fact, the liquid argon scintillation mechanism is rather complicate as it tends to form dimers and de-excite with a fast and a slow component.

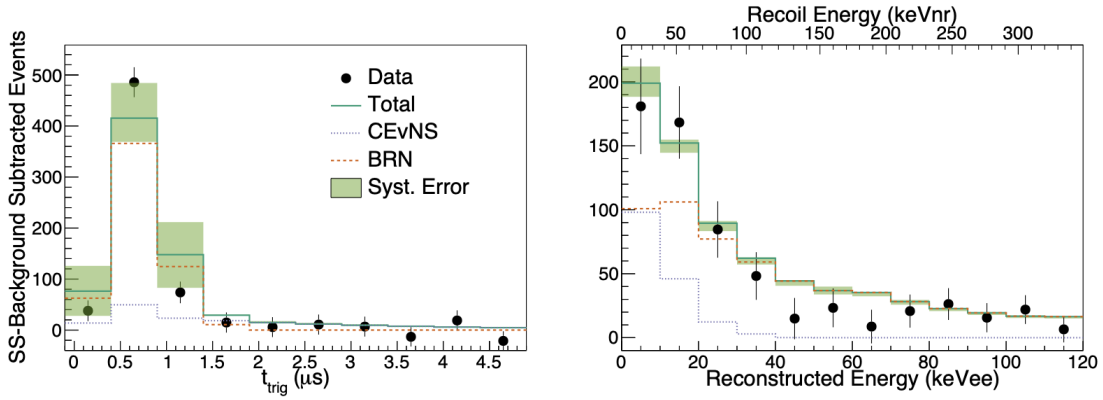

Figure 2.29: Excess counts as a function of the arrival time (left) and the recoil energy (right). The figure shows the data residuals and the contribution of the BRN background component [53].

Practically speaking, what is observed is that a nuclear recoil signal produces almost all the light within the first 90 ns, while electron recoils tend to produce the majority of the light after that time window, providing very useful information to discriminate nuclear recoils from electron recoils [53]. However, in our analysis of

the COHERENT LAr data, we neglect the F_{90} variable, using only the energy and time information, as it is done for the case of the CsI detector.
The quenching factor considered corresponds to a linear fit of the available data shown in Fig. 2.30 (left) in the nuclear recoil range between 0-125 $\mathrm{keV_{nr}}$. After that energy, the quenching is assumed to flatten and becomes a constant, so that the quenching model is given by [53, 91]

$$f_Q^{\mathrm{Ar}}(T_{\mathrm{nr}}) = \begin{cases} 0.00078 \times T_{\mathrm{nr}} + 0.246 & T_{\mathrm{nr}} \leq 125\,\mathrm{keV_{nr}}\,, \\ 0.3435 & T_{\mathrm{nr}} > 125\,\mathrm{keV_{nr}}\,. \end{cases} \tag{2.76}$$

In Fig. 2.30 (right) also the energy acceptance as a function of the recoil energy is shown. The COHERENT Collaboration performed two different analyses so that the corresponding acceptances are shown. In particular, we employed the analysis indicated as analysis A. For more details see Refs. [53, 91].

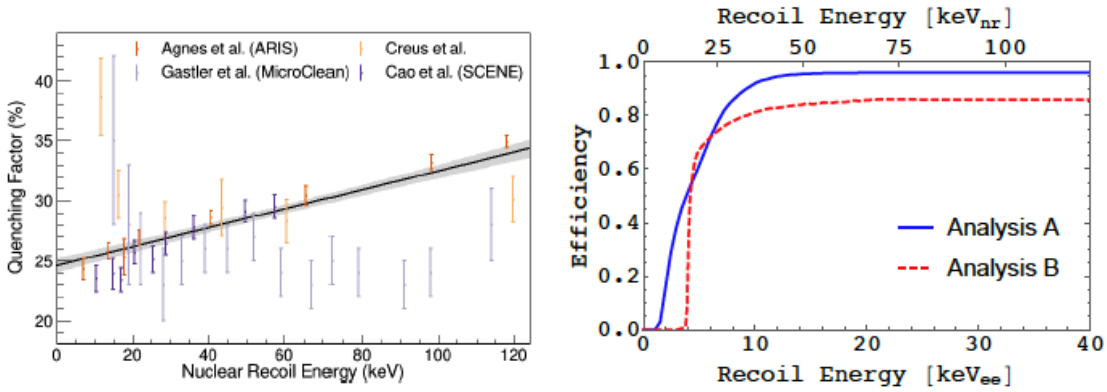

Figure 2.30: (Left) Quenching factor campaign measurement for liquid-Ar as a function of the nuclear recoil energy taken from Ref. [53]. (Right) Signal acceptance as a function of both the nuclear, T_{nr}, and electron, T_e, recoil energies, taken from Ref. [53].

More details about the arrival time distribution and time acceptance can be found in the data release in Ref. [91], but the discussion is rather similar to the one of the CsI measurement.
A crucial difference with respect to the CsI data set, besides the different detector location, is the number of protons of targets. In the case of the argon measurement, $N_{\mathrm{POT}} = 1.37 \cdot 10^{23}$, and the π fraction is $r = 0.09$.
To analyze COHERENT LAr data, we have calculated the experimental event rates following the same procedure adopted for the COHERENT CsI measurement. The theoretical event rate as a function of the nuclear recoil energy for CEνNS on argon is shown in Fig. 2.31, together with the curves from each of the neutrino flux components. By comparing the rate for argon with the one for CsI (see Fig. 2.28), we can notice that the rate on argon is smaller due to the argon being a lighter nucleus, but it expands on a larger nuclear recoil range. In fact, the suppression due to the form factors becomes significant at higher recoil energies, around $T_{\mathrm{nr}} \sim 120\,\mathrm{keV}$.

To fit the data, we have defined a Gaussian least-square function [5]

$$\chi^2_{\rm Ar} = \sum_{i=1}^{12}\sum_{j=1}^{10}\left(\frac{N_{ij}^{\rm exp} - \sum_{z=1}^{4}(1+\eta_z+\sum_l \eta^{\rm sys}_{zl,ij})N^z_{ij}}{\sigma_{ij}}\right)^2 + \\ + \sum_{z=1}^{4}\left(\frac{\eta_z}{\sigma_z}\right)^2 + \sum_{z,l}(\epsilon_{zl})^2\,, \tag{2.77}$$

where also here i refers to the energy bins and j to the time bins. Here, $z = 1,2,3,4$ stands for the theoretical prediction of CEνNS, Steady-State (SS), Prompt Beam-Related Neutron (PBRN) and Delayed Beam-Related Neutron (DBRN) backgrounds, and $N_{ij}^{\rm exp}$ is the number of observed events in each energy and time bin.

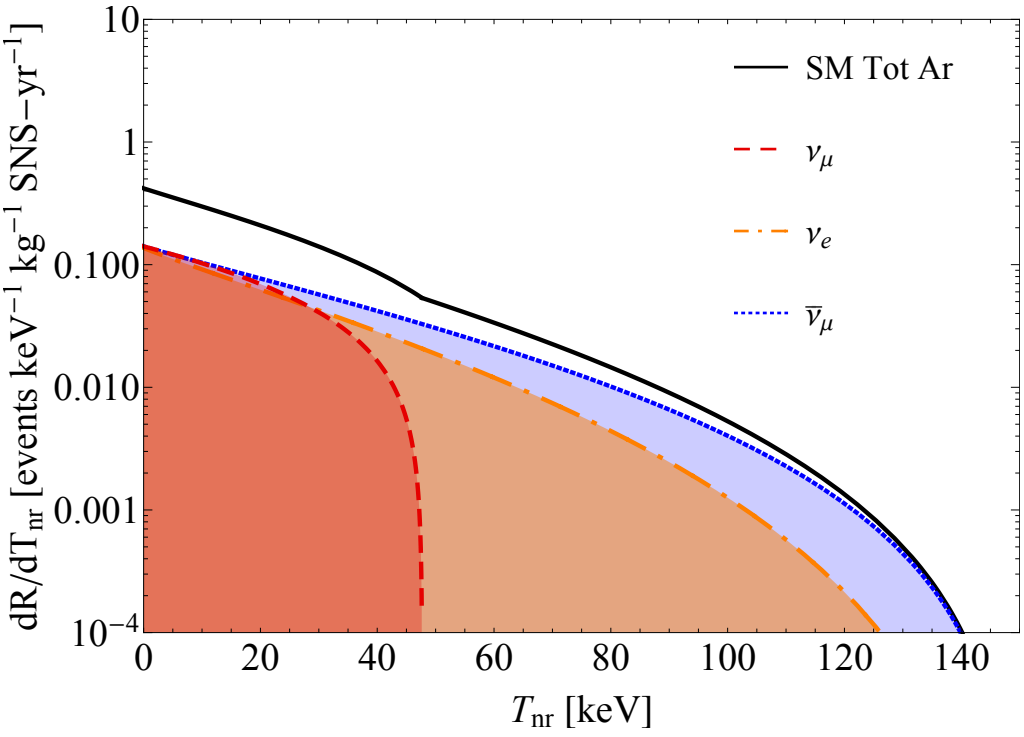

Figure 2.31: Standard model CEνNS event rate as a function of the nuclear recoil energy considering an Ar target. The different colored regions indicate the three different neutrino flux components, while the black curve is the total expected event rate.

The statistical uncertainty σ_{ij} is given by

$$(\sigma_{ij})^2 = (\sigma_{ij}^{\rm exp})^2 + (\sigma_{ij}^{\rm SS})^2, \tag{2.78}$$

where $\sigma_{ij}^{\rm exp} = \sqrt{N_{ij}^{\rm exp}}$ and $\sigma_{ij}^{\rm SS} = \sqrt{N_{ij}^{\rm SS}/5}$. The factor 1/5 is due to the 5 times longer sampling time of the SS background with respect to the signal time window. The nuisance parameters η_z quantify the systematic uncertainties of the event rate for the theoretical prediction of CEνNS, SS, PBRN, and DBRN backgrounds,

with the corresponding uncertainties $\sigma_{\mathrm{CE}\nu\mathrm{NS}} = 0.13$, $\sigma_{\mathrm{PBRN}} = 0.32$, $\sigma_{\mathrm{DBRN}} = 1$, and $\sigma_{\mathrm{SS}} = 0.0079$. We considered also the systematic uncertainties of the shapes of CEνNS and PBRN spectra using the information in the COHERENT data release [91]. This is done in Eq. (2.77) through the nuisance parameters ϵ_{zl} and the terms $\eta^{\mathrm{sys}}_{zl,ij}$ given by

$$\eta^{\mathrm{sys}}_{zl,ij} = \epsilon_{zl}\,\frac{N^{\mathrm{sys}}_{zl,ij} - N^{\mathrm{CV}}_{zl,ij}}{N^{\mathrm{CV}}_{zl,ij}}, \tag{2.79}$$

where l is the index of the source of the systematic uncertainty. Here $N^{\mathrm{sys}}_{zl,ij}$ and $N^{\mathrm{CV}}_{zl,ij}$ are, respectively, 1σ probability distribution functions (PDFs) described in Table 3 of Ref. [91] and the central-value (CV) SM predictions described in Table 2 of Ref. [91]. For the theoretical prediction of CEνNS ($z = 1$), the sources of systematic shape uncertainties are the F_{90} energy dependence and the mean time to trigger (t_{trig}) distribution. For the PBRN background ($z = 2$), the sources of systematic shape uncertainties are the energy, t_{trig} mean, and t_{trig} width distributions.
As already discussed in the case of COHERENT CsI data, in case of beyond the standard model scenarios, $N^{\mathrm{CE}\nu\mathrm{NS}}$, will be properly modified inside the chi-square function. In order to perform combined analysis using both data sets, the least-squares function will be obtained by summing the function in Eq. 2.77 and the one in Eq. 2.75.

2.4.2 —— Dresden-II ——

In 2022, the first evidence of CEνNS from reactor neutrinos has been reported by the Dresden-II collaboration, using a 2.924 kg p-type point contact germanium detector, named NCC-1701 [92] with a low experimental threshold, namely $T_e = 0.2\,\mathrm{keV}_{ee}$. The detector is located in close proximity ($L \sim 10.39$ m) to the core of the Dresden-II boiling water reactor power plant, in Illinois.

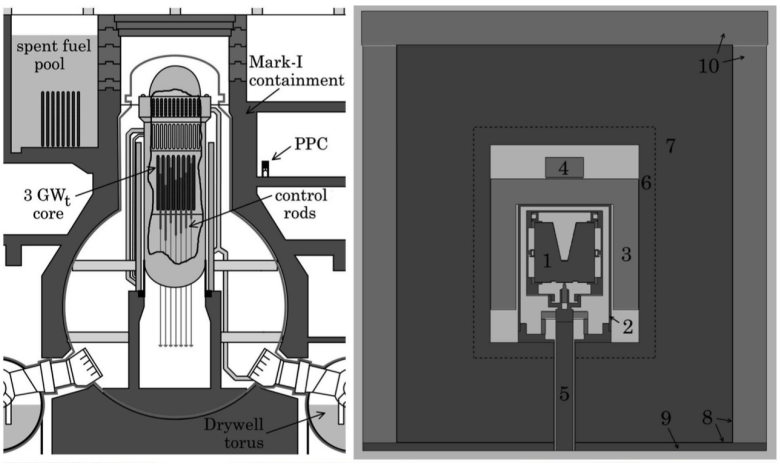

Figure 2.32: (Left) Schematic of the detector location within the Dresden-II boiling water reactor plant. (Right) Cross section of the NCC-1701 detector and its shielding system. Image taken from Ref. [93].

A schematic of the location of the detector and a cross section of the system are shown in Fig. 2.32. More technical details about the detector, shielding and acquisition system can be found in Ref. [93].
The data of interest have been collected between 22/1/2021 and 8/5/2021, with a reactor power of 2.96 $\mathrm{GW_{th}}$, resulting in 96.4 days of effective exposure. The flux normalization estimate at the reactor location during the operational period is $4.8 \cdot 10^{13}\,\overline{\nu}_e/\mathrm{cm^2 s}$, as in Fig. 2.19.
The quenching factor for the germanium crystal was measured by the same authors, and in particular they refer to two different possible models, fitting different data sets, namely the iron-filter (Fef) and the photo-neutron (YBe) ones [92, 94].

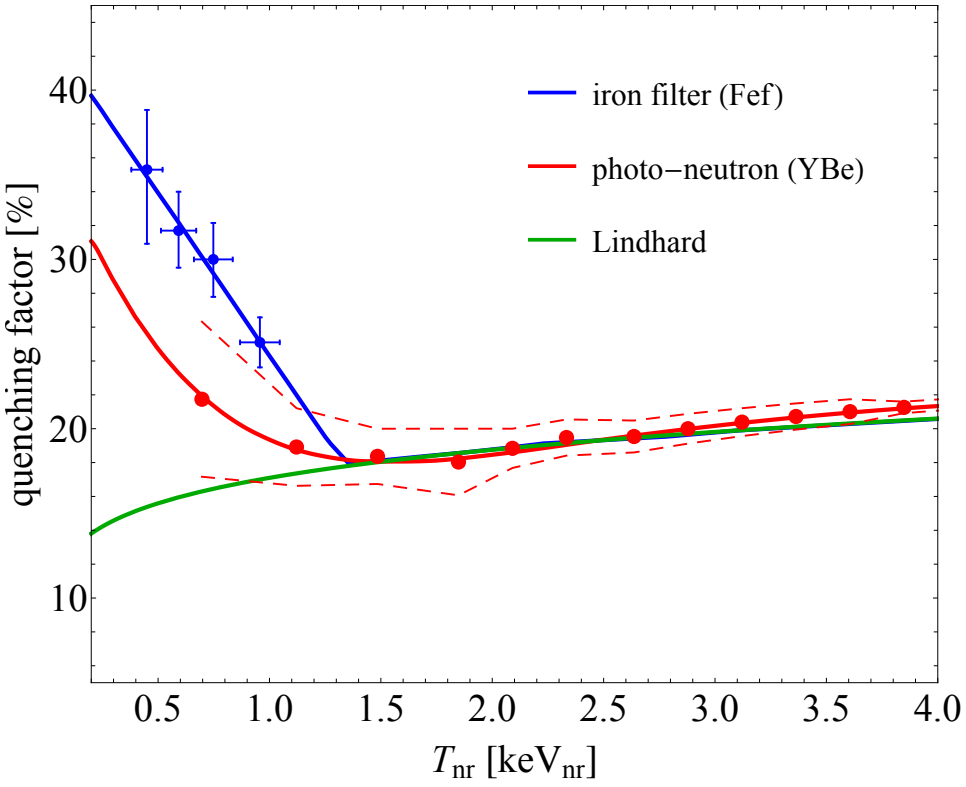

Figure 2.33: Germanium quenching factor measurement as a function of the nuclear recoil energy. The blue points and line correspond to the iron filter data, the red ones to the photo-neutron ones [92, 94]. The green line shows the standard Lindhard prediction of the quenching factor for germanium [95, 96].

These new measurements show a rather large quenching factor at tiny nuclear recoil energies (below $\sim 1\,\mathrm{keV_{nr}}$), with respect to the expectation of traditional quenching factor models, such as the Lindhard model.
The Lindhard model for the quenching factor is considered a standard quenching reference in the community, and in particular for germanium it is defined by [95, 96]

$$f_Q^{\mathrm{Ge}}(T_{\mathrm{nr}}) = \frac{k_{\mathrm{Ge}} \cdot g_{\mathrm{Ge}}(T_{\mathrm{nr}})}{1 + k_{\mathrm{Ge}} \cdot g_{\mathrm{Ge}}(T_{\mathrm{nr}})}\,, \tag{2.80}$$

with $k_{\mathrm{Ge}} = 0.157$, and $g_{\mathrm{Ge}}(T_{\mathrm{nr}}) = 3[\epsilon_{\mathrm{Ge}}(T_{\mathrm{nr}})]^{0.15} + 0.7 \cdot [\epsilon_{\mathrm{Ge}}(T_{\mathrm{nr}})]^{0.6} + \epsilon_{\mathrm{Ge}}(T_{\mathrm{nr}})$ and $\epsilon_{\mathrm{Ge}}(T_{\mathrm{nr}}) = 11.5\, Z_{\mathrm{Ge}}^{-7/3} \cdot T_{\mathrm{nr}}$.

According to the authors, the Lindhard theory is not suitable to describe the microscopic mechanisms that govern the quenching factor at low recoil energies. However, there is not even a clear physical explanation for such larger values of the quenching. Therefore, many discussions are ongoing in the community, in the direction of the need for further quenching measurements in the full recoil range. Since the data are provided as a function of the electron recoil energy, we need to account for the quenching factor to determine the rate, when making the convolution of the CEνNS cross section[7] in Eq. 2.46 with the reactor neutrino flux shown in Fig. 2.19. The theoretical number of CEνNS events in each electron recoil energy bin is given by [6]

$$N_i^{\mathrm{CE}\nu\mathrm{NS}}(\mathcal{N}) = N(\mathrm{Ge}) \int_{T_\mathrm{e}^i}^{T_\mathrm{e}^{i+1}} dT_\mathrm{e} \int_{T_\mathrm{nr}^{\prime\min}}^{T_\mathrm{nr}^{\prime\max}} dT'_\mathrm{nr}\, R(T_\mathrm{e}, T'_\mathrm{e}(T'_\mathrm{nr})) \times \\ \times \int_{E_{\min}(T'_\mathrm{nr})}^{E_{\max}} dE \frac{dN_{\overline{\nu}}}{dE}(E) \frac{d\sigma_{\overline{\nu}-\mathcal{N}}}{dT'_\mathrm{nr}}(E, T'_\mathrm{nr}), \tag{2.81}$$

where $\mathcal{N} = {}^A_Z\mathrm{Ge}$ with $A = 70, 72, 73, 74, 76$, and $N_i^{\mathrm{CE}\nu\mathrm{NS}}(\mathrm{Ge}) = \sum_A f({}^A_Z\mathrm{Ge}) \cdot N_i^{\mathrm{CE}\nu\mathrm{NS}}({}^A_Z\mathrm{Ge})$, where $f({}^A_Z\mathrm{Ge})$ are the germanium isotopic abundances. Moreover, $N(\mathrm{Ge}) = 2.43 \times 10^{25}$ is the number of germanium atoms, $T_\mathrm{nr}^{\prime\min} \simeq 2.96$ eV is the minimum average ionization energy in Ge and $R(T_\mathrm{e}, T'_\mathrm{e}(T'_\mathrm{nr}))$ is the detector energy resolution function. The detector energy-resolution function is described as a truncated Gaussian [6]

$$R\left(T_\mathrm{e}, T'_\mathrm{e}(T'_\mathrm{nr})\right) = \left(\frac{2}{1 + \mathrm{Erf}\left(\frac{T'_\mathrm{e}(T'_\mathrm{nr})}{\sqrt{2}\sigma'_e}\right)} \right) \frac{1}{\sqrt{2\pi}\sigma'_e} e^{-\frac{\left(T_\mathrm{e} - T'_\mathrm{e}(T'_\mathrm{nr})\right)^2}{2{\sigma'_e}^2}}, \tag{2.82}$$

with a standard deviation equal to $\sigma'_e = \sqrt{\sigma_n^2 + \eta F_f T_\mathrm{e}}$, where the average energy of electron-hole formation is $\eta = 2.96$ eV and the Fano factor is $F_f = 0.11$ for Ge [92]. Finally, in Eq. (2.81) the experimental acceptance does not appear since the data points provided in the data release are already corrected for it.
In the energy region of interest of Dresden-II, $0.2\,\mathrm{keV_{ee}} < T_\mathrm{e} < 1.5\,\mathrm{keV_{ee}}$, the main background components come from the elastic scattering of epithermal neutrons and the electron capture in ^{71}Ge. The epithermal neutron contribution, which is the dominant one in the CEνNS recoil-energy region, $T_\mathrm{e} \lesssim 0.5\,\mathrm{keV_{ee}}$, is described by an exponential function with decay constant T_epith plus a constant term N_epith. Instead, the electron capture peaks from ^{71}Ge, namely the L1-, L2- and M-shell peaks, are described each by a Gaussian function. The latter is parameterized by an amplitude A_i, the centroid T_i and the standard deviation σ_i, where $i =$ L1, L2 and M. Thus, the expected event rate of background is given by

$$\frac{dN^\mathrm{bkg}}{dT_\mathrm{e}} = N_\mathrm{epith} + A_\mathrm{epith} e^{-T_\mathrm{e}/T_\mathrm{epith}} + \sum_{i=\mathrm{L1,L2,M}} \frac{A_i}{\sqrt{2\pi}\sigma_i} e^{-\frac{(T_\mathrm{e} - T_i)^2}{2\sigma_i^2}}. \tag{2.83}$$

[7] Let us note that since the typical neutrino energies of reactor neutrinos are $E_\nu \sim 2\,\mathrm{MeV}$, the form factors in the cross section have a negligible impact.

Following Ref. [6, 92], the total amount of free parameters for the background prediction reduces to: $N_{\rm epith}$, $A_{\rm epith}$, $T_{\rm epith}$, $A_{\rm L1}$, $E_{\rm L1}$, $\sigma_{\rm L1}$ and $\beta_{\rm M/L1}$. In fact, the amplitude of the L2 shell contribution can be expressed in terms of the amplitude of the L1 shell ($A_{\rm L1}$), in particular $A_{\rm L2}/A_{\rm L1} = 0.008$, and $\sigma_{\rm L2} = \sigma_{\rm L1}$. The centroid of the L1 Gaussian has nominal value $T_{\rm L1} = 1.297$ keV, while the L2 Gaussian one can be safely set to $T_{\rm L2} = 1.142$ keV. The standard deviation of the M-shell contribution can be fixed to the electronic noise uncertainty, which is $\sigma_n = 68.5$ eV for the Rx-ON (reactor operation period) data.

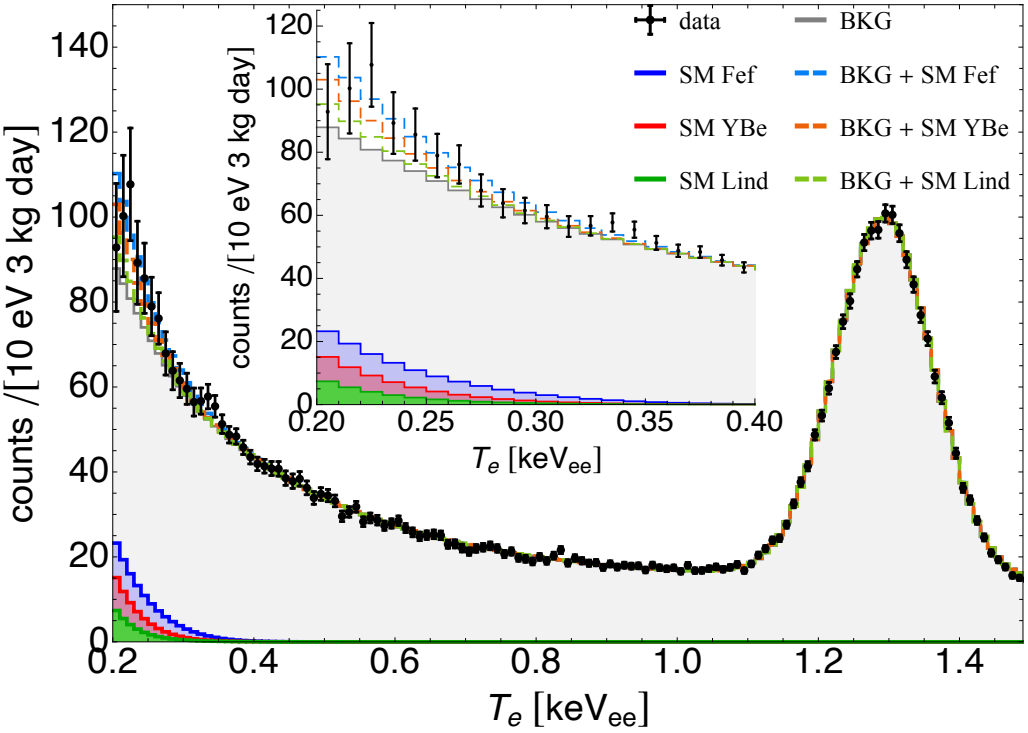

Figure 2.34: Event count rate as a function of the electron recoil energy T_e for the Dresden-II measurement. The black points correspond to the dataset provided by the authors in Ref. [92]. The gray curve instead shows the best fit of the background model (using the CEνNS with Fef). The blue, red and green curves correspond to the SM CEνNS rates obtained using the Fef, YBe and Lindhard quenching, respectively. The lighter blue, red and green dashed curves represent the background plus CEνNS rates for the corresponding quenching models. The inset shows a zoom of the rates in the region of interest of CEνNS searches.

The centroid of the M-shell Gaussian is fixed to its nominal value $T_{\rm M} = 0.158$ keV, being smaller than the experimental threshold whereas its amplitude is left free to vary in the fit with a constraint corresponding to the experimentally determined ratio $\beta_{\rm M/L1} = A_{\rm M}/A_{\rm L_1} = 0.16 \pm 0.03$.
To analyze the Dresden-II data, we build the following least-squares function [6]

$$\chi^2_{\rm Ge} = \sum_{i=1}^{130} \left(\frac{N_i^{\rm bkg} + \alpha(N_i^{\rm CE\nu NS}) - N_i^{\rm exp}}{\sigma_{\rm exp}} \right)^2 + \left(\frac{\beta - \beta_{\rm M/L1}}{\sigma_{\beta_{\rm M/L1}}} \right)^2 + \left(\frac{\alpha - 1}{\sigma_\alpha} \right)^2, \quad (2.84)$$

where $N_i^{\rm bkg}$ and $N_i^{\rm CE\nu NS}$ are the predictions in the i-th electron recoil energy bin

for the background and the CEνNS signal signal, respectively, and $N_i^{\rm exp}$ is the experimental number of events in the i-th bin. The nuisance parameter α takes into account the uncertainty on the neutrino flux (with $\sigma_\alpha = 2\%$), while $\beta_{\rm M/L1}$ is a prior for the M- to L1-shells ratio, with $\beta_{\rm M/L1} = 0.16$ and $\sigma_{\beta_{\rm M/L1}} = 0.03$.
In Fig. 2.34, we show the event rate predicted in the SM for CEνNS in the NCC-1701 detector considering the three different quenching models presented in Fig. 2.33. In the figure also the data set is shown together with an example of the expected background event rate (in gray), obtained by fitting the data assuming SM CEνNS and Fef quenching. To give an idea of how the CEνNS rate compares directly to the data, we show the rate for background plus CEνNS and an inset with a zoomed range in the low recoil regime. In fact, the SM CEνNS signal is all concentrated at low electron recoil energies, $T_e \lesssim 0.4\,\mathrm{keV}_{ee}$. Therefore, low thresholds are needed to measure CEνNS using reactor anti-neutrinos.
From Fig. 2.34, it is clear that the expected CEνNS event rate is rather low, especially compared to the counts due to the background components. Thus, for reactor CEνNS experiments, it is crucial to characterize the background, as it is difficult to reduce it, since for example, the timing information is missing (differently from the π-DAR experiments). Moreover, we see that the CEνNS event rate is strongly dependent on the considered quenching model. Using Fef (blue), the rate of events is significantly enhanced with respect to the one obtained according to the standard Lindhard theory (green), while the YBe quenching stands in the middle. Hence, in order to perform precision CEνNS measurements at reactor power plants, it is crucial to have a well tested and understood quenching factor, especially at low recoil energies.
In some beyond the standard model scenario, we will consider also the contribution given by the νES process. The discussion is rather similar, but for the different cross section. Additionally, the νES rate does not depend on the quenching factor model as it intrinsically depends on the elector recoil energy. When we will account for the νES contribution, in practice, the χ^2 function in Eq. 2.84 will be modified by adding to the $N_i^{\rm CE\nu NS}$ contribution the number of νES events in the same energy bin, $N_i^{\rm ES}$, weighted by the same α nuisance parameter.

2.4.3 —— Xenon based Dark Matter detectors: Lux-Zeplin ——

In this section, we will move from experiments developed in order to measure CEνNS, to experiments whose aim is to search for hypothetical dark matter particles interacting with target materials.
Among this very wide research field, we will concentrate on noble-elements dual-phase TPCs, and in particular, those filled with xenon (Xe) or argon (Ar). With dual-phase TPC, we refer to a time projection chamber filled with a liquid for most of its volume, but for a small gas pocket on the top, which constitutes the second phase of the chamber.
This technology is adopted widely in direct dark matter searches, where one looks for possible recoil signals in the TPC by dark matter particles coming from space. Such recoils would produce a first scintillation signal, called S1, that can be detected by a system of photo-multiplier tubes located at the top and at the bottom

of the chamber. Following the scintillation, material electrons get ionized, and thanks to an electric field applied between the bottom and the top of the chamber, they drift toward the gas phase (also known as gas pocket). Once the electrons reach the interface with the gas phase, they emit again light that is detected by the photo-multipliers. A schematic of the working mechanism of a LXe dual-phase TPC is shown in Fig. 2.35.

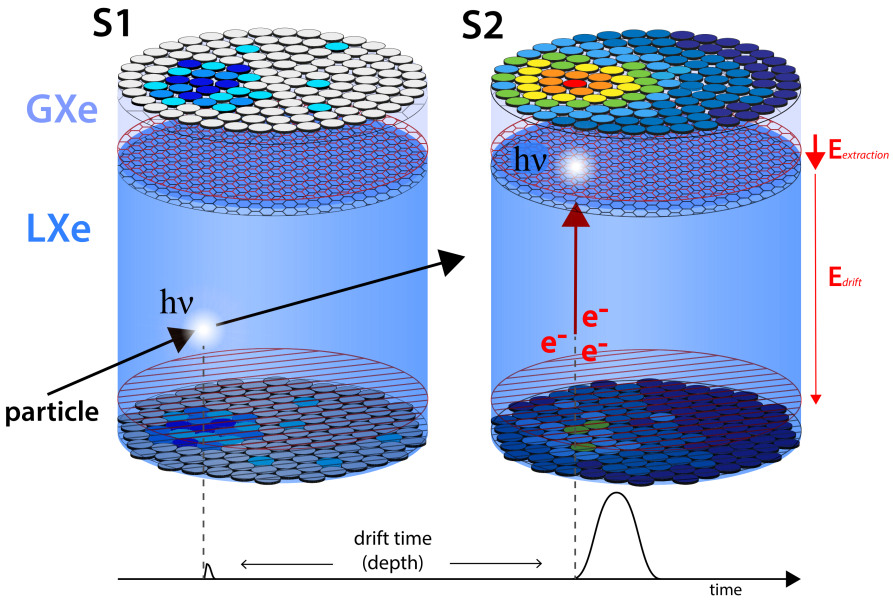

Figure 2.35: Schematic of the signals produced in a dual-phase TPC filled with xenon, taken from Ref. [97]. In particular, the left part of the picture shows the S1 signal, so the light produced by the recoil in the liquid xenon. The right part shows the S2 signal, so the one produced by the ionized electrons that after having been drifted, emit photons at the interface between the liquid phase and the gas pocket.

The collection of light in the photo-multipliers planes allows the reconstruction of the x-y position of the recoil event. Instead, the drift time, i.e. the time between the S1 and S2 signal, allows one to reconstruct the depth at which the event was generated in the chamber (z position), providing a quite good 3D reconstruction. This mechanism is rather general and can be applied also in the case of dual-phase TPC filled with argon or other noble liquids, although the scintillation mechanism can be slightly different from material to material. The electric field applied can also be different from detector to detector. The same applies to the read-out system and other technical details.
We will concentrate on the Lux-Zeplin (LZ) Collaboration, which has recently reported their first weakly interacting massive particles (candidate of dark matter) search [98] using an exposure of 60 live days and 7 t of LXe (5.5 t fiducial mass) at the Sandford Underground Research Facility in Lead, South Dakota.
Let us note that almost at the same time, also the XENON-nT Collaboration released their data, using a very similar LXe dual-phase TPC located at the Laboratori Nazionali del Gran Sasso (LNGS), in Italy, with 4.37 t of active mass and

a total exposure of 1.16 t yr. A discussion of their measurement can be found in Ref. [99].
Technical details on the LZ detector can be found in Ref. [98] and Ref. [100], while a schematic of it is shown in Fig. 2.36.
Like the other direct dark matter detectors, the LZ detector is located underground to exploit the ground rock as a natural shield from cosmogenic backgrounds. In particular, the LZ detector is shielded by an overburden of 4300 m water-equivalent.

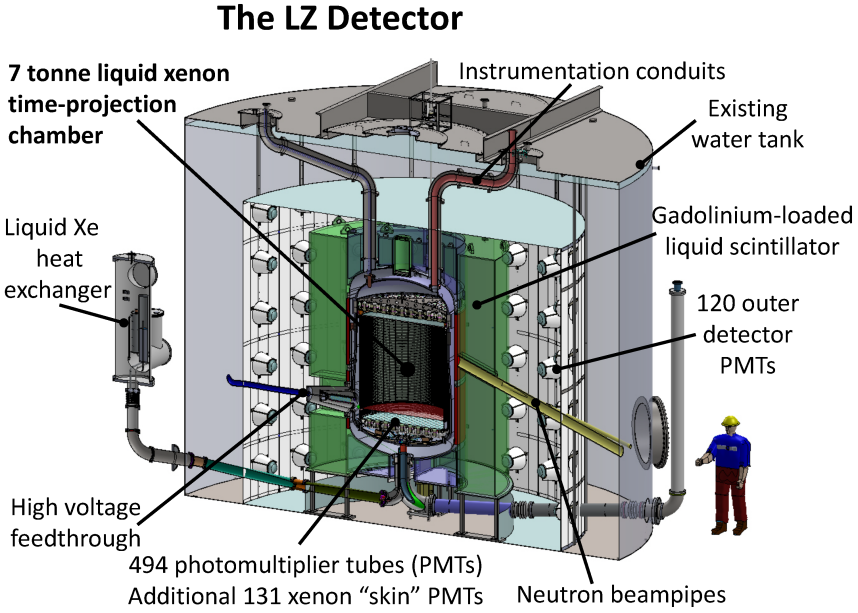

Figure 2.36: Schematic of the Lux-Zeplin dual-phase TPC located in the Sandford Underground Research Facility in South Dakota [98, 100].

Therefore, one of the backgrounds for direct dark matter detectors is due to solar neutrinos, as thanks to their weak cross section, they do not get shielded by the rock. Moreover, the dark matter particle searched for by this kind of experiments is expected to interact weakly and to produce a similar signature to the one produced by neutrinos interacting with nuclei in the active volume of the TPC, so it is not trivial to distinguish a signal from such hypothetical dark matter candidate and a neutrino. It is clear that CEνNS and νES are crucial to determine the background and analyse data of a direct dark matter experiment.
Furthermore, as we will discuss later in this thesis, dark matter detectors can also become "neutrino detectors", as some of their technical features made for dark matter searches, turn out to be very suitable and powerful when looking from beyond the standard model neutrino properties.
One interesting aspect of dark matter detectors is that they are designed to have very low energy thresholds. For instance, the LZ detector has a threshold around $\sim 5\,\mathrm{keV}_{\mathrm{nr}}$ ($\sim 1.5\,\mathrm{keV}_{ee}$).
The LZ Collaboration reported around 27 νES events in their region of interest (ROI), while the contribution of CEνNS results to be significantly smaller in that

recoil energy range, around 0.15 events, coming mainly from the contribution of ^{8}B solar neutrinos.
The total νES cross section to be considered is given by the weighted sum of the different neutrino flavor cross sections according to the oscillation mechanism, so that [7]

$$\frac{d\sigma_\nu}{dT_e}(E, T_e) = P_{ee}\frac{d\sigma_{\nu_e}}{dT_e} + \sum_{f=\mu,\tau} P_{ef}\frac{d\sigma_{\nu_f}}{dT_e}, \tag{2.85}$$

where $P_{ee} = \sin^4\theta_{13} + \cos^4\theta_{13}P^{2\nu}$ [101] is the average survival probability for solar neutrinos reaching the detector when considering the dominant pp and ^{7}Be fluxes and $P^{2\nu} \simeq 0.55$ [25, 38] is the ν_e survival probability in the two-neutrino oscillation scheme. Here, $P_{e\mu} = (1 - P_{ee})\cos^2\theta_{23}$ and $P_{e\tau} = (1 - P_{ee})\sin^2\theta_{23}$ are the transition probabilities. The values of the corresponding mixing angles θ_{13} and θ_{23} were taken from Ref. [25]. The cross sections are the ones defined in Eq. 2.16.

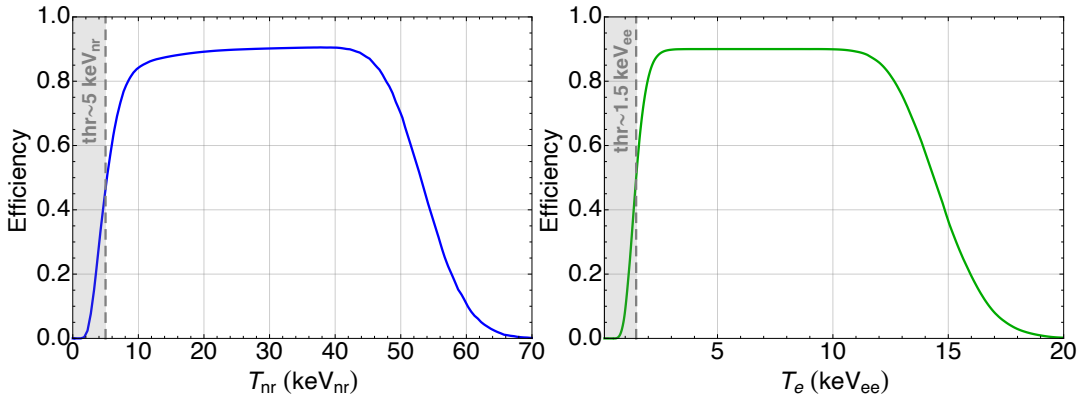

Figure 2.37: (Left) Signal efficiency of the LZ detector as a function of the nuclear recoil energy as provided by the collaboration in Ref. [98]. (Right) Signal efficiency of the LZ detector as a function of the electron recoil energy as obtained converting the nuclear recoil one using the NEST 2.3.7 software [7]. The gray vertical dashed lines indicate the energy thresholds in both cases.

The main components that contribute to the νES event rate in the ROI, are the pp flux and the monochromatic ^{7}Be 861 keV line, which have been presented in Fig. 2.13. Following a very similar strategy to the one used to analyse COHERENT data, we calculated the expected number of νES in each electron recoil energy bin by [7]

$$N_i^{\nu\mathrm{ES}} = N(\mathrm{Xe})\int_{T_e^i}^{T_e^{i+1}} dT_e\, A(T_e)\int_{E_{\min}(T_e)}^{E_{\max}} dE \sum_j \frac{dN_{\nu,j}}{dE}(E)\frac{d\sigma_\nu}{dT_e}(E, T_e), \tag{2.86}$$

where $N(\mathrm{Xe})$ is the number of xenon targets contained in the detector, $A(T_e)$ is the energy-dependent detector efficiency, $E_{\min}(T_e) = (T_e + \sqrt{T_e^2 + 2m_eT_e})/2$, and $E_{\max} \sim 2$ MeV. The number of target xenon atoms in the detector is given by $N(\mathrm{Xe}) = N_A M_{\mathrm{det}}/M_{\mathrm{Xe}}$, where N_A is the Avogadro number, $M_{\mathrm{det}} = 5.5$ t is the detector fiducial mass and M_{Xe} is the average xenon molar mass.
In principle, in Eq. 2.86 also the energy resolution should appear to convert the

recoil energy, into the true recoil energy. The energy resolution is measured to be very precise by the LZ Collaboration, so that it has little effect on the calculation of the rates. To check this, the theoretical spectra were smeared using a Gaussian distribution with an energy-dependent width, which has been determined using an empirical fit of mono-energetic peaks [102]. In particular, we employed $\sigma(T_e) = K/\sqrt{T_e}$, with $K = 0.323 \pm 0.001$ as reported in Ref. [103].

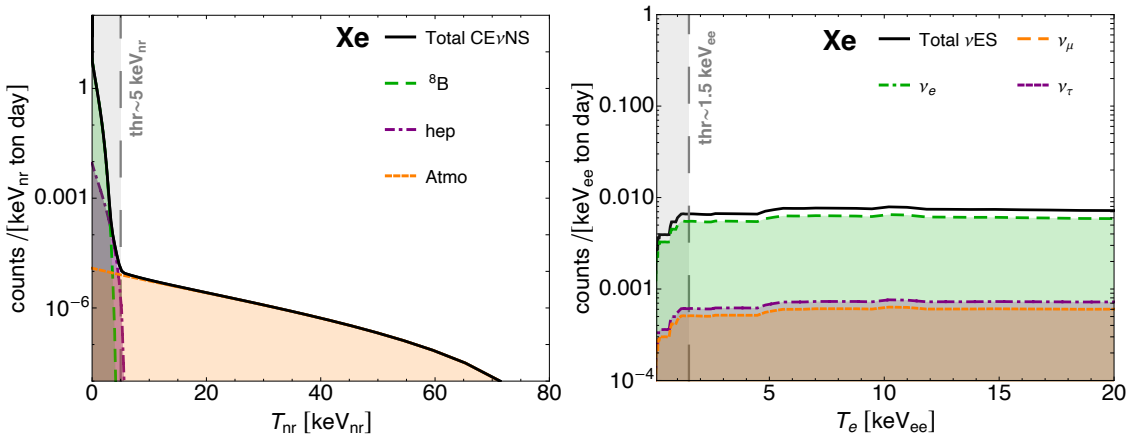

Figure 2.38: (Left) Theoretical CEνNS event rate on xenon as a function of the nuclear recoil energy. The three different flux components contributing to the total rate are shown through the different colors: green for ^{8}B, purple for hep and orange for atmospheric neutrinos. The vertical gray band indicates the experimental threshold of the LZ detector. (Right) Theoretical νES event rate on xenon as a function of the electron recoil energy. The three different flavors are shown through the different colors: green for ν_e, orange for ν_μ and purple for ν_τ. The vertical gray band indicates the experimental threshold of the LZ detector.

The detector efficiency has been provided by the LZ Collaboration as a function of the nuclear recoil energy, so that it was necessary to convert it into the observed energy, i.e. electron recoil energy. In order to do so, we used the NEST 2.3.7 software [104]. The efficiency as a function of the nuclear recoil energy (left) and of the electron recoil energy (right) is shown in Fig. 2.37. In the figure, the gray vertical line indicates the energy threshold of the experiment, and the gray bands show the energy range that is not accessible to the experiment.
In Fig. 2.38, we present the theoretical event rates on xenon in units of $\mathrm{keV}^{-1}\mathrm{ton}^{-1}\mathrm{day}^{-1}$ for CEνNS (left) and νES (right), as a function of the nuclear (left) and electron (right) recoil energy. From the comparison between the two images, it is clear that the event rate of νES is significantly higher than the CEνNS event rate, if one considers the LZ ROIs identified by the efficiencies in Fig. 2.37. To further stress this, in the figure, the vertical gray bands indicate the below threshold energy regions, to show the part of the spectra which is excluded by the analysis. In this sense, the solar neutrino contribution to CEνNS rate, results to be completely below the threshold, so that only atmospheric neutrinos can contribute to the ROI, however, this results in a rate which is about a factor 10^3 lower than the νES contribution. Instead, the steps in the right image of Fig. 2.37 reflect the $Z_{\mathrm{eff}}^{\mathrm{Xe}}$ function in the νES cross section.

Indeed, we can neglect the CEνNS contribution when calculating the number of events in each experimental bin, and consider only the νES contribution, since the acceptance would exclude completely the contribution of solar neutrino CEνNS. To obtain the count rate, we need to consider also the experimental exposure, which is given by the product of the active detector mass (5.5 t for LZ) and total time of data collecting (60.3 days for LZ).

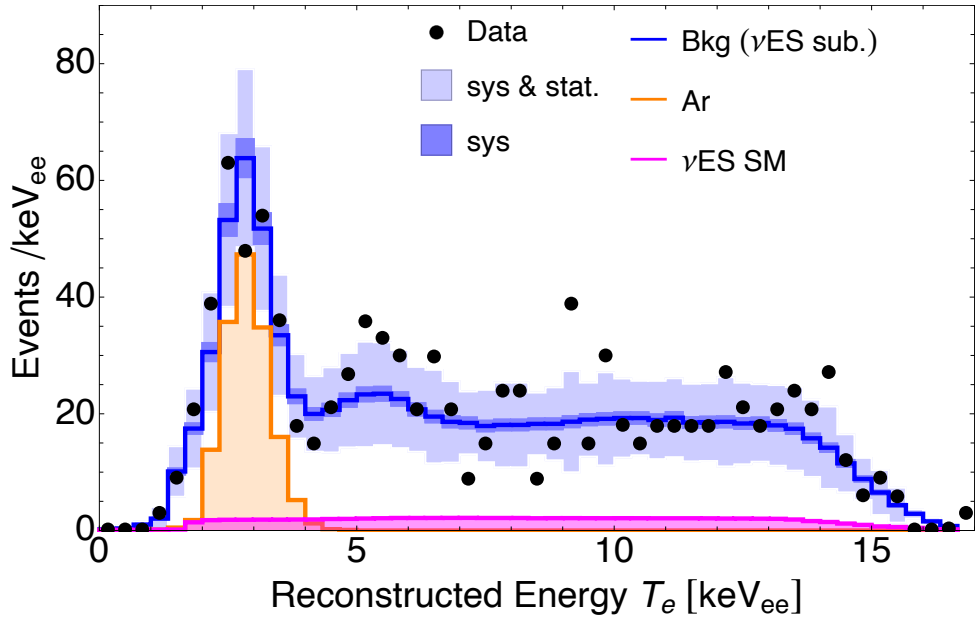

Figure 2.39: LZ data set as a function of the electron recoil energy T_e, together with the systematic and statistical error budgets [98]. The magenta line shows the experimental νES rate, the orange one indicates the ^{37}Ar background component, and the blue line shows the total background, subtracted for the νES component.

In Fig. 2.39, we show the experimental νES rate of events as a function of the electron recoil energy, expected for the LZ detector, which corresponds to a total of $\sim$27 events in the ROI. In the figure, also the data points provided by the Collaboration are shown, together with the residual background component (background at which we have subtracted the νES contribution) and the ^{37}Ar background component, which is one of the dominating background for the LZ measurement [7, 98]. The latter is an unstable argon isotope with a half-life of about 35 days, which thus, undergoes the β decay process producing electrons at $T_e \sim 3\,\mathrm{keV}_{ee}$.
To analyze the LZ data, we have built the following Poissonian chi-square function [7]

$$\chi^2 = 2\sum_{i=1}^{51}\Big[(1+\alpha)N_i^{\mathrm{bkg}} + (1+\beta)N_i^{\nu\mathrm{ES}} - N_i^{\mathrm{exp}} + \\ + N_i^{\mathrm{exp}}\ln\left(\frac{N_i^{\mathrm{exp}}}{(1+\alpha)N_i^{\mathrm{bkg}} + (1+\beta)N_i^{\nu\mathrm{ES}}}\right)\Big] + \left(\frac{\alpha}{\sigma_\alpha}\right)^2 + \left(\frac{\beta}{\sigma_\beta}\right)^2, \qquad (2.87)$$

where N_i^{bkg} is the number of residual background events found in the i-th bin fit by the LZ Collaboration and N_i^{exp} is the experimental number of events in the i-th

bin [98]. The nuisance parameter α takes into account the uncertainty on the neutrino background[8] (with $\sigma_\alpha = 5.1\%$), while β accounts for the uncertainty on the neutrino flux[9] (with $\sigma_\beta = 7\%$). However, in order to keep into account the large uncertainty on the ^{37}Ar background component, we analyze the LZ data also with a different least-squares function [7]

$$\begin{aligned}\chi^2_{^{37}\mathrm{Ar}} = 2\sum_{i=1}^{51}\Big[&\alpha N_i^{\mathrm{bkg}} + \beta N_i^{\nu\mathrm{ES}} + \delta N_i^{^{37}\mathrm{Ar}} - N_i^{\mathrm{exp}} + \\ &+ N_i^{\mathrm{exp}} \ln\left(\frac{N_i^{\mathrm{exp}}}{\alpha N_i^{\mathrm{bkg}} + \beta N_i^{\nu\mathrm{ES}} + \delta N_i^{^{37}\mathrm{Ar}}}\right)\Big] \\ &+ \left(\frac{\alpha-1}{\sigma_\alpha}\right)^2 + \left(\frac{\beta-1}{\sigma_\beta}\right)^2 + \left(\frac{\delta-1}{\sigma_\delta}\right)^2, \end{aligned} \tag{2.88}$$

where N_i^{bkg} is the number of residual background events at which we have subtracted also the ^{37}Ar contribution as found in the i-th electron recoil energy bin fit by the LZ Collaboration, and $N_i^{^{37}\mathrm{Ar}}$ is the number of ^{37}Ar background events found in the i-th bin fit by the LZ Collaboration, scaled such that the integral is equal to 96 events, as estimated in Ref. [98]. In such a way, we leave the latter contribution free to vary in the fit with a Gaussian constraint given by the additional nuisance parameter δ, which takes into account the uncertainty on the ^{37}Ar background, with $\sigma_\delta = 100\%$. In this case, we set $\sigma_\alpha = 13\%$, which is the uncertainty on the expected number of background events provided in Ref. [98] when not considering the ^{37}Ar contribution.

2.4.4 —— Argon based Dark Matter detector: DarkSide-20k ——

The counterpart of direct dark matter searches with LXe detectors is represented by the LAr detectors. They employ the same dual-phase TPC technology, but with a lighter target nucleus like argon.
Argon has the advantage with respect to xenon that it can be easily purified from electro-negative impurities and it is very abundant in the atmosphere (it is usually called atmospheric argon, AAr). However, the interaction of cosmic rays with AAr, activates some radiative argon isotopes, namely $^{39}\mathrm{Ar}$, $^{37}\mathrm{Ar}$ and $^{42}\mathrm{Ar}$, which being β-emitter, introduce an intrinsic background in the detectors. $^{39}\mathrm{Ar}$ constitutes the dominant source of background at low energies for argon-based detectors, requiring dedicated studies to reduce its contribution. In addition, the scintillation mechanism of argon allows for an efficient discrimination between nuclear and electron recoil signals, which is very profitable for dark matter searches.
The DarkSide-50 Collaboration, which leads the argon-based direct dark matter searches using a dual-phase TPC, cleverly decided to use an argon from a different source, known as underground argon (UAr), which can be extracted by

[8] We note that this procedure ignores the fact that the different background contributions have a different relative uncertainty. However, given that the total background is dominated by the β decays this approximation is valid.

[9] The flux uncertainty is about 7% for ^{7}Be and 0.6% for pp [105], we conservatively use the first one for both fluxes.

underground natural gas reservoirs [106]. UAr is argon from natural gas wells which is depleted of $^{39}\mathrm{Ar}$, as its activation process due to cosmic rays is strongly suppressed, thanks to the natural rock shielding. The DarkSide-50 Collaboration demonstrated that the UAr has an $^{39}\mathrm{Ar}$ rate of 7.3×10^{-4} Bq kg^{-1}, which is a factor of about 1400 below atmospheric levels [107].
Recently, the Aria Project, which is part of the DarkSide scientific program, demonstrated also that a very tall cryogenic column can be used to further purify argon from its problematic radiative isotope [19, 20]. The prototype of the Aria distillation column is running in the mine shaft at Carbosulcis S.p.A. in Nuraxi-Figus, in Sardinia, and the final 350 m tall column is currently under construction.
The DarkSide-50 detector is now dismantled after its successful measurements started in 2013. Meanwhile, the DarkSide Collaboration has been designing the next argon-based dual-phase TPC detector to search for dark matter signals. The new detector, known as DarkSide-20k (DS-20k), is under installation at the LNGS in Italy, and will be filled with 50 tons of active mass of UAr argon coming from Colorado and then further purified using the Aria column.
The detector has a similar technology to the LZ and XENON-nT detectors, however it will have a light readout made of silicon photo-multipliers planes, instead of the canonical photo-multiplier tubes. A schematic of the DarkSide-20k detector is shown in Fig. 2.40.

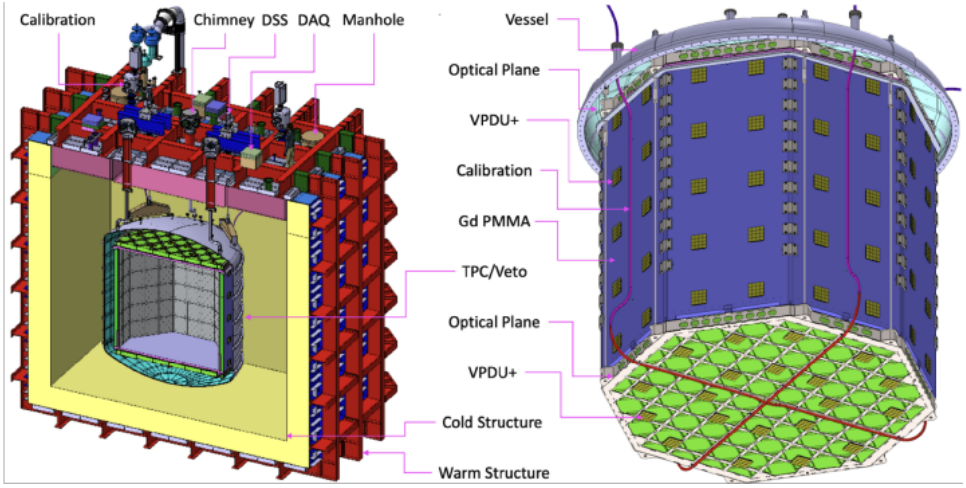

Figure 2.40: Schematic of the DarkSide-20k dark matter detector which is under construction at the Gran Sasso National Laboratories with a closeup of the inner detector shown on the right [108].

In a similar way to what we have discussed for the LZ detector, we can determine the CEνNS and νES theoretical rate for a 50 ton (20 ton after fiducialization) LAr dual-phase TPC, to understand the impact of neutrinos as a background source, in the context of the DarkSide-20k detector.
As the detector is not taking data and finalised, we only consider theoretical rates. In particular, the CEνNS event rate on argon is shown in the left image in Fig. 2.41 (left), while the νES one in the right one of the same figure.
These rates can be compared to the ones obtained for the case of a xenon target, in Fig. 2.38. The CEνNS event rate on argon results to be higher, especially

for the atmospheric neutrino contribution, as a given nuclear recoil energy corresponds to a smaller momentum transfer in the case of argon, because of the lighter nuclear mass. In this sense, the CEνNS event rate expands toward much higher nuclear recoil energies. However, the energy threshold for argon detectors is usually high enough to still cut the solar neutrino contribution out of the ROI. In the Fig. 2.41 (Left), we fixed the threshold to $\sim 30\,\mathrm{keV_{nr}}$ to indicate an estimate of the possible nuclear recoil energy threshold for the DS-20k detector. Considering such energy threshold, and integrating up to $\sim 200\,\mathrm{keV_{nr}}$, we estimate around 2.9 CEνNS events in the DS-20k ROI with an exposure of 200 ton yr.

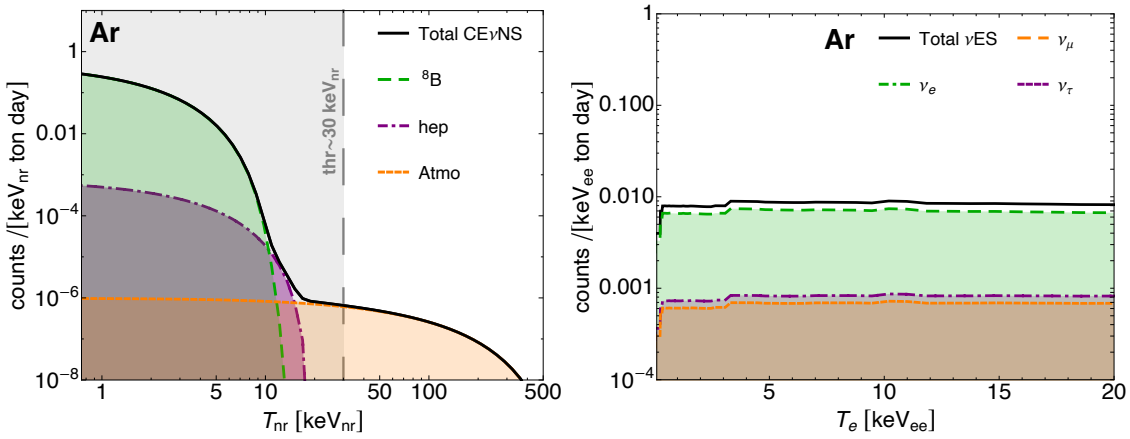

Figure 2.41: (Left) Theoretical CEνNS event rate on argon as a function of the nuclear recoil energy. The three different flux components contributing to the total rate are shown through the different colors: green for ^{8}B, purple for hep and orange for atmospheric neutrinos. The vertical gray band indicates an estimate of the experimental threshold for DS-20k. (Right) Theoretical νES event rate on argon as a function of the electron recoil energy. The three different flavors are shown through the different colors: green for ν_e, orange for ν_μ and purple for ν_τ.

Also the νES event rate is similar between the case of LAr and LXe (for the latter see Fig. 2.38), although the rate on argon is slightly higher. In this case, we didn't indicate an energy threshold, as the details of the DS-20k on this kind of measurement are not available yet. In particular, this threshold can also depend on the quenching factor model of argon considered by the Collaboration.

2.4.4.1 The Single Electron "problem" in the DarkSide-50 detector

We have just discussed the intriguing characteristics of direct dark matter detectors, in particular in the context of noble liquid dual-phase TPCs. The detectors are optimized in order to reach very low background levels together with low energy thresholds, which makes them suitable also to search for neutrino BSM signals as we will discuss later on.
Reaching lower thresholds represents one of the main challenges for future dark matter detectors as well as for neutrino detectors, however, achieving lower recoil energies is not trivial. Indeed, one limiting factor that has been observed in a plethora of different experiments is the presence of a still-to-be-understood

excess of events in the low recoil region, which has motivated many discussions around the community. In particular, this excess of events has been observed in various crystal based detectors, motivating the creation of a common initiative, called EXCESS [109], in order to join the efforts looking for a possible explanation. However, similar events have been detected also in noble liquid dark matter TPCs, among which the DarkSide-50 (DS-50) detector [9]. The careful characterization of this unexpected background component is crucial especially as the community is developing the next generation devices, which aim to reach even lower background levels and thresholds besides being scaled up significantly. This applies, for instance, to the DarkSide-20k (DS-20k) [110] detector, which is currently under construction.
As we have already discussed, a typical interaction in the active volume of the TPC yields a prompt scintillation signal, S1, and one or more clouds of ionization electrons, depending on the single- or multi-scatter nature of the interaction. Inside the DS-50 LAr TPC, the extracted electrons drift upwards under a uniform electric field until they reach the gas pocket and induce electroluminescence signals, S2. We will call S1+S2 events, those in which both the scintillation and the ionization signals are observed. In fact, low energy interactions may yield only S2 signals above the detection threshold. These single-pulse events were used to extend the search for dark matter to lower masses [111].
In addition to S1+S2 and S2 only events, other event types were also observed in the DS-50 detector [9]. We discuss prompt emission events, namely events with an additional small amplitude S2 pulse, occurring in the same $440\ \mu\mathrm{s}$ data acquisition window as standard events; we refer to these pulses as Single Electron Candidates (SEC). We classify these events into two different categories: echo events, when the SEC has a definite temporal relationship with the preceding S1 or S2 signals, and bulk events, when the SEC does not have a definite temporal relationship with the preceding S1 or S2, but is consistent with being due to a single electron. Therefore, both these event types have features that clearly distinguish them from the common multi-scatter photon background interactions, for which the S2 pulses have a wide spectrum of charges. We also provide a tentative interpretation of the observed event types [9].
Events with single electron signals occurring outside the acquisition window of a previous standard event, i.e. due to delayed emission, were also observed in DS-50 [111] and will be discussed and analyzed in an upcoming DS-50 publication, currently under finalization.
Similar kinds of events were also observed and studied with liquid-xenon based detectors, indicating that the source of this background component may be common throughout different detector materials. The most comprehensive study was performed by the LUX Collaboration [112], to which, therefore, we refer for comparison. Other previous papers reporting similar event types can be found in Refs. [113–116].
The DS-50 LAr TPC is a cylinder, whose active volume has a height of $35.6\ \mathrm{cm}$ and a diameter of $35.6\ \mathrm{cm}$ at warm, and contains $(46.4 \pm 0.7)\ \mathrm{kg}$ of low-radioactivity argon (UAr) extracted from underground [106, 117, 118]. Arrays of $19\ 3''$ photomultipliers (PMTs) at each end detect the S1 and S2 signals. The PMTs are im-

mersed in liquid argon and view the active volume through fused silica windows. These are coated on both faces with transparent conductive indium tin oxide (ITO) films $15\,\mathrm{nm}$ thick. The inner faces of the window define the grounded anode (top) and the HV cathode (bottom) of the TPC, while the outer faces are kept at the average photocathode potential of each 19-PMT array.
The cylindrical side wall is made of $2.54\ \mathrm{cm}$-thick polytetrafluoroethylene (PTFE) reflector that was sintered using a special annealing cycle to increase its reflectivity. The PTFE reflector and the fused silica windows are coated with a tetraphenyl butadiene (TPB) wavelength shifter, which absorbs the $128\,\mathrm{nm}$ LAr scintillation photons and re-emits visible photons with a peak wavelength of $420\,\mathrm{nm}$, which can be detected by the PMTs. The specific thickness of the TPB coating on the windows corresponds to a few $\mu\mathrm{m}$ thickness [9].

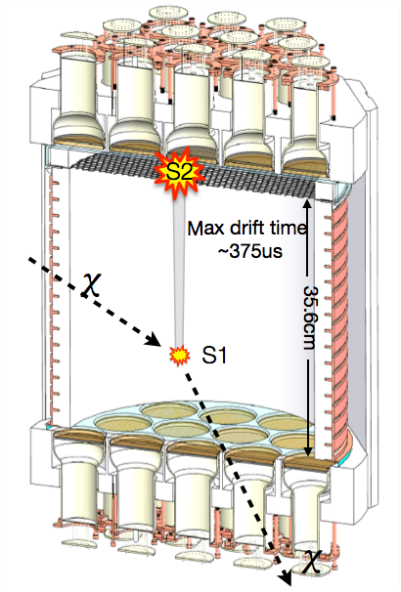

Figure 2.42: Schematic of the DarkSide-50 detector in which we also show an example of the S1 and S2 signals [119].

The electric fields needed for drifting and extracting electrons are formed by the ITO-coated cathode and anode planes, a field cage made of a stack of copper rings behind the PTFE reflector held at graded potentials, and a grid that separates the drift and electron extraction regions. The grid is placed $5\ \mathrm{mm}$ below the liquid surface. It is made from hexagonal mesh photo-etched from a $50\ \mu\mathrm{m}$-thick stainless steel foil and has an optical transparency of 95% at normal incidence. The data employed in this analysis [9] were collected between July 2015 and October 2017, with a TPC drift field of $200\,\mathrm{V/cm}$, an extraction field of $2.8\,\mathrm{kV/cm}$, and an electroluminescence field of $4.2\,\mathrm{kV/cm}$. At this extraction field, the grid is fully transparent to electrons and the efficiency for extracting ionization electrons into the gas layer is estimated to be close to 100% [120, 121]. The electron drift time, $t_{\mathrm{drift}} = \Delta t_{\mathrm{S2-S1}}$, has a maximum value at $t_{\mathrm{drift}}^{\mathrm{max}} = 376\ \mu\mathrm{s}$, corresponding to interactions located right above the cathode. The electron drift speed is $(0.93 \pm 0.01)\ \mathrm{mm}/\mu\mathrm{s}$ [122]. A schematic of the DS-50 TPC is shown in Fig. 2.42, where an exemplification of the S1 and S2 signals is shown. The time acquisition

window is set to record from all 38 PMTs for 440 μs starting $\sim$ 10 μs before the trigger, which, for this analysis, is the S1 signal. Software pulse-finding algorithms are then applied to the digitized data, including the pre-trigger data. The software classifies the pulses into two categories (S1 or S2) based on the fraction of light detected within the first $90\,\mathrm{ns}$ (f_{90}). The f_{90} variable is used to distinguish between electron and nuclear recoils, as for electron recoils, its value is clustered around 0.3, while for nuclear recoils, it is around 0.7 [9]. The efficiency of the software pulse-finding algorithm is essentially $100\,\%$ for S2 signals larger than $30\,\mathrm{PE}$ [123]. The pulse finder uses an integration window of 30 μs, which is long enough to include the entire S2 signal.
We select three-pulse events, with an S1 followed by two S2, one of which is called a SEC. The S1 pulse provides the event trigger. We classify the selected events into two groups, according to the time sequence of the three pulses: S1-S2-SEC, with the SEC occurring after the S2 pulse, and S1-SEC-S2, with the SEC occurring between S1 and S2 [9]. The S2 light yield drops by about 60% from the center to the sides of the detector [124]. To avoid efficiency corrections for the pulse finder, we only select SEC pulses with the maximum signal in the top central PMT [9]. In this analysis, only electron recoil events are selected, by requiring $f_{90}< 0.5$. Moreover, to limit the effects of saturation and pulse overlaps, we require S2$<$ 50000 PE and 100 PE $<$S1$<$ 1500 PE [9]. Moreover, in DS-50, the typical S2 to S1 charge ratio for electron recoils is between 10 and 30. To further strengthen the identification of the pulse sequence, the S2 to S1 ratio is required to be larger than 10.

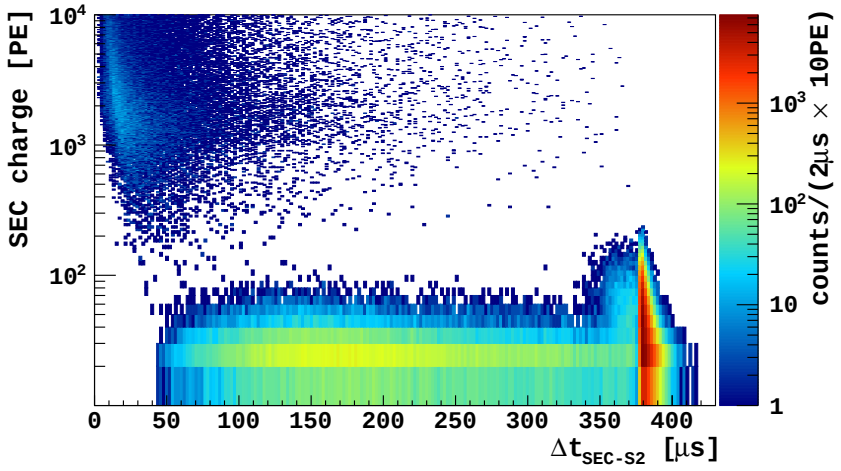

Figure 2.43: Distribution of SEC charge vs. time difference between the SEC and the preceding S2 pulse, $\Delta t_{\mathrm{SEC-S2}}$. The set of events at small values of $\Delta t_{\mathrm{SEC-S2}}$ and large values of charge is related to double-scatter γ-ray interactions [9].

In Fig. 2.43, we show the charge of the SEC pulse vs. the time difference, $\Delta t_{\mathrm{SEC-S2}}$, between the SEC pulse and the preceding S2, in the case of S1-S2-SEC events. We observe three main features in the plot, corresponding to three sets of events. One set of events in 2.43 is clustered around $\Delta t_{\mathrm{SEC-S2}} \sim 380$ μs, corresponding to the maximum TPC drift time, and SEC charges up to a few hundred PEs. It seems plausible that these events are due to S2 photons extracting electrons from the cathode. The electrons then drift through the whole TPC length. We call

these events S2-echo events. In Fig. 2.44, we show the SEC charge spectrum for these events. The peak related to the signal from one ionization electron is clearly visible and its corresponding SEC charge[10] is in agreement with the observation of a previous DS-50 publication [111] of $\sim$ 23 PE. The distribution also shows a tail extending to several electrons. The S2 pulses are quite large signals and can induce the emission of more than one electron from the cathode.

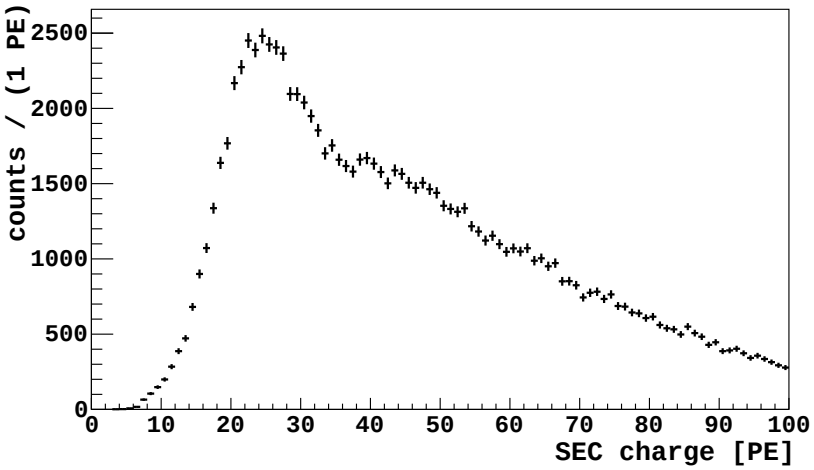

Figure 2.44: SEC charge distribution for S2-echo events [9].

From now on, we require the SEC to be a small amplitude electroluminescence pulse, i.e. to have a charge smaller than 200 PE, which corresponds to about eight extracted electrons.
The number of recorded S2-echo events is affected by the data acquisition window of 430 μs after the trigger. This time window is smaller than $2 \times t_{\rm drift}^{\rm max}$, the time that would be required for recording all S2-echo events. In practice, the DS-50 data acquisition only records S2-echo events originating from interactions in the top section of the TPC, with drift times, $\Delta t_{\rm S2-S1}$, smaller than $430\ \mu{\rm s} - t_{\rm drift}^{\rm max}$, which is $\sim 50\ \mu$s [9].
The fraction of events containing an S2-echo, $F_{\rm S2\text{-}echo}$, as a function of the drift time, is

$$F_{\rm S2\text{-}echo}(t_{\rm drift}) = N_{\rm S2\text{-}echo}(t_{\rm drift})/N_{\rm S2}(t_{\rm drift}). \tag{2.89}$$

The drift time, $\Delta t_{\rm S2-S1}$, depends on the depth of the interaction, z, with $z = 0$ corresponding to $\Delta t_{\rm S2-S1} = 0$, the gas-liquid interface. In Fig. 2.45, we show the SEC charge vs S2 charge distribution for S2-echo events. From the figure, we observe that larger S2 charges correspond to a greater probability of inducing photoelectric emission from the cathode of more than one electron. This corroborates our interpretation of S2-echo events [9].
We also expect that the probability of S2-echo events, independent of the SEC pulse charge, increases with the S2 pulse charge. Indeed, this is clearly visible in Fig. 2.46, which shows the fraction of S2-echo events as a function of the S2

[10]Charge $\sim$ 23 PE corresponds to one extracted electron, from which we speak about Single Electron signals.

charge. The fraction is found to increase with the S2 charge, leading to an event fraction of about 0.5 at the maximum S2 selected energy.

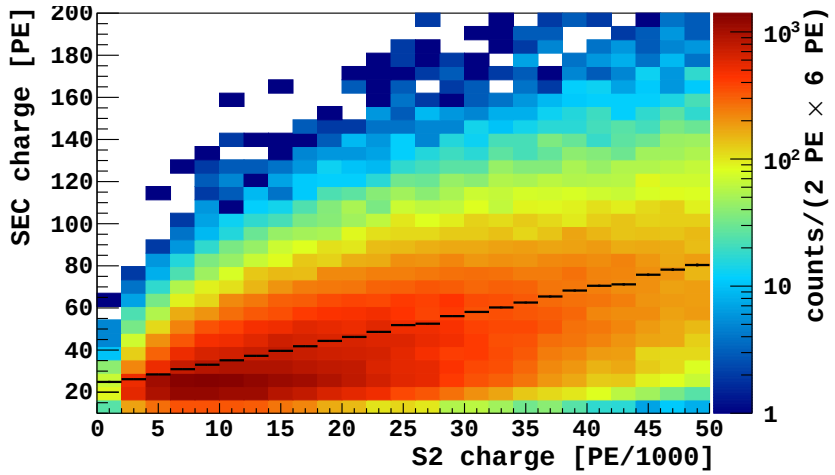

Figure 2.45: SEC charge vs S2 charge distribution for S2-echo events. Overlaid is the profile histogram. A linear fit gives an intercept of ~ 23.3 PE and a slope of $\sim 1.2 \times 10^{-3}$ [9].

This translates into a probability of observing an echo of about $\sim 20\%$ for a S2 of 30000 PE. Since we selected only the events with the maximum signal in the central top PMT, which causes a restricted geometric acceptance for the SEC, for the events with S2 above this size essentially every event produced an echo signal in the detector [9]. However, due to the limited data acquisition time window, most of the third pulses are not recorded.

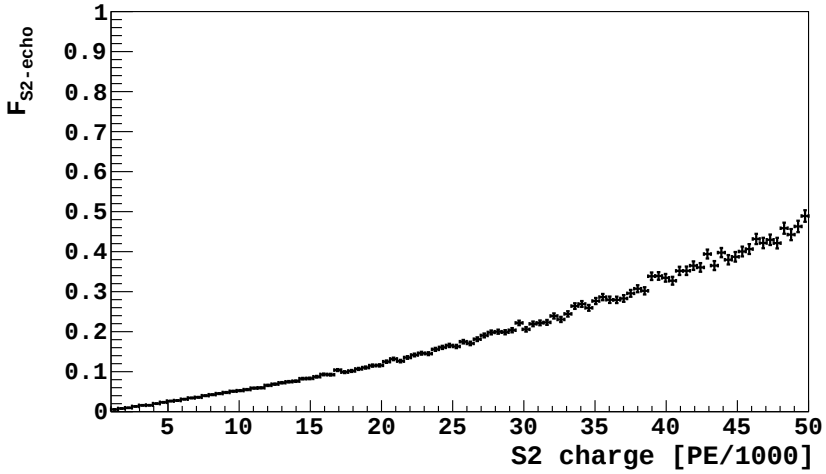

Figure 2.46: Fraction of S2-echo events vs S2 charge, with $5\ \mu\text{s} < \Delta t_{\text{S2}-\text{S1}} < 45\ \mu\text{s}$ [9].

Another set of events in Fig. 2.43 is clustered at SEC charges peaking at ~ 25 PE, the single ionization electron response, and spanning the time axis from $50\ \mu$s to $375\ \mu$s. These events are well separated from those with SEC charges larger than a few 100 PEs, which are identified as S2 events from standard double-scatter γ-ray interactions in the detector. It can be noticed that the pulse finder is not able

to reconstruct SEC pulses below $\sim$ 100 PE that are less than $\sim$ 40 μs after an S2 pulse, as they would be incorporated inside the S2 signal. The origin of these events can be understood from Fig. 2.47, which shows the distribution of $\Delta t_{\mathrm{SEC-S2}}$ vs. $\Delta t_{\mathrm{SEC-S1}}$, when selecting events with SEC$<$ 50 PE.

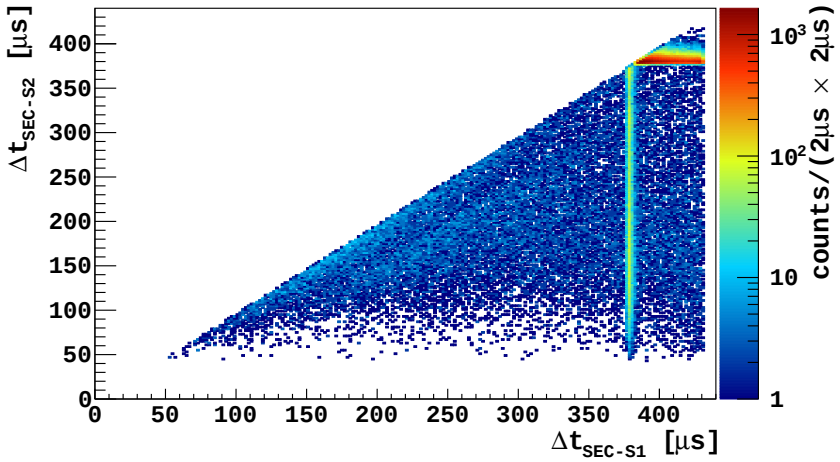

Figure 2.47: Time difference $\Delta t_{\mathrm{SEC-S2}}$ vs time difference $\Delta t_{\mathrm{SEC-S1}}$ distribution for events with SEC$<$ 50 PE [9].

Three event categories are clearly visible in the distribution: a horizontal band at $\Delta t_{\mathrm{SEC-S2}} \sim 380$ μs, corresponding to the S2-echo events discussed previously, a continuum of events without a specific time relation of the SEC with either S1 or S2, which will be discussed later, and a vertical band, corresponding to $\Delta t_{\mathrm{SEC-S1}} \sim 380$ μs, about one maximum drift time after the S1 signal. We interpret these events as photoelectric emissions from the cathode induced by S1 photons and call them S1-echo events, in analogy with S2-echo.
In Fig. 2.48, we show the time distribution, $\Delta t_{\mathrm{SEC-S1}}$, for events with SEC$<$ 50 PE and $\Delta t_{\mathrm{SEC-S2}} < 350\mu$s. The narrowness of the peak for the S1-echo events and the similarity between the rates before and after the peak imply that there is no substantial delayed emission from the liquid surface on the scale of 10 to 100 μs. This finding agrees with the electron extraction efficiency into the gas pocket being close to 100%. The events before and after the peak belong to the S2-bulk category, that is the third type of SEC considered in this analysis, and will be discussed later.
Fig. 2.49 shows the fraction of S1-echo events, $F_{\text{S1-echo}}$, as a function of the drift time, t_{drift}, defined as [9]

$$F_{\text{S1-echo}}(t_{\mathrm{drift}}) = \frac{N_{\text{S1-echo}}(t_{\mathrm{drift}})}{N_{\mathrm{T}}(t_{\mathrm{drift}})}, \tag{2.90}$$

with $N_{\mathrm{T}}(t_{\mathrm{drift}})$ the selected total number of events (two pulses and three pulses). The fraction $F_{\text{S1-echo}}$ rises with t_{drift} up to about 250 μs, due to solid angle effect, whereas it drops at large t_{drift}, when the time of the SEC becomes closer to the preceding S2. This drop is due to a pulse finder inefficiency, similar to the effect seen in Fig. 2.43, which tends to merge small signals with a preceding S2.

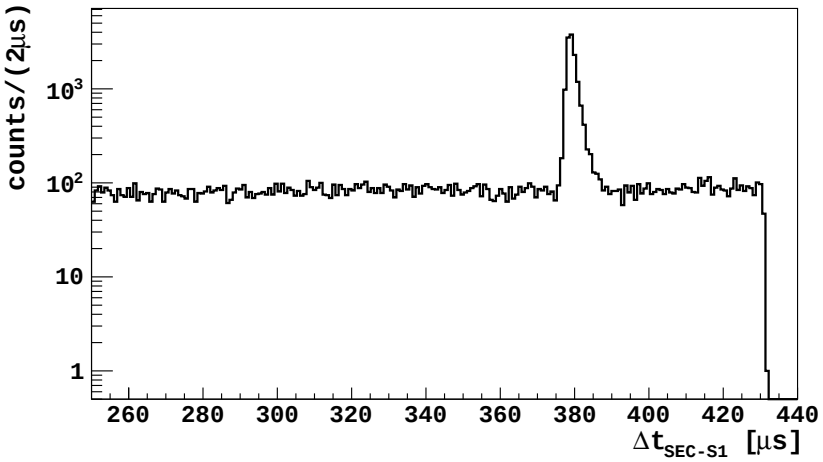

Figure 2.48: Time difference $\Delta t_{\mathrm{SEC-S1}}$ distribution, for events with SEC<50 PE and $\Delta t_{\mathrm{SEC-S2}} < 350$ μs [9].

Indeed, when for instance, we select low energy events, such as with S1<800 PE and S2<5000 PE, we find that the drop at large $\Delta t_{\mathrm{S2-S1}}$ only starts at ~ 300 μs. No tuning of the pulse finder algorithm was made to cope with this effect [9]. We tested the hypothesis that the drop could be due to the SEC being captured by the ion cloud of the S2 signal, by selecting events for which the S2 signal maximum is not in the central PMT. The corresponding distribution in Fig. 2.49 does not change, and we therefore discard this hypothesis. The presence of a time gap between the S2 and the subsequent SEC is also visible in the continuum of events at the bottom of Fig. 2.47.
The geometric acceptance for S1 UV photons, $\epsilon(r, t_{\mathrm{drift}})$, defined as the fraction of photons, for which we assume 4π emission at a given r and z position in the chamber, that hits a cathode area corresponding to the central PMT, was calculated with a simple Monte Carlo, and a schematic representation of the situation is pictured in the left image of Fig. 2.51. In the following, we made the simplifying assumption, true to a good approximation, that the event distribution in t_{drift} and r factorizes. Then, the average $\hat{\epsilon}(t_{\mathrm{drift}})$ is obtained by weighting the geometric acceptance $\epsilon(r, t_{\mathrm{drift}})$ by the normalized radial distribution, $f(r)$, of the S2 pulses measured with data, as

$$\hat{\epsilon}(t_{\mathrm{drift}}) = \sum_r \epsilon(r, t_{\mathrm{drift}}) f(r)\,. \tag{2.91}$$

For $t_{\mathrm{drift}} < 330$ μs, the calculated efficiency is a rising function of t_{drift} and can be parameterized as [9]

$$\hat{\epsilon}(t_{\mathrm{drift}}) = 0.0072 \cdot e^{0.0024 \cdot t_{\mathrm{drift}}} - 0.0054, \tag{2.92}$$

with t_{drift} expressed in μs. The fraction of S1-echo events vs drift time after S1 UV photon acceptance corrections, defined as

$$F^{\epsilon}_{\mathrm{S1\text{-}echo}}(t_{\mathrm{drift}}) = \frac{N_{\mathrm{S1\text{-}echo}}(t_{\mathrm{drift}})}{\hat{\epsilon}(t_{\mathrm{drift}}) N_{\mathrm{T}}(t_{\mathrm{drift}})}, \tag{2.93}$$

is shown in red in Fig. 2.49. Below ~ 200 μs we retrieve a flat distribution.

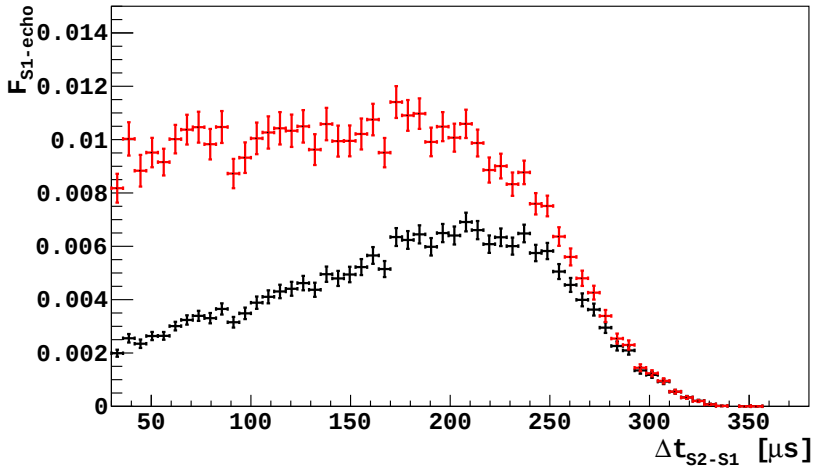

Figure 2.49: Fraction of S1-echo events, $F_{\text{S1-echo}}$, vs drift time $\Delta t_{\text{S2}-\text{S1}}$ (black dots) and after S1 UV photon corrections (red dots), $F^{\epsilon}_{\text{S1-echo}}$ [9].
$F^{\epsilon}_{\text{S1-echo}}$ is multiplied by 0.01 to fit conveniently on the plot.

By repeating the results in Fig. 2.46, but applied to S1-echo events (for 50 μs $< \Delta t_{\text{S2}-\text{S1}} < 200$ μs), we observe that the probability of S1-echo events increases with the S1 charge (see Fig. 9 of Ref. [9]).
Moreover, by repeating also the results in Fig. 2.44 for the S1-echo events, we observe that similarly to the S2-echo case, the SEC charge distribution shows a clear peak corresponding to one extracted electron and a lower shoulder due to two extracted electrons (see Fig. 10 of Ref. [9]).
From the measured fraction of both S1-echo and S2-echo events, it is possible to estimate the quantum efficiency of the cathode in liquid argon, i.e. the photoelectron emission probability per UV photon, γ_{UV}, at the liquid argon emission wavelengths of $\sim$128 nm [9].
For the calculation of the quantum efficiency measured with S1 photons, QE_{S1}, we select events with 50 μs $< \Delta t_{\text{S2}-\text{S1}} < 200$ μs. Indeed, we have shown in Fig. 2.49 that, for these drift times, we retrieve a flat distribution as a function of t_{drift}, after acceptance corrections. The number of S1-echo events is given by [9]

$$N_{\text{S1-echo}}(t_{\text{drift}}) = \hat{\epsilon}(t_{\text{drift}}) N^{S1}_{\gamma_{UV}}(t_{\text{drift}}) \frac{QE_{S1}}{\langle N_{el} \rangle_{S1}}, \tag{2.94}$$

where the number of S1 UV photons is

$$N^{S1}_{\gamma_{UV}}(t_{\text{drift}}) = N_{\text{T}}(t_{\text{drift}}) \langle S1 \rangle_e / g_1. \tag{2.95}$$

$N_{\text{T}}(t_{\text{drift}})$ is the selected total number of events (two pulses and three pulses), $\langle S1 \rangle_e$ the S1 mean charge expressed in PE, and $g_1 \sim 0.16$ PE/γ_{UV} the average number of photoelectrons per UV photon [124]. The presence of the average number of electrons per S1-echo event, $\langle N_{el} \rangle_{S1}$, in the denominator of Eq. 2.94 takes into account that an S1-echo event might have more than one extracted electron and is defined by [9]

$$\langle N_{el} \rangle_{S1} = \langle \text{SEC} \rangle_{\text{S1}} / g, \tag{2.96}$$

with $\langle \mathrm{SEC} \rangle_{\mathrm{S1}}$ the average SEC charge (see the distribution in Fig. 10 of Ref. [9]), and $g \sim 23\,\mathrm{PE}/e^-$ the photoelectric gain in the central PMT. In the selected $\Delta t_{\mathrm{S2-S1}}$ range, the average fraction of S1-echo events, $\langle F^{\epsilon}_{\text{S1-echo}} \rangle$, is $\sim$ 1.0 (see Fig. 2.49), and from Eq. 2.93, Eq. 2.94, and Eq. 2.95, we obtain [9]

$$QE_{\mathrm{S1}} \sim \langle F^{\epsilon}_{\text{S1-echo}} \rangle \frac{g_1}{\langle S1 \rangle_e} \langle N_{el} \rangle_{S1}. \tag{2.97}$$

The mean value of S1, $\langle S1 \rangle_e$, is ~ 730 PE, while the average number of electrons, $\langle N_{el} \rangle_{S1}$, is ~ 1.1, giving [9]

$$QE_{\mathrm{S1}} \sim 2.4 \times 10^{-4} / \gamma_{UV}. \tag{2.98}$$

The S2-echo photons are induced by S2 signals, which are all produced within the thin gas region at the top of the TPC, shown by the light gray rectangle at the top of the images in Fig. 2.51. Therefore, the average acceptance for S2 UV photons, $\hat{\epsilon}_{S2}$, is the value calculated from Eq. 2.92 at $t_{\mathrm{drift}} \sim 0$. For S2-echo events, Eq. 2.97 gets modified into [9]

$$QE_{\mathrm{S2}} \sim \frac{\langle F_{\text{S2-echo}} \rangle}{\hat{\epsilon}_{\mathrm{S2}}} \frac{g_2}{\langle S2 \rangle_e} \langle N_{el} \rangle_{S2}. \tag{2.99}$$

where the average of $F_{\mathrm{S2-echo}}$, $\langle F_{\text{S2-echo}} \rangle \sim 0.055$, is taken from Fig. 3 of Ref. [9] over the interval $5\ \mu\mathrm{s} < \Delta t_{\mathrm{S2-S1}} < 45\ \mu\mathrm{s}$, $\langle S2 \rangle_e$ is the mean S2 charge, $\langle N_{el} \rangle_{S2}$ is the average number of electrons per S2-echo event,

$$\langle N_{el} \rangle_{S2} = \langle \mathrm{SEC} \rangle_{\mathrm{S2}} / g, \tag{2.100}$$

with $\langle \mathrm{SEC} \rangle_{\mathrm{S2}}$ the average charge of the distribution from Fig. 2.44, yielding $\langle N_{el} \rangle_{S2} \sim 2.1$. The mean S2 charge, $\langle S2 \rangle_e$, is ~ 23430 PE, $g_2 \sim g_1 \sim 0.16$ PE/γ_{UV} [124, 125], and $\hat{\epsilon}_{\mathrm{S2}} \sim 1.8 \times 10^{-3}$, giving [9]

$$QE_{\mathrm{S2}} \sim 4.4 \times 10^{-4} / \gamma_{UV}. \tag{2.101}$$

The two measurements of the quantum efficiency, QE_{S1} in Eq. 2.98 and QE_{S2} in Eq. 2.101, are in broad agreement with each other. They are affected by systematic uncertainties due to the dependence of both g_1 and g_2 on the interaction position in the detector, at most a $10 - 20\%$ effect, and to the acceptance calculation for S1 and S2 UV photons. Indeed, both $\hat{\epsilon}(t_{\mathrm{drift}})$ and $\hat{\epsilon}_{\mathrm{S2}}$ were calculated under the simplifying assumption that the SEC signals with the maximum charge in the top center PMT are only those with electrons extracted from the cathode area corresponding to the center PMT. In this way, the efficiency is slightly underestimated, since electrons extracted just outside that area can still give the same kind of signal. A quick evaluation of the uncertainty on the geometric efficiency calculation can be obtained from the fraction of the detector cross-section which is not covered by the PMTs, which amounts to $\sim 15\%$ [9].
Moreover, Rayleigh scattering was also not included in the acceptance calculation. An upper bound on the size of this effect could be obtained by re-calculating $\hat{\epsilon}(t_{\mathrm{drift}})$ and $\hat{\epsilon}_{\mathrm{S2}}$ with the inclusion in the Monte Carlo simulation of the Rayleigh

scattering probability for the UV-photons, assuming that every scattered photon is lost. In this extreme case, with a scattering length of 90 cm [126], $\hat{\epsilon}_{\mathrm{S2}}$ would decrease by $\sim 30\%$, whereas $\hat{\epsilon}(t_{\mathrm{drift}})$ by only $\sim 15\%$ [9].
Furthermore, in the calculations of the acceptance for S1 and S2 UV photons, we assumed no dependence on the angle of incidence on the cathode of the photoelectric efficiency and that UV light attenuation in liquid argon is negligible.
The measured absorption length of TPB at 128 nm is about 400 nm [127]. Since this thickness is much smaller than the few microns of the TPB on the DS-50 cathode, most of the photoelectric effect we observe is due to electron emission from the TPB itself. The QE we measure is therefore the previously unmeasured quantum efficiency of the TPB in liquid argon. It should also be noted that this may be different from the value measured in vacuum since the effective work function of the TPB could be modified by the electron affinity of the liquid argon, as is expected for liquid xenon [112].
In Fig. 2.47, there is also a continuum of events with no specific values of time differences between SEC and either S1 or S2, which are not interpretable in terms of S1-echo and S2-echo events. Since our selection constrains the SEC pulse to follow the S2 one, these events follow the S2 signal, we call them *S2-bulk* events (see a schematic representation in the right image of Fig. 2.51). However, it is also possible to observe other events with no specific values of the time difference between SEC and S1, by studying events with the time sequence S1-SEC-S2, and they will be called *S1-bulk* events [9]. An understanding of the origin of S2-bulk and S1-bulk events is no simple matter. However, at least two observations support that there is a correlation with the S2 and S1 UV photon emission, respectively. The first observation is that the ratio of the number of observed events (the number of S2-bulk events divided by the number of S1-bulk events) is similar to the ratio of the pulse charge of S2 and S1. The former ratio is ~ 19, whereas the latter one is ~ 24 [9].
To compute the event ratio, we selected the S2-bulk events by requiring $5\ \mu\mathrm{s} < \Delta t_{\mathrm{S2-S1}} < 45\ \mu\mathrm{s}$ and the S1-bulk ones by requiring $\Delta t_{\mathrm{S2-S1}} > 354\ \mu\mathrm{s}$, i.e. with S2 events at the top of the chamber and the S1 events at the bottom, and normalizing them. We also require $\Delta t_{\mathrm{S1-SEC}} > 30\ \mu\mathrm{s}$ to avoid events which could be related to grid ionization. In this way we find 8348 S2-bulk events and 432 S1-bulk events, giving a ratio of ~ 19 [9].
Note that while we ascribe all SEC after S2 as S2-bulk events, in fact for $\Delta t_{\mathrm{SEC-S1}}$ up to the maximum drift time, the source (S1 or S2) is not determined. Given the observed ratio of a SEC formation by S2 or S1, this is a small correction.
The second observation is that the fraction of both S2-bulk and S1-bulk events increases with S2 and S1 charge, respectively, as shown in the plots in Fig. 2.50.
A candidate explanation for S2-bulk events is the photoionization of contaminants by S2 photons (or S1 photons). One possibility is a contaminant that captured an electron during a previous event, such as, for instance, the O_2^- ion, which has an ionization energy lower than the 9.76 eV energy of VUV argon photons. Photoionization of neutral molecules such as O_2 or H_2O is less likely since the first ionization energy is above 9.76 eV. Another potential contaminant is TPB, which can detach from the walls and dissolve in the liquid [128].

Due to the SEC pulse selection requirement of having the signal maximum in the central PMT, we tend to rule out the interpretation of S2-bulk events as photoelectric emissions from the TPC walls.
We do not favor the possible interpretation of the S2-bulk events as being due to recombination or de-excitation of contaminant molecules since these mechanisms are not expected to yield electrons.

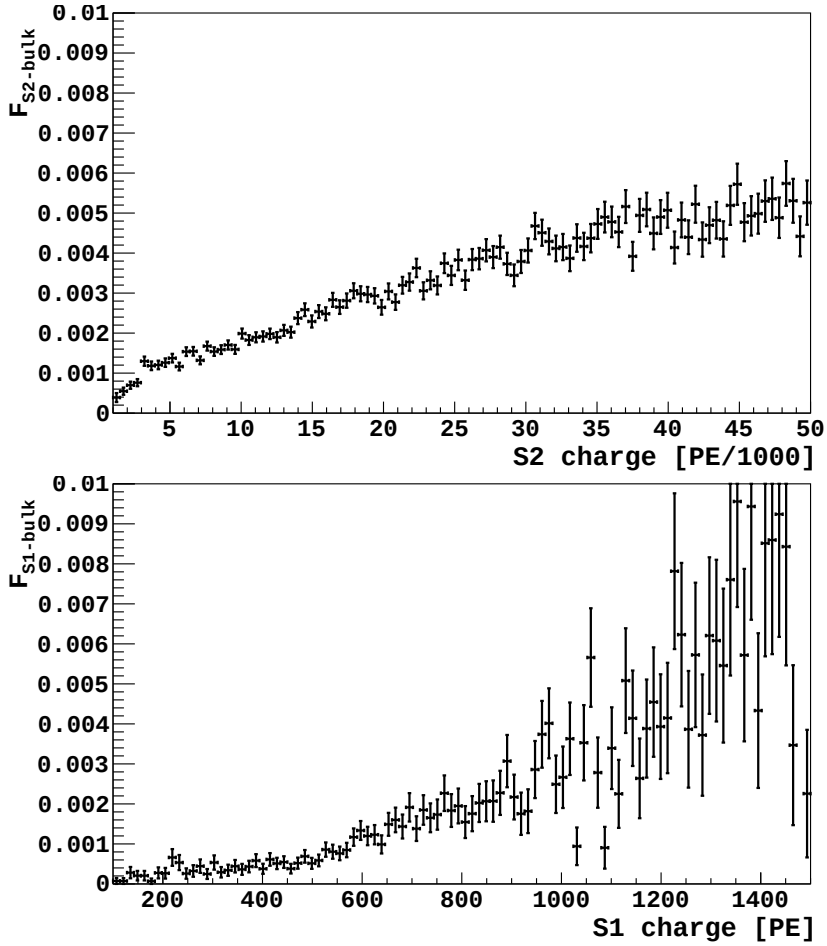

Figure 2.50: Fraction of S2-bulk (S1-bulk) events vs S2 (S1) charge, with $\Delta t_{\mathrm{S2-S1}} > 50\ \mu$s ($5\ \mu\mathrm{s} < \Delta t_{\mathrm{S2-S1}} < 45\ \mu$s) [9].

From the fraction of S2-bulk events,

$$F_{\text{S2-bulk}} = \frac{N_{\text{S2-bulk}}}{N_{\mathrm{T}}}, \tag{2.102}$$

with $N_{\text{S2-bulk}}$ the number of selected S2-bulk events and N_{T} the total number of selected events (two pulses and three pulses), we derive the probability of photoelectric extraction from the liquid per unit length and per UV photon, PEP_{S2}. Averaging over the interval $5\ \mu s < \Delta t_{\mathrm{S2-S1}} < 45\ \mu s$, we have [9]

$$PEP_{S2} = \frac{1}{\hat{L}_{\mathrm{S2}}} \frac{g_2}{\langle S2 \rangle_b} \langle F_{\text{S2-bulk}} \rangle, \tag{2.103}$$

with $\langle S2 \rangle_b$ the mean S2 charge for selected S2-bulk events. The quantity $\hat{L}_{\mathrm{S2}}$ is the average S2 path length, defined as [9]

$$\hat{L}_{\mathrm{S2}} = \sum_r L_{\mathrm{S2}}(r) f(r), \tag{2.104}$$

where $L_{\mathrm{S2}}(r)$ is the path length of an S2 photon generated at the radial distance r, that falls inside a cylinder of diameter equal to that of the central PMT and height equal to the maximum TPC drift length (see the azure rectangle in the schemes in Fig. 2.51). Since $\langle F_{\text{S2-bulk}} \rangle \sim 0.006$, $\hat{L}_{\mathrm{S2}} \sim 1.5$ cm, and $\langle S2 \rangle_b \sim 18000$ PE, we obtain $PEP_{S2} \sim 4 \times 10^{-6}\ e^-/\gamma_{UV}/\mathrm{m}$.
For $\Delta t_{\mathrm{S1-SEC}} < 30\ \mu$s, we have observed a higher than average number of events per unit $\Delta t_{\mathrm{SEC-S1}}$, as well as a higher SEC charge (see Fig. 11 of Ref. [9]). A possible interpretation of these events is the photoionization of the extraction grid by S1 signals, as was observed with the LUX detector [112].
To further test our interpretation of bulk events as photoionization of contaminants, we performed two more studies. For S2-bulk events, we analyzed a set of data taken during a time period of five days in July 2015, when the getter used in the closed loop to remove contaminants in the liquid argon was turned off for maintenance. Over this period, we expect an increase in contaminants and, if our hypothesis is correct, in bulk photoionization. This is indeed what we observe with the data, but the increase is relatively modest. Indeed, the fraction of S2-bulk events increased by $\sim 35\%$ [9].

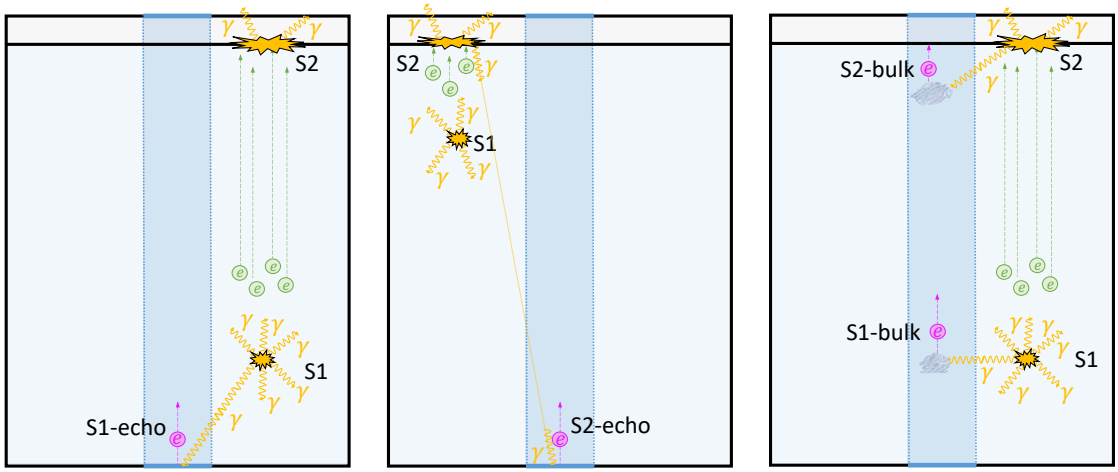

Figure 2.51: Schematic of the three different SEC types studied in this work. The left scheme shows the S1-echo type, the central one the S2-echo type and the right one the bulk events (both S1-bulk and S2-bulk).

For S1-bulk events, although it is plausible that the SEC may originate from the S1 light, there are two possible interpretations for the origin of the SECs: either they are due to S1 or they are remnants from a previous event, e.g. an electron captured by some electronegative impurity and then released randomly in the time window between S1 and S2. To test this hypothesis, we looked at a possible time correlation with the previous events. By considering a time window of 10 s and

with no specific selection of the previous events, we do not observe any correlated component with $\tau \gtrsim 20$ ms [9].
We observed several categories of single isolated electrons in association with standard scintillation-ionization S1-S2 signals with the DS-50 LAr TPC. A graphical schematic is shown in Fig. 2.51, which summarizes the different event types.
Since this is the first study with an argon detector, it is interesting to compare our results to the abundant literature available with xenon detectors. One of the most comprehensive studies was performed by the LUX Collaboration [112] and we mostly compare our results to this one in the following. Section III of that paper reports about our kinds of phenomena: a) photoionization electrons that are detected within hundreds of microseconds after the S1 and S2 pulses, b) delayed emission of individual electrons at the millisecond-to-second scale, c) electron emission that appears independent of prior interactions, and d) clustered electron emission that occurs within tens of milliseconds after S2. The present study gives our experience with the first phenomenon; the second and third are briefly discussed in Ref. [111] and will be treated in more detail in an upcoming DS-50 publication. We do not observe the clustered electron emission that occurs within tens of milliseconds after S2.
S1-echo and S2-echo events are observed both with xenon detectors, namely LUX [112], ZEPLIN-III [114], XENON100 [115] and with DS-50. The main structural difference between these detectors in this respect is that the DS-50 cathode and anode planes are continuous planes, with the surface facing the active volume coated with ITO and TPB, whereas LUX uses metal grids and there is no wavelength shifting of the light. The quantum efficiency of TPB in DS-50 and that of metal grids in LUX were measured. In both experiments, they were calculated with both S1 and S2 photons, and the results agreed in both cases within a factor of two. In both LUX and DS-50 we observe events that are compatible with photoionization from the extraction grid, right below the gas-liquid interface.
S1-bulk and S2-bulk events are observed by both LUX [112] and DS-50 Collaborations [9]. Interesting considerations about the origin of S2-bulk events in LUX were obtained from the $\Delta t_{\mathrm{S2-S1}}$ distribution. Unfortunately, due to the limited time window of our data acquisition, we have a severe restriction on the time range of the S2-bulk events, preventing us from making similar considerations. LUX attributed both S1-bulk and S2-bulk events to the photoionization of impurities dissolved in liquid xenon, more likely neutral molecules than negative ions. The hypothesis of photoionization in the liquid xenon was likewise suggested by the XENON-100 [115] Collaboration, which also showed a correlation of the rate with the electron lifetime, and by the ZEPLIN-II [113] and ZEPLIN-III Collaborations [114]. We observed with DS-50 a correlation with impurity concentration, as the rate of S2-bulk events increased by about 35% during a period of time with the getter switched off [9]. We note that, during the same time period, as described in a previous DS-50 paper [111], we observed a five-fold increase in isolated, i.e., far in time from a standard event, single electrons. Hence, while our data point to an impurity-related origin for photoionozation events, our understanding remains incomplete and inconclusive.
Both LUX and DS-50 measured the probability of photoelectric emission per unit

length in the bulk. LUX measured $(5-20)\times 10^{-5} e^-/\gamma_{UV}/\mathrm{m}$ [112] while DS-50 with S2-bulk events measured $\sim 4\times 10^{-6} e^-/\gamma_{UV}/\mathrm{m}$ [9], i.e. smaller by more than a factor of 10. While there is no a priori reason the LUX and the DS-50 values for photoelectric emission should be the same, it may be of interest to identify the factors that contribute to the difference in values observed. The measured electron lifetime in DS-50 is much larger than both the lifetime measured by LUX (by more than a factor of 10) and the DS-50 maximum drift time (by a factor of 30). Since the electron attachment rate at the drift field of 200 V/cm (the same for DS-50 and LUX) is about the same for argon and xenon for e.g. O_2 [129], it is plausible that the lifetime difference is mostly driven by a lower concentration of contaminants in DS-50 than in LUX. This conclusion is also coherent with the higher expected outgassing load in a liquid xenon system due to the higher temperature. Concerning the photoionization of negative ions, the different affinities and UV emission energies between liquid argon and liquid xenon may also play a role in the measured PEP_{S2} values.
Unfortunately, identification of the impurity molecules was not possible in both experiments and will have to wait for future research.
It should be noted that the report by LUX [112] is a snapshot in time and that xenon-based experiments have to-date achieved much improved lifetimes. Given that the same wavelength shifter will be deposited on the cathode of DS-20k, the S1-echo and S2-echo events observed with DS-50 are most likely to be present in DS-20k as well. Given that the aspect ratios of the DS-50 and DS-20k TPCs are almost identical, and that the S2 gain is intended to be the same, the number of echo events will scale with the event rate in the detector, i.e. the size of the detector. In addition to the event rate factor, there will be a factor of five more S2-bulk events due to the longer drift length of DS-20k, assuming the level of contaminants remains the same.

To summarize, the excess at low energy observed in various dark matter and neutrino detectors has been observed also in the DS-50 experiment. We have provided a tentative interpretation of some of the observed events as due to photoelectric emission from the cathode of the TPC from S1 or S2 photons, as well as a bulk component from the extraction of electrons in the liquid, as a consequence of a still-to-understand mechanism. However, also other components are present, that are still-to-be studied. Efforts from the community are needed to completely understand the mechanism regulating the single electron background component in order to reduce it and characterize it for next generation detectors. Getting rid of this background will definitely help in lowering the experimental threshold and in reaching a significantly improved sensitivity.

Chapter 3

Low energy electron interactions

Short introduction

In this chapter, we will introduce the basics of low energy electron processes, considering one scattering process, namely the electron-nucleus scattering, and a particular process known as atomic parity violation, which involves parity violating transition in atomic systems. The common idea is to consider electron scattering by isolating the parity violating contribution in order to study the weak part of their interactions.

3.1 PVES: Parity Violation Electron Scattering

Electrons have been the main characters of late 1800s and early 1900s physics. In 1897, J.J. Thomson discovered the electron, a tiny elementary particle with negative charge. Since then, electrons have been used in many experiments as the research was developing. At the beginning of the 1900s, E. Rutherford, together with his students Geiger and Marsden, used α particles to study the atomic structure, leading to the actual discovery of the nucleus, and paving the way toward a successful model for the atoms. The Rutherford model for the atom was not perfect, as the electron orbits could not be stable in classical theory, but thanks to N. Bohr and the quantum mechanics theory, the Rutherford model was perfected, leading to the model still adopted in today's description of the atom.
Although the nucleus was discovered through α particle scattering from thin gold foils, the actual field of nuclear structure studies was brought on during the years using electron scattering. Electrons are easier to accelerate, allowing one to study the nuclear structure at different energy scales, and being leptons, their interactions can be described in a rather simple fashion. α particles have hadronic nature, thus requiring a more complicated description when interacting with the nucleus. The electron energy can be adjusted to obtain a de Broglie wavelength of the particle mediating the interaction of the order of nuclear dimensions. In particular, by using MeV-GeV electron energies, one can extract information for instance on the nuclear radii. Still today, electrons are used to probe nuclei to understand the

mechanisms at the basis of their structure.
In first approximation, the elastic scattering process of an electron off a nucleus A, with Z protons and N neutrons,

$$e^- + {}^Z_N A \rightarrow e^- + {}^Z_N A, \tag{3.1}$$

can be described by an electromagnetic process in which we can assume the nucleus to have infinite mass and to be point-like. The electron, travelling in the proximity of the nucleus, feels the Coulomb potential generated by the nuclear electric charge.

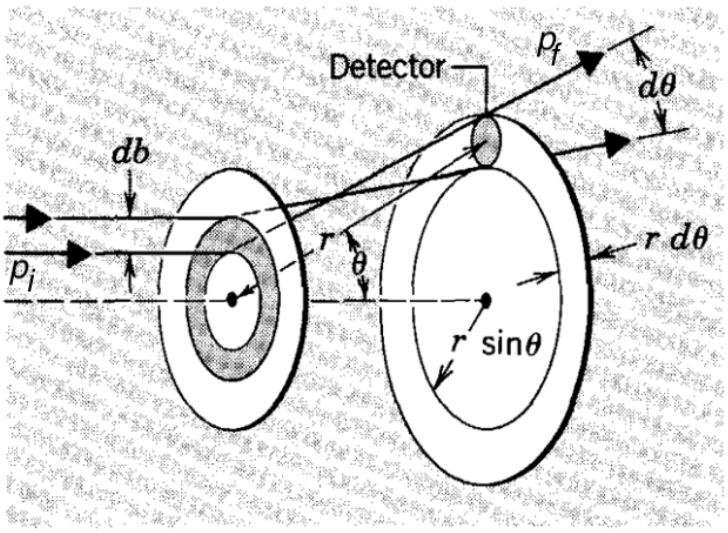

Figure 3.1: Schematic of the geometry of the elastic scattering of electrons off a point-like nucleus [130].

In Fig. 3.1, a schematic of the geometry of the system is shown, where the parameter r describes the distance between the electron and the target nucleus during the trajectory, b the impact parameter, θ the scattering angle at which the electron exits after the scattering and p_i and p_f the initial and final electron momenta, respectively. As it can be noticed, the system has cylindrical symmetry, so it is convenient to consider polar coordinates.
Considering the incoming electrons with impact parameter in the interval $[b, b+db]$, these will be deflected at a scattering angle in the interval $[\theta, \theta+d\theta]$, corresponding to e solid angle $d\Omega$ once the detector position is fixed. We can define the number of incoming electrons per unit of time and area as N_0, so that, the number of electrons collected by the detector per unit of time is

$$dN = N_0 \cdot (2\pi b db)\,, \tag{3.2}$$

where the term in between parenthesis indicates the infinitesimal area, $d\sigma$, through which the particles get diffused. Thus, the elastic cross section is [1]

$$d\sigma(\theta) = \frac{d\sigma}{d\Omega} d\Omega = \frac{d\sigma}{d\Omega} 2\pi \sin\theta d\theta = -2\pi b db\,, \tag{3.3}$$

[1]Let us notice that the minus sign in the last term of Eq. 3.3 is due to the definition of dN as the difference between the initial and final number of particles.

where we defined the solid angle as

$$d\Omega = 2\pi \sin\theta d\theta \,. \tag{3.4}$$

Rearranging the latter equations, we obtain that the cross section reads

$$\frac{d\sigma}{d\Omega} = -\frac{b}{\sin\theta}\frac{db}{d\theta} \,. \tag{3.5}$$

Using the energy conservation principle and the kinematic of the process, one can obtain a relation between the scattering angle and the impact parameter b [130], so that

$$\tan\frac{\theta}{2} = \frac{Ze^2}{(4\pi\epsilon_0)2E_e b} \,, \tag{3.6}$$

which translates in

$$b = \frac{Ze^2}{(4\pi\epsilon_0)2E_e}\cot\frac{\theta}{2} \,, \tag{3.7}$$

where E_e is the incoming electron energy, ϵ_0 the vacuum dielectric constant, and Ze represents the electric charge of the target nucleus. We can now calculate the differential

$$\frac{db}{d\theta} = -\frac{Ze^2}{(4\pi\epsilon_0)8E_e}\frac{1}{\sin^2\frac{\theta}{2}} \,. \tag{3.8}$$

This discussion leads to the calculation of the classical Rutherford cross section for electron elastic scattering off nuclei, which is given by

$$\left(\frac{d\sigma}{d\Omega}\right)_{\text{Ruth}} = -\frac{b}{\sin\theta}\frac{db}{d\theta} = \frac{(Ze^2)^2}{(4\pi\epsilon_0)^2(4E_e)^2}\frac{1}{\sin^4\frac{\theta}{2}} = \frac{Z\alpha^2}{4E_e^2}\frac{1}{\sin^4\frac{\theta}{2}} \,, \tag{3.9}$$

where we used the fine structure constant definition[2] $\alpha = e^2/(4\pi\epsilon_0)$.
However, the Rutherford theory for electron scattering neglects the effect due to relativistic regimes. In fact, to probe nuclei, the needed electron energies are in the range of the hundreds of MeV up to a few GeV, which make the electron be relativistic ($m_e \simeq 511\,\text{keV}$). To this purpose, the Mott theory of electron scattering accounts for these relativistic effects and also for the spin of the involved particles. The Mott cross section is built as a correction to the Rutherford one, with an additional factor, resulting in

$$\left(\frac{d\sigma}{d\Omega}\right)_{\text{Mott}} = \left(\frac{d\sigma}{d\Omega}\right)_{\text{Ruth}}\left(1 - \beta^2\sin^2\frac{\theta}{2}\right) \,, \tag{3.10}$$

where β is the relativistic factor, i.e. the velocity of the electrons in units of the speed of light[3], that can be set to 1 for the considered energy regimes.
Therefore, the cross section becomes

$$\left(\frac{d\sigma}{d\Omega}\right)_{\text{Mott}} = \frac{Z\alpha^2}{4E_e^2}\frac{\cos^2\frac{\theta}{2}}{\sin^4\frac{\theta}{2}} \,. \tag{3.11}$$

[2] We are considering natural units, $\hbar = c = 1$.

[3] Reintroducing the speed of light, the relativistic factor reads $\beta = v/c$, with v being the electron velocity.

In a similar way to what was discussed in the context of elastic neutrino scattering off nuclei ($\mathrm{CE}\nu\mathrm{NS}$), the cross section has to be corrected to consider an extended distribution for the nucleus, so going beyond the point-like approximation of the nucleus. The correction factor is the form factor. In fact, in the case of electron scattering off nuclei is easy to understand that the interaction is with a charge density distribution and not with a point-like Ze electric charge. Thus, we can define the nuclear charge density[4] $\rho_{\mathrm{ch}}(r)$, which will be normalized to the total charge in units of electron charge, e_0, so to the atomic number Z.
However, the cross section does not depend directly on the nuclear density, but on its Fourier transform, which is known as the nuclear form factor. Given a generic density, we can define the form factor as

$$F(q) = \int \rho(\vec{r})\, e^{i\vec{q}\cdot\vec{r}} d^3\vec{r}\,. \tag{3.12}$$

Considering the case of nuclear densities, with spherical symmetry, the integral reduces to

$$F(q^2) = \frac{4\pi}{q} \int \rho(r)\ \sin(qr)\, r dr\,, \tag{3.13}$$

which being the Fourier transform of a spatial-dependent quantity, depends on the momentum space. Usually, a factor $1/\mathrm{normalization}$ is introduced in the nuclear form factor definition, in order to normalize it to unity for $q^2 \to 0$.
The charge form factor will be defined by substituting the nuclear charge density, ρ_{ch}, inside the form factor definition in the latter equation, considering the normalization being the atomic number Z.
The cross section will scale as the square of the charge form factor. In particular, one can consider the so-called *Plane Wave Born Approximation*, PWBA, in which the wave function of the incident electron is considered to be a plane wave before and after the scattering. Under this approximation, the elastic cross section for the scattering of relativistic electrons off nuclei can be obtained by simply multiplying the Mott cross section in Eq. 3.11 by the charge form factor squared, namely

$$\left(\frac{d\sigma}{d\Omega}\right)_{\mathrm{PWBA}} = \left(\frac{d\sigma}{d\Omega}\right)_{\mathrm{Mott}} |F_{\mathrm{ch}}(q^2)|^2\,. \tag{3.14}$$

As the nuclear charge density is a property of the specific target nucleus considered, the form factor is a target-dependent quantity in principle. Therefore, a measurement of the charge form factor gives information on the charge distribution of the nucleus.
In experimental measurements, the cross section is measured as a function of the scattering angle, and it is easy to understand that this translates into a measurement of the form factor as a function of the scattering angle, and thus as a function of the momentum transfer. In this sense, it is useful to define the charge density as the anti-Fourier transform of the charge form factor, instead of the opposite. Hence, the density is given by

$$\rho_{\mathrm{ch}}(r) = \frac{Z}{2\pi^2 r} \int_0^\infty F_{\mathrm{ch}}(q^2)\ \sin(qr)\, q dq\,, \tag{3.15}$$

[4]Usually the nuclear densities are assumed to be spherically symmetric, as there is generally a central potential structure. So, the densities only depend on the module of the radial distance.

and this can be employed to convert an experimental measurement of the cross section (i.e. form factor) into a measurement of the nuclear charge density and the corresponding nuclear charge radius. By considering a simple Taylor expansion of the $\sin(qr)$ in the form factor definition in Eq. 3.13, the interconnection between the form factor and the radius of the distribution can be made explicit:

$$F_{\rm ch}(q^2) = \frac{1}{Z}\frac{4\pi}{q}\int \rho_{\rm ch}(r)\Big[qr - \frac{1}{3!}(qr)^3 + ...\Big] r\, dr = \\ = \frac{1}{Z}\int \rho_{\rm ch}(r)\Big[4\pi r^2 - \frac{1}{6}q^2\, 4\pi r^4\Big] dr + ... = \Big[1 - \frac{1}{6}q^2\langle r^2_{\rm ch}\rangle + ...\Big]\,, \qquad (3.16)$$

where we considered the charge distribution as an example. The term of order q^2, depends on the expectation value of the square of the nuclear radius, also known as *root-mean-square* radius, $\langle r^2\rangle$. From this expansion, but in general, from the presence of a sinusoidal term in the form factor definition, it is clear that the cross section in the PWBA presents periodical minima.
Experimental measurements of the cross section for the elastic scattering of electrons off nuclei showed great disagreement between the expression in Eq. 3.14 and the data points. In particular, the experimental cross section does not show big drops and deeps in the cross section, so that the minima are not well defined. This is not compatible with the PWBA or Mott and Rutherford theories.

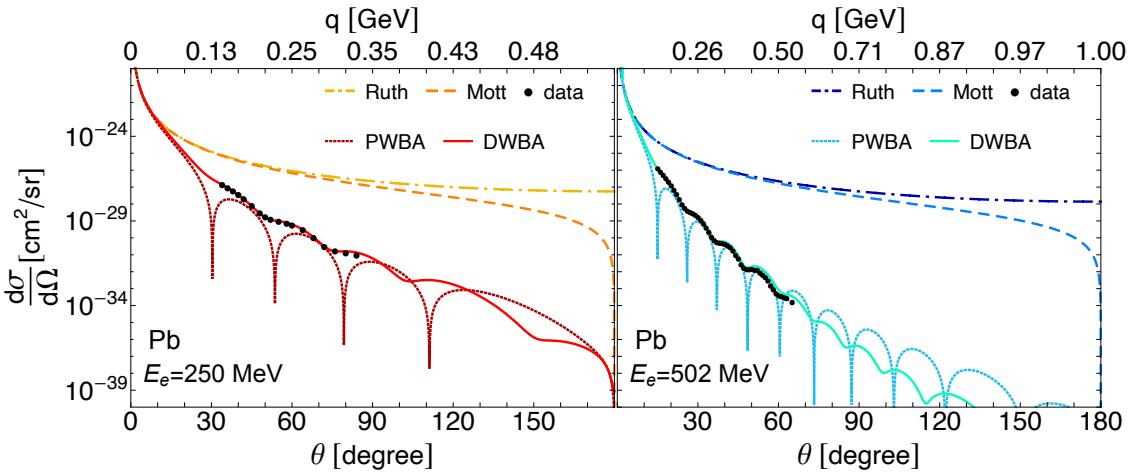

Figure 3.2: Comparison between the experimental measurements of the cross section for the elastic scattering of electrons off lead ^{208}Pb with the theoretical predictions in the Rutherford, Mott, PWBA and DWBA theories. The left panel refers to an electron energy $E_e \simeq 250$ MeV [131], while the right one to $E_e \simeq 502$ MeV [132, 133]. The cross section is given as a function of the scattering angle (and the corresponding momentum transfer).

The PWBA does not hold in the realistic case of experimental setups because the electron wavelengths are not plane waves. They are distorted by the intense nuclear electromagnetic field. To account for the wave distortion due to such nuclear force fields, the developed theory is called *Distorted Wave Born Approximation*, or DWBA [134, 135].

The effect of the electromagnetic field on the electron wave function has a double outcome: it shifts the initial and final electron momenta toward higher values in the proximity of the nucleus because of the attractive electrostatic potential, and then, the attractive potential focuses the wave function toward the nuclear region. Practically speaking, the cross section has to be calculated by solving the Dirac equation for the elastic scattering of electrons in the nuclear field, and this is usually done by exploiting a partial wave expansion and then numerically solving the Dirac equation in the radial form for each partial wave.
In Fig. 3.2, we compare the experimental data for the elastic scattering cross section for electron off lead $^{208}\mathrm{Pb}$ nuclei taken from Ref. [131] (for $E_e \simeq 250\,\mathrm{MeV}$) and from Refs. [132, 133] (for $E_e \simeq 502\,\mathrm{MeV}$), with the theoretical predictions in the Rutherford model (dot-dashed curves), Mott model (dashed curves), PWBA (dotted curves) and DWBA (solid curves). The cross section is shown as a function of the scattering angle but also of the corresponding momentum transfer. In fact, due to the kinematics, the scattering angle defines the momentum transfer given a certain electron energy and a fixed target mass. In particular, it results that the momentum transfer can be defined as calculated in Appendix B

$$q^2(\theta) = \frac{4E_e^2 \sin^2(\theta/2)}{1 + \dfrac{2E_e}{M_{\mathrm{T}}} \sin^2(\theta/2)}\,, \tag{3.17}$$

where in this case, we considered M_T being the $^{208}\mathrm{Pb}$ mass.
From Fig. 3.2, we obtain a clear comparison between the different theoretical predictions. The effect of the form factor has a significant impact on the cross section, and this is clearly visible by looking at the difference in the magnitude of the Mott and Rutherford cross section with respect to the PWBA and DWBA. The effect is dependent on the scattering angle, and thus the momentum transfer, and becomes more significant as the momentum transfer grows. This is visible also by comparing the left and the right panel of the figure. For higher electron energies, the momentum transfer is larger fixing the scattering angle, and thus the impact of the form factor is larger. This is due to the fact that a larger momentum transfer corresponds to a smaller de Broglie wavelength, so a smaller spatial dimension probed in the scattering. In this sense, higher momentum transfer corresponds to probing the nucleus on a smaller scale, so probing its constituents instead of the entire object. From the figure, it is also shown the effect of Coulomb distortions. The cross section in PWBA shows clear minima and drops, and evidently does not describe well the experimental data points, while the DWBA curves are in great agreement with the data.
The comparison of theoretical predictions for the cross section with data, considering different form factor parametrizations and different nuclear parameters (such as the radius), allowed us to extract information on the nuclear structure of the targets.
To give an idea of the possible procedure to extract the radius and the density of the lead nucleus using the data presented in Fig. 3.2, one can use a simple parametrization for the charge form factor, namely the symmetrized 2pF defined in Eq. 2.71. This parametrization is particularly useful, as it allows one to describe

the nuclear density as given by a box density, whose sharp drop is mitigated by the convolution with a Gaussian drop. This translates into a two parameters dependent density, whose Fourier transform (i.e. correspondent form factor) is analytic. The symmetrized 2pF (SF) is known to be a fairly good model to describe nuclear densities. In this model, the density has the form

$$\rho_{\mathrm{ch,\,2pF}}(r) = Z\rho_0 \frac{\sinh(c/a)}{\cosh(c/a) + \cosh(r/a)}\,, \tag{3.18}$$

where ρ_0 is a normalization factor and it is defined as

$$\rho_0 = \frac{3}{4\pi c(c^2 + \pi^2 a^2)}\,. \tag{3.19}$$

In the density definition, we have considered the density as normalized to unity, for consistency with the precedent definition. Let us note that one could also redefine the density as normalized to unity instead to the electric charge. In the latter case, also the other definitions have to be redefined accordingly.
The parameters that define the density and the form factor are c and a. c is known as *half-density radius*, as it is the radius at which the density becomes 50%. The a parameter is called *diffuseness* and it is related to the way the density drops at the edge, so basically how steep is the Gaussian drop. The diffuseness parameter is usually converted into the so-called *thickness* parameter, t, which quantifies the distance on which the density drops from 90% to 10%. The thickness is obtained from the diffuseness from $t = 4\,a\,\ln 3$.

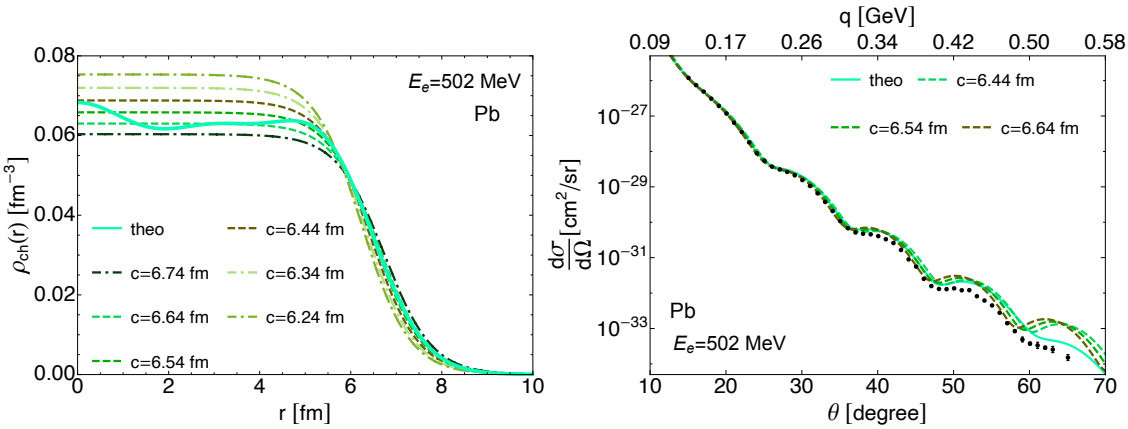

Figure 3.3: (Left) Comparison between a theoretical nuclear model density and the symmetrized 2pF density, with $t = 2.3\,\mathrm{fm}$ and various c values, for the case of a lead nucleus. (Right) Comparison between the experimental data at $E_e = 502\,\mathrm{MeV}$ [132, 133] and the predictions in DWBA obtained using the symmetrized 2pF density with different c values (dashed lines) compared with the theoretical prediction given by a nuclear model (solid line).

One advantage of the symmetrized 2pF model is the fact that the distribution radius is expressed analytically in terms of c and a, through the formula

$$R_{\mathrm{2pF}} \equiv \sqrt{\frac{3}{5}c^2 + \frac{7}{5}\pi^2 a^2}\,. \tag{3.20}$$

For reference, also a different model with a similar form is known as 2pF (not symmetrized). This model is very similar, but it does not provide an analytic result for the form factor. In that model, also Eq. 3.20 is formally not valid.
Using the symmetrized 2pF model, we can now generate many densities by varying the two model parameters. Experimentally, what is commonly seen is that the drop of the density is expected to be rather constant from nucleus to nucleus, while the c parameter gives the actual difference. For our demonstrative purpose, we fixed $t = 2.3\,\mathrm{fm}$, which is the typical value for lead, and let only the c parameter free to vary.
In Fig. 3.3 (left), we show the densities generated by varying the c parameter in a reasonable range for $^{208}\mathrm{Pb}$, compared with a density obtained from a theoretical nuclear model (solid line). In the right panel of the same figure, we show the prediction for the cross section corresponding to the densities in the left panel compared to the experimental data at $E_e \simeq 502$ MeV. Varying the c parameter, clearly also the cross section is modified. The solid cyan line shows the prediction for the theoretical nuclear model considered as a comparison.
By fitting the different predictions obtained by varying c, one can find the best fit parameter value which better reproduces the experimental data, and thus, using Eq. 3.20 translate it into a measurement of the charge radius. In this particular case, we obtained $c_{\mathrm{BF}} \simeq 6.64\,\mathrm{fm}$, which corresponds to $R_{\mathrm{ch}} \simeq 5.5\,\mathrm{fm}$.
This represents a simple estimate of the charge radius of $^{208}\mathrm{Pb}$, but it is meant to be an example of the procedure to extract a charge radius measurement from the experimental cross section data. This procedure, of course, can be complicated by letting a free-to-vary, but also by considering more complicated models for the nuclear densities, such as the *Sum-of-Gaussians* (SOG), the *Fourier-Bessel* (FB), the *3-parameter-Fermi* (3pF) models, and many others. In this way, the charge radius of a large sample of nuclei has been measured during the decades, reaching high precision levels, and they have been collected in rather complete tables, such as the ones reported in Ref.[136].

All the above discussions consider the interaction of electrons with the electric charge distribution of the nuclear matter. In practice, we have considered a photon exchange between an incoming electron with the charge density of a target nucleus, and this allowed us to study the nuclear charge distribution and to extract information such as the nuclear charge radius.
However, the same interaction can be mediated by a Z boson and happens through the weak interaction. In Fig. 3.4 we show the two diagrams contributing to the scattering process: the electromagnetic process (left) and the weak one (right). The weak contribution is subdominant to the electromagnetic one, so that, the elastic cross section is correctly the one discussed above. Nevertheless, it is interesting to investigate the possibility of measuring the weak contribution to the scattering. In fact, the Z boson does not couple to the electric charge of the nucleus, but to the weak counterpart, i.e. the nuclear weak charge. Therefore, the measurement of the weak interaction between electrons and nuclei, allows one to probe the nuclear weak density distribution. To further show it graphically, in the diagrams in Fig. 3.4 we used different colors for the nuclei vertices to indicate that

the coupling is not with the exact same distribution in the two diagrams.

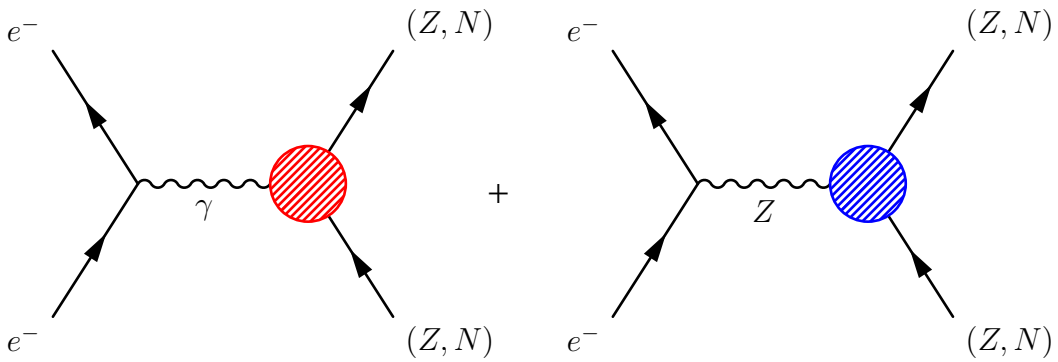

Figure 3.4: Diagram of the elastic scattering of electrons off nuclei, where the blob indicates the interaction vertex between the nucleus and the γ/Z boson which mediates the interaction. On the left, the diagram mediated by the photon is shown, and the red color of the blob indicates the interaction with the nuclear electric charge distribution. On the right, the Z mediated diagram is displayed, and the blue color indicates the interaction with the nuclear weak density distribution.

Considering the contribution from both diagrams, the scattering amplitude is given by the sum of the two amplitudes, so that in principle also an interference can occur. The cross section will be obtained by taking the module squared of the total amplitude:

$$\sigma_{\mathrm{TOT}} \propto |\mathcal{A}_{\mathrm{EM}} + \mathcal{A}_{\mathrm{wk}}|^2 \,, \tag{3.21}$$

where $\mathcal{A}_{\mathrm{EM\,(wk)}}$ represents the electromagnetic (weak) amplitude. Usually, the weak amplitude is neglected because it is of order G_F, and hence significantly smaller than the electromagnetic one. By solving the square, the cross section becomes proportional to

$$\sigma_{\mathrm{TOT}} \propto |\mathcal{A}_{\mathrm{EM}}|^2 + |\mathcal{A}_{\mathrm{wk}}|^2 + 2|\mathcal{A}_{\mathrm{EM}}| \cdot |\mathcal{A}_{\mathrm{wk}}| \,, \tag{3.22}$$

where the second term can be safely neglected as it is order G_F^2. If one wants to be able to measure the weak part of the interaction, one has to find a manner to isolate its contribution, as otherwise it would be incorporated in the measurement of the electromagnetic one. The solution is given by exploiting the non-conservation of parity in the weak interaction and conservation in the electromagnetic one. Therefore, the total cross section for different electron helicities reads

$$\sigma^{\uparrow}_{\mathrm{TOT}} \propto |\mathcal{A}^{\uparrow}_{\mathrm{EM}}|^2 + 2|\mathcal{A}^{\uparrow}_{\mathrm{EM}}| \cdot |\mathcal{A}^{\uparrow}_{\mathrm{wk}}| \,, \tag{3.23}$$

$$\sigma^{\downarrow}_{\mathrm{TOT}} \propto |\mathcal{A}^{\downarrow}_{\mathrm{EM}}|^2 + 2|\mathcal{A}^{\downarrow}_{\mathrm{EM}}| \cdot |\mathcal{A}^{\downarrow}_{\mathrm{wk}}| = |\mathcal{A}^{\uparrow}_{\mathrm{EM}}|^2 - 2|\mathcal{A}^{\uparrow}_{\mathrm{EM}}| \cdot |\mathcal{A}^{\uparrow}_{\mathrm{wk}}| \,, \tag{3.24}$$

where $\uparrow$ / $\downarrow$ refer to the helicity of the incoming electron. In the latter equations, we made use of the fact that electromagnetic interactions are parity conserving, while weak interactions maximally violate parity.
In principle, it can be understood that building an asymmetry, as a difference between cross sections for different electron helicities, it would be possible to isolate

the weak amplitude, namely

$$\text{Asym.} \propto \frac{\sigma^{\uparrow}_{\text{TOT}} - \sigma^{\downarrow}_{\text{TOT}}}{\sigma^{\uparrow}_{\text{TOT}} + \sigma^{\downarrow}_{\text{TOT}}} \propto \frac{|\mathcal{A}^{\uparrow}_{\text{EM}}| \cdot |\mathcal{A}^{\uparrow}_{\text{wk}}|}{|\mathcal{A}^{\uparrow}_{\text{EM}}|^2} = \frac{|\mathcal{A}^{\uparrow}_{\text{wk}}|}{|\mathcal{A}^{\uparrow}_{\text{EM}}|} \,. \tag{3.25}$$

By building this asymmetry as the difference between the cross section for different helicities, normalized to the sum of the cross sections, it is clear that one isolates the weak contribution.
Substituting the actual cross section for right- and left-handed electrons, one obtains an asymmetry in the form of

$$A_{\text{pv}} = \frac{d\sigma/d\Omega_+ - d\sigma/d\Omega_-}{d\sigma/d\Omega_+ + d\sigma/d\Omega_-} = -\frac{G_F Q^2}{4\sqrt{2}\pi\alpha} \frac{Q_W}{Z} \frac{F_{\text{wk}}(q^2)}{F_{\text{ch}}(q^2)} \,, \tag{3.26}$$

where now $+/-$ indicate the electron helicity, Q^2 is the four-momentum squared transfer and F_{wk} is the weak form factor, i.e. the weak counterpart of the charge form factor. In the latter definition, we have made explicit use of the normalizations of the form factors, which gives the term Q_W/Z, so the ratio between the nuclear weak charge and the nuclear electric charge.
This asymmetry is the actual observable of what is commonly known as parity violating electron scattering (PVES) experiments, in which polarized electrons are delivered on a target, and the detectors measure the number of scattered electrons with a certain helicity, and by measuring both helicities, a measurement of the parity violation asymmetry, A_{pv}, is obtained.
Let us recall that the nuclear weak charge represents basically the weak coupling to the entire nucleus and it is defined at the tree-level as

$$Q_W = -2[Z g^{\text{ep}}_{\text{AV}} + N g^{\text{en}}_{\text{AV}}] \,, \tag{3.27}$$

with $g^{\text{ep}}_{\text{AV}}$ and $g^{\text{em}}_{\text{AV}}$ being the electron-proton and electron-neutron weak couplings[5].
The dependence on the nuclear weak charge is interesting as it is similar to the one discussed for CEνNS searches. Also in the case of electrons, the coupling with protons introduces a dependence on the weak mixing angle. In this sense, also the parity violating asymmetry depends on the weak mixing angle (and enables one to measure it), and not only on the nuclear distributions.
All the considerations discussed for the charge form factor are applicable to the weak form factor. It is defined as the Fourier transform of the nuclear weak density, ρ_{wk}, and it is related to the so-called weak radius R_{wk}. The main difference between the two form factors is the knowledge we have about them today. The charge radius is well known for a large compilation of nuclei, while the weak distribution is still relatively unknown. The main reason is because of the difficulty of accessing the weak distribution, as the parity violating asymmetry is a small quantity. The weak distribution is of course accessible through weak processes, like CEνNS, but there are not many high precision electroweak measurements of the weak density available. There are some hadronic probes that allow one to get

[5]A more detailed discussion of these couplings and the corresponding radiative corrections to be applied can be found in Appendix A.

some information on the nuclear weak distribution, however, they suffer from theoretical model uncertainties due to the Quantum Chromodynamics (QCD) theory. At the same time, nuclear theorists are trying to develop solid models to describe the nuclear structure starting from the microscopic mechanisms that regulate the interactions between the nucleons, but this field is still under development, and up to now a robust theoretical calculation applicable to all the nuclei has not been achieved. This said, the need for electroweak measurements of the nuclear weak densities is crucial to understanding the interactions at the basis of nuclear structure, which in turn have consequences also on the description of much larger objects, such as neutron stars. Neutron stars' inner structure is still a mystery, but it is expected that the fundamental mechanisms regulating their structure are not different from the ones governing heavy nuclei, making PVES measurement a sort of open window toward neutron stars' nature [137–139].
Before going into the discussion of the available (and future) electroweak measurements of the weak nuclear radius and the corresponding density, let us discuss a crucial detail about the definition of the asymmetry in Eq. 3.26.
Often, the asymmetry is expressed in terms of other two form factors, that we have already discussed in the context of CEνNS, namely the nuclear proton and neutron form factors. They are related to the distribution of protons and neutrons inside the nucleus, instead of the distributions of charge and weak charge. This is due to the fact that, since the neutrons are neutral particles, they could be expected to not contribute to the nuclear charge distribution. Similarly, since the weak coupling to protons is suppressed with respect to the coupling to neutrons, the contribution of protons to the nuclear weak charge is expected to be negligible. In this sense, the asymmetry is sometimes presented as

$$A_{\rm pv} \propto -\frac{G_F Q^2}{4\sqrt{2}\pi\alpha}\frac{F_n(q^2)}{F_p(q^2)}\,. \tag{3.28}$$

From this, it can be understood that the measurements of the charge distribution through the elastic scattering of electrons off nuclei can be thought of as a measurement of the proton distribution inside the nucleus. Instead, the PVES process can lead to a measurement of the neutron nuclear distribution. By combining the two measurements, we obtain information about both the *root-mean-square* ($\langle r^2\rangle^{1/2}$) nuclear proton and neutron radii, R_p and R_n, respectively, whose squares are defined by

$$R^2_{p,n} = \int r^2\rho_{p,n}(r)d^3r \Big/ \int \rho_{p,n}(r)d^3r\,, \tag{3.29}$$

where $\rho_{p(n)}(r)$ is the proton(neutron) nuclear density distribution.
However, the quantity of interest of a PVES measurement is not the actual nuclear radius, but the difference between the neutron and the proton radii, which is known as neutron skin (a scheme of which can be found in Fig. 3.5), i.e.

$$\Delta R_{\rm np} \equiv R_n - R_p\,. \tag{3.30}$$

One could expect the existence of a neutron skin as due to the Coulomb repulsion between protons, which being localized inside the nucleus would tend to push

each other outer of the nucleus. However, the neutron skin is a more complicated quantity, as it is the result of the competition of many forces inside the system, besides the Coulomb force only. Inside the nucleus, there are effects due to the surface tension that keeps the nucleus together, the symmetry energy that characterizes the variation of the binding energy as the neutron-to-proton ratio varies, some possible isospin-breaking effects and in general the fact that the number of neutrons and protons inside the nucleus usually differs [139]. The balancing between all these effects leads to a stiff or soft nuclear matter depending on the prevalent contribution.
In general, light nuclei tend to have few nucleons, usually balanced between the number of neutrons and protons. In this case, the skin is expected to be very small and even negative (sometimes this is called proton-skin to indicate the dominance of the proton contribution over the neutron one), as the dominating effect is expected to be Coulombian repulsion.

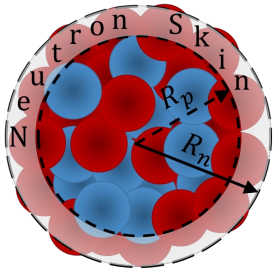

Figure 3.5: Pictorial representation of the neutron and proton distribution inside the nucleus, with the indication of the neutron skin.

Instead, for heavy nuclei the number of neutrons is usually larger than the number of protons (in fact it is often referred to as neutron-rich matter) [140], and thus it is expected that nucleons distribute to form an outer layer of neutrons, a sort of crust, toward the nuclear surface which constitutes a positive skin, i.e. a neutron skin (as shown in Fig. 3.5).
In a similar way, we can define also the so-called weak skin, as the difference between the nuclear weak and charge radii, namely

$$\Delta R_{\mathrm{wk,\,skin}} \equiv R_{\mathrm{wk}} - R_{\mathrm{ch}}\,. \tag{3.31}$$

The two skins are different, in fact, the approximation of the charge density being constituted only by the contribution of protons in reality does not hold. The neutrons contribute to the charge density, as well as the protons contribute to the weak density. In Fig. 3.6, we show an example of nuclear densities from a nuclear mean field model, FSUGold [141, 142], for the case of $^{208}\mathrm{Pb}$. From the image, the difference between charge (blue) and proton (red) density distributions can be appreciated. Also, the difference between the weak (black) and the neutron (green) ones is visible in the plot. It is clear that the main contribution to the charge distribution comes from protons, with a small contribution coming from the neutrons, and to the weak one is given by neutrons, even if protons contribute up to about 10-15%. Therefore, to obtain the charge and weak densities in Fig. 3.6 we accounted for the contribution of both proton and neutron distributions.

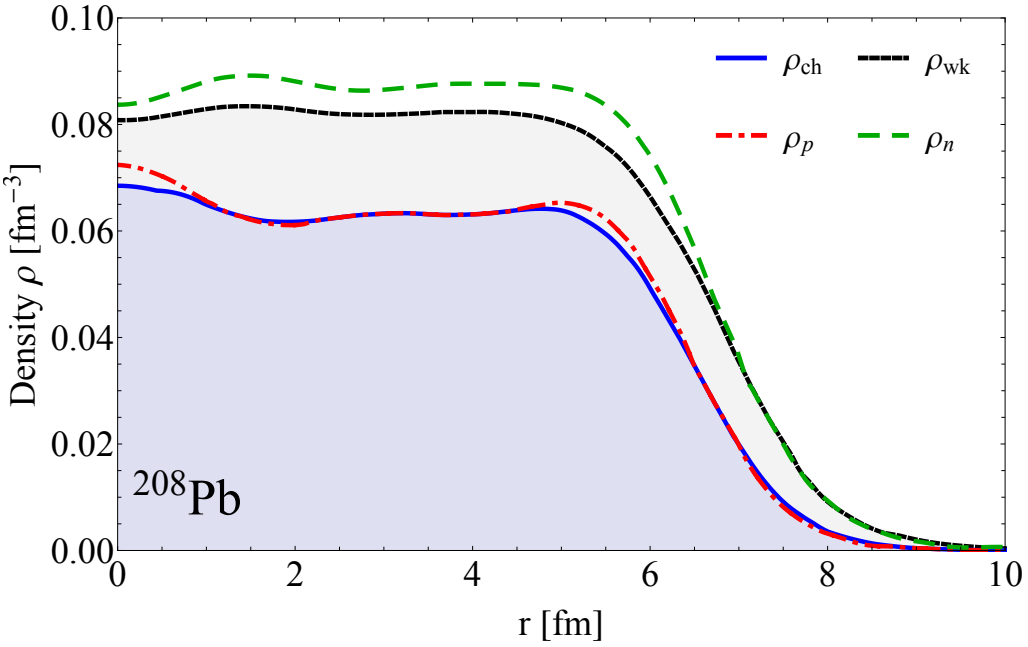

Figure 3.6: Nuclear density distributions as a function of the radial distance for the case of the lead $^{208}\mathrm{Pb}$ nucleus from the FSUGold nuclear model [139]. The different colors indicate the different densities: the proton, neutron, charge and weak ones.

To further understand it, we can consider some approximated expressions which allow one to go from the point[6] proton and neutron radii, R_p^{point} and R_n^{point}, to charge and weak radii [143] without knowing the specific density distribution. In particular, the nuclear charge radius can be expressed as [143, 144]

$$R_{\text{ch}}^2 = R_p^{\text{point},2} + r_p^2 + \frac{N}{Z} r_n^2 + \frac{3}{4M_N^2} + r_{\text{so}}^2 \,, \tag{3.32}$$

where $3/4M_N^2 \simeq 0.033\ \text{fm}^2$, with M_N the average nucleon mass, is the Darwin correction. $r_p^2 = 0.707954\ \text{fm}^2$ and $r_n^2 = -0.116\ \text{fm}^2$ are the physical proton and neutron radii, respectively [145], while r_{so}^2 represents the spin-orbit correction [143] ($r_{\text{so}}^2 \simeq -0.028\ \text{fm}^2$ for lead-208). Similarly, the weak radius is given by [143]

$$R_{\text{wk}}^2 = \frac{\mathcal{Q}_W^n N}{Q_W} R_n^{\text{point},2} + \frac{\mathcal{Q}_W^p Z}{Q_W} R_{\text{ch}}^2 + \frac{\mathcal{Q}_W^n}{Q_W}[N r_p^2 + Z r_n^2] - \frac{Z+N}{Q_W} r_s^2 \,, \tag{3.33}$$

where r_s^2 is the nucleon strangeness radius ($r_s^2 \simeq -0.013\ \text{fm}^2$ [146]) and $\mathcal{Q}_W^{n,p}$ are the nucleon weak charges, defined as twice the opposite of the couplings of electrons to nucleons, g_{AV}^{ep} and g_{AV}^{en}. In the standard model and taking into account radiative corrections [25, 147, 148], one obtains $g_{AV}^{ep} = -0.0357$ and $g_{AV}^{en} = 0.495$, where we notice that the coupling to protons is suppressed[7].

[6] The point radius does not account for the nucleon form factor, so that $R_{p,n}^2 = R_{p,n}^{\text{point},2} + r_{p,n}^2$.

[7] Let us note that some authors define the factor -2 directly inside the coupling definition, so that in that case the couplings are identical to the nucleon weak charges. For example in Ref. [145], the couplings are defined including the -2 factor, so that have to be compared to our $\mathcal{Q}_W^{p,n}$ charges.

In Refs. [145, 149], the authors clearly explain the procedure to be followed in order to go from the proton and neutron point densities, ρ_p and ρ_n, to the actual charge and weak densities, by defining how protons and neutrons contribute to them. The latter procedure was employed to produce the curves in Fig. 3.6. We define with point density the nucleon density not folded with the nucleon form factor. The starting point is the nuclear charge density definition

$$\rho_{\rm ch}(\mathbf{r}) = \frac{Z}{(2\pi)^3}\int d^3q e^{-i\mathbf{q}\cdot\mathbf{r}} F_{\rm ch}(\mathbf{q})\,, \tag{3.34}$$

where with the $\mathbf{r}$ and $\mathbf{q}$ we indicate the position vector and the momentum vector respectively.
We can define the charge form factor as [149]

$$F_{\rm ch}(\mathbf{q}) = \sum_{t=p,n}\Big[G_E^t(\mathbf{q})\Big(1-\frac{1}{2}\mathbf{q}^2\mathcal{D}\Big)F_t(\mathbf{q}) - \mathcal{D}\Big(2G_M^t(\mathbf{q}) - G_E^t(\mathbf{q})\Big)F_{ls}^t(\mathbf{q})\Big], \tag{3.35}$$

with $\mathcal{D} = \dfrac{\hbar^2}{(2M_Nc)^2}$ (M_N being the nucleon mass), and where $F_t(\mathbf{q})$ is the point-proton (neutron) form factor, while $F_{ls,t}(\mathbf{q})$ is a form factor related to the current density, and are defined as

$$F_t(\mathbf{q}) = \int d^3r e^{i\mathbf{q}\cdot\mathbf{r}}\rho_t(\mathbf{r})\,, \tag{3.36}$$

$$F_{ls,t}(\mathbf{q}) = \int d^3r e^{i\mathbf{q}\cdot\mathbf{r}}\nabla\cdot\mathbf{J}_t(\mathbf{r})\,. \tag{3.37}$$

$G_{E,\,M}^t$ are the electric and magnetic form factors, necessary to fold the point-proton and neutron form factors (and the current contributions). There are measurements of the latter form factors and some phenomenological parametrizations for them. A simple model to define the electric form factor is to assume a dipole parametrization [145], so that it results

$$G_E^p(\mathbf{q}) = G_D(\mathbf{q}) = \Big(1+\frac{q^2}{12}r_p^2\Big)^{-2}, \tag{3.38}$$

$$G_E^n(\mathbf{q}) = -\Big(\frac{q^2r_n^2/6}{1+q^2/M_N^2}\Big)G_D(\mathbf{q}). \tag{3.39}$$

The magnetic form factors can also be assumed to follow the dipole form,

$$G_M^p(\mathbf{q}) = \mu_pG_E^p(\mathbf{q}), \tag{3.40}$$

$$G_M^n(\mathbf{q}) = \mu_nG_E^n(\mathbf{q}), \tag{3.41}$$

with $\mu_p = 2.79$ and $\mu_n = -1.91$ the proton and neutron magnetic moments in units of the Bohr magneton μ_B, respectively.
Similarly, the weak density is defined as the Fourier transform of the weak form factor, which can be expressed in an analogue form to the charge form factor in Eq. (3.35), namely

$$F_{\rm wk}(\mathbf{q}) = \sum_{t=p,n}\Big[G_{E,\rm wk}^t(\mathbf{q})\Big(1-\frac{1}{2}\mathbf{q}^2\mathcal{D}\Big)F_t(\mathbf{q}) - \mathcal{D}\Big(2G_{M,\rm wk}^t(\mathbf{q}) - G_{E,\rm wk}^t(\mathbf{q})\Big)F_{ls}^t(\mathbf{q})\Big]\,, \tag{3.42}$$

where we have introduced the weak nucleon form factors, $G^t_{E,\mathrm{wk}}$ and $G^t_{M,\mathrm{wk}}$. These weak nucleon form factor can be obtained from the electric form factor as

$$G^p_{E,\mathrm{wk}}(\mathbf{q}) = \mathcal{Q}^p_W G^p_E(\mathbf{q}) + \mathcal{Q}^n_W G^n_E(\mathbf{q}), \quad (3.43)$$
$$G^n_{E,\mathrm{wk}}(\mathbf{q}) = \mathcal{Q}^n_W G^p_E(\mathbf{q}) + \mathcal{Q}^p_W G^n_E(\mathbf{q}), \quad (3.44)$$
$$G^p_{M,\mathrm{wk}}(\mathbf{q}) = \mathcal{Q}^p_W G^p_M(\mathbf{q}) + \mathcal{Q}^n_W G^n_M(\mathbf{q}), \quad (3.45)$$
$$G^n_{M,\mathrm{wk}}(\mathbf{q}) = \mathcal{Q}^n_W G^p_M(\mathbf{q}) + g^{ep}_{AV} G^n_M(\mathbf{q})\,. \quad (3.46)$$

Moreover, as it is clear from the above equations, we have neglected the strangeness contribution to the weak form factors. However, this is known to be significantly smaller, and thus it can be safely neglected [145].
In any case, from the latter discussion, it is clear that both the charge and density distributions and form factors incorporate in them the contributions of both the protons and the neutrons, properly weighted and scaled.
This procedure is usually used in the context of theoretical nuclear models, such as the mean-field nuclear models, that calculate the point-proton and neutron densities from an interaction Hamiltonian arising from some microscopical chosen interactions. Starting from those densities and assuming a form for the nucleon form factors, the charge and weak densities are obtained. Nevertheless, from a phenomenological point of view, it is also possible to describe the weak density, as already shown for the charge density, using some phenomenological parameterizations such as the symmetrized 2pF model and many others. It is clear from Fig. 3.6 that theoretical nuclear models can give a much more complicated shape for the density with respect to the ones shown in Fig. 3.3 (left) obtained using the "simple" SF model. There are some more complicated phenomenological models that try to emulate the dips of the theoretical models, usually obtained by adding some other model parameters.
The above discussion about the definition of the parity violating asymmetry (see Eq. 3.26) and the form factors is valid when considering the PWBA, in a similar way to what we have discussed for elastic scattering of (non-polarized) electrons on nuclei. However, also in this case it is necessary to go beyond the PWBA, thus considering the effect of Coulomb distortions on the electron wave functions. The difference in the case of PVES is given by the definition of the nuclear potential. Since we are now considering the contribution to the scattering from both the electromagnetic and the weak processes, also the nuclear potential is not due to the Coulomb force alone. In fact, it is now necessary to solve the Dirac equation in the presence of a different potential, namely [150]

$$\hat{V}(r) = V(r) + \gamma^5 A(r)\,, \quad (3.47)$$

where $V(r)$ is the conventional Coulomb potential, while $A(r)$ is the weak neutral current potential and it is given by [150]

$$A(r) = \frac{G_F}{2^{3/2}} \rho_{\mathrm{wk}}(r)\,. \quad (3.48)$$

This procedure can be implemented and some numerical codes have been developed over the years to precisely calculate the parity violating asymmetry in

the DWBA. The numerical solver that we have used in this thesis work is called DREPHA [151], and as a reference another popular code that gives similar results is called ELSEPA package [152].

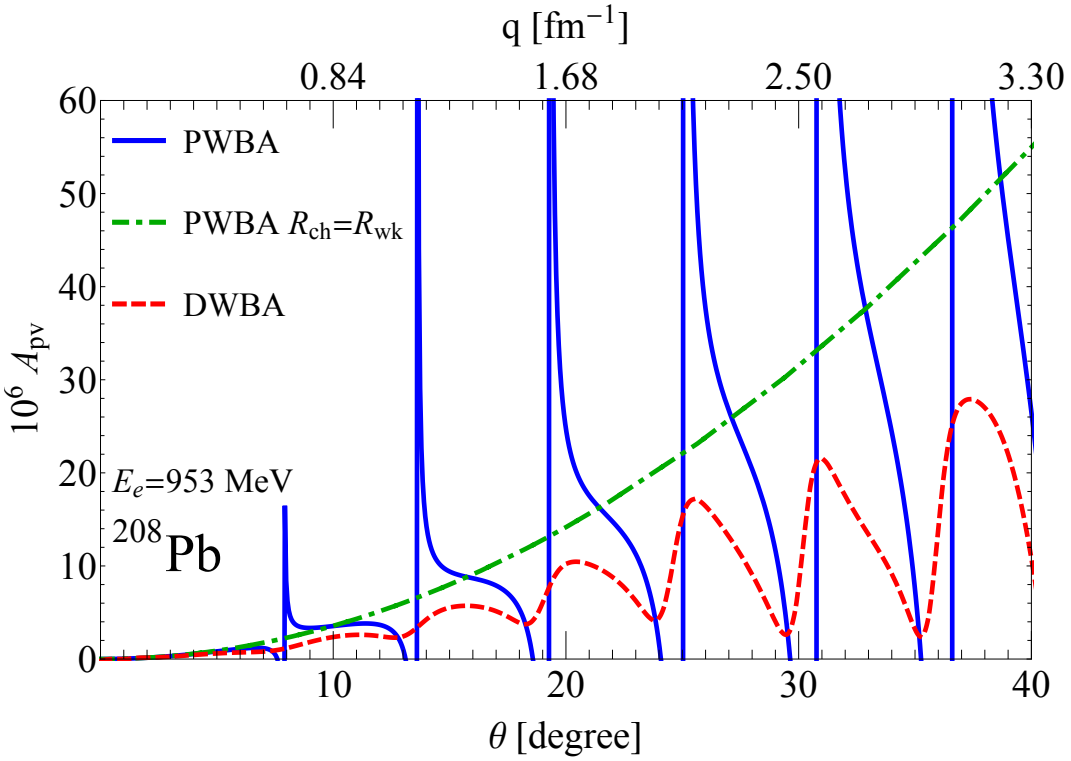

Figure 3.7: Comparison between the asymmetries calculated in PWBA and DWBA with different assumed nuclear densities as a function of the scattering angle (momentum transfer) considering 953 MeV electrons on ^{208}Pb. The solid blue line refers to the PWBA result considering a symmetrized 2pF for both charge and weak densities with $t_{\rm ch} = t_{\rm wk} = 2.3\,{\rm fm}$, $c_{\rm ch} = 6.65\,{\rm fm}$ and $c_{\rm wk} = 6.90\,{\rm fm}$. The red line shows the same assumption but in DWBA. Instead, the green line shows the case of $\rho_{\rm wk} = \rho_{\rm ch}$.

An example of the importance of considering the DWBA when calculating the parity violating asymmetry, $A_{\rm pv}$, is shown in Fig. 3.7 as a function of the scattering angle and the corresponding momentum transfer. The curves have been obtained considering $E_e = 953\,{\rm MeV}$ and a lead $^{208}{\rm Pb}$ target and using different assumptions for the densities. In particular, we have considered a SF for both the charge and the weak densities with the same thickness parameter ($t_{\rm ch} = t_{\rm wk} = 2.3\,{\rm fm}$) but different half-density parameters, namely $c_{\rm ch} = 6.65\,{\rm fm}$ and $c_{\rm wk} = 6.90\,{\rm fm}$, which correspond to $R_{\rm ch} \simeq 5.50\,{\rm fm}$ and $R_{\rm wk} \simeq 5.69\,{\rm fm}$, respectively. In Fig. 3.7, we show also the prediction for the asymmetry in PWBA when considering the same density for both the proton and the weak contributions through the green dot-dashed line. The three predictions show very different behaviors. The blue PWBA curve shows very well defined minima due to the drops in the weak form factor and some divergences due to the dips in the charge form factor in Eq. 3.26. As a matter of fact, the two form factors do not present the minima at the same momentum

transfer as they correspond to two different density distributions. These structures of course disappear when one considers the same density for both the charge and weak distributions, as the form factors would cancel out, leading to the smooth line in green. That line, in practice, shows only the kinematic dependence of the asymmetry on the scattering angle (or momentum transfer).
The curve obtained in DWBA (red line) is very different from the corresponding one in PWBA (blue curve). The effect of Coulomb distortions smooths the minima (taking away all the divergences) and slightly shifts the minima position. From the figure, it is evident that the Coulomb distortions have to be carefully included in the calculations for the parity violating asymmetry, as it can not be neglected without introducing a significant bias in the predictions. This effect is more evident and more significant for heavier nuclei (such as the case of lead-208) for which the Coulomb potential is larger.

3.1.1 —— PVES at JLab: PREX ——

The PREX experiment, also now as the "Lead Radius Experiment", is an experiment meant to measure the parity violating asymmetry on lead-208 nuclei with ∼GeV electrons to extract information on the lead neutron radius up to a 1% accuracy. The experiment was performed in the Hall A of the Jefferson Laboratory in Virginia and performed a first measurement released in 2012 [153] and then an improved measurement in 2021 [154].
The target nucleus, $^{208}\mathrm{Pb}$, is a heavy nucleus with significantly more neutrons than protons, as $Z = 82$ and $N = 126$, so that it constitutes an ideal candidate to measure the neutron skin. It is expected that the lead-208 should have a neutron skin thickness $\Delta R_{\mathrm{np}} \approx 0.13 - 0.19\,\mathrm{fm}$.
The first measurement (PREX-I) performed by the PREX Collaboration employed 1.06 GeV longitudinally polarized electrons impinging on a thick lead foil and then, collected the scattered electrons with high-resolution spectrometers located at forward angle ($\theta_{\mathrm{lab}} \sim 5^\circ$) after passing through a collimator which enables to improve the angular resolution. The spectrometer has a certain angular acceptance, $\epsilon(\theta)$, so that the measured quantity is not the actual asymmetry at a fixed momentum transfer (and scattering angle), but it is average over the angular detection range.
The outcome of the PREX-I measurement found an asymmetry of [153]

$$A_{\mathrm{pv}}^{\mathrm{PREX-I}} = 656 \pm 60(\mathrm{stat}) \pm 14(\mathrm{syst})\,\mathrm{ppb}\,, \tag{3.49}$$

at an average momentum transfer $\langle Q^2 \rangle = 0.00880 \pm 0.00011\,\mathrm{GeV}^2$.
The second PREX measurement, PREX-II, reached higher levels of precision employing 953 MeV electrons on an improved lead target. The scattered electrons have been collected by the same spectrometers with an average scattering angle $\theta_{\mathrm{lab}} \sim 5^\circ$. In particular, the angular acceptance for the PREX-II measurement has been provided by the PREX Collaboration as a function of the scattering angle in 100 bins from 3° to 8°, normalized in such a way that the sum over the full

acceptance goes to unity, namely

$$\sum_i \epsilon(\theta_i)\sin(\theta_i)\Delta\theta = 1\,, \tag{3.50}$$

with a bin size of $\Delta\theta = 0.05°$, and it is shown in Fig. 3.8.

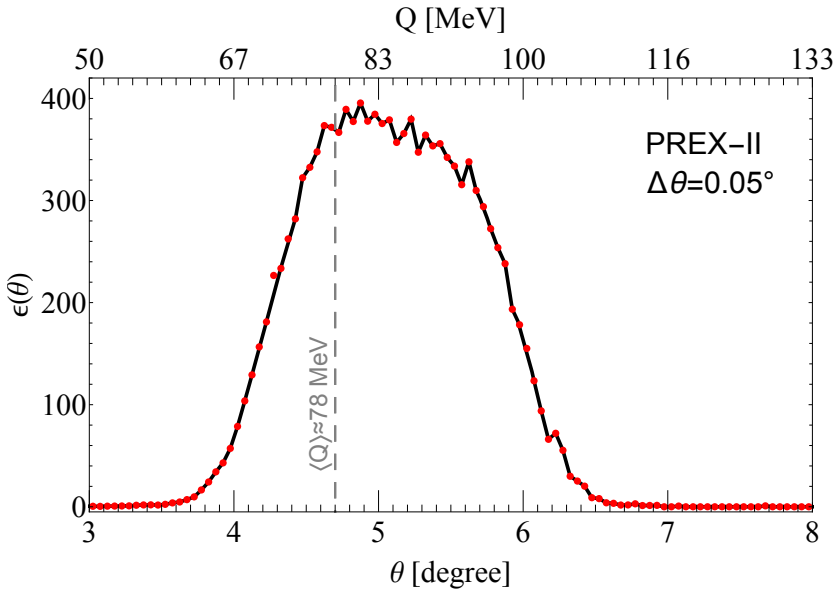

Figure 3.8: Acceptance function for the PREX-II measurement as a function of the scattering angle and momentum transfer [154]. The dashed vertical line indicates the experimental rate-averaged scattering angle and the corresponding mean momentum transfer.

In the figure, we indicate the rate-averaged scattering angle, and thus momentum transfer, through the dashed vertical line, and it corresponds to $\langle Q\rangle \approx 78\,\mathrm{MeV}$.
The PREX-II result is [154]

$$A_{\rm pv}^{\rm meas} = 550 \pm 16(\mathrm{stat}) \pm 8(\mathrm{syst})\,\mathrm{ppb}\,, \tag{3.51}$$

at an average momentum transfer $\langle Q^2\rangle = 0.00616 \pm 0.00005\,\mathrm{GeV}^2$. It is easy to observe that the PREX-II measurement has improved uncertainties of both statistical and systematic origins.
Since the second measurement from the PREX Collaboration is sensibly more precise, we will describe the procedure only in the context of the PREX-II measurement. However, it is worth to remark that the procedure can be easily extended to the PREX-I measurement by using the correct kinematics and the correct angular acceptance.
In general, the experimentally measured value for the asymmetry has to be compared to the theoretical predictions in order to be translated into a measurement of the neutron skin, or the weak and neutron radii. To compare to the experimentally measured asymmetry, one has to average the theoretically predicted asymmetry, in Eq. 3.26, over the angular distribution, so that

$$\langle A_{\rm pv}\rangle = \frac{\int d\theta \sin\theta A_{\rm pv}(\theta)\frac{d\sigma}{d\Omega}\epsilon(\theta)}{\int d\theta \sin\theta \frac{d\sigma}{d\Omega}\epsilon(\theta)}\,, \tag{3.52}$$

where $\frac{d\sigma}{d\Omega}$ is the non-polarized cross section and $\epsilon(\theta)$ is the angular acceptance of the experimental setup (for PREX-II it is shown in Ref. 3.8).
To be able to extract $R_{\rm wk}$ (or R_n), the charge density of lead-208 was fixed inside the calculation. The charge distribution of the latter nucleus has been precisely tested through electromagnetic scattering processes, and the currently accepted value for the charge distribution radius is $R_{\rm ch}(^{208}{\rm Pb}) = 5.503 \pm 0.002$ fm [136]. This charge radius corresponds to a proton radius of $R_p(^{208}{\rm Pb}) = 5.449$ fm [143]. Since the asymmetry depends on the nuclear weak charge, as it is obvious from Eq. 3.26, it is crucial to precisely calculate its value. Such quantity has to be evaluated accounting for the radiative correction (see Appendix A), and in particular for the $\gamma - Z$ box. The latter contribution arises from box diagrams in which the interaction is exchanged by a Z boson and a photon, γ. Indeed, it has been shown that this correction depends on the experimental kinematic regime, so that it has to be calculated for every target nucleus for the specific experimental setup in the case of PVES measurements [155–158]. The calculated value of the nuclear weak charge of the lead nucleus in the standard model is $Q_W(^{208}{\rm Pb}) = -117.9 \pm 0.3$.

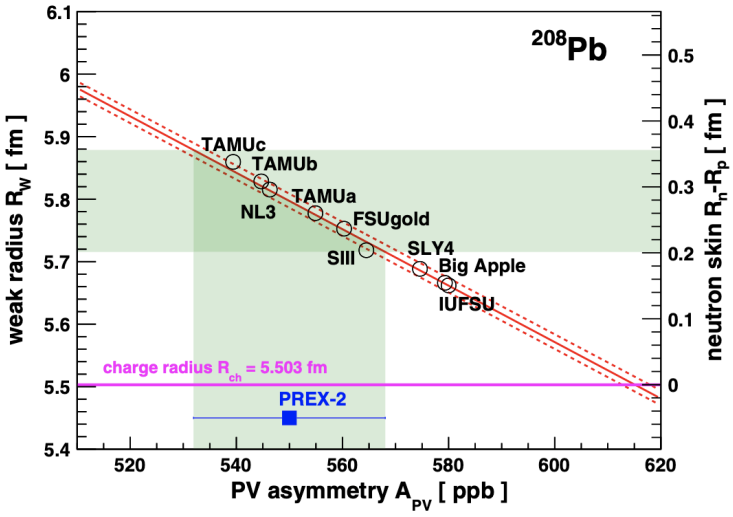

Figure 3.9: PREX-II measurement result [154] in the plane weak radius (or neutron skin) vs measured parity violating asymmetry. The black circles show the predictions from a collection of EDF models, and the red lines show the best fit and $\pm 1\sigma$ of the diffuseness parameter. The green bands indicate the $\pm 1\sigma$ results. Figure taken from Ref. [154].

The chosen parametrization to describe the weak density is a SF distribution, but with a thickness parameter larger than the typical $2.3\,{\rm fm}$ value used to describe charge densities. In fact, the collaboration worked together with nuclear theorists to extract an average value for the thickness (or better for the diffuseness parameter a) from their predictions, in particular considering a set of energy density functionals (EDFs). The adopted diffuseness is $a = 0.605 \pm 0.025\,{\rm fm}$, where the uncertainty represents the range of values suggested by the considered nuclear models.
By fixing the diffuseness, it is clear that the SF presents a direct correlation be-

tween weak radius and half-density radius (see Eq. 3.20). In this sense, the best fit value for the weak radius is retrieved by fitting the experimental asymmetry letting the half-density parameter as a free parameter in the fit. Each c parameter corresponds uniquely to a certain neutron (or weak) radius, so that we can build a chi-square function

$$\chi^2_{\rm PREX-II}(R_n) = \Big(\frac{A_{\rm pv}(R_n) - A_{\rm pv}^{\rm meas}}{\sigma_{A_{\rm pv}^{\rm meas}}}\Big)^2 , \tag{3.53}$$

where $\sigma_{A_{\rm pv}^{\rm meas}}$ is the total uncertainty on measured asymmetry for the PREX-II measurement and $A_{\rm pv}(R_n)$ is the prediction after having averaged over the angular distribution. We show explicitly the dependence of the latter on the neutron radius R_n.
The PREX-II result is shown in Fig. 3.9 in the plane $A_{\rm pv}$ vs $R_{\rm wk}$ (or $\Delta R_{\rm np}$). The numerical results are

$$R_{\rm wk}(^{208}{\rm Pb}) = 5.795 \pm 0.082({\rm exp.}) \pm 0.013({\rm theo.})\,{\rm fm}\,, \tag{3.54}$$
$$\Delta R_{\rm np}(^{208}{\rm Pb}) = R_n - R_p = 0.278 \pm 0.078({\rm exp.}) \pm 0.012({\rm theo.})\,{\rm fm}\,. \tag{3.55}$$

These results are in agreement with the PREX-I measurement [153], but in tension with the other available determinations, such as those coming from electric-dipole polarizability [159–161], antiprotonic atoms [162–164], proton-nucleus scattering [165, 166], coherent pion photoproduction [167] and the indirect measurements of neutron star observables [138, 168–178]. All these non-electroweak measurements are in fair agreement with each other, being also compatible with the predictions of different energy density functional (EDF) nuclear models [159–161], $\Delta R_{\rm np}^{\rm th}(^{208}{\rm Pb}) = [0.13, 0.19]\,{\rm fm}$, and the first *ab-initio* estimate of the lead neutron skin, $\Delta R_{\rm np}^{\textit{ab-initio}}(^{208}{\rm Pb}) = [0.14, 0.20]\ {\rm fm}$ [179]. Recently, a novel measurement of the lead-208 neutron skin from ultrarelativistic nuclear collisions at LHC was released, finding $\Delta R_{\rm np}^{\rm LHC}(^{208}{\rm Pb}) = 0.217 \pm 0.058\ {\rm fm}$ [180], showing a competitive uncertainty with respect to PVES measurements, and being rather in between the theoretical predictions and the PREX determination.
Moreover, in this definition of the asymmetry, we are considering the weak mixing angle, which is hidden inside the nuclear weak charge definition, to be the standard model one. Later in this thesis, we will consider also the scenario in which we allow the weak mixing angle to be non-standard. In this sense, we show that the PVES measurements can be considered also weak mixing angle measurements, and since the PREX-II measurement is at $Q \sim 78\,{\rm MeV}$, it is important, as the weak mixing angle at low energies is still poorly constrained. In this case, we will modify the weak mixing angle, and thus the nuclear weak charge inside $A_{\rm pv}$, and we will define the following chi-square function

$$\chi^2_{\rm PREX-II}(\sin^2\theta_W,\, R_n) = \Big(\frac{A_{\rm pv}(\sin^2\theta_W,\, R_n) - A_{\rm pv}^{\rm meas}}{\sigma_{A_{\rm pv}^{\rm meas}}}\Big)^2 , \tag{3.56}$$

where we explicitly include the $\sin^2\theta_W$ dependence.

3.1.2 —— PVES at JLab: CREX ——

The CREX experiment is the PREX twin experiment at JLab. It exploits the same apparatus to measure the parity violating asymmetry on a different target, namely a $^{48}\mathrm{Ca}$ target. The choice of this particular target is due to its relatively large number of neutrons ($N = 28$) compared to the proton one ($Z = 20$), which makes it a suitable example for neutron rich matter[8] and it is a double magic nucleus like lead-208. Moreover, calcium is an interesting atomic species, as it counts a variety of isotopes, ranging from a symmetric example, $^{40}\mathrm{Ca}$ ($Z = N = 20$), which is the most abundant in nature, the intermediate $^{42}\mathrm{Ca}$ which is relevant for superallowed β-decays, up to $^{48}\mathrm{Ca}$ whose is expected to have a rather large neutron skin due to the neutron excess. Furthermore, there have been attempts to build a correlation between the theoretical predictions of the neutron skins for neutron rich species, such as $^{208}\mathrm{Pb}$ and $^{48}\mathrm{Ca}$, so that the measurements performed on both nuclear species could be interpreted as a confirmation (or not) of the microscopic physics governing nuclear structure.
The charge density of calcium-48 has been measured from electron scattering [181] for the nuclear ground state. However, the CREX Collaboration, used a more accurate description of the density, as explained in the supplemental material of Ref. [158]. In particular, they built the charge density using as a starting point the sum-of-Gaussians (SOG) description of the charge density of $^{40}\mathrm{Ca}$ [182], and then adding the difference of the charge densities of $^{48}\mathrm{Ca}$ and $^{40}\mathrm{Ca}$ expressed as a Fourier Bessel (FB) expansion [183], so that

$$\rho_{\mathrm{ch}}^{^{48}\mathrm{Ca}}(r) = \rho_{40}^{\mathrm{SOG}}(r) + \rho_{48}^{\mathrm{FB}}(r) - \rho_{40}^{\mathrm{FB}}(r)\,. \tag{3.57}$$

This description reproduces well the electron scattering data and in particular gives a more accurate value of the charge radius than using the FB parametrization alone [136].
The sum-of-Gaussians parametrization for the nuclear density consists on defining the density as the sum of Gaussian functions conveniently weighted, namely

$$\rho^{\mathrm{SOG}} = \sum_i A_i \left[e^{-\left(\frac{r-R_i}{\gamma}\right)^2} + e^{-\left(\frac{r+R_i}{\gamma}\right)^2} \right], \tag{3.58}$$

where R_i is the position of the $i-th$ Gaussians and A_i, which is the amplitude, is given by

$$A_i = Ze\frac{Q_i}{2\pi^{3/2}\gamma^3(1+2R_i^2/\gamma^2)}\,. \tag{3.59}$$

Q_i indicates the fraction of the total charge contained in the $i-th$ Gaussian and it is normalized such that $\sum_i Q_i = 1$. γ is related to the *root-mean-square* (rms) radius of the Gaussians (RP), namely $\gamma = RP\sqrt{2/3}$ (RP=1.45 for calcium-48) [136].
Instead, the FB parametrization consists on defining the nuclear density as a superposition of spherical Bessel functions properly normalized, so that

$$\rho^{\mathrm{FB}} = \begin{cases} \sum_n a_n j_0(n\pi r/R) & \text{for} \quad r \le R\,, \\ 0 & \text{for} \quad r > R\,, \end{cases} \tag{3.60}$$

[8] In fact, $N/Z = 1.4$ for calcium-48, while for lead-208 $N/Z \sim 1.5$.

where j_0 is the spherical Bessel function of order 0 and R is the cut-off density, i.e. the radius beyond which the charge density is assumed to be identical to zero. In particular, $R(^{40}\mathrm{Ca}) = R(^{48}\mathrm{Ca}) = 8\,\mathrm{fm}$ [136]. The normalization is chosen such that the integral of the density is equal to the total electric charge.

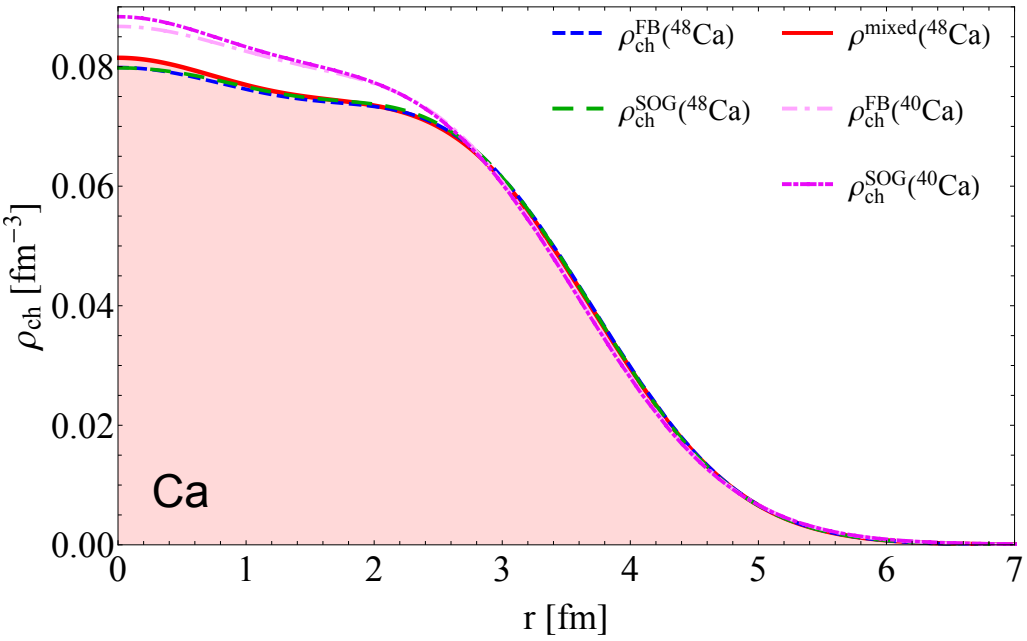

Figure 3.10: Charge density distribution for calcium as a function of the distance from the center of the nucleus. We consider three different parametrizations for the charge density of the $^{48}\mathrm{Ca}$ isotope: blue for FB, green for SOG and red for the mixed [158]. In purple and lilac for the $^{40}\mathrm{Ca}$ isotope.

The coefficients for the SOG and the FB charge densities for $^{40}\mathrm{Ca}$ and $^{48}\mathrm{Ca}$ have been taken from the compilation in Ref. [136].
In Fig. 3.10, we show a comparison of the different charge densities considered for calcium-40 and calcium-48. In particular, we notice that the lilac and purple curves refer to the calcium-40 case, while the other curves to the calcium-48 curves. The red filled region indicates the mixed density defined in Eq. 3.57, which is the charge density considered in evaluating the asymmetries for the CREX science case. By comparing the red curve with the green and the blue ones, it is possible to see that they are rather similar.
After fixing the choice of the charge density, in a similar way to what was done for the case of PREX, we can parametrize the weak density using a SF 2pF, with fixed diffuseness parameter $a_{\mathrm{wk}} = 0.605\,\mathrm{fm}$ and letting the half-density parameter c_{wk} free to vary in order to extract the best fit weak radius.
In Fig. 3.11, we compare the theoretical asymmetries calculated in PWBA and in DWBA. In particular, the green curve corresponds to the case of PWBA with $R_{\mathrm{ch}} = R_{\mathrm{wk}}$ (i.e. no weak skin), the blue curve the PWBA considering the experimental value for the charge radius, namely $R_{\mathrm{ch}} = 3.481\,\mathrm{fm}$ [136], and for the weak part a SF 2pF with $t_{\mathrm{wk}} = 2.66\,\mathrm{fm}$ and $c_{\mathrm{wk}} = 3.90\,\mathrm{fm}$. Indeed, the latter curve presents the divergences and marked minima expected in the PWBA. The red curve instead shows the asymmetry in DWBA for the same parameter

choices as the blue curve. From the figure, we can see that even if calcium-48 is a lighter nucleus with respect to lead-208, also in this case the effect of DWBA is not negligible. Moreover, it must be remarked that the energy of electron beam is much higher for the CREX measurement with respect to the PREX one, in particular $E_e = 2.18\,\mathrm{GeV}$ [158] instead of $E_e = 953\,\mathrm{MeV}$ used in the PREX-II measurement [154]. Thus, the experimental momentum transfer results to be larger, namely $\langle Q \rangle \approx 172\,\mathrm{MeV}$.
The value of the parity violating asymmetry measured by the CREX Collaboration is [158]

$$A_{\mathrm{pv}}^{\mathrm{meas}} = 2668 \pm 106(\mathrm{stat}) \pm 40(\mathrm{syst})\,\mathrm{ppb}\,, \tag{3.61}$$

at an average momentum transfer $\langle Q^2 \rangle = 0.0297 \pm 0.0002\,\mathrm{GeV}^2$.

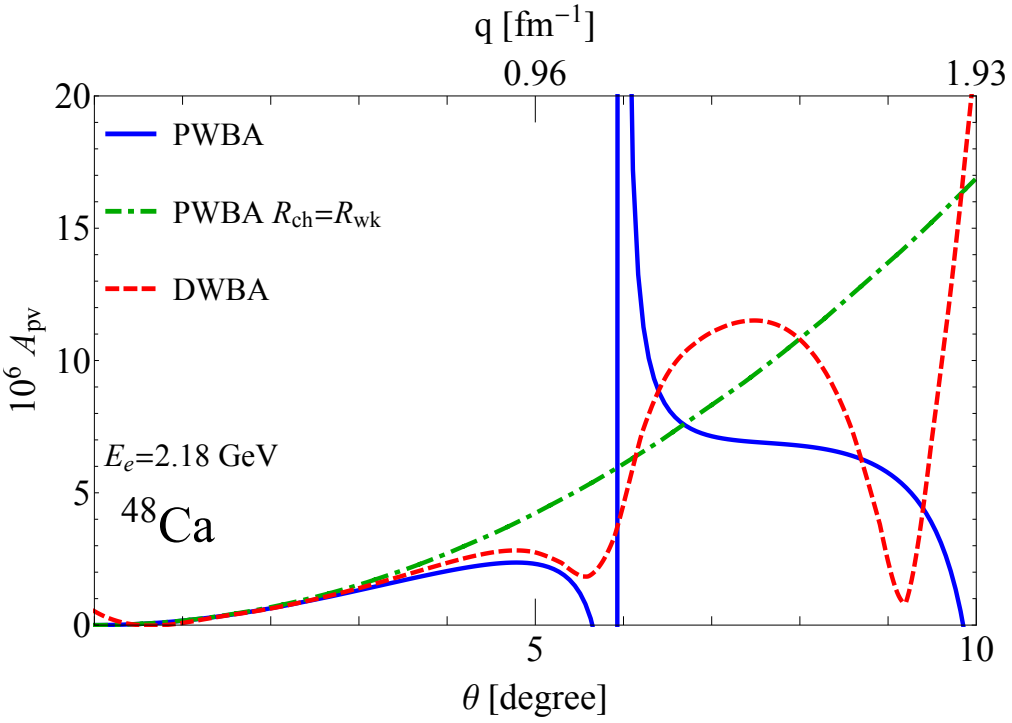

Figure 3.11: Comparison between the asymmetries calculated in PWBA and DWBA with different assumed nuclear densities as a function of the scattering angle (momentum transfer) considering 2.18 GeV electrons on $^{48}\mathrm{Ca}$. The solid blue line refers to the PWBA result considering a symmetrized 2pF for both charge and weak densities with $t_{\mathrm{ch}} = 2.3\,\mathrm{fm}$, $c_{\mathrm{ch}} = 3.73\,\mathrm{fm}$, $t_{\mathrm{wk}} = 2.66\,\mathrm{fm}$ and $c_{\mathrm{wk}} = 3.90\,\mathrm{fm}$. The red line shows the same assumption but in DWBA. Instead, the green line shows the case of $\rho_{\mathrm{wk}} = \rho_{\mathrm{ch}}$.

The experimental angular acceptance function is shown in Fig. 3.12, and it has been provided in 100 bins from 3° to 8° with a bin size of 0.05°.
Using the definition of the asymmetry averaged over the angular distribution in Eq. 3.52, and considering the standard model prediction of the nuclear weak charge for calcium-48 accounting for the radiative corrections and the contribution of the $\gamma - Z$ boxes, namely $Q_W(^{48}\mathrm{Ca}) = -26.0 \pm 0.1$, one can perform the

extraction of the weak skin and the neutron skin, resulting in [158]

$$\Delta R_{\rm wk}(^{48}{\rm Ca}) = R_{\rm wk} - R_{\rm ch} = 0.159 \pm 0.026({\rm exp.}) \pm 0.023({\rm model})\,{\rm fm}\,, \quad (3.62)$$
$$\Delta R_{\rm np}(^{48}{\rm Ca}) = R_n - R_p = 0.121 \pm 0.026({\rm exp.}) \pm 0.024({\rm model})\,{\rm fm}\,. \quad (3.63)$$

In reality, it is worth mentioning that the CREX Collaboration made a great effort to estimate the model error, i.e. the uncertainty coming from the translation of the results in terms of the form factor to the nuclear radii. In fact, in the CREX analysis, very careful attention has been devoted to understanding the impact of fixing a parameterization of the form factor, the specific shape chosen for the densities, and more in general from the fact that the quantity which is actually measured is not the radius, but the form factor at a certain momentum transfer. In this sense, the main result presented by the collaboration in Ref. [158], is the extraction of the difference between the charge and the weak form factors of $^{48}{\rm Ca}$ at the experimental value for the momentum transfer, namely

$$F_{\rm ch}(q) - F_{\rm wk}(q) = 0.0277 \pm 0.0055({\rm exp.})\,, \quad (3.64)$$

which then should be translated into the skin measurements.

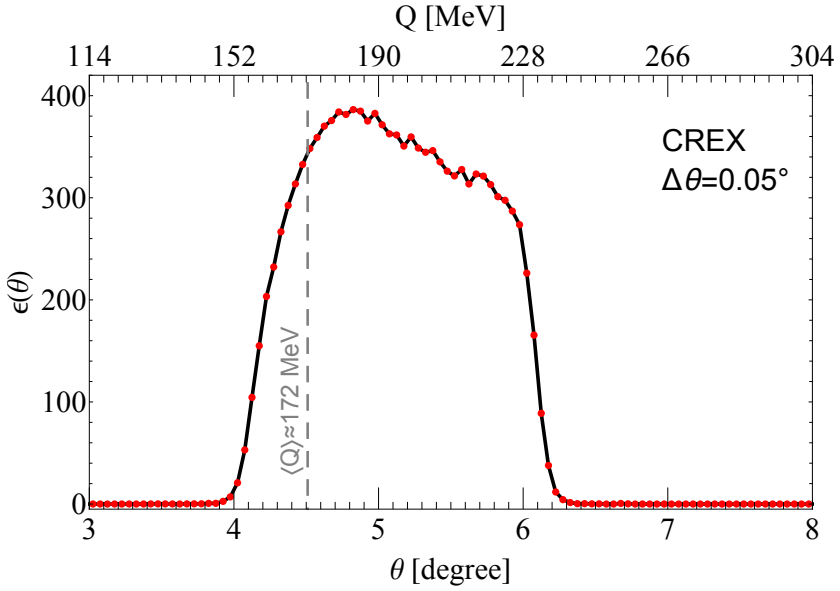

Figure 3.12: Acceptance function for the CREX measurement as a function of the scattering angle and momentum transfer [158]. The dashed vertical line indicates the experimental rate-averaged scattering angle and the corresponding mean momentum transfer.

In other words, we could make the statement that the experimental observable of a PVES measurement is the asymmetry, which, thanks to the current knowledge about the charge distribution and form factor, translates directly to the weak form factor. Since the experimental setup is made in such a way that the measurement is performed at a fixed momentum transfer (or better on a restricted range of momenta), the measured quantity is the weak form factor at a certain energy

scale. This has to be translated into a measurement of the neutron skin (or the weak skin), but in order to do so, some assumptions have to be made, resulting in the necessity of introducing a model uncertainty to account for them.
In Fig. 3.13 we show the results as reported by the CREX Collaboration [158]. In the left plot, the measurement of the difference between the charge and weak form factors at the CREX momentum transfer is shown together with the predictions from a set of density functionals as a function of the momentum transfer. From there, it seems that the experimental measurement is relatively smaller than the theoretical predictions considered.

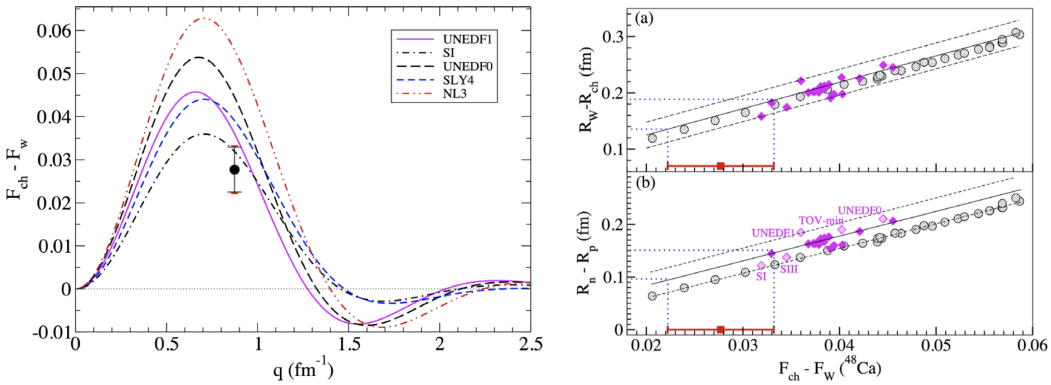

Figure 3.13: (Left) Difference between the charge and weak form factors for $^{48}\mathrm{Ca}$ as a function of the momentum transfer as reported by the CREX Collaboration [158]. The lines correspond to a set of EDF nuclear models. The error bar of the CREX experimental dot shows the total experimental uncertainty. (Right) weak skin (upper panel) and neutron skin (lower panel) as a function of the difference between the charge and the weak form factors at the CREX momentum transfer from a series of relativistic (gray) and non relativistic (magenta) density functionals. The red data point indicates the CREX result with its uncertainties. Both figures are taken from Ref. [158].

In the right plot in Fig. 3.13, the weak skin (neutron skin) as a function of the difference between form factors is shown. The gray and magenta points indicate the predictions from a compilation of density functionals, relativistic and non relativistic respectively. These predictions are used to translate the measured difference between form factors in a measurement of the weak and neutron skins. The width of the dashed bands indicates the uncertainty introduced by the spread of models. In principle, also the procedure followed in the PREX-II case can be applied to the CREX case. So that, one can consider a SF 2pF density for the weak density of $^{48}\mathrm{Ca}$ and after fixing the thickness parameter $t_{\mathrm{wk}} = 2.66\,\mathrm{fm}$, one can fit the experimental result to extract the half-density radius which better reproduces the datum with a chi-square function defined as

$$\chi^2_{\mathrm{CREX}}(R_n) = \left(\frac{A_{\mathrm{pv}}(R_n) - A_{\mathrm{pv}}^{\mathrm{meas}}}{\sigma_{A_{\mathrm{pv}}^{\mathrm{meas}}}}\right)^2 . \tag{3.65}$$

At this point, one can build the weak nuclear radius from c_{wk} and t_{wk}, and the corresponding neutron radius.

3.1.3 —— PVES at MESA ——

Both the PREX and CREX Collaborations have now completed their successful experimental campaigns at JLab, so that no further PVES measurements are foreseen in the near future in the same laboratory. However, a great effort is being carried out at the Johannes Gutenberg University (JGU) in Mainz, Germany, to build a novel PVES setup at the MESA (Mainz Energy recovery Superconducting Accelerator) accelerator facility, in the context of the P2 Collaboration [184].

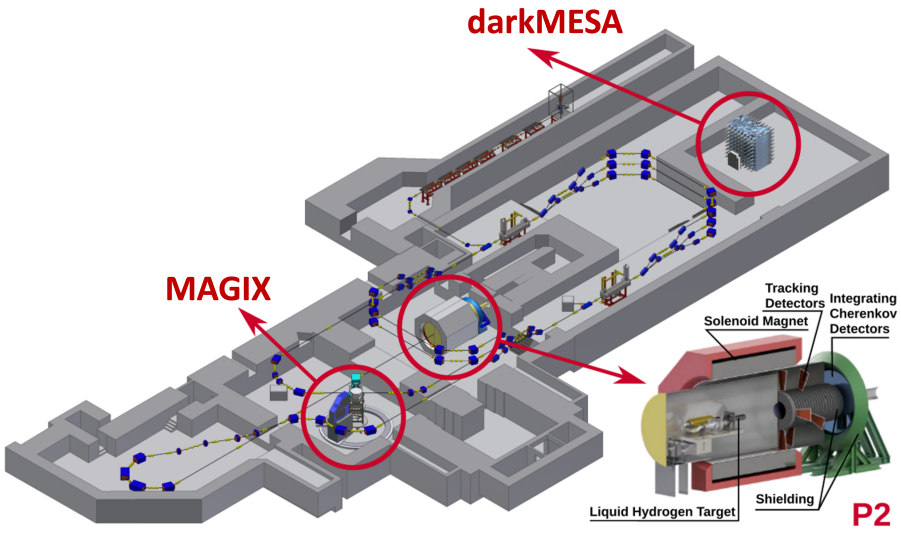

Figure 3.14: Schematic of the MESA accelerator and the main experiments foreseen in the MESA facility at the Johannes Gutenberg University in Mainz. Figure adapted from Ref. [185].

In Mainz, a new linear acceleration called MESA, is being built to replace the previous apparatus, MAMi, to provide JGU of a novel laboratory that will become the center for PVES (and not only) studies. The P2 experiment will employ a solenoid spectrometer with fused silica detectors to collect the scattered electrons.
The MESA facility will accelerate electrons that start with an initial kick of energy 5 MeV, which will be circulated in an acceleration ring for three times, increasing their energy of 50 MeV every round. After having reached $E_e = 155\,\mathrm{MeV}$ some electrons will be extracted from the main acceleration branch to be sent to a secondary line, in which they will be focalized and sent toward the P2 target and detector. A schematic of the facility and the detector is shown in Fig. 3.14, together with the other experiments planned in the facility, namely MAGIX and darkMESA [184, 185].
The P2 experiment has been designed with the purpose of measuring the weak charge of the proton, in order to perform a new measurement of it following the $\mathrm{Q_{weak}}$ one [33], by considering the asymmetry for the scattering of electrons off a liquid hydrogen target. The weak charge of the proton is of particular interest to the community, as it provides a direct measurement of the weak mixing angle at low energies, and it has already been demonstrated by the $\mathrm{Q_{weak}}$ Collaboration that it allows one to reach world-leading precision measurements. However, there

are also plans to use the P2 detector to measure the parity violating asymmetry for PVES off some to-be-selected targets. Up to the date of this thesis work the plan is to perform a PVES measurement on lead, to collect a new point to be compared with the PREX results. This possibility is often referred to by the name MREX (Mainz Radius EXperiment). Furthermore, the idea of placing a carbon-12 target inside the laboratory is under serious consideration, to measure the weak mixing angle using a different target. In fact, as we can see in the definition of the asymmetry in Eq. 3.26, it directly depends on the nuclear weak charge, and thus, on the weak mixing angle.
Indeed, we have considered PVES experiments as measurements of nuclear structure, through the extraction of the nuclear form factors and the nuclear radii, however, in the case of a light nucleus, such as carbon-12, the effect of nuclear structure is expected to be less significant, as the neutron skin is expected to be very tiny. This is true especially considering the lower beam energies exploited at MESA with respect to the ones used in PREX and CREX, since the momentum transfer can result in being rather small depending on the scattering angle at which the detector operates. Even though, in principle, the momentum transfer can also reach large values if one considers the possibility of measuring the scattered electrons at high angles (backward scattering).

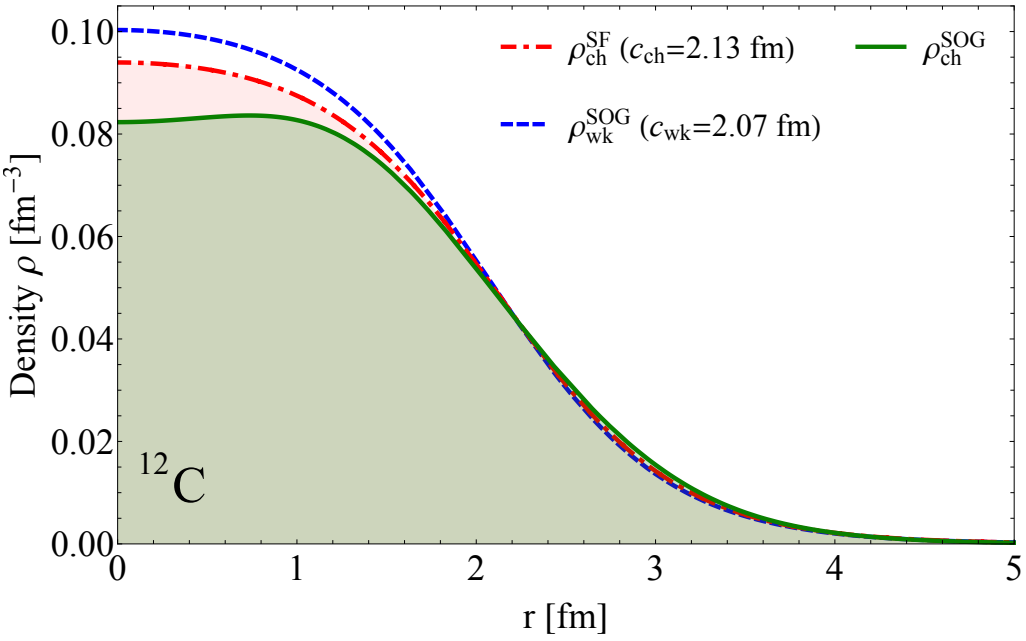

Figure 3.15: Examples of densities for the carbon-12 nucleus. The red curve shows a SF 2pF for charge density with $c_{\text{ch}} = 2.13\,\text{fm}$, while the blue one a SF 2pF for the weak density with $c_{\text{wk}} = 2.13\,\text{fm}$. For both densities we fixed $t_{\text{ch}} = t_{\text{wk}} = 2.17\,\text{fm}$. The green curve instead shows the SOG description for the carbon-12 charge density as reported in Ref. [136].

The experimental program, currently, foresees two detectors, one located at forward angle ($\theta_f \sim 29°$) and one at backward angle ($\theta_b \sim 145°$), with a still to be defined angular resolution. The forward angle has been chosen to match the momentum transfer of the PREX measurement, so that $\langle Q_f \rangle \approx 78\,\text{MeV}$, and should

lead to an intriguing precision on the weak mixing angle measurement practically free of any nuclear structure dependence. Instead, the backward measurement happens at a much larger momentum transfer, $\langle Q_b \rangle \approx 290\,\mathrm{MeV}$, and thus, it should depend mainly on the weak skin. The combination of the two measurements could in principle lead to the simultaneous measurement of both the weak mixing angle and the weak skin in the same experimental apparatus.
Such a possibility has been recently investigated in Ref. [186], showing nice perspectives for the measurement of both quantities with the P2 experiment.
In this thesis work, we will describe some further studies that have been performed to improve the previous sensitivity study to investigate the possibilities of the $^{12}\mathrm{C}$ measurement at MESA.

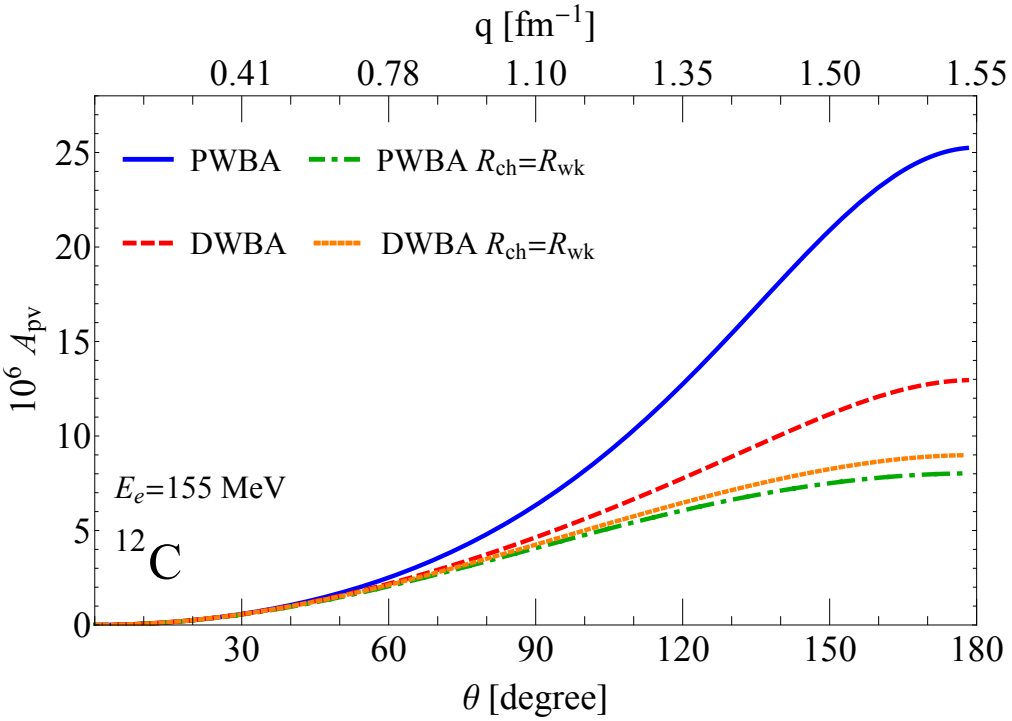

Figure 3.16: Comparison between the asymmetries calculated in PWBA and DWBA with different assumed nuclear densities as a function of the scattering angle (momentum transfer) considering 155 MeV electrons on $^{12}\mathrm{C}$. The solid blue line refers to the PWBA result considering a SOG charge density with $R_{\mathrm{ch}} \sim 2.47\,\mathrm{fm}$ and a symmetrized 2pF for the weak density with $t_{\mathrm{wk}} = 2.17\,\mathrm{fm}$ and $c_{\mathrm{wk}} = 2.07\,\mathrm{fm}$. The red line is the asymmetry in DWBA with the same density assumptions. The green line shows the PWBA result with both charge and weak densities fixed to the SOG density with $R_{\mathrm{ch}} \sim 2.47\,\mathrm{fm}$ and the orange one the DWBA with the same density choice.

The measured charge density for carbon-12 is reported in Ref. [136], and has been fitted with a SOG parametrization, resulting in a charge radius $R_{\mathrm{ch}}^{\mathrm{SOG}}(^{12}\mathrm{C}) = 2.469(6)\ \mathrm{fm}$. We show such density in Fig. 3.15, by the green solid line, compared to two SF 2pF densities, one describing a charge density which matches the charge radius with $t_{\mathrm{ch}} = 2.17\,\mathrm{fm}$ and $c_{\mathrm{ch}} = 2.13\,\mathrm{fm}$, and one which resembles the weak density considering $t_{\mathrm{wk}} = 2.17\,\mathrm{fm}$ and $c_{\mathrm{wk}} = 2.07\,\mathrm{fm}$ (which translates

to $R_{\rm wk} \approx 2.44\,{\rm fm}$). The latter SF 2pF densities have been employed to evaluate the asymmetry in both the PWBA and DWBA. The results are shown in Fig. 3.16, where we show the predictions of the asymmetry as a function of the scattering angle in the two approximations considering the case of skin and no skin. The difference between the PWBA and DWBA is clearly evident in the case with $R_{\rm ch} \neq R_{\rm wk}$, while it is much less significant for the no-skin case. However, it is clear that also in the case of a light nucleus such as $^{12}{\rm C}$, the effect of Coulomb distortions is not negligible. In any case, the difference is more visible at backward angle. In fact, at forward angle, all the curves result to be very close to each other. Let us note, that differently from the plot shown for calcium-48 and lead-208 (see Fig. 3.11 and Fig. 3.7), we do not see any pick or dip in the asymmetry. The low electron energy, in fact, makes the kinematic to be such that we are safe from the first minimum.

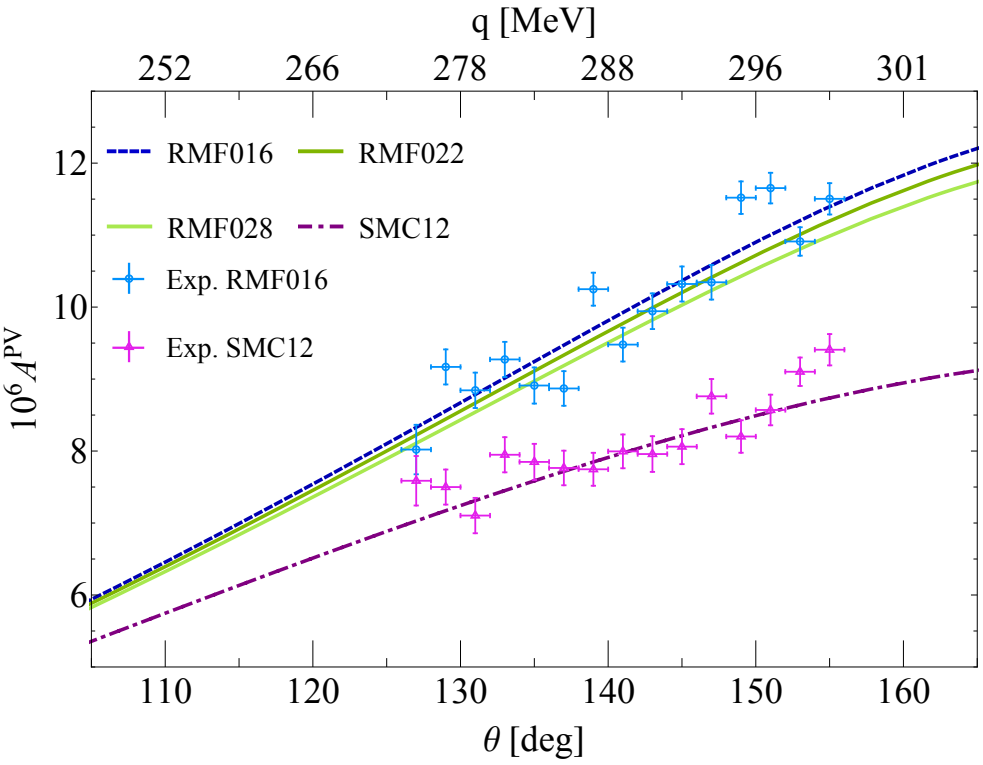

Figure 3.17: Predictions of the asymmetry from four different nuclear mean field models [186] as a function of the scattering angle and the momentum transfer considering the MESA beam line ($E_e = 155\,{\rm MeV}$). The blue and magenta data points show an example of the possible data set for the backward measurement considering the fragmented backward detector. The data points are 2° wide and run between $\theta = 126^\circ$ to $\theta = 156^\circ$.

Since the P2 experiment is not operational yet, we will consider as a starting point for the sensitivity study the theoretical predictions for the carbon-12 nuclear system from nuclear energy density functionals [142, 187, 188] considering the same sample used in Ref. [186]. By comparing the theoretical predictions with the experimental precision goal we investigated the sensitivity of the P2 experiment on

the weak mixing angle and the carbon-12 weak skin. In particular, the experimental program foresees reaching a $\sim 0.3\%$ precision on the measured asymmetry at forward angle, $A_{\rm pv}^{{\rm meas},\,f}$, and a $\sim 3-7\%$ precision on the asymmetry at backward angle, $A_{\rm pv}^{{\rm meas},\,b}$. However, there are ongoing discussions about the possibility of considering a fragmented detector at backward kinematics, which by employing pixel strips could enable the measurement of multiple points at different kinematics (i.e. momentum transfer), improving the expected precision on the backward asymmetry, with a total expected precision around $\sim 1\%$. An example of the possible data set of the P2 measurement at MESA at backward angle considering the pixel-like technology for the backward detector is shown in Fig. 3.17. The data points have been simulated considering as a reference prediction a particular nuclear mean field model, namely the blue points from the RMF016 model and the violet points from the SMC12 model [186]. In the figure, we also show other two nuclear model predictions to give an idea of the discrimination potential between theoretical prediction given by the experimental precision goal achievable with such technology[9].
The actual discussion of the sensitivity study, the analysis prescription and the main results will be discussed in Sec. 4.3.

3.2 APV: Atomic parity Violation

Another process involving electrons and nuclei at low energies is known as atomic parity violation (APV), also known as *parity non-conservation* (PNC). In atoms, electronic transitions usually happen via a photon exchange, thus through an electromagnetic process. However, some specific transitions can not happen, due to the selection rules arising from parity conservation. In this specific scenario, the electron-nucleus weak interaction becomes dominant and the transition happens via a Z boson exchange, as pictorially schematized in Fig. 3.18. As the Z boson couples to the weak charge, the observable of APV experiments is definitely the nuclear weak charge, from which one can extract information on the weak mixing angle at low energy ($\sim$ few MeV). Indeed, these measurements have been performed on a set of different nuclei, such as ytterbium, bismuth, thallium, cesium and lead [189]. However, we will consider only the case of lead, for its complementary with PVES measurements, and cesium, for its complementary with CEνNS measurements and for its much better precision with respect to the other APV measurements. These probes provide the lowest energy determinations of $\sin^2\theta_W$, being the momentum transfer of few MeVs [190], i.e., $Q_{\rm APV(Cs)} \sim 2.4\ \mathrm{MeV}$ for cesium atoms and $Q_{\rm APV(Pb)} \sim 8\ \mathrm{MeV}$ for lead atoms.
From a microscopic point of view, the Hamiltonian which describes the weak interaction between atomic electrons and the nucleus can be expressed as [189, 191]

$$\hat{h}_{\rm PNC} = \frac{G_F}{\sqrt{2}} \sum_B (C_{1B}\overline{B}\gamma_\mu B\overline{e}\gamma^\mu\gamma_5 e + C_{2B}\overline{B}\gamma_\mu\gamma_5 B\overline{e}\gamma^\mu e)\,, \tag{3.66}$$

[9] Study still in progress in collaboration with M. Boonekamp and M. Gorchtein.

where the sum is over all the nucleons ($B = p, n$) and the Hamiltonian contains a spin-independent and a spin-dependent terms.

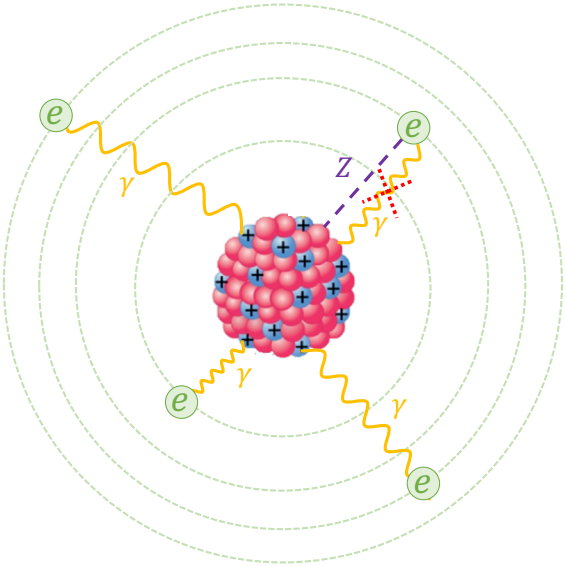

Figure 3.18: Pictorial representation of the atomic parity violation process in atoms. The different orbitals indicate different atomic shells. Almost all the atomic transitions happen through an electromagnetic process (photon exchange), some specific transitions instead can not happen through the photon exchange due to selection rules, and thus, the process is mediated by a Z boson.

The above Hamiltonian does not conserve parity, but it preserves the time reversal symmetry. The C_{1B} and C_{2B} coefficients can be calculated in the standard model for protons and neutrons, and at tree-level they are [191]

$$C_{1p} = \frac{1}{2}(1 - 4\sin^2\theta_W) \approx 0.04\,, \tag{3.67}$$

$$C_{1n} = -\frac{1}{2}\,, \tag{3.68}$$

$$C_{2p} = -C_{2n} = \frac{1}{2}(1 - 4\sin^2\theta_W)g_A \approx 0.05\,, \tag{3.69}$$

where we have considered the nucleon axial charge $g_A \approx 1.26$.
The spin-independent (SI) contribution stems from the coupling of electron axial current and nucleon vector current, while the spin-dependent (SD) part from the electron vector current and the nucleon axial current. The nucleon contribution to the SI part is in principle coherent, however, the protons give a rather small contribution, being $C_{1p} << C_{1n}$. The situation is different for the SD contribution, as only valence nucleon contributes and both the couplings, C_{2p} and C_{2n} are small. Other SD contributions should also be incorporated, and a detailed discussion can be found in the review in Ref. [189].
Considering non-relativistic nucleons, it is convenient to write the Hamiltonian as an effective single-electron operator [189, 191, 192]

$$\hat{h}_{\rm SI} = \frac{G_F}{\sqrt{2}}[C_{1p}Z\rho_p(r) + C_{1n}N\rho_n(r)]\gamma_5\,, \tag{3.70}$$

where we have assumed a point-like nature for nucleons and used the fact that $\sum_B \langle \overline{B}(r) B(r) \rangle = \#_B \rho_B(r)$, for $B = p, n$ and $\#_B$ is the number of B nucleons [193], with $\rho_B(r)$ being the nucleon density distribution. Often, the difference between the two is neglected ($\rho(r) = \rho_p(r) = \rho_n(r)$), so that the definition assumes a simplified form, namely

$$\hat{h}_{\mathrm{SI},\,0} = \frac{G_F}{2\sqrt{2}} Q_W \rho(r) \gamma_5 \,, \tag{3.71}$$

where we can define the nuclear weak charge in terms of the C_{1N} coefficients, namely[10] $Q_W = 2ZC_{1p} + 2NC_{1n} \approx -N$. Indeed, we have already discussed the fact that the equal proton-neutron densities approximation is not fully correct. In particular, the difference between the nucleon densities gives rise to the neutron skin.
As we are interested in the impact of the neutron skin in low energy electroweak probes, we need to consider $\rho_p \neq \rho_n$, and thus, we can define the matrix element between two different atomic states with relativistic wave functions $\psi_{i,j}$ as [191]

$$\begin{aligned} \mathcal{M} &= \langle j | \hat{h}_{\mathrm{SI}} | i \rangle \\ &= \frac{G_F}{2\sqrt{2}} \Big[2C_{1p} Z \int \rho_p(r) \psi_j^\dagger \gamma_5 \psi_i d^3 r + \\ &+ 2C_{1n} N \int \rho_n(r) \psi_j^\dagger \gamma_5 \psi_i d^3 r \Big] \,. \end{aligned} \tag{3.72}$$

Using the Dirac wave functions for the s and $p_{1/2}$ orbital states inside a uniformly charged spherical nucleus, and integrating over angles, the matrix element becomes

$$\mathcal{M} = \frac{G_F}{2\sqrt{2}} \mathcal{A}_{ps} \mathcal{N} \tilde{Q}_W \propto G_F \tilde{Q}_W \,, \tag{3.73}$$

where $\mathcal{A}_{ps}$ is the atomic factor which has no dependence on nuclear parameters and $\mathcal{N}$ is the normalization factor dependent on the nuclear charge radius. With $\tilde{Q}_W$, we define

$$\tilde{Q}_W = Z q_p (1 - 4 \sin^2 \theta_W) - N q_n \,. \tag{3.74}$$

The redefined couplings $q_{p,n}$ are defined as [2]

$$q_{p,n} = 4\pi \int_0^\infty \rho_{p,n}(r) f(r) r^2 \mathrm{d}r, \tag{3.75}$$

where $f(r)$ is the radial matrix element of the electron axial current between the atomic $s_{1/2}$ and $p_{1/2}$ wave functions inside the nucleus normalized to $f(0) = 1$. We can expand the function $f(r)$ as a series in power of $(Z\alpha)$, and for most of the atomic systems of interest, in particular, for $(Z\alpha)$ up to ~ 0.7, cutting off the series at $(Z\alpha)^2$ is more than adequate to fulfill the requirements of precision for

[10] Let us note that, by comparing with the nuclear weak charge definition in Eq. 3.27, we can observe that $g_{\mathrm{AV}}^{\mathrm{ep}} = -C_{1p}$ e $g_{\mathrm{AV}}^{\mathrm{en}} = -C_{1n}$.

the comparison with currently available experimental observation. At order $(Z\alpha)^2$, for any nucleus, $f(r)$ is given by [194]

$$f(r) = 1 - 2\int_0^r \frac{V(r')}{r'^2}\int_0^{r'} V(r'')r''^2 \mathrm{d}r''\mathrm{d}r' + \left(\frac{1}{r}\int_0^r V(r')r'^2\mathrm{d}r'\right)^2 , \tag{3.76}$$

where $V(r)$ represents the radial electric potential determined by the nuclear charge distribution $\rho_{\rm ch}(r)$. By using the Poisson equation, we can obtain the potential through

$$\frac{1}{r}\frac{d^2}{dr^2}[rV(r)] = -4\pi Z\alpha\rho_{\rm ch}(r)\,, \tag{3.77}$$

whose general solution is

$$V(r) = 4\pi Z\alpha\left[\frac{1}{r}\int_0^r \rho_{\rm ch}(r')r'^2\mathrm{d}r' + \int_r^\infty \rho_{\rm ch}(r')r'\mathrm{d}r'\right] . \tag{3.78}$$

At this point, the parametrization for the charge density has to be fixed in order to perform the calculation, and the easiest choice is to imagine the nucleus as a uniformly charged sphere (cd) of radius $R_{\rm ch}$, so that

$$\rho_{\rm c}^{\rm cd}(r) = \frac{3}{4\pi R_{\rm ch}^3}\,\Theta(R_{\rm ch} - r)\,, \tag{3.79}$$

where $\Theta(R_{\rm ch} - r)$ is the Heaviside function, and the potential, using Eq. (3.78) turns out to be

$$V^{\rm cd}(r) = \begin{cases} \frac{Z\alpha}{2R_{\rm ch}}\left(3 - \frac{r^2}{R_{\rm ch}^2}\right) & \text{for } r < R_{\rm ch} \\ \frac{Z\alpha}{r} & \text{for } r > R_{\rm ch} \end{cases} . \tag{3.80}$$

By using Eq. (3.76), it is possible to derive the analytical form of the radial matrix element $f^{\rm cd}(r)$ for $r < R_{\rm ch}$

$$f^{\rm cd}(r) = 1 - \frac{(Z\alpha)^2}{2}\left(\frac{r^2}{R_{\rm ch}^2} - \frac{r^4}{5R_{\rm ch}^4} + \frac{r^6}{75R_{\rm ch}^6}\right), \tag{3.81}$$

and for $r > R_{\rm ch}$

$$f^{\rm cd}(r) = 1 - \frac{(Z\alpha)^2}{2}\left(\frac{13}{30} + \frac{2R_{\rm ch}^2}{5r^2} - \frac{R_{\rm ch}^4}{50r^4} + 2\ln\left(\frac{r}{R_{\rm ch}}\right)\right). \tag{3.82}$$

Using the above results and Eq. (3.75), one can calculate the proton and neutron integrals. Indeed, when considering a constant density, the integrals in Eq. (3.75) have a cut-off at the value of the proton distribution radius R_p, and the neutron distribution radius R_n. Since both R_p and R_n are in general larger than $R_{\rm ch}$, one has to use both forms for $f(r)$, depending on the regimes of integration. These considerations lead to [2]

$$q_{p,n}^{\rm cd} = 1 - (Z\alpha)^2\Big(-\frac{7}{60} + \frac{3}{5}\frac{R_{\rm ch}^2}{R_{p,n}^2} - \frac{16}{63}\frac{R_{\rm ch}^3}{R_{p,n}^3} + \frac{3}{100}\frac{R_{\rm ch}^4}{R_{p,n}^4} + \ln\frac{R_{p,n}}{R_{\rm ch}}\Big). \tag{3.83}$$

Under the approximation $R_{\rm ch} \simeq R_p$ and for $R_n^2/R_p^2 - 1 \ll 1$, it is possible to obtain the typically used forms of $q_{p,n}$

$$q_p^{\rm cd} \simeq 1 - \frac{817}{3150}(Z\alpha)^2, \tag{3.84}$$

$$q_n^{\rm cd} \simeq 1 - (Z\alpha)^2 \left[\frac{817}{3150} + \frac{116}{525}\left(\frac{R_n^2}{R_p^2} - 1\right)\right]. \tag{3.85}$$

However, the constant density approximation is useful mainly for illustrative purposes, as it is known to not be the most accurate description of heavy nuclei. Therefore, we performed the calculations considering the more accurate charge, proton and neutron distribution densities that correspond to the form factors discussed previously, namely, we used the Helm parametrization [88] or the symmetrized 2pF distribution, with the appropriate values of the charge, proton and neutron radii [2, 4].
The experimental extraction of the nuclear weak charge is slightly different for different atomic systems, so that we will discuss it in more detail in the proper sections, however, the common procedure employs the ratio of a purely experimental quantity and a theoretical one. The crucial quantity entering inside the ratio is the parity violating amplitude $E_{\rm PNC}$, which can be calculated theoretically in terms of the nuclear weak charge. Its imaginary part assumes the form of $\mathrm{Im}\, E_{\rm PNC} \sim \text{coeff} \times (Q_W/N)$, where the coefficient depends on the specific atomic system considered. In the original atomic theory derivation of the parity violating amplitude, a charge-density distribution has been used instead of $\rho_W(\mathbf{r})$ since the charge radius was better determined. To keep this into account, a so-called neutron-skin correction was applied to the final calculation using the proper density distribution. Such neutron skin correction takes the form [2, 4, 191, 193–198]

$$\delta E_{\rm PNC}^{\rm n.s.}(R_n) = \left[\frac{\rm N}{Q_W}\Big(1 - \frac{q_n(R_n)}{q_p}\Big) E_{\rm PNC}^{\rm w.n.s.}\right], \tag{3.86}$$

where $E_{\rm PNC}^{\rm w.n.s.}$ is the parity violating amplitude calculated considering the charge density distribution without any neutron skin correction applied[11].
In the latter correction, the $q_{p,n}$ coefficients defined above enter in order to account for the radial distribution of protons and neutrons inside the nucleus, and we have explicitly introduced the R_n dependence to underline the unknown quantity at which we are interested. Let us note that in calculating q_p inside Eq. 3.86, it is necessary to adopt the same charge density considered in the calculation of $E_{\rm PNC}^{\rm w.n.s.}$, in which no neutron skin correction was yet introduced. Indeed, this is necessary as we want to remove the contribution of q_p, in order to replace it with the one due to the neutron density distribution, namely q_n. Therefore, if one does not employ the correct charge distribution in calculating q_p, it would introduce a bias in the calculation. Instead, for the q_n calculation one can consider any chosen parametrization for the nuclear neutron density.

[11] The superscript w.n.s. stands for without neutron skin and is used to indicate the amplitude corrected for the neutron skin.

3.2.1 —— APV on Lead ——

Interestingly, one of the atomic systems exploited to perform atomic parity violation experiments is $^{208}\mathrm{Pb}$, the same nucleus used by PREX for PVES measurement. Thus, it is rather important as it provides an independent measurement of analogue quantities, namely the nuclear weak charge (i.e. the weak mixing angle) and the neutron skin. We will see that it is possible and convenient to combine the two experimental probes to obtain more information.
The parity nonconserving nuclear-spin-independent part of the electron-nucleus interaction Hamiltonian [199] depends on $\rho_W(\mathbf{r})$. In the original calculation of E_{PNC}, a charge-density distribution has been used instead of $\rho_W(\mathbf{r})$ since the charge radius was better determined. In particular, for the amplitude calculation of APV(Pb), a uniformly charged ball density was assumed, with $R_{\mathrm{ch}}(^{208}\mathrm{Pb}) = 5.5010\,\mathrm{fm}$ [199].
Once E_{PNC} is obtained[12], the quantity $R_{\mathrm{th}} = (\mathrm{Im}\, E_{\mathrm{PNC}}/M_1)_{\mathrm{th.}}$ can be defined, where M_1 represents the reduced electric-dipole transition of the magnetic-dipole operator for the $6p^2\,{}^3P_0 \rightarrow 6p^2\,{}^3P_1$ transition relevant for lead. The theoretical calculated value is $R_{\mathrm{th}} = -10.6(4) \times 10^{-8}(-Q_W^{\mathrm{APV(Pb)}}/N)$ [199] while experimentally two measurements are available, $R_{\mathrm{exp}} = -9.86(12) \times 10^{-8}$ [200] and $R_{\mathrm{exp}} = -9.80(33) \times 10^{-8}$ [201], therefore we consider the experimental average value, $R_{\mathrm{exp}}^{\mathrm{av.}}$. The lead nuclear weak charge is then obtained through the ratio between R_{exp} and R_{th}, which gives $Q_W^{\mathrm{APV(Pb)}} = -117(5)$ [199].
Considering the neutron skin correction defined in Eq. 3.86, we can define the correction to be applied in the case of APV on lead-208. Namely, for the q_p calculation we follow the original calculation, and thus, we consider the charge density used in Ref. [199], while for q_n calculation the symmetrized 2pF was adopted, to be consistent to what we have employed in the PREX analysis.
Following the above definitions, the nuclear weak charge measurement can then be obtained through

$$Q_W^{\mathrm{APV(Pb)}}(R_n) = -N R_{\mathrm{exp}}^{\mathrm{av.}} \Big(\frac{M_1}{\mathrm{Im}(E_{\mathrm{PNC}}^{\mathrm{w.n.s}} + \delta E_{\mathrm{PNC}}^{\mathrm{n.s.}}(R_n))} \Big)_{\mathrm{th.}}, \tag{3.87}$$

where Im stands for imaginary part. A completely analogue procedure will be discussed in the next section applied to the case of cesium atoms [2, 198].
The APV measurement, contrary to PREX, is mainly sensitive to s_W^2 and only feebly on ΔR_{np}. We build the following χ^2 function to analyze the APV(Pb) measurement

$$\chi^2_{\mathrm{APV(Pb)}}(\sin^2\theta_W, R_n) = \Big(\frac{Q_W^{\mathrm{th,APV}}(\sin^2\theta_W) - Q_W^{\mathrm{APV(Pb)}}(R_n)}{\sigma^{\mathrm{APV(Pb)}}(\sin^2\theta_W, R_n)} \Big)^2, \tag{3.88}$$

where $\sigma^{\mathrm{APV(Pb)}}(\sin^2\theta_W, R_n)$ is the total uncertainty. It is worth mentioning that the weak mixing angle dependence is inside the calculation of the theoretical value of the nuclear weak charge, while the nuclear neutron radius enters inside the theoretical contribution to the experimental determination of the nuclear weak charge.

[12] Let us note that in some references, as in Ref. [4], the notation is E_{APV}, which is completely equivalent.

The weak charge $Q_W^{\rm th,APV}$ for APV experiments is slightly different from the one discussed in the context of PVES experiments, due to different radiative corrections. In particular, adopting the description in Refs. [2, 25], $Q_W^{\rm th,APV} = -118.79(5)$, accounting for the radiative corrections.
The APV(Pb) measurement, considering a fixed nuclear neutron radius $R_n = 5.609\,\mathrm{fm}$, gives a determination of the weak mixing angle of $\sin^2\theta_W = 0.235 \pm 0.013$. In order to perform a combined fit of the APV(Pb) and PREX-II measurements, we summed the χ^2 functions in Eq. 3.56 and Eq. 3.88 to fully exploit their correlations, with the only hidden assumption of requiring $\sin^2\theta_W$ to be constant between the corresponding experimental momentum transfers, $8 \lesssim Q \lesssim 78\ \mathrm{MeV}$.

3.2.2 —— APV on Cs ——

The most precise APV measurement was performed on cesium atoms and it is extracted from the ratio of the parity violating amplitude, $E_{\rm PNC}$, to the Stark vector transition polarizability, β, and by calculating theoretically $E_{\rm PNC}$ in terms of the nuclear weak charge Q_W [25, 31, 202]

$$Q_W^{\rm APV(Cs)}(R_n) = N \left(\frac{\mathrm{Im}\, E_{\rm PNC}}{\beta}\right)_{\rm exp.} \left(\frac{Q_W^{\rm SM,\,Cs}}{N\,\mathrm{Im}\,(E_{\rm PNC}^{\rm w.n.s.} + \delta E_{\rm PNC}^{\rm n.s.}(R_n))}\right)_{\rm th.} \beta_{\rm exp.+th.}\,, \tag{3.89}$$

where $\beta_{\rm exp.+th.}$ and $(E_{\rm PNC})_{\rm th.}^{\rm w.n.s.}$ are determined from atomic theory [25, 203]. We have already applied the neutron skin correction $\delta E_{\rm PNC}^{\rm n.s.}(R_n)$, defined in Eq. 3.86, following the same procedure discussed for the APV(Pb) measurement. Let us notice that the above definition of $Q_W^{\rm APV(Cs)}(R_n)$ has a rather similar structure to the one in Eq. 3.87. The term $Q_W^{\rm SM,\,Cs}$ indicates the SM value of the nuclear weak charge for cesium, namely $Q_W^{\rm SM\,Cs} = -73.23(1)$, and it is important to remark that this will remain the SM value also when we will allow the weak mixing angle free to vary in the theoretical prediction of the nuclear weak charge. We use $(\mathrm{Im}\, E_{\rm PNC}/\beta)_{\rm exp} = (-3.0967 \pm 0.0107) \times 10^{-13}|e|/a_B^2$ [25, 203], where a_B is the Bohr radius and $|e|$ is the absolute value of the electric charge, and $\beta_{\rm exp.+th.} = (27.064 \pm 0.033)\, a_B^3$ [25, 203]. For the imaginary part of $E_{\rm PNC}$ we use $(\mathrm{Im}\, E_{\rm PNC})_{\rm th.}^{\rm w.n.s.} = (0.8995 \pm 0.0040) \times 10^{-11}|e| a_B \frac{Q_W}{N}$ [2, 31], where we subtracted the neutron skin correction, introduced in Ref. [204] to take into account the difference between R_n and R_p that is not considered in the nominal atomic theory derivation. Here we remove this correction in order to be able to directly evaluate R_n, so that practically speaking we are reintroducing the neutron skin correction ourselves. We will also discuss the implications of considering the result of the more recent calculation reported in Ref. [205] which yields to a smaller value of the parity violating amplitude, namely $(\mathrm{Im}\, E_{\rm PNC})_{\rm th.}^{\rm w.n.s.} = (0.8930 \pm 0.0027) \times 10^{-11}|e| a_B \frac{Q_W}{N}$, adopting the same procedure.
When performing the analysis of the APV data, we use the least-squares function given by [8]

$$\chi^2_{\rm APV(Cs)}(\sin^2\theta_W, R_n) = \left(\frac{Q_W^{\rm th,APV}(\sin^2\theta_W) - Q_W^{\rm APV(Cs)}(R_n)}{\sigma^{\rm APV(Cs)}(\sin^2\theta_W, R_n)}\right)^2, \tag{3.90}$$

where $\sigma_{\rm APV}$ is the total uncertainty. Finally, when performing a combined analysis of the COHERENT CsI data with APV(Cs), we sum the latter chi-square function with the one defined in Eq. 2.75.
According to our calculation, reported in Ref. [8], the APV(Cs) measurement, considering a fixed nuclear neutron radius $R_n({\rm Cs}) = 5.09\,{\rm fm}$ [8, 60] and the $({\rm Im}\,E_{\rm PNC})^{\rm w.n.s.}_{\rm th.}$ from Refs. [2, 31], gives a determination of the weak mixing angle of

$$\sin^2\theta_W({\rm APV\ PDG}) = 0.2375 \pm 0.0019\,(1\sigma) \pm 0.0031\,(90\%{\rm CL}) \pm 0.0038\,(2\sigma)\,, \quad (3.91)$$

where the denomination APV PDG has been added to indicate the $({\rm Im}\,E_{\rm PNC})^{\rm w.n.s.}_{\rm th.}$ value adopted. While, using $({\rm Im}\,E_{\rm PNC})^{\rm w.n.s.}_{\rm th.}$ from Refs. [205], it gives

$$\sin^2\theta_W({\rm APV\ 2021}) = 0.2399 \pm 0.0016\,(1\sigma) \pm 0.0026\,(90\%{\rm CL}) \pm 0.0032\,(2\sigma)\,, \quad (3.92)$$

result that we refer to with the denomination APV 2021 [8]. Let us note that the two values are different with respect to the ones reported in the original references [31, 205], that we will refer to as APV(Cs) 2020 and APV(Cs) Sahoo 2021, as we use a larger value for the nuclear neutron radius of cesium with respect to the value adopted inside their calculations.

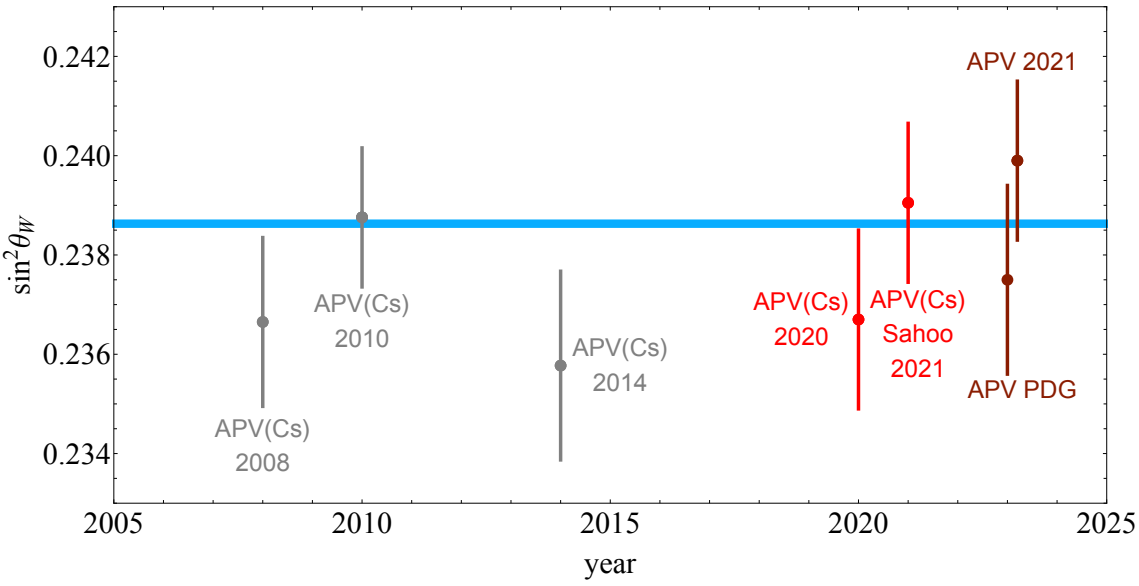

Figure 3.19: Summary of the weak mixing angle measurements from APV(Cs) during the years. The light blue line shows the SM value of the weak mixing angle at low energies. The gray points show the measurements from APV on cesium atoms during the years [206–208], while the red points the two determinations from APV PDG 2020 and APV 2021 as reported in Refs. [25, 203, 205]. Our re-determinations of the two are shown with the darker red point [8].

In fact, at the time of Refs. [31, 204], there was not any cesium neutron radius measurement. Therefore, the neutron skin correction was evaluated by fixing the nuclear neutron radius to an extrapolation from antiprotonic atom x-rays data [162]. From such data, which have been collected for many nuclei, but

not cesium, they extrapolated the cesium neutron skin, namely $\Delta R_{\rm np}^{\rm had}(^{133}{\rm Cs}) = 0.13(4)$ fm (which implies $R_n^{\rm had} = 4.951\,{\rm fm}$), by assuming a linear dependence on the so-called asymmetry parameter, $I = (N-Z)/A$. They found an empirical fitted function

$$\Delta R_{\rm np}^{\rm had}(\mathcal{N}) = (-0.04 \pm 0.03) + (1.01 \pm 0.15) I\,{\rm fm}\,. \tag{3.93}$$

Unfortunately, these hadronic determinations of the neutron skin are known to be affected by considerable model dependencies and uncontrolled approximations [139], differently from electroweak measurements.
By considering $\Delta R_{\rm np}^{\rm had}(^{133}{\rm Cs})$ inside the calculations one obtains a nuclear weak charge measurement of [32, 203, 209]

$$Q_W^{^{133}{\rm Cs},\,{\rm had}} = -72.82(42)\,. \tag{3.94}$$

Furthermore, it is interesting to notice how the theoretical value of $(\mathrm{Im}\,E_{\rm PNC})_{\rm th.}^{\rm w.n.s.}$ has varied significantly during the years due to the redetermination of the theoretical value by different atomic calculations and different choices of the neutron skin correction. To give an idea of the impact on the weak mixing angle extraction, in Fig. 3.19 we show the status of the weak mixing angle measurement from APV(Cs) in the last years. The weak mixing angle measurement has bounced up and down during the years keeping the uncertainty almost constant, and also the two latest results, APV PDG and APV 2021 are rather far apart from one another (slightly more than 1σ) but both in good agreement with the SM expected value.
It is important to notice how the choice of the poorly known neutron radius impacts the measurement, moving the extracted value. This has been discussed in detail in Refs. [2, 8, 198] and also in Ref. [3], where the neutron skin correction was calculated starting from an extrapolation of the cesium neutron skin from the PREX measurement on lead. In fact, it is possible to exploit the correlation between the predictions of the neutron skin of cesium and lead from nuclear mean field models, to infer a value of the cesium neutron skin from a measurement of the lead one. Such result is shown in Fig. 3.20, where we report a variety of nuclear models [142, 187, 210–223], and by the gray black line we present the result of a linear fit, with its 1σ and 3σ constraints through the gray dashed regions. Exploiting such correlation is possible to infer the neutron skin of cesium from the combined PREX-I and PREX-II measurement of the neutron skin of lead, resulting in [3]

$$\Delta R_{\rm np}^{\rm point}(^{133}{\rm Cs}) = 0.22(5)\,{\rm fm}\,, \tag{3.95}$$

which indeed leads to an experimental value for the nuclear weak charge (using $E_{\rm PNC}$ from PDG 2020) of $Q_W^{^{133}{\rm Cs}} = -72.94(43)$ and a neutron radius of $R_n(^{133}{\rm Cs}) = 5.03(5)\,{\rm fm}$. These values are compatible with the ones obtained relying on the neutron radius from the nuclear shell model estimation used as reference values in this thesis work, and discussed previously. Moreover, we find similar uncertainties with respect to the result reported in Refs. [32, 203, 209] (see Eq. 3.94) but with a slightly different central value. However, due to the model dependencies and uncontrolled approximations affecting the hadronic determination of the neutron skin, we decided to rely on the extrapolation exploiting the PREX measurement, or as we will see later to leave it as a free parameter in the fit when possible.

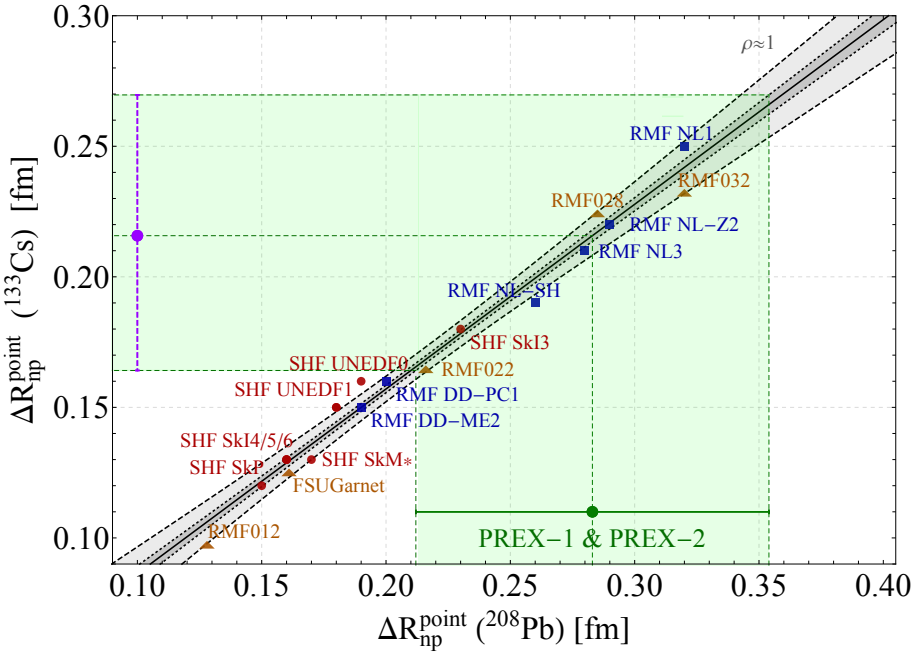

Figure 3.20: Point neutron skin predictions for ^{208}Pb and ^{133}Cs according to different models (red circles [210, 217–221], orange triangles [142, 187, 222, 223], and blue squares [211–216]). A linear fit is superimposed in solid black, where the 1σ and 3σ constraints are also shown by the dark-gray dotted and light-gray dashed regions, respectively. Constraints set by the combined PREX result [143, 153, 154, 224] and the ones on $\Delta R_{\rm np}^{\rm point}(^{133}{\rm Cs})$ derived in Ref. [3] are also shown by the green and purple point, respectively.

In conclusion, it is interesting to see the deep interconnection between the electroweak probes we are dealing with, such that a measurement using polarized electron scattering on lead can help in understanding the atomic parity violation process on a different target, such as cesium, and then this reflects also on neutrino scattering measurements such as CEνNS. This gives a clear picture of the power of the combination of different electroweak probes to test the SM and try to go beyond it.
In general, it is clear that the most correct procedure to analyze APV measurements and extract physical quantities from them is to leave the neutron skin (or equivalently the neutron radius) as a free parameter in the fit as well as the weak mixing angle, in order to avoid possible biases in the extraction of $\sin^2\theta_W$. One fundamental remark is to notice that the COHERENT CsI measurement basically depends on the same quantity of APV(Cs), as they both extract the neutron skin of cesium and the weak mixing angle. To be more precise, in the COHERENT case, the target is not exactly cesium, but cesium iodine, and we will see later the implications of this aspect. It is interesting to combine the two probes to fully exploit the constraining power of such electroweak probes.

Part II

Precision standard model test and beyond

Chapter 4

Nuclear Structure and theory perspective in PVES measurements

Short introduction

In this chapter, we will discuss the main results obtained by analyzing the PVES and APV measurements to extract nuclear structure information and also measurements on the weak mixing angle. Some of the results are taken from Ref. [4] and other ones are still not published.

4.1 The case of lead 208: PREX

We analyzed the PREX-II measurement as it is more precise than the first PREX result, and the details can be found in Ref. [4]. The first analysis aimed to reproduce the official result released by the PREX Collaboration. In order to do so, we fixed the weak mixing angle to its SM value, $\sin^2\theta_W = \sin^2\theta_W^{\rm SM}$, and used the chi-square function in Eq. 3.53, to find the best fit values of the neutron radius, and thus to retrieve the neutron skin. We found $\Delta R_{\rm np}(\sin^2\theta_W^{\rm SM}) = 0.276 \pm 0.078$ fm, which confirms the PREX-II published result, $\Delta R_{\rm np}^{\rm PREX-II}(^{208}{\rm Pb}) = 0.278 \pm 0.078$ fm [154], via an independent analysis.
Then, we showed the impact of the weak mixing angle on the analysis by leaving it as a free-to-vary parameter in the fit, using the chi-square in Eq. 3.56. Practically speaking we varied the weak mixing angle inside the nuclear weak charge definition entering the parity violating asymmetry. Since at this point, the experimental asymmetry value measured is only one single value to be interpreted in terms of two free parameters, the result is a degenerate band whose width depends on the chosen confidence level, as shown in Fig. 4.1 by the gray, brown and red shaded bands which correspond to the 1, 2 and 3σ confidence level (C.L.) contours, respectively. The red data point shows the PREX-II result [154] and it is set to the SM value of the weak mixing angle, shown by the horizontal blue line. The green vertical band indicates the prediction from theoretical models and *ab-initio* calculations, $\Delta R_{\rm np}^{\rm th}(^{208}{\rm Pb})$. Therefore, it is easy to conclude that smaller values of the

neutron skin can be accessed for lower values of $\sin^2\theta_W$, so that a neutron skin compatible with $\Delta R_{\rm np}^{\rm th}(^{208}{\rm Pb})$ can be obtained if $\sin^2\theta_W \approx 0.225$.

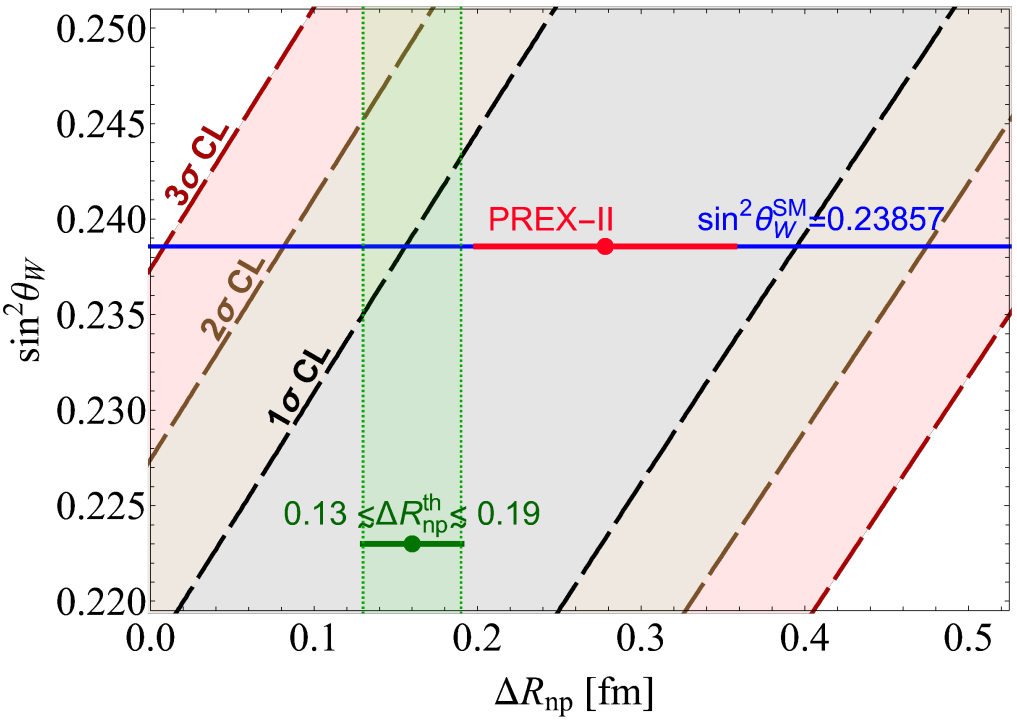

Figure 4.1: Favored regions in the $\sin^2\theta_W$ vs $\Delta R_{\rm np}(^{208}{\rm Pb})$ plane given by the reanalysis of the PREX-II data in Ref. [4]. The gray, brown and red shaded areas represent the 1, 2 and 3σ confidence level contours. The red horizontal bar shows the PREX-II result [154] for $\sin^2\theta_W^{\rm SM}$ (blue line). The green vertical band corresponds to the theoretical prediction, $\Delta R_{\rm np}^{\rm th}(^{208}{\rm Pb})$.

From the figure, it appears clear that the PREX-II measurement is visibly more sensitive to the neutron skin than the weak mixing angle (the band is more oriented toward the vertical direction). Instead, we have seen that atomic parity violation represents a fruitful probe to measure the weak mixing angle, even if it depends on the neutron skin. By fitting the atomic parity violation on lead in terms of the weak mixing angle and the neutron skin, one would obtain an almost horizontal band in the parameter space. Thus, it is evident that, by combining the two electroweak measurements, one could break the degenerate bands and end out with a closed elliptical favored region.
In Fig. 4.2, we show the results of the combined analysis of APV(Pb) and PREX-II (called "comb") obtained by summing the chi-squares in Eq. 3.53 and Eq. 3.88, through the dashed contours. In particular, the orange and darker red closed regions represent the 1σ and 3σ C.L. contours, respectively. By marginalizing the elliptical contours, one obtains the following best-fit values (orange square point) and relative uncertainties

$$\Delta R_{\rm np}^{\rm Comb} = 0.262 \pm 0.136 \text{ fm}, \tag{4.1}$$

$$\sin^2\theta_W(8 \lesssim Q \lesssim 78 \text{ MeV}) = 0.237 \pm 0.014. \tag{4.2}$$

The neutron skin value obtained is slightly smaller than the PREX-II one [154], but with about double the uncertainty, so that now it is in agreement with $\Delta R_{\rm np}^{\rm th}$ as well as with other non-electroweak measurements [138, 159–178]. The weak mixing angle is in full agreement with the SM prediction, also due to the rather large uncertainties which are dominated by the relatively poor precision of APV(Pb). Moreover, the result on the weak mixing angle has to be considered to be valid for momenta $8 \lesssim Q \lesssim 78\,\mathrm{MeV}$, so between the two experimental energy scales, in the sense that the weak mixing angle could assume a different value with respect to the SM value, but remaining constant in between such scales.

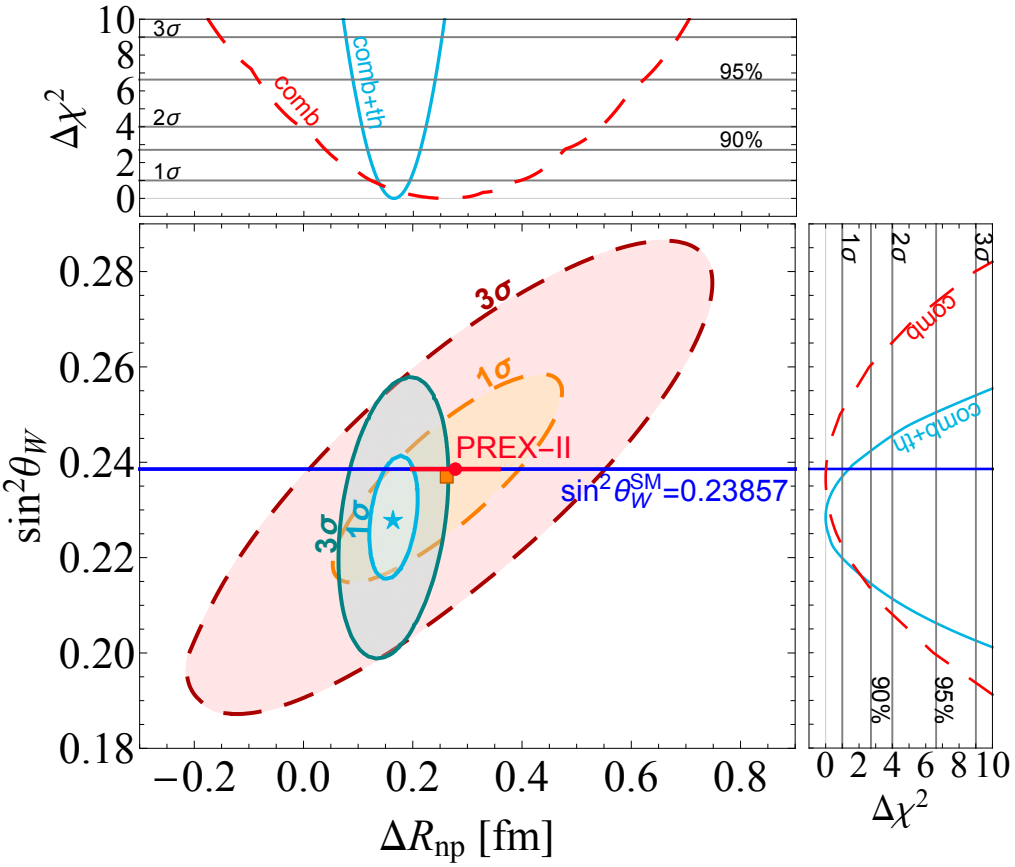

Figure 4.2: Combined fit results of APV(Pb)+PREX-II (dashed orange and dark red contours) and APV(Pb)+PREX-II+theory (solid cyan and blue contours), with their corresponding best fits (orange square and cyan star, respectively), shown at 1σ and 3σ confidence levels [4]. The side panels show the one-dimensional marginalizations (red line for APV(Pb)+PREX-II, cyan line for APV(Pb)+PREX-II+theory) for both fits. The red horizontal bar shows the PREX-II result [154] set at $\sin^2\theta_W^{\rm SM}$ (blue line).

Finally, we combine the two experimental determinations by adding a Gaussian prior $\Delta R_{\rm np}^{\rm th}(^{208}\mathrm{Pb}) = 0.16 \pm 0.03$ fm to the chi-square function, namely in the form of

$$\chi^2_{\rm prior} = \left(\frac{\Delta R_{\rm np} - \Delta R_{\rm np}^{\rm th}(^{208}\mathrm{Pb})}{\sigma_{\Delta R_{\rm np}^{\rm th}}}\right)^2, \tag{4.3}$$

to see what happens if we "force" the fit toward the theoretical predicted value of the neutron skin. The result of this combined fit (called "comb+th") is shown in Fig. 4.2 through the blue and lighter blue solid contours. Clearly, the prior forces the fit to favor smaller values of $\sin^2\theta_W$, resulting in a smaller value of the neutron skin. The best-fit values are shown by the star point and correspond to

$$\Delta R_{\rm np}^{\rm comb+th} = 0.164 \pm 0.029 \text{ fm}, \tag{4.4}$$

$$\sin^2\theta_W(8 \lesssim Q \lesssim 78 \text{ MeV}) = 0.228 \pm 0.008. \tag{4.5}$$

The $\sin^2\theta_W$ best fit results in a value lower than the SM predicted one, and with smaller uncertainty with respect to the PREX-II+APV(Pb) combined fit result.
To underline the power of combining different electroweak probes, we summarize the 1σ confidence level contours obtained by the three different analyses in Fig. 4.3 [4].

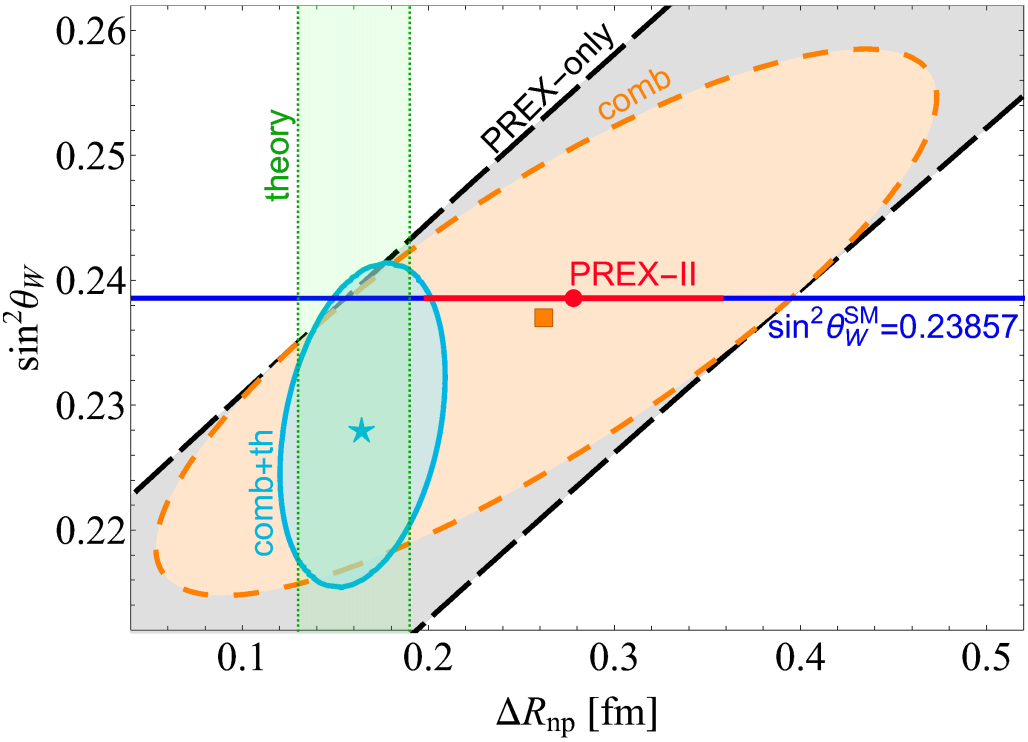

Figure 4.3: Summary of the PREX-only (grey long dashed), combined (orange dashed) and combined+theory (cyan solid) 1σ confidence level contours. The orange square and the cyan star points are the best fits of combined and combined+theory, respectively [4]. The green vertical band shows $\Delta R_{\rm np}^{\rm th}$, while the red dot the PREX-II result [154] and it is set at $\sin^2\theta_W^{\rm SM}$(blue line).

To give a basis for comparison, we summarize the state-of-the-art of low energy ($Q \lesssim 200\,\text{MeV}$) weak mixing angle measurements in Fig. 4.4 through processes involving electrons.
The data point at the lowest energy belongs to APV(Cs), which is about 1σ lower than the SM value [203]. The APV(Cs) value displayed corresponds to a neutron skin correction determined from an extrapolation of neutron skin measurements

from antiprotonic data [31, 162, 204, 225], which is compatible with the EDF estimate on cesium. At higher energies ($Q \approx 160$ MeV), the Q_{weak} [33] and the E158 [34] measurements precisely determine $\sin^2\theta_W$ to be compatible with the SM prediction. The orange square and the light blue star points are the results obtained in this work for the combined PREX-II+APV(Pb) fit, see Eq. 4.2, and the PREX-II+APV(Pb)+theory fit, see Eq. 4.5, respectively [4]. The horizontal error bars indicate that we assume $\sin^2\theta_W$ to remain constant between the APV(Pb) and PREX-II experimental energy scales.

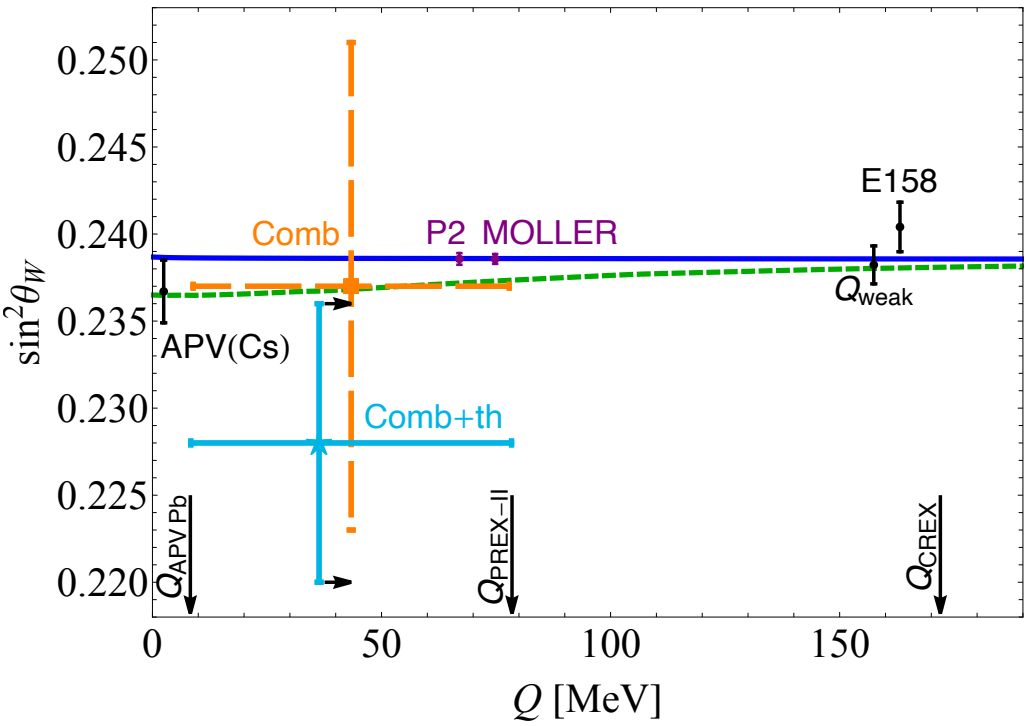

Figure 4.4: Weak mixing angle running with the energy scale Q. The SM prediction (solid blue curve) is compared with some experimental determinations (black dots) [31–34, 203, 226], and future measurements (purple dots) [184, 227, 228]. The orange dashed and the cyan solid points come from the combined and the combined+theory fits, respectively [4]. The cyan result is shifted towards lower energies for illustrative purposes, as indicated by the arrows. The vertical arrows indicate the momentum transfer for APV(Pb), PREX-II and CREX, while the green dashed curve represents the modified running of $\sin^2\theta_W$ in a scenario involving a new mediator [3].

Since PREX-II and APV(Pb) are not so precise in measuring the weak mixing angle, future determinations at the same energy scale are awaited. In particular, we show the P2 [184, 227] and the MOLLER [228] experiments projections, since the latter experiments are going to measure $\sin^2\theta_W$ with high precision at a momentum transfer slightly smaller than the PREX-II one.
The $\sin^2\theta_W$ dependence on the energy scale is a fundamental assumption behind these results. In fact, the presence of beyond the SM light particles could significantly modify the running of $\sin^2\theta_W$ only at low energies, and not induce a simple

constant shift. The green dashed curve in Fig. 4.4 shows an example of a dark Z boson [229, 230] of mass around $50\ \mathrm{MeV}$ as discussed in Ref. [3]. Such BSM model will be discussed in more detail in Sec. 6.1.3. In this context, the curve has been shown in order to give an example of a BSM scenario that can modify sensibly the weak mixing angle at low energies while remaining compatible with the SM for $Q \gtrsim 150$ MeV, so that Q_{weak} and PREX-II could be measuring different $\sin^2\theta_W$ values.

4.2 The case of calcium 48: CREX

We applied practically the same strategy used in the analysis of the PREX measurement to the case of calcium-48. Indeed, The CREX measurement (see Eq. 3.63) results to be in agreement with the expected neutron skin from *ab-initio* calculations [231], which prediction $\Delta R_{\mathrm{np}}(^{48}\mathrm{Ca}) \simeq [0.12, 0.15]$ fm. Therefore, the motivation in this case is not to try to alleviate the tension between nuclear theory calculations and the experimental measurement, but rather to study the impact of the weak mixing angle in a measurement at a different energy scale.

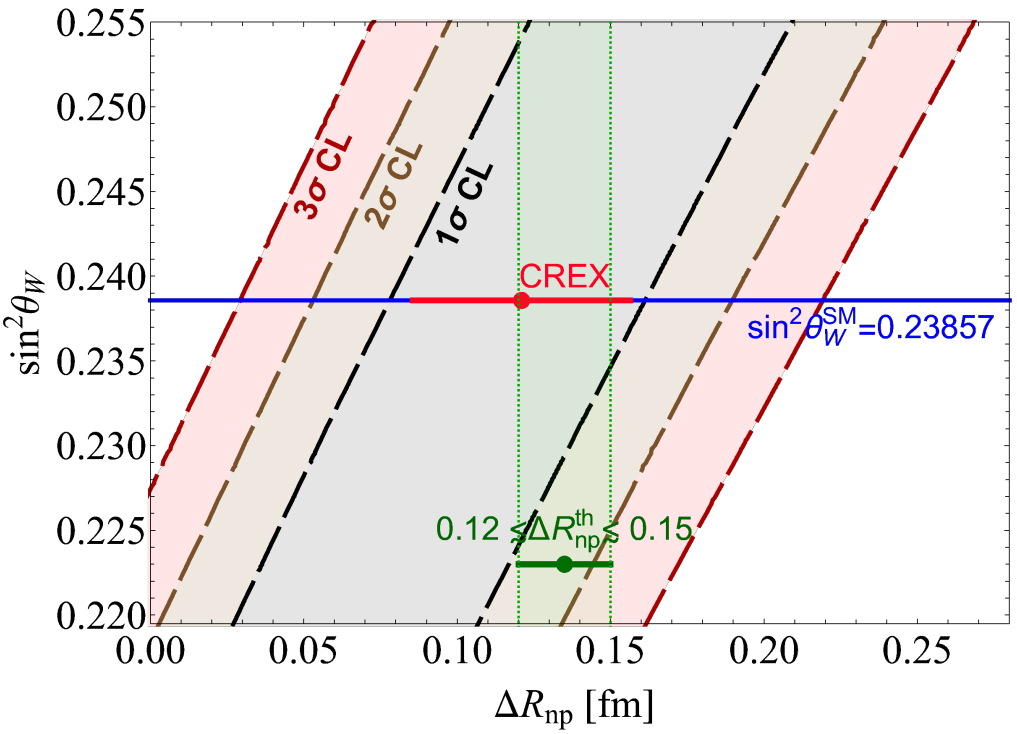

Figure 4.5: Favored regions in the $\sin^2\theta_W$ vs $\Delta R_{\mathrm{np}}(^{48}\mathrm{Ca})$ plane given by the re-analysis of the CREX data. The gray, brown and red shaded areas represent the 1, 2 and 3σ confidence level contours. The red horizontal bar shows the CREX result [158] for $\sin^2\theta_W^{\mathrm{SM}}$ (blue line). The green vertical band corresponds to the theoretical prediction, $\Delta R_{\mathrm{np}}^{\mathrm{th}}(^{48}\mathrm{Ca})$.

By re-analysing the CREX data [158], using the chi-square function in Eq. 3.65

with fixed weak mixing angle, we found

$$\Delta R_{\rm np}(^{48}{\rm Ca}) = 0.119 \pm 0.028\,{\rm fm}\,, \tag{4.6}$$

which is similar to the official result released by the collaboration, reported in Eq. 3.63. The central value is slightly smaller but still compatible, and the uncertainty is similar to the experimental uncertainty of the collaboration. Differently from what was done in Ref. [158], we did not carry out a careful model uncertainty estimation, which should then be added to the experimental one.
In Fig. 4.5, we show the effect of leaving the weak mixing angle as a free parameter in the theoretical prediction in the chi-square function in Eq. 3.65. The shaded bands represent the favored regions at different C.Ls, while the red data point indicates the official results found by the CREX Collaboration. The blue horizontal line shows the SM value of the weak mixing angle, while the vertical green band the suggested neutron skin values from *ab-initio* calculations [231]. From the figure, it is clear that the two-parameter fit leads to a degenerate diagonal band, as we obtained in the case of PREX. However, in this case, to retrieve a skin value compatible with the theoretical calculations, the weak mixing angle has to match the SM prediction. A lower weak mixing angle value, like the ones obtained in the PREX case, would lead to a much smaller neutron skin, ruining the current agreement between theory and experiment.
Nevertheless, it is fundamental to consider that the PREX and CREX measurements were performed at significantly different momentum transfers. The momentum transfer for the PREX measurement is roughly $Q_{\rm PREX-II} \sim 80$ MeV, while the CREX one is $Q_{\rm CREX} \sim 170$ MeV, as shown in Fig. 4.4. The green curve in the latter figure, showing the effect of a SM extension at low energies, suggests that in principle a variation of the weak mixing angle at the PREX energy scale could leave the weak mixing angle practically unmodified at the CREX energy scale. In this sense, the weak mixing angle running could produce an effect on the PREX extraction of the neutron skin, leaving the CREX analysis unvaried. Moreover, at a similar energy scale to CREX, other two weak mixing angle measurements are available, namely E158 and $Q_{\rm weak}$, which anchor pretty solidly the weak mixing angle to its SM value.
The $Q_{\rm weak}$ Collaboration [33] measured the weak charge of the proton Q_p very precisely at $Q \sim 160$ MeV by electron scattering off protons. They found $Q_p^{\rm exp} = 0.0719 \pm 0.0045$, which agrees well with the SM prediction, $Q_p^{\rm SM} = 0.0711(2)$ [203]. Since the weak charge of the proton is intimately bound to the electron proton coupling, it provides a rather clear measurement of the weak mixing angle. In fact, we can define the weak charge of the proton by

$$Q_p(\sin^2\theta_W) = -2(g_{\rm AV}^{\rm ep}(\sin^2\theta_W))\Big(1 - \frac{\alpha}{2\pi}\Big)\,, \tag{4.7}$$

where we have explicitly shown the weak mixing angle dependence. Interestingly, the coupling is the same entering the nuclear weak charge inside the parity violating asymmetry in Eq. 3.26. Thus, it is evident the complementarity between the two electroweak measurements. Since the proton weak charge measurement does not depend on the calcium neutron skin, the fit of the $Q_{\rm weak}$ data leads to a

horizontal band, finding $\sin^2\theta_W(Q_{\text{weak}}) = 0.238 \pm 0.001$.
We performed a combined analysis of the CREX and Q_{weak} measurements, by adding to the χ^2 function the following one

$$\chi^2_{Q_{\text{weak}}} = \left(\frac{Q_p(\sin^2\theta_W) - Q_p^{\text{exp}}}{\sigma_{\text{exp}}}\right)^2, \tag{4.8}$$

where σ_{exp} is the experimental uncertainty on the proton weak charge measurement. The result of the combined fit is shown in Fig.4.6 by the magenta and purple contours.

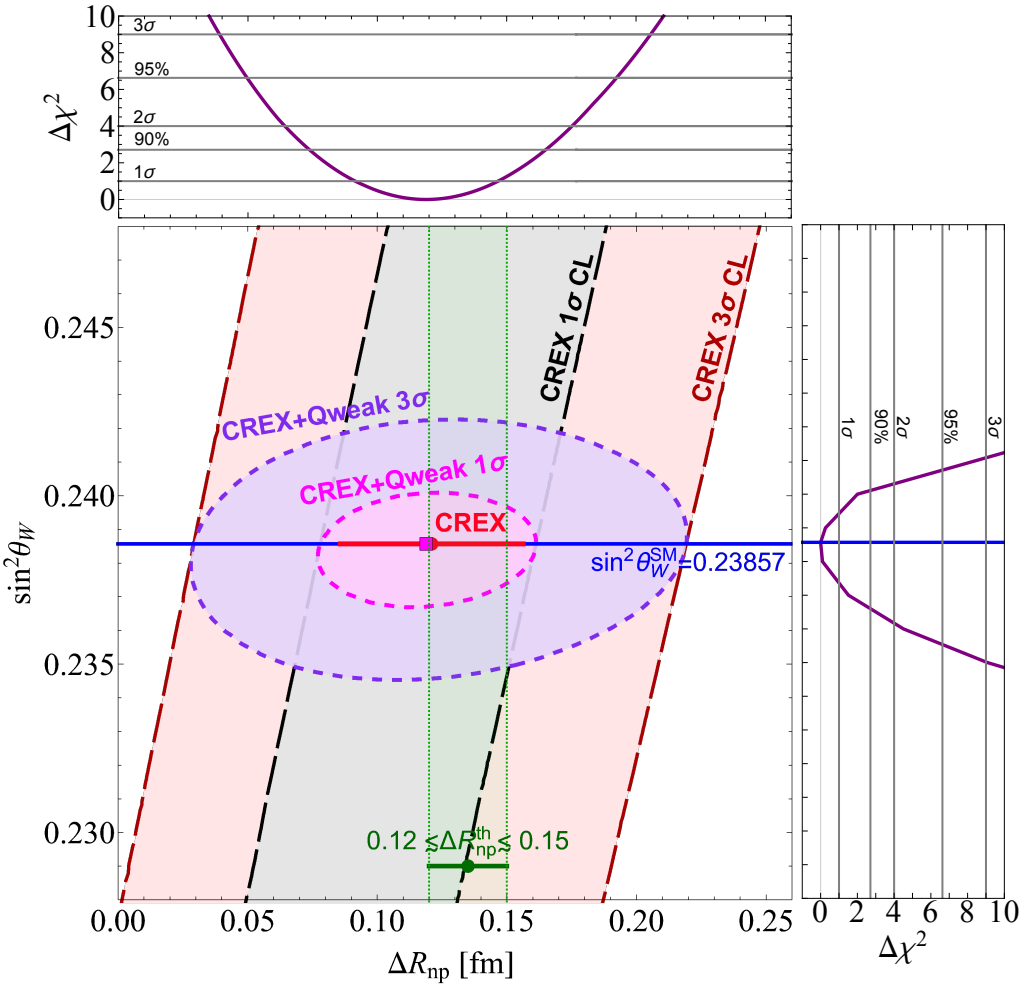

Figure 4.6: Combined fit results of Q_{weak}+CREX (magenta and purple contours) and CREX only results (red and black bands), shown at 1σ and 3σ confidence levels. The side panels show the one-dimensional marginalizations for the combined fit. The red horizontal bar shows the CREX result [158], while the magenta square the best fit of the analysis.

It is clear that since the Q_{weak} contribution is a flat horizontal band, the resulting contours are closed elliptical regions, whose precision on the weak mixing angle

is dominated by the Q_{weak} precision, while on the neutron skin by the CREX measurement. The magenta dot, showing the best fit result, is practically coincident with the CREX official result and numerically corresponds to

$$\Delta R_{\text{np}}^{Q_{\text{weak}}+\text{CREX}} = 0.119 \pm 0.028 \text{ fm}\,, \tag{4.9}$$

$$\sin^2\theta_W(157 \lesssim Q \lesssim 172 \text{ MeV}) = 0.2386^{+0.0010}_{-0.0013}\,. \tag{4.10}$$

We can easily notice that the best fit value for the neutron skin, as well as the uncertainties, are unchanged from the fit of CREX only considering the SM value for the weak mixing angle. The weak mixing angle measurement instead is similar to the Q_{weak} result, even if the central values and the uncertainties are slightly larger. We can conclude, that the two probes are in perfect agreement with each other, and allow one to break the degeneracy between weak mixing angle and neutron skin, keeping the uncertainties at a world leading level.

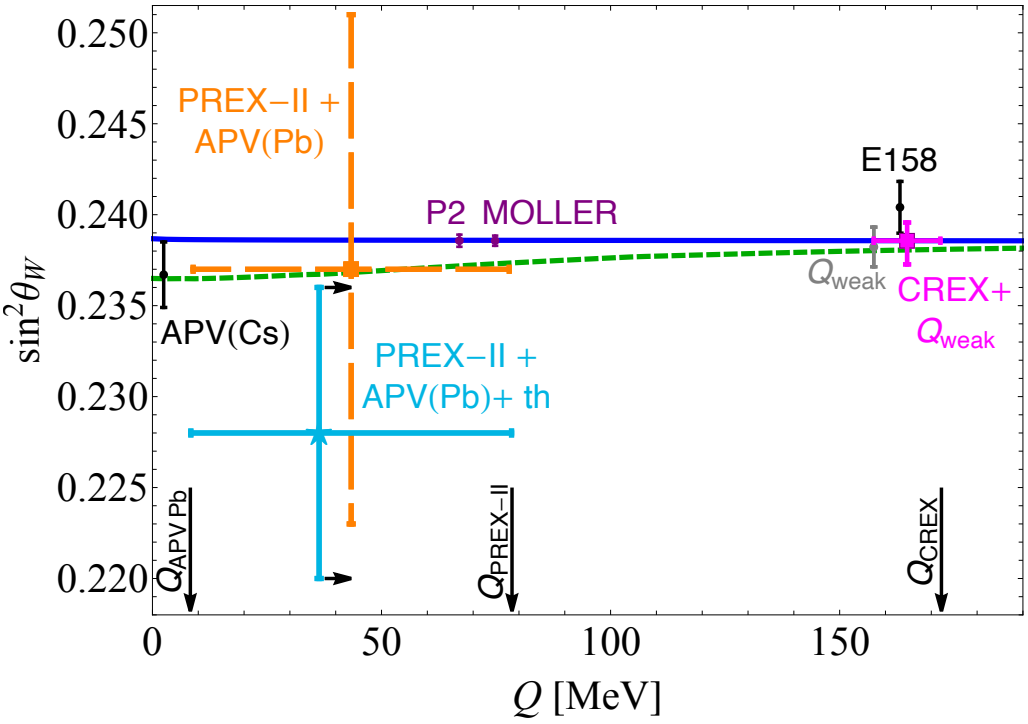

Figure 4.7: Weak mixing angle running with the energy scale Q. The SM prediction (solid blue curve) is compared with some experimental determinations (black dots) [31, 32, 34, 203, 226], and future measurements (purple dots) [184, 227, 228]. The orange dashed and the cyan solid points come from our analysis of the PREX-II data (see Fig. 4.4). The vertical arrows indicate the momentum transfer for APV(Pb), PREX-II and CREX, while the green dashed curve represents the modified running of $\sin^2\theta_W$ in a scenario involving a new mediator [3]. The gray data shows the Q_{weak} result [33], while the magenta one is our combined analysis of Q_{weak} and CREX.

To further emphasise this, in Fig. 4.7 we re-propose the same figure shown in Fig. 4.4, but with the new result from the combined Q_{weak} and CREX analysis (shown by the magenta data point). In the figure, we display in gray the result

from Q_{weak} for comparison: it is possible to see that our combined analysis gives a data point that has comparable precision to the standard Q_{weak} analysis. We associate to the data point a horizontal uncertainty to account for the different energy scales between Q_{weak} and CREX. From the results, we can see that the possibility of a scale dependent modification for the running of the weak mixing angle is compatible with our re-analysis of PREX-II and CREX, so that the weak mixing angle could alleviate the tension in between the PREX neutron skin measurement and the theoretical predictions for lead-208, without spoiling the excellent agreement of the calcium neutron skin from CREX with the theoretical estimates.

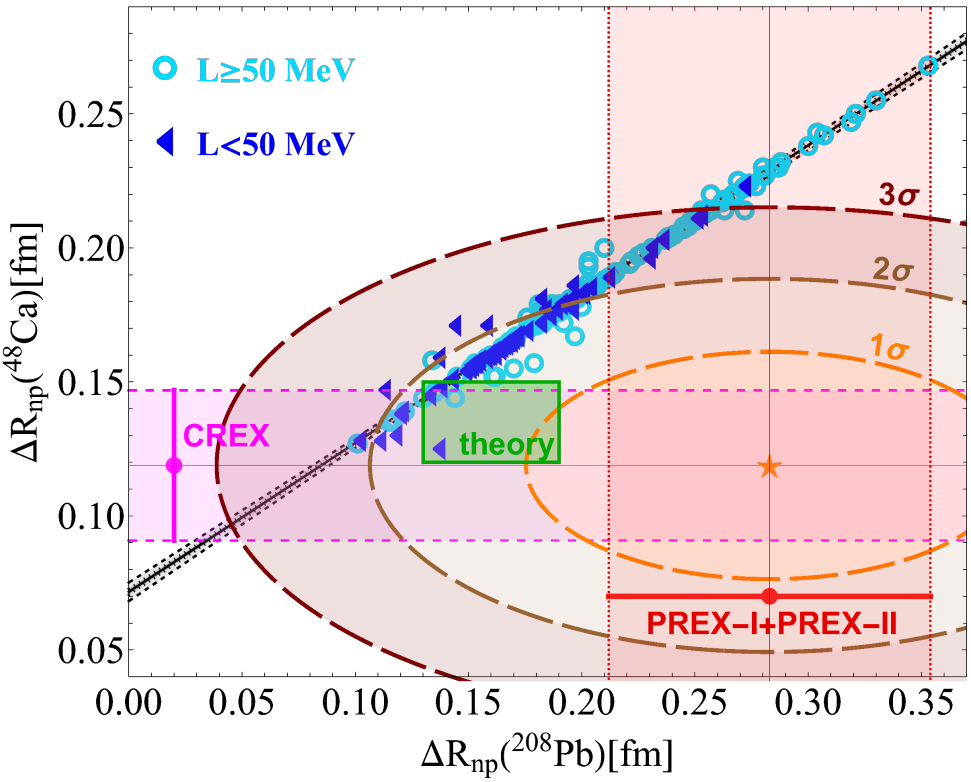

Figure 4.8: Collection of neutron skins of $^{48}\mathrm{Ca}$ and $^{208}\mathrm{Pb}$ from 206 equation of states calculations [232] divided into two groups based on their prediction of the slope parameter L, compared with the allowed region by the PREX+CREX fit at different confidence levels. The black lines show a linear fit of the predictions. The red (magenta) data point shows the neutron skin obtained by the analysis of PREX (CREX), while the green box indicates the theoretical predictions considered in the previous discussions [4].

A different way to compare the PREX and CREX results is to show their determinations against a collection of model predictions applied to both nuclei. In particular, we considered the 206 equation of states calculations reported in Table 1 of Ref. [232], in order to produce the results shown in Fig. 4.8. The blue and light-blue points indicate the predictions in the $\Delta R_{\text{np}}(^{48}\mathrm{Ca})$ vs $\Delta R_{\text{np}}(^{208}\mathrm{Pb})$ plane from the aforementioned calculations, distinguished in two groups depending on the value they predict for the slope parameter L. The predictions show a correlation between them, so that we performed a linear fit, whose result is shown by

the black lines, together with its uncertainties. The magenta point indicates the CREX result [158], the red on the combined PREX-I + PREX-II result [154], while the orange/light-brown/brown shaded regions indicate the 1-2-3σ C.L. contours obtained by the fit of the latter measurement obtained by the chi-square function

$$\chi^2 = \left(\frac{\Delta R_{\rm np}(^{208}{\rm Pb}) - \Delta R_{\rm np}^{\rm PREX}}{\sigma_{\rm PREX}}\right) + \left(\frac{\Delta R_{\rm np}(^{48}{\rm Ca}) - \Delta R_{\rm np}^{\rm CREX}}{\sigma_{\rm CREX}}\right). \tag{4.11}$$

The green box instead indicates the predictions from the theory considered as reference values in the PREX and CREX analysis.
In general, we can see that none of the light-blue and blue points falls within the orange 1σ contour, while a part of them falls in the 2σ region. However, the combined fit does not provide a preference on L. At the same time, a corner of the green box falls within the 1σ region, showing that in general, even if the two measurements seem to give different indications for the behaviour of neutron rich matter, they are still in relative agreement with each other.

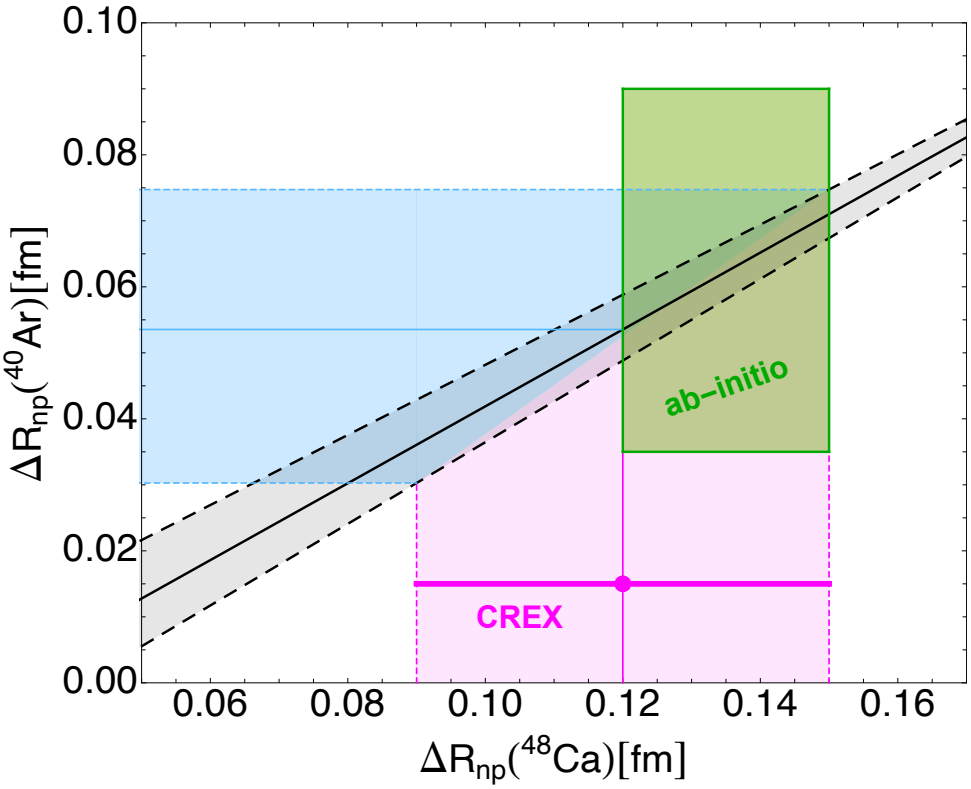

Figure 4.9: Correlation between the neutron skin of argon-40 and calcium-40 obtained by extending the correlation found in Ref. [223]. The magenta point shows the CREX result [158], while the green box indicates the predictions from *ab-initio* calculations [231, 233].

A consequence of the CREX measurement of the calcium-48 neutron skin is that it can provide indications on the nuclear neutron distribution of argon-40. Similar to what we have discussed already in many occasions, the possible correlation between model predictions of the neutron skin of two different nuclear systems

from different nuclear models can allow one to translate a measurement of one neutron skin in an indication on the neutron skin of the other nucleus. In this sense, in Ref. [223], it was shown that by considering some nuclear energy density functional models, one can obtain a correlation function between the neutron skin of argon-40 and calcium-48, such that

$$\Delta R_{\rm np}(^{40}{\rm Ar}) = 0.572 \times \Delta R_{\rm np}(^{48}{\rm Ca}) - 0.015\,{\rm fm}\,, \tag{4.12}$$

with an uncertainty attached to it. We show such correlation in Fig. 4.9 by the black line and gray shaded region, by assuming that the correlation remains linear toward smaller skin values with respect to the ones considered in Ref. [223]. It must be remarked that this is a qualitative study, to first approach the extraction of the argon-40 neutron skin from the CREX measurement (shown with the magenta data point).
By relying on such correlation, the CREX measurement of $^{48}{\rm Ca}$ neutron skin suggests a skin value in the range of (azure region in Fig. 4.9)

$$\Delta R_{\rm np}(^{40}{\rm Ar}) \approx [0.030, 0.075]\,{\rm fm}\,. \tag{4.13}$$

It is interesting to notice that this estimate is in good agreement with the *ab-initio* calculations on argon-40 [233], which indicate $\Delta R_{\rm np}^{\textit{ab-initio}}(^{40}{\rm Ar}) = [0.035, 0.090]\,{\rm fm}$, as well as the consistency of the CREX measurements with the calculations on calcium-48 [231]. The *ab-initio* predictions are shown through the green box in the figure.
Moreover, let us notice that if confirmed, this would indicate a smaller value of the neutron skin of argon-40 with respect to the one considered in our CEνNS calculation for COHERENT and with respect to the R_n value reported in Tab. 2.2, which comes from nuclear shell model calculations and leads to $\Delta R_{\rm np}(^{40}{\rm Ar}) \sim 0.10\,{\rm fm}$ [60].

4.3 The case of carbon 12: measurements at MESA

Regarding the physics case of Carbon-12 future measurements at MESA, we have repeated the sensitivity study performed in Ref. [186], and extended it in order to explore some possible different scenarios. In the latter work, the authors carried out a feasibility study of the simultaneous extraction of the weak mixing angle and the $^{12}{\rm C}$ neutron skin with a competitive precision by combining two measurements, one performed at forward angle and one at backward.
In the work, the parity violating asymmetry in the plane-wave Born approximation was defined as

$$A_{\rm pv} = -\frac{G_F Q^2}{4\sqrt{2}\pi\alpha}\frac{Q_W}{Z}(1+\Delta)\,, \tag{4.14}$$

where the nuclear weak charge for carbon-12 is $Q_W^{^{12}{\rm C}} \approx -24\sin^2\theta_W$ ($Q_W^{^{12}{\rm C}} = -5.499$ accounting for radiative corrections) and the Δ term incorporates the nuclear structure dependence, and is defined as

$$\Delta \equiv F_{\rm wk}(Q^2)/F_{\rm ch}(Q^2) - 1\,. \tag{4.15}$$

For $Q^2 \to 0$, it is obvious that $\Delta \to 0$, so that we can define the remaining term as A_0, or equivalently the value of the asymmetry in the point-like nucleus limit. The A_0 term depends on the momentum transfer Q^2 and is evaluated by fixing the weak mixing angle to its SM predicted value. It is convenient to define also another parameter, called λ, which is defined as the weak skin normalized to the charge radius, namely

$$\lambda = \frac{R_{\rm wk} - R_{\rm ch}}{R_{\rm ch}} \,. \tag{4.16}$$

Since the charge radius of carbon-12 is well known, the λ parameter effectively represents the weak radius, or the weak skin, $R_{\rm wskin} = R_{\rm wk} - R_{\rm ch}$.
In Ref. [186], the authors discussed the fact that a particular form of the weak density distribution introduces a model dependence in the calculation. So that, the usual choice of parameterizing the weak density distribution by using a symmetrized 2pF distribution (SF) could lead to a model dependence in the final extraction of the neutron skin and the weak mixing angle. In order to avoid this, they proposed a different method, that aims to disentangle the effect of the weak skin from higher order effects. The ^{12}C nucleus is special, in fact, it is symmetric ($N = Z$). For this reason, its weak density distribution is expected to be very similar to the charge one. In this sense, the small differences between the two can be quantified through the definition of a "weak skin" distribution,

$$\rho_{\rm wskin}(r) \equiv \rho_{\rm wk}(r) - \rho_{\rm ch}(r) \,. \tag{4.17}$$

Let us note that the weak skin density is normalized to zero, and that its second moment can be fixed to

$$\rho_{\rm wskin}(r) r^2 d^3 r = R^2_{\rm wk} - R^2_{\rm ch} = 2\lambda R^2_{\rm ch} + \mathcal{O}(\lambda^2) \,, \tag{4.18}$$

which allows one to define the weak skin density in terms of a ζ parameter representative of the introduced model dependence,

$$\rho_{\rm wskin}(r) = \lambda \overline{\rho}(r;\zeta) \,. \tag{4.19}$$

This particular parametrization for the weak skin density is advantageous because it allows the explicit separation of the dependence on the λ parameter from the effects of the higher moments of the weak charge density, where the model dependence lies, encapsulated in a set of model parameters ζ. In fact, if we choose the SF parametrization for the weak density, this translates in

$$\rho_{\rm wskin}(r) = (\lambda/\lambda_{\rm SF})(\rho_{\rm SF}(r,c,a) - \rho_{\rm ch}(r)) \,, \tag{4.20}$$

where $\lambda_{\rm SF} = \lambda_{\rm SF}(c_{\rm mod}, a_{\rm mod}) = R_{\rm SF}(c_{\rm mod}, a_{\rm mod})/R_{\rm ch} - 1$. So, by considering some nuclear models, which come with certain SF parameters $c_{\rm mod}$ and $a_{\rm mod}$, one obtains a certain $\lambda^{\rm mod}_{\rm SF}$.
The choice of this modelization translates into a redefinition of the Δ term in Eq. 4.15 which assumes the following form [186]

$$\begin{aligned} \Delta &= -\frac{\lambda}{3} Q^2 R^2_{\rm ch} + \Big(\frac{F_{\rm wk}}{F_{\rm ch}} - 1 + \frac{\lambda}{3} Q^2 R^2_{\rm ch} \Big) = \\ &= -\frac{\lambda}{3} Q^2 R^2_{\rm ch} + \Big[\frac{\lambda}{\lambda_{\rm SF}} \Big(\frac{F^{\rm SF}_{\rm wk}}{F_{\rm ch}} - 1 \Big) + \frac{\lambda}{3} Q^2 R^2_{\rm ch} \Big] \,, \end{aligned} \tag{4.21}$$

where now the weak form factor is described through a SF parametrization. Thanks to this method, the nuclear model predictions [142, 187, 188], can be used to set the range of values to be explored to quantify the model uncertainty in Δ, rather than to predict the weak density distribution.

Model	c [fm]	a [fm]	$R_{\rm wk}^{\rm SF}$ [fm]	$\lambda_{\rm SF}$ [%]
RMF016	2.06065	0.49389	2.43274	-1.48
RMF022	2.06849	0.49445	2.43830	-1.26
RMF028	2.07585	0.49544	2.44482	-0.99
RMF032	2.06421	0.49433	2.43578	-1.36
SMC12	2.22693	0.47318	2.46358	-0.23

Table 4.1: Table reporting the c and a parameters for each of the models considered, together with the corresponding weak radius and $\lambda_{\rm SF}$ value.

The five models considered in the work are all built considering the charge radii and binding energies of a variety of nuclei including ^{12}C. They all predict $|\lambda_{\rm SF}| \leq 2\%$ with a central value of $\lambda_0 = -0.90\%$ [186]. Indeed, in Tab. 4.1 we collect the c and a parameters of each model, together with the corresponding weak radius and the value of the $\lambda_{\rm SF}$ parameter.
We can notice that the $\lambda_{\rm SF}$ values are slightly different from the ones reported in Table I of the supplemental material of Ref. [186], due to a different choice of the reference value for the charge radius of ^{12}C, since we have chosen to consider the one obtained by fitting the data using a SOG distribution reported in Ref. [136], which results in a charge radius of $R_{\rm ch}^{\rm SOG}(^{12}{\rm C}) = 2.469(6)$ fm. However, the final results are practically unaffected by such choice.

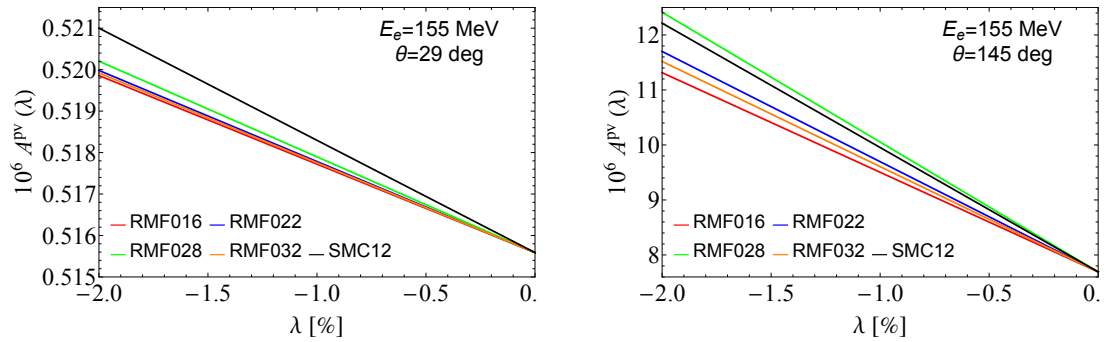

Figure 4.10: Asymmetry predictions from the input of the five nuclear models considered as a function of the λ parameter. The left panel corresponds to the forward kinematics ($\theta = 29°$ and $E_e = 155\,{\rm MeV}$), while the right one to the backward kinematic ($\theta = 145°$ and $E_e = 155\,{\rm MeV}$)

In Fig. 4.10, we show the predicted asymmetries as a function of the λ parameters obtained from the DWBA calculations of the parity violating asymmetry obtained by fixing the charge density to the SOG one in the calculation and by defining the weak density as

$$\rho_{\rm wk}(\lambda, r) = \rho_{\rm ch}^{\rm SOG}(r) + \rho_{\rm wskin}(\lambda, r)\,, \tag{4.22}$$

where we made the dependence on the λ parameter explicit and where the ρ_{wskin} is the density defined in Eq. 4.20.
The different colors indicate each different nuclear model used inside of the weak skin density calculation. The left plot corresponds to the forward setup expected at MESA, so $\theta = 29°$ and $E_e = 155\,\text{MeV}$, while the right one to the backward scenario, so $\theta = 145°$ and $E_e = 155\,\text{MeV}$. It is interesting to notice that the asymmetry is much larger at backward angle, as already shown in Fig. 3.16.
The spread between the models represents the model uncertainty, so that the actual prediction for the asymmetry is obtained as the bisector of the predictions, and the width associated with it is such that we go from the lowest among the predictions up to the highest one. This can be seen in Fig. 4.11, where we represent the previous results but in the form of the central line with the light blue band representing the uncertainty.

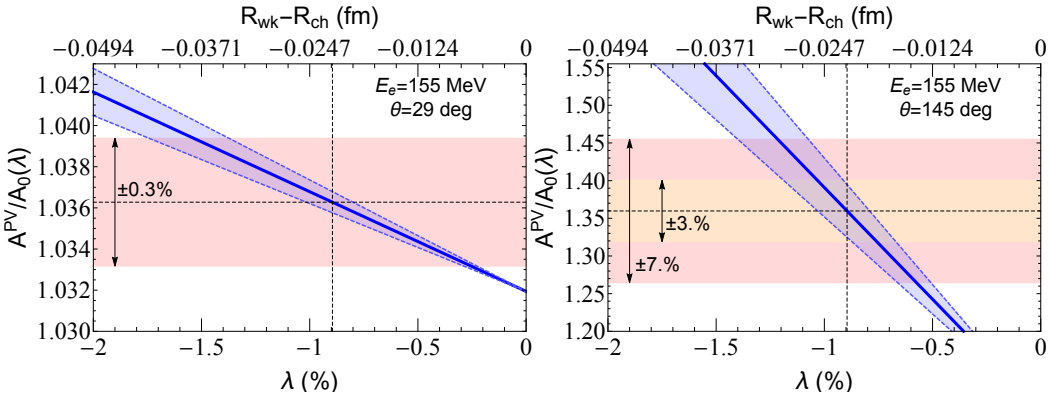

Figure 4.11: Asymmetry normalized to the proper value of A_0 as a function of the λ parameter (and neutron skin) for the forward (left) and backward (right) kinematics. The blue band indicates the prediction from the models with the attached uncertainty. The pink and orange bands indicate the expected precision goal on the asymmetry (indicated also with the vertical arrows) while the black dashed lines indicate the reference value for the weak skin and for the asymmetry.

In Fig. 4.11 we decided to normalize the asymmetry to the A_0 value calculated at the proper kinematic conditions, so that in some sense we isolate the contribution due to the nuclear structure. Indeed, one could expect that for $\lambda = 0$, which means $R_{\text{wk}} = R_{\text{ch}}$, the displayed ratio should go to unity. However, it is clear from the figures that the ratio goes to a number higher than 1. This is attributable to the effect of Coulomb distortions. In fact, the ratio would go to unity at tree-level (PWBA), but not in the DWBA. Moreover, the horizontal pink and orange bands show the precision goal of the measurement, namely $\sim 0.3\%$ on the forward asymmetry, while something between $\sim 3 - 10\%$ on the backward one. With the black dashed lines, we indicate the reference value for λ, namely $\lambda_0 = -0.90\%$, which corresponds to a weak skin around $R_{\text{wskin}} \simeq -0.022\,\text{fm}$. Indeed, by looking at the horizontal scale of the figure, it is clear that the models indicated a negative value of λ, which means a negative value for the weak skin, which implies that the charge radius is expected to be larger than the weak radius. It is also clear that the skin is expected to be very tiny in such a special system as ^{12}C.

The important result shown in Fig. 4.11 is that the slope of the blue bands gives us an idea of the sensitivity to the weak skin. In fact, the two parameters, in which we are interested, are the weak mixing angle, whose modification by entering the nuclear weak charge would produce a vertical shift of the asymmetry value, and the weak skin, which instead produces a diagonal shift in the plane. The steeper the blue band is, the more sensitive to the weak skin the measurement is. By qualitatively comparing the precision goal (pink/orange bands) with the theoretical prediction, we can understand that the forward measurement should be rather independent of the weak skin, but sensitive to the weak mixing angle. Instead, the backward measurement shows an interesting sensitivity to the weak skin, even if the precision is lower than the one for the forward angle. These results already suggest that the combination of a backward and forward measurement could allow one to disentangle the weak mixing angle and the weak skin measurements, allowing for a simultaneous extraction of the two observable keeping interesting precision.
In order to perform a sensitivity study, we can describe the asymmetry prediction (blue band) by the following formula [186]

$$A^{\mathrm{pv}} = -\frac{G_F Q^2}{4\sqrt{2}\pi\alpha}\frac{Q_W}{Z}\Big(1 + p_0 + (p_1 + p_2\zeta)\lambda\Big)\,, \tag{4.23}$$

where the ζ parameter is introduced in order to account for the width of the blue band. In fact, it is defined in such a way that $\zeta = \zeta_0 = 0$ corresponds to the central prediction, while $\zeta = \pm 1$ corresponds to the upper and lower limits of the error band. The other coefficients, p_0, p_1 and p_2 can be obtained by the calculation of the asymmetry considering the Coulomb distortion effects.
Indeed, it can be easily understood that the p_0 coefficient which quantifies the intrinsic Coulomb distortion effect (is obtained by fixing $\lambda = 0$). Instead, p_1 can be extracted from the central prediction ($\zeta = 0$), while p_2 from either the upper or lower bound, since $\zeta = \pm 1$ for them. In particular, the results of our calculations are collected in Tab. 4.2 for both kinematic scenarios. Also in this case, the results are slightly different with respect to the ones reported in Table II of the supplemental material of Ref. [186], but lead to very similar conclusions.

Coefficient	$\theta = 29^\circ$	$\theta = 145^\circ$
p_0	0.03193	0.09422
p_1	-0.48444	-29.6647
p_2	-0.06825	-3.91652

Table 4.2: Table reporting the results for the p_0, p_1 and p_2 coefficients for both the backward and forward measurements.

We perform a χ^2 fit for both the forward (A_f^{pv}) and backward (A_b^{pv}) asymmetries using the definition in Eq. 4.23, with respect to the three free parameters, that now are the weak mixing angle, $\sin^2\theta_W$, λ and ζ. The χ^2 function is defined as [186]

$$\chi^2(\sin^2\theta_W, \lambda, \zeta) = \sum_{i=f,b}\Big(\frac{A_i^{\mathrm{exp}} - A_i^{\mathrm{pv}}(\sin^2\theta_W, \lambda, \zeta)}{\epsilon_i}\Big)^2 + \Big(\frac{\zeta - \zeta_0}{\delta\zeta}\Big)^2\,, \tag{4.24}$$

where $i = f, b$ refers to the forward and backward kinematics, respectively, and for the "experimental" value of the asymmetry we considered the value of the asymmetry for $\lambda = \lambda_0$ obtained from the central blue curves in Fig. 4.11.

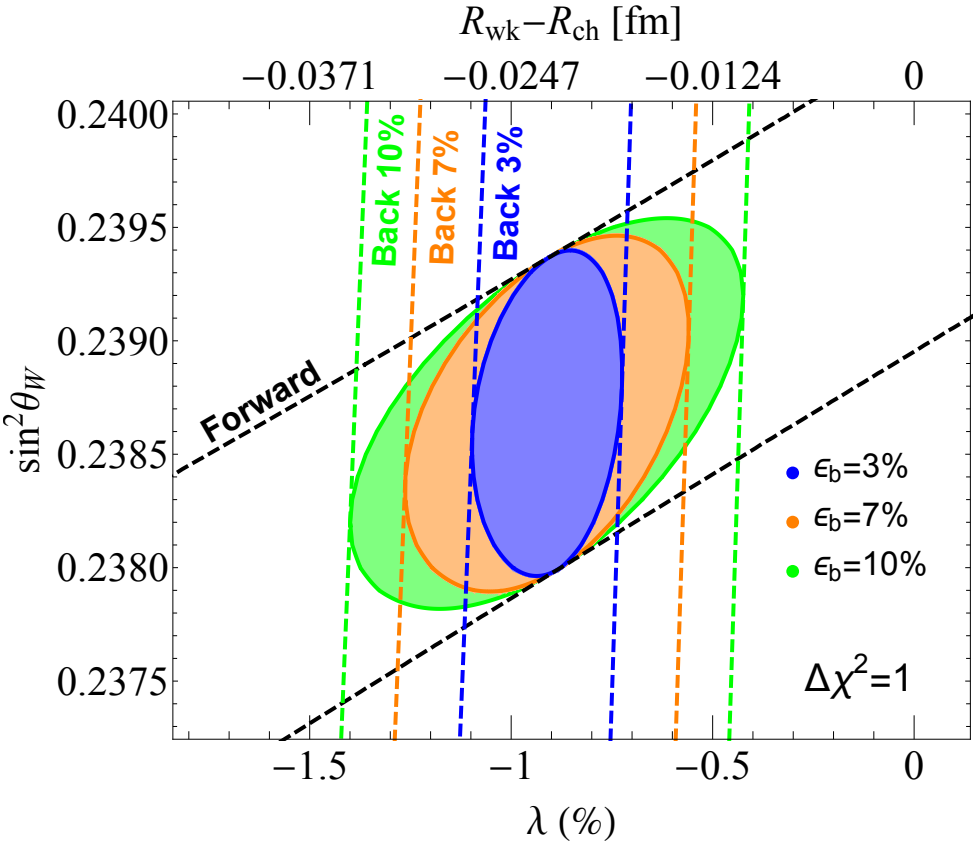

Figure 4.12: $\Delta\chi^2 = 1$ contours from the combined fit of the forward and backward measurements in the plane $\sin^2\theta_W$ vs λ from the χ^2 function defined in Eq. 4.24. The different colors correspond to the different precision for the backward measurement, $\epsilon_b = 3,\ 7,\ 10\,\%$, while for the forward we considered always a precision of 0.3%. The dashed lines show the fit of the only forward (black) or backward (blue, orange, green) asymmetries.

In Eq. 4.24, ϵ_i is the expected precision on the asymmetry, and in particular, for ϵ_f we consider the 0.3%, while for the backward asymmetry we will consider three different scenarios, $\epsilon_b = 3\%,\ 7\%\ 10\%$. Instead, we consider $\delta\zeta = 1$, as we have defined that variation as the range to be considered for estimating the model uncertainty. The results of the combined forward and backward analysis are shown by the closed contours in Fig. 4.12 and the obtained precision on the extraction of the weak mixing angle and λ are reported in Table 4.3.
We can notice that the precision on the weak mixing angle is roughly constant for the different ϵ_b considered, and it is practically identical to ϵ_f. Indeed, the forward asymmetry alone depends poorly on the skin parameter. In fact, the fit of the forward measurement only (dashed black line) results in a non-very-steep diagonal band, so that, it can not alone provide a completely clean weak mixing angle measurement (there is some dependence on the skin). Instead, the back-

ward measurement depends strongly on the skin parameter, resulting in the three practically vertical dashed lines (the width depends on the backward precision). In conclusion, the precision on the forward measurement determines the precision at which the experiment will extract the weak mixing angle, while the precision on λ depends on ϵ_b. In fact, by considering smaller ϵ_b values, the precision on λ improves significantly.

ϵ_f [%]	ϵ_b [%]	$\Delta \sin^2\theta_W / \sin^2\theta_W$ [%]	$\Delta\lambda$ [%]
0.3	3	$\pm$ 0.31	$\pm$ 0.16-0.20
	7	$\pm$ 0.34	$\pm$ 0.33-0.37
	10	$\pm$ 0.37	$\pm$ 0.46-0.51

Table 4.3: Summary of the results from the sensitivity study on the weak mixing angle and on the skin parameter λ for the three different scenarios for the precision on the backward asymmetry, ϵ_b.

In order to extend the study carried out in Ref. [186], we consider also the scenario of a backward measurement performed in the initial working period of the MESA accelerator, in which the electrons could be travelling with lower energy, namely considering only one circulation, at $E_e = 55\,\mathrm{MeV}$. Indeed, the momentum transfer for a backward measurement with $E_e = 55\,\mathrm{MeV}$ is very similar to the one for the forward measurement with $E_e = 155\,\mathrm{MeV}$, namely $Q_f(E_e = 155\,\mathrm{MeV}) \simeq 78$ MeV and $Q_b(E_e = 55\,\mathrm{MeV}) \simeq 104$ MeV.

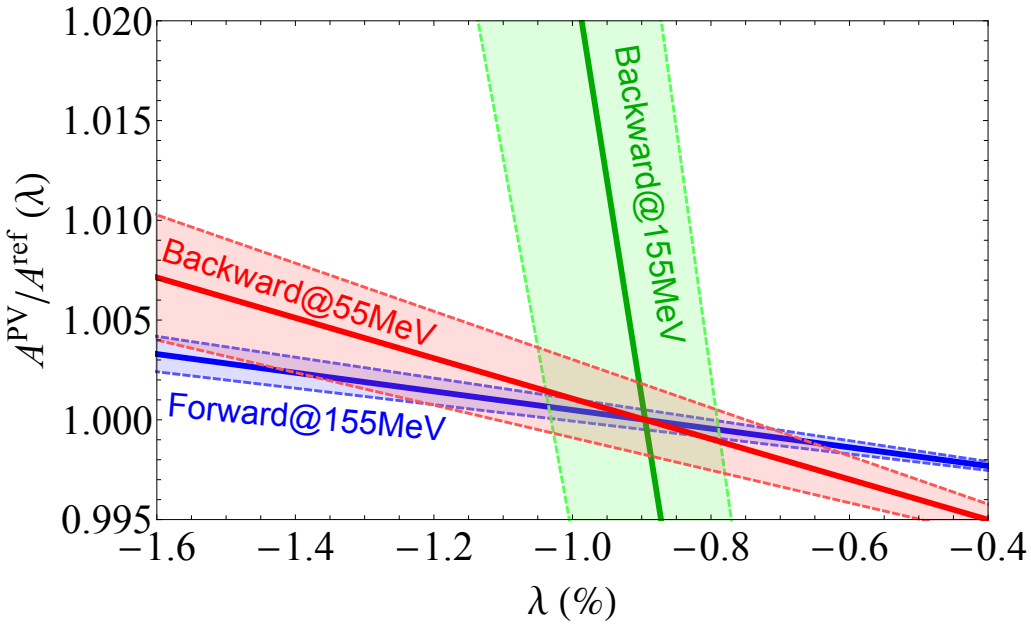

Figure 4.13: Asymmetry normalized to the reference value $A^{\mathrm{ref}} = A^{\mathrm{pv}}(\lambda_0)$ at the proper kinematic as a function of the λ parameter for three different kinematics, namely the forward measurement with $E_e = 155\,\mathrm{MeV}$, the backward measurement with $E_e = 155\,\mathrm{MeV}$ and a hypothetical backward measurement with lower electron energy $E_e = 55\,\mathrm{MeV}$.

In this sense, it is intriguing to study the feasibility of a combined backward measurement with $E_e = 55\,\mathrm{MeV}$ with a forward measurement with $E_e = 155\,\mathrm{MeV}$, since the latter two would be performed at approximately the same momentum transfer.
In Fig. 4.13, we show the prediction of the asymmetry with the corresponding band width for the three different kinematic scenarios normalized to the reference value $A^{\mathrm{ref}} = A^{\mathrm{pv}}(\lambda_0)$ at the corresponding kinematic. Such normalization was chosen in order to display the asymmetry on the same scale. In fact, the three predictions cross for $\lambda = \lambda_0$ at $A^{\mathrm{pv}}/A^{\mathrm{ref}} = 1$.
This figure clearly shows that the forward measurement with $E_e = 155\,\mathrm{MeV}$ is rather horizontal, and thus, poorly sensitive to the skin, while the backward one, with the same beam energy, is rather steep. It is interesting to notice that the backward measurement with a lower beam energy does not present the same steepness as the one at higher energies. Instead, it is rather flat and quite similar to the forward measurement at $E_e = 155\,\mathrm{MeV}$. This naively shows that the sensitivity to the skin parameter is driven by the momentum transfer instead of the energy or the scattering angle.

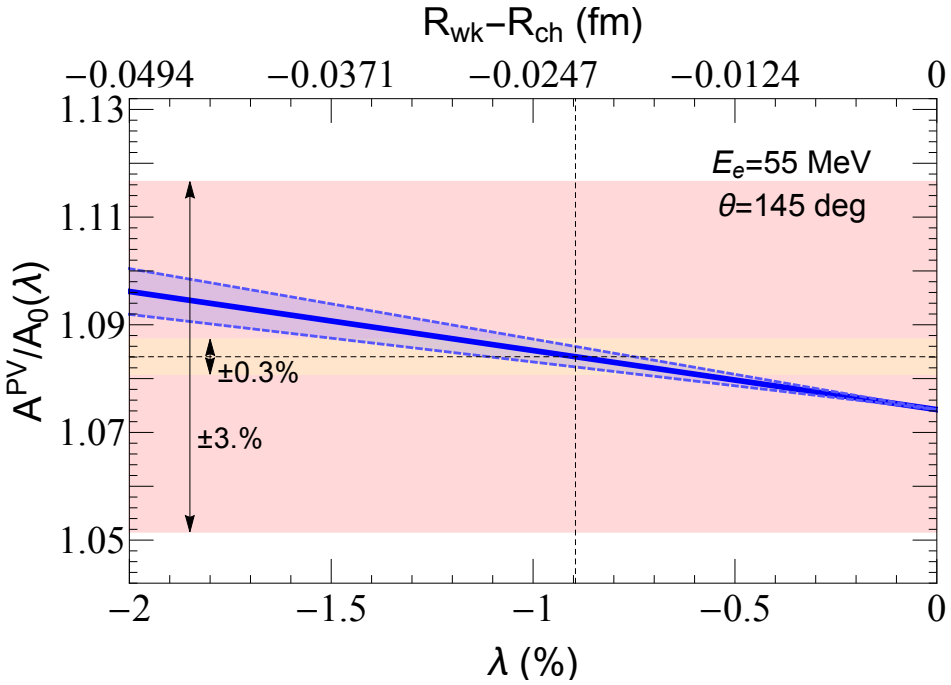

Figure 4.14: Asymmetry normalized to the proper value of A_0 as a function of the λ parameter (and neutron skin) for the backward measurement with $E_e = 55\,\mathrm{MeV}$. The blue band indicates the prediction from the models with the attached uncertainty. The orange and pink bands indicate possible precision on the asymmetry (indicated also with the vertical arrows), namely 0.3% and 3%, while the black dashed lines indicate the reference value for the weak skin and for the asymmetry.

To make it even more evident that the backward measurement with $E_e = 55\,\mathrm{MeV}$ is poorly sensitive to the weak skin, in Fig. 4.14, we show the asymmetry normalized to A_0 in analogy to what we presented in Fig. 4.11 for $E_e = 155\,\mathrm{MeV}$. The

horizontal bands show some possible precision (ϵ_b^{55}) scenarios, namely the orange one to $\epsilon_b^{55} = 0.3\%$ while the pink one to $\epsilon_b^{55} = 3\%$. Of course, to reach a higher precision level, the data taking should last longer, so that the $\epsilon_b^{55} = 0.3\%$ scenario results are highly optimistic.
From the figure, it is clear that the behaviour of such measurement is similar to that of the nominal forward measurement, although the reachable precision is expected to be poorer.

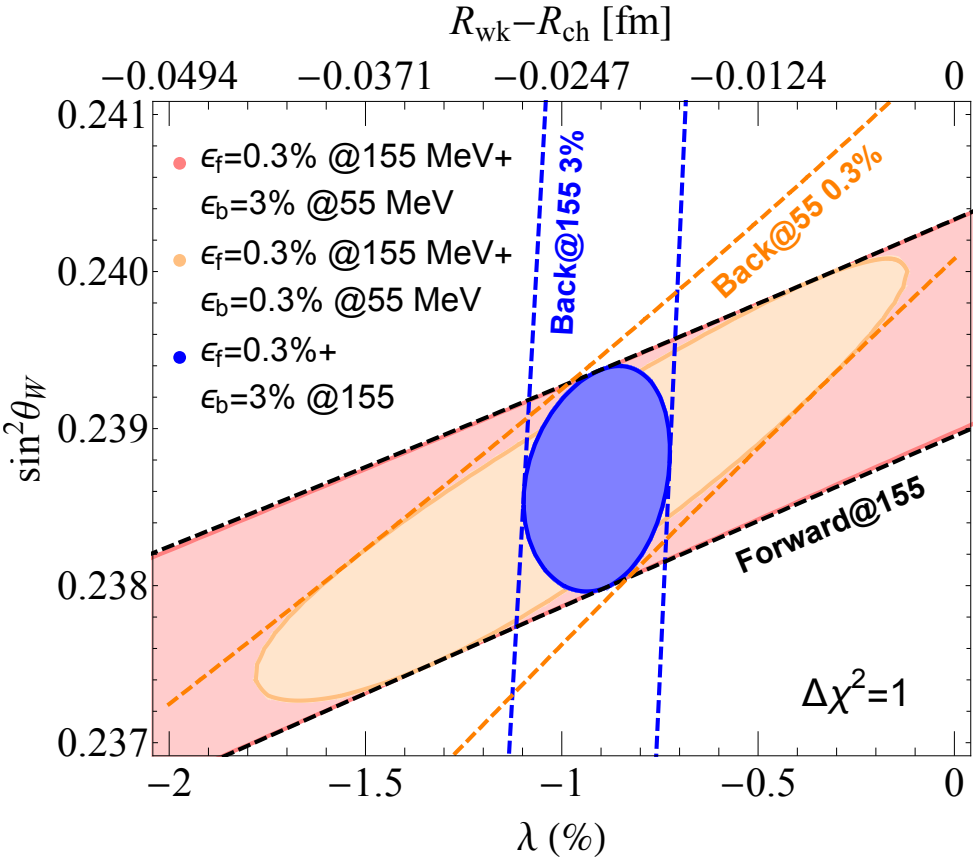

Figure 4.15: Favored contours for $\Delta\chi^2 = 1$ obtained from the combined forward+backward measurements considering different combinations. The light red band is obtained by the nominal forward combined with the backward at $E_e = 55\,\mathrm{MeV}$ measurement with $\epsilon_b^{55} = 3\%$, while the orange one with $\epsilon_b^{55} = 0.3\%$. The blue ellipse instead is obtained by combining the nominal backward measurement with $\epsilon_b^{155} = 3\%$. The orange dashed lines show the fit of the backward measurement at $E_e = 55\,\mathrm{MeV}$ with $\epsilon_b^{55} = 0.3\%$ alone, the blue ones correspond to the backward measurement at $E_e = 155\,\mathrm{MeV}$ with $\epsilon_b^{55} = 3\%$ alone, while the black dashed lines the nominal forward fit alone.

At this point, we performed two χ^2 analysis, one by fitting the backward measurement with $E_e = 55\,\mathrm{MeV}$ only, namely by using the following function

$$\chi^2_{55}(\sin^2\theta_W, \lambda, \zeta) = \left(\frac{A_b^{\mathrm{exp},55} - A_b^{\mathrm{pv},55}(\sin^2\theta_W, \lambda, \zeta)}{\epsilon_b^{55}}\right)^2 + \left(\frac{\zeta - \zeta_0}{\delta\zeta}\right)^2, \qquad (4.25)$$

and one by combining it with the forward measurement at $E_e = 155\,\mathrm{MeV}$, using the chi-square function

$$\chi^2_{55+155}(\sin^2\theta_W, \lambda, \zeta) = \Big(\frac{A_b^{\mathrm{exp},55} - A_b^{\mathrm{pv},55}(\sin^2\theta_W, \lambda, \zeta)}{\epsilon_b^{55}}\Big)^2 + \quad (4.26)$$
$$+ \Big(\frac{A_f^{\mathrm{exp},155} - A_f^{\mathrm{pv},155}(\sin^2\theta_W, \lambda, \zeta)}{\epsilon_f^{155}}\Big)^2 + \Big(\frac{\zeta - \zeta_0}{\delta\zeta}\Big)^2,$$

where we have introduced the superscript "155" to indicate the nominal forward scenario, in order to avoid any confusion.
The results of the two analyses are shown in Fig. 4.15, where we show the $E_e = 55\,\mathrm{MeV}$ backward fit only, for $\epsilon_b^{55} = 0.3\%$, with the dashed orange lines, while the black ones correspond to the nominal forward measurement and the blue ones to the nominal backward with $\epsilon_b^{155} = 3\%$. It is evident that the measurement at lower energy alone would not allow one to simultaneously extract the weak mixing angle and the skin parameter λ, as the fit results in almost horizontal degenerate bands.
By combining the latter measurement with the nominal forward one, it is possible to break the degenerate band, but dependently on the precision that can be reached on the backward asymmetry at $E_e = 55\,\mathrm{MeV}$. Indeed, the red shaded degenerate band corresponds to the combination of the forward measurement with the backward at $E_e = 55\,\mathrm{MeV}$ with $\epsilon_b^{55} = 3\%$, while the orange one with $\epsilon_b^{55} = 0.3\%$. So that, $\epsilon_b^{55} = 3\%$ does not allow one to solve the degeneracy. If one achieves a better precision, namely $\epsilon_b^{55} = 0.3\%$, it is possible to find a closed contour, which however is significantly larger than the ellipse for the nominal measurement, resulting in a less precise extraction of the two parameters. To give a clear comparison, in the figure, we show with the blue ellipse, the result previously discussed from the combined nominal backward and forward measurement, with $\epsilon_b^{155} = 3\%$, which is much smaller than the orange one, obtained with a factor 10 better precision on the backward asymmetry. The numerical comparison can be found in Tab. 4.4, where we compare the precision on the two observable from the forward+backward analysis, considering the two backward measurements at different beam energies, and $\epsilon_b^{155} = 3\%$ and $\epsilon_b^{55} = 0.3\%$.

ϵ_b^{155} [%]	$\Delta\sin^2\theta_W/\sin^2\theta_W$ [%]	$\Delta\lambda$ [%]
3	$\pm$ 0.31	$\pm$ 0.16-0.20
ϵ_b^{55} [%]	$\Delta\sin^2\theta_W/\sin^2\theta_W$ [%]	$\Delta\lambda$ [%]
0.3	$\pm$ 0.60	$\pm$ 0.76-0.90

Table 4.4: Comparison between the combined forward+backward analysis with the backward measurements at different beam energies.

This said, it is clear that a backward measurement with $E_e = 55\,\mathrm{MeV}$ would not help in better measuring the two parameters, especially the skin parameter, but it could provide an honest measurement of the weak mixing angle, if one restricts the skin parameter in the suggested range. Moreover, as we have shown, the precision necessary on the backward asymmetry is about a factor of 10 better than

the best case scenario foreseen in the nominal setup. Thus, it would require a significant effort in data taking, without significantly improving the physics reach. Nonetheless, it is fundamental to show the precision level at which the weak mixing angle can be measured in the different scenarios considered in this study, compared to the currently available measurements and to the results previously discussed from the PREX and CREX analysis. Therefore, in Fig. 4.16, we show the running of the weak mixing angle with a compilation of the current status of determination as reported by the Particle Data Group in Ref. [25, 31–35], and the previous results (orange and azure data from the PREX analysis, and magenta from CREX). Indeed, the figure represents an updated version of Fig. 4.4 and Fig. 4.7.

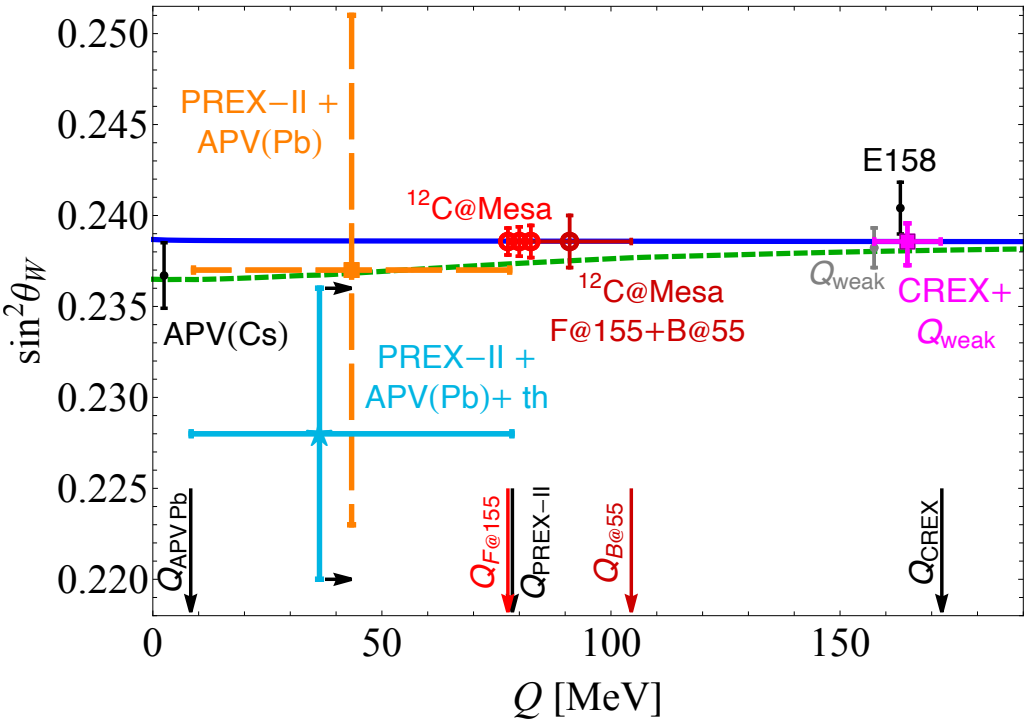

Figure 4.16: Running of the weak mixing angle with the energy scale evaluated in the RGE formalism. The black points show the currently available experimental measurements, as reported by the Particle Data Group in Ref. [25, 31–35]. The dot shows the expected precision on the weak mixing angle for the PVES measurement on Carbon-12 that will be performed at MESA.

In the figure, we show with the red circles the results from the 155 MeV run set at the forward momentum transfer (the points are shifted to the right for showing purposes), since the weak mixing angle determination is mainly driven by the forward asymmetry measurement. The three different error bands correspond to the three different scenarios, following the values in Tab. 4.3. The darker red data instead, correspond to the combined fit with the backward measurement at $E_e = 55$ MeV for $\epsilon_b^{55} = 0.3\%$ (see Tab. 4.4), and it is set to an average momentum transfer between the one of the forward measurement at $E_e = 155$ MeV and the one for the backward measurement at $E_e = 55$ MeV.

It is interesting to notice how the expected precision for the nominal setup represents a great improvement with respect to the currently available measurements. Moreover, they are at an intermediate momentum between the APV(Cs) measurement and the Q_{weak} one. It is also remarkable that the sensitivity considering the lower beam energy scenario still provides a determination of the weak mixing angle which well compares to the other available measurements, even being a factor 2 less precise than the nominal result. In fact, the precision is not very different from the one achieved in our CREX+Q_{weak} analysis (magenta point).
To conclude, such future measurements will have a crucial role in testing the new physics scenario represented by the green dashed line in the figure. The foreseen precision level will help in excluding or indicating the presence of a new mediator by testing the running in that intermediate energy range.

Chapter 5

Weak mixing angle and nuclear information from neutrino scattering

Short introduction

In this chapter, we will present the current status of weak mixing angle and nuclear neutron radius measurements from neutrino-nucleus coherent scattering. We will show the results obtained by analysing the data released by the COHERENT Collaboration and from the recent measurement of CEνNS from reactor neutrinos reported by the Dresden-II Collaboration. We will also discuss some future projections relative to the experimental program foreseen by the COHERENT Collaboration in the next years [84]. Moreover, we will present a combined analysis of COHERENT CsI data and APV(Cs) measurements to show the power of combining the two different electroweak probes. Most of the results are reported in Refs. [2, 6, 8, 234].

5.1 COHERENT LAr

The COHERENT data allow one to extract both the weak mixing angle and the nuclear neutron radius, since the cross section depends on both the nuclear weak charge and the neutron form factor (see the CEνNS cross section in Eq. 2.46). Therefore, one can decide to fix one of the two parameters to its standard prediction: the SM in the case of the weak mixing angle, while the chosen reference value for the neutron radius of argon-40 coming from nuclear shell models [60]. In this way, by using the chi-square function in Eq. 2.77 and the experimental details described in Sec. 2.4.1, one can measure the parameter of interest.
In reference to the COHERENT data with the LAr detector [53, 91, 234], and fixing the weak mixing angle to its SM value, namely $\sin^2\theta_W^{\rm SM} = 0.23857$, we fit the data using different parameterizations for the neutron form factor. Interestingly, we found that for the current precision of the argon data set the choice of the parametrization of the form factor does not produce any effect on the results, making the measurement of the neutron radius model independent. The results

of the neutron radius are shown in the left panel of Fig. 5.1, where we present the marginalized curves obtained by the fit considering the SF form factor (green dots), the Helm [88] form factor (blue dashed line) and the Klein-Nystrand [235] form factor (solid red line). The latter one is the parametrization considered by the COHERENT Collaboration.

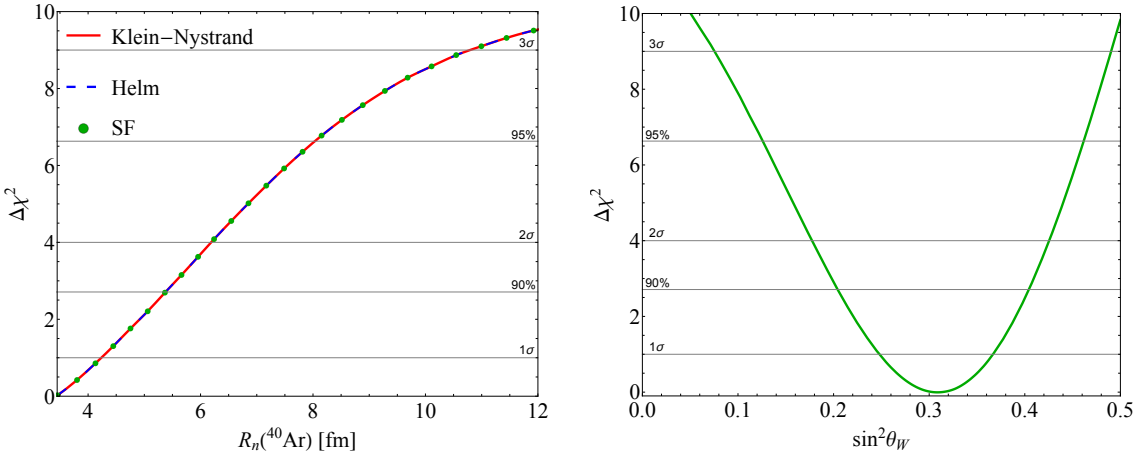

Figure 5.1: Marginalized $\Delta\chi^2$ curves for the fit of the neutron nuclear radius $R_n(^{40}\mathrm{Ar})$ (Left) and weak mixing angle (Right) [234]. The neutron radius has been obtained by considering three different parametrizations for the neutron form factor, represented by the different dashing and colors.

From the figure, it is clear that the COHERENT LAr data do not allow one to determine the neutron radius of argon-40, but only to set an upper bound, namely

$$R_n(^{40}\mathrm{Ar}) < 4.2(1\sigma), 6.2(2\sigma), 10.8(3\sigma)\,\mathrm{fm}\,, \tag{5.1}$$

however, it is expected that with the next data set and future detectors [84], the precision will be sufficient to perform a first measurement of the neutron radius of argon from CEνNS. In fact, in Ref. [84], the COHERENT Collaboration presented the foreseen precision goal for the next generation LAr TPC detector, which will be a ton-scale detector filled with 750 kg of liquid argon. In their estimate, the neutron radius will be measured with a precision of about $\sigma_{R_n}^{\mathrm{COH-Ar-750}} \approx 0.24$ fm ($\sim 4.6\%$) (see also Ref. [236]). To give a meter of comparison, in Fig. 5.2 we compare the current measurement from COHERENT LAr [234] (orange) and the expected sensitivity [84] (blue) to the CREX measurement of the neutron radius of calcium-48. Indeed, the two nuclear systems are expected to have similar dimensions, even if argon is not as rich in neutrons as calcium. We already showed that there is a correspondence between the two nuclei in Fig. 4.9, so that it is worth comparing the available measurements on both nuclei.
It is evident that even if the expected precision of the future COHERENT LAr detector is intriguing, it remains worse than the one achieved by CREX. On the contrary, the CREX experimental program does not foresee any future measurement, so, in principle, with next-to-next generation CEνNS LAr detector, there might be a chance to reach the current PVES precision.

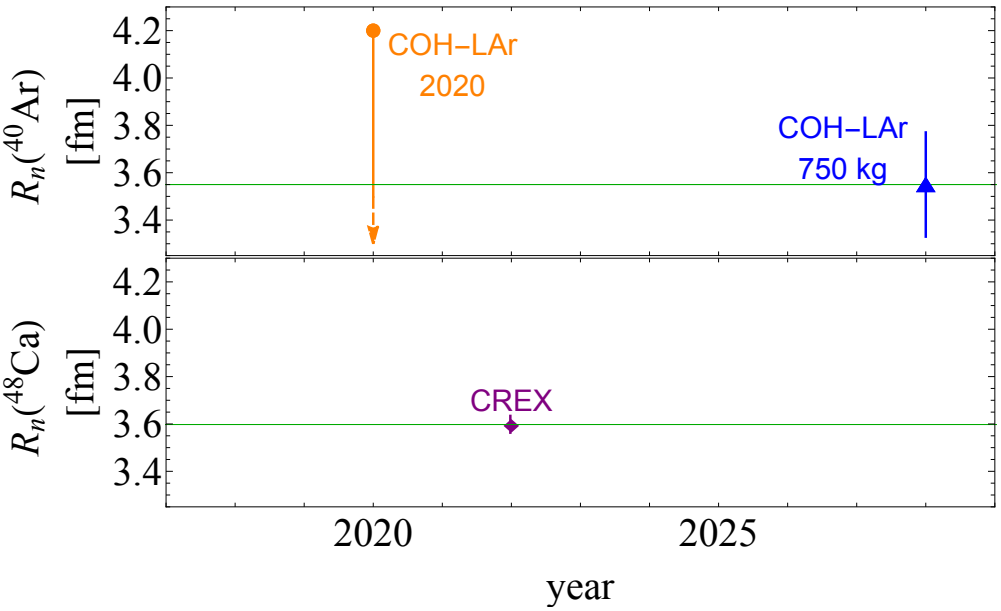

Figure 5.2: Current status and future projections for the neutron radii measurements on argon-40 and calcium-48 as a function of the year of the measurement. The orange point corresponds to our analysis of COHERENT LAr data [234], while the purple one to the CREX data [158]. The blue point shows the projected sensitivity for the future COHERENT LAr 750 kg detector [84]. The green lines correspond to the neutron radius reference value.

Instead, after fixing the neutron radius to the chosen theoretical reference value [60], $R_n^{\mathrm{ref}}(^{40}\mathrm{Ar}) = 3.55\,\mathrm{fm}$, we can perform a measurement of the weak mixing angle at the experimental energy scale, namely $Q_{\mathrm{COH\,LAr}} \approx 50 - 60$ MeV. The result of the fit is shown in the right panel of Fig. 5.1, and numerically it corresponds to

$$\sin^2\theta_W(\mathrm{Ar}) = 0.31 \pm 0.06(1\sigma)^{+0.11}_{-0.13}(2\sigma)^{+0.18}_{-0.23}(3\sigma)\,, \tag{5.2}$$

which is about 1.2σ above the SM prediction. By looking at the data in Fig. 2.29, one can understand the reason behind this small discrepancy. Indeed, the fit of the data set improves for a larger value of the weak mixing angle, which translates in a larger CEνNS cross section, with respect to the SM one, as there is a small excess of events in the first energy bins.
Furthermore, we have repeated the weak mixing angle measurement by releasing the condition on the neutron radius. Since leaving both parameters free-to-vary would not allow one to simultaneously determine them, as it would result in a degenerate region, we allowed the neutron radius to vary in between $3.45 < R_n{}^{40}(\mathrm{Ar}) < 4\,\mathrm{fm}$, ranging from the proton radius of argon-40 to a rather large skin value. We found that the weak mixing angle determination does not change under this different assumption.
In Fig. 5.3 we compare the result from the COHERENT LAr data analysis (green point) with the weak mixing angle measurement reported by the Particle Data Group [25, 203]. Since our determination has rather large uncertainties and a central value quite far away from the SM running (light blue curve), we displayed

the data point in the inset, whose x scale coincides with the one of the main plot, while the vertical scale is much larger.

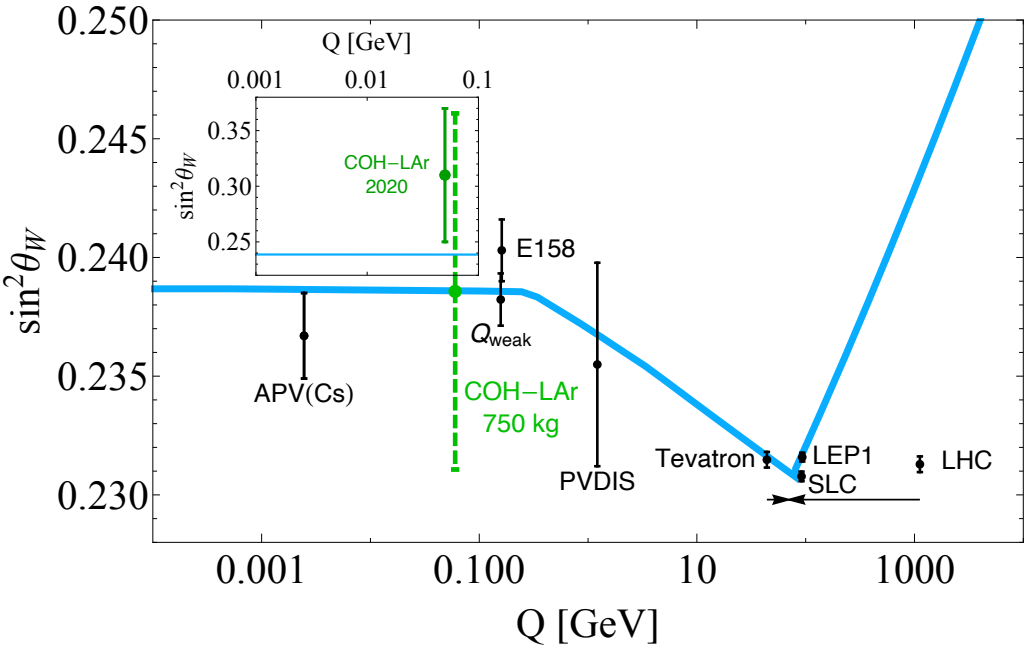

Figure 5.3: Running of $\sin^2\theta_W$ with energy scale Q. The SM prediction is shown by the light blue curve, together with experimental determinations in black [31–35, 226, 237]. The result from the analysis of COHERENT LAr data is shown by the green point in the inset. With the dashed green data point we report the expected precision foreseen for the COHERENT LAr-750 kg detector [84].

It is evident that the current precision of COHERENT data on argon does not allow one to retrieve a competitive measurement of the weak mixing angle. However, it is able to test the SM running of the weak mixing angle in the intermediate energy scale between Q_{weak} and APV(Cs), where we lack of other measurements. It will certainly represent a powerful tool to test the weak mixing angle with next generation detectors, such as the ton-scale LAr TPC foreseen by COHERENT [84]. To this purpose, in the figure we show with the dashed green data point the experimental precision on the weak mixing angle expected by the COHERENT Collaboration from the ton-scale LAr detector, as reported in Fig. 19 of Ref. [84]. The foreseen precision, $\sigma^{\text{COH}-\text{Ar}-750}_{\sin^2\theta_W} \sim 0.0075$, will be roughly a factor 10 better than the current one, and will be still rather large compared to the precision achieved using different probes. However, it will start to be competitive, so that the CEνNS measurement will be able to contribute to the overall picture.

5.2 COHERENT CsI

The situation is slightly different when dealing with COHERENT CsI data [51, 54]. The first difference is that the detector is made of a crystal of cesium and iodide, which are similar nuclei, but still two different ones. Therefore, the CEνNS process

is not probing a specific nuclear species, like in the case of the liquid argon target, but rather two nuclei, or in some sense a sort of average of the two. Moreover, the COHERENT Collaboration released the first measurement in 2017 [51], but also updated the results in 2021 [54]. We will discuss the results from the latest cesium-iodide data [2, 8] in terms of measurements of the weak mixing angle at the experimental energy scale, $Q^2 \simeq (50\ \mathrm{MeV})^2$. Furthermore, the advantage of dealing with the COHERENT CsI data is that we can perform combined analysis exploiting the APV(Cs) measurement performed at lower momentum transfer, $Q^2 \simeq (2.4\ \mathrm{MeV})^2$, which incidentally is on cesium, so that it measures the same parameters extracted by CEνNS.
Indeed, we can first perform the same analysis carried out for the COHERENT LAr data: fixing the neutron radius of Cs and I to the chosen reference values from nuclear shell models (NSM) [60], namely $R_n^{\mathrm{ref}}(\mathrm{Cs}) = 5.09$ fm and $R_n^{\mathrm{ref}}(\mathrm{I}) = 5.03$ fm, and fitting for the weak mixing angle, and then the opposite, fixing the weak mixing angle and fitting for the neutron radius. Since the COHERENT data do not allow us to disentangle the contribution of the two nuclei in the crystal, we fit for an average CsI nuclear radius. This assumption is justified by the fact that the two nuclei are expected to have similar neutron radii, at least compared to the current precision.

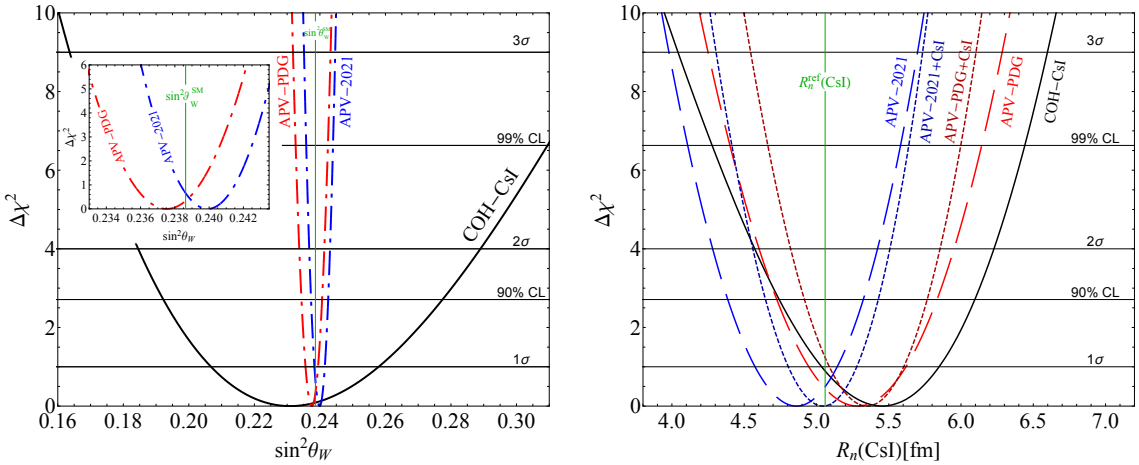

Figure 5.4: Constraints on the weak mixing angle (Left) and on the average rms CsI neutron radius (Right) at different confidence levels (C.L.). The different curves refer to the COHERENT CsI data (CsI), the APV data using the PNC amplitude of Ref. [31] (APV PDG) and that recently calculated in Ref. [205] (APV 2021), as well as their combination (APV-PDG+CsI and APV-2021+CsI). In (Left) the combined curves are practically indistinguishable from the APV only fit. The green lines represent (Left) the low-energy SM value of the weak mixing angle and (Right) the average rms CsI neutron radius from the nuclear shell model prediction [8, 60]. In the inset in the top left of (Left), a zoom of x-axes is shown to better appreciate the APV only determinations (whose 1σ values were shown already in Fig. 3.19 through the dark red data points).

We performed the COHERENT CsI and APV data analysis separately but also their combination, using the chi-square functions in Eq. 2.75 and Eq. 3.90. In particular,

for the APV(Cs) result we considered both the PNC amplitude calculations, as previously discussed in Sec. 3.2.2, referring to them by APV PDG [31] and APV 2021 [205].
The result of the fit of the weak mixing angle is shown graphically in the left plot in Fig. 5.4 (black curve) and numerically it corresponds to

$$\sin^2\theta_W(\mathrm{COH-CsI}) = 0.231^{+0.027}_{-0.024}(1\sigma)^{+0.046}_{-0.039}(90\%\mathrm{CL})^{+0.058}_{-0.047}(2\sigma), \tag{5.3}$$

which is in agreement with the theoretical SM prediction (vertical green line) and the result recently presented in Ref. [238] when fitting the COHERENT CsI data with a different approach. Another derivation performed by the COHERENT Collaboration [54] reports $\sin^2\theta_W(\mathrm{CsI}) = 0.220^{+0.028}_{-0.026}$, which agrees rather well with our result although some small differences are expected due to the different description of the nuclear structure, i.e. different choices of the reference values for the neutron nuclear radii, and a different approach to radiative corrections for neutrino-nucleus scattering.

	$\sin^2\theta_W$		$R_n(\mathrm{CsI})[\mathrm{fm}]$	
	best-fit$^{+1\sigma}_{-1\sigma}$	χ^2_{min}	best-fit$^{+1\sigma}_{-1\sigma}$	χ^2_{min}
COH-CsI	$0.231^{+0.027}_{-0.024}$	86.0	$5.47^{+0.38}_{-0.38}$	85.2
APV PDG	$0.2375^{+0.0019}_{-0.0019}$	-	$5.29^{+0.33}_{-0.34}$	-
APV 2021	$0.2399^{+0.0016}_{-0.0016}$	-	$4.86^{+0.28}_{-0.29}$	-
APV PDG + CsI	$0.2374^{+0.0020}_{-0.0018}$	86.0	$5.35^{+0.25}_{-0.26}$	85.3
APV 2021 + CsI	$0.2398^{+0.0016}_{-0.0015}$	86.0	$5.04^{+0.23}_{-0.24}$	86.6

Table 5.1: Summary of the constraints obtained in this work on the weak mixing angle $\sin^2\theta_W$ and on the average rms CsI neutron radius $R_n(\mathrm{CsI})$ with the relative uncertainties. The different labels refer to the COHERENT CsI data (COH-CsI), the APV data using the PNC amplitudes of Ref. [31] (APV-PDG) and Ref. [205] (APV-2021), as well as the combined APV and COHERENT fit (APV-PDG+CsI and APV-2021+CsI). For each constraint, we also report the minimum value of the least square function provided by the fit.

This result can be compared with those obtained using the APV experiment on Cs[1], shown by the red and blue curves in the Fig. 5.4, namely (see also Eq. 3.91 and Eq. 3.92)

$$\sin^2\theta_W(\mathrm{APV\ PDG}) = 0.2375 \pm 0.0019\,(1\sigma) \pm 0.0031\,(90\%\mathrm{CL}) \pm 0.0038\,(2\sigma), \tag{5.4}$$
$$\sin^2\theta_W(\mathrm{APV\ 2021}) = 0.2399 \pm 0.0016\,(1\sigma) \pm 0.0026\,(90\%\mathrm{CL}) \pm 0.0032\,(2\sigma). \tag{5.5}$$

It is possible to see that the APV data allows us to achieve a factor of more than 10 better precision in the determination of $\sin^2\theta_W$. As shown in the insert of Fig. 5.4 (Left), the two PNC amplitudes point to a value of the weak mixing angle that is

[1]The same APV results were shown through the dark red data points in Fig. 3.19.

below and above the theoretical prediction, respectively, by less than 1σ. From the combination of the APV and COHERENT CsI dataset we obtain[2]

$$s^2_W(\text{APV PDG} + \text{COH} - \text{CsI}) = 0.2374^{+0.0020}_{-0.0018}(1\sigma)^{+0.0032}_{-0.0031}(90\%\text{CL})^{+0.0039}_{-0.0037}(2\sigma), \quad (5.6)$$

$$s^2_W(\text{APV 2021} + \text{COH} - \text{CsI}) = 0.2398^{+0.0016}_{-0.0015}(1\sigma)^{+0.0026}_{-0.0026}(90\%\text{CL})^{+0.0032}_{-0.0031}(2\sigma). \quad (5.7)$$

Clearly, the combination is vastly dominated by the APV result, with the PNC amplitude from Ref. [205] being slightly more precise. All the numerical results shown are summarised in Table 5.1.

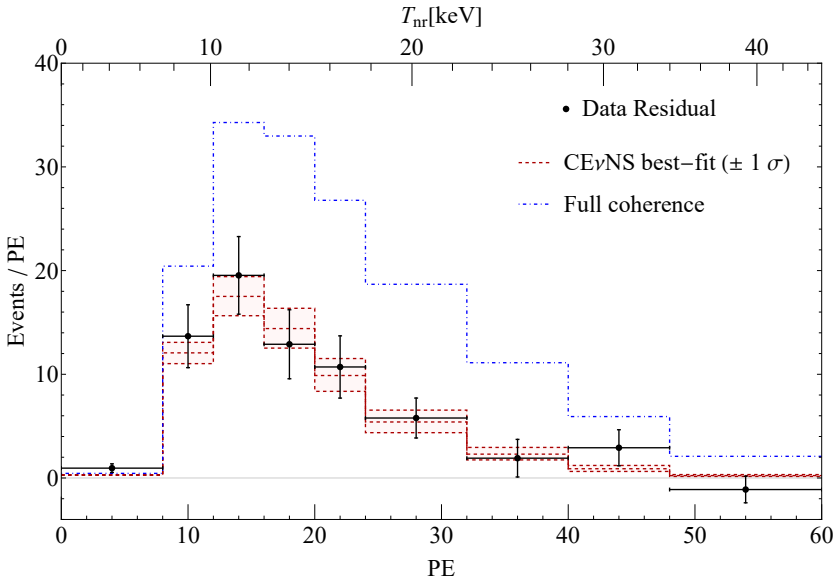

Figure 5.5: COHERENT CEνNS only data versus the number of photoelectrons (PE) and the nuclear recoil energy ($T_{\rm nr}$). The histograms represent the theoretical prediction in the case of full coherence (blue dash-dotted line) and the best fit obtained leaving R_n free to vary (red dashed line) [8].

Moving to the extraction of the neutron nuclear radius, we fixed the weak mixing angle to its SM low-energy value, to let the average CsI neutron distribution radius $R_n(\text{CsI})$ free to vary in the fit. Clearly, in this case, the contribution due to the neutron form factor to the total systematic uncertainty on $N_{ij}^{\text{CE}\nu\text{NS}}$ is removed in the evaluation of the least-square function in Eq. 2.75. The result of the fit is shown in the right plot in Fig. 5.4 and numerically it corresponds to

$$R_n(\text{COH} - \text{CsI}) = 5.47^{+0.38}_{-0.38}(1\sigma)^{+0.63}_{-0.72}(90\%\text{CL})^{+0.76}_{-0.89}(2\sigma)\ \text{fm}, \quad (5.8)$$

which is in agreement, within the uncertainty, with the NSM expected value for $R_n^{\text{NSM}}(\text{CsI})$, despite the central value pointing toward a large neutron skin. Moreover, this result is almost 10% more precise than the previous determination of Ref. [2]. To better appreciate the sensitivity of CEνNS to R_n, in Fig. 5.5 we show the impact of the nuclear structure on the theoretical prediction of the CEνNS event rates. In particular, we show the COHERENT excess counts, namely the

[2]In the equations we used s^2_W to indicate $\sin^2\theta_W$ for graphical purposes.

background subtracted COHERENT data, as a function of both the photoelectrons (PE) and the corresponding nuclear recoil energy ($T_{\rm nr}$) and we compare them with the prediction obtained in case of full coherence, i.e., setting all nuclear form factors equal to unity, and with the best fit obtained leaving R_n free to vary, as described in this section. We find that COHERENT data show a 6σ evidence of the nuclear structure suppression of the full coherence, making it an extremely powerful probe to determine nuclear parameters.
Also, APV data is sensitive to R_n, so that we can fix the weak mixing angle and fit for the cesium neutron radius by using the chi-square function in Eq. 3.90, getting

$$R_n(\text{APV PDG}) = 5.29^{+0.33}_{-0.34}(1\sigma)^{+0.55}_{-0.56}(90\%\text{CL})^{+0.66}_{-0.68}(2\sigma)\ \text{fm}, \tag{5.9}$$
$$R_n(\text{APV 2021}) = 4.86^{+0.28}_{-0.29}(1\sigma)^{+0.46}_{-0.48}(90\%\text{CL})^{+0.56}_{-0.58}(2\sigma)\ \text{fm}. \tag{5.10}$$

Differently from the case of the weak mixing angle, the precision achieved in this case is only slightly better than that achieved with COHERENT, such that the constraints improve significantly by performing a combination of these two experiments. The χ^2-curves we obtain are summarised in Fig. 5.4 (Right) and the numerical values we find are

$$R_n(\text{APV PDG} + \text{COH} - \text{CsI}) = 5.35^{+0.25}_{-0.26}(1\sigma)^{+0.41}_{-0.43}(90\%\text{CL})^{+0.50}_{-0.53}(2\sigma)\ \text{fm}, \tag{5.11}$$
$$R_n(\text{APV 2021} + \text{COH} - \text{CsI}) = 5.04^{+0.23}_{-0.24}(1\sigma)^{+0.38}_{-0.40}(90\%\text{CL})^{+0.46}_{-0.48}(2\sigma)\ \text{fm}. \tag{5.12}$$

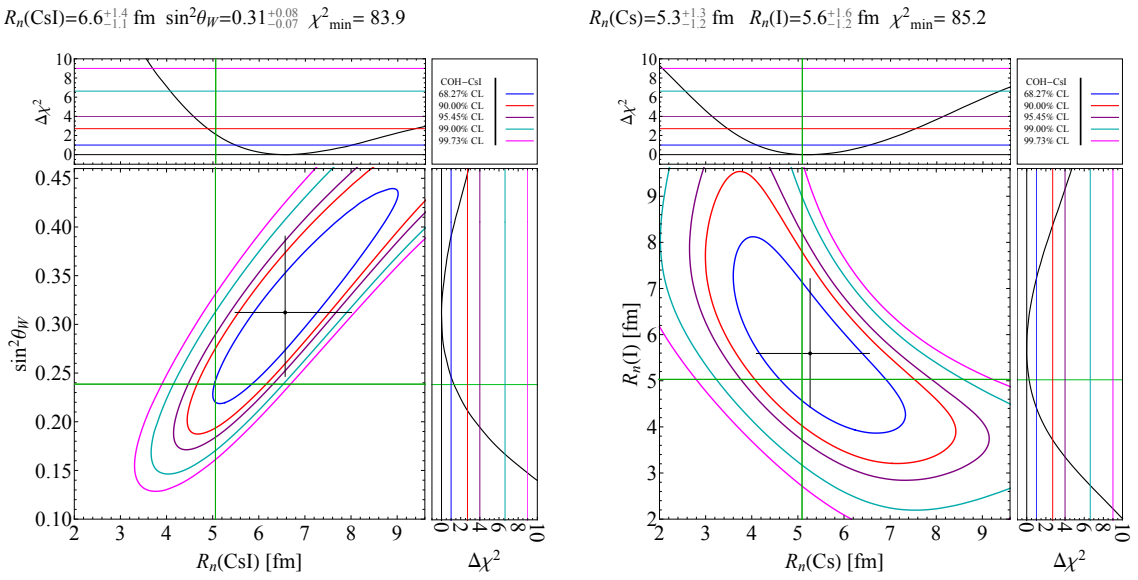

Figure 5.6: Constraints obtained fitting the COHERENT CsI data on the weak mixing angle and the average rms CsI neutron radius (Left) and on the plane of $R_n(^{133}\text{Cs})$ and $R_n(^{127}\text{I})$ (Right) together with their marginalizations, at different C.Ls. The green lines indicate the theoretical low-energy value of the weak mixing angle and the nuclear shell model (NSM) [60] prediction for the corresponding rms neutron distribution radius, chosen as reference values.

It is possible to see that the combination obtained using the 2021 PNC amplitude of Ref. [205] returns a neutron distribution rms radius that is very well in agreement with the theoretical prediction, while both COHERENT and the PDG PNC amplitude of Ref. [31] suggest a larger neutron skin. Given that in the latter case the two datasets point toward a similar value, we also get a smaller value for the minimum χ^2, as shown in Table 5.1. In both scenarios, a precision of less than 5% is obtained in the determination of R_n.
Although these analyses in which we allow only one parameter to vary are significant to understand the general sensitivity of the considered experimental probes, it is also crucial to repeat the analysis by letting free both the physical parameters in the fit in order to obtain a completely data driven measurement. Therefore, we performed a simultaneous fit of the average neutron radius of CsI and the weak mixing angle by considering the COHERENT CsI data alone, and then in combination with APV data, in order to exploit the different dependence of the two experiments on these two parameters. This allows us to get a more precise and solid determination of both quantities that uses the overall constraining power of two different electroweak probes. Moreover, we performed also a different kind of analysis: by fixing again the weak mixing angle to its SM value, we can fit for the two distinct neutron radii, trying to disentangle the contribution to the CEνNS process from the two nuclei.

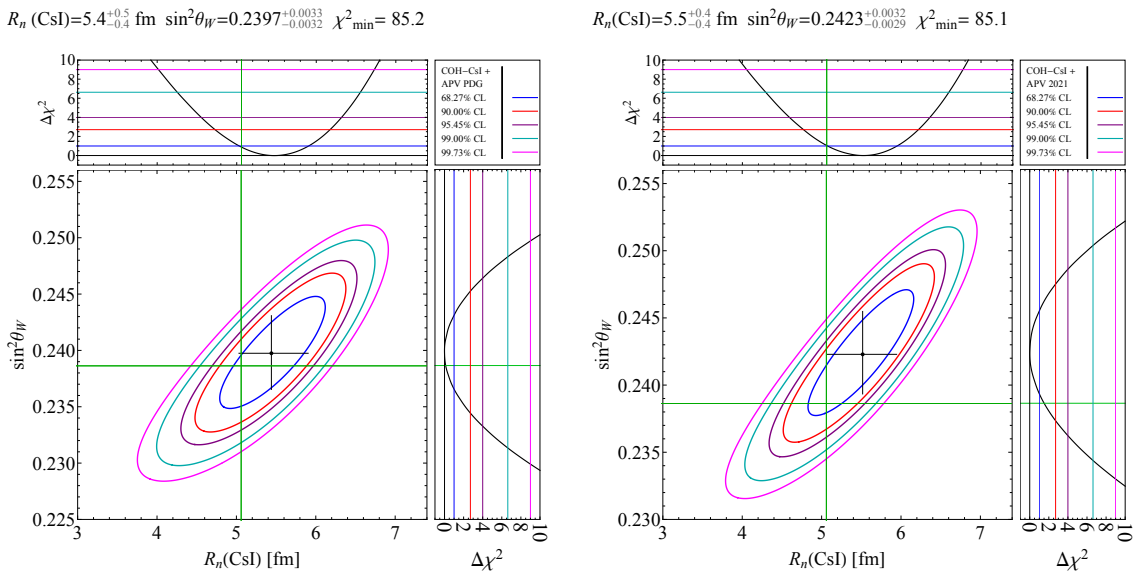

Figure 5.7: Constraints on the weak mixing angle and the average rms CsI neutron radius together with their marginalizations, at different C.Ls obtained fitting the COHERENT CsI data in combination with APV data, using the value for the neutron skin corrections of Ref. [31] (Left) and Ref. [205] (Right). The green lines indicate the theoretical low-energy value of the weak mixing angle and the NSM prediction [60] for the average rms CsI neutron radius.

The contours at different C.Ls of the allowed regions in the plane of the weak mixing angle and the average CsI neutron radius are reported in the left plot in

Fig. 5.6, using COHERENT CsI data alone. At the 1σ C.L. we obtain

$$\mathrm{COH-CsI}: \quad \sin^2\theta_W = 0.31^{+0.08}_{-0.07}, \quad R_n(\mathrm{CsI}) = 6.6^{+1.4}_{-1.1}\ \mathrm{fm}. \tag{5.13}$$

The fit tends to prefer large values for both parameters, with the theoretical value of the weak mixing angle and the rms average neutron radius of CsI that lie respectively at $\sim 1\sigma$ and $\sim 1.3\sigma$ outside the marginalized allowed region, despite the large uncertainties [8]. The results obtained by the combined analyses with APV(Cs) are reported in Fig. 5.7, using the experimental value of Q_W obtained with the theoretical prediction of the PNC amplitude of Ref. [31] (Left) and that recently calculated in Ref. [205] (Right). We obtain

$$\mathrm{APV\,PDG + COH-CsI}: \ \sin^2\theta_W = 0.2397^{+0.0033}_{-0.0032}, \quad R_n(\mathrm{CsI}) = 5.4^{+0.5}_{-0.4}\ \mathrm{fm}\,, \tag{5.14}$$

$$\mathrm{APV\,2021 + COH-CsI}: \ \sin^2\theta_W = 0.2423^{+0.0032}_{-0.0029}, \quad R_n(\mathrm{CsI}) = 5.5^{+0.4}_{-0.4}\ \mathrm{fm}\,. \tag{5.15}$$

The impact of including the APV data is noticeable, both in the uncertainty of the parameters, which is improved by more than one order of magnitude for the weak mixing angle and by a factor of ~ 3 for $R_n(\mathrm{CsI})$, as well as in their central values, that are moved towards the expected values, especially for $\sin^2\theta_W$.

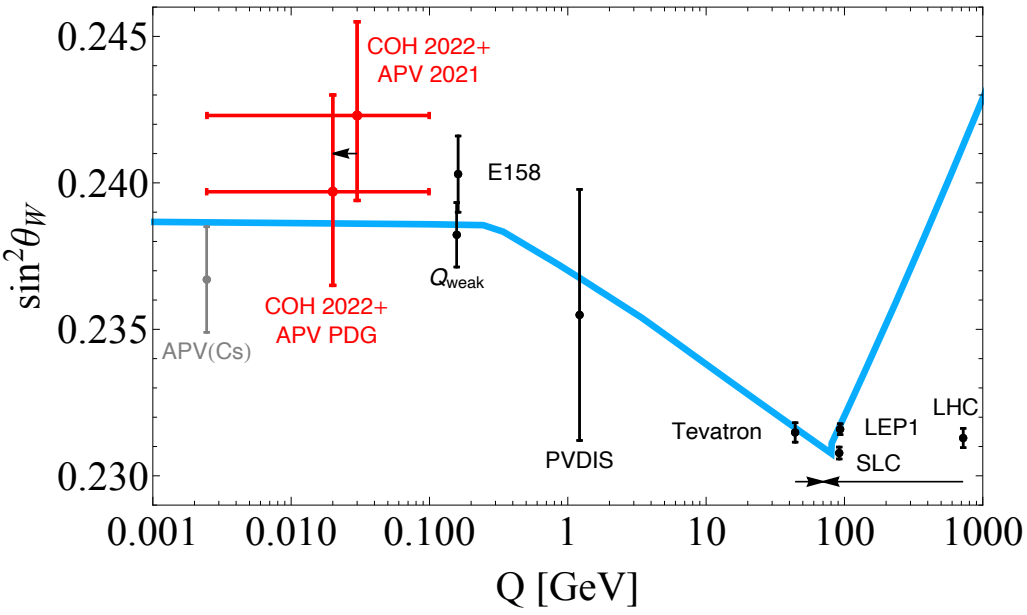

Figure 5.8: Running of the weak mixing angle in the SM (light blue line) as a function of the energy scale Q. The black experimental determination represent the status of the art of the measurements at different energy scales [25, 31, 33–35, 237]. The red points show the determinations from the combined analysis of APV(Cs) and COHERENT-CsI measurements retrieved in this work, which supersedes the nominal APV determination depicted in gray [32].

These results are depicted by the red data points in Fig. 5.8, where a summary of the weak mixing angle measurements as a function of the energy scale Q is shown along with the SM predicted running. They represent an alternative extraction of the weak mixing angle from APV that is fully data-driven and that keeps into

account the correlation with the value of R_n determined simultaneously using two electroweak probes, that are known to be practically model independent. Indeed, the nominal derivation of the weak mixing angle from APV data reported by the PDG [25], which is depicted by the gray point in Fig. 5.8, uses a value of R_n that is extrapolated from hadronic experiments using antiprotonic atoms, which are known to be affected by considerable model dependencies, as already discussed in Sec. 3.2.2. By comparing the two new determinations reported in this work, it is possible to see that the weak mixing angle is especially affected by the particular choice of the PNC amplitude, underlying thus the importance for the future to clarify the discrepancies between the two different approaches used in Refs. [31, 205].

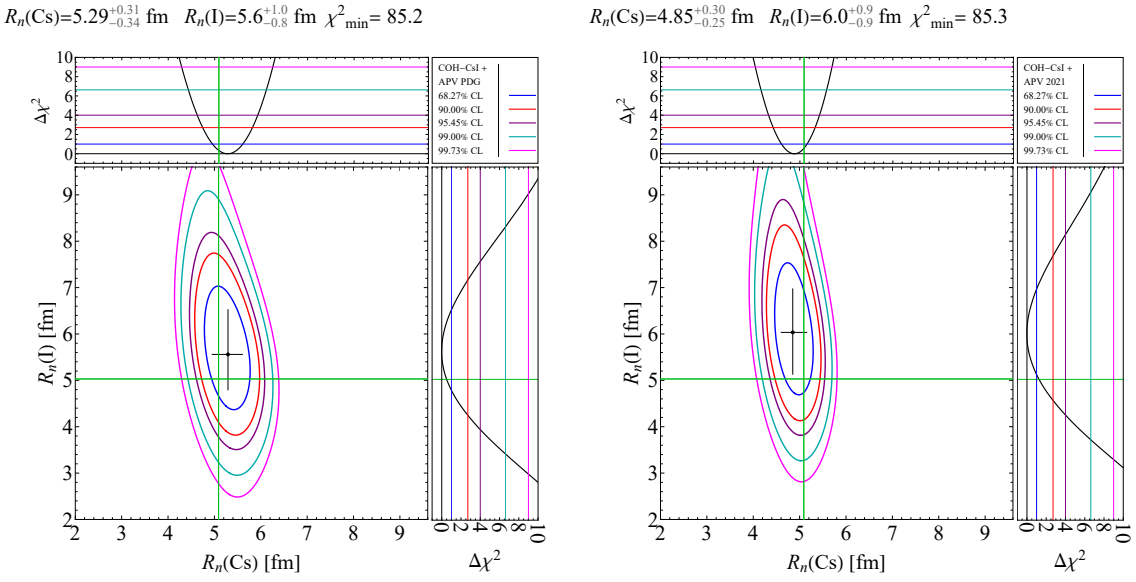

Figure 5.9: Constraints on the plane of $R_n(^{133}\mathrm{Cs})$ and $R_n(^{127}\mathrm{I})$ together with their marginalizations, at different C.Ls obtained fitting the COHERENT CsI data in combination with APV data, using the value for the neutron skin corrections of Ref. [31] (Left) and Ref. [205] (Right). The green lines indicate the corresponding NSM prediction for the average rms neutron radius of Cs and I.

We can now move to the study of the correlation between $R_n(\mathrm{Cs}) - R_n(\mathrm{I})$ using the latest COHERENT CsI data alone and combined with APV Cs to obtain the up-to-date and more accurate constraints on both these quantities, by relying on the precise SM prediction of the weak mixing angle at low energy. The result of the COHERENT CsI analysis is reported in Fig. 5.6 (Right), where we show the contours at different C.Ls in the plane of $R_n(\mathrm{Cs})$ and $R_n(\mathrm{I})$. Namely, we get

$$\mathrm{COH-CsI}: \quad R_n(\mathrm{Cs}) = 5.3^{+1.3}_{-1.2}\ \mathrm{fm}, \quad R_n(\mathrm{I}) = 5.6^{+1.6}_{-1.2}\ \mathrm{fm}. \tag{5.16}$$

As expected, COHERENT CsI data alone does not allow to disentangle the two contributions, motivating the need to perform a combined analysis with APV data. In fact, since APV depends only on the Cs neutron radius, while the COHERENT CsI result depends on both $R_n(^{133}\mathrm{Cs})$ and $R_n(^{127}\mathrm{I})$, we are able to break their degeneracy by combining them.

The results of such combined analysis are reported in Fig. 5.9, using the two experimental values of Q_W obtained with the theoretical predictions of the PNC amplitude considered in this work. In these two scenarios, we obtain

$$\text{APV PDG} + \text{COH} - \text{CsI} : R_n(\text{Cs}) = 5.29^{+0.31}_{-0.34}\ \text{fm},\ R_n(\text{I}) = 5.6^{+1.0}_{-0.8}\ \text{fm}, \quad (5.17)$$

$$\text{APV 2021} + \text{COH} - \text{CsI} : R_n(\text{Cs}) = 4.85^{+0.30}_{-0.25}\ \text{fm},\ R_n(\text{I}) = 6.0^{+0.9}_{-0.9}\ \text{fm}. \quad (5.18)$$

These values of the neutron radii can be converted into neutron skins determinations, and in particular, they correspond to $\Delta R_{\text{np}}(\text{Cs}) = 0.20^{+0.31}_{-0.34}$ fm-$\Delta R_{\text{np}}(\text{I}) = 0.57^{+1.0}_{-0.8}$ fm and $\Delta R_{\text{np}}(\text{Cs}) = -0.24^{+0.30}_{-0.25}$ fm-$\Delta R_{\text{np}}(\text{I}) = 1.0^{+0.9}_{-0.9}$ fm, respectively. Also in this case the different PNC amplitudes play a major role and with the second analysis, the slightly larger value of the iodine rms neutron radius is compensated by a significantly smaller value of $R_n(\text{Cs})$, which translates in an almost-zero neutron skin for cesium, with smaller uncertainties than those obtained in the first analysis.

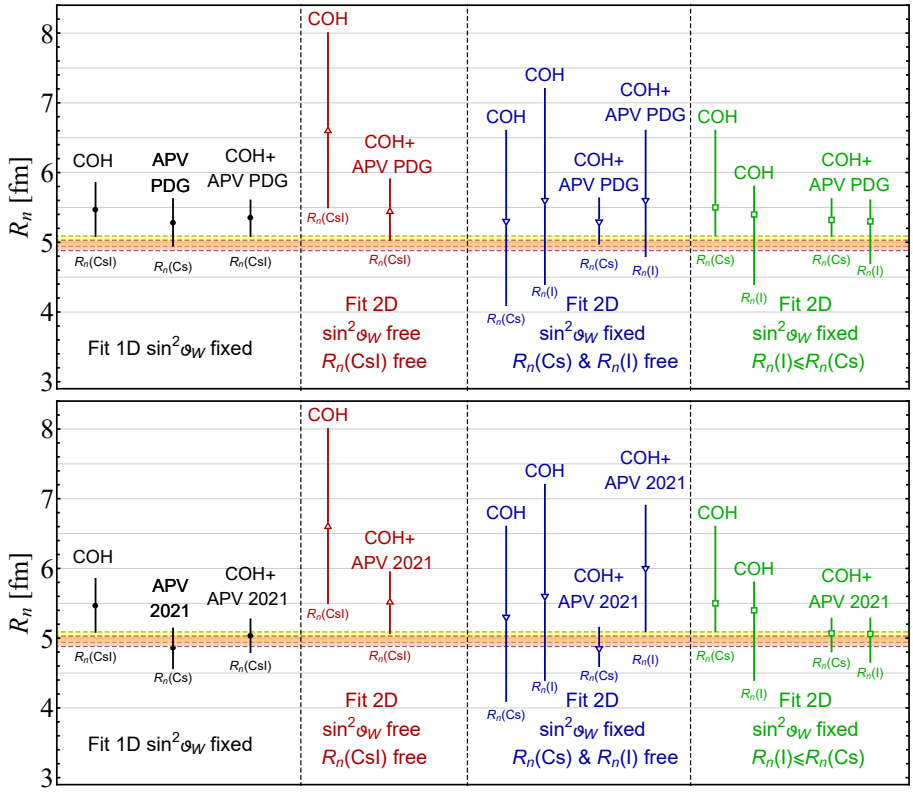

Figure 5.10: Overview of the different results presented in this section obtained using CEνNS CsI COHERENT (COH) data and APV with the PNC amplitude (Upper plot) from Ref. [31] (APV PDG) or (Lower plot) from Ref. [205] (APV 2021) as well as their combination [8]. The different markers and colors refer to the different fitting conditions. The yellow and orange areas represent the regions where the theoretical predictions of $R_n(\text{Cs})$ and $R_n(\text{I})$ can be found [2, 60].

Moreover, in all the scenarios, the central values suggest that $R_n(\text{I}) > R_n(\text{Cs})$, while all theoretical models (see e.g. Table I of Ref. [2]) predicts the opposite.

We thus redetermine these measurements after imposing the well-motivated constraint $R_n(\mathrm{I}) \leq R_n(\mathrm{Cs})$. In this case the measurements become [8]

$$\mathrm{COH-CsI}\,[R_n(\mathrm{I}) \leq R_n(\mathrm{Cs})] : \begin{bmatrix} R_n(\mathrm{Cs}) = 5.5^{+1.1}_{-0.4}\ \mathrm{fm}, \\ R_n(\mathrm{I}) = 5.4^{+0.4}_{-1.0}\ \mathrm{fm}, \end{bmatrix} \tag{5.19}$$

$$\mathrm{APV\,PDG + COH-CsI}\,[R_n(\mathrm{I}) \leq R_n(\mathrm{Cs})] : \begin{bmatrix} R_n(\mathrm{Cs}) = 5.32^{+0.30}_{-0.23}\ \mathrm{fm}, \\ R_n(\mathrm{I}) = 5.30^{+0.30}_{-0.6}\ \mathrm{fm}, \end{bmatrix} \tag{5.20}$$

$$\mathrm{APV\,2021 + COH-CsI}\,[R_n(\mathrm{I}) \leq R_n(\mathrm{Cs})] : \begin{bmatrix} R_n(\mathrm{Cs}) = 5.07^{+0.21}_{-0.26}\ \mathrm{fm}, \\ R_n(\mathrm{I}) = 5.06^{+0.22}_{-0.4}\ \mathrm{fm}. \end{bmatrix} \tag{5.21}$$

Imposing this constraint, we achieve an uncertainty as low as 4% on $R_n(\mathrm{Cs})$.
Given the vast amount of measurements of the neutron rms radius distribution presented by our analysis of the COHERENT CsI data under different hypotheses, we summarised all of them in Fig. 5.10 when using APV with the PNC amplitude from Ref. [31] (Upper plot) or from Ref. [205] (Lower plot). Despite the different fit configurations used to extract the values of $R_n(\mathrm{CsI})$, $R_n(\mathrm{Cs})$ and $R_n(\mathrm{I})$, a coherent picture emerges with an overall agreement between the COHERENT and APV results and the theoretical predictions. However, we would like to note that using APV PDG we obtain on average larger values on the radii, even if still compatible within the uncertainties. On the contrary, APV 2021 shifts downwards the measured radii towards the predictions, but in the simultaneous 2D fit with $\sin^2\theta_W$ where the correlation with the latter increases the extracted central value of $R_n(\mathrm{CsI})$.
Moreover, we checked the impact of using a different quenching factor, by comparing our nominal results obtained using Refs. [54, 86] and the derivation in Ref. [239]. The latter lower QF decreases the total number of CEνNS events resulting in a smaller $R_n(\mathrm{CsI})$ by about 10%.
To contextualize even further the importance of CEνNS measurements using the COHERENT CsI detector, we compared the measurements of the CsI neutron radius from the COHERENT experiment with the state-of-art measurements using other electroweak probes.
The current level of accuracy of CEνNS in the determination of the neutron radius, both the CsI one reported in this section as well as the argon one reported in Ref. [234] and shown in Fig. 5.1 (Left) and Fig. 5.2, is still lower with respect to that obtained using parity-violating electron scattering on similar nuclei. This is shown in Fig. 5.11 for the case of CsI by comparing it to the situation on lead-208. In the figure, we show the current status for different neutron distribution radii measured via diverse electroweak probes. As shown, the precision achieved by the PREX experiments [153, 154] and the one expected for the future MREX measurement at the MESA facility [184] is indeed greater than that obtained through CEνNS for CsI [2, 8, 197, 240].
Luckily, the COHERENT Collaboration has additional existing and planned near-future deployments in the Neutrino Alley at the SNS with exciting physics potential. In particular, the experimental program under development includes a large scale CsI cryogenic detector. Moreover, the European Spallation Source (ESS) is

currently under construction in Lund, Sweden [241]. There are plans of measuring CEνNS with a 31.5 kg CsI target kept at 80 K [241, 242]. Meanwhile, a new CEνNS detection experiment is under construction in China, where undoped CsI crystals coupled with two photon multiplier tubes each, will be cooled down to 77 K and placed at the China Spallation Neutron Source (CSNS) [243].

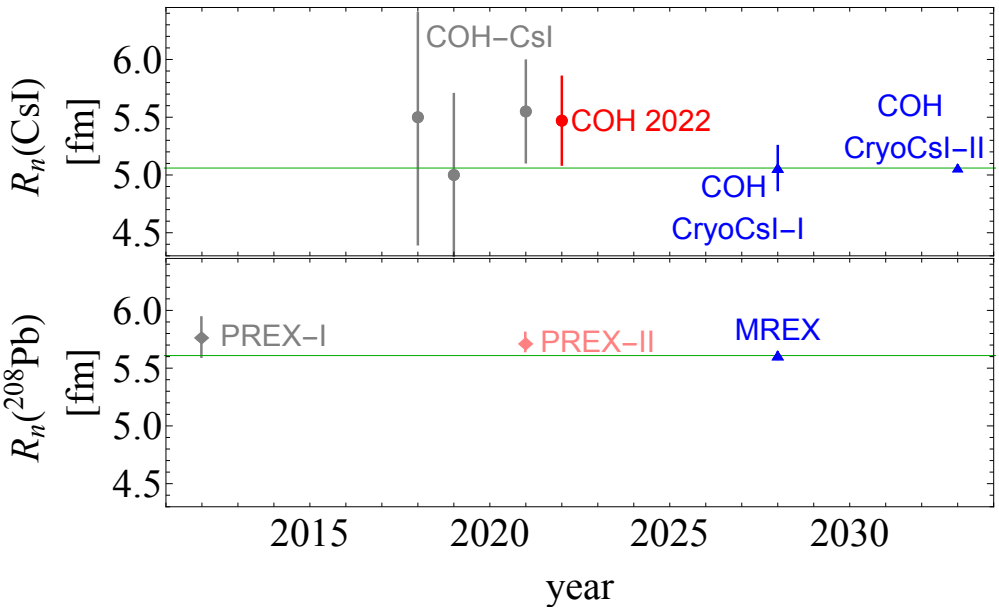

Figure 5.11: Current status and future projections for neutron distribution radii of different nuclei measured via electroweak probes. We show the current and foreseen measurements of $R_n(\mathrm{Cs})$ (upper panel) from CEνNS with CsI crystal detectors [2, 8, 84, 197, 240] compared to the current and foreseen measurements from parity-violating electron scattering on Pb [153, 154, 184] (lower panel). For CsI, similar uncertainties are expected to be achieved thanks to the detectors planned at the ESS [241] and at the CSNS [243].

Thus, it is interesting to perform a sensitivity study using COHERENT plans as described in Ref. [84]. However, similar conclusions and prospects can also be drawn for the already mentioned CsI detectors expected at the ESS and the CSNS as they foresee similar technologies. The aim of this study is to assess to which extent CEνNS will be competitive in the future [8].
The first upgrade of the SNS is planned for 2025, where the proton beam energy (E_p) will be increased up to 1.3 GeV (the current one is 0.984 GeV) and the beam power P_{beam} will increase to 2 MW (the current one is 1.4 MW) so that the number of neutrinos per flavor produced for each proton-on-target (POT) will increase to a value of 0.12. Moreover, a second target station is planned in the 2030s, for a final power of 2.8 MW. The so-called COH-CryoCsI-I experiment, scheduled for 2025, will have a mass of about 10 kg and will exploit an undoped CsI crystal at cryogenic temperature $(\sim 40\mathrm{K})$, with an almost doubled light yield. The following upgrade will be the COH-CryoCsI-II experiment, planned in the 2030s, that will operate in similar conditions with a 700 kg undoped CsI detector. Both the COH-CryoCsI-I and COH-CryoCsI-II detectors will be able to lower the energy

threshold, that we considered to be of $1.4\ \mathrm{keV_{nr}}$ [84]. In addition, the systematic uncertainty on the neutrino flux will be strongly reduced thanks to the installation of a heavy water detector, and it will approach 4.7(2)% statistical uncertainty after 2(5) SNS-years of operation. Thus, we considered the value of 4.7% for the statistical uncertainty on the neutrino flux for the Cryo-CsI-I detector, while we used 2% for the Cryo-CsI-II detector. The quenching factor will be directly measured by the COHERENT Collaboration, but for this sensitivity study, we will consider a quenching factor of 5% as reported in Ref. [84] and as it has already been established in Ref. [239]. The resulting total systematic uncertainty for the CEνNS prediction is $\sigma_{\mathrm{CE}\nu\mathrm{NS}} = 0.062$ for the Cryo-CsI-I detector and $\sigma_{\mathrm{CE}\nu\mathrm{NS}} = 0.046$ for the Cryo-CsI-II detector. Assuming three years of data taking, $\sim 2 \cdot 10^3$ and $\sim 2 \cdot 10^5$ events are expected for COH-CryoCsI-I and COH-CryoCsI-II, respectively, to be compared with the current CsI available statistics of ~ 300 events[3].

We used the same least-square function defined in Eq. (2.75), using the same time binning of the data and time efficiency of the latest CsI data release [54] also for the sensitivity study. In particular, we rescaled the SS background measured by the current CsI detector for the exposure time and the mass of COH-CryoCsI-I and COH-CryoCsI-II, respectively, and we extended it below the current threshold. For more details look at Refs. [8, 84].

In Fig. 5.11, we report the projections on the neutron radius of CsI as obtained from this sensitivity study. We find that COH-CryoCsI-I will be able to measure the neutron rms CsI radius[4] with a precision of $\sigma(R_n(\mathrm{CsI})) = 0.19\,\mathrm{fm}$ corresponding to a relative accuracy of about 4%. Similarly, for the COH-CryoCsI-II scenario we obtain a sensitivity projection for $R_n(\mathrm{CsI})$ that corresponds to $\sigma(R_n(\mathrm{CsI})) = 0.023\,\mathrm{fm}$, meaning that COH-CryoCsI-II will be able to reach a per-mille accuracy level, i.e., about 0.5%. It is worth noticing that, in this regime, the projected uncertainty on the neutron radius will become smaller than the difference between the Cs and I radius, expected to be $\sim 0.06\,\mathrm{fm}$. Thus, it will be of paramount importance to keep into account the different contributions of Cs and I by performing a simultaneous fit on these two quantities. This precision, which is also expected to be achieved at the ESS with a similar amount of foreseen CEνNS events, will represent an unprecedented window into nuclear physics, making CEνNS very competitive with respect to the other weak probes. Specifically, the other available and currently world-leading measurements on the neutron radius of heavy and neutron-rich nuclei come from parity-violating electron scattering as shown in Fig. 5.11, for the case of $^{208}\mathrm{Pb}$ [153, 154] as measured by PREX-I and PREX-II, respectively. It is worth noticing that the MREX experiment [184] also plans to measure the $^{208}\mathrm{Pb}$ neutron radius with an accuracy of about 0.5%.

In Fig. 5.12, we report the projections on the weak mixing angle as obtained from this sensitivity study [8], along with a comprehensive review of the current and future measurements that are known for an energy scale below $100\ \mathrm{MeV}$. In particular we depicted the evolution of the APV determination in the last decade [25, 203,

[3] For comparison, at the ESS a compact 31.5 kg cryogenic CsI detector is expected to measure $\sim 1.2 \cdot 10^4$ CEνNS events per year [241].

[4] For these studies, we consider a value of $R_n(\mathrm{CsI}) = 5.06\ \mathrm{fm}$ as provided by the nuclear shell model calculations.

206–208], that moved significantly due to different theoretical re-evaluations (see Fig. 3.19), the value of the weak mixing angle extracted from the CsI COHERENT in Ref. [2] and in this work as well as the values obtained from the combination with APV. As it can be seen, many measurements of $\sin^2\theta_W$ are expected in the near future in the low energy sector, as those coming from the P2 [184, 227] and MOLLER [228] experiments, and from future CEνNS experiments (COνUS [244], TEXONO [245], CONNIE [246], and MIνER [247]) that will be really powerful for further constraining such a quantity.
It is worth noticing that CEνNS from reactor antineutrinos already proved to be able to provide a determination of the weak mixing angle. Indeed, this has been shown in Refs. [6, 96], even if the uncertainty so far is still too large to be depicted in Fig. 5.12, but will be discussed in the following section.

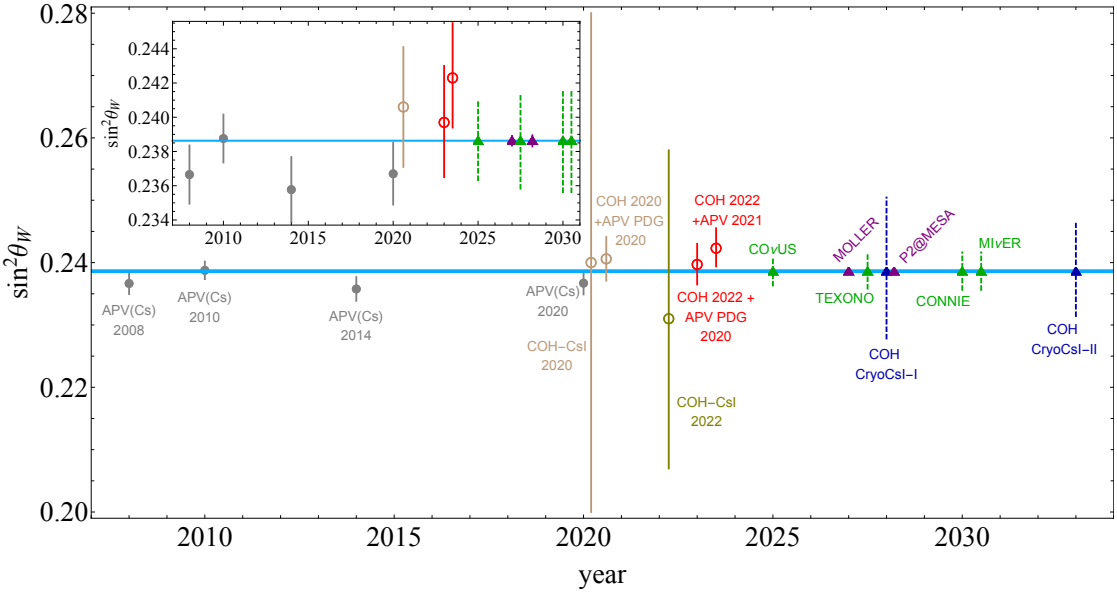

Figure 5.12: Current status and future projections for weak mixing angle measurements below $Q \lesssim 100$ MeV. The gray points show the measurements from APV on cesium atoms during the years [25, 203, 206–208]. The brown measurements refer to the COHERENT only and the combination between COHERENT and APV as determined in 2020 in our previous work (see Ref. [2]), while the olive, dark blue and red points refer to our updated measurements [8], with the dark blue triangles being the projections for the future CryoCsI-I and CryoCsI-II determinations [8]. The projections for future CEνNS experiments (COνUS [244], TEXONO [245], CONNIE [246], and MIνER [247]), shown by the green triangles and dashed error bars, are taken from Ref. [248]. The purple triangles are the projections for the future electron scattering experiment MOLLER [228] and P2@MESA [184, 227]. In the inset in the top left, a zoom of the y axes is shown to better appreciate the statistical uncertainties of the reported measurements and projections, removing the measurements from COHERENT-only which suffer from larger uncertainties.

In this scenario, CEνNS determinations with CsI will help with both the Cryo-CsI-I detector that will reach a precision of about $\sigma(\sin^2\theta_W) = 0.012$ and in particular with COH-CryoCsI-II, where a precision of about $\sigma(\sin^2\theta_W) = 0.007$ could be

achieved. The sensitivity projection on the weak mixing angle for the Cryo-CsI-I detector has been reported also in Ref. [84] by the COHERENT Collaboration, where a slightly better precision corresponding to $\sigma(\sin^2\theta_W) \sim 0.009$ has been found. The different result can be explained considering that the sensitivity to the weak mixing angle depends strongly on the values of $R_n(\mathrm{Cs})$ and $R_n(\mathrm{I})$ used to describe the loss of coherence for increasing recoil energies. The values from the NSM calculations adopted in our work differ significantly from the value used in the aforementioned work, which seems to be $R_n(\mathrm{CsI}) \sim 6$ fm. We verified that we are able to obtain a better agreement with their projections using the latter value for the nuclear radius. When more data becomes available, it will be therefore essential to perform a simultaneous determination of these parameters, as investigated in this work.

5.3 Dresden-II

Differently from the case of the COHERENT data analysis, the Dresden-II CEνNS data do not depend significantly on the form factor effects. Indeed, the lower energy of reactor neutrinos, together with the low recoil regime considered in the experimental region-of-interest, make the data analysis independent of the particular choice of the nuclear neutron radius of germanium inside the CEνNS cross section. This allows one to extract the weak mixing angle directly from fitting the data, without the need of performing a two parameter fit. Indeed, in this CEνNS cross section, we fixed the form factors to unity. Of course, the drawback is that the Dresden-II data do not allow us to extract information on the neutron distribution inside the germanium nucleus.

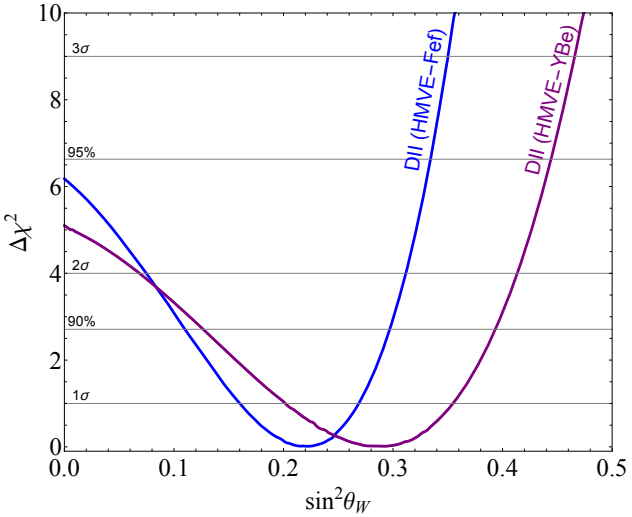

Figure 5.13: Marginal $\Delta\chi^2$'s for $\sin^2\theta_W$ obtained from the analysis of the Dresden-II data assuming the HMVE reactor antineutrino flux and the Fef (blue) or YBe (purple) quenching factors.

Therefore, we performed a fit of the weak mixing angle using the chi-square function in Eq. 2.84 [6], considering the different parameterizations for the reactor

neutrino spectra and the two different quenching factor models, namely the Fef and the YBe.
In Fig. 5.13 we show the marginal $\Delta\chi^2$ results from the Dresden-II data fit considering the HMVE reactor antineutrino flux and two different quenching factors [6]. Indeed, the results obtained with the other parametrizations are very similar and the graphical comparison can be seen in Fig. 2(a) of Ref. [6]. The numerical results of these fits are summarized in Tab. 5.2 for all the six combinations of neutrino fluxes and QFs, where we provide the best fit values with the range for different confidence levels. The impact of the different antineutrino fluxes is marginal. On the contrary, the impact of the different QFs is non-negligible, being the YBe result shifted toward larger values of the weak mixing angle and also less precise. However, the two results are still in agreement with each other within the 1σ confidence level. Focusing on the HMVE flux, our results are [6]

$$\sin^2\theta_W(\mathrm{Dresden-II\,Fef}) = 0.219^{+0.06}_{-0.05}\,(1\sigma),^{+0.11}_{-0.08}\,(90\%),^{+0.14}_{-0.09}\,(2\sigma)\,, \quad (5.22)$$

$$\sin^2\theta_W(\mathrm{Dresden-II\,YBe}) = 0.286^{+0.08}_{-0.07}\,(1\sigma),^{+0.16}_{-0.11}\,(90\%),^{+0.22}_{-0.13}\,(2\sigma)\,, \quad (5.23)$$

for the Fef and YBe quenching factors, respectively. These results are also depicted in Fig. 5.14, where a summary of low energy weak mixing angle measurements (black data points) as a function of the energy scale Q is shown along with the SM predicted running of $\sin^2\theta_W$, calculated in the $\overline{\mathrm{MS}}$ scheme [27, 28, 226]. The results of the fit are shown by the blue (Fef) and purple (YBe) and are set at the experimental momentum transfer, namely $Q \simeq \sqrt{2m_N T_{\mathrm{nr}}} \sim 20\,\mathrm{MeV}$.

Dresden-II	$\sin^2\theta_W^{\mathrm{b.f.}}$	1σ	90%	2σ	3σ
HMVE-Fef	0.219	(0.159, 0.268)	(0.110, 0.296)	(0.0742, 0.311)	< 0.349
HMK-Fef	0.219	(0.159, 0.268)	(0.110, 0.296)	(0.0742, 0.311)	< 0.349
EFK-Fef	0.226	(0.164, 0.275)	(0.113, 0.304)	(0.0772, 0.319)	< 0.358
HMVE-YBe	0.286	(0.202, 0.354)	(0.127, 0.393)	(0.0693, 0.413)	< 0.465
HMK-YBe	0.286	(0.201, 0.353)	(0.127, 0.392)	(0.0693, 0.412)	< 0.464
EFK-YBe	0.293	(0.206, 0.362)	(0.129, 0.402)	(0.0683, 0.423)	< 0.476

Table 5.2: Best-fit value and bounds on $\sin^2\theta_W$ obtained from the analysis of the Dresden-II data assuming the HMVE, HMK, or EFK reactor antineutrino flux and the Fef or YBe quenching.

Since the current precision of the Dresden-II measurement is far from being competitive compared to other existing measurements (black dots) we display the determinations in an inset with an enlarged y scale. In the inset, we compare the weak mixing angle determinations with the ones obtained by the COHERENT data analysis, which have been discussed in the previous section. Namely, the green point corresponds to the COHERENT LAr data (see Eq. 5.2), while the olive point to the COHERENT CsI data (see Eq. 5.3).
The measurements from CEνNS experiments cover an energy scale region which is still untested. However, they have all rather large uncertainties, even if the latest COHERENT CsI one shows already a significantly better precision with respect to

the others. Nonetheless, this measurement from Dresden-II has to be considered the first weak mixing angle measurement from reactor CEνNS, and in the future, it could be significantly improved, also by considering some combination of different electroweak probes. In fact, we have shown that combining the COHERENT CsI measurement with the APV(Cs) one can lead to more precise determinations, thus, obtaining significantly reduced uncertainties and completely data driven results (see Fig. 5.8). In future, some similar combined analysis could be employed to improve the precision, also, for example, by considering combined CEνNS measurements.

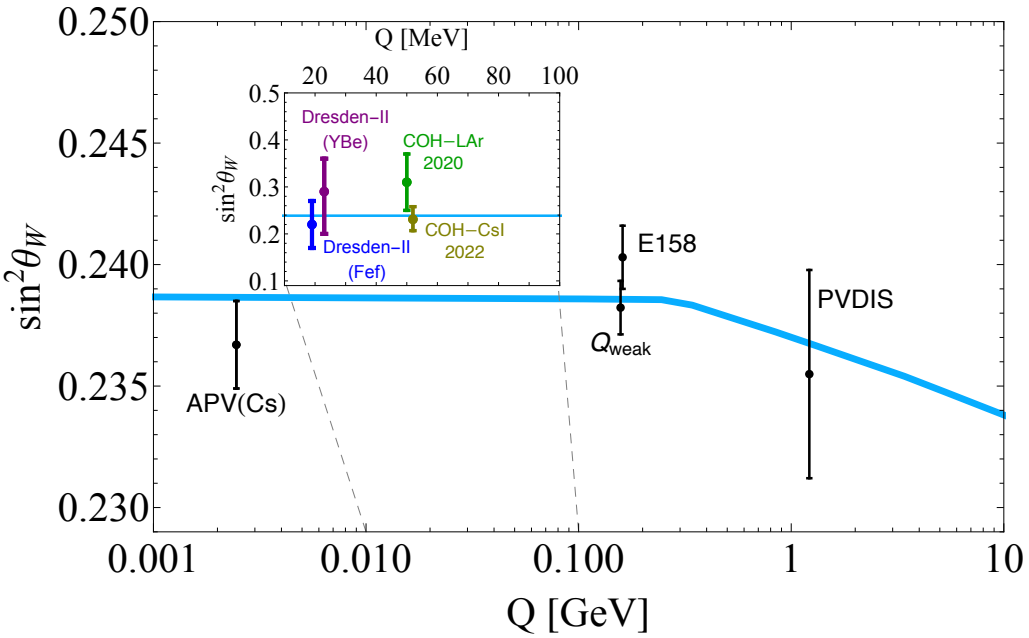

Figure 5.14: Variation of $\sin^2\theta_W$ with the energy scale Q. The SM prediction is shown as the light blue curve, together with the available non-CEνNS experimental determinations [31–35]. The results derived in this work using the Dresden-II data are shown in blue and purple for the Fef and YBe quenching factor, respectively, and are shown on a different scale in the inset to better appreciate them. In the inset, the determinations are compared to the ones from COHERENT-LAr (green) and COHERENT-CsI (olive). The dashed gray lines indicate the corresponding energy scale in the larger figure.

In principle, the Dresden-II data could correspond to a superposition of CEνNS and νES events, so that we repeated all the above measurements including also the νES contribution in the Dresden-II data set. As already discussed, this is accounted for by substituting in the function in Eq. 2.84 the sum of the CEνNS and νES events in each bin to the CEνNS only one. However, no effect is found due to νES on the weak mixing angle, thus the results are independent of its inclusion. This is also comprehensible, since the SM number of νES events is orders of magnitude smaller than the CEνNS one, and the weak mixing angle variation does not produce a significant shape distortion, but rather an overall shift of the rate of events.
Other bounds on $\sin^2\theta_W$ have also been obtained exploiting the CEνNS data from COHERENT and Dresden-II in Refs. [96, 249], leading to similar results.

Chapter 6

$U(1)'$ extensions of the standard model

Short introduction

In this chapter, we will discuss a variety of beyond the standard model scenarios in which the SM is extended by the introduction of an extra $U(1)'$ gauge group following the results published in Refs. [1, 3, 5]. In these BSM scenarios, a novel vector mediator is introduced and in particular it is expected to behave like a standard Z boson although being lighter, so that it is usually referred to as Z'. We will consider also a scenario in which the extra mediator is not a vector-like boson, but a scalar boson, in which case it will be called ϕ boson. We will present the latest constraints on such new physics scenarios from CEνNS measurement, namely by the analysis of COHERENT and Dresden-II data, following closely Refs. [1, 5].
In addition, we will investigate a more complicated model, called Z_d, in which the extra boson induces a parity violating interaction. In particular, we will consider the impact of a Z_d boson in low energy processes involving electrons, such as APV, proton weak charge measurement and also anomalous magnetic moment measurements, together with the implications on the running of the weak mixing angle. The latter discussion will follow closely the publication in Ref. [3].

6.1 Light mediators framework

Here, we consider beyond the SM scenarios in which the new physics manifests through a novel interaction mediated by a light vector boson, usually called Z', or scalar boson, usually named ϕ. In particular, we consider those models which contribute to the CEνNS process and to other low energy electroweak probes such as APV(Cs) and the proton weak charge measurement by the $\mathrm{Q}_{\mathrm{weak}}$ experiment.
Each model presents two model parameters, namely the mass of the new boson and the coupling of the new mediator to the SM fermions, but for the one particular model, called dark Z, Z_d, which has a more complicated phenomenology, since it provides an additional source of parity violation. We will discuss the model

structure mainly for the more general Z' models, and leave the discussion of the Z_d for the section dedicated to it.
One of the strongest motivations behind the Z' searches in CEνNS data and in other experimental measurements is to test the SM looking for possible explanations for a long-standing tension between experimental measurements and SM theory: the muon anomalous magnetic moment, $(g-2)_\mu$. The current status of the comparison between the theoretical prediction [250–275] and the combined experimental measurement from the campaign at Brookhaven National Laboratory [276] and the recent one at the Fermi National Laboratory [277], leads to a 4.2σ tension[1] (see Appendix. D for a brief explanation of the anomaly). This so-called $(g-2)_\mu$ anomaly is a putative signal of physics beyond the SM, which has been studied in many papers (see, e.g., Refs. [279, 280]). Indeed, several light vector mediator models have been proposed as a candidate solution for such anomaly [3, 281–288], but in principle also a light scalar mediator could solve the tension [289].
The candidate models are in particular those which present a direct interaction with the muon (or in general the muonic flavor), so that it is crucial to test these models using processes involving such flavor to look for compatible signatures in different measurements, or to discard them. In this sense, the COHERENT measurements of CEνNS provide a suitable setup to search for the mentioned signatures thanks to the presence of a ν_μ neutrino flux.
The models that will be considered represent some simple extensions of the SM built via the addition of an extra $U(1)$ gauge group, either with a scalar or vector structure, which introduces to the particle zoo an extra light mediator.
We will present the constraints obtained by analyzing the COHERENT 2021 CsI data [54] and the COHERENT 2020 LAr data [53, 91] when considering the vector and scalar models. We will consider a smaller ensemble of models with respect to Ref. [5], where a rather complete discussion of Z' is presented. The constraints will be presented as exclusion limits in the mass and coupling of the light vector or scalar boson mediator parameter space, and will be compared to the constraints coming from other experimental measurements. Let us note that some constraints using CEνNS data were derived in the previous publication in Ref. [1], where we considered a smaller selection of models and used the older COHERENT CsI data set [51].
In the section related to the Z_d model, we will present the results obtained through a combined electroweak fit at low energies obtained considering APV(Cs), the $\mathrm{Q_{weak}}$ measurement of the proton weak charge, anomalous magnetic moment measurements of both electrons and muons, and some future measurements [3]. This model presents three free parameters, as an additional coupling is introduced to account for the contribution of parity violation. We will concentrate our attention on the impact of having such a boson on the running of the weak mixing angle.

[1] During the writing process of this thesis, a new experimental result has been released by the Muon g-2 Collaboration, relative to the Run-2 and Run-3 at FermiLab [278]. The new data improved significantly the uncertainty on the experimental results, remaining consistent with the previous data set. The updated discrepancy from the average experimental value is now $\Delta a_\mu = 249(48) \times 10^{-11}$ (5σ tension). However, the theory is currently under debate, so that the picture could change in the near future.

6.1.1 —— Vector models: Z' ——

The simplest extension of the SM that can be considered is known as non-standard neutrino interactions (NSI). In this scenario, an additional contribution from an heavy[2] (and decoupled) new particle is added to the SM couplings of neutrinos. However, these models are introduced as a "simple" constant contribution to be added to the couplings, without any scale dependence, at least in the regime at which experiments work. Of course, NSI models can get complicated by introducing particular flavor structures, but they will not be discussed in this thesis work (an example of COHERENT analysis of NSI models can be found in Ref. [290]). In the case of NSI the specifics of the new mediator are not important, since they arise in an effective four-fermion theory.
Instead, we are interested in looking for signature from a new light mediator, light with respect to the standard model Z boson (i.e. $M_{Z'} \approx \mathrm{MeV} - \mathrm{GeV}$), in which case, the details of the model and boson alter the nuclear recoil energy spectrum, since the boson propagator depends on the momentum transfer. in this sense, the simplest extension that we can consider happens via the addition of a $U(1)'$ gauge group to the canonical gauge structure of the SM theory. Associated with this additional gauge, a new neutral vector gauge boson is introduced (see, e.g., the review in Ref. [291]), and it is usually referred to as Z' boson[3] due to its similarities to the classical Z gauge boson. The specific model features are defined by the charges of the fermions under the newly introduced gauge symmetry, as they determine the contributions to CEνNS of the interactions mediated by the Z' vector boson. In fact, the effect of the new boson is quantified by additional terms in the nuclear weak charge in Eq. 2.47.
The easiest Z' model is called universal Z' model in which all the standard model fermions have the same charge [1, 292–297] under the new gauge symmetry. This model is not anomaly-free per se, but it can be extended with new non-standard particles to make it anomaly-free. Then, we consider several $U(1)'$ models in which quarks and leptons have appropriate non-zero charges that cancel the quantum anomalies (e.g., the popular $B - L$ model [291, 298, 299], where B is the baryon number and L is the total lepton number). Since in these models, the Z' vector boson interacts directly with both neutrinos and nucleons, the contribution to the CEνNS process occurs at tree-level and thus, it is possible to obtain stringent constraints on the mass and coupling of the new vector boson from the COHERENT CEνNS data. One can also consider some anomaly-free models based on a flavor structure, such as $L_e - L_\mu$, $L_e - L_\tau$, and $L_\mu - L_\tau$ $U(1)'$ models [300–303] (where L_α are the lepton generation numbers, for $\alpha = e, \mu, \tau$) in which the charges are exclusively leptonic. Therefore, in these models a direct coupling between the Z' boson and the nucleons is forbidden, and the contribution to the CEνNS process arises from a kinetic mixing process of the boson with the photon at one-loop level [304–306]. Indeed, these interactions can be thought of as a Z' interacting

[2]With "heavy" we refer to a mass greater than the momentum transfer, so that the propagator in Eq. 1.2 becomes the simplified one in Eq. 1.3.

[3]Let us note that in literature sometimes the Z' is included inside the dark photon, γ_d, class of models, as the structure behind them is rather similar.

with the neutrinos, then mixing with a photon, which then interacts with protons in the nucleons (the neutrons are not contributing as they are neutral particles). An example of Feynman diagrams describing the Z' interaction can be found in Fig. 6.1, where the left diagram shows the contribution of a generic Z' which couples with all the involved fermions, while the right one refers to the case in which the Z' couples only to a leptonic structure involving the α and β flavors. In the latter case, the Z' has a direct coupling only to the vertex with the appropriate neutrino flavor and then it mixes kinetically at one-loop level with a Z boson or a γ. The mixing with the Z boson has a negligible contribution when compared to the photon one, so that typically one considers the amplitude where the photon interacts with the protons inside the nucleus. In principle, one could consider the diagram with a neutrino of flavor $\delta \neq \alpha, \beta$, however, the interaction would require two loops, and thus, it can be safely neglected. In the diagrams, we used the green color for the vertices to indicate that the couplings are not the SM ones, because they depend on the specific gauge symmetry at the basis of the new mediator, and hence, on the new gauge charges associated with each fermion.

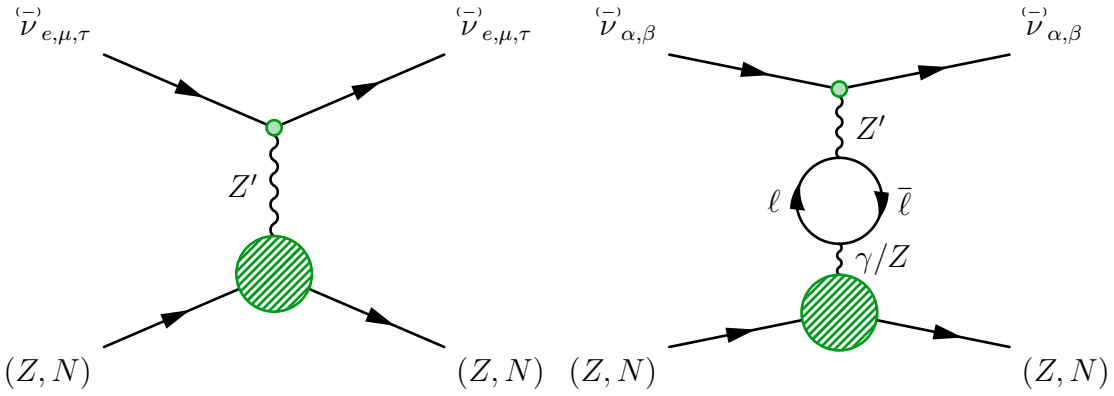

Figure 6.1: Diagram contributing the CEνNS process in the presence of a generic Z' which couples to all the involved fermions (left) and of a Z' model based on a flavor structure involving only the α and β flavors (right), and thus presents a loop involving leptons of flavor $\ell = \alpha, \beta$. The loops indicate the kinetic mixing between the Z' boson and the SM Z and γ. The green color for the vertices is used to indicate that the couplings are not the SM one, but are scaled via the fermion charges under the new gauge symmetry.

By considering the interaction of a Z' vector boson coupling to both neutrinos and quarks, we can write the generic Lagrangian

$$\mathcal{L}^V_{Z'} = -Z'_\mu \left[\sum_{\ell=e,\mu,\tau} g^{\nu_\ell V}_{Z'} \, \overline{\nu_{\ell L}} \gamma^\mu \nu_{\ell L} + \sum_{q=u,d} g^{qV}_{Z'} \, \bar{q} \gamma^\mu q \right] , \tag{6.1}$$

where $g^{qV}_{Z'}$ and $g^{\nu_\ell V}_{Z'}$ are the couplings constants due to the new interaction, while Z'_μ is the gauge field of the new mediator.
In the case of a new vector mediator, the coupling constants are proportional to the charges Q'_q and Q'_ℓ of quarks and neutrinos under the new gauge symmetry: $g^{qV}_{Z'} = g_{Z'} Q'_q$ and $g^{\nu_\ell V}_{Z'} = g_{Z'} Q'_\ell$, where $g_{Z'}$ is the coupling constant of the symmetry

group. Since both the SM and the Z' interactions are of vector type, they contribute coherently to the CEνNS cross section, so that the amplitudes arising from the specific diagram related to the considered model in Fig. 6.1 has to be summed to the SM CEνNS amplitude, relative to the diagram in Fig. 2.6. Moreover, since the vector current is conserved, the proton and neutron couplings are given by the sums of the couplings of their valence quarks. Therefore, the total cross section is obtained by replacing the SM weak charge $Q^V_{\ell,\mathrm{SM}}$ in Eq. 2.47 with the new total weak charge[4]

$$Q^V_{\ell,\mathrm{SM+V}} = Q^V_{\ell,\mathrm{SM}} + \frac{g^2_{Z'} Q'_\ell}{\sqrt{2} G_F \left(|\vec{q}|^2 + M^2_{Z'}\right)} \left[(2Q'_u + Q'_d)\, Z F_Z(|\vec{q}|^2) + (Q'_u + 2Q'_d)\, N F_N(|\vec{q}|^2) \right] . \tag{6.2}$$

In Ref. [5], a rather complete list of models was considered, some of which were already considered in Ref. [1]. To summarise the studied models we report them in Table 6.1, where the name of each model is shown together with the associated gauge charges.

Model	Q'_u	Q'_d	Q'_e	Q'_μ	Q'_τ
universal	1	1	1	1	1
$B-L$	$1/3$	$1/3$	-1	-1	-1
$B-3L_e$	$1/3$	$1/3$	-3	0	0
$B-3L_\mu$	$1/3$	$1/3$	0	-3	0
$B-2L_e-L_\mu$	$1/3$	$1/3$	-2	-1	0
$B-L_e-2L_\mu$	$1/3$	$1/3$	-1	-2	0
$B_y+L_\mu+L_\tau$	$1/3$	$1/3$	0	1	1
L_e-L_μ	0	0	1	-1	0
L_e-L_τ	0	0	1	0	-1
$L_\mu-L_\tau$	0	0	0	1	-1

Table 6.1: The $U(1)'$ charges of quarks and leptons in the vector mediator models considered in Ref. [5].

There are many BSM scenarios involving an additional massive Z' vector boson associated with a new $U(1)'$ gauge symmetry (see, e.g., the review in Ref. [291]). A common requirement is that the theory is anomaly-free. However, it is also possible to consider effective anomalous models that describe the interactions of SM fermions with the implicit requirement that the anomalies are canceled by the contributions of the non-standard fermions of the full theory. This is the case of the first model that we consider: a Z' boson which couples universally to all SM

[4]We have added here the superscript V to indicate that we are considering vector-type models and the underscript ℓ since the couplings are flavor dependents when considering radiative corrections.

fermions [1, 5, 292–297]. In this case $Q'_\ell = Q'_u = Q'_d = 1$, and the coupling is same for all the fermions.
Other models that we consider are anomaly-free if the SM is extended with the introduction of three right-handed neutrinos (see, e.g., Ref. [307]), which are also beneficial for the generation of the neutrino masses that are necessary for the explanation of the oscillations of neutrinos observed in many experiments (see, e.g., Refs. [24, 203]). In this case, there is an infinite set of anomaly-free $U(1)'$ gauge groups generated by

$$G(c_1, c_2, c_3, c_e, c_\mu, c_\tau) = c_1 B_1 + c_2 B_2 + c_3 B_3 - c_e L_e - c_\mu L_\mu - c_\tau L_\tau, \tag{6.3}$$

where B_1, B_2, and B_3 are the baryon numbers of the three generations and L_α are the lepton numbers for $\alpha = e, \mu, \tau$. We assume that for each generation the $U(1)'$ couplings of the right-handed neutrino are the same as that of the left-handed neutrino in order to have vectorial $U(1)'$ interactions. Therefore, when we extend the SM gauge group $SU(3)_C \times SU(2)_L \times U(1)_Y$ to $SU(3)_C \times SU(2)_L \times U(1)_Y \times U(1)'$, the only remaining anomalies are $[SU(2)_L]^2 U(1)'$ and $[U(1)_Y]^2 U(1)'$, which are canceled with the constraint [5]

$$c_1 + c_2 + c_3 - c_e - c_\mu - c_\tau = 0\,. \tag{6.4}$$

It is often assumed that the quark charges are universal, in order to avoid unobserved flavor-changing neutral currents in the quark sector. In this case, we have

$$G_B(c_B, c_e, c_\mu, c_\tau) = c_B B - c_e L_e - c_\mu L_\mu - c_\tau L_\tau\,, \tag{6.5}$$

with the constraint [308, 309]

$$3c_B - c_e - c_\mu - c_\tau = 0\,. \tag{6.6}$$

Here $B = B_1 + B_2 + B_3$ is the usual baryon number. The latter condition is very helpful as it directly provides the relation between the fermion charges given a particular model. For example, one can consider the following anomaly-free models that correspond to different choices of the coefficients in Eq. (6.3) or (6.5) and contribute to CEνNS interactions of ν_e and ν_μ:

$B - L = G_B(1, 1, 1, 1)$ Here $L = L_e + L_\mu + L_\tau$ is the total lepton number. This is the most popular Z' model [291, 298, 299]). It was considered recently in several CEνNS phenomenological analyses [1, 5, 297, 310–312]. Note that, since there are no ν_τ's in the COHERENT neutrino beam, bounds on the coupling constant in the anomaly-free model generated by

$$G_B(1, 3/2, 3/2, 0) = B - \frac{3}{2}\left(L_e + L_\mu\right)\,, \tag{6.7}$$

considered, e.g., in Ref. [313], can be obtained from the bounds on the coupling constant $g_{Z'}$ in the $B - L$ model by rescaling it by the factor $\sqrt{2/3}$, because the ν_e and ν_μ couplings are changed by the same factor $3/2$.

$B_y + L_\mu + L_\tau = G(1, -y, y - 3, 0, -1, -1)$ In this model [311, 314], $B_y = B_1 - yB_2 + (y - 3)B_3$.

$\boldsymbol{B-3L_e=G_B(1,3,0,0)}$ This model was considered, e.g., in Refs. [311–313, 315]. In this case, only the ν_e CEνNS cross section is affected by the new Z'-mediated interaction. Moreover, since there are no ν_τs in the COHERENT neutrino beam, the bounds on the coupling constant $g_{Z'}$ obtained in this model can be extended to all the anomaly-free models generated by

$$G_B(1, 3w_e, 0, 3(1-w_e)) = B - 3w_e L_e - 3(1-w_e)L_\tau \tag{6.8}$$

through a rescaling of the coupling constant by a factor $1/\sqrt{w_e}$.

$\boldsymbol{B-3L_\mu=G_B(1,0,3,0)}$ This model was considered, e.g., in Refs. [311, 312, 315]. In this case, only the ν_μ CEνNS cross section is affected by the new Z'-mediated interaction and, in analogy with the argument in the previous item, the bounds on the coupling constant $g_{Z'}$ obtained in this model can be extended to all the anomaly-free models generated by

$$G_B(1, 0, 3w_\mu, 3(1-w_\mu)) = B - 3w_\mu L_\mu - 3(1-w_\mu)L_\tau \tag{6.9}$$

through a rescaling of the coupling constant by a factor $1/\sqrt{w_\mu}$. For example, the $B-(3/2)(L_\mu+L_\tau)$ [311, 315] model is obtained with $w_\mu = 1/2$.

$\boldsymbol{B-2L_e-L_\mu=G_B(1,2,1,0)}$ This model was considered in Ref. [312]. In analogy with the discussion in the previous items, the bounds on the coupling constant $g_{Z'}$ obtained in this model can be extended to all the anomaly-free models generated by

$$G_B(1, 2w_1, w_1, 3(1-w_1)) = B - 2w_1 L_e - w_1 L_\mu - 3(1-w_1)L_\tau \tag{6.10}$$

through a rescaling of the coupling constant by a factor $1/\sqrt{w_1}$.

$\boldsymbol{B-L_e-2L_\mu=G_B(1,1,2,0)}$ This model was considered in Ref. [312]. Again, in analogy with the discussion in the previous items, the bounds on the coupling constant $g_{Z'}$ obtained in this model can be extended to all the anomaly-free models generated by

$$G_B(1, w_2, 2w_2, 3(1-w_2)) = B - w_2 L_e - 2w_2 L_\mu - 3(1-w_2)L_\tau \tag{6.11}$$

through a rescaling of the coupling constant by a factor $1/\sqrt{w_2}$.

It is clear that one could restrict the analysis to a smaller class of models, and then derive afterwards the constraints on other ones.
The effects of some of the models discussed above on the CEνNS differential event rates that are predicted for the COHERENT Ar and CsI detectors are illustrated in Fig. 6.2. In these figures, we set $g_{Z'} = 10^{-4}$ and $M_{Z'} = 10$ MeV in order to compare the model predictions with the SM one for both argon and CsI detectors. The effect of the light mediator is rather similar for the two target nuclei considered and in particular the vector boson mediator contribution increases for small values of the recoil energy because of the propagator in Eq. 6.2. The different scales of $T_{\rm nr}$ in the left and right plots are obviously due to the different masses of the nuclei.

In the case of the universal Z' model, there is a deep dip generated by a cancellation between the negative SM and the positive Z' contributions to the nuclear weak charge in Eq. 6.2. In fact, in the universal model, all the gauge charges are positive, so that the Z' contribution to the nuclear weak charge is positive, contrary to the negative value of the SM contribution.

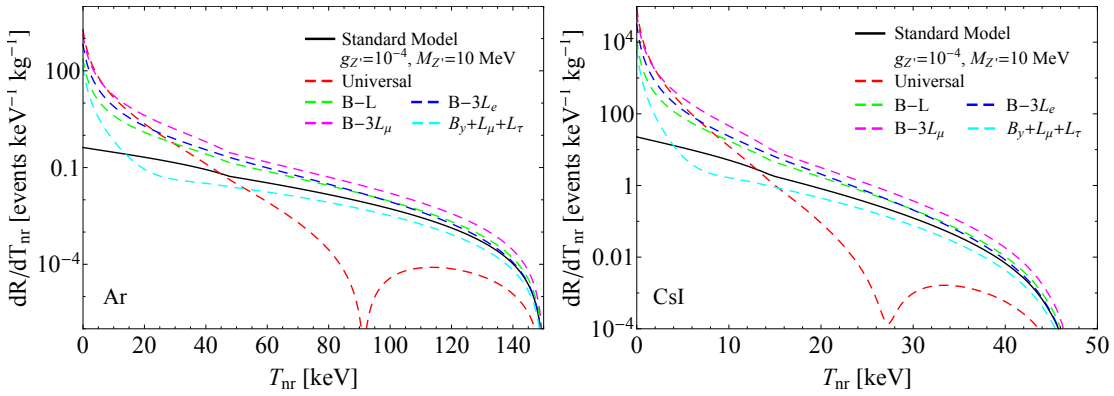

Figure 6.2: Predicted CEνNS differential event rates corresponding to the experimental configuration and data taking time of the COHERENT Ar (Left) and CsI (Right) detectors for some of the vector mediator models coupling to nucleons considered in Ref. [5].

Indeed, it can be retrieved that the cancellation occurs for [1, 5]

$$T_{\rm nr} = -\frac{1}{2m_N}\left(\frac{3g_{Z'}^2}{\sqrt{2}G_F}\frac{ZF_Z(|\vec{q}|^2)+NF_N(|\vec{q}|^2)}{g_V^pZF_Z(|\vec{q}|^2)+g_V^nNF_N(|\vec{q}|^2)}+M_{Z'}^2\right), \tag{6.12}$$

which corresponds to $T_{\rm nr} \simeq 92$ keV for Ar and $T_{\rm nr} \simeq 27$ keV for CsI in in Fig. 6.2 left and right, respectively.
By looking at the charges in Tab. 6.1, one can notice that a cancellation is present also for ν_μ in the $B_y + L_\mu + L_\tau$ model, since the quarks and ν_μ have both positive charges. In this case, the cancellation occurs at [5]

$$T_{\rm nr} = -\frac{1}{2m_N}\left(\frac{g_{Z'}^2}{\sqrt{2}G_F}\frac{ZF_Z(|\vec{q}|^2)+NF_N(|\vec{q}|^2)}{g_V^pZF_Z(|\vec{q}|^2)+g_V^nNF_N(|\vec{q}|^2)}+M_{Z'}^2\right), \tag{6.13}$$

which corresponds to $T_{\rm nr} \simeq 29$ keV for Ar and $T_{\rm nr} \simeq 8$ keV for CsI. Since the cancellation is present only for ν_μ and for ν_e, the SM contribution from ν_e can not be cancelled. Therefore, there are only shallow dips at these energies for this model in Fig. 6.2. Note that the total differential rate is smaller than the SM differential rate for energies above the dip, because the positive and smaller Z' contribution to $Q^V_{\mu,\rm SM+V}$ is added to the dominant negative SM contribution, decreasing the absolute value of $Q^V_{\mu,\rm SM+V}$.
In all the other models above the quarks and leptons have opposite charges and thus, the Z' contribution to the weak charge is negative as the SM contribution. Therefore, the total differential rate is always larger than the SM rate for all values of $T_{\rm nr}$.

We also consider the following three possible $L_\alpha - L_\beta$ models that are anomaly-free and can be gauged without extending the SM content with right-handed neutrinos [300–303]:

$\boldsymbol{L_e - L_\mu = G_B(0,-1,1,0)}$ This model, obtained from Eq. (6.5) with $c_B = 0$, $c_e = -1$ $c_\mu = 1$, and $c_\tau = 0$, was considered, e.g., in Refs. [5, 302, 311, 316].

$\boldsymbol{L_e - L_\tau = G_B(0,-1,0,1)}$ This model, obtained from Eq. (6.5) with $c_B = 0$, $c_e = -1$ $c_\mu = 0$, and $c_\tau = 1$, was considered, e.g., in Refs. [5, 302, 311, 316].

$\boldsymbol{L_\mu - L_\tau = G_B(0,0,-1,1)}$ This model, obtained from Eq. (6.5) with $c_B = 0$, $c_e = 0$ $c_\mu = -1$, and $c_\tau = 1$, was considered in many papers, e.g., in Refs. [1, 5, 281, 297, 302, 304–306, 317].

Since in these models, the Z' vector boson does not couple to quarks, there are no tree-level interactions that contribute to CEνNS.

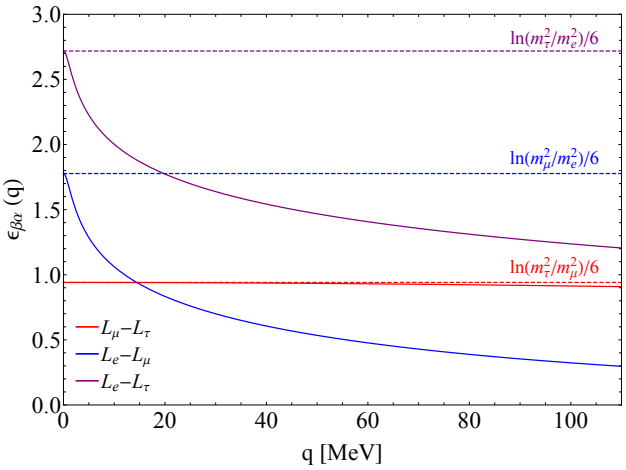

Figure 6.3: Values of $\varepsilon_{\beta\alpha}$ in Eq. (6.15) for each of the three $L_\alpha - L_\beta$ symmetries as a function of the momentum transfer $q \simeq \sqrt{2MT_{\rm nr}}$ in the range of the COHERENT CEνNS data.

However, there is kinetic mixing of the Z' and the photon at the one-loop level that induces a contribution to CEνNS through the photon interaction with quarks [304–306] as shown by the right diagram in Fig. 6.1. The CEνNS cross section in these three models is [1, 5, 304]

$$\left(\frac{d\sigma}{dT_{\rm nr}}\right)^{\nu_\ell - \mathcal{N}}_{L_\alpha - L_\beta}(E, T_{\rm nr}) = \frac{G_F^2 m_N}{\pi}\left(1 - \frac{T_{\rm nr}}{E_\nu} - \frac{m_N T_{\rm nr}}{2E_\nu^2}\right) \tag{6.14}$$
$$\times \left\{\left[g_V^p(\nu_\ell) + \frac{\sqrt{2}\alpha g_{Z'}^2\left(\delta_{\ell\alpha}\varepsilon_{\beta\alpha}(|\vec{q}|) + \delta_{\ell\beta}\varepsilon_{\alpha\beta}(|\vec{q}|)\right)}{\pi G_F\left(|\vec{q}|^2 + M_{Z'}^2\right)}\right] Z F_Z(|\vec{q}|^2) + g_V^n N F_N(|\vec{q}|^2)\right\}^2,$$

where α is the electromagnetic fine-structure constant and $\varepsilon_{\beta\alpha}(|\vec{q}|)$ is the one-loop kinetic mixing coupling, that is given by [305, 306]

$$\varepsilon_{\beta\alpha}(|\vec{q}|) = \int_0^1 x(1-x)\ln\left(\frac{m_\beta^2 + x(1-x)|\vec{q}|^2}{m_\alpha^2 + x(1-x)|\vec{q}|^2}\right) dx\,, \tag{6.15}$$

where m_β and m_α are the charged lepton masses. Note that the Z' contribution is invariant for $\alpha \leftrightarrows \beta$, as it should be, since $L_\alpha - L_\beta$ and $L_\beta - L_\alpha$ are physically equivalent. Note also that the sign of the loop contribution of the i charged lepton to ν_ℓ scattering is given by $-Q'_i Q'_\ell$, where the minus comes from the negative electric charge of the charged lepton propagating in the loop. Therefore, the mass of the charged lepton with the same flavor ℓ of the scattering neutrino is always at the denominator of the logarithm in Eq. (6.15) and the mass of the other charged lepton taking part to the new symmetry is always at the numerator. Figure 6.3 shows the value of $\varepsilon_{\beta\alpha}(|\vec{q}|)$ for each of the three $L_\alpha - L_\beta$ symmetries as a function of momentum transfer $|\vec{q}|$ in the range of the COHERENT CEνNS. One can see that only $\varepsilon_{\tau\mu}$ is almost constant, because $|\vec{q}| \ll m_\tau$ and $|\vec{q}| < m_\mu$. In this case it is possible to approximate $\varepsilon_{\tau\mu} \simeq \ln(m_\tau^2/m_\mu^2)/6$, as done in Refs. [1, 297, 304]. On the other hand, for the symmetries $L_e - L_\mu$ and $L_e - L_\tau$ the $|\vec{q}|$ dependence of $\varepsilon_{\beta\alpha}$ on $|\vec{q}|$ must be taken into account, because $|\vec{q}| \gg m_e$.

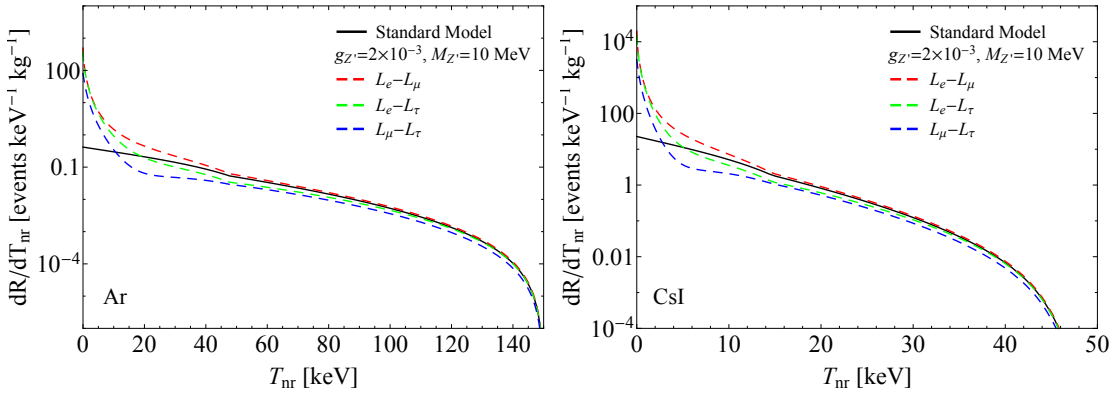

Figure 6.4: Predicted CEνNS differential event rates corresponding to the experimental configuration and data taking time of the COHERENT Ar (Left) and CsI (Right) detectors in the vector mediator models coupling only to a specific flavor structure considered in Ref. [5].

In Fig. 6.4, we show the effects of the Z' contribution to the CEνNS differential event rates that are predicted for the COHERENT Ar (Left) and CsI (Right) detectors in the $L_\alpha - L_\beta$ models. In this figure, we set $g_{Z'} = 2 \times 10^{-3}$ and $M_{Z'} = 10$ MeV and we compared the model predictions with that of the SM. One can see that, as for the models in Fig. 6.2 discussed above, the effects of the light mediator are similar for the Ar and CsI detectors and the vector boson mediator contribution increases for small recoil energies because of the propagator in Eq. 6.14.
In the case of the $L_\mu - L_\tau$ model the Z' contribution to $Q^V_{\mu,\mathrm{SM+V}}$ is positive and there can be a cancellation with the negative SM contribution, as in the case of the universal model considered before. The cancellation occurs at [1, 5]

$$T_{\mathrm{nr}} = -\frac{1}{2m_N}\left(\frac{\alpha g_{Z'}^2}{3\pi\sqrt{2}G_F}\ln\left(\frac{m_\tau^2}{m_\mu^2}\right)\frac{ZF_Z(|\vec{q}|^2)}{g_V^p ZF_Z(|\vec{q}|^2) + g_V^n NF_N(|\vec{q}|^2)} + M_{Z'}^2\right), \quad (6.16)$$

which corresponds to $T_{\mathrm{nr}} \simeq 23$ keV for Ar and $T_{\mathrm{nr}} \simeq 6$ keV for CsI. Since there is no interaction of ν_e with the Z', the correspondent SM contribution can not be

cancelled. Therefore, similarly to the discussion for the $B_y + L_\mu + L_\tau$ model, there are only shallow dips at these energies in Figs. 6.4 for this model, and after those energies, the rate remains below the SM one.
In the case of the $L_e - L_\tau$ model, there can be a cancellation as well, but it is difficult to estimate for which value of $T_{\rm nr}$ this would happen, because of the strong dependence of $\varepsilon_{\tau e}$ on momentum transfer, and thus the recoil energy, shown in Fig. 6.3. However, one can see from Fig. 6.4 that there are shallow dips of the differential rates at larger values of $T_{\rm nr}$ than those in the $L_\mu - L_\tau$ model, because $\varepsilon_{\tau e} > \varepsilon_{\tau\mu}$, as shown in Fig. 6.3. In the case of the $L_e - L_\mu$ model, the situation is more complicated, because the Z' contribution to $Q^V_{e,\rm SM+V}$ is positive, since $\varepsilon_{\mu e} > 0$, but the Z' contribution to $Q^V_{\mu,\rm SM+V}$ is negative, since $\varepsilon_{e\mu} < 0$. Therefore, the Z' contributions of the dominant ν_μ and $\bar{\nu}_\mu$ fluxes enhance the CEνNS differential event rate with respect to the SM prediction, whereas the subdominant ν_e flux generate a decrease for sufficiently large values of $T_{\rm nr}$ (about 40 keV for Ar and 15 keV for CsI). As a result of these opposite contributions, the total CEνNS differential rates of the $L_e - L_\mu$ model shown in Fig. 6.4 are only slightly larger than the SM rates in almost the considered recoil energy range.

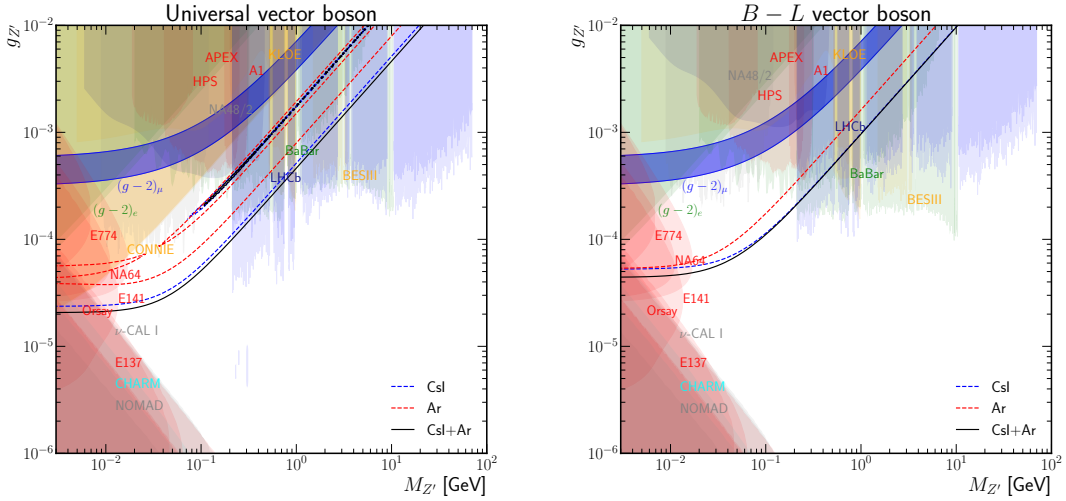

Figure 6.5: Excluded regions (2σ) in the $M_{Z'}$-$g_{Z'}$ plane for the universal vector mediator model (Left) and for the $B - L$ model (Right). The blue dashed, the red dashed and the black solid curves correspond to the results of the analysis of COHERENT CsI, LAr and their combination, respectively. The other colored regions represent the allowed contours coming from several other experimental measurements obtained by using the *darkcast* code [318].

We have analyzed the COHERENT CsI [54] and LAr [53] data to obtain constraints on the aforementioned light mediator models, and all the results are reported in Ref. [5]. Here, we present only the results on a smaller selection of significant models, such as the universal model, the $B-L$ and the $L_\mu-L_\tau$ to give an insight on three different model types, one anomalous model, one that can be made anomaly-free and which has direct coupling to all fermions, and one that couples only to

muons and taus. In order to derive such constraints, the chi-square in Eq. 2.75 for CsI and Eq. 2.77 have been modified by calculating the number of CEνNS events in each experimental bin using the proper interaction cross section. By varying the values of the coupling and the boson mass, it is possible to find an exclusion contour, and the results are shown in Fig. 6.5 for the universal (Left) and $B-L$ (Right) models, respectively, and in Fig. 6.6 for the $L_\mu - L_\tau$ model. Our results are compared to the constraints coming from other experiments, obtained by using the *darkcast* [318] code, represented by the colored regions.
In the exclusion plots, the black line delimits the 2σ allowed regions obtained from the combined analysis of the CsI and Ar data, while the blue and red lines delimit the excluded regions obtained from the CsI and Ar data, respectively [5].
Considering as an example the combined analysis of the CsI and Ar data, one can see that in the low-mass region the black line, which represents the upper boundary of the 2σ allowed region, flattens due to the fact that the contribution of the Z' boson to $Q^V_{\ell,\mathrm{SM+V}}$ does not depend on $M_{Z'}$ since $|\vec{q}| \gg M_{Z'}$ in the Z' boson propagator. On the other hand, for higher masses, the contribution of the Z' boson is suppressed by a large $M_{Z'}$, and the boundary is given by a diagonal line proportional to $M_{Z'}$. The numerical values of the 2σ limits for all the models are reported in Table II of Ref. [5].
In the left plot in Fig. 6.5, one can notice the presence of a thin diagonal black strip, which corresponds to the parameter space in which $Q^V_{\ell,\mathrm{SM+V}} \simeq -Q^V_{\mathrm{SM}}$, that leads to a degeneracy with the SM cross section, as explained in Ref. [1, 5]. The model parameters corresponding to the strips are

$$(g^{\mathrm{univ}}_{Z'})_{\mathrm{strip}} \simeq \sqrt{\frac{N}{A}\frac{\sqrt{2}G_F M^2_{Z'}}{3}} \simeq 1.8\times 10^{-3}\,\frac{M_{Z'}}{\mathrm{GeV}}. \tag{6.17}$$

Let us note that such strip is not present in the right plot of Fig. 6.5, as its existence is correlated to the possibility of having a cancellation of the CEνNS differential event rate, as discussed before, which is present for the universal model but not for the $B-L$ one. Indeed, all the models that can have a cancellation of the CEνNS differential (i.e. the universal, $B_y + L_\mu + L_\tau$, $L_e - L_\tau$, and $L_\mu - L_\tau$ models) have an allowed strip. The cancellation for the universal model occurs in the excluded parameter space between the lower allowed region and the thin allowed strip for

$$(g^{\mathrm{univ}}_{Z'})_{\mathrm{canc}} \simeq \sqrt{\frac{N}{A}\frac{\sqrt{2}G_F M^2_{Z'}}{6}} \simeq 1.3\times 10^{-3}\,\frac{M_{Z'}}{\mathrm{GeV}}. \tag{6.18}$$

However, since the Ar data are less constraining than the CsI one, in the case of the universal model the strip is wide and it extends to small values of $M_{Z'}$. It is represented by the two red dashed lines that cross around $M_{Z'} \sim 50\,\mathrm{MeV}$.
The strip in the case of the $L_\mu - L_\tau$ model shown in Fig. 6.6 occurs for

$$(g^{L_\mu - L_\tau}_{Z'})_{\mathrm{strip}} \approx \sqrt{\frac{N}{Z}\frac{6\pi G_F M^2_{Z'}}{\sqrt{2}\alpha\ln(m^2_\tau/m^2_\mu)}} \approx 7\times 10^{-2}\,\frac{M_{Z'}}{\mathrm{GeV}}. \tag{6.19}$$

In general, the limits obtained from the CsI data are stricter than those obtained from the Ar data and are close to those of the combined fit.

For the universal model, we show also the limits obtained from the CONNIE reactor CEνNS experiment [319] (orange shaded region), which are rather similar to the ones obtained by analyzing COHERENT data, although less stringent.
In Fig. 6.5 and in Fig. 6.6, we show the $(g-2)_\mu$ 2σ allowed band, i.e. the parameter space which could provide an explanation of the anomalous magnetic moment of the muon under the considered model [277, 289]. One can see that the explanation of the $(g-2)_\mu$ anomaly with the universal model is excluded by the combination of the non-CEνNS exclusion limits, and also by both the CONNIE CEνNS bounds and the COHERENT ones. Instead, for the $B-L$ model, the COHERENT constraints are the one that completely rule out the $(g-2)_\mu$ explanation, improving significantly the previous bound, especially in the intermediate region $20\text{ MeV} \lesssim M_{Z'} \lesssim 200\text{ MeV}$ and $5\times10^{-5} \lesssim g_{Z'} \lesssim 3\times10^{-4}$. It is in such intermediate range that COHERENT results to be strongly constraining also for the universal model, namely for $20\text{ MeV} \lesssim M_{Z'} \lesssim 200\text{ MeV}$ and $2\times10^{-5} \lesssim g_{Z'} \lesssim 10^{-4}$. It is clear from Fig. 6.5, that COHERENT data play a major role in covering this intermediate parameter space for both the universal and the $B-L$ models.

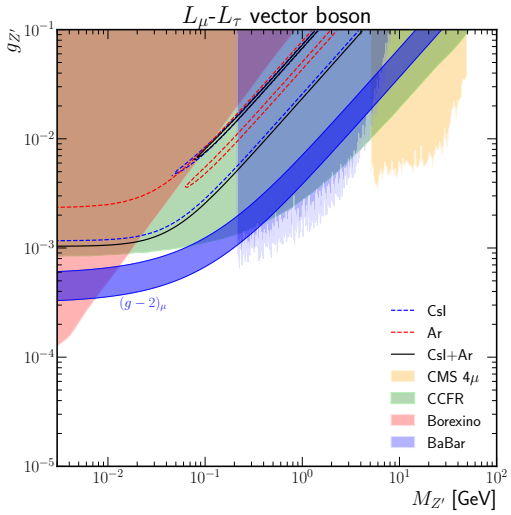

Figure 6.6: Excluded regions (2σ) in the $M_{Z'}$-$g_{Z'}$ plane for the $L_\mu - L_\tau$ vector mediator model. The blue dashed, the red dashed and the black solid curves correspond to the results of the analysis of COHERENT CsI, LAr and their combination, respectively. The other colored regions represent other experimental constraints [318].

From Fig. 6.6, it is evident that less experimental constraints are available, because of the necessity of studying processes involving the μ or τ flavors. Nevertheless, the COHERENT constraints are rather loose, since they are all less stringent than the constraints coming from the neutrino trident production constraints from CCFR [320, 321]. The COHERENT constraints are not very stringent also because the rate from the ν_e part of the flux is not modified by the presence of a new Z' under the $L_\mu - L_\tau$ symmetry, and there is no ν_τ contribution. All this said, it is interesting to notice that for $10\text{ MeV} \lesssim M_{Z'} \lesssim 200\text{ MeV}$ and $3\times10^{-4} \lesssim g_{Z'} \lesssim 10^{-3}$, the $(g-2)_\mu$ strip still eludes the exclusions. It will be fundamental, with next gen-

eration COHERENT detectors [84], to try to exclude completely such parameter space, or perhaps to find a signature of new physics.

6.1.2 —— Scalar models ——

We consider also contributions to the CEνNS process of interactions mediated by a light scalar boson [5, 244, 322–325], which differ from those mediated by a light vector boson for two fundamental reasons. First, the helicity-flipping interactions mediated by a scalar boson contribute incoherently to the CEνNS process with respect to the helicity-conserving SM contribution. Therefore, in the scalar case, the new contribution consists in an addition to the cross section, not to the amplitude of the process as in the vector case, so that the diagrams can not interfere. Second, the scalar charges of the nucleons are not simply given by the sum of the charges of the valence quarks as in the vector case, because the scalar currents are not conserved as the vector currents. Hence, the scalar charges of the nucleons must be calculated and the results may suffer from large theoretical uncertainties.

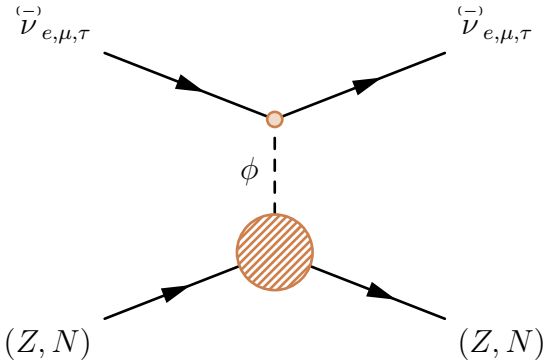

Figure 6.7: Diagram contributing the CEνNS process in presence of a new scalar boson mediator ϕ. The gold color for the vertices are used to indicate that the couplings are not the SM one, but are the ones relative to the new gauge symmetry.

The generic Lagrangian that describes the interaction of a scalar mediator ϕ with neutrinos and quarks is

$$\mathcal{L}_{\phi}^{S} = -\phi \left[\sum_{\ell=e,\mu,\tau} g_{\phi}^{\nu_\ell}\, \overline{\nu_\ell}\, \nu_\ell + \sum_{q=u,d} g_{\phi}^{q}\, \overline{q}\, q \right] , \tag{6.20}$$

where $\nu_\ell = \nu_{\ell L} + \nu_{\ell R}$ and $g_{\phi}^{\nu_\ell}$ and g_{ϕ}^{q} are the coupling constants. Let us note, that in order to consider the scalar model we need to introduce also the right-handed neutrinos.
In Fig. 6.7 we show the ϕ-mediated diagram contributing to the CEνNS process. Since the contribution of the scalar boson interaction to the CEνNS cross section adds incoherently to the SM cross section [244, 322–325], the total cross section would be

$$\frac{d\sigma_{\nu_\ell\text{-}\mathcal{N}}}{dT_{\text{nr}}} = \left(\frac{d\sigma_{\nu_\ell\text{-}\mathcal{N}}}{dT_{\text{nr}}}\right)_{\text{SM}} + \left(\frac{d\sigma_{\nu_\ell\text{-}\mathcal{N}}}{dT_{\text{nr}}}\right)_{\text{scalar}} , \tag{6.21}$$

with the scalar cross section defined as

$$\left(\frac{d\sigma_{\nu_\ell\text{-}\mathcal{N}}}{dT_{\rm nr}}\right)_{\rm scalar} = \frac{m_N^2 T_{\rm nr}}{4\pi E_\nu^2}\,\frac{(g_\phi^{\nu_\ell})^2\mathcal{Q}_\phi^2}{(|\vec{q}|^2+M_\phi^2)^2}, \tag{6.22}$$

where M_ϕ is the mass of the new scalar mediator and $\mathcal{Q}_\phi$ is the scalar charge of the nucleus, given by

$$\mathcal{Q}_\phi = ZF_Z(|\vec{q}|^2)\sum_{q=u,d} g_\phi^q\langle p|\bar{q}q|p\rangle + NF_N(|\vec{q}|^2)\sum_{q=u,d} g_\phi^q\langle n|\bar{q}q|n\rangle. \tag{6.23}$$

It is sometimes written in the form of [322–325]

$$\mathcal{Q}_\phi = ZF_Z(|\vec{q}|^2)\sum_{q=u,d} g_\phi^q\frac{m_p}{m_q}f_q^p + NF_N(|\vec{q}|^2)\sum_{q=u,d} g_\phi^q\frac{m_n}{m_q}f_q^n, \tag{6.24}$$

where m_p, m_n and m_q being the proton, neutron and quark masses, respectively, and with the quark contributions to the nucleon masses defined as

$$f_q^{\mathbb{N}} = \frac{m_q}{m_n}\,\langle \mathbb{N}|\bar{q}q|\mathbb{N}\rangle, \tag{6.25}$$

for $\mathbb{N} = p, n$. Since the scalar currents are not conserved, the scalar charges of the nucleons are not simply given by the sums of the charges of their valence quarks, as in the case of a vector boson mediator (see Eq. (6.2)). Hence, the proton and neutron matrix elements of the scalar quark current must be calculated (see, e.g., the recent Refs. [326–329]). For simplicity, one can consider equal couplings for the u and d quarks and equal couplings for ν_e and ν_μ

$$g_\phi^u = g_\phi^d = g_\phi^q \quad \text{and} \quad g_\phi^{\nu_e} = g_\phi^{\nu_\mu} = g_\phi^\nu. \tag{6.26}$$

In this simplified framework, the nuclear scalar charge becomes

$$\mathcal{Q}_\phi = g_\phi^q\left[ZF_Z(|\vec{q}|^2)\langle p|\bar{u}u+\bar{d}d|p\rangle + NF_N(|\vec{q}|^2)\langle n|\bar{u}u+\bar{d}d|n\rangle\right]. \tag{6.27}$$

Considering the isospin approximation, we obtain[5]

$$\langle p|\bar{u}u+\bar{d}d|p\rangle = \langle n|\bar{u}u+\bar{d}d|n\rangle = \langle N|\bar{u}u+\bar{d}d|N\rangle = \frac{\sigma_{\pi N}}{\overline{m}_{ud}}, \tag{6.28}$$

where $\overline{m}_{ud} = (m_u+m_d)/2$ and $\sigma_{\pi N}$ is the pion-nucleon σ-term that has been determined in different ways in the literature (see the recent review in Ref. [330]). Recent values have been obtained from pionic atoms and pion-nucleon scattering [326, 331, 332] and from lattice calculations [327, 329]. Since there are large uncertainties on the values of $\sigma_{\pi N}$ and $\overline{m}_{ud}$, we choose a reference value for $\sigma_{\pi N}/\overline{m}_{ud}$ given by the ratio of the central value of $\sigma_{\pi N}$ determined in Ref. [326] ($\sigma_{\pi N} = 59.1\,$MeV) and the central PDG values [203] $m_u = 2.16\,$MeV $m_d = 4.67\,$MeV, that gives

$$\left(\frac{\sigma_{\pi N}}{\overline{m}_{ud}}\right)_{\rm ref} = 17.3, \tag{6.29}$$

[5]Let us note that we are neglecting the small $|\vec{q}|$-dependent corrections discussed in Ref. [60].

that allows us to write the scalar cross section (6.22) as

$$\left(\frac{d\sigma_{\nu_\ell\text{-}\mathcal{N}}}{dT_{\rm nr}}\right)_{\rm scalar} = \frac{m_N^2 T_{\rm nr}}{4\pi E_\nu^2}\,\frac{\tilde{g}_\phi^4}{(|\vec{q}|^2+M_\phi^2)^2}\left(\frac{\sigma_{\pi N}}{\overline{m}_{ud}}\right)^2_{\rm ref}\left[ZF_Z(|\vec{q}|^2)+NF_N(|\vec{q}|^2)\right]^2, \tag{6.30}$$

with

$$\tilde{g}_\phi^2 = g_\phi^{\nu_\ell} g_\phi^q\,\frac{\sigma_{\pi N}/\overline{m}_{ud}}{(\sigma_{\pi N}/\overline{m}_{ud})_{\rm ref}}. \tag{6.31}$$

In this way, the results of other calculations can be compared with our results by appropriate rescaling of $\tilde{g}_\phi$ according to the assumptions. The approach followed is different from that in Refs. [296, 322, 333], which considered different values for the proton and neutron matrix elements in Eq. (6.27): $\langle p|\bar{u}u+\bar{d}d|p\rangle = 15.1$ and $\langle n|\bar{u}u+\bar{d}d|n\rangle = 14$. These values correspond to a rather large 8% violation of the isospin symmetry.
Furthermore, we are neglecting the contribution given by the strange and heavier quarks, whose contributions to the nucleon mass have very large uncertainties [334].

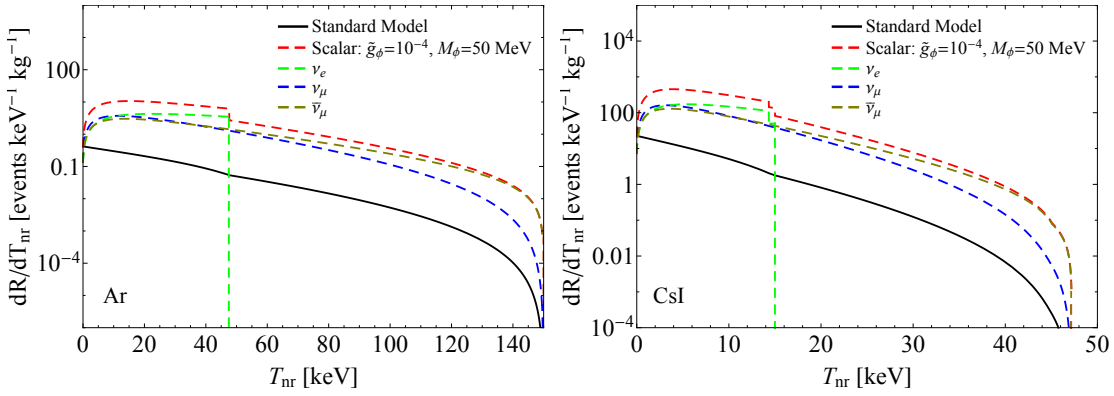

Figure 6.8: Predicted CEνNS differential event rates corresponding to the experimental configuration and data taking time of the COHERENT Ar (a) and CsI (b) detectors in the universal scalar mediator model considering $\tilde{g}_\phi = 10^{-4}$ and $M_\phi = 50\,\text{MeV}$ compared to the SM prediction (black).

In Fig. 6.8, we illustrate the effect of the scalar boson mediator on the CEνNS differential event rates for the COHERENT Ar and CsI detectors fixing $\tilde{g}_\phi = 10^{-4}$ and $M_\phi = 50$ MeV. We show by using different colors also the single neutrino flavor component contributing to the total rate. One can see that the total CEνNS rates are larger than the SM rates, because the scalar boson cross section adds incoherently to the SM cross section, and hence, no interference effect can occur. One can also notice that the total CEνNS rates represented by the red-dashed lines have small discontinuities at $T_{\rm nr} \simeq 48$ keV for Ar and $T_{\rm nr} \simeq 15$ keV for CsI. These values correspond to the maximum nuclear kinetic energy $T_{\rm nr}^{\rm max} = 2E_\nu^2/m_N$ for the monoenergetic ν_μ from pion decay ($E_\nu = 29.8$ MeV), as shown by the green-dashed lines that represent the ν_μ contributions. Furthermore, the presence of $T_{\rm nr}$ in the numerator of the scalar cross section in Eq. (6.22) produces the decrease of the

scalar contribution for low recoil energies, which is visible in Fig. 6.8.
Following the same procedure adopted for the vector boson mediator, we modified the number of CEνNS events in the χ^2s defined in Eq. 2.77 and Eq. 2.75 by using the cross section defined in Eq. 6.21, and then perform a two-parameter fit by letting both the coupling $\tilde{g}_\phi$ and the mass M_ϕ free-to-vary. The exclusion contours at 2σ C.L. are shown in Fig. 6.9, together with the constraints coming from other experimental probes and the allowed band for the explanation of the $(g-2)_\mu$ anomaly. Indeed, also a scalar boson could produce an effect on the muon anomalous magnetic moment, however, the derived constraints from the analysis of the COHERENT data completely excludes such explanation in the whole mass range considered [5]. It is also interesting to notice how the COHERENT data [53, 54] allow one to significantly improve the previously existing constraints. Of course, the considered scalar model is quite a simplified one, since it assumes universal couplings, but in principle, one could extend the model similarly to what was discussed in the case of vector mediators.

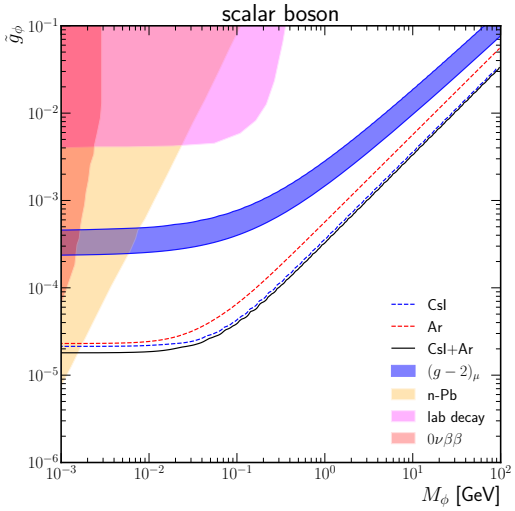

Figure 6.9: Excluded regions (2σ) in the $M_{Z'}$-$g_{Z'}$ plane for the scalar mediator model obtained by the COHERENT analysis, compared to other constraints [5].

Let us note, that also in the case of the scalar mediator, the constraints from the COHERENT CsI data are more stringent than the ones coming from COHERENT Ar data, so that the combined limits (black curve in Fig. 6.9) are practically identical to the CsI limits (in blue), but for a slight improvement for masses below ~ 100 MeV.

6.1.3 —— Parity violating model: Z_d ——

The $U(1)'$ models discussed so far are characterized by either a direct coupling between the new mediator and the SM fermion or a coupling through a kinetic mixing effect. We will now discuss a particular model, known as 'dark Z', Z_d, in which the dominant effect is the mass mixing. This model was introduced

and then discussed in Refs. [3, 335–338], where the new boson is assumed to be lighter than the usual Z boson, and it manifests its properties through the kinetic and mass mixing with the SM Z boson and the photon γ.
In Fig. 6.10 the Feynman diagram representing an example of Z_d interaction is shown in the case of the APV process. In the diagram, we show that the Z_d is produced through kinetic mixing (brown loop) with the γ and then it produces itself a Z boson through mass mixing (brown cross). The strength of such mixing processes depends on the model parameters, which in this case are three: ε which quantifies the kinetic mixing, δ which is related to the mass matrix mixing and the boson mass, m_{Z_d}.

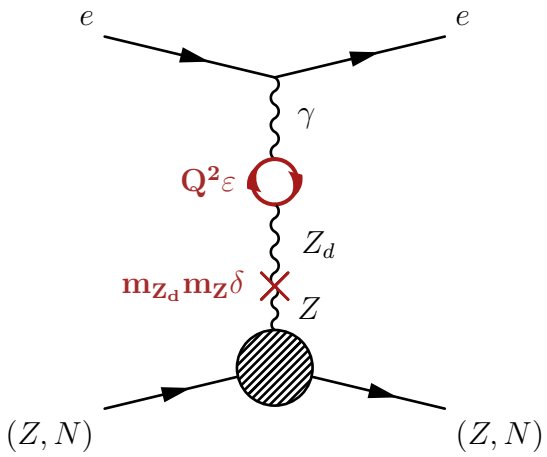

Figure 6.10: Example of diagram characterizing the interaction modes of the dark Z, boson Z_d contributing to the APV process. The loop indicates the kinetic mixing between the photon γ and the dark Z boson Z_d, while the cross indicates the mass mixing between the Z_d and the SM Z bosons. The brown color indicates the fact that such couplings are unknown as they depend on the model. The other two vertices are not colored because there the couplings are the SM ones.

The $Z - Z_d$ mass matrix mixing is usually parameterized by introducing the ε_Z coupling, in analogy with the kinetic mixing parameter ε, which is defined by $\varepsilon_Z = (m_{Z_d}/m_Z\delta)$.
However, in more recent works, the δ parameter has often been replaced by the following expression [3, 339]

$$\delta' \simeq \delta + \frac{m_{Z_d}}{m_Z}\,\varepsilon\,\tan\theta_W, \tag{6.32}$$

which incorporates higher order corrections, even if small for $m_{Z_d} \ll m_Z$. Here, θ_W is the SM predicted running of the Weinberg angle [28, 203].
As a consequence of the mixing, the Z_d coupling with the SM results into an interaction Lagrangian [335, 337, 338]

$$\mathcal{L}_{\text{int}} = \Big(- e_0\varepsilon J_\mu^{em} - \frac{g}{2\cos\theta_W}\frac{m_{Z_d}}{m_Z}\delta' J_\mu^{NC}\Big) Z_d^\mu, \tag{6.33}$$

where e_0 is the electric charge, J_μ^{NC} and J_μ^{em} are respectively the neutral and electromagnetic currents, whereas Z_d^μ is the new boson field. Already from the

Lagrangian it is possible to see that ε is related to the mixing process with the photon, while δ (or better δ') to the $Z - Z_d$ mixing.
Effectively, the contribution to the weak neutral current amplitudes induced by the Z_d boson can be accounted for by substituting $G_F \to \rho_d G_F$ and $\sin^2\theta_W(Q^2) \to \kappa_d \sin^2\theta_W(Q^2)$ [335, 336, 339, 340], where

$$\rho_d = 1 + (\delta + \frac{m_{Z_d}}{m_Z}\,\varepsilon\,\tan\theta_W)^2 f\Big(\frac{Q^2}{m_{Z_d}^2}\Big), \tag{6.34}$$

and

$$\kappa_d = 1 - \varepsilon(\delta + \frac{m_{Z_d}}{m_Z}\,\varepsilon\,\tan\theta_W)\frac{m_Z}{m_{Z_d}}\cot\theta_W f\Big(\frac{Q^2}{m_{Z_d}^2}\Big). \tag{6.35}$$

The term $f(Q^2/m_{Z_d}^2)$ is related to the propagator of the new boson and it may assume different forms depending on the experimental process [190, 341]. Clearly, we see that the effect of the new boson directly affects the running of the weak mixing angle.
Moreover, the existence of a Z_d boson would contribute to the leptonic magnetic moment, a_ℓ (with $\ell = e,\ u$), at one-loop level. This motivated the study of such BSM model as a possible explanation of the muon anomalous magnetic moment tension. However, differently from the Z' and the scalar boson cases, the dark Z boson would contribute both via a vector and an axial contribution, although the latter one is usually negligible. As the axial contribution scales with the δ parameter, while the vector one mainly depends on ε, we can say that the contribution to the anomalous magnetic moment practically does not depend on δ. The details of the form of such contributions can be found in Appendix D.
Another consequence of the existence of this additional Z_d boson, besides the modification of the lepton magnetic moment, would be the introduction of a new source of parity violation that could be tested by experiments sensitive to the weak charge, Q_W, of both protons and nuclei. In particular, the proton weak charge has been measured by the $\mathrm{Q_{weak}}$ Collaboration at JLAB [33] at a momentum transfer of $Q^2 = 0.0248\,\mathrm{GeV}^2$. The $\mathrm{Q_{weak}}$ Collaboration found

$$Q_W^{p,\,\mathrm{exp}} = 0.0719(45), \tag{6.36}$$

which has to be compared with the SM prediction [147, 203] that, taking into account radiative corrections, can be expressed by

$$Q_W^{p,\,\mathrm{SM}} = -2g_{AV}^{ep}(\sin^2\theta_W)\Big(1 - \frac{\alpha}{2\pi}\Big) = 0.0711(2), \tag{6.37}$$

where we have considered the value of the weak mixing angle predicted by the SM at low energies. Of course, a modification of the weak mixing angle at low energies due to the effect of the dark Z boson would result in a modification of the proton weak charge.
The same discussion applies to the atomic parity violation (APV) experiments, since they provide the measurement of the weak charge of a nucleus, which is also very sensitive to the weak mixing angle, and thus, to new vector bosons. As

we have already discussed, the most precise measurement has been performed at $Q \approx 2.4$ MeV using cesium atoms ($N_{\rm Cs} = 78$ and $Z_{\rm Cs} = 55$), so that we have studied the impact of the Z_d only considering the APV(Cs) measurement. Let us recall that the SM prediction [203] of the nuclear weak charge of Cs including radiative corrections[6] leads to [3]

$$\begin{aligned} Q_W^{^{133}\mathrm{Cs,\,SM}} &= -2\,[\,Z_{\rm Cs}(g_{AV}^{ep}(\sin^2\theta_W) + 0.00005) \\ &\quad + N_{\rm Cs}(g_{AV}^{en} + 0.00006)]\Big(1 - \frac{\alpha}{2\pi}\Big) \\ &= -73.23(1)\,. \end{aligned} \tag{6.38}$$

As previously discussed (see Sec. 3.2), we consider the experimental value of the nuclear weak charge of Cs being

$$Q_W^{^{133}\mathrm{Cs,\,exp}} = -72.94(43)\,, \tag{6.39}$$

which has been recalculated in Ref. [3], by relying on an electroweak model-independent extrapolation from the PREX lead neutron skin measurement[7].
The measurements of Q_W in Eqs. (6.39) and (6.36) can be used to set limits on the available phase space for the Z_d model. Indeed, the presence of a Z_d mediator would change the experimental extraction of Q_W. More precisely, adopting the substitutions described before, the expression for the proton weak charge becomes

$$Q_W^{p,Z_d} = -2\rho_d\; g_{AV}^{ep}(\kappa_d \sin^2\theta_W)\,\Big(1 - \frac{\alpha}{2\pi}\Big), \tag{6.40}$$

where, in the case of polarized electron scattering experiments, such as for the measurement of the proton weak charge, the propagator term inside Eqs. (6.34) and (6.35) becomes [190, 341]

$$f\Big(\frac{Q^2}{m_{Z_d}^2}\Big) = \frac{m_{Z_d}^2}{m_{Z_d}^2 + Q^2}, \tag{6.41}$$

where Q^2 is the typical experimental momentum transfer.
Similarly, the expression for the cesium weak charge is

$$\begin{aligned} Q_W^{^{133}\mathrm{Cs},\;Z_d} &= -\,2\rho_d\Big[Z_{\rm Cs}(g_{AV}^{ep}(\kappa_d \sin^2\theta_W) + 0.00005) \\ &\quad + N_{\rm Cs}(g_{AV}^{en} + 0.00006)\Big]\Big(1 - \frac{\alpha}{2\pi}\Big). \end{aligned} \tag{6.42}$$

In the case of parity violation in heavy atoms, such as for cesium, the propagator assumes a different form due to the nuclear structure. In particular, for ^{133}Cs it becomes $f(Q^2/m_{Z_d}^2) = K(^{133}\mathrm{Cs})$, as described in Refs. [190, 341]. For example,

[6] The calculation of the couplings entering the nuclear weak charge can be found in Appendix A.

[7] It is necessary to mention that at the time of Ref. [3], where these results have been reported, the updated COHERENT CsI data [54] had not been publicly released yet, so that we could not consider the combined COHERENT CsI+ APV(Cs) result discussed in Sec. 5.2, which is free of assumptions on the neutron skin of cesium, inside the fit. The analysis will be updated by considering also the other available measurements discussed in this thesis in an upcoming work.

$K(^{133}\mathrm{Cs}) \simeq 0.5$ for masses of the Z_d boson of the order of the typical momentum transfer of APV, $Q \approx 2.4$ MeV, while $K(^{133}\mathrm{Cs}) \simeq 0.83, 1$ for $m_{Z_d} \simeq 20, 100$ MeV. In order to determine information on ε, δ and m_{Z_d}, we performed several fits with the common least-squares function

$$\chi^2_i(\varepsilon,\, \delta,\, m_{Z_d}) = \frac{(X_i^{\mathrm{exp}} - X_i^{\mathrm{th}}(\varepsilon,\, \delta,\, m_{Z_d}))^2}{\sigma_i^2}\,, \tag{6.43}$$

where i stands for $\mathrm{Q_{weak}}$, $\mathrm{APV(Cs)}$, a_μ, and a_e, such that $X^{\mathrm{exp}} = \{Q_W^{p,\,\mathrm{exp}},\, Q_W^{^{133}\mathrm{Cs},\,\mathrm{exp}},\, a_\mu^{\mathrm{exp}},\, a_e^{\mathrm{exp}}\}$, $X^{\mathrm{th}} = \{Q_W^{p,\,Z_d}, Q_W^{^{133}\mathrm{Cs},\,Z_d},\, a_\mu^{Z_d},\, a_e^{Z_d}\}$ and σ_i are the corresponding experimental and theoretical uncertainties summed in quadrature.

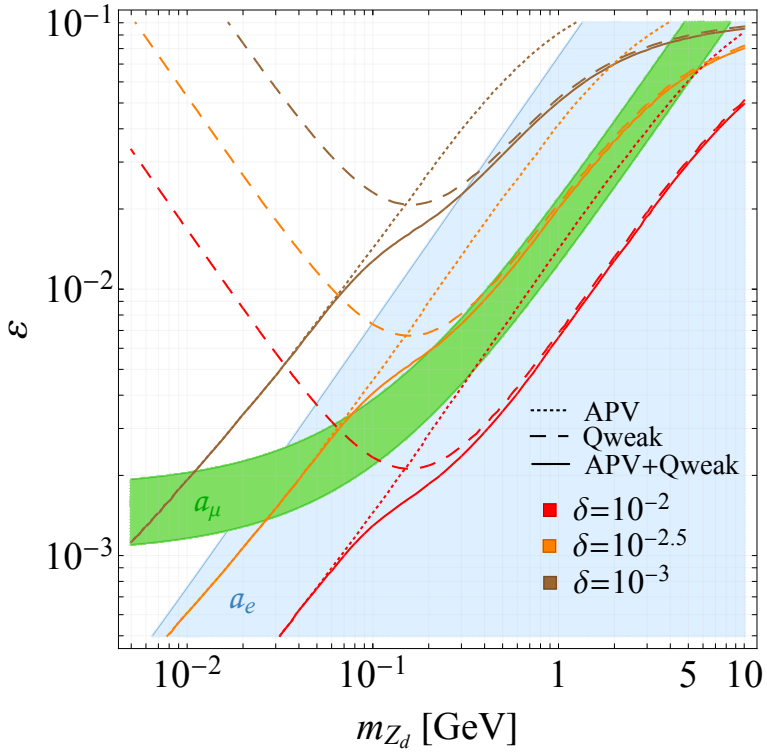

Figure 6.11: Limits at 90% C.L. in ε vs m_{Z_d} parameter space, for both $\mathrm{Q_{weak}}$ (dashed line) and APV(Cs) (dotted line) experiments, and also their combination (solid line), for different values of δ. The green band and the light blue area are the favored regions at 90% C.L. needed to explain the anomalous magnetic moment of the muon and of the electron, respectively.

For the muon anomalous magnetic moment, we have considered the experimental average value between the BNL measurement and the Run-1 data of the FNAL measurement [3, 276, 277], which considering the currently accepted theoretical value, leads to[8] $\Delta a_\mu = 251(59) \times 10^{-11}$. For the electron anomalous magnetic moment instead, we have considered the recent reevaluation of the electron

[8]Let us remind the presence of the new result released during the completion of this thesis by the Muon g-2 Collaboration, which is discussed in Appendix D.

magnetic moment from the determination of the fine structure constant [342], obtained from the measurement of the recoil velocity on rubidium atoms, which leads to $\Delta a_e = 0.48(30) \times 10^{-12}$. This re-determination is interesting, as it brings the anomaly in the same direction as the ones on muons, although it is only at 1.6σ C.L..
In Fig. 6.11 we show the limits or allowed regions at 90% confidence level (C.L.) in the plane of m_{Z_d} and ε for different values of δ. In particular, we show the limits of APV(Cs), $\mathrm{Q_{weak}}$ and their combination, and how they depend significantly on the δ parameter. In particular, larger values of δ, lead to smaller values of ε. Moreover, we also show the 90% CL favored regions for the explanation of the muon and electron anomalous magnetic moments. Since the latter two are practically independent of δ, such parameter becomes fundamental in order to exclude or not the a_μ and a_e interpretations under the Z_d model. In fact, for $\delta > 10^{-2}$ the entire Δa_μ discrepancy is already completely ruled out, not only by the combined result but also by the APV(Cs) only limit. Other experiments that are also sensitive to Z_d bosons are those able to measure rare flavor-changing weak neutral-current decays of K and B mesons and the Higgs boson decays to ZZ_d bosons [335, 339, 340]. In both cases, the constraints obtained depend on the assumed branching fraction (BF) of the Z_d boson decay and on its mass (for a more detailed discussion look at Ref. [3]).

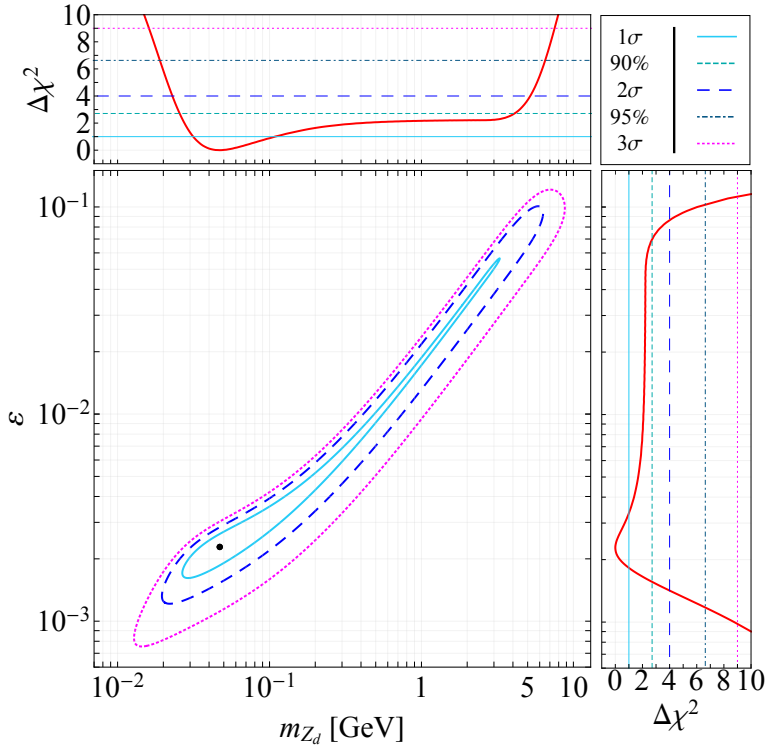

Figure 6.12: Contours at different C.Ls of the allowed regions in the plane of m_{Z_d} and ε, together with their marginalizations, obtained from the combined fit of the $\mathrm{Q_{weak}}$, APV(Cs), a_μ and a_e experimental results. The best fit result is indicated by the black dot.

By looking at Fig. 6.11, it is clear that it is possible to find combinations of δ, m_{Z_d} and ε, for which one obtains an overlap between all the different experimental constraints. To better highlight it, we performed a combined fit by summing all the four χ^2's in Eq. (6.43). In order to remove the ambiguity on δ, we marginalized the result over this parameter and the results are shown in Fig. 6.12 [3], where we show the 1σ, 2σ, and 3σ C.L. contours in the plane of m_{Z_d} and ε, as well as the best fit result corresponding to a minimum $\chi^2_{\rm min} = 0.007$. We get the following results for m_{Z_d}, ε and δ at 1σ C.L. [3]

$$m_{Z_d} = 47^{+61}_{-16}\,\text{MeV}, \tag{6.44}$$
$$\varepsilon = 2.3^{+1.1}_{-0.4} \times 10^{-3}, \tag{6.45}$$
$$\delta < 2 \times 10^{-3}\ \left(\delta^{\rm BF} = 7.9 \times 10^{-4}\right). \tag{6.46}$$

Using these best fit values and their 1σ ranges, in Fig. 6.13 we show how the running of $\sin^2\theta_W$ changes at low energies due to the contribution of a Z_d boson by the orange and green dashed curves.

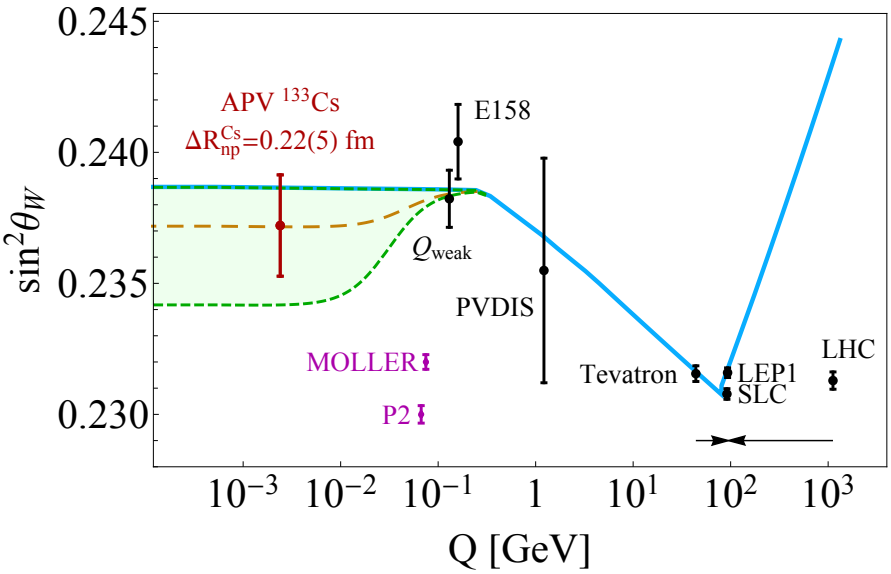

Figure 6.13: Running of $\sin^2\theta_{\rm W}$ with energy scale Q. The SM prediction is shown as the solid light blue curve, together with experimental determinations in black [31–35, 226, 237] and future projections in violet [184, 228] with a central value shown at an arbitrary position. The result derived in this work for APV(Cs) is shown in red. With the dashed orange and green lines we indicate the best fit result and the $\pm1\sigma$ variations, respectively, for the running of $\sin^2\theta_W$ in the presence of a Z_d boson as described in the text [3].

Clearly, further measurements of $\sin^2\theta_W$ in the low energy sector, as those coming from the P2 [184, 227] and MOLLER [228] experiments, from the coherent elastic neutrino scattering on nuclei [8, 234] (whose precision are not competitive yet) and finally from future atomic parity violation with francium, radium and rubidium [189, 343] would be really powerful for further constraining such a model. It is worth mentioning that, as shown in Fig. 4.16, our analyses of PREX and CREX

are in agreement with the presence of such new boson, and that also the future PVES measurements on ^{12}C will play a crucial role in testing this model.
To highlight the near future prospects that can be achieved thanks to upcoming results from MOLLER and P2, considering the SM value for the central value, as well as the improved measurement of a_μ presented in Ref. [278], we show in Fig. 6.14 the limits at 90% C.L. in the plane of m_{Z_d} and ε for different values of δ. As clearly visible, P2 and MOLLER will allow one to exclude a large portion of the a_μ band already for values of δ as small as 10^{-3}.

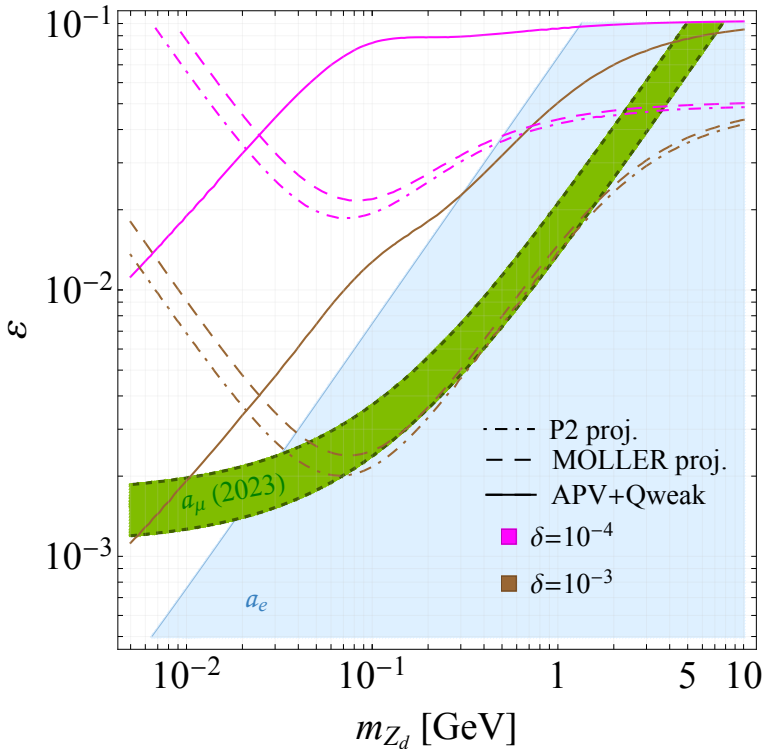

Figure 6.14: Limits at 90% C.L. in the plane of m_{Z_d} and ε, for the combined Q_{weak}+APV(Cs) analysis (solid), the projected MOLLER (dashed) and P2 (dot-dashed) proposed experiments, for different values of δ as depicted in the label. The green band and the light blue area are the favored regions at 90% C.L. needed to explain the anomalous magnetic moment of the muon and of the electron, respectively. In this figure, for the a_μ band we considered the updated experimental average value from Ref. [278].

As it is clear by looking at this figure, the allowed region for the explanation of the muon anomalous magnetic moment is not significantly modified, but only slightly narrowed. Moreover, in the Supplemental Material of Ref. [3], we have also shown a tentative sensitivity study, obtained by considering an optimistic future precision for a_μ, namely considering the Δa_μ central value considered in such work, but with an uncertainty reduced by a factor of two. The combined analysis of the latter probes leads to a significantly smaller allowed region, further stressing the need for such low energy weak mixing angle measurement to confirm the SM or to possibly indicate the existence of such a new light boson mediator.

Chapter 7

Neutrino Electromagnetic Properties

Short introduction

In this chapter, we will discuss a particular class of neutrino properties of great interest in the neutrino and dark matter communities: the so-called neutrino electromagnetic properties. Such properties describe possible photon mediated neutrino interactions, and in particular, we will present the current status of constraints on the neutrino charge radius, the neutrino magnetic moment and the neutrino electric charge from CEνNS and νES by the analysis of COHERENT, Dresden-II and LZ data. We will also talk about the momentum dependence of the neutrino charge radius radiative correction, and its possible implication for future neutrino searches. Most of the results have been taken from Ref. [6] regarding the results from COHERENT and Dresden-II experiments and from Ref. [7] in the case of LZ data.

7.1 Neutrino Charge Radius

Neutrinos are neutral particles, therefore, they can not couple directly to photons. However, even if the electric charge is null, the electric form factor[1] of the neutrino, $\mathbb{f}_Q(q^2)$, can encode nontrivial information about the neutrino electric properties. In principle, a neutral particle can be characterized by a superposition of two different charge distributions of opposite signs. Indeed, this can be described by a form factor, $\mathbb{f}_Q(q^2)$, which is nonzero for momentum transfer $q^2 \neq 0$ [37]. We can expand in series of powers of q^2 the form factor

$$\mathbb{f}_Q(q^2) = \mathbb{f}_Q(0) + q^2 \frac{d\mathbb{f}_Q(q^2)}{dq^2}\Big|_{q^2=0} + \dots . \tag{7.1}$$

In the "Breit frame", the charge form factor depends only on $|\vec{q}|$. In this frame, it can be interpreted as the Fourier transform of a spherically symmetric charge

[1] The electric form factor is not connected to the spatial distribution of nucleons inside the nuclei, but is instead an intrinsic neutrino property. Thus, it should not be confused with the charge form factor discussed in scattering processes off nuclei.

distribution, $\rho(r)$, so that [37]

$$\frac{d\mathbb{f}_Q(q^2)}{dq^2} = \int \rho(r) e^{-i\vec{q}\cdot\vec{r}} d^3r = \int \rho(r) \frac{\sin(qr)}{qr} d^3r \,. \tag{7.2}$$

From this interpretation of the electric form factor, we can understand that the first term in the expansion in Eq. 7.1 has to be zero, since the particle is neutral, while the second term corresponds to the neutrino charge radius, i.e. the radius of the electric charge distribution. By deriving the expression in Eq. 7.2 with respect to q^2 and taking the limits of $q^2 \to 0$, we obtain

$$\lim_{q^2\to 0} \frac{d\mathbb{f}_Q(q^2)}{dq^2} = \int \rho(r) \frac{r^2}{6} d^3r = \frac{\langle r^2 \rangle}{6} \,, \tag{7.3}$$

from which the squared neutrino charge radius is given by

$$\langle r^2 \rangle = 6 \frac{d\mathbb{f}_Q(q^2)}{dq^2}\Big|_{q^2=0} \,. \tag{7.4}$$

Let us note that $\langle r^2 \rangle$ has no defined sign because $\rho(r)$ is not a positively defined quantity.

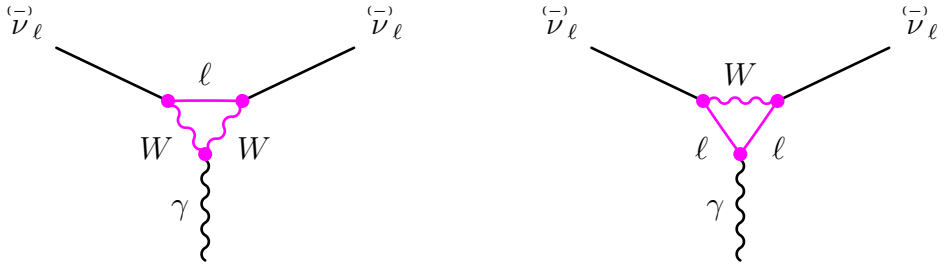

Figure 7.1: Diagrams describing the neutrino charge radius contributions to the neutrino vertices.

In general, the charge radius of a neutrino is generated by a loop insertion into the ν_ℓ line, consisting of a W boson and the charged lepton ℓ, as shown in the diagrams in Fig. 7.1. In the figure, we show the two diagrams contributing, one named $WW\ell$ loop (left diagram), and the other one $\ell\ell W$ loop (right diagram). Indeed, the Neutrino Charge Radius (NCR)[2] is the only nonzero electromagnetic property of neutrinos in the SM and it introduces a flavor dependence in the cross section. It can be calculated, and according to Refs. [344–346] it is a physical observable, being gauge invariant. In particular, the SM calculation gives

$$\langle r^2_{\nu_\ell} \rangle_{\rm SM} = -\frac{G_F}{2\sqrt{2}\pi^2} \left[3 - 2\ln\left(\frac{m_\ell^2}{m_W^2}\right) \right] , \tag{7.5}$$

where we can see that the value of the NCR depends on the charged lepton mass, m_ℓ. We can notice that the definition of the neutrino charge radius is the sum of two contributions: one constant term arising from the $WW\ell$ loop diagram, where

[2]We will sometimes also refer to it as neutrino CR (Charge Radius).

we attach the photon to the W boson (left diagram in Fig. 7.1), and the other one which is generated attaching the photon to the lepton ℓ (right diagram in Fig. 7.1). The latter generates an electroweak logarithm, which is divergent in the UV range, that is regularized at the lepton mass, m_ℓ.
Moreover, we can easily see that the NCR is a flavor dependent quantity, and numerically it can be calculated, leading to

$$\langle r^2_{\nu_e} \rangle \simeq -8.3 \times 10^{-33}\,\mathrm{cm}^2\,, \tag{7.6}$$
$$\langle r^2_{\nu_\mu} \rangle \simeq -4.8 \times 10^{-33}\,\mathrm{cm}^2\,, \tag{7.7}$$
$$\langle r^2_{\nu_\tau} \rangle \simeq -3.0 \times 10^{-33}\,\mathrm{cm}^2\,. \tag{7.8}$$

The neutrino charge radius has an effect on the scattering of neutrinos with charged particles. Therefore, it contributes to the νES scattering process, whereas in the case of CEνNS it contributes only to the neutrino-proton coupling (and not to the neutron one). The NCR contribution is accounted for through a shift of the vector coupling constant [6, 37, 197], namely

$$\begin{aligned} g_V^{\nu_\ell e} &\to g_V^{\nu_\ell e} + \frac{2}{3} m_W^2 \langle r^2_{\nu_\ell} \rangle \sin^2\theta_W = g_V^{\nu_\ell e} + \frac{\sqrt{2}\pi\alpha}{3G_F} \langle r^2_{\nu_\ell} \rangle\,, \\ g_V^{p}(\nu_\ell) &\to g_V^{p}(\nu_\ell) - \frac{2}{3} m_W^2 \langle r^2_{\nu_\ell} \rangle \sin^2\theta_W = g_V^{p}(\nu_\ell) - \frac{\sqrt{2}\pi\alpha}{3G_F} \langle r^2_{\nu_\ell} \rangle\,, \end{aligned} \tag{7.9}$$

for the neutrino-electron coupling, $g_V^{\nu_\ell e}$, and for the neutrino-proton coupling, $g_V^p(\nu_\ell)$, entering the νES and CEνNS cross sections, respectively. In this sense, the neutrino charge radius is effectively introduced as a radiative correction [147]. Historically, the NCR was considered as one of the radiative corrections to be included in the calculation of the running of the weak mixing angle in the case of neutrino scattering processes [347]. However, the commonly accepted definition of the weak mixing angle is not dependent on the scattering particle, whether one considers neutrino or electron processes, and the NCR is incorporated as an additional radiative correction to the coupling constant.
Despite representing a fundamental quantity to measure in order to test the SM theory, the current precision reached is still insufficient to provide a first measurement of the NCR. However, it is possible to set constraints on its value and to investigate possible BSM effects that could modify the SM value of the neutrino charge radius. In the SM, the neutrino charge radius is associated with a certain lepton flavor, ℓ. By considering BSM effects, it is also possible to have the so-called off-diagonal contributions. In fact, in BSM theories, one can build a flavor matrix describing the contribution of the new physics, and it is convenient to distinguish diagonal terms (flavor conserving) and off-diagonal terms (flavor changing). The off-diagonal terms are referred to as transition charge radii as they change the neutrino flavor between the initial and the final state.
We can consider the general case in which neutrinos can have both diagonal and off-diagonal charge radii. To account for this, we rename the charge radius in $\langle r^2_{\nu_{\ell\ell'}} \rangle$, where for $\ell = \ell'$ we retrieve the diagonal terms, while for $\ell \neq \ell'$ the off-diagonal ones.
The differential CEνNS cross section that takes into account the contribution of

the neutrino charge radii in addition to the SM neutral-current weak interaction is

$$\frac{d\sigma^{\rm NCR}_{\nu_\ell\text{-}\mathcal{N}}}{dT_{\rm nr}}(E_\nu, T_{\rm nr}) = \frac{G_{\rm F}^2 m_N}{\pi}\left(1 - \frac{m_N T_{\rm nr}}{2E_\nu^2}\right)\left\{\left[\left(\tilde{g}_V^p - \tilde{Q}_{\ell\ell}\right) Z F_Z(q^2) + g_V^n N F_N(q^2)\right]^2 + \right.$$
$$\left. + Z^2 F_Z^2(q^2) \sum_{\ell' \neq \ell} |\tilde{Q}_{\ell\ell'}|^2 \right\}, \tag{7.10}$$

where $\tilde{g}_V^p$ is the neutrino-proton coupling including radiative corrections but the contribution of the SM neutrino CR one. The effects of the charge radii $\langle r^2_{\nu_{\ell\ell'}}\rangle$ in the cross section are expressed as [43]

$$\tilde{Q}_{\ell\ell'} = \frac{\sqrt{2}\pi\alpha}{3G_{\rm F}}\langle r^2_{\nu_{\ell\ell'}}\rangle, \tag{7.11}$$

which can be easily be brought back to the SM NCR radiative correction defined in Eq. 7.9.
The diagonal CR contribute to the cross section coherently with the neutrino-proton neutral current interaction, generating an effective shift of $\sin^2\theta_W$. In the case of $\bar{\nu}_\ell$-$\mathcal{N}$ scattering, it is sufficient to operate the substitutions: $g_V^{p,n} \to -g_V^{p,n}$ and $\langle r_{\nu_{\ell\ell'}}\rangle \to \langle r_{\bar{\nu}_{\ell\ell'}}\rangle = -\langle r_{\nu_{\ell\ell'}}\rangle$. Therefore, the CR of flavor neutrinos and antineutrinos contribute with the same sign to the shift of $\sin^2\theta_W$ in the CEνNS cross section.
Considering the COHERENT neutrino flux and the Dresden-II one, there are five CR that can be determined with the available CEνNS data: the two diagonal charge radii $\langle r^2_{\nu_{ee}}\rangle$ and $\langle r^2_{\nu_{\mu\mu}}\rangle$, that sometimes are denoted with the simpler notation $\langle r^2_{\nu_e}\rangle$ and $\langle r^2_{\nu_\mu}\rangle$, to be reconnected to the SM charge radii defined in Eq. 7.5, and the absolute values of the three off-diagonal CR $\langle r^2_{\nu_{e\mu}}\rangle = \langle r^2_{\nu_{\mu e}}\rangle^*$, $\langle r^2_{\nu_{e\tau}}\rangle$, and $\langle r^2_{\nu_{\mu\tau}}\rangle$.
Similarly, in the presence of the neutrino charge radii, the νES cross section in Eq. 2.16, is modified to [43]

$$\left(\frac{d\sigma^{\rm ES,CR}_{\nu_\ell-\mathcal{A}}}{dT_{\rm e}}\right)_{\rm SM+\tilde{Q}} = \left(\frac{d\sigma^{\rm ES,CR}_{\nu_\ell-\mathcal{A}}}{dT_{\rm e}}\right)_{\rm SM+\tilde{Q}_{\ell\ell}} + \sum_{\ell'\neq\ell}\left(\frac{d\sigma^{\rm ES,CR}_{\nu_\ell-\mathcal{A}}}{dT_{\rm e}}\right)_{\tilde{Q}_{\ell\ell'}}, \tag{7.12}$$

where $(d\sigma^{\rm ES,CR}_{\nu_\ell-\mathcal{A}}/dT_{\rm e})_{\rm SM+\tilde{Q}_{\ell\ell}}$ is given by Eq. (2.5) with

$$g_V^{\nu_\ell} \to g_V^{\nu_\ell} + \tilde{Q}_{\ell\ell}, \tag{7.13}$$

while for $\ell' \neq \ell$, the cross section is

$$\left(\frac{d\sigma^{\rm ES,CR}_{\nu_\ell-\mathcal{A}}}{dT_{\rm e}}\right)_{\tilde{Q}_{\ell\ell'}} = Z^{\mathcal{A}}_{\rm eff}(T_e)\,\frac{\pi\alpha^2 m_e}{9}\left[1 + \left(1 - \frac{T_e}{E_\nu}\right)^2 - \frac{m_e T_e}{E_\nu^2}\right]|\langle r^2_{\nu_{\ell\ell'}}\rangle|^2. \tag{7.14}$$

In this scenario, the FEA approach corrected by the stepping function as discussed in Sec. 2.1, slightly overestimates the cross section with respect to *ab-initio* calculations in the Relativistic Random Phase Approximation (RRPA), which account

for many body interactions, for $T_e \lesssim 1$ keV, but they rapidly converge for $T_e > 1$ keV [44], causing a negligible difference.

	1σ	90%	2σ	3σ
		CsI		
$\langle r^2_{\nu_{ee}} \rangle$	$(-62, 10)$	$(-68, 14)$	$(-70, 16)$	$(-77, 22)$
$\langle r^2_{\nu_{\mu\mu}} \rangle$	$(-37.9, 0.5)$	$(-57.4, 2.9)$	$(-59.2, 4.4)$	$(-64.0, 8.6)$
$\lvert\langle r^2_{\nu_{e\mu}} \rangle\rvert$	< 26	< 30	< 31	< 34
$\lvert\langle r^2_{\nu_{e\tau}} \rangle\rvert$	< 36	< 41	< 43	< 49
$\lvert\langle r^2_{\nu_{\mu\tau}} \rangle\rvert$	< 27	< 30	< 32	< 36
		Ar		
$\langle r^2_{\nu_{ee}} \rangle$	$(-79, 29)$	$(-88, 38)$	$(-93, 43)$	$(-110, 59)$
$\langle r^2_{\nu_{\mu\mu}} \rangle$	$(-59.2, 8.6)$	$(-64.9, 14.6)$	$(-67.6, 17.3)$	$(-74.8, 24.5)$
$\lvert\langle r^2_{\nu_{e\mu}} \rangle\rvert$	< 33	< 36	< 38	< 44
$\lvert\langle r^2_{\nu_{e\tau}} \rangle\rvert$	< 54	< 63	< 68	< 84
$\lvert\langle r^2_{\nu_{\mu\tau}} \rangle\rvert$	< 34	< 40	< 42	< 50
		CsI + Ar		
$\langle r^2_{\nu_{ee}} \rangle$	$(-66, 11)$	$(-69, 14)$	$(-71, 16)$	$(-77, 22)$
$\langle r^2_{\nu_{\mu\mu}} \rangle$	$(-54.7, 0.8)$	$(-57.7, 3.2)$	$(-59.2, 4.7)$	$(-63.1, 8.3)$
$\lvert\langle r^2_{\nu_{e\mu}} \rangle\rvert$	< 28	< 30	< 31	< 34
$\lvert\langle r^2_{\nu_{e\tau}} \rangle\rvert$	< 38	< 42	< 44	< 50
$\lvert\langle r^2_{\nu_{\mu\tau}} \rangle\rvert$	< 28	< 31	< 32	< 36

Table 7.1: Bounds on the neutrino charge radii in units of 10^{-32} cm^2 obtained from the analysis of the COHERENT CsI and Ar data.

We have analysed the latest COHERENT LAr and CsI data [53, 54] together with the Dresden-II one [92], in order to set constraints on the neutrino charge radii [6], by using the chi-square in Eq. 2.77, Eq. 2.75 and Eq. 2.84 modifying the CEνNS rate according to the above cross section definitions. The results of fit of the COHERENT data are summarized in Tab. 7.1. We can notice that the bounds obtained for the Ar data set are of the same order of magnitude but, as expected due to statistics, less stringent than those obtained from the COHERENT CsI data, which therefore dominate the combined fit.

	1σ	90%	2σ	3σ
	Dresden-II (HMVE-Fef)			
$\langle r^2_{\nu_{ee}} \rangle$	$(-54, 2)$	$(-56, 4)$	$(-58, 5)$	$(-61, 8)$
$\lvert\langle r^2_{\nu_{e\mu}} \rangle\rvert$, $\lvert\langle r^2_{\nu_{e\tau}} \rangle\rvert$	< 28	< 30	< 32	< 35
	Dresden-II (HMVE-YBe)			
$\langle r^2_{\nu_{ee}} \rangle$	$(-61, 9)$	$(-65, 12)$	$(-66, 14)$	$(-71, 18)$
$\lvert\langle r^2_{\nu_{e\mu}} \rangle\rvert$, $\lvert\langle r^2_{\nu_{e\tau}} \rangle\rvert$	< 35	< 38	< 40	< 44

Table 7.2: Bounds on the neutrino charge radii in units of 10^{-32} cm^2 obtained from the analysis of the Dresden-II data assuming the HMVE reactor antineutrino flux and the Fef or YBe quenching.

Similarly, the results from the fit of the Dresden-II data set for the neutrino charge radii are summarized in Tab. 7.2. In this case only $\langle r^2_{\nu_{ee}} \rangle$, $|\langle r^2_{\nu_{e\mu}} \rangle|$, and $|\langle r^2_{\nu_{e\tau}} \rangle|$ could

be constrained by the data. In the table, we show the results obtained by fitting the data with the HMVE antineutrino flux parameterization considering the two different germanium QF functional forms, Fef and YBe. Indeed, considering the different flux parametrizations (HMVE, HMK and EFK) induces very small differences in the final bounds, while the QF plays a more important role. Therefore, we will present only the numerical results obtained with the HMVE parametrization. The complete tables can be found in Ref. [6].
All in all, the bounds obtained from the Dresden-II data set are comparable with those obtained from the CsI and Ar data set, with a precision similar to the CsI data set.
Finally, in Tab. 7.3 we show the bounds on the NCR obtained from the combined analysis of the COHERENT CsI and Ar data and the Dresden-II data assuming the HMVE antineutrino flux and the two different QFs. An improvement with respect to the results obtained fitting the COHERENT data set alone is visible.

	1σ	90%	2σ	3σ
CsI + Ar + Dresden-II (HMVE-Fef)				
$\langle r^2_{\nu_{ee}} \rangle$	$(-52, 3)$	$(-56, 5)$	$(-58, 6)$	$(-61, 9)$
$\langle r^2_{\nu_{\mu\mu}} \rangle$	$(-55.6, 1.8)$	$(-58.2, 4.0)$	$(-59.8, 5.1)$	$(-63.1, 8.7)$
$\lvert\langle r^2_{\nu_{e\mu}} \rangle\rvert$	< 28	< 29	< 30	< 32
$\lvert\langle r^2_{\nu_{e\tau}} \rangle\rvert$	< 28	< 31	< 32	< 35
$\lvert\langle r^2_{\nu_{\mu\tau}} \rangle\rvert$	< 29	< 32	< 33	< 36
CsI + Ar + Dresden-II (HMVE-YBe)				
$\langle r^2_{\nu_{ee}} \rangle$	$(-60, 7)$	$(-63, 10)$	$(-65, 12)$	$(-69, 15)$
$\langle r^2_{\nu_{\mu\mu}} \rangle$	$(-54.3, 0.74)$	$(-57.3, 3.2)$	$(-58.9, 4.3)$	$(-62.2, 7.8)$
$\lvert\langle r^2_{\nu_{e\mu}} \rangle\rvert$	< 28	< 30	< 31	< 33
$\lvert\langle r^2_{\nu_{e\tau}} \rangle\rvert$	< 35	< 37	< 38	< 42
$\lvert\langle r^2_{\nu_{\mu\tau}} \rangle\rvert$	< 28	< 30	< 32	< 35

Table 7.3: Bounds on the neutrino charge radii in units of 10^{-32} cm^2 obtained from the combined analysis of the COHERENT CsI and Ar data and the Dresden-II data assuming the HMVE reactor antineutrino flux and the Fef or YBe quenching.

The contours of the 90% C.L. allowed regions in the $(\langle r^2_{\nu_{ee}} \rangle, \langle r^2_{\nu_{\mu\mu}} \rangle)$ plane obtained from the analysis of the COHERENT CsI and Ar data, and from the combined analysis of the COHERENT data and Dresden-II data assuming the HMVE, HMK, or EFK reactor antineutrino flux and the Fef or YBe quenching are shown in Fig. 7.2 together with the SM values in Eq. 7.6 and Eq. 7.7 and the 90% bounds on $\langle r^2_{\nu_{ee}} \rangle$ and $\langle r^2_{\nu_{\mu\mu}} \rangle$ obtained, respectively, in the TEXONO [348] and BNL-E734 [349] experiments.
In Fig. 7.3 we show the marginal $\Delta\chi^2$'s for $\langle r^2_{\nu_{ee}} \rangle$ together with the SM value in Eq. (7.6) and the lower and upper 90% bounds on $\langle r^2_{\nu_{ee}} \rangle$ obtained in the TEXONO [348] experiment. As visible, the point corresponding to the SM value of the diagonal CR lies at the edge of the 1σ allowed region and very close to the best fit value for $\langle r^2_{\nu_{ee}} \rangle$ in the combined CsI+Ar+Dresden-II fit. For a better comparison, in Tab. 7.4 we report a summary of the most recent and precise bounds on $\langle r^2_{\nu_{ee}} \rangle$ and $\langle r^2_{\nu_{\mu\mu}} \rangle$. Please note that some of these limits have been corrected by a factor of two due to a different convention, see Ref. [350] for a detailed explanation.

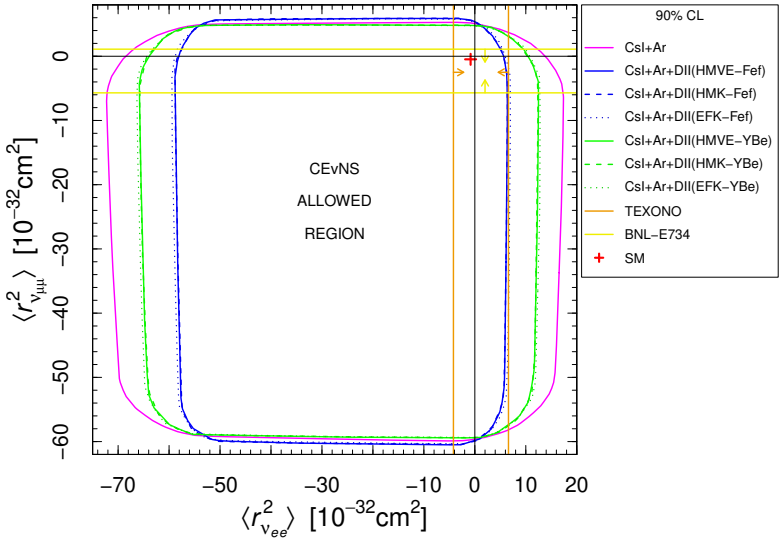

Figure 7.2: Contours of the 90% C.L. allowed regions in the $(\langle r^2_{\nu_{ee}} \rangle, \langle r^2_{\nu_{\mu\mu}} \rangle)$ plane obtained from the analysis in the presence of transitional CR of the COHERENT CsI and Ar data (magenta), and the combined one with the Dresden-II data assuming the HMVE, HMK, or EFK reactor antineutrino flux and the Fef (blue) or YBe (green) quenching. The red cross indicates the Standard Model value. The orange and yellow lines delimit, respectively, the 90% bounds on $\langle r^2_{\nu_{ee}} \rangle$ and $\langle r^2_{\nu_{\mu\mu}} \rangle$ obtained in the TEXONO [348] and BNL-E734 [349] experiments.

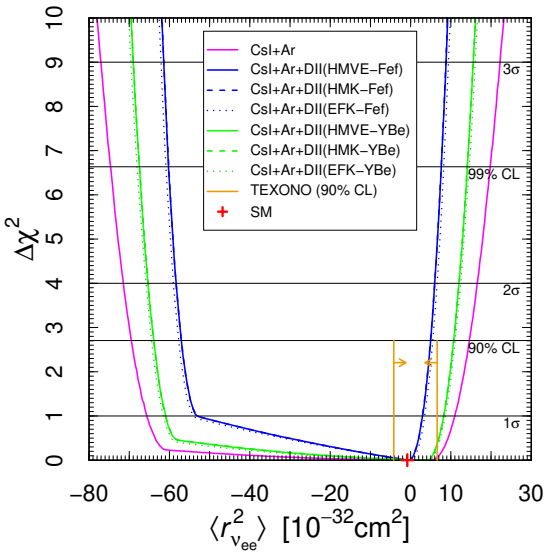

Figure 7.3: Marginal $\Delta\chi^2$'s for $\langle r^2_{\nu_{ee}} \rangle$ obtained from the analysis in presence of transitional CR of the COHERENT CsI and Ar data (magenta), and the combined one with the Dresden-II data assuming the HMVE, HMK, or EFK reactor antineutrino flux and the Fef (blue) or YBe (green) quenching. The red cross indicates the Standard Model value. The short vertical orange lines show the lower and upper 90% bounds on $\langle r^2_{\nu_{ee}} \rangle$ from the TEXONO [348] experiment.

In Tab. 7.4 we also summarized the results found in this work from the combined Dresden-II + COHERENT analysis when considering non-null transition CR. Interestingly, we are able to improve the best upper bound limit for $\langle r^2_{\nu_{ee}} \rangle$ previously set by TEXONO.

Process	Collaboration	Limit [10^{-32} cm^2]	C.L.	Ref.
Reactor $\bar{\nu}_e$-e	Krasnoyarsk	$\lvert\langle r^2_{\nu_e}\rangle\rvert < 7.3$	90%	[351]
	TEXONO	$-4.2 < \langle r^2_{\nu_e}\rangle < 6.6$	90%	[348][a]
Accelerator ν_e-e	LAMPF	$-7.12 < \langle r^2_{\nu_e}\rangle < 10.88$	90%	[352][a]
	LSND	$-5.94 < \langle r^2_{\nu_e}\rangle < 8.28$	90%	[353][a]
Accelerator	BNL-E734	$-5.7 < \langle r^2_{\nu_\mu}\rangle < 1.1$	90%	[349][a,b]
ν_μ-e and $\bar{\nu}_\mu$-e	CHARM-II	$\lvert\langle r^2_{\nu_\mu}\rangle\rvert < 1.2$	90%	[354][a]
COHERENT	w/o transition CR	$-7.1 < \langle r^2_{\nu_e}\rangle < 5$	90%	our work [6][c]
+ Dresden-II	w transition CR	$-56 < \langle r^2_{\nu_e}\rangle < 5$	90%	our work [6][c]
COHERENT	w/o transition CR	$-5.9 < \langle r^2_{\nu_\mu}\rangle < 4.3$	90%	our work [6][c]
+ Dresden-II	w transition CR	$-58.2 < \langle r^2_{\nu_\mu}\rangle < 4.0$	90%	our work [6][c]

[a] Corrected by a factor of two due to a different convention, see Ref. [350].
[b] Corrected in Ref. [355]. [c] Using the Fef quenching factor.

Table 7.4: Experimental limits on the diagonal neutrino charge radii.

Finally, in Fig. 7.4 we show the marginal $\Delta\chi^2$'s for $\lvert\langle r^2_{\nu_{e\mu}}\rangle\rvert$ and $\lvert\langle r^2_{\nu_{e\tau}}\rangle\rvert$. We note that by combining COHERENT with the Dresden-II with the Fef QF we obtain significantly more stringent bounds.

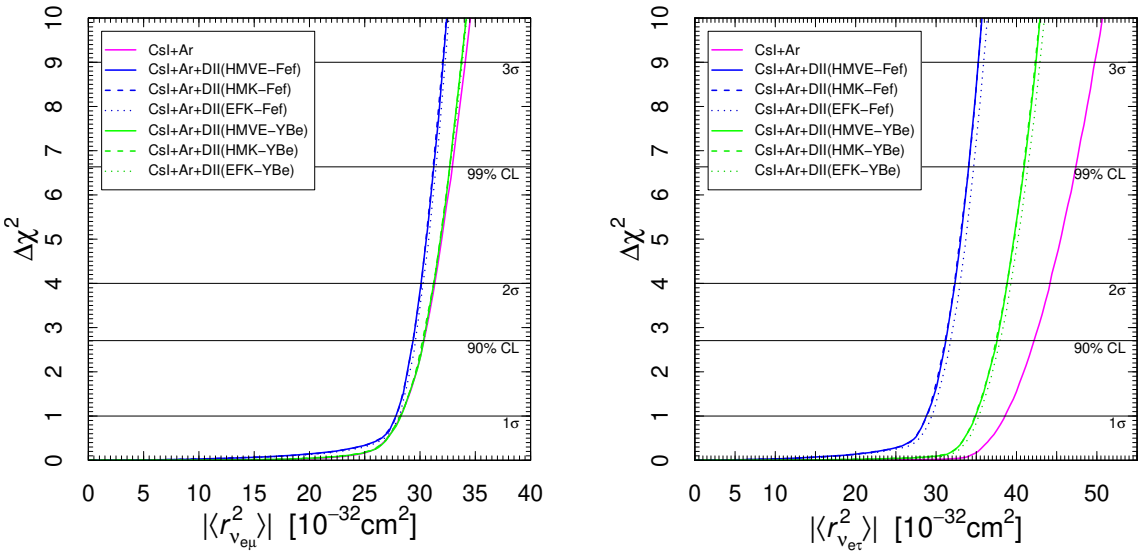

Figure 7.4: Marginal $\Delta\chi^2$'s for $\lvert\langle r^2_{\nu_{e\mu}}\rangle\rvert$ and $\lvert\langle r^2_{\nu_{e\tau}}\rangle\rvert$ obtained from the analysis in the presence of transitional CR of the COHERENT CsI and Ar data (magenta), and from the combination with the Dresden-II data assuming the HMVE, HMK, or EFK reactor antineutrino flux and the Fef (blue) or YBe (green) quenching.

We also assumed the absence of transition CR, fitting thus only for the diagonal charge radii $\langle r^2_{\nu_e} \rangle \equiv \langle r^2_{\nu_{ee}} \rangle$ and $\langle r^2_{\nu_\mu} \rangle \equiv \langle r^2_{\nu_{\mu\mu}} \rangle$ [6]. In this way, we directly probe the values of the neutrino CR in the SM. However, since it is also possible that BSM physics generates off-diagonal neutrino CR that are much smaller than the diagonal ones and that can thus be neglected in a first approximation, also new physics models can be tested in this scenario. The bounds are shown in Tabs. 7.5, 7.6 and 7.7 from the analysis of COHERENT data only, Dresden-II data only for the HMVE reactor antineutrino fluxes and the two germanium QFs (only $\langle r^2_{\nu_e} \rangle$ can be tested in this case) and their combinations, respectively [6].

	1σ	90%	2σ	3σ
		CsI		
$\langle r^2_{\nu_e} \rangle$	$(-62.4, -57.2)$ $(-2.9, 10.1)$	$(-68.1, -49.4)$ $(-8.6, 13.8)$	$(-70.4, -45.1)$ $(-12.4, 15.8)$	$(-76.8, 21.6)$
$\langle r^2_{\nu_\mu} \rangle$	$(-7.0, 0.5)$	$(-57.4, -49.0)$ $(-9.7, 2.9)$	$(-59.2, -46.9)$ $(-11.2, 4.4)$	$(-64.0, -41.8)$ $(-16.0, 8.6)$
		Ar		
$\langle r^2_{\nu_e} \rangle$	$(-79.3, -37.7)$ $(-12.4, 28.8)$	$(-88.5, 38.0)$	$(-93.4, 43.1)$	$(-109.8, 59.2)$
$\langle r^2_{\nu_\mu} \rangle$	$(-59.2, -36.4)$ $(-13.9, 8.6)$	$(-64.9, 14.6)$	$(-67.6, 17.3)$	$(-75.1, 24.5)$
		CsI + Ar		
$\langle r^2_{\nu_e} \rangle$	$(-65.5, -54.6)$ $(-1.7, 10.9)$	$(-69.3, -49.2)$ $(-6.9, 14.4)$	$(-71.3, -45.4)$ $(-10.6, 16.4)$	$(-77.0, 22.1)$
$\langle r^2_{\nu_\mu} \rangle$	$(-54.7, -51.4)$ $(-6.4, 0.8)$	$(-57.7, -47.8)$ $(-8.8, 3.2)$	$(-59.2, -46.3)$ $(-10.3, 4.7)$	$(-63.1, -41.8)$ $(-14.8, 8.6)$

Table 7.5: Bounds on the diagonal neutrino charge radii in units of 10^{-32} cm^2 obtained from the analysis of the COHERENT CsI and Ar data in the absence of transition charge radii.

	1σ	90%	2σ	3σ
		Dresden-II (HMVE-Fef)		
$\langle r^2_{\nu_e} \rangle$	$(-54.3, -45.0)$ $(-7.4, 1.6)$	$(-56.7, -40.8)$ $(-11.6, 4.0)$	$(-58.0, -38.0)$ $(-14.7, 5.4)$	$(-61.1, 8.4)$
		Dresden-II (HMVE-YBe)		
$\langle r^2_{\nu_e} \rangle$	$(-61.5, -48.5)$ $(-3.9, 8.9)$	$(-64.8, -42.4)$ $(-10.3, 12.2)$	$(-66.4, -37.5)$ $(-15.1, 13.9)$	$(-70.8, 18.3)$

Table 7.6: Bounds on the electron neutrino charge radius $\langle r^2_{\nu_e} \rangle$ in units of 10^{-32} cm^2 obtained from the analysis of the Dresden-II data with the HMVE reactor antineutrino flux and the Fef or YBe quenching in the absence of transition charge radii.

	1σ	90%	2σ	3σ
	CsI + Ar + Dresden-II (HMVE-Fef)			
$\langle r^2_{\nu_e} \rangle$	$(-53.5, -52.1)$	$(-57.0, -47.4)$	$(-58.4, -45.3)$	$(-61.4, -38.6)$
	$(-4.2, 2.9)$	$(-7.1, 5.0)$	$(-8.9, 5.9)$	$(-15.4, 8.8)$
$\langle r^2_{\nu_\mu} \rangle$	$(-56.2, -52.9)$	$(-58.9, -50.5)$	$(-60.0, -49.4)$	$(-63.5, -46.3)$
	$(-3.9, 2.3)$	$(-5.9, 4.3)$	$(-7.0, 5.4)$	$(-10.0, 8.9)$
	CsI + Ar + Dresden-II (HMVE-YBe)			
$\langle r^2_{\nu_e} \rangle$	$(-61.0, -54.6)$	$(-63.9, -50.6)$	$(-65.4, -48.4)$	$(-69.0, -40.3)$
	$(-0.52, 8.3)$	$(-4.1, 10.8)$	$(-6.3, 12.0)$	$(-14.3, 15.6)$
$\langle r^2_{\nu_\mu} \rangle$	$(-54.7, -51.6)$	$(-57.6, -48.8)$	$(-58.9, -47.4)$	$(-62.4, -43.5)$
	$(-5.6, 0.96)$	$(-7.8, 3.2)$	$(-9.2, 4.3)$	$(-12.9, 8.0)$

Table 7.7: Bounds on the diagonal neutrino charge radii in units of 10^{-32} cm^2 obtained from the combined analysis of the COHERENT CsI and Ar data and the Dresden-II data assuming the HMVE reactor antineutrino flux and the Fef or YBe quenching in the absence of transition charge radii.

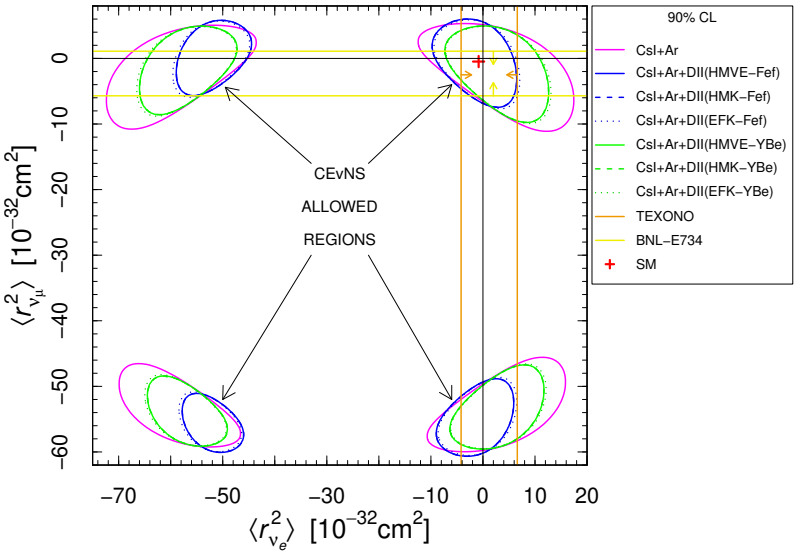

Figure 7.5: Contours of the 90% C.L. allowed regions in the $(\langle r^2_{\nu_e} \rangle, \langle r^2_{\nu_\mu} \rangle)$ plane obtained from the analysis of the COHERENT CsI and Ar data (magenta), and from the combined analysis of the COHERENT data and Dresden-II data assuming the HMVE, HMK, or EFK reactor antineutrino flux and the Fef (blue) or YBe (green) quenching, in the absence of transition charge radii. The red cross near the origin indicates the Standard Model values. The orange and yellow lines delimit, respectively, the 90% bounds on $\langle r^2_{\nu_e} \rangle$ and $\langle r^2_{\nu_\mu} \rangle$ obtained in the TEXONO [348] and BNL-E734 [349] experiments.

The corresponding contours of the 90% C.L. allowed regions in the $(\langle r^2_{\nu_e} \rangle, \langle r^2_{\nu_\mu} \rangle)$ plane are shown in Fig. 7.5 [6]. One can see that the contribution of the Dresden-

II data leads to a considerable restriction of the allowed regions, especially when using the Fef QF (blue contours). Here, we also show the SM values in Eq. 7.6 and Eq. 7.7 and the 90% bounds on $\langle r^2_{\nu_e} \rangle$ and $\langle r^2_{\nu_\mu} \rangle$ obtained, respectively, in the TEXONO [348] and BNL-E734 [349] experiments. Indeed, by comparing the allowed regions in Fig. 7.5 with the one shown in Fig. 7.2, we notice how by allowing for nonzero off-diagonal charge radii the allowed regions gets significantly larger, while, the assumption of only diagonal terms ends up with four smaller allowed regions, one of which is centered in the SM predictions for the charge radii (top right in the plot).
In Fig. 7.6 we also show the marginal $\Delta\chi^2$'s for $\langle r^2_{\nu_e} \rangle$. As summarized in Tab. 7.4, assuming the absence of the transition CR we obtain a very competitive limit at 90% C.L. with respect to that set by TEXONO and the one by BNL-E734 when using the Fef QF, namely

$$-7.1 < \langle r^2_{\nu_e} \rangle < 5, \tag{7.15}$$
$$-5.9 < \langle r^2_{\nu_\mu} \rangle < 4.3 \tag{7.16}$$

in units of $10^{-32}\,\text{cm}^2$.

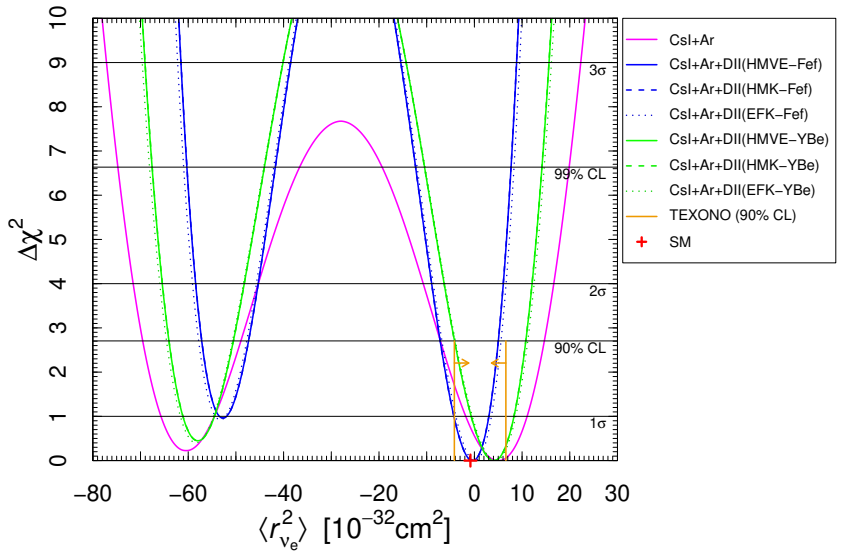

Figure 7.6: Marginal $\Delta\chi^2$'s for $\langle r^2_{\nu_e} \rangle$ obtained from the analysis of the COHERENT CsI and Ar data (magenta), and from the combined analysis of the COHERENT data and Dresden-II data assuming the HMVE, HMK, or EFK reactor antineutrino flux and the Fef (blue) or YBe (green) quenching, in the absence of transition charge radii. The red cross near the origin indicates the Standard Model value in Eq. 7.6. The short vertical orange lines show the lower and upper 90% bounds on $\langle r^2_{\nu_e} \rangle$ obtained in the TEXONO [348] experiment.

In particular, we are able to restrict the upper bound limit from $6.6 \times 10^{-32}\,\text{cm}^2$ to $5 \times 10^{-32}\,\text{cm}^2$. When using the YBe QF, the limit becomes $-4.1 < \langle r^2_{\nu_e} \rangle < 10.8$ in units of $10^{-32}\,\text{cm}^2$, with a slightly better lower bound with respect to that set by TEXONO. In both cases, the limits obtained are practically independent of the

particular reactor antineutrino flux used.
We repeated all of the above bound calculations including also the ES contribution for both the CsI and Dresden-II data sets. However, no effect is found due to ES on the neutrino CR, thus the results are independent of its inclusion.

7.1.1 —— Effective momentum dependent neutrino charge radius ——

As we have already discussed, the neutrino charge radius was introduced in the context of the radiative corrections to be considered when calculating the running of the weak mixing angle for neutrino scattering processes [347]. Indeed, the running of the weak mixing angle was evaluated only at one-loop level using a slightly different formalism with respect to the one considered in Refs. [27, 28] (see Sec. 1.1). The formalism presented in Ref. [347] consists of an effective form factor which allows one to define the weak mixing angle at a certain energy scale from its value at the Z mass energy scale, namely

$$\sin^2\theta_W(q^2) = k_{\nu_\ell}(q^2)\sin^2\theta_W(m_Z) \equiv k_{\nu_\ell}(q^2)s_Z^2\,, \tag{7.17}$$

where $k_{\nu_\ell}(q^2)$ is defined by

$$\begin{aligned} k_{\nu_\ell}(q^2) = 1 - \frac{\alpha}{2\pi s_Z^2}\Big[2\sum_f (T_{3f}Q_f - 2s_Z^2Q_f^2)J_f(q^2) - 2R_\ell(q^2) + \\ + \frac{c_Z^2}{3} + \frac{1}{2} + \frac{1}{c_Z^2}\Big(\frac{19}{8} + \frac{17}{4}s_Z^2 + 3s_Z^4\Big) - \Big(\frac{7}{2}c_Z^2 + \frac{1}{12}\Big)\ln c_Z^2\Big]\,, \end{aligned} \tag{7.18}$$

where we defined $s_Z^2 \equiv \sin^2\theta_W(m_Z)$ and $c_Z^2 \equiv \cos^2\theta_W(m_Z)$. T_{3f} is the fermion weak isospin third component, Q_f the fermion charge. The sum runs over all the fermions f. It is crucial to notice that while the $J_f(q^2)$ term is relative to all the fermions f, the $R_\ell(q^2)$ one is relative only to the lepton flavor ℓ of the neutrino involved in the scattering process. The latter terms are defined by the following integrals

$$J_f(q^2) = \int_0^1 dx\, x(1-x)\ln\Big[\frac{m_f^2 - q^2x(1-x)}{m_Z^2}\Big]\,, \tag{7.19}$$

$$R_\ell(q^2) = \int_0^1 dx\, x(1-x)\ln\Big[\frac{m_\ell^2 - q^2x(1-x)}{m_W^2}\Big]\,, \tag{7.20}$$

from which we can notice that the two terms have the same structure, but for the different mass in the denominator.
In principle, if no neutrino is involved in the scattering process, the $R_\ell(q^2)$ term vanishes, obtaining the definition of the weak mixing angle running for a generic scattering process.
It is easy to understand that the approximated running described in this formalism results to be much easier than the one obtained in the RGE formalism, although it is not complete.
By comparing the two descriptions of the running of the weak mixing angle in

Eq. 7.17 and Eq. 1.23 in the zero momentum limit, $q^2 \to 0$ it can be noticed that the weak mixing angle value obtained differs only for a constant term, namely

$$\sin^2\theta_W(0) = (k_{\nu_\ell} s_W^2) - s_0^2(\mathrm{RGE}) = -\frac{2\alpha}{9\pi} + \mathcal{O}(\alpha^2)\,, \tag{7.21}$$

in the case one neglects the flavor dependent term, R_ℓ. In fact, the R_ℓ term is not included in the RGE running, as in the RGE discussion, it is included as a radiative correction to the coupling. However, since the two formalisms are consistent among them but for the aforementioned constant term, the flavor dependent radiative correction in the RGE formalism should coincide with the R_ℓ term, at least in the $q^2 \to 0$ limit [27, 28].
By calculating $R_\ell(0)$ one obtains

$$R_\ell(0) = \frac{1}{6}\ln\frac{m_\ell^2}{m_W^2}\,. \tag{7.22}$$

In reality, in the running definition in Ref. [347], there is also a constant term $(1/4)$ which is added in the case of neutrino scattering, which together with R_ℓ constitutes the NCR radiative contribution.
Therefore, we can define the NCR radiative correction which is common in both descriptions [147, 347]

$$\phi_{\nu_\ell W} = -\frac{\alpha}{6\pi}\left(\ln\frac{m_W^2}{m_\ell^2} + \frac{3}{2}\right)\,, \tag{7.23}$$

which can be easily obtained also by considering the definitions in Eq. 7.9 and Eq. 7.5, and in the formalism of Ref. [347] can be defined as

$$\phi_{\nu_\ell W} = -\frac{\alpha}{\pi}\left(-R_\ell(0) + \frac{1}{4}\right)\,. \tag{7.24}$$

The interesting aspect of the latter definition is that it can be easily extended to consider the case of a nonzero momentum transfer just by letting the momentum in the R_ℓ integral being different from zero. This can easily be considered a more realistic scenario, since the experiments are run at a nonzero momentum transfer. However, it is necessary to make a clarification: we need to distinguish between the NCR radiative correction and the actual physical NCR. In fact, the NCR is an observable by definition at zero momentum transfer, as it represents the value of the form factor derivative at zero momentum transfer, as shown in Eq. 7.4, while the NCR radiative correction could have a momentum dependence, as it is a correction to the coupling.
Thus, we can generalize the NCR radiative correction by defining

$$\begin{aligned}\phi_{\nu_\ell W}^{\mathrm{eff}}(q^2) &= -\frac{\alpha}{\pi}\left(-R_\ell(q^2) + \frac{1}{4}\right) \\ &= -\frac{\alpha}{\pi}\left(-\int_0^1 dx\, x(1-x)\ln\left[\frac{m_\ell^2 - q^2x(1-x)}{m_W^2}\right] + \frac{1}{4}\right)\,.\end{aligned} \tag{7.25}$$

Since the experimental extraction of the neutrino charge radius does not happen at $q^2 = 0$ but at the experimental energy scale, it may be important to account for the momentum dependence of the neutrino charge radius radiative correction. Thus, to extract the actual NCR value, one should carefully correct for the momentum dependence.
To match the previous definition of the neutrino charge radius correction to the couplings in the case of νES and CEνNS, we can define an effective NCR, namely

$$\langle r^2 \rangle_\ell^{\text{eff}} = \frac{6G_F}{\sqrt{2}\pi\alpha}\phi_{\nu_\ell W}^{\text{eff}}(q^2) = -\frac{G_F}{2\sqrt{2}\pi^2}\left[3 - 12R_\ell(q^2)\right], \tag{7.26}$$

so that, we can obtain the couplings by using this effective NCR instead of the classical one inside Eq. 7.9 and analogously for the case of the neutrino-electron coupling. Indeed, we can notice that this is fully in agreement with the classical procedure to include radiative corrections to the coupling as described in Appendix A, where we consider the standard NCR radiative correction defined in Eq. 7.23.

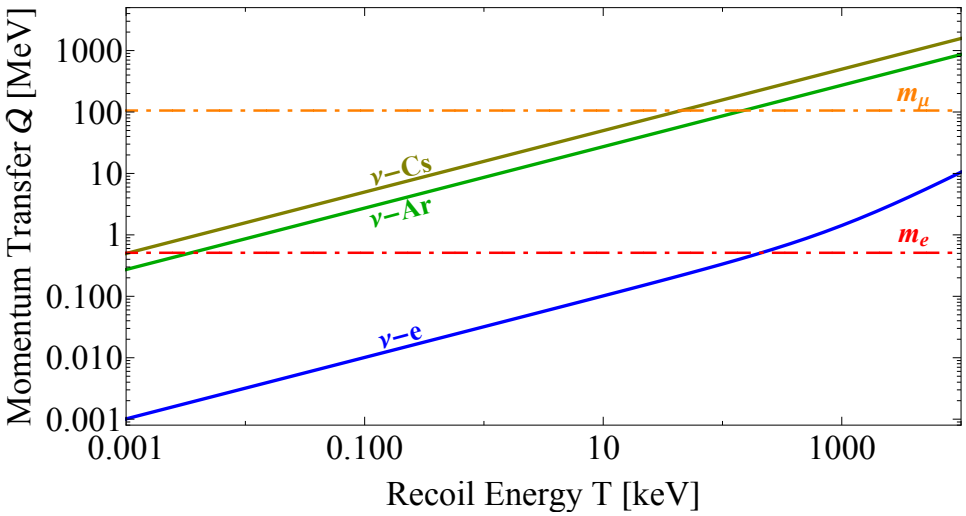

Figure 7.7: Momentum transfer as a function of the recoil energy for the case of neutrino scattering off electrons (blue) and on nuclei (cesium in olive and argon in green). The horizontal lines indicate the electron (red) and muon (orange) masses.

The momentum dependence of $\phi_{\nu_\ell W}^{\text{eff}}$ is thus described by the momentum dependence in $R_\ell(q^2)$, and given the form of $R_\ell(q^2)$ (see Eq. 7.20), it is possible to understand that this correction due to the nonzero momentum becomes effective for momenta larger than the mass of the charged lepton ℓ, $q^2 \gtrsim m_\ell^2$. In this sense, the impact on the couplings becomes visible for $q \geq 1\,\text{MeV}$ in the case of ν_e processes, while above $\sim 100\,\text{MeV}$ for ν_μ. In the case of ν_τ one has to go to even a higher momentum transfer, which is not relevant for the momenta of the νES and CEνNS experiments that we are considering. Let us remind that we can calculate the momentum transfer as a function of the recoil energy (either nuclear or electron recoil) by

$$Q^2 = -q^2 \sim 2m_{\text{tar}}T\,, \tag{7.27}$$

where $m_{\rm tar}$ is the target mass, so either the nuclear or the electron mass, and T the recoil energy, $T_{\rm nr}$ or T_e depending on the case. From a purely kinematic analysis, we can thus understand whether the momentum dependence of the NCR radiative correction may or may not produce an effect in current analysis. Therefore, in Fig. 7.7 we show the momentum transfer as a function of the recoil energy considering the case of neutrino scattering off electrons (blue), argon nuclei (green) and cesium nuclei (olive), compared to the momentum transfer correspondent to the mass of electrons and muons, which represent a sort of threshold for the momentum dependence. From the figure, we already understand that in order to have an effect in the νES case, it is necessary to reach very high electron recoil energies (above $\sim 100\,\mathrm{keV}$ for the electron case), while, thanks to the large nuclear masses, in the CEνNS case, we are above the electron mass threshold already for eV scale nuclear recoils.

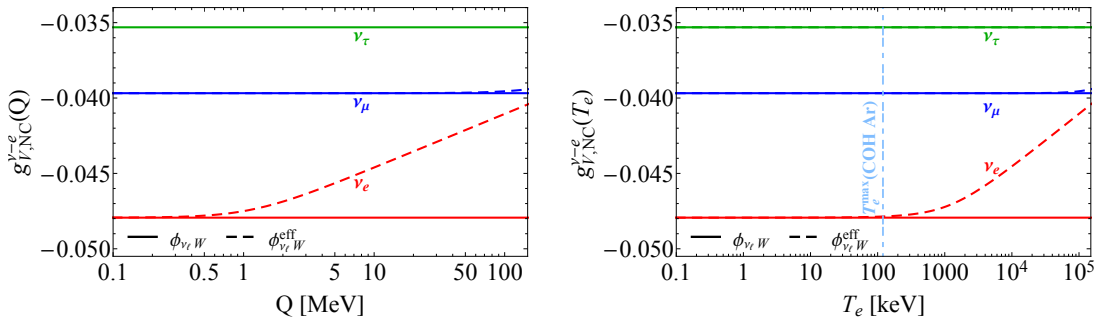

Figure 7.8: Neutral current neutrino-electron coupling as a function of the momentum transfer (Left) and the electron recoil energy (Right). The solid lines refer to the canonical values of the couplings (considering the SM NCR), while the dashed ones to the couplings evaluated considering the effective neutrino charge radius radiative corrections. The vertical light blue line indicates the maximum electron recoil energy relative to the COHERENT argon data set [53].

In Fig. 7.8 (Left) we compare the neutrino-electron neutral current couplings calculated considering the momentum dependent NCR radiative correction (dashed lines) and the ones with the constant NCR radiative correction (solid lines) for the three different neutrino flavors. In the right panel of the same plot, we show the same results as a function of the electron recoil energy instead of the momentum transfer. It is evident that, as we guessed, the effect of the momentum dependence becomes visible after the threshold given by the lepton mass. For electron neutrinos, we clearly observe a deviation after $Q \sim 1\,\mathrm{MeV}$, and we start observing it for the muon neutrinos, above $Q \sim 100\,\mathrm{MeV}$. However, as we see in the right plot, these momentum transfers correspond to relatively large electron recoil energies, i.e. above ~ 100 keV for electron neutrinos, which are above the typical electron recoil energies of CEνNS experimental data. To give an idea, we show the maximum electron recoil energy of the COHERENT argon data [53] by the vertical light blue line, which is well below the recoils for which the momentum dependence is not negligible. Therefore, we can conclude, that concerning CEνNS experiment data analysis, we can safely consider the classical constant NCR radiative correc-

tion in the νES channel.

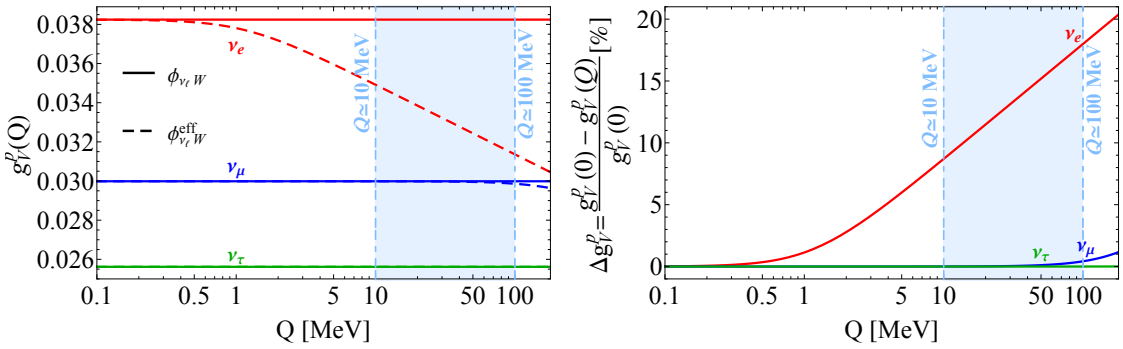

Figure 7.9: (Left) Neutrino-proton coupling for CEνNS process as a function of the momentum transfer. The solid lines refer to the couplings considering the constant NCR radiative correction, while the dashed ones to the momentum dependent neutrino charge radius radiative corrections case. (Right) Percentage variation of the neutrino-proton coupling by considering or not the momentum dependence in the neutrino charge radius radiative correction. The vertical blue lines and the shaded area indicate the typical momentum transfer of CEνNS experiments.

We can now consider the effect on neutrino-proton couplings. In fact, as we already discussed, the NCR radiative correction does not contribute to the neutrino-neutron coupling because there is no photon-neutron vertex. In Fig. 7.9 (Left) we show the variation of the neutrino-proton coupling as a function of the momentum transfer comparing the two NCR radiative correction schemes. Clearly, if we consider the typical momentum transfer of CEνNS experiments $Q \sim 10 - 100\,\mathrm{MeV}$ (shown by the shaded light blue area), we can notice that the variation of the coupling is already non-negligible for the ν_e case.
The effect on the $\nu_\mu - p$ coupling is in general significant for heavier momentum transfer, so that, for ν_μ CEνNS we can safely employ the constant NCR radiative correction.
To quantify the impact of such effect on the couplings, in the right plot in Fig. 7.9 we show the percentage variation of the coupling as a function of the momentum transfer. In the momentum transfer region of interest, the variation of the $\nu_e - p$ coupling due to this effect is between $\sim 10 - 20\%$, while we see that there is almost no effect for the other two neutrino flavors.
In Fig. 7.10, we re-propose the variation of the $\nu_\ell - p$ couplings but as a function of the nuclear recoil energy by considering argon nuclei (left) and cesium nuclei (right) as examples of CEνNS targets. It is evident that in both cases, the $\nu_e - p$ coupling should be evaluated accounting for this momentum dependence of the NCR radiative correction, while for the other neutrino flavor, the constant radiative correction is sufficient.
Although the effect on the $\nu_e - p$ coupling does not seem to be small, being around the 10-20% level, the overall effect on the cross section and the experimental rate is rather small. Indeed, this effect involves only ν_e, so that in the case of COHERENT, only one flux component would be affected.
Moreover, the variation is only for the coupling to protons, which are naturally

suppressed by the weak mixing angle inside the nuclear weak charge in Eq. 2.47, so that in practice we are dealing with a not so large effect affecting a suppressed quantity.

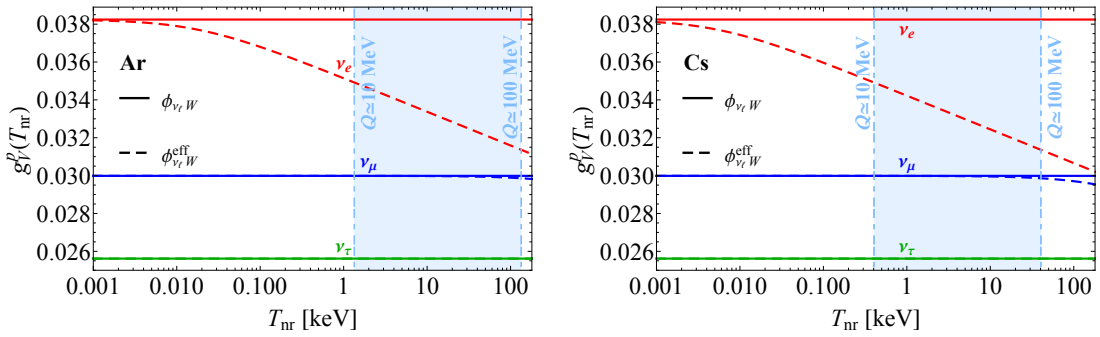

Figure 7.10: Neutrino-proton coupling as a function of the nuclear recoil energy for the CEνNS process on argon (Left) and cesium (Right). The solid lines refer to the canonical values of the couplings (considering the SM NCR), while the dashed ones to the couplings evaluated considering the effective neutrino charge radius radiative corrections. The vertical blue lines and the shaded area indicate the typical nuclear recoil energies of CEνNS experiments.

We estimate that the effect on the $\nu_e - \mathcal{N}$ scattering cross section is around $1-2\%$, which results, taking the COHERENT measurements as an example, in an effect below 1% on the total event rate (around 1-2% on the ν_e only event rate). Thus, it is evident that, due to the current precision of experimental measurements, the constant NCR radiative correction is sufficient to well describe also the CEνNS process. For reference, the current precision on the flux averaged CEνNS cross section measured by COHERENT results in about 15-20% for the CsI data [54] and about $\sim 35\%$ for the Ar ones [53]. Nonetheless, for future measurements, it will become crucial to account for this additional momentum dependence, especially as the community is putting a great effort into reaching the high precision frontier. Furthermore, if one wants also to perform the first neutrino charge radius measurement (and not only constraint its value), this effect could potentially mislead the extraction, as the quantity that one measures, in the case of the electron neutrinos, is the effective NCR, which has to be corrected for the momentum dependence in order to extract the physical NCR.
Additionally, it is worth mentioning the radiative corrections calculated in Ref. [356], in which an Effective Field Theory (EFT) approach has been employed in order to determine the radiative corrections to the CEνNS process. The formalism is rather different with respect to the one considered in our work, however, the two descriptions should be equivalent. In this EFT approach, the flavor dependent contribution, given by the neutrino charge radius, has been evaluated through a polarization diagram, which is indeed equivalent to the integral defined in Eq. 7.20. In Ref. [356], the authors themselves compared the prescription commonly adopted in literature [346, 350] with their EFT approach, however, considering only the zero-momentum limit, so that a more complete and careful comparison is left for future studies.

7.2 Neutrino Magnetic Moment

The neutrino magnetic moment (MM) is the most investigated neutrino electromagnetic property by theorists. They also attract the interest of experimentalists, although the value of the magnetic moments of Dirac neutrinos predicted in the simplest extension of the SM (adding right-handed neutrinos) is proportional to the neutrino mass, and thus, it is orders of magnitude smaller than the present experimental limits. Indeed, the existence of neutrino magnetic moments is also predicted by many BSM theories, especially those that include right-handed neutrinos, see the reviews in Refs. [37, 357], in which the new physics can enhance their values making them potentially observable in current and future experiments.
In the minimal extension of the SM with right-handed neutrinos the magnetic moment cannot flip chirality, as the vertices involve only left-handed neutrinos. At the leading order, the diagonal magnetic moments for Dirac neutrinos are expected to have a value of [37]

$$\mu_{kk}^{\mathrm{D}} \simeq 3.2 \times 10^{-19} \left(\frac{m_k}{\mathrm{eV}}\right) \mu_{\mathrm{B}} \,, \tag{7.28}$$

where we use the superscript D in the magnetic moment μ_{kk} to indicate that we are referring to Dirac neutrinos, μ_{B} is the Bohr magneton, and m_ℓ the mass of the k flavor neutrino. Given that the current limit on the neutrino mass is ~ 1 eV [358], one can estimate the order of magnitude of the neutrino magnetic moment. In this framework, off-diagonal magnetic moments, μ_{kj}^{D}, following a similar flavor structure to the one discussed for NCR, can be nonzero, however, they result to be suppressed with respect to the diagonal terms [37], at least of a factor of the order of 10^{-4}. Instead, in the case of Majorana neutrinos, only transition (off-diagonal) magnetic moments are allowed, and are expected to be of the same order of magnitude of the Dirac transition magnetic moments [37]. The differences between Majorana and Dirac neutrino magnetic moments have gained a lot of popularity as it could, in principle, help in unveiling the nature of the neutrino.

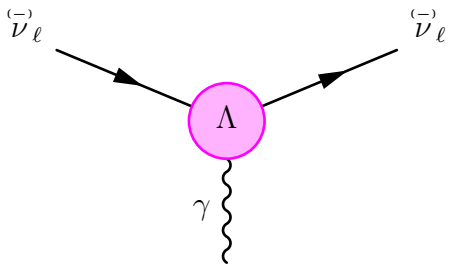

Figure 7.11: Diagram showing the effective one-photon coupling of a neutrino with a photon. The magenta blob and Λ describe the effective operator describing the neutrino electromagnetic interaction [37].

In Fig. 7.11, we show a representation of the effective one-photon coupling of a neutrino with a photon arising from BSM neutrino electromagnetic properties,

such as the neutrino magnetic moment. The blob generically includes the vertices arising from the specific operator describing the neutrino electromagnetic interaction.
Historically, the most used method to test neutrino MMs has been νES either by reactor antineutrinos, accelerator neutrinos or solar neutrinos. In the case of neutrino-electron scattering, the cross section in the presence of neutrino magnetic moments receives an additional contribution equal to

$$\frac{d\sigma^{\text{ES, MM}}_{\nu_\ell\text{-}\mathcal{A}}}{dT_\text{e}}(E, T_\text{e}) = Z^{\mathcal{A}}_{\text{eff}}(T_\text{e})\frac{\pi\alpha^2}{m_e^2}\left(\frac{1}{T_\text{e}} - \frac{1}{E}\right)\left|\frac{\mu_{\nu_\ell}}{\mu_\text{B}}\right|^2, \tag{7.29}$$

with $Z^{\mathcal{A}}_{\text{eff}}(T_e)$ being the effective coupling which accounts for the binding energies of atomic electrons as discussed in Sec. 2.1 (numerical values can be found in Appendix C), and where μ_{ν_ℓ} is the effective MM of the flavor neutrino ν_ℓ in elastic scattering (see Ref. [37]). This cross section is summed with the SM one in Eq. 2.15. It is worth noticing that the cross section for the MM contribution scales as $\propto 1/T_e$, which means that the cross section is highly enhanced at low recoil energies. This BSM property is thus testable if one is able to measure very tiny recoil energies. As in the case of neutrino charge radii, the cross section obtained with the corrected FEA approach, thus using $Z^{\mathcal{A}}_{\text{eff}}(T_e)$, is slightly larger than the MCR-RPA one only for $T_e \lesssim 1$ keV [44]. Therefore, in the analysis of the COHERENT data and the Dresden-II one, we will consider the corrected FEA method.

	1σ	90%	2σ	3σ	Interaction
Dresden-II (HMVE-Fef)					
$\lvert\mu_{\nu_e}\rvert$	< 1.65	< 2.34	< 2.66	< 3.41	CEvNS
	< 1.45	< 2.13	< 2.45	< 3.20	CEvNS+ES
Dresden-II (HMVE-YBe)					
$\lvert\mu_{\nu_e}\rvert$	< 3.02	< 3.68	< 4.00	< 4.79	CEvNS
	< 2.51	< 3.25	< 3.58	< 4.41	CEvNS+ES

Table 7.8: Bounds on the electron neutrino magnetic moment $|\mu_{\nu_e}|$ in units of 10^{-10} μ_B obtained from the analysis of the Dresden-II data assuming the HMVE and the Fef or YBe quenching. We show the results obtained with CEνNS only interactions and with CEνNS+ES interactions.

Similarly, the differential CEνNS cross section that takes into account the contribution of the neutrino magnetic moment is given by adding to the SM cross section in Eq. 2.46 the MM contribution, namely

$$\frac{d\sigma^{\text{MM}}_{\nu_\ell\text{-}\mathcal{N}}}{dT_\text{nr}}(E_\nu, T_\text{nr}) = \frac{\pi\alpha^2}{m_e^2}\left(\frac{1}{T_\text{nr}} - \frac{1}{E_\nu}\right)Z^2F_Z^2(q^2)\left|\frac{\mu_{\nu_\ell}}{\mu_\text{B}}\right|^2. \tag{7.30}$$

We study the bounds on the neutrino MM [6], namely on $|\mu_{\nu_e}|$ and $|\mu_{\nu_\mu}|$ using the COHERENT data [53, 54] and $|\mu_{\nu_e}|$ only using the Dresden-II data [92], using the χ^2 functions in Eq. 2.75, Eq. 2.77 and Eq. 2.84. The numerical results of our analysis for the neutrino MM are shown in Tab. 7.8 and Tab. 7.9 for the Dresden-II

data and for COHERENT CsI and Ar data set and their combination, respectively. In both cases, we separate the scenarios in which ES is not considered, from those in which the ES contribution is added in the COHERENT CsI and the Dresden-II data set analyses.

	1σ	90%	2σ	3σ	1σ	90%	2σ	3σ
	CsI (CEvNS)				**CsI (CEvNS+ES)**			
$\lvert\mu_{\nu_e}\rvert$	< 36	< 44	< 49	< 62	< 32	< 41	< 46	< 58
$\lvert\mu_{\nu_\mu}\rvert$	< 12	< 18	< 21	< 28	< 11	< 17	< 19	< 27
	Ar (CEvNS)							
$\lvert\mu_{\nu_e}\rvert$	< 53	< 65	< 72	< 91				
$\lvert\mu_{\nu_\mu}\rvert$	< 32	< 39	< 43	< 54				
	CsI (CEvNS) + Ar (CEvNS)				**CsI (CEvNS+ES) + Ar (CEvNS)**			
$\lvert\mu_{\nu_e}\rvert$	< 37	< 44	< 48	< 59	< 34	< 42	< 46	< 56
$\lvert\mu_{\nu_\mu}\rvert$	< 13	< 19	< 21	< 28	< 12	< 18	< 20	< 27

Table 7.9: Bounds on the neutrino magnetic moments in units of 10^{-10} $\mu_{\rm B}$ obtained from the analysis of the COHERENT CsI and Ar data. We show the results of the analyses of CsI data with CEνNS only interactions and with CEνNS+ES interactions.

For the Dresden-II results, we show only the numerical results obtained considering the HMVE parametrization of the reactor antineutrino flux as the choice of the parametrization leads to marginal differences in the bounds. The complete table can be found in Ref. [6].
By comparing Tab. 7.8 and Tab. 7.9, it is clear that the Dresden-II data allow us to significantly improve the bound on $|\mu_{\nu_e}|$ with respect to COHERENT by more than one order of magnitude. Also in this case, the two QFs produce a noticeable effect, with the Fef QF limits being almost a factor of two more precise. The COHERENT Ar bounds are less stringent than the CsI ones, so that, the combined COHERENT results are practically driven by COHERENT CsI data, and we observe that the inclusion of the ES leads only to small improvements. The inclusion of ES results in a marginal improvement of about 10% also for the Dresden-II limits. At 90% C.L., the bounds on the neutrino MM obtained in this work are

$$|\mu_{\nu_e}| < 2.13 \times 10^{-10}\,\mu_{\rm B} \quad {\rm Dresden-II\,(CE\nu NS+ES)}, \tag{7.31}$$

$$|\mu_{\nu_\mu}| < 18 \times 10^{-10}\,\mu_{\rm B} \quad {\rm CsI\,(CE\nu NS+ES) + Ar\,(CE\nu NS)}, \tag{7.32}$$

where for the Dresden-II data the Fef QF has been considered. For the Ar data set no contribution from νES was considered as thanks to the pulse shape discrimination technique, nuclear and electron recoil signals can be distinguished by looking at the different shapes of the signal in the data acquisition. These limits can be compared with the bounds obtained in accelerator experiments with $\nu_\mu - e$ scattering (see Table IV of Ref. [37]).
The most stringent is the LSND bound $|\mu_{\nu_\mu}| < 6.8 \times 10^{-10}\,\mu_{\rm B}$ at 90% C.L. [353], and that on $|\mu_{\nu_e}|$ established in reactor neutrino experiments, namely $|\mu_{\nu_e}| < 2.9 \times 10^{-11}\,\mu_{\rm B}$ [37, 226].
In Fig. 7.12 we show the marginal $\Delta\chi^2$'s for $|\mu_{\nu_e}|$ and $|\mu_{\nu_\mu}|$ obtained from the COHERENT Ar and CsI data as well as their combination with the CEνNS-only analyses of Dresden-II data assuming the HMVE reactor antineutrino flux and the YBe

or Fef QF. We also show the impact of the ES contribution assuming the HMVE, HMK, or EFK reactor antineutrino flux and the YBe or Fef QF. For comparison, we also show the 90% C.L. upper bounds on $|\mu_{\nu_e}|$ obtained in the MUNU [359], TEXONO [245], and GEMMA [360] experiments; and $|\mu_{\nu_\mu}|$ obtained in the BNL-E734 [349], LAMPF [352], and LSND [353] experiments.

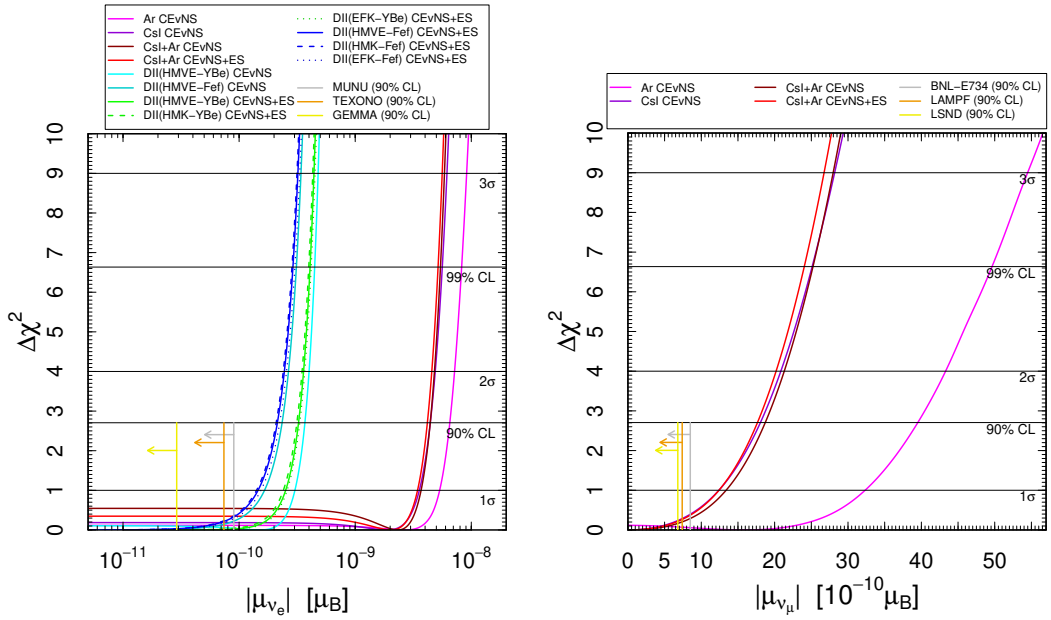

Figure 7.12: Marginal $\Delta\chi^2$'s for $|\mu_{\nu_e}|$ (Left) and $|\mu_{\nu_\mu}|$ (Right) obtained from: the separate analyses of the COHERENT Ar (magenta) and CsI (purple) data with CEνNS interactions; the combined analyses of the COHERENT Ar and CsI data with CEνNS interactions only (dark red) and with CEνNS+ES interactions (red); the CEνNS-only analyses of Dresden-II data assuming the HMVE reactor antineutrino flux and the YBe (cyan) or Fef (dark cyan) quenching; the CEνNS+ES analyses of Dresden-II data assuming the HMVE, HMK, or EFK reactor antineutrino flux and the YBe (green) or Fef (blue) quenching. The short vertical gray, orange, and yellow lines show, respectively, the 90% C.L. upper bounds on: $|\mu_{\nu_e}|$ (Left) obtained in the MUNU [359], TEXONO [245], and GEMMA [360] experiments; $|\mu_{\nu_\mu}|$ (Right) obtained in the BNL-E734 [349], LAMPF [352], and LSND [353] experiments.

Other analyses in which the authors have studied the CEνNS impact on the neutrino MM by analyzing COHERENT and Dresden-II data can be found in Refs. [96, 361, 362]. Similar bounds to those found by us in Ref. [6] have been obtained, although with some differences among the various data analyses, due to different assumptions and procedures. In particular, in Ref. [361], a bound at 90% C.L. of $|\mu_{\nu_e}| < 2.2 \times 10^{-10}\,\mu_B$ is found when using the Dresden-II data using the Fef QF and including the ES contribution as in our work. In this latter case, a very similar treatment of the Dresden-II data with respect to this work has been followed by the authors, with only minimal differences in the antineutrino flux treatment and least-squares function definition.

7.3 Neutrino Electric Charge

In the SM the neutrino is strictly a neutral particle, i.e. its electric charge is exactly zero. However, in some extensions of the SM, the neutrinos can acquire a tiny electric charge (EC), q_ν, usually referred to as millicharge given the very small value of it [37]. The tightest constraint on the neutrino EC comes directly from the neutrality of matter [363, 364], which makes the hypothetical EC of neutrinos so small. Other strong constraints are obtained by exploiting the observation of astrophysical objects, such as supernovae explosions or the rotation of magnetized stars [37].
In the presence of a millicharge, an interaction between the neutrino and the photon would arise, giving rise to a diagram like the one shown in Fig. 7.11, where the blob would indicate the vertex from the new electric charge acquired by the neutrino.
Together with other experimental probes, CEνNS and νES processes are sensitive to the existence of neutrino electric charges. The differential CEνNS cross section taking into account the contribution of the neutrino electric charges in addition to SM neutral-current weak interactions is similar to that derived for the neutrino charge radii (see Eq. 7.10). The cross section is defined by considering the SM couplings g_V^p and g_V^n (with the inclusion of the SM NCR radiative correction) and by replacing $\tilde{Q}_{\ell\ell'}$ with $Q_{\ell\ell'}$ inside Eq. 7.10 [6, 37, 43, 197, 234], where

$$Q_{\ell\ell'} = \frac{2\sqrt{2}\pi\alpha}{G_{\rm F} q^2}\, q_{\nu_{\ell\ell'}}\,, \tag{7.33}$$

with $q_{\nu_{\ell\ell'}}$ being the neutrino EC. Being the momentum transfer inside $Q_{\ell\ell'}$ defined as $q^2 \simeq -2m_N T_{\rm nr}$, we notice that the EC contribution scales as $\propto 1/T_{\rm nr}^2$, so even steeper than the MM contribution, making the low recoil energy threshold a fundamental requirement to strictly constraint neutrino ECs. Given the extremely low momentum transfer and low-energy thresholds of reactor experiments, the constraints from the Dresden-II data are expected to be more stringent than the ones from COHERENT data. As in the case of neutrino CR, the contribution of neutrinos and antineutrinos to the neutrino EC will also shift $\sin^2\theta_W$ with the same sign, since the electric charges of neutrino and antineutrino are opposite as well as the weak neutral current couplings.
If neutrinos have electric charges, the neutrino-electron elastic scattering cross section in Eq. (2.16) becomes [6, 43]

$$\left(\frac{d\sigma^{\rm ES,EC}_{\nu_\ell-\mathcal{A}}}{dT_{\rm e}}\right)_{\rm SM+Q} = \left(\frac{d\sigma^{\rm ES,EC}_{\nu_\ell-\mathcal{A}}}{dT_{\rm e}}\right)_{{\rm SM}+Q_{\ell\ell}} + \sum_{\ell'\neq\ell}\left(\frac{d\sigma^{\rm ES,EC}_{\nu_\ell-\mathcal{A}}}{dT_{\rm e}}\right)_{Q_{\ell\ell'}}, \tag{7.34}$$

where $(d\sigma^{\rm ES,EC}_{\nu_\ell-\mathcal{A}}/dT_{\rm e})_{{\rm SM}+Q_{\ell\ell}}$ is given by Eq. (2.16) with

$$g_V^{\nu_\ell} \to g_V^{\nu_\ell} + Q_{\ell\ell}, \tag{7.35}$$

and

$$\left(\frac{d\sigma^{\rm ES,EC}_{\nu_\ell-\mathcal{A}}}{dT_{\rm e}}\right)_{Q_{\ell\ell'}} = Z^{\mathcal{A}}_{\rm eff}(T_e)\,\frac{\pi\alpha^2}{m_e T_{\rm e}^2}\left[1+\left(1-\frac{T_{\rm e}}{E_\nu}\right)^2 - \frac{m_e T_{\rm e}}{E_\nu^2}\right]|q_{\nu_{\ell\ell'}}|^2, \tag{7.36}$$

for $\ell' \neq \ell$. In neutrino-electron elastic scattering $|q^2| = 2m_e T_e$, which is much smaller than the CEνNS $|q^2|$, given the lighter mass of the electron. Therefore, the analysis of the COHERENT CsI and Dresden-II data taking into account ES scattering allows us to enhance substantially the sensitivity to neutrino millicharges. Let us note that, for neutrino millicharges, the MCRRPA cross section for $T_e \lesssim 1$ keV is more than one order of magnitude bigger than that obtained with the corrected FEA [44]. In this respect, we can consider our Dresden-II ES limits as conservative and tighter limits are expected if the MCRRPA approach is used.

	1σ	90%	2σ	3σ
		CsI (CEvNS)		
$q_{\nu_{ee}}$	$(-1.6, 45.2) \times 10^{-8}$	$(-1.6, 5.8) \times 10^{-7}$	$(-1.9, 6.2) \times 10^{-7}$	$(-2.6, 7.0) \times 10^{-7}$
$q_{\nu_{\mu\mu}}$	$(-8.0, 136.0) \times 10^{-9}$	$(-3.2, 25.2) \times 10^{-8}$	$(-4.4, 30.8) \times 10^{-8}$	$(-8.4, 43.2) \times 10^{-8}$
$\lvert q_{\nu_{e\mu}}\rvert$	$< 1.8 \times 10^{-7}$	$< 2.3 \times 10^{-7}$	$< 2.5 \times 10^{-7}$	$< 2.9 \times 10^{-7}$
$\lvert q_{\nu_{e\tau}}\rvert$	$(1.5, 4.0) \times 10^{-7}$	$< 4.3 \times 10^{-7}$	$< 4.6 \times 10^{-7}$	$< 5.2 \times 10^{-7}$
$\lvert q_{\nu_{\mu\tau}}\rvert$	$< 1.8 \times 10^{-7}$	$< 2.3 \times 10^{-7}$	$< 2.5 \times 10^{-7}$	$< 3.0 \times 10^{-7}$
		CsI (CEvNS+ES)		
$q_{\nu_{ee}}$	$(-3.6, 3.6) \times 10^{-10}$	$(-5.0, 5.0) \times 10^{-10}$	$(-5.6, 5.6) \times 10^{-10}$	$(-7.5, 7.5) \times 10^{-10}$
$q_{\nu_{\mu\mu}}$	$(-1.2, 1.2) \times 10^{-10}$	$(-1.9, 1.9) \times 10^{-10}$	$(-2.2, 2.2) \times 10^{-10}$	$(-3.2, 3.2) \times 10^{-10}$
$\lvert q_{\nu_{e\mu}}\rvert$	$< 1.2 \times 10^{-10}$	$< 1.8 \times 10^{-10}$	$< 2.2 \times 10^{-10}$	$< 3.1 \times 10^{-10}$
$\lvert q_{\nu_{e\tau}}\rvert$	$< 3.5 \times 10^{-10}$	$< 5.0 \times 10^{-10}$	$< 5.6 \times 10^{-10}$	$< 7.5 \times 10^{-10}$
$\lvert q_{\nu_{\mu\tau}}\rvert$	$< 1.2 \times 10^{-10}$	$< 1.9 \times 10^{-10}$	$< 2.2 \times 10^{-10}$	$< 3.2 \times 10^{-10}$
		Ar (CEvNS)		
$q_{\nu_{ee}}$	$(-1.3, 1.7) \times 10^{-7}$	$(-1.7, 3.2) \times 10^{-7}$	$(-2.0, 3.5) \times 10^{-7}$	$(-2.7, 4.4) \times 10^{-7}$
$q_{\nu_{\mu\mu}}$	$(-4.4, 10.0) \times 10^{-8}$	$(-6.8, 21.6) \times 10^{-8}$	$(-8.0, 24.4) \times 10^{-8}$	$(-1.2, 3.0) \times 10^{-7}$
$\lvert q_{\nu_{e\mu}}\rvert$	$< 1.0 \times 10^{-7}$	$< 1.4 \times 10^{-7}$	$< 1.5 \times 10^{-7}$	$< 1.8 \times 10^{-7}$
$\lvert q_{\nu_{e\tau}}\rvert$	$< 2.0 \times 10^{-7}$	$< 2.5 \times 10^{-7}$	$< 2.8 \times 10^{-7}$	$< 3.6 \times 10^{-7}$
$\lvert q_{\nu_{\mu\tau}}\rvert$	$< 1.1 \times 10^{-7}$	$< 1.5 \times 10^{-7}$	$< 1.7 \times 10^{-7}$	$< 2.1 \times 10^{-7}$
		CsI (CEvNS) + Ar (CEvNS)		
$q_{\nu_{ee}}$	$(-12.4, 8.0) \times 10^{-8}$	$(-1.6, 1.7) \times 10^{-7}$	$(-1.7, 2.2) \times 10^{-7}$	$(-2.2, 3.5) \times 10^{-7}$
$q_{\nu_{\mu\mu}}$	$(-1.2, 7.6) \times 10^{-8}$	$(-3.2, 11.2) \times 10^{-8}$	$(-4.0, 12.8) \times 10^{-8}$	$(-6.8, 18.4) \times 10^{-8}$
$\lvert q_{\nu_{e\mu}}\rvert$	$< 1.1 \times 10^{-7}$	$< 1.4 \times 10^{-7}$	$< 1.5 \times 10^{-7}$	$< 1.9 \times 10^{-7}$
$\lvert q_{\nu_{e\tau}}\rvert$	$< 2.4 \times 10^{-7}$	$< 2.9 \times 10^{-7}$	$< 3.1 \times 10^{-7}$	$< 3.7 \times 10^{-7}$
$\lvert q_{\nu_{\mu\tau}}\rvert$	$< 1.2 \times 10^{-7}$	$< 1.5 \times 10^{-7}$	$< 1.6 \times 10^{-7}$	$< 2.0 \times 10^{-7}$
		CsI (CEvNS+ES) + Ar (CEvNS)		
$q_{\nu_{ee}}$	$(-3.5, 3.5) \times 10^{-10}$	$(-5.0, 5.0) \times 10^{-10}$	$(-5.6, 5.6) \times 10^{-10}$	$(-7.5, 7.5) \times 10^{-10}$
$q_{\nu_{\mu\mu}}$	$(-1.2, 1.2) \times 10^{-10}$	$(-1.9, 1.9) \times 10^{-10}$	$(-2.2, 2.2) \times 10^{-10}$	$(-3.2, 3.2) \times 10^{-10}$
$\lvert q_{\nu_{e\mu}}\rvert$	$< 1.2 \times 10^{-10}$	$< 1.8 \times 10^{-10}$	$< 2.2 \times 10^{-10}$	$< 3.1 \times 10^{-10}$
$\lvert q_{\nu_{e\tau}}\rvert$	$< 3.6 \times 10^{-10}$	$< 5.0 \times 10^{-10}$	$< 5.6 \times 10^{-10}$	$< 7.5 \times 10^{-10}$
$\lvert q_{\nu_{\mu\tau}}\rvert$	$< 1.2 \times 10^{-10}$	$< 1.9 \times 10^{-10}$	$< 2.2 \times 10^{-10}$	$< 3.2 \times 10^{-10}$

Table 7.10: Bounds on the neutrino electric charges in units of the elementary charge e_0 obtained from the analysis of the COHERENT CsI and Ar data. We show the results of the analyses of CsI data with CEνNS only interactions and with CEνNS+ES interactions.

In analogy to what we have done in the NCR analysis, there are five electric charges that can be determined with the COHERENT CEνNS data, namely the two diagonal EC $q_{\nu_{ee}}$ and $q_{\nu_{\mu\mu}}$, and the absolute values of the three transition EC $q_{\nu_{e\mu}} = q^*_{\nu_{\mu e}}$, $q_{\nu_{e\tau}}$, and $q_{\nu_{\mu\tau}}$. Instead, using the Dresden-II data, only $q_{\nu_{ee}}$, $|q_{\nu_{e\mu}}|$ and $|q_{\nu_{e\tau}}|$ can be tested. We performed an analysis of the COHERENT data [53, 54] and the Dresden-II ones [92], using the χ^2 functions in Eq. 2.77, Eq. 2.75 and Eq. 2.84 in order to set bounds on the accessible neutrino millicharges.
The results of our analyses are shown in Tab. 7.10 and Tab. 7.11 for the COHERENT CsI and Ar data set and for the Dresden-II data, respectively.
Focusing on the results shown in Tab. 7.10, differently from the analysis of the neutrino CR, the contribution of Ar data is dominant in the combined COHERENT analysis of the neutrino electric charges, although the CsI data set has more statistics. This behaviour follows from the enhancement of the neutrino electric charge effect in CEνNS at low q^2, because of the denominator in Eq. (7.33). However, the expected enhancement due to the different CsI and Ar masses, is mitigated by the different sizes of the energy bins: in the Ar experiment, the first bin includes energies from the threshold, of about 5 $\mathrm{keV_{nr}}$, to about 36 $\mathrm{keV_{nr}}$, whereas the first CsI energy bin has a much smaller size. Therefore, the enhancement of the EC effect occurs only in the first energy bin of the Ar experiment. Nevertheless, this enhancement is sufficient to achieve a slightly better performance of the Ar data in constraining the neutrino EC in spite of the larger uncertainties. In Tab. 7.10 we also explicitly show the impact of including the ES in the CsI analysis, also when combining it with Ar. Thanks to the presence of the q^2 term in the denominator of Eq. (7.33), a large improvement of more than 2 orders of magnitude with respect to the limits derived ignoring the ES contribution is obtained.

	1σ	90%	2σ	3σ
Dresden-II (HMVE-Fef CEvNS)				
$q_{\nu_{ee}}$	$(-1.5, 10.1) \times 10^{-10}$	$(-3.4, 12.5) \times 10^{-10}$	$(-4.3, 13.6) \times 10^{-10}$	$(-6.5, 16.0) \times 10^{-10}$
$\lvert q_{\nu_{e\mu}}\rvert$, $\lvert q_{\nu_{e\tau}}\rvert$	$< 6.0 \times 10^{-10}$	$< 8.2 \times 10^{-10}$	$< 9.1 \times 10^{-10}$	$< 1.1 \times 10^{-9}$
Dresden-II (HMVE-Fef CEvNS+ES)				
$q_{\nu_{ee}}$	$(-7.3, 7.6) \times 10^{-12}$	$(-9.3, 9.5) \times 10^{-12}$	$(-1.0, 1.0) \times 10^{-11}$	$(-1.2, 1.3) \times 10^{-11}$
$\lvert q_{\nu_{e\mu}}\rvert$, $\lvert q_{\nu_{e\tau}}\rvert$	$< 7.4 \times 10^{-12}$	$< 9.4 \times 10^{-12}$	$< 1.0 \times 10^{-11}$	$< 1.3 \times 10^{-11}$
Dresden-II (HMVE-YBe CEvNS)				
$q_{\nu_{ee}}$	$(-4.8, 12.4) \times 10^{-10}$	$(-6.6, 15.2) \times 10^{-10}$	$(-7.5, 16.3) \times 10^{-10}$	$(-9.8, 18.9) \times 10^{-10}$
$\lvert q_{\nu_{e\mu}}\rvert$, $\lvert q_{\nu_{e\tau}}\rvert$	$< 8.9 \times 10^{-10}$	$< 1.1 \times 10^{-9}$	$< 1.2 \times 10^{-9}$	$< 1.4 \times 10^{-9}$
Dresden-II (HMVE-YBe CEvNS+ES)				
$q_{\nu_{ee}}$	$(-1.1, 1.1) \times 10^{-11}$	$(-1.2, 1.3) \times 10^{-11}$	$(-1.3, 1.3) \times 10^{-11}$	$(-1.5, 1.5) \times 10^{-11}$
$\lvert q_{\nu_{e\mu}}\rvert$, $\lvert q_{\nu_{e\tau}}\rvert$	$< 1.1 \times 10^{-11}$	$< 1.2 \times 10^{-11}$	$< 1.3 \times 10^{-11}$	$< 1.5 \times 10^{-11}$

Table 7.11: Bounds on the neutrino electric charges in units of the elementary charge e_0 obtained from the analysis of the Dresden-II data assuming the HMVE reactor antineutrino flux and the Fef or YBe quenching. We show the results obtained with CEνNS only interactions and with CEνNS+ES interactions.

In Tab. 7.11 we show the bounds on the EC found using the Dresden-II data. As for

the neutrino CR and the MM limits discussed above, the different flux parameterizations cause only negligible differences in the obtained bounds. Thus, we show only the results obtained with the HMVE flux, considering both the CEνNS only case and the one in which we include the ES contribution. The more complete table can be found in Ref. [6].
As already discussed, the q^2 corresponding to ES is much smaller than the CEνNS q^2 (for a certain recoil energy), resulting in improved sensitivity when the ES contribution is included with respect to CEνNS only. Namely, with CEνNS only we still obtain an improvement with respect to COHERENT CEνNS only of about 2 orders of magnitude, while considering CEνNS $+\nu$ES the improvement is of about 4 orders of magnitude.

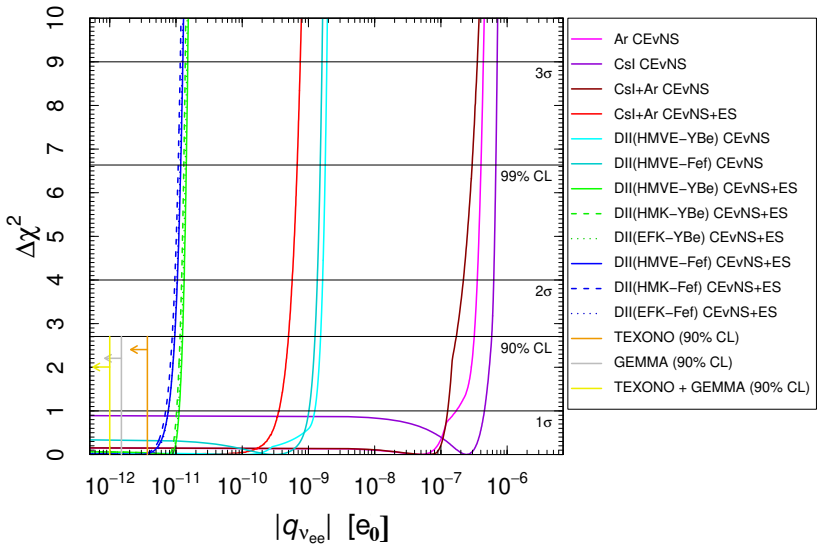

Figure 7.13: Marginal $\Delta\chi^2$'s for $|q_{\nu_{ee}}|$ obtained from: the separate analyses of the COHERENT Ar (magenta) and CsI (purple) data with CEνNS interactions; the combined analyses of the COHERENT Ar and CsI data with CEνNS interactions only (dark red) and with CEνNS +ES interactions (red); the CEνNS -only analyses of Dresden-II data assuming the HMVE reactor antineutrino flux and the YBe (cyan) or Fef (dark cyan) quenching; the CEνNS +ES analyses of Dresden-II data assuming the HMVE, HMK, or EFK reactor antineutrino flux and the YBe (green) or Fef (blue) quenching. The short vertical orange, gray, and yellow lines show the 90% C.L. upper bounds on $|q_{\nu_{ee}}|$ obtained, respectively, in Ref. [365] from TEXONO data [366], in Ref. [367] from the GEMMA [360] bound on $|\mu_{\nu_e}|$, and in Ref. [368] from TEXONO data [245] and GEMMA data [360].

In Fig. 7.13 we show the marginal $\Delta\chi^2$'s for $|q_{\nu_{ee}}|$ obtained from the separate analyses of the COHERENT Ar and CsI data and their combinations, with CEνNS interactions only and with the ES contribution, as well as the CEνNS-only analyses of Dresden-II data assuming the HMVE reactor antineutrino flux and the YBe or Fef QF. Moreover, also the CEνNS + ES analysis of Dresden-II data assuming the HMVE, HMK, or EFK reactor antineutrino flux and the YBe or Fef QF is drawn. We also show the 90% C.L. upper bounds on $|q_{\nu_{ee}}|$ obtained, respectively, in Ref. [365]

from TEXONO data [366], in Ref. [367] from the GEMMA [360] bound on $|\mu_{\nu_e}|$, and in Ref. [368] from TEXONO data [245] and GEMMA data [360]. Intriguingly, the bounds on $|q_{\nu_{ee}}|$ obtained from the combination of COHERENT with the Dresden-II CEνNS + ES data set are much more stringent than the COHERENT ones and the CEνNS only fit, namely at 90% C.L. and using the Fef quenching factor

$$-9.3 < q_{\nu_{ee}} < 9.5, \tag{7.37}$$

in units of $10^{-12}\, e_0$. This limit is competitive with respect to the other aforementioned bounds, that are at the level of $10^{-12}\, e_0$, the best limit being $|q_{\nu_{ee}}| < 1.0 \times 10^{-12}\, e_0$ [368]. However, when comparing these limits one has to keep in mind that, differently from our work [6], the limits in Ref. [368] have been derived using the neutrino-electron cross section the MCRRPA theory [39–41]. This becomes relevant for data from Ge detectors at sub-keV sensitivities and allows them to achieve more stringent limits with respect to FEA in particular for the neutrino EC. Thus, the limits obtained in this work can be considered as very conservative and we will investigate the impact of using a random-phase approximation theory in a future work.

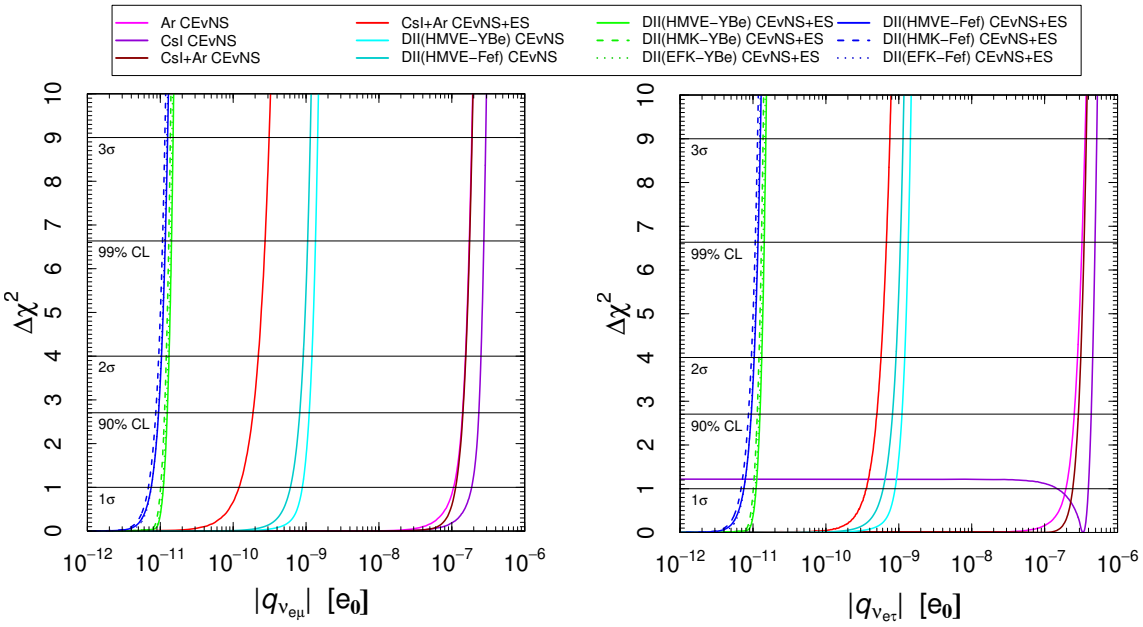

Figure 7.14: Marginal $\Delta\chi^2$'s for $|q_{\nu_{e\mu}}|$ and $|q_{\nu_{e\tau}}|$ obtained from: the separate analyses of the COHERENT Ar (magenta) and CsI (darkviolet) data with CEνNS interactions; the combined analyses of the COHERENT Ar and CsI data with CEνNS interactions only (dark red) and with CEνNS + ES interactions (red); the CEνNS -only analyses of Dresden-II data assuming the HMVE reactor antineutrino flux and the YBe (cyan) or Fef (dark cyan) quenching; the CEνNS + ES analyses of Dresden-II data assuming the HMVE, HMK, or EFK reactor antineutrino flux and the YBe (green) or Fef (blue) quenching.

In Fig. 7.14 (Left) and (Right) we show the marginal $\Delta\chi^2$'s for $|q_{\nu_{e\mu}}|$ and $|q_{\nu_{e\tau}}|$, respectively, obtained from the separate analyses of the COHERENT Ar and CsI

data with CEνNS interactions and the combined analyses of the COHERENT Ar and CsI data with CEνNS interactions only and with the ES contribution, as well as the CEνNS-only analyses of the Dresden-II data assuming the HMVE reactor antineutrino flux and the two QFs, and the CEνNS + ES analyses of Dresden-II data assuming the HMVE, HMK, or EFK reactor antineutrino flux and the two QFs. Also in this case it is possible to see that the different fluxes result in negligible differences, while the impact of the QF is visible. Again, the inclusion of the ES contribution significantly improves the bounds obtained for both Dresden-II and COHERENT.

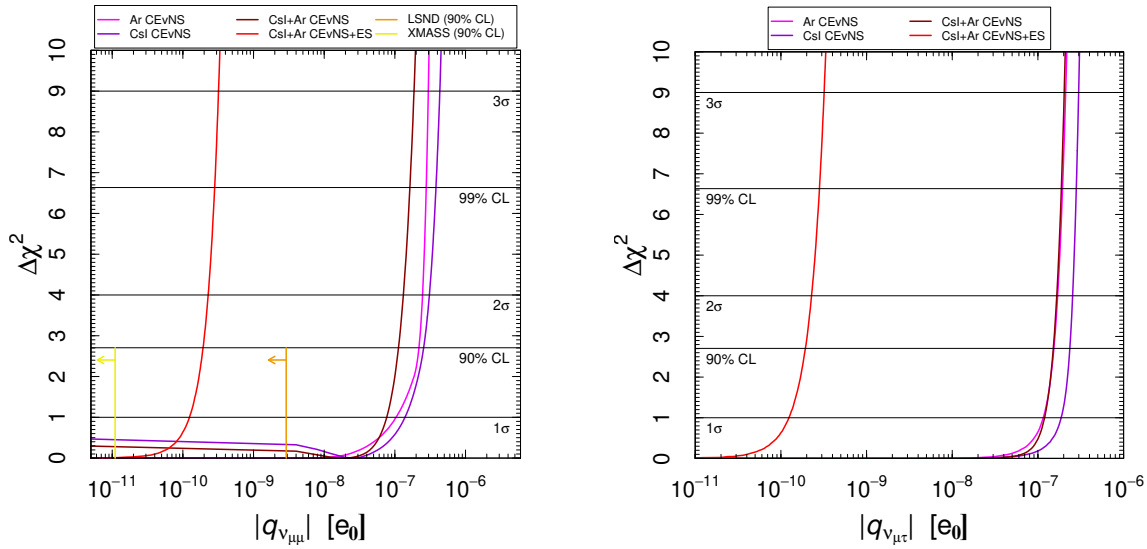

Figure 7.15: Marginal $\Delta\chi^2$'s for $|q_{\nu_{\mu\mu}}|$ and $|q_{\nu_{\mu\tau}}|$ obtained from: the separate analyses of the COHERENT Ar (magenta) and CsI (darkviolet) data with CEνNS interactions; the combined analyses of the COHERENT Ar and CsI data with CEνNS interactions only (dark red) and with CEνNS+ES interactions (red). The short vertical orange and yellow lines show the 90% C.L. upper bounds on $|q_{\nu_{\mu\mu}}|$ obtained, respectively, in Ref. [369] from the LSND [353] bound on $|\mu_{\nu_\mu}|$ and in the XMASS-I experiment [370] from solar neutrino ES.

Finally, in Fig. 7.15 (Left) and (Right) we show similar marginal $\Delta\chi^2$'s $|q_{\nu_{\mu\mu}}|$ and $|q_{\nu_{\mu\tau}}|$, respectively, using COHERENT data only. Here, together with the various bounds obtained in this work we also show the 90% C.L. upper bounds on $|q_{\nu_{\mu\mu}}|$ obtained, respectively, in Ref. [369] from the LSND [353] bound on $|\mu_{\nu_\mu}|$ and in the XMASS-I experiment [370] from solar neutrino ES. Let us notice that also in the case of the XMASS-I limit, that is the most stringent one for $|q_{\nu_{\mu\mu}}|$, the electron-neutrino cross section is derived using an *ab-initio* multi-configuration relativistic random phase approximation [370] that allows them to set more stringent limits. Also in this case, the inclusion of the ES contribution significantly improves the bounds obtained for COHERENT, superseding the existing bounds from LSND concerning $|q_{\nu_{e\mu}}|$, while our bounds represent the only existing laboratory bounds for $|q_{\nu_{e\tau}}|$.

7.4 Neutrino Magnetic Moment and Electric Charge in Dark Matter detectors

As already widely discussed, the neutrino MM and the neutrino EC require a low threshold experiment to be properly tested. In fact, we showed that reactor CEνNS experiments, such as the Dresden-II one, are able to reach low thresholds leading to very stringent constraints. As we have examined in Sec. 2.4.3 and Sec. 2.4.4, direct dark matter detectors are able to reach very low energy thresholds and are sensitive to solar neutrinos, representing thus a very powerful tool to search for such neutrino electromagnetic properties.
Since solar neutrinos are a mixture of mass eigenstates due to the phenomenon of oscillations, the MM measured for solar CEνNS and νES is an effective one

$$\mu_\nu^{2,\text{eff}} = \sum_j |\sum_k \mu_{jk} A_k(E_\nu, L)|^2, \tag{7.38}$$

where μ_{jk} is an element of the neutrino electromagnetic moments matrix and $A_k(E_\nu, L)$ is the amplitude of the k-mass state at the point of scattering [101]. Similarly, it is possible to define also an effective neutrino millicharge parameter q_ν^{eff} as a combination of the three flavor components.

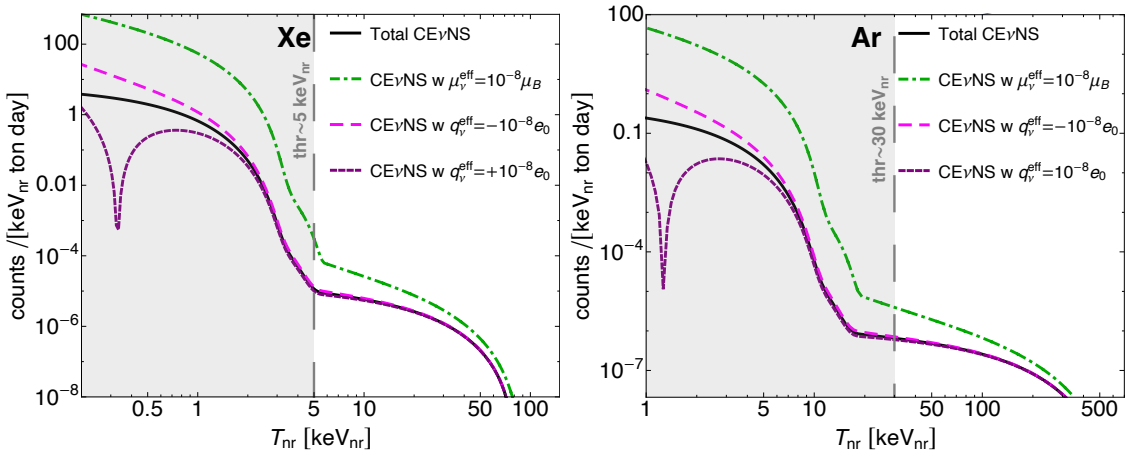

Figure 7.16: Theoretical CEνNS event rate on xenon (Left) and argon (Right) as a function of the nuclear recoil energy. The black curve corresponds to the SM CEνNS rate, while the green curve to a neutrino MM of $\mu_\nu = 10^{-8}\mu_\text{B}$, the magenta curve to a neutrino EC of $q_\nu = -10^{-8}e_0$ and the purple one to $q_\nu = +10^{-8}e_0$. The vertical gray bands indicate the typical experimental threshold of current and future direct dark matter dual-phase TPCs, such as the LZ and the DS-20k ones.

In Fig. 7.16, we show the theoretical CEνNS rate for a generic xenon (left) and argon (right) direct dark matter detector as a function of the nuclear recoil energy. The black curve shows the SM event rate, already shown in Fig. 2.38 and Fig. 2.41, compared with the rate predicted in the presence of BSM neutrino electromagnetic properties. With the green curves, we consider a neutrino MM of $\mu_\nu^{\text{eff}} = 10^{-8}\mu_\text{B}$, while with the magenta and purple lines the rate in the presence of

a neutrino electric charge of $q_\nu^{\rm eff} = -10^{-8} e_0$ and $q_\nu^{\rm eff} = +10^{-8} e_0$, respectively. The gray shaded region shows the below threshold part of the spectrum, considering the typical threshold of current direct dark matter dual-phase TPCs.
It is evident that the main effects due to the neutrino electromagnetic properties manifest at low recoil energies, and mainly below the experimental thresholds. The MM produces an interesting enhancement already above the threshold, however, it must be remarked that a MM of $\mu_\nu^{\rm eff} = 10^{-8} \mu_{\rm B}$ is about two orders of magnitude larger than the current constraint derived from Dresden-II data. It is worth noticing how a rather large value of the neutrino EC produces a different signature depending on the sign of the electric charge. Indeed, the cross section in the presence of a neutrino EC was obtained by shifting the neutrino-proton coupling by the term in Eq. 7.33, which depends linearly on q_ν. Therefore, depending on the size and sign of the EC, an interference effect with the SM coupling could occur. This is visible in Fig. 7.16, where the purple curves (positive EC) are always below the SM rate, and present a sharp minimum, while the magenta curves (negative EC) do not present any interference, resulting in a rate always larger than the SM one. Given these intriguing signatures, it is fundamental to reach lower experimental thresholds in order to probe the part of the spectrum where most of the effects happen.

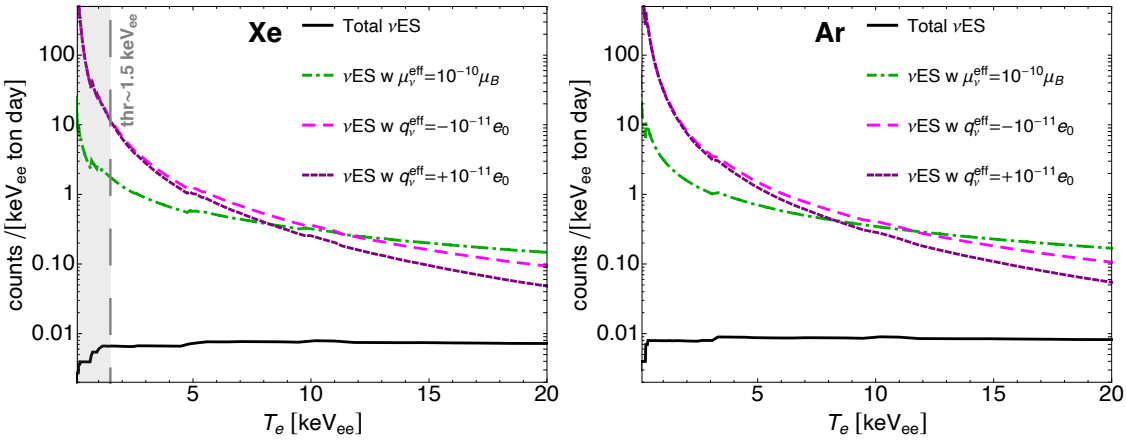

Figure 7.17: Theoretical νES event rate on xenon (Left) and argon (Right) as a function of the electron recoil energy. The black curve corresponds to the SM νES rate, while the green curve to a neutrino MM of $\mu_\nu^{\rm eff} = 10^{-10} \mu_{\rm B}$, the magenta curve to a neutrino EC of $q_\nu^{\rm eff} = -10^{-11} e_0$ and the purple one to $q_\nu^{\rm eff} = +10^{-11} e_0$. The vertical gray band in the left plot indicates the experimental threshold of the LZ detector.

In Fig. 7.17, we show the theoretical νES rate for a generic xenon (left) and argon (right) direct dark matter detectors as a function of the nuclear recoil energy. The black curve shows the SM event rate, already shown in Fig. 2.38 and Fig. 2.41, compared with the rate predicted in the presence of BSM neutrino electromagnetic properties. With the green curves, we consider a neutrino MM of $\mu_\nu^{\rm eff} = 10^{-10} \mu_{\rm B}$, while with the magenta and purple lines the rate in presence of a neutrino electric charge of $q_\nu^{\rm eff} = -10^{-11} e_0$ and $q_\nu^{\rm eff} = +10^{-11} e_0$, respectively. The gray shaded region in the left plot, indicates the below threshold part of the spectrum, considering the

experimental threshold of the LZ detector [98].
It is interesting to notice that the rate in the presence of electromagnetic properties is significantly enhanced already for smaller μ_ν and q_ν than the ones shown for CEνNS. Already for values of the order of the constraints derived from Dresden-II data [6], the rate results to be evidently higher than the SM one. Moreover, considering as a reference threshold the LZ one, we see that the effect is already significant above that energy. We can notice that moving toward even lower recoil energies, the rate increases steeply, so that reaching lower thresholds would result in an even enhanced sensitivity. Moreover, we can notice that for the displayed EC values, the rates for positive and negative charges are very similar, with no evident interference. Although, some small differences are still present, especially for $T_e \gtrsim 5\ \mathrm{keV}_{ee}$.
It is clear that direct dark matter detectors provide a very powerful tool to investigate neutrino electromagnetic properties, in particular through the νES scattering process, which is able to provide the most evident signature.

7.4.1 —— Lux-Zeplin science case ——

To give a practical proof of the potentialities of direct dark matter detectors to probe neutrino electromagnetic properties, we analyzed the latest Lux-Zeplin (LZ) data [98], as discussed in Sec. 2.4.3, where we presented the experimental details and the procedure followed to analyse the data.

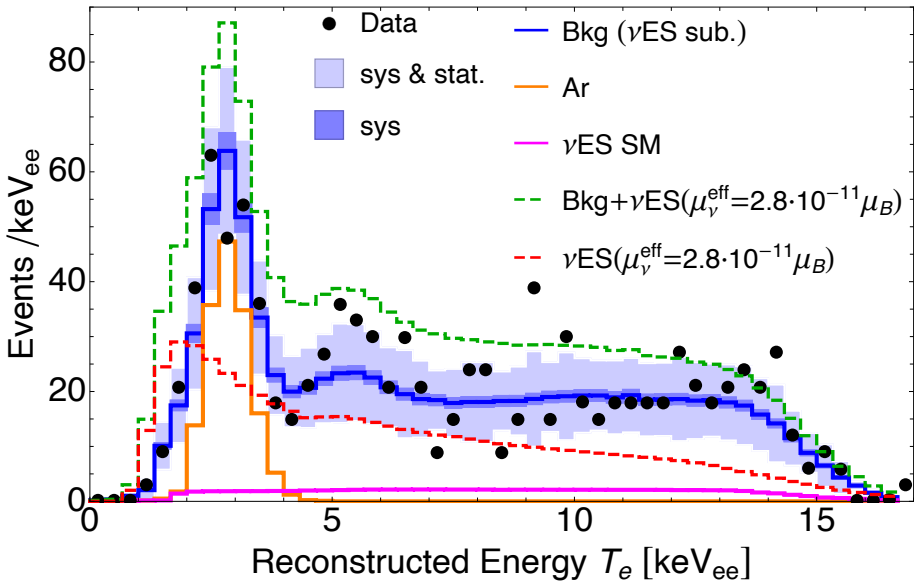

Figure 7.18: LZ energy spectrum [98] with superimposed the total background subtracted for the νES contribution (blue solid), the ^{37}Ar contribution (orange), the νES SM prediction (purple), and for illustration purposes the νES with $\mu_\nu^{\mathrm{eff}} = 2.8 \times 10^{-11}\ \mu_\mathrm{B}$, with (green dashed) and without (red dashed) the background.

Firstly, in Fig. 7.18 we show the νES prediction in presence of a nonzero neutrino magnetic moment, namely considering an effective neutrino MM of $\mu_\nu^{\mathrm{eff}} = 2.8 \cdot 10^{-11}\ \mu_\mathrm{B}$ (red curve), which corresponds to the BOREXINO 90% C.L. limit [101],

compared to the SM νES rate and the LZ data (see also Fig. 2.39). From the figure, we clearly understand that a subdominant background component, such as the one due to neutrinos scattering elastically off the target electrons, can become rather large, and thus not negligible, in the presence of neutrino electromagnetic properties. In this sense, what is classically considered an almost negligible background component, could actually become an opportunity to search for new physics signals[3].

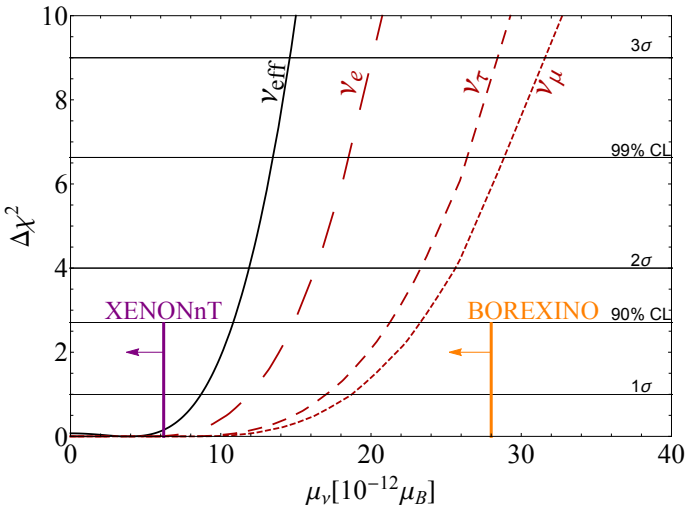

Figure 7.19: Marginal $\Delta\chi^2$s for $\mu_\nu^{\rm eff}$ obtained from the analysis of the LZ data with the χ^2 in Eq. 2.87 (black solid line) and the marginalized flavor components (dashed red lines) [7]. The solid purple (orange) line shows the 90% C.L. upper bound on the effective neutrino MM obtained in the XENONnT [99] (BOREXINO [101]) experiment.

In Fig. 7.19 we show the marginal $\Delta\chi^2$s at different confidence levels, obtained using the χ^2 in Eq. 2.87, for both the effective MM and the marginalization over the three flavor components. The numerical values of the limits derived considering the three different flavors are reported in Table 7.12. At 90% C.L., the bound on the effective neutrino MM obtained in this work is

$$\mu_\nu^{\rm eff} \;<\; 1.1 \times 10^{-11}\,\mu_{\rm B}, \tag{7.39}$$

which corresponds to an integrated number of ∼50 νES events. Our result can be compared with the official result from the LZ Collaboration, namely $\mu_\nu^{\rm eff} < 1.36 \times 10^{-11}\,\mu_{\rm B}$ [371], which is slightly less constraining due to a better treatment of the different background components inside the fit. Moreover, we can compare it with the limit recently reported by the XENONnT Collaboration corresponding to $\mu_\nu^{\rm eff} < 6.4 \times 10^{-12}\,\mu_{\rm B}$ [99], which is about a factor of 2 more stringent due to their lower background with respect to LZ. Further neutrino MM analyses exploiting XENONnT data can be found in Refs. [372, 373]. These LZ and

[3]If the neutrino truly has a magnetic moment or a millicharge, the background component due to νES can become non negligible, and thus become a signal.

XENONnT limits, both obtained using a LXe double-phase TPC technology originally designed to search for dark matter and a similar analysis approach, are significantly tighter than the previous laboratory bounds, highlighting the potentiality that such a technique can offer thanks to the low energy threshold and low level of background achieved. Indeed, they can be compared to the limit obtained by the Super-Kamiokande Collaboration of $3.6 \times 10^{-10}\mu_B$ (90% C.L.), derived by fitting day/night solar neutrino spectra above 5 MeV. With additional information from other solar neutrino and KamLAND experiments a limit of $1.1\times10^{-10}\mu_B$ (90% C.L.) was obtained [374]. The Borexino Collaboration reported the previous best current limit on the effective MM by laboratory experiments of $2.8\times10^{-11}\mu_B$ (90% C.L.) using the ER spectrum from solar neutrinos [101].

	$\lvert\mu_\nu\rvert[\times10^{-11}\mu_B]$	q_ν $[\times10^{-13}e_0]$	
		FEA	EPA
ν_{eff}	< 1.1	[-3.0, 4.7]	[-1.5, 1.5]
ν_e	< 1.5	[-3.6, 6.5]	[-2.1, 2.0]
ν_μ	< 2.3	[-8.9, 8.8]	[-3.1, 3.1]
ν_τ	< 2.1	[-8.1, 8.1]	[-2.8, 2.8]

Table 7.12: Limits on the neutrino magnetic moment and neutrino millicharge at 90% C.L. obtained with a χ^2 analysis as defined in Eq. 2.87. For the neutrino millicharge, the limits are reported for both the FEA and the EPA formalism [7].

The best MM limit from reactor antineutrinos is $2.9 \times 10^{-11}\mu_B$ (90% C.L.) [375]. Finally, the analysis of the CEνNS data from Dresden-II and COHERENT Collaborations permits to set limits on $|\mu_{\nu_e}| < 2.13\times10^{-10}\,\mu_\text{B}$ and $|\mu_{\nu_\mu}| < 18\times10^{-10}\,\mu_\text{B}$ [6], also exploiting νES. When considering nonlaboratory experiments, the most stringent limits on the neutrino MM of up to $\sim 10^{-12}\mu_B$ come from astrophysical observations [376–378], which however are rather indirect. A complete historical record of limits on the neutrino MM can be found in Ref. [25] and a large collection of existing bounds is summarized in Fig. 7.22 (Left). It is possible to see that in our analysis of the LZ data we significantly improve the limits on the electron, muon and tau neutrino MM compared to the other laboratory bounds.
To perform a more accurate analysis, we investigated the possibility of leaving the ^{37}Ar component free to vary in the fit using a prior similar to that implemented by the LZ Collaboration, as defined in Eq. 2.88. Interestingly, the fit retrieves a number of ^{37}Ar events similar to that found by LZ, namely ~ 48 with $\chi^2_{\text{min}} = 99.6$. Thus, also in this case, the limits do not substantially change and for reference the bound on the effective neutrino MM at 90% C.L. becomes $\mu_\nu^{\text{eff}}(^{37}\text{Ar}) < 1.2 \times 10^{-11}\,\mu_\text{B}$, which is closer to the official LZ result [371].
It is worth mentioning that, although the neutrino MM cross section within the corrected FEA framework adopted in our work is known to be in good agreement with that of *ab-initio* theories even for sub-keV ERs, in the same regime the Random Relativistic Phase Approximation (RRPA) cross section for a neutrino with a nonzero EC is more than one order of magnitude bigger than that obtained with the corrected FEA definition [44, 45]. In this regard, we can determine the constraints on the neutrino EC by considering the FEA formalism as a conservative

one. Moreover, it is well known that another approximation, known as Equivalent Photon Approximation (EPA), is able to reproduce well the RRPA cross section for a millicharged neutrino [44, 45]. Therefore, we exploit the EPA formalism in order to go beyond the FEA approach and better describe the interaction in the case of a millicharged neutrino. This improved approach should lead to tighter constraints on the neutrino millicharge, as the cross section is larger.
In particular, the EPA cross section for a millicharged neutrino reads [44, 45]

$$\frac{d\sigma_{\nu_\ell}}{dT_\mathrm{e}}\Big|^{\mathrm{EC}}_{\mathrm{EPA}} = \frac{2\alpha}{\pi}\frac{\sigma_\gamma(T_e)}{T_e}\log\left[\frac{E_\nu}{m_\nu}\right] q^2_{\nu_\ell}, \tag{7.40}$$

where m_ν is the neutrino mass, and $\sigma_\gamma(T_e)$ is the photoelectric cross section by a real photon, which can be extracted from Ref. [48] for Xe. By looking at Eq. 7.40 it can be seen that the cross section in the EPA approximation is independent of the sign of the electric charge, differently from what we discussed in the case of the FEA approximation.
We show a comparison between the cross section on xenon for a millicharged neutrino with $|q^{\mathrm{eff}}_\nu| = 10^{-11}\, e_0$ in Fig. 7.20. The cross section in the EPA approach is larger than the corrected FEA one. Moreover, in the figure, we show again that the sign of the EC produces a small difference between the cross sections in the corrected FEA approach. The particular shape of the EPA cross section derives from the contribution to the photoelectric cross section from different atomic shells.

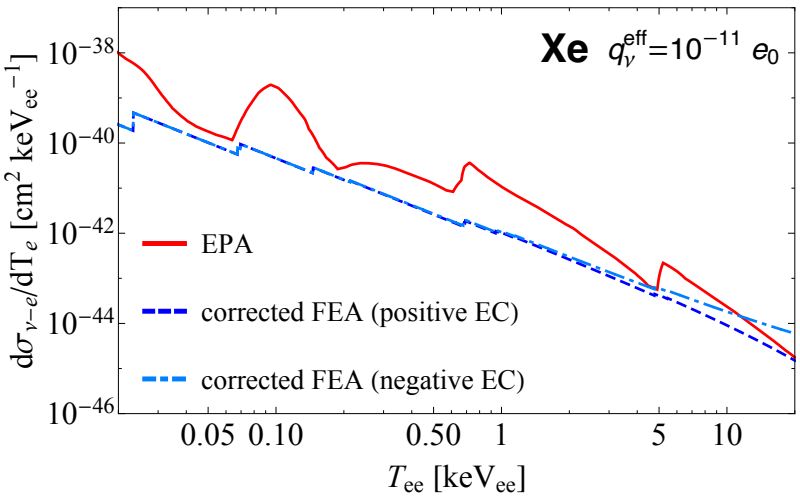

Figure 7.20: Comparison between the differential cross section for the νES of a millicharge neutrino with $|q^{\mathrm{eff}}_\nu| = 10^{-11}\, e_0$ on xenon in the EPA (red) and in the corrected FEA approaches. For the FEA case, we consider the two different EC signs. For the EPA case we conservatively set $m_\nu = 1$ eV.

We should underline that, although the EPA approach describes very well the cross section for ER energies below a few keVs, it is known to underestimate the scattering cross section for larger energies where the FEA formalism works better. For this reason, we will rely on the EPA scheme only when its cross section is larger than that of the corrected FEA, following the same procedure adopted in Ref. [379]. In the following, for simplicity, we will refer to this strategy as EPA.

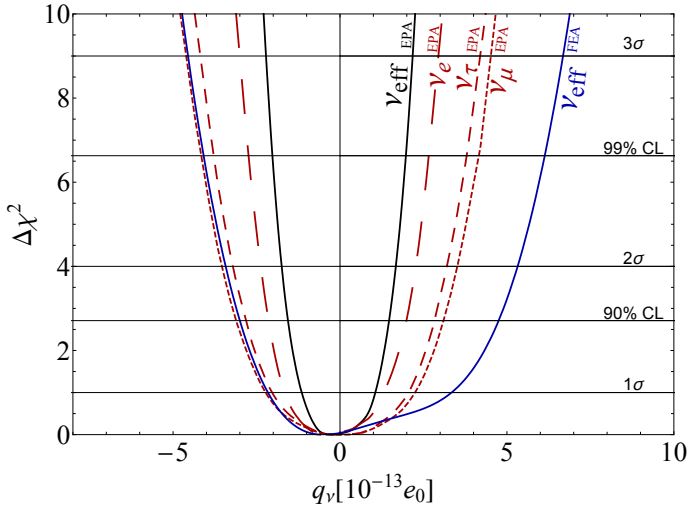

Figure 7.21: $\Delta\chi^2$ profiles of the effective (solid black) and flavor dependent (dashed red) neutrino millicharge obtained adopting the EPA formalism. As a comparison, the curve for the effective neutrino millicharge under the FEA approximation is also shown (solid blue).

In Fig. 7.21 we present the limits on the neutrino EC obtained in this work within the FEA and EPA formalisms, using the χ^2 in Eq. 2.87. We note that the EPA cross section depends on the neutrino mass, as it can be seen in Eq. 7.40, which is not yet precisely measured. We used a conservative value of $m_\nu = 1$ eV, which is close to the current laboratory upper bounds on the neutrino mass [25]. On the other hand, we verified that the limit is not significantly modified even when considering smaller values for m_ν. The 90% C.L. bounds on the effective millicharge are

$$\text{FEA}: \quad -3.0 < q_\nu^{\rm eff}\ [10^{-13}\ e_0] < 4.7, \tag{7.41}$$

$$\text{EPA}: \quad -1.5 < q_\nu^{\rm eff}\ [10^{-13}\ e_0] < 1.5\,. \tag{7.42}$$

It is interesting to notice that the bounds obtained in the FEA approach are asymmetrical due to the effect of the EC sign in the cross section, while in the case of the EPA approach, the constraint is symmetrical, as the sign does not matter.
The values for the flavor-dependent neutrino millicharges are summarized in Table 7.12 both for the FEA and EPA analyses. It is clear that the limits obtained with the more realistic EPA formalism are much stronger than those obtained within FEA and hence, for simplicity, in Fig. 7.21 we showed only the effective EC limit for FEA. We note also that the limits obtained in this work with FEA are comparable with those reported in Ref. [372], which exploits the ER energy efficiency derived in this work for the LZ analysis, and are less stringent than those obtained with XENONnT [372, 373]. On the other hand, as expected, the limits obtained in this work adopting EPA when analyzing the LZ data are even stronger than the XENONnT limits obtained in Refs. [372, 373] that were determined using FEA.
In Fig. 7.22 (Right) a collection of existing bounds on the neutrino millicharge coming from different experiments is shown. It can be seen that the limits derived in our work using the LZ data and the more realistic EPA formalism significantly improve the previous best laboratory limits [7], that for the electron

neutrino electric charge was obtained in Ref. [368] by combining TEXONO [245] and GEMMA [360] data, finding $|q_{\nu_e}| < 1.0 \times 10^{-12}\ e_0$. We expect, however, that adopting the EPA or the RRPA formalism to analyse the XENONnT data would allow us to further constrain the limit on this fundamental quantity.
For completeness, we fitted again the LZ data leaving the ^{37}Ar component free to vary also in the case of neutrino EC. In this case, the bounds on the effective neutrino millicharge become

$$\text{FEA}: \quad -3.3 < q_\nu^{\text{eff}}(^{37}\text{Ar})\ [10^{-13}\ e_0] < 5.0, \tag{7.43}$$

$$\text{EPA}: \quad -1.6 < q_\nu^{\text{eff}}(^{37}\text{Ar})\ [10^{-13}\ e_0] < 1.5, \tag{7.44}$$

As before, leaving the ^{37}Ar component free to vary does not impact significantly the results. Moreover, our result within EPA is slightly more stringent than the LZ official one [371].

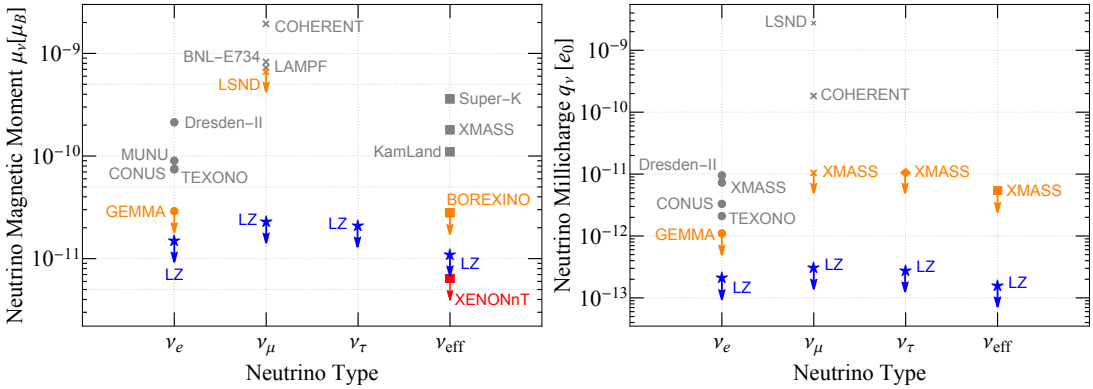

Figure 7.22: Summary of existing limits at 90% C.L. on the neutrino magnetic moment (Left) and the neutrino millicharge (Right) coming from a variety of experiments [6, 25, 37, 101, 245, 349, 352, 359, 360, 370, 374, 380, 381].The limits are divided in flavor components μ_{ν_e} (q_{ν_e}) (dots), μ_{ν_μ} (q_{ν_μ}) (crosses), and μ_{ν_τ} (q_{ν_τ}) (diamonds) and also the ones on the effective magnetic moment μ_ν^{eff} (q_ν^{eff}) (squares) are shown. In orange, we highlighted the best limits before the LZ data release and in red the XENONnT limit on the MM [99]. The results derived in our work [7] are shown by the blue stars and for the millicharge we show the results obtained in the EPA approach.

To summarize, we showed that dark matter detectors such as LZ and XENONnT are able to significantly improve constraints on the neutrino MM and EC thanks to their low background and threshold. Moreover, we foresee that in the future the LZ detector will reach a lower background level due to the decay of the ^{37}Ar background component, which having a half-life of about 35 days should not be present in future data samples.
Other existing dark matter detectors together with the planned ones will help as well to improve the big picture, and potentially reach (and supersede) the bounds from indirect astrophysical sources [376–378]. In this sense, when the DS-20k detector will become operational, also liquid argon dark matter detectors will enter the game, helping to unveil these intriguing neutrino electromagnetic properties.

Conclusions

In this thesis work, we have vastly discussed the main aspects of low energy neutrino scattering processes off nuclei and atomic electrons. Indeed, we have shown a series of physical implications and applications of measurements of the cross section for the coherent elastic neutrino nucleus scattering (CEνNS), ranging from standard model tests to scenarios in which the neutrinos acquire a small electric charge.
We have calculated the cross section for CEνNS and for the elastic scattering of neutrinos off electrons paying careful attention to the radiative corrections, considering the well established framework employed in the standard renormalization scheme of the low energy electroweak theory. The CEνNS process has been studied in the context of the available measurements, namely the ones performed by the COHERENT Collaboration, which, by employing neutrinos from the stopped pion decay-at-rest, measured the CEνNS cross section with a cesium-iodide detector and a liquid argon one, and by the NCC-1701 germanium detector at the Dresden-II reactor power plant.
In this thesis, we have shown the vast physics reach of CEνNS measurements by presenting many implications of cross section measurements. Meanwhile, we have discussed the impact of the νES process within CEνNS experimental data, which may be fundamental in some beyond the standard model scenarios. Furthermore, we have discussed the importance of CEνNS and νES in the context of direct dark matter detectors, which, thanks to their very low experimental thresholds (see Fig. 7.16 and Fig. 7.17)) and ultra-low background levels, result to be very promising in testing some beyond the standard model properties, such as the neutrino magnetic moment and the neutrino electric charge.
However, the achievement accomplished within this thesis is the proof of the power of combining different electroweak probes. In fact, we have shown how the scattering of electrons off nuclei and the atomic parity violation process, despite being due to very different mechanisms, are complementary to low energy neutrino scattering. The common ingredient is the weak mixing angle, which in practice governs the size of the electroweak couplings, and thus provides a direct test of the standard model theory. The weak mixing angle has been precisely measured at higher energies, while in the low energy sector (i.e. below the production threshold of quarks) is still poorly measured. Therefore, a measurement of the weak mixing angle in this energy region would represent a key test of the standard model theory, or possibly indicate the effect of new physics.
In this thesis, we spent a large amount of time discussing the difficulties in mea-

suring the weak mixing angle at low energy with high precision via processes involving nuclei. The main issue is the almost always present degeneracy with the effect of nuclear structure, which arises from the presence of the product of the nuclear weak charge with the nuclear form factor in the theoretical predictions (i.e. see Eq. 2.46 and Eq. 3.26). Indeed, both in atomic parity violation, parity violating electron scattering and CEνNS, we have observed a degeneration of the information due to the competition of the effects due to the weak mixing angle and the nuclear form factor. In this sense, the resulting picture indicates that a fully data driven approach to extract the two observable simultaneously from this kind of probes is hardly achievable, as shown in Fig. 4.1 and Fig. 5.6. However, the different dependence of the measurement on the two quantities allows one to disentangle the contribution by considering combined measurements on similar nuclei. This has been shown for example by the combined analysis of the PVES measurement on $^{208}\mathrm{Pb}$ by the PREX Collaboration and the atomic parity violation measurement on the same nucleus in Ref. [4] and in Fig. 4.3. The combination allows one to extract the weak mixing angle and the nuclear neutron radius simultaneously, although the poor precision achievable (about ~ 6 % on $\sin^2\theta_W$ and ~ 50 % on the neutron skin $\Delta R_{\mathrm{np}}(^{208}\mathrm{Pb})$). The same has been shown by combining the PVES measurement on calcium by the CREX Collaboration with the proton weak charge measurement by the $Q_{\mathbf{weak}}$ Collaboration, whose precision is significantly better. In this context, we have also performed some tentative studies on the precision achievable through a novel PVES measurement on a much lighter nucleus, namely carbon, which thanks to the combination of a backward and a forward scattering measurements will be able to simultaneously extract the weak mixing angle and the nuclear neutron radius with a precision of the order of $\sim 0.3 - 0.4$ %, which would represent one of the most precise measurements in that energy regime. A summary of the latter results on the weak mixing angle is shown in Fig. 4.16.
Similarly, we have extracted the weak mixing angle and the nuclear neutron radius by the available CEνNS measurements, and in particular, for the COHERENT cesium-iodide detector we have shown in Fig. 5.7 how a combined analysis with the APV measurement on cesium atoms reaches a significantly improved precision through a completely data driven approach [2, 8], namely around ~ 1.3 % on $\sin^2\theta_W$ and ~ 9 % on $R_n(\mathrm{CsI})$. These studies are fundamental as in the next few years new measurements of the weak mixing angle and the neutron radii will be available, so that the overall picture will be clarified. In this sense, in Fig. 5.11 we show a summary of current and near future precision on the extraction of the neutron radius of CsI compared to the ones of $^{208}\mathrm{Pb}$, from which one can see that the precision foreseen by COHERENT with their future cryogenic CsI detector will reach about ~ 0.5 % in the CryoCsI-II scenario. Similarly, in Fig. 5.12 we summarize the status of weak mixing angle measurements from CEνNS probes, presenting also the near future projections from many experimental probes in the same energy region. In particular, we show that the CryoCsI-II detector foreseen by the COHERENT Collaboration is expected to reach a precision of about ~ 3 % on $\sin^2\theta_W$. Moreover, we have shown in Fig. 5.14 that the only available $\sin^2\theta_W$ measurement of CEνNS from reactor antineutrinos by the NCC-1701 germanium

detector [6] is less precise with respect to the COHERENT ones, and it also depends significantly on the quenching factor model, which is still under debate in the community.
In this thesis, we have also illustrated a selected compilation of beyond the standard model scenarios that can be tested through the CEνNS and the νES processes. For example, we have discussed the category of $U(1)'$ extensions of the standard model, which are based on the introduction of a new mediator related to a new gauge symmetry. In particular, this boson, which is generically referred to as Z' due to its similarities to the standard Z boson but lighter in mass, would introduce a new interaction that could show as a signature in the data. We have presented different scenarios, with either a vector or scalar mediator. We have analyzed the COHERENT data in order to set constraints on the size of the new interaction and the mass of the extra mediator. In most of the considered models, the COHERENT data allowed one to extend the other existing bounds, mostly in the intermediate mass range, around the hundreds of MeV [1, 5]. The obtained constraints can be seen in Fig. 6.5 for two selected vector models, namely the universal and the $B - L$ ones.
In addition, in the context of light mediators, we have discussed also the muon anomalous magnetic moment, which at the moment represents one of the most intriguing measurements available, as the experimental result is in tension with the standard model prediction, motivating the search for solid beyond the standard model theories. Thanks to the obtained bounds, the explanation of the muon anomalous magnetic moment anomaly in terms of an extra light mediator is rather disfavored. It is worth mentioning that the particular $L_\mu - L_\tau$ models, which is based upon a novel flavor symmetry involving the μ and τ flavors, is still unconstrained for masses $M_{Z'} \sim [10 - 200]\,\mathrm{MeV}$, as shown in Fig. 6.6. However, this model will be definitely probed with next generation CEνNS measurements.
We have considered also a particular standard model extension, in which the new light mediator introduces a new source of parity violation, called Z_d [3]. In this more complicated model, there is an additional free parameter, which enables one to loosen some bounds. We have explored this model as a possible explanation of existing tension between the experimental determinations of the muon and electron magnetic moments and their standard model predictions, by considering the APV measurement on cesium and the proton weak charge measurement by the Q_{weak} Collaboration. Indeed, we find a small preference for a light Z_d with a mass around $50\,\mathrm{MeV}$ (see Eqs. 6.44-6.45-6.46). This model is particularly interesting as the presence of such a boson would significantly impact the running of the weak mixing angle at low energies, as shown in Fig. 6.13. Therefore, precise measurement of the weak mixing angle at low energy would directly test the effect of the Z_d model.
Finally, we have presented various analyses in which we searched for signatures of possible neutrino electromagnetic properties introduced in a plethora of beyond the standard model theories. In particular, we have drawn the current status of neutrino electric charge and neutrino magnetic moment measurements, adding to the already available bounds the one obtained by analysing the COHERENT and Dresden-II data [6]. Although the bound obtained from CEνNS measurements

are still far from the most stringent ones, we have shown how reactor experiments can provide a very sensitive tool to search for such signatures, especially by analysing the νES channel, which results to be enhanced in this kind of models. Moreover, we have shown how direct dark matter detectors, thanks to their low background level and threshold, allow one to obtain some of the strongest available constraints of such quantities. We have applied this to the Lux-Zeplin data, obtaining the second strongest laboratory bounds on the neutrino electric charge and magnetic moment [7]. Since the most sensitive channel is the νES one, we have carefully studied the problem of the description of the interaction of neutral particles, in particular neutrinos, with bound atomic electrons, so that we have considered different approaches to deal with this interaction. A rather complete summary of the current status of neutrino electric charge and magnetic moment bounds is shown in Fig. 7.22, from which it emerges that the current constraints from direct dark matter detectors have reached $\sim 10^{-12} - 10^{-11}\ \mu_B$ on the neutrino magnetic moment and $\sim 10^{-13}\ e_0$ on the electric charge, while the ones from COHERENT and Dresden-II data are around 3 and 2 order of magnitude weaker, respectively.
We have also discussed the bounds on the only standard model neutrino electromagnetic property, i.e. the neutrino charge radius, by the COHERENT and Dresden-II data analysis [6]. We have considered non standard neutrino charge radius scenarios, however, the obtained bounds are of the order of $\sim 10^{-32} - 10^{-31}\,\mathrm{cm}^2$, so about one order of magnitude larger than the standard model prediction of the actual neutrino charge radius values. In Tab. 7.4 we collected the current status of the bounds on diagonal neutrino charge radii.
Since with next generation detectors, such bounds could improve significantly, we have discussed a theoretical redefinition of the radiative correction commonly employed to include the neutrino charge radius effect in the CEνNS and νES cross sections. We have shown that the neutrino charge radius contribution actually encodes a momentum dependence, which can sensibly affect the extraction of the neutrino charge radius. We estimate that such momentum dependent radiative correction will have an impact below 1% on the total CEνNS number of events for the COHERENT science case, so still below the current experimental precision. Therefore, we have paved the way for more precise radiative correction calculation for CEνNS, which will become relevant in future data analyses.

In conclusion, the CEνNS process represents a unique opportunity for exploring a vast class of beyond the standard model scenarios as well as for performing standard model tests at low energy. The complementary of CEνNS with νES and neutral current electron interactions shows a very promising future in this sense. When new data will become available the global picture at low energy will significantly improve, and potentially suggest the research path to be followed in the next decades.

Bibliography

[1] M. Cadeddu et al. “Constraints on light vector mediators through coherent elastic neutrino nucleus scattering data from COHERENT”. In: *JHEP* 01 (2021), p. 116. DOI: 10.1007/JHEP01(2021)116. arXiv: 2008.05022 [hep-ph].

[2] M. Cadeddu et al. “New insights into nuclear physics and weak mixing angle using electroweak probes”. In: *Phys. Rev. C* 104.6 (2021), p. 065502. DOI: 10.1103/PhysRevC.104.065502. arXiv: 2102.06153 [hep-ph].

[3] M. Cadeddu et al. “Muon and electron g-2 and proton and cesium weak charges implications on dark Zd models”. In: *Phys. Rev. D* 104.1 (2021), p. 011701. DOI: 10.1103/PhysRevD.104.L011701. arXiv: 2104.03280 [hep-ph].

[4] M. Atzori Corona et al. “Incorporating the weak mixing angle dependence to reconcile the neutron skin measurement on Pb208 by PREX-II”. In: *Phys. Rev. C* 105.5 (2022), p. 055503. DOI: 10.1103/PhysRevC.105.055503. arXiv: 2112.09717 [hep-ph].

[5] M. Atzori Corona et al. “Probing light mediators and $(g-2)_\mu$ through detection of coherent elastic neutrino nucleus scattering at COHERENT”. In: *JHEP* 05 (2022), p. 109. DOI: 10.1007/JHEP05(2022)109. arXiv: 2202.11002 [hep-ph].

[6] M. Atzori Corona et al. “Impact of the Dresden-II and COHERENT neutrino scattering data on neutrino electromagnetic properties and electroweak physics”. In: *JHEP* 09 (2022), p. 164. DOI: 10.1007/JHEP09(2022)164. arXiv: 2205.09484 [hep-ph].

[7] M. Atzori Corona et al. “New constraint on neutrino magnetic moment and neutrino millicharge from LUX-ZEPLIN dark matter search results”. In: *Phys. Rev. D* 107.5 (2023), p. 053001. DOI: 10.1103/PhysRevD.107.053001. arXiv: 2207.05036 [hep-ph].

[8] M. Atzori Corona et al. “Nuclear neutron radius and weak mixing angle measurements from latest COHERENT CsI and atomic parity violation Cs data”. In: *Eur. Phys. J. C* 83.7 (2023), p. 683. DOI: 10.1140/epjc/s10052-023-11849-5. arXiv: 2303.09360 [nucl-ex].

[9] P. Agnes et al. “A study of events with photoelectric emission in the DarkSide-50 liquid argon Time Projection Chamber”. In: *Astropart. Phys.* 140 (2022), p. 102704. DOI: 10.1016/j.astropartphys.2022.102704. arXiv: 2107.08015 [physics.ins-det].

[10] M. Atzori Corona et al. “On the impact of the Migdal effect in reactor CEνNS experiments”. In: (July 2023). arXiv: 2307.12911 [hep-ph].

[11] P. Agnes et al. “Directionality of nuclear recoils in a liquid argon time projection chamber”. In: (July 2023). arXiv: 2307.15454 [physics.ins-det].

[12] P. Agnes et al. “Sensitivity projections for a dual-phase argon TPC optimized for light dark matter searches through the ionization channel”. In: *Phys. Rev. D* 107.11 (2023), p. 112006. DOI: 10.1103/PhysRevD.107.112006. arXiv: 2209.01177 [physics.ins-det].

[13] M. Cadeddu et al. “Muon and electron g-2 and proton and cesium weak charges implications on dark Z_d models”. In: *Nuovo Cim. C* 45.1 (2021), p. 4. DOI: 10.1393/ncc/i2022-22004-1.

[14] P. Agnes et al. “Search for Dark-Matter–Nucleon Interactions via Migdal Effect with DarkSide-50”. In: *Phys. Rev. Lett.* 130.10 (2023), p. 101001. DOI: 10.1103/PhysRevLett.130.101001. arXiv: 2207.11967 [hep-ex].

[15] P. Agnes et al. “Search for Dark Matter Particle Interactions with Electron Final States with DarkSide-50”. In: *Phys. Rev. Lett.* 130.10 (2023), p. 101002. DOI: 10.1103/PhysRevLett.130.101002. arXiv: 2207.11968 [hep-ex].

[16] P. Agnes et al. “Search for low-mass dark matter WIMPs with 12 ton-day exposure of DarkSide-50”. In: *Phys. Rev. D* 107.6 (2023), p. 063001. DOI: 10.1103/PhysRevD.107.063001. arXiv: 2207.11966 [hep-ex].

[17] P. Agnes et al. “Search for low mass dark matter in DarkSide-50: the bayesian network approach”. In: *Eur. Phys. J. C* 83 (2023), p. 322. DOI: 10.1140/epjc/s10052-023-11410-4. arXiv: 2302.01830 [hep-ex].

[18] P. Agnes et al. “Search for dark matter annual modulation with DarkSide-50”. In: (July 2023). arXiv: 2307.07249 [hep-ex].

[19] P. Agnes et al. “Separating ^{39}Ar from ^{40}Ar by cryogenic distillation with Aria for dark-matter searches”. In: *Eur. Phys. J. C* 81.4 (2021), p. 359. DOI: 10.1140/epjc/s10052-021-09121-9. arXiv: 2101.08686 [physics.ins-det].

[20] E. Aaron et al. “Measurement of isotopic separation of argon with the prototype of the cryogenic distillation plant Aria for dark matter searches”. In: *Eur. Phys. J. C* 83.5 (2023), p. 453. DOI: 10.1140/epjc/s10052-023-11430-0. arXiv: 2301.09639 [physics.ins-det].

[21] A. Elersich et al. “Study of cosmogenic activation above ground for the DarkSide-20k experiment”. In: *Astropart. Phys.* 152 (2023), p. 102878. DOI: 10.1016/j.astropartphys.2023.102878. arXiv: 2301.12970 [astro-ph.IM].

[22] K. Zuber. *Neutrino Physics*. Boca Raton: Taylor & Francis, 2020. DOI: 10.1201/9781315195612.

[23] A. Tarek Abouelfadl Mohamed. *The Standard Model of Particle Physics*. Cham: Springer International Publishing, 2020, p. 3. ISBN: 978-3-030-59516-6. DOI: 10.1007/978-3-030-59516-6_1. URL: https://doi.org/10.1007/978-3-030-59516-6_1.

[24] C. Giunti and C. W. Kim. *Fundamentals of Neutrino Physics and Astrophysics*. 2007. ISBN: 978-0-19-850871-7.

[25] R. L. Workman et al. "Review of Particle Physics". In: *PTEP* 2022 (2022), p. 083C01. DOI: 10.1093/ptep/ptac097.

[26] T. D. Lee and S. Drell. "Particle Physics and Introduction to Field Theory". In: *Physics Today* 34.12 (Dec. 1981), p. 55. ISSN: 0031-9228. DOI: 10.1063/1.2914386. eprint: https://pubs.aip.org/physicstoday/article-pdf/34/12/55/8288693/55_1_online.pdf. URL: https://doi.org/10.1063/1.2914386.

[27] J. Erler and M. J. Ramsey-Musolf. "Weak mixing angle at low energies". In: *Phys. Rev. D* 72 (7 Oct. 2005), p. 073003. DOI: 10.1103/PhysRevD.72.073003. URL: https://link.aps.org/doi/10.1103/PhysRevD.72.073003.

[28] J. Erler and R. Ferro-Hernández. "Weak Mixing Angle in the Thomson Limit". In: *JHEP* 03 (2018), p. 196. DOI: 10.1007/JHEP03(2018)196. arXiv: 1712.09146 [hep-ph].

[29] A. Czarnecki and W. J. Marciano. "Polarized Moller scattering asymmetries". In: *Int. J. Mod. Phys. A* 15 (2000). Ed. by C. A. Heusch, p. 2365. DOI: 10.1016/S0217-751X(00)00243-0. arXiv: hep-ph/0003049.

[30] S. Sarantakos, A. Sirlin, and W. J. Marciano. "Radiative Corrections to Neutrino-Lepton Scattering in the SU(2)-L x U(1) Theory". In: *Nucl. Phys. B* 217 (1983), p. 84. DOI: 10.1016/0550-3213(83)90079-2.

[31] V. A. Dzuba et al. "Revisiting parity non-conservation in cesium". In: *Phys. Rev. Lett.* 109 (2012), p. 203003. DOI: 10.1103/PhysRevLett.109.203003. arXiv: 1207.5864 [hep-ph].

[32] C. S. Wood et al. "Measurement of parity nonconservation and an anapole moment in cesium". In: *Science* 275 (1997), p. 1759. DOI: 10.1126/science.275.5307.1759.

[33] D. Androic et al. "Precision measurement of the weak charge of the proton". In: *Nature* 557.7704 (2018), p. 207. DOI: 10.1038/s41586-018-0096-0.

[34] P. L. Anthony et al. "Precision measurement of the weak mixing angle in Moller scattering". In: *Phys. Rev. Lett.* 95 (2005), p. 081601. DOI: 10.1103/PhysRevLett.95.081601. eprint: hep-ex/0504049 (hep-ex).

[35] D. Wang et al. "Measurement of parity violation in electron–quark scattering". In: *Nature* 506.7486 (2014), p. 67. DOI: 10.1038/nature12964.

[36] F. J. Hasert et al. "Search for Elastic ν_μ Electron Scattering". In: *Phys. Lett. B* 46 (1973), p. 121. DOI: 10.1016/0370-2693(73)90494-2.

[37] C. Giunti and A. Studenikin. “Neutrino electromagnetic interactions: a window to new physics”. In: *Rev. Mod. Phys.* 87 (2015), p. 531. DOI: 10.1103/RevModPhys.87.531. arXiv: 1403.6344 [hep-ph].

[38] J.W. Chen et al. “Low-energy electronic recoil in xenon detectors by solar neutrinos”. In: *Physics Letters B* 774 (Nov. 2017), p. 656. DOI: 10.1016/j.physletb.2017.10.029. URL: https://doi.org/10.1016%5C%2Fj.physletb.2017.10.029.

[39] K. -N. Huang and W. R. Johnson. “Multiconfiguration relativistic random-phase approximation. Theory”. In: *Phys. Rev. A* 25 (2 Feb. 1982), p. 634. DOI: 10.1103/PhysRevA.25.634. URL: https://link.aps.org/doi/10.1103/PhysRevA.25.634.

[40] K.N. Huang. “Relativistic many-body theory of atomic transitions. The relativistic equation-of-motion approach”. In: *Phys. Rev. A* 26 (2 Aug. 1982), p. 734. DOI: 10.1103/PhysRevA.26.734. URL: https://link.aps.org/doi/10.1103/PhysRevA.26.734.

[41] J.W. Chen et al. “Atomic ionization of germanium by neutrinos from an ab initio approach”. In: *Phys. Lett. B* 731 (2014), p. 159. DOI: 10.1016/j.physletb.2014.02.036. arXiv: 1311.5294 [hep-ph].

[42] K. A. Kouzakov and A. I. Studenikin. “Theory of neutrino-atom collisions: the history, present status and BSM physics”. In: *Adv. High Energy Phys.* 2014 (2014), p. 569409. DOI: 10.1155/2014/569409. arXiv: 1406.4999 [hep-ph].

[43] K. A. Kouzakov and A. I. Studenikin. “Electromagnetic properties of massive neutrinos in low-energy elastic neutrino-electron scattering”. In: *Phys. Rev. D* 95.5 (2017). [Erratum: Phys.Rev.D 96, 099904 (2017)], p. 055013. DOI: 10.1103/PhysRevD.95.055013. arXiv: 1703.00401 [hep-ph].

[44] J. W. Chen et al. “Constraining neutrino electromagnetic properties by germanium detectors”. In: *Phys. Rev. D* 91.1 (2015), p. 013005. DOI: 10.1103/PhysRevD.91.013005. arXiv: 1411.0574 [hep-ph].

[45] C.C. Hsieh et al. “Discovery potential of multiton xenon detectors in neutrino electromagnetic properties”. In: *Phys. Rev. D* 100 (7 Oct. 2019), p. 073001. DOI: 10.1103/PhysRevD.100.073001. URL: https://link.aps.org/doi/10.1103/PhysRevD.100.073001.

[46] L. A. Mikaelyan. “Investigation of neutrino properties in experiments at nuclear reactors: Present status and prospects”. In: *Phys. Atom. Nucl.* 65 (2002), p. 1173. DOI: 10.1134/1.1495017. arXiv: hep-ph/0210047.

[47] S. A. Fayans, L. A. Mikaelyan, and V. V. Sinev. “Weak and magnetic inelastic scattering of anti-neutrinos on atomic electrons”. In: *Phys. Atom. Nucl.* 64 (2001), p. 1475. DOI: 10.1134/1.1398940. arXiv: hep-ph/0004158.

[48] B.L. Henke, E.M. Gullikson, and J.C. Davis. "X-Ray Interactions: Photoabsorption, Scattering, Transmission, and Reflection at E = 50-30,000 eV, Z = 1-92". In: *Atomic Data and Nuclear Data Tables* 54.2 (1993), p. 181. ISSN: 0092-640X. DOI: https://doi.org/10.1006/adnd.1993.1013. URL: https://www.sciencedirect.com/science/article/pii/S0092640X83710132.

[49] A. Thompson et al. *X-ray data booklet, https://xdb.lbl.gov/*. 2009. URL: https://xdb.lbl.gov/.

[50] D. Z. Freedman. "Coherent Neutrino Nucleus Scattering as a Probe of the Weak Neutral Current". In: *Phys. Rev. D* 9 (1974), p. 1389. DOI: 10.1103/PhysRevD.9.1389.

[51] D. Akimov et al. "Observation of Coherent Elastic Neutrino-Nucleus Scattering". In: *Science* 357.6356 (2017), p. 1123. DOI: 10.1126/science.aao0990. arXiv: 1708.01294 [nucl-ex].

[52] M. Cadeddu, F. Dordei, and C. Giunti. "A view of Coherent Elastic Neutrino-Nucleus Scattering". In: (July 2023). arXiv: 2307.08842 [hep-ph].

[53] D. Akimov et al. "First Measurement of Coherent Elastic Neutrino-Nucleus Scattering on Argon". In: *Phys. Rev. Lett.* 126.1 (2021), p. 012002. DOI: 10.1103/PhysRevLett.126.012002. arXiv: 2003.10630 [nucl-ex].

[54] D. Akimov et al. "Measurement of the Coherent Elastic Neutrino-Nucleus Scattering Cross Section on CsI by COHERENT". In: *Phys. Rev. Lett.* 129.8 (2022), p. 081801. DOI: 10.1103/PhysRevLett.129.081801. arXiv: 2110.07730 [hep-ex].

[55] D. J Griffiths. *Introduction to elementary particles; 2nd rev. version*. Physics textbook. New York, NY: Wiley, 2008. URL: https://cds.cern.ch/record/111880.

[56] P. An et al. "Measurement of ^{nat}Pb(ν_e,Xn) production with a stopped-pion neutrino source". In: (Dec. 2022). arXiv: 2212.11295 [hep-ex].

[57] J. Sansonetti and W. Martin. *Handbook of Basic Atomic Spectroscopic Data*. en. 2005.

[58] G. Fricke et al. "Nuclear Ground State Charge Radii from Electromagnetic Interactions". In: *Atom. Data Nucl. Data Tabl.* 60 (1995), p. 177. DOI: 10.1006/adnd.1995.1007.

[59] I. Angeli and K. P. Marinova. "Table of experimental nuclear ground state charge radii: An update". In: *Atom. Data Nucl. Data Tabl.* 99.1 (2013), p. 69. DOI: 10.1016/j.adt.2011.12.006.

[60] M. Hoferichter, J. Menéndez, and A. Schwenk. "Coherent elastic neutrino-nucleus scattering: EFT analysis and nuclear responses". In: *Phys. Rev. D* 102.7 (2020), p. 074018. DOI: 10.1103/PhysRevD.102.074018. arXiv: 2007.08529 [hep-ph].

[61] J. N. Bahcall and R. L. Sears. "Solar neutrinos". In: *Ann. Rev. Astron. Astrophys.* 10 (1972), p. 25. DOI: 10.1146/annurev.aa.10.090172.000325.

[62] W. C. Haxton. "The solar neutrino problem". In: *Ann. Rev. Astron. Astrophys.* 33 (1995). Ed. by G. Burbidge and A. Sandage, p. 459. DOI: 10.1146/annurev.aa.33.090195.002331. arXiv: hep-ph/9503430.

[63] M. Agostini et al. "Comprehensive measurement of pp-chain solar neutrinos". In: *Nature* 562.7728 (2018), p. 505. DOI: 10.1038/s41586-018-0624-y.

[64] M. Agostini et al. "First Directional Measurement of Sub-MeV Solar Neutrinos with Borexino". In: *Phys. Rev. Lett.* 128.9 (2022), p. 091803. DOI: 10.1103/PhysRevLett.128.091803. arXiv: 2112.11816 [hep-ex].

[65] S. Appel et al. "Improved Measurement of Solar Neutrinos from the Carbon-Nitrogen-Oxygen Cycle by Borexino and Its Implications for the Standard Solar Model". In: *Phys. Rev. Lett.* 129.25 (2022), p. 252701. DOI: 10.1103/PhysRevLett.129.252701. arXiv: 2205.15975 [hep-ex].

[66] N. Grevesse and A. J. Sauval. "Standard Solar Composition". In: *Space Sci. Rev.* 85 (1998), p. 161. DOI: 10.1023/A:1005161325181.

[67] A. Yu. Smirnov. "The MSW effect and solar neutrinos". In: *10th International Workshop on Neutrino Telescopes*. May 2003, p. 23. arXiv: hep-ph/0305106.

[68] S. Kumaran et al. "Borexino Results on Neutrinos from the Sun and Earth". In: *Universe* 7.7 (2021), p. 231. DOI: 10.3390/universe7070231. arXiv: 2105.13858 [hep-ex].

[69] E. Vitagliano, I. Tamborra, and G. Raffelt. "Grand Unified Neutrino Spectrum at Earth: Sources and Spectral Components". In: *Rev. Mod. Phys.* 92 (2020), p. 45006. DOI: 10.1103/RevModPhys.92.045006. arXiv: 1910.11878 [astro-ph.HE].

[70] M. Agostini et al. "Experimental evidence of neutrinos produced in the CNO fusion cycle in the Sun". In: *Nature* 587 (2020), p. 577. DOI: 10.1038/s41586-020-2934-0. arXiv: 2006.15115 [hep-ex].

[71] J. Bergstrom et al. "Updated determination of the solar neutrino fluxes from solar neutrino data". In: *JHEP* 03 (2016), p. 132. DOI: 10.1007/JHEP03(2016)132. arXiv: 1601.00972 [hep-ph].

[72] T. Kajita. "Atmospheric Neutrinos". In: *New Journal of Physics* 6 (Dec. 2004), p. 194. DOI: 10.1088/1367-2630/6/1/194.

[73] M. Honda et al. "Improvement of low energy atmospheric neutrino flux calculation using the JAM nuclear interaction model". In: *Phys. Rev. D* 83 (12 June 2011), p. 123001. DOI: 10.1103/PhysRevD.83.123001. URL: https://link.aps.org/doi/10.1103/PhysRevD.83.123001.

[74] G. Battistoni et al. "The atmospheric neutrino flux below 100-MeV: The FLUKA results". In: *Astropart. Phys.* 23 (2005), p. 526. DOI: 10.1016/j.astropartphys.2005.03.006.

[75] P. Vogel and J. Engel. "Neutrino electromagnetic form factors". In: *Phys. Rev. D* 39 (11 June 1989), p. 3378. DOI: 10.1103/PhysRevD.39.3378. URL: https://link.aps.org/doi/10.1103/PhysRevD.39.3378.

[76] Th. A. Mueller et al. “Improved Predictions of Reactor Antineutrino Spectra”. In: *Phys. Rev. C* 83 (2011), p. 054615. DOI: 10.1103/PhysRevC.83.054615. arXiv: 1101.2663 [hep-ex].

[77] P. Huber. “On the determination of anti-neutrino spectra from nuclear reactors”. In: *Phys. Rev. C* 84 (2011). [Erratum: Phys.Rev.C 85, 029901 (2012)], p. 024617. DOI: 10.1103/PhysRevC.85.029901. arXiv: 1106.0687 [hep-ph].

[78] M. Estienne et al. “Updated Summation Model: An Improved Agreement with the Daya Bay Antineutrino Fluxes”. In: *Phys. Rev. Lett.* 123.2 (2019), p. 022502. DOI: 10.1103/PhysRevLett.123.022502. arXiv: 1904.09358 [nucl-ex].

[79] V. I. Kopeikin, L. A. Mikaelyan, and V. V. Sinev. “Search for the neutrino magnetic moment in the nonequilibrium reactor anti-neutrino energy spectrum”. In: *Phys. Atom. Nucl.* 63 (2000), p. 1012. DOI: 10.1134/1.855741. arXiv: hep-ph/9904384.

[80] V. I. Kopeikin. “Flux and spectrum of reactor antineutrinos”. In: *Phys. Atom. Nucl.* 75 (2012), p. 143. DOI: 10.1134/S1063778812020123.

[81] Y. Declais et al. “Study of reactor anti-neutrino interaction with proton at Bugey nuclear power plant”. In: *Phys. Lett. B* 338 (1994), p. 383. DOI: 10.1016/0370-2693(94)91394-3.

[82] P. S. Barbeau, Yu. Efremenko, and K. Scholberg. “COHERENT at the Spallation Neutron Source”. In: (Nov. 2021). arXiv: 2111.07033 [hep-ex].

[83] B. J. Scholz. “First Observation of Coherent Elastic Neutrino-Nucleus Scattering”. PhD thesis. Chicago U., 2017. DOI: 10.1007/978-3-319-99747-6. arXiv: 1904.01155 [nucl-ex].

[84] D. Akimov et al. “The COHERENT Experimental Program”. In: *Snowmass 2021*. Apr. 2022. arXiv: 2204.04575 [hep-ex].

[85] D. Akimov et al. “COHERENT 2018 at the Spallation Neutron Source”. In: (Mar. 2018). arXiv: 1803.09183 [physics.ins-det].

[86] D. Akimov et al. “Measurement of scintillation response of CsI[Na] to low-energy nuclear recoils by COHERENT”. In: *JINST* 17.10 (2022), P10034. DOI: 10.1088/1748-0221/17/10/P10034. arXiv: 2111.02477 [physics.ins-det].

[87] J. Piekarewicz et al. “Power of two: Assessing the impact of a second measurement of the weak-charge form factor of ^{208}Pb”. In: *Phys. Rev. C* 94.3 (2016), p. 034316. DOI: 10.1103/PhysRevC.94.034316. arXiv: 1604.07799 [nucl-th].

[88] R. H. Helm. “Inelastic and Elastic Scattering of 187-Mev Electrons from Selected Even-Even Nuclei”. In: *Phys. Rev.* 104 (1956), p. 1466. DOI: 10.1103/PhysRev.104.1466.

[89] J. Friedrich and N. Voegler. “The salient features of charge density distributions of medium and heavy even-even nuclei determined from a systematic analysis of elastic electron scattering form factors”. In: *Nucl. Phys. A* 373 (1982), p. 192. DOI: 10.1016/0375-9474(82)90147-6.

[90] S. Baker and R. D. Cousins. "Clarification of the Use of Chi Square and Likelihood Functions in Fits to Histograms". In: *Nucl. Instrum. Meth.* 221 (1984), p. 437. DOI: 10.1016/0167-5087(84)90016-4.

[91] D. Akimov et al. "COHERENT Collaboration data release from the first detection of coherent elastic neutrino-nucleus scattering on argon". In: (June 2020). DOI: 10.5281/zenodo.3903810. arXiv: 2006.12659 [nucl-ex].

[92] J. Colaresi et al. "Measurement of Coherent Elastic Neutrino-Nucleus Scattering from Reactor Antineutrinos". In: *Phys. Rev. Lett.* 129.21 (2022), p. 211802. DOI: 10.1103/PhysRevLett.129.211802. arXiv: 2202.09672 [hep-ex].

[93] J. Colaresi et al. "First results from a search for coherent elastic neutrino-nucleus scattering at a reactor site". In: *Phys. Rev. D* 104.7 (2021), p. 072003. DOI: 10.1103/PhysRevD.104.072003. arXiv: 2108.02880 [hep-ex].

[94] J. I. Collar, A. R. L. Kavner, and C. M. Lewis. "Germanium response to sub-keV nuclear recoils: a multipronged experimental characterization". In: *Phys. Rev. D* 103.12 (2021), p. 122003. DOI: 10.1103/PhysRevD.103.122003. arXiv: 2102.10089 [nucl-ex].

[95] J. Lindhard et al. "INTEGRAL EQUATIONS GOVERNING RADIATION EFFECTS. (NOTES ON ATOMIC COLLISIONS, III)". In: *Kgl. Danske Videnskab., Selskab. Mat. Fys. Medd.* Vol: 33: No. 10 (Jan. 1963). URL: https://www.osti.gov/biblio/4701226.

[96] D. Aristizabal Sierra, V. De Romeri, and D. K. Papoulias. "Consequences of the Dresden-II reactor data for the weak mixing angle and new physics". In: *JHEP* 09 (2022), p. 076. DOI: 10.1007/JHEP09(2022)076. arXiv: 2203.02414 [hep-ph].

[97] P. Di Gangi. "The Xenon Road to Direct Detection of Dark Matter at LNGS: The XENON Project". In: *Universe* 7.8 (2021), p. 313. DOI: 10.3390/universe7080313.

[98] J. Aalbers et al. "First Dark Matter Search Results from the LUX-ZEPLIN (LZ) Experiment". In: *Phys. Rev. Lett.* 131.4 (2023), p. 041002. DOI: 10.1103/PhysRevLett.131.041002. arXiv: 2207.03764 [hep-ex].

[99] E. Aprile et al. "Search for New Physics in Electronic Recoil Data from XENONnT". In: *Phys. Rev. Lett.* 129.16 (2022), p. 161805. DOI: 10.1103/PhysRevLett.129.161805. arXiv: 2207.11330 [hep-ex].

[100] V. A. Kudryavtsev. "Recent Results from LUX and Prospects for Dark Matter Searches with LZ". In: *Universe* 5.3 (2019), p. 73. DOI: 10.3390/universe5030073.

[101] M. Agostini et al. "Limiting neutrino magnetic moments with Borexino Phase-II solar neutrino data". In: *Phys. Rev. D* 96.9 (2017), p. 091103. DOI: 10.1103/PhysRevD.96.091103. arXiv: 1707.09355 [hep-ex].

[102] D. S. Akerib et al. "The LUX-ZEPLIN (LZ) Experiment". In: *Nucl. Instrum. Meth. A* 953 (2020), p. 163047. DOI: 10.1016/j.nima.2019.163047. arXiv: 1910.09124 [physics.ins-det].

[103] G. Pereira. *Energy resolution of the LZ detector for High-Energy Electronic Recoils*. presentation at the 5th XeSAT conference. 2022. URL: https://indico.in2p3.fr/event/20879/contributions/109640/attachments/70740/100409/GuilhermePereira_%5C%20Energy%5C%20resolution%5C%20of%5C%20LZ%5C%20detector%5C%20for%5C%20High%5C%20Energy%5C%20Electronic%5C%20Recoils.pdf.

[104] M. Szydagis et al. "NEST: a comprehensive model for scintillation yield in liquid xenon". In: *Journal of Instrumentation* 6.10 (Oct. 2011). [https://nest.physics.ucdavis.edu/], P10002. DOI: 10.1088/1748-0221/6/10/p10002. URL: https://doi.org/10.1088%2F1748-0221%2F6%2F10%2Fp10002.

[105] A. Serenelli. "Alive and well: a short review about standard solar models". In: *Eur. Phys. J. A* 52.4 (2016), p. 78. DOI: 10.1140/epja/i2016-16078-1. arXiv: 1601.07179 [astro-ph.SR].

[106] D. Acosta-Kane et al. "Discovery of underground argon with low level of radioactive 39Ar and possible applications to WIMP dark matter detectors". In: *Nucl. Instrum. Meth. A* 587 (2008). Ed. by Kunio Inoue, Atsuto Suzuki, and Tadao Mitsui, p. 46. DOI: 10.1016/j.nima.2007.12.032. arXiv: 0712.0381 [astro-ph].

[107] P. Agnes et al. "Results From the First Use of Low Radioactivity Argon in a Dark Matter Search". In: *Phys. Rev. D* 93.8 (2016). [Addendum: Phys.Rev.D 95, 069901 (2017)], p. 081101. DOI: 10.1103/PhysRevD.93.081101. arXiv: 1510.00702 [astro-ph.CO].

[108] P. Agnes. "Direct Detection of Dark Matter with DarkSide-20k". In: *EPJ Web Conf.* 280 (2023), p. 06003. DOI: 10.1051/epjconf/202328006003.

[109] P. Adari et al. "EXCESS workshop: Descriptions of rising low-energy spectra". In: *SciPost Phys. Proc.* 9 (2022). Ed. by A. Fuss et al., p. 001. DOI: 10.21468/SciPostPhysProc.9.001. arXiv: 2202.05097 [astro-ph.IM].

[110] C. E. Aalseth et al. "DarkSide-20k: A 20 tonne two-phase LAr TPC for direct dark matter detection at LNGS". In: *Eur. Phys. J. Plus* 133 (2018), p. 131. DOI: 10.1140/epjp/i2018-11973-4. arXiv: 1707.08145 [physics.ins-det].

[111] P. Agnes et al. "Low-Mass Dark Matter Search with the DarkSide-50 Experiment". In: *Phys. Rev. Lett.* 121.8 (2018), p. 081307. DOI: 10.1103/PhysRevLett.121.081307. arXiv: 1802.06994 [astro-ph.HE].

[112] D.S. Akerib et al. "Investigation of background electron emission in the LUX detector". In: *Phys. Rev. D* 102.9 (2020), p. 092004. DOI: 10.1103/PhysRevD.102.092004. arXiv: 2004.07791 [physics.ins-det].

[113] B. Edwards et al. "Measurement of single electron emission in two-phase xenon". In: *Astropart. Phys.* 30 (2008), p. 54. DOI: 10.1016/j.astropartphys.2008.06.006. arXiv: 0708.0768 [physics.ins-det].

[114] E. Santos et al. “Single electron emission in two-phase xenon with application to the detection of coherent neutrino-nucleus scattering”. In: *JHEP* 12 (2011), p. 115. DOI: 10.1007/JHEP12(2011)115. arXiv: 1110.3056 [physics.ins-det].

[115] E. Aprile et al. “Observation and applications of single-electron charge signals in the XENON100 experiment”. In: *J. Phys. G* 41 (2014), p. 035201. DOI: 10.1088/0954-3899/41/3/035201. arXiv: 1311.1088 [physics.ins-det].

[116] D.Y. Akimov et al. “Observation of delayed electron emission in a two-phase liquid xenon detector”. In: *Journal of Instrumentation* 11.03 (Mar. 2016), p. C03007. DOI: 10.1088/1748-0221/11/03/c03007. URL: https://doi.org/10.1088%2F1748-0221%2F11%2F03%2Fc03007.

[117] P. Agnes et al. “DarkSide-50 532-day Dark Matter Search with Low-Radioactivity Argon”. In: *Phys. Rev. D* 98.10 (2018), p. 102006. DOI: 10.1103/PhysRevD.98.102006. arXiv: 1802.07198 [astro-ph.CO].

[118] J. Xu et al. “A Study of the Residual ^{39}Ar Content in Argon from Underground Sources”. In: *Astropart. Phys.* 66 (2015), p. 53. DOI: 10.1016/j.astropartphys.2015.01.002. arXiv: 1204.6011 [physics.ins-det].

[119] N. Canci. “Long term operation with the DarkSide-50 detector”. In: *JINST* 15.03 (2020), p. C03026. DOI: 10.1088/1748-0221/15/03/C03026. arXiv: 1912.05461 [astro-ph.IM].

[120] A. Bondar et al. “Electron emission properties of two-phase argon and argon-nitrogen avalanche detectors”. In: *Journal of Instrumentation* 4.09 (Sept. 2009), P09013. DOI: 10.1088/1748-0221/4/09/p09013. URL: https://doi.org/10.1088/1748-0221/4/09/p09013.

[121] E. M. Gushchin, A. A. Kruglov, and I. M. Obodovskil. “ Emission of hot electrons from liquid and solid argon and xenon”. In: *Zh.Eksp.Teor.Fi.* 82 (1982), p. 1485. DOI: 10.1088/1748-0221/16/07/p07014.

[122] P. Agnes et al. “The electronics, trigger and data acquisition system for the liquid argon time projection chamber of the DarkSide-50 search for dark matter”. In: *Journal of Instrumentation* 12.12 (Dec. 2017), P12011. DOI: 10.1088/1748-0221/12/12/p12011. URL: https://doi.org/10.1088/1748-0221/12/12/p12011.

[123] P. Agnes et al. “First Results from the DarkSide-50 Dark Matter Experiment at Laboratori Nazionali del Gran Sasso”. In: *Phys. Lett. B* 743 (2015), p. 456. DOI: 10.1016/j.physletb.2015.03.012. arXiv: 1410.0653 [astro-ph.CO].

[124] P. Agnes et al. “Simulation of argon response and light detection in the DarkSide-50 dual phase TPC”. In: *Journal of Instrumentation* 12.10 (2017), P10015. DOI: 10.1088/1748-0221/12/10/P10015. arXiv: 1707.05630 [physics.ins-det].

[125] P. Agnes et al. “Performance of the ReD TPC, a novel double-phase LAr detector with silicon photomultiplier readout”. In: *Eur. Phys. J. C* 81.11 (2021), p. 1014. DOI: 10.1140/epjc/s10052-021-09801-6. arXiv: 2106.13168 [physics.ins-det].

[126] M. Babicz et al. “A measurement of the group velocity of scintillation light in liquid argon”. In: *Journal of Instrumentation* 15.09 (Sept. 2020), P09009. DOI: 10.1088/1748-0221/15/09/p09009. URL: https://doi.org/10.1088/1748-0221/15/09/p09009.

[127] C. Benson, G. Orebi Gann, and V. Gehman. “Measurements of the intrinsic quantum efficiency and absorption length of tetraphenyl butadiene thin films in the vacuum ultraviolet regime”. In: *Eur. Phys. J. C* 78.4 (2018), p. 329. DOI: 10.1140/s10052-018-5807-z. arXiv: 1709.05002 [physics.ins-det].

[128] J. Asaadi et al. “Emanation and bulk fluorescence in liquid argon from tetraphenyl butadiene wavelength shifting coatings”. In: *JINST* 14.02 (2019), P02021. DOI: 10.1088/1748-0221/14/02/P02021. arXiv: 1804.00011 [physics.ins-det].

[129] G. Bakale, U. Sowada, and W. F. Schmidt. “Effect of an electric field on electron attachment to sulfur hexafluoride, nitrous oxide, and molecular oxygen in liquid argon and xenon”. In: *The Journal of Physical Chemistry* 80.23 (1976), p. 2556. DOI: 10.1021/j100564a006. eprint: https://doi.org/10.1021/j100564a006. URL: https://doi.org/10.1021/j100564a006.

[130] K. S. Krane. *Introductory nuclear physics*. New York, NY: Wiley, 1988. URL: https://cds.cern.ch/record/359790.

[131] J. B. Bellicard and K. J. van Oostrum. “Elastic Electron Scattering from Lead-208 at 175 and 250 MeV”. In: *Phys. Rev. Lett.* 19 (5 July 1967), p. 242. DOI: 10.1103/PhysRevLett.19.242. URL: https://link.aps.org/doi/10.1103/PhysRevLett.19.242.

[132] J. L. Friar and J. W. Negele. “The determination of the nuclear charge distribution of Pb-208 from elastic electron scattering and muonic x-rays”. In: *Nucl. Phys. A* 212 (1973), p. 93. DOI: 10.1016/0375-9474(73)90039-0.

[133] J. Heisenberg et al. “Elastic Electron Scattering by $^{208}\mathrm{Pb}$ And New Information About the Nuclear Charge Distribution”. In: *Phys. Rev. Lett.* 23 (24 Dec. 1969), p. 1402. DOI: 10.1103/PhysRevLett.23.1402. URL: https://link.aps.org/doi/10.1103/PhysRevLett.23.1402.

[134] R. Hofstadter. “Electron scattering and nuclear structure”. In: *Rev. Mod. Phys.* 28 (1956), p. 214. DOI: 10.1103/RevModPhys.28.214.

[135] J.D. Walecka. *Theoretical Nuclear And Subnuclear Physics (Second Edition)*. World Scientific Publishing Company, 2004. ISBN: 9789813102170. URL: https://books.google.it/books?id=Rc47DQAAQBAJ.

[136] H. De Vries, C. W. De Jager, and C. De Vries. "Nuclear charge and magnetization density distribution parameters from elastic electron scattering". In: *Atom. Data Nucl. Data Tabl.* 36 (1987), p. 495. DOI: 10.1016/0092-640X(87)90013-1.

[137] C. J. Horowitz and J. Piekarewicz. "Neutron star structure and the neutron radius of Pb-208". In: *Phys. Rev. Lett.* 86 (2001), p. 5647. DOI: 10.1103/PhysRevLett.86.5647. arXiv: astro-ph/0010227.

[138] B. T. Reed et al. "Implications of PREX-2 on the Equation of State of Neutron-Rich Matter". In: *Phys. Rev. Lett.* 126.17 (2021), p. 172503. DOI: 10.1103/PhysRevLett.126.172503. arXiv: 2101.03193 [nucl-th].

[139] M. Thiel et al. "Neutron skins of atomic nuclei: per aspera ad astra". In: *J. Phys. G* 46.9 (2019), p. 093003. DOI: 10.1088/1361-6471/ab2c6d. arXiv: 1904.12269 [nucl-ex].

[140] S. S. M. Wong. "Bulk Properties of Nuclei". In: *Introductory Nuclear Physics*. John Wiley and Sons, Ltd, 1998. Chap. 4, p. 105. ISBN: 9783527617906. DOI: https://doi.org/10.1002/9783527617906.ch4. eprint: https://onlinelibrary.wiley.com/doi/pdf/10.1002/9783527617906.ch4. URL: https://onlinelibrary.wiley.com/doi/abs/10.1002/9783527617906.ch4.

[141] B. G. Todd-Rutel and J. Piekarewicz. "Neutron-Rich Nuclei and Neutron Stars: A New Accurately Calibrated Interaction for the Study of Neutron-Rich Matter". In: *Phys. Rev. Lett.* 95 (2005), p. 122501. DOI: 10.1103/PhysRevLett.95.122501. arXiv: nucl-th/0504034.

[142] W.C. Chen and J. Piekarewicz. "Building relativistic mean field models for finite nuclei and neutron stars". In: *Phys. Rev. C* 90.4 (2014), p. 044305. DOI: 10.1103/PhysRevC.90.044305. arXiv: 1408.4159 [nucl-th].

[143] C. J. Horowitz et al. "Weak charge form factor and radius of 208Pb through parity violation in electron scattering". In: *Phys. Rev. C* 85 (2012), p. 032501. DOI: 10.1103/PhysRevC.85.032501. arXiv: 1202.1468 [nucl-ex].

[144] A. Ong, J. C. Berengut, and V. V. Flambaum. "Effect of spin-orbit nuclear charge density corrections due to the anomalous magnetic moment on halonuclei". In: *Phys. Rev. C* 82 (1 July 2010), p. 014320. DOI: 10.1103/PhysRevC.82.014320. URL: https://link.aps.org/doi/10.1103/PhysRevC.82.014320.

[145] C. J. Horowitz and J. Piekarewicz. "Impact of spin-orbit currents on the electroweak skin of neutron-rich nuclei". In: *Phys. Rev. C* 86 (2012), p. 045503. DOI: 10.1103/PhysRevC.86.045503. arXiv: 1208.2249 [nucl-th].

[146] C. J. Horowitz. "Weak radius of the proton". In: *Phys. Lett. B* 789 (2019), p. 675. DOI: 10.1016/j.physletb.2018.12.029. arXiv: 1809.06478 [nucl-th].

[147] J. Erler and S. Su. "The Weak Neutral Current". In: *Prog. Part. Nucl. Phys.* 71 (2013), p. 119. DOI: 10.1016/j.ppnp.2013.03.004. arXiv: 1303.5522 [hep-ph].

[148] J. Erler et al. "Weak Polarized Electron Scattering". In: *Ann. Rev. Nucl. Part. Sci.* 64 (2014), p. 269. DOI: 10.1146/annurev-nucl-102313-025520. arXiv: 1401.6199 [hep-ph].

[149] P.G. Reinhard and W. Nazarewicz. "Nuclear charge densities in spherical and deformed nuclei: towards precise calculations of charge radii". In: *Phys. Rev. C* 103 (2021), p. 054310. DOI: 10.1103/PhysRevC.103.054310. arXiv: 2101.00320 [nucl-th].

[150] C. J. Horowitz. "Parity violating elastic electron scattering and Coulomb distortions". In: *Phys. Rev. C* 57 (1998), p. 3430. DOI: 10.1103/PhysRevC.57.3430. arXiv: nucl-th/9801011.

[151] S. Klein, B. Dreher, and J. Friedrich. *Drepha: A phase-shift calculation code for elastic electron scattering*. 1986.

[152] F. Salvat, A. Jablonski, and C. J. Powell. *elsepa—Dirac partial-wave calculation of elastic scattering of electrons and positrons by atoms, positive ions and molecules*. 2005. DOI: 10.1016/j.cpc.2004.09.006..

[153] S. Abrahamyan et al. "Measurement of the Neutron Radius of ^{208}Pb through Parity Violation in Electron Scattering". In: *Physical Review Letters* 108.11 (Mar. 2012). ISSN: 1079-7114. DOI: 10.1103/physrevlett.108.112502. URL: http://dx.doi.org/10.1103/PhysRevLett.108.112502.

[154] D. Adhikari et al. "Accurate Determination of the Neutron Skin Thickness of $^{208}\mathrm{Pb}$ through Parity-Violation in Electron Scattering". In: *Phys. Rev. Lett.* 126 (17 Apr. 2021), p. 172502. DOI: 10.1103/PhysRevLett.126.172502. URL: https://link.aps.org/doi/10.1103/PhysRevLett.126.172502.

[155] M. Gorchtein and C. J. Horowitz. "Dispersion gamma Z-box correction to the weak charge of the proton". In: *Phys. Rev. Lett.* 102 (2009), p. 091806. DOI: 10.1103/PhysRevLett.102.091806. arXiv: 0811.0614 [hep-ph].

[156] M. Gorchtein, C. J. Horowitz, and M. J. Ramsey-Musolf. "Model-dependence of the γZ dispersion correction to the parity-violating asymmetry in elastic ep scattering". In: *Phys. Rev. C* 84 (2011), p. 015502. DOI: 10.1103/PhysRevC.84.015502. arXiv: 1102.3910 [nucl-th].

[157] J. Erler et al. "Reduced uncertainty of the axial γZ-box correction to the proton's weak charge". In: *Phys. Rev. D* 100.5 (2019), p. 053007. DOI: 10.1103/PhysRevD.100.053007. arXiv: 1907.07928 [hep-ph].

[158] D. Adhikari et al. "Precision Determination of the Neutral Weak Form Factor of Ca48". In: *Phys. Rev. Lett.* 129.4 (2022), p. 042501. DOI: 10.1103/PhysRevLett.129.042501. arXiv: 2205.11593 [nucl-ex].

[159] J. Piekarewicz et al. "Electric dipole polarizability and the neutron skin". In: *Phys. Rev. C* 85 (4 Apr. 2012), p. 041302. DOI: 10.1103/PhysRevC.85.041302. URL: https://link.aps.org/doi/10.1103/PhysRevC.85.041302.

[160] X. Roca-Maza et al. “Neutron skin thickness from the measured electric dipole polarizability in ^{68}Ni, ^{120}Sn, and ^{208}Pb”. In: *Phys. Rev. C* 92 (6 Dec. 2015), p. 064304. DOI: 10.1103/PhysRevC.92.064304. URL: https://link.aps.org/doi/10.1103/PhysRevC.92.064304.

[161] J. Piekarewicz. “Implications of PREX-2 on the electric dipole polarizability of neutron-rich nuclei”. In: *Phys. Rev. C* 104.2 (2021), p. 024329. DOI: 10.1103/PhysRevC.104.024329. arXiv: 2105.13452 [nucl-th].

[162] A. Trzci ńska et al. “Neutron Density Distributions Deduced from Antiprotonic Atoms”. In: *Phys. Rev. Lett.* 87 (8 Aug. 2001), p. 082501. DOI: 10.1103/PhysRevLett.87.082501. URL: https://link.aps.org/doi/10.1103/PhysRevLett.87.082501.

[163] J. T. Zhang et al. “Systematic trends of neutron skin thickness versus relative neutron excess”. In: *Phys. Rev. C* 104.3 (2021), p. 034303. DOI: 10.1103/PhysRevC.104.034303. arXiv: 2109.03417 [nucl-th].

[164] B. Klos et al. “Neutron density distributions from antiprotonic Pb-208 and Bi-209 atoms”. In: *Phys. Rev. C* 76 (2007), p. 014311. DOI: 10.1103/PhysRevC.76.014311. arXiv: nucl-ex/0702016.

[165] J. Zenihiro et al. “Neutron density distributions of $^{204,206,208}\mathrm{Pb}$ deduced via proton elastic scattering at $E_p = 295$ MeV”. In: *Phys. Rev. C* 82 (4 Oct. 2010), p. 044611. DOI: 10.1103/PhysRevC.82.044611. URL: https://link.aps.org/doi/10.1103/PhysRevC.82.044611.

[166] V. E. Starodubsky and N. M. Hintz. “Extraction of neutron densities from elastic proton scattering by Pb-206, Pb-207, Pb-208 at 650-MeV”. In: *Phys. Rev. C* 49 (1994), p. 2118. DOI: 10.1103/PhysRevC.49.2118.

[167] C. M. Tarbert et al. “Neutron skin of ^{208}Pb from Coherent Pion Photoproduction”. In: *Phys. Rev. Lett.* 112.24 (2014), p. 242502. DOI: 10.1103/PhysRevLett.112.242502. arXiv: 1311.0168 [nucl-ex].

[168] R. Essick et al. “Astrophysical Constraints on the Symmetry Energy and the Neutron Skin of Pb208 with Minimal Modeling Assumptions”. In: *Phys. Rev. Lett.* 127.19 (2021), p. 192701. DOI: 10.1103/PhysRevLett.127.192701. arXiv: 2102.10074 [nucl-th].

[169] B. P. Abbott et al. “GW170817: Observation of Gravitational Waves from a Binary Neutron Star Inspiral”. In: *Phys. Rev. Lett.* 119.16 (2017), p. 161101. DOI: 10.1103/PhysRevLett.119.161101. arXiv: 1710.05832 [gr-qc].

[170] B. P. Abbott et al. “GW170817: Measurements of neutron star radii and equation of state”. In: *Phys. Rev. Lett.* 121.16 (2018), p. 161101. DOI: 10.1103/PhysRevLett.121.161101. arXiv: 1805.11581 [gr-qc].

[171] B. P. Abbott et al. “GW190425: Observation of a Compact Binary Coalescence with Total Mass $\sim 3.4 M_{\odot}$”. In: *Astrophys. J. Lett.* 892.1 (2020), p. L3. DOI: 10.3847/2041-8213/ab75f5. arXiv: 2001.01761 [astro-ph.HE].

[172] F. J. Fattoyev, J. Piekarewicz, and C. J. Horowitz. "Neutron Skins and Neutron Stars in the Multimessenger Era". In: *Phys. Rev. Lett.* 120.17 (2018), p. 172702. arXiv: 1711.06615 [nucl-th]. URL: https://doi.org/10.1103/PhysRevLett.120.172702.

[173] W. G. Newton and G. Crocombe. "Nuclear symmetry energy from neutron skins and pure neutron matter in a Bayesian framework". In: *Phys. Rev. C* 103 (6 June 2021), p. 064323. DOI: 10.1103/PhysRevC.103.064323. URL: https://link.aps.org/doi/10.1103/PhysRevC.103.064323.

[174] J. R. Stone. "Nuclear Physics and Astrophysics Constraints on the High Density Matter Equation of State". In: *Universe* 7.8 (2021), p. 257. DOI: 10.3390/universe7080257.

[175] R. Essick et al. "Detailed examination of astrophysical constraints on the symmetry energy and the neutron skin of Pb208 with minimal modeling assumptions". In: *Phys. Rev. C* 104.6 (2021), p. 065804. DOI: 10.1103/PhysRevC.104.065804. arXiv: 2107.05528 [nucl-th].

[176] T. E. Riley et al. "A NICER View of the Massive Pulsar PSR J0740+6620 Informed by Radio Timing and XMM-Newton Spectroscopy". In: *Astrophys. J. Lett.* 918.2 (2021), p. L27. DOI: 10.3847/2041-8213/ac0a81. arXiv: 2105.06980 [astro-ph.HE].

[177] M. C. Miller et al. "The Radius of PSR J0740+6620 from NICER and XMM-Newton Data". In: *Astrophys. J. Lett.* 918.2 (2021), p. L28. DOI: 10.3847/2041-8213/ac089b. arXiv: 2105.06979 [astro-ph.HE].

[178] B. Biswas. "Impact of PREX-II and Combined Radio/NICER/XMM-Newton's Mass–radius Measurement of PSR J0740+6620 on the Dense-matter Equation of State". In: *Astrophys. J.* 921.1 (2021), p. 63. DOI: 10.3847/1538-4357/ac1c72. arXiv: 2105.02886 [astro-ph.HE].

[179] B. Hu et al. *Ab initio predictions link the neutron skin of ^{208}Pb to nuclear forces*. 2021. arXiv: 2112.01125 [nucl-th].

[180] G. Giacalone, G. Nijs, and W. van der Schee. "Determination of the Neutron Skin of ^{208}Pb from Ultrarelativistic Nuclear Collisions". In: *Phys. Rev. Lett.* 131.20 (2023), p. 202302. DOI: 10.1103/PhysRevLett.131.202302. arXiv: 2305.00015 [nucl-th].

[181] H. J. Emrich et al. "RADIAL DISTRIBUTION OF NUCLEONS IN ISOTOPES CA-48, CA-40." In: *Nucl. Phys. A* 396 (1983). Ed. by A. Van Der Woude and B. J. Verhaar, p. 401C. DOI: 10.1016/0375-9474(83)90034-9.

[182] I. Sick et al. "CHARGE DENSITY OF CA-40". In: *Phys. Lett. B* 88 (1979), p. 245. DOI: 10.1016/0370-2693(79)90458-1.

[183] B. Dreher et al. "The determination of the nuclear ground state and transition charge density from measured electron scattering data". In: *Nucl. Phys. A* 235 (1974), p. 219. DOI: 10.1016/0375-9474(74)90189-4.

[184] D. Becker et al. "The P2 experiment". In: *Eur. Phys. J. A* 54.11 (2018), p. 208. DOI: 10.1140/epja/i2018-12611-6. arXiv: 1802.04759 [nucl-ex].

[185] L. Doria et al. “Dark Matter at the Intensity Frontier: the new MESA electron accelerator facility”. In: *PoS* ALPS2019 (2020), p. 022. DOI: 10.22323/1.360.0022. arXiv: 1908.07921 [hep-ex].

[186] O. Koshchii et al. “Weak charge and weak radius of ^{12}C”. In: *Phys. Rev. C* 102.2 (2020), p. 022501. DOI: 10.1103/PhysRevC.102.022501. arXiv: 2005.00479 [nucl-th].

[187] W.C. Chen and J. Piekarewicz. “Searching for isovector signatures in the neutron-rich oxygen and calcium isotopes”. In: *Phys. Lett. B* 748 (2015), p. 284. DOI: 10.1016/j.physletb.2015.07.020. arXiv: 1412.7870 [nucl-th].

[188] X. Roca-Maza, G. Colò, and H. Sagawa. “New Skyrme interaction with improved spin-isospin properties”. In: *Phys. Rev. C* 86 (3 Sept. 2012), p. 031306. DOI: 10.1103/PhysRevC.86.031306. URL: https://link.aps.org/doi/10.1103/PhysRevC.86.031306.

[189] B. M. Roberts, V. A. Dzuba, and V. V. Flambaum. “Parity and Time-Reversal Violation in Atomic Systems”. In: *Ann. Rev. Nucl. Part. Sci.* 65 (2015), p. 63. DOI: 10.1146/annurev-nucl-102014-022331. arXiv: 1412.6644 [physics.atom-ph].

[190] C. Bouchiat and C.A. Piketty. “Parity violation in atomic cesium and alternatives to the standard model of electroweak interactions”. In: *Physics Letters B* 128.1 (1983), p. 73. ISSN: 0370-2693. DOI: https://doi.org/10.1016/0370-2693(83)90076-X. URL: https://www.sciencedirect.com/science/article/pii/037026938390076X.

[191] A. V. Viatkina et al. “Dependence of atomic parity-violation effects on neutron skins and new physics”. In: *Phys. Rev. C* 100.3 (2019), p. 034318. DOI: 10.1103/PhysRevC.100.034318. arXiv: 1903.00123 [physics.atom-ph].

[192] J. S. M. Ginges and V. V. Flambaum. “Violations of fundamental symmetries in atoms and tests of unification theories of elementary particles”. In: *Phys. Rept.* 397 (2004), p. 63. DOI: 10.1016/j.physrep.2004.03.005. arXiv: physics/0309054.

[193] S. J. Pollock, E. N. Fortson, and L. Wilets. “Atomic parity nonconservation: Electroweak parameters and nuclear structure”. In: *Phys. Rev. C* 46 (6 Dec. 1992), p. 2587. DOI: 10.1103/PhysRevC.46.2587. URL: https://link.aps.org/doi/10.1103/PhysRevC.46.2587.

[194] J. James and P. G. H. Sandars. “A parametric approach to nuclear size and shape in atomic parity nonconservation”. In: *Journal of Physics B: Atomic, Molecular and Optical Physics* 32.14 (July 1999), p. 3295. DOI: 10.1088/0953-4075/32/14/301. URL: https://doi.org/10.1088/0953-4075/32/14/301.

[195] S.J. Pollock and M.C. Welliver. “Effects of neutron spatial distributions on atomic parity nonconservation in cesium”. In: *Physics Letters B* 464.3-4 (Oct. 1999), p. 177. ISSN: 0370-2693. DOI: 10.1016/s0370-2693(99)00987-9. URL: http://dx.doi.org/10.1016/S0370-2693(99)00987-9.

[196] C. J. Horowitz et al. “Parity violating measurements of neutron densities”. In: *Physical Review C* 63.2 (Jan. 2001). ISSN: 1089-490X. DOI: 10.1103/physrevc.63.025501. URL: http://dx.doi.org/10.1103/PhysRevC.63.025501.

[197] M. Cadeddu et al. “Neutrino, electroweak, and nuclear physics from COHERENT elastic neutrino-nucleus scattering with refined quenching factor”. In: *Phys. Rev.* D101.3 (2020), p. 033004. DOI: 10.1103/PhysRevD.101.033004. arXiv: 1908.06045 [hep-ph].

[198] M. Cadeddu and F. Dordei. “Reinterpreting the weak mixing angle from atomic parity violation in view of the Cs neutron rms radius measurement from COHERENT”. In: *Phys. Rev. D* 99.3 (2019), p. 033010. DOI: 10.1103/PhysRevD.99.033010. arXiv: 1808.10202 [hep-ph].

[199] S. G. Porsev et al. “Development of the configuration-interaction + all-order method and application to the parity-nonconserving amplitude and other properties of Pb”. In: *Phys. Rev. A* 93 (1 Jan. 2016), p. 012501. DOI: 10.1103/PhysRevA.93.012501. URL: https://link.aps.org/doi/10.1103/PhysRevA.93.012501.

[200] D. M. Meekhof et al. “High-precision measurement of parity nonconserving optical rotation in atomic lead”. In: *Phys. Rev. Lett.* 71 (21 Nov. 1993), p. 3442. DOI: 10.1103/PhysRevLett.71.3442. URL: https://link.aps.org/doi/10.1103/PhysRevLett.71.3442.

[201] S. J. Phipp et al. “A measurement of parity non-conserving optical rotation in atomic lead”. In: *Journal of Physics B: Atomic, Molecular and Optical Physics* 29.9 (May 1996), p. 1861. DOI: 10.1088/0953-4075/29/9/028. URL: https://doi.org/10.1088/0953-4075/29/9/028.

[202] S. C. Bennett and C. E. Wieman. “Measurement of the 6S —> 7S transition polarizability in atomic cesium and an improved test of the Standard Model”. In: *Phys. Rev. Lett.* 82 (1999). [Erratum: Phys. Rev. Lett.83,889(1999)], p. 2484. URL: http://dx.doi.org/10.1103/PhysRevLett.82.2484.

[203] P.A. Zyla et al. “Review of Particle Physics”. In: *PTEP* 2020.8 (2020), p. 083C01. DOI: 10.1093/ptep/ptaa104.

[204] A. Derevianko. “Correlated many-body treatment of the Breit interaction with application to cesium atomic properties and parity violation”. In: *Phys. Rev. A* 65 (1 Dec. 2001), p. 012106. DOI: 10.1103/PhysRevA.65.012106. URL: https://link.aps.org/doi/10.1103/PhysRevA.65.012106.

[205] B. K. Sahoo, B. P. Das, and H. Spiesberger. “New physics constraints from atomic parity violation in Cs133”. In: *Phys. Rev. D* 103.11 (2021), p. L111303. DOI: 10.1103/PhysRevD.103.L111303. arXiv: 2101.10095 [hep-ph].

[206] C. Amsler et al. “Review of Particle Physics”. In: *Phys. Lett. B* 667 (2008), p. 1. DOI: 10.1016/j.physletb.2008.07.018.

[207] K. Nakamura et al. “Review of particle physics”. In: *J. Phys. G* 37 (2010), p. 075021. DOI: 10.1088/0954-3899/37/7A/075021.

[208] K. A. Olive et al. “Review of Particle Physics”. In: *Chin. Phys. C* 38 (2014), p. 090001. DOI: 10.1088/1674-1137/38/9/090001.

[209] J. Guena, M. Lintz, and M. A. Bouchiat. “Measurement of the parity violating 6S-7S transition amplitude in cesium achieved within 2×10^{-13} atomic-unit accuracy by stimulated-emission detection”. In: *Phys. Rev. A* 71 (2005), p. 042108. DOI: 10.1103/PhysRevA.71.042108. arXiv: physics/0412017.

[210] J. Dobaczewski, H. Flocard, and J. Treiner. “Hartree-Fock-Bogolyubov descriptions of nuclei near the neutrino dripline”. In: *Nucl. Phys.* A422 (1984), p. 103. DOI: 10.1016/0375-9474(84)90433-0.

[211] M. M. Sharma, M. A. Nagarajan, and P. Ring. “rho meson coupling in the relativistic mean field theory and description of exotic nuclei”. In: *Phys. Lett.* B312 (1993), p. 377. DOI: 10.1016/0370-2693(93)90970-S.

[212] M. Bender et al. “Shell structure of superheavy nuclei in selfconsistent mean field models”. In: *Phys. Rev.* C60 (1999), p. 034304. DOI: 10.1103/PhysRevC.60.034304. eprint: nucl-th/9906030 (nucl-th).

[213] G. A. Lalazissis, J. Konig, and P. Ring. “A New parametrization for the Lagrangian density of relativistic mean field theory”. In: *Phys. Rev.* C55 (1997), p. 540. DOI: 10.1103/PhysRevC.55.540. eprint: nucl-th/9607039 (nucl-th).

[214] P. G. Reinhard et al. “Nuclear Ground State Properties in a Relativistic Meson Field Theory”. In: *Z. Phys. A* 323 (1986), p. 13.

[215] T. Niksic, D. Vretenar, and P. Ring. “Relativistic Nuclear Energy Density Functionals: Adjusting parameters to binding energies”. In: *Phys. Rev.* C78 (2008), p. 034318. DOI: 10.1103/PhysRevC.78.034318. eprint: arXiv:0809.1375 (nucl-th).

[216] T. Niksic et al. “Relativistic Hartree-Bogolyubov model with density dependent meson nucleon couplings”. In: *Phys. Rev.* C66 (2002), p. 024306. DOI: 10.1103/PhysRevC.66.024306. eprint: nucl-th/0205009 (nucl-th).

[217] J. Bartel et al. “Towards a better parametrisation of Skyrme-like effective forces: A Critical study of the SkM force”. In: *Nucl. Phys.* A386 (1982), p. 79. DOI: 10.1016/0375-9474(82)90403-1.

[218] M. Kortelainen et al. “Nuclear energy density optimization: Large deformations”. In: *Phys. Rev.* C85 (2012), p. 024304. DOI: 10.1103/PhysRevC.85.024304. eprint: arXiv:1111.4344 (nucl-th).

[219] M. Kortelainen et al. “Nuclear Energy Density Optimization”. In: *Phys. Rev.* C82 (2010), p. 024313. DOI: 10.1103/PhysRevC.82.024313. eprint: arXiv:1005.5145 (nucl-th).

[220] E. Chabanat et al. “A Skyrme parametrization from subnuclear to neutron star densities. 2. Nuclei far from stablities”. In: *Nucl. Phys.* A635 (1998), p. 231. DOI: 10.1016/S0375-9474(98)00570-3,10.1016/S0375-9474(98)00180-8.

[221] P. G. Reinhard and H. Flocard. "Nuclear effective forces and isotope shifts". In: *Nucl. Phys.* A584 (1995), p. 467. DOI: 10.1016/0375-9474(94)00770-N.

[222] J. A. Hernandez. "Weak Nuclear Form Factor: Nuclear Structure & Coherent Elastic Neutrino-Nucleus Scattering". MA thesis. Florida State U., Tallahassee (main), 2019.

[223] J. Yang, J. A. Hernandez, and J. Piekarewicz. "Electroweak probes of ground state densities". In: *Phys. Rev. C* 100.5 (2019), p. 054301. DOI: 10.1103/PhysRevC.100.054301. arXiv: 1908.10939 [nucl-th].

[224] B. Reed. "Measuring the weak charge radius of ^{208}Pb with PREX-II". In: *Presentation on behalf of the PREX-II Collaboration at the Magnificent CEvNS 2020 workshop* (2020). URL: https://indico.cern.ch/event/943069/contributions/4105294/attachments/2145999/3617186/CEvNS_2020.pdf.

[225] A. Derevianko. "Reconciliation of the Measurement of Parity Nonconservation in Cs with the Standard Model". In: *Phys. Rev. Lett.* 85 (8 Aug. 2000), p. 1618. DOI: 10.1103/PhysRevLett.85.1618. URL: https://link.aps.org/doi/10.1103/PhysRevLett.85.1618.

[226] M. Tanabashi et al. "Review of Particle Physics". In: *Phys. Rev.* D98.3 (2018), p. 030001. DOI: 10.1103/PhysRevD.98.030001.

[227] P. S. Bhupal Dev et al. *Searching for Z' bosons at the P2 experiment*. Mar. 2021. arXiv: 2103.09067 [hep-ph].

[228] J. Benesch et al. *The MOLLER Experiment: An Ultra-Precise Measurement of the Weak Mixing Angle Using Moller Scattering*. 2014. arXiv: 1411.4088 [nucl-ex].

[229] H. Davoudiasl, H.S. Lee, and W. J. Marciano. "Muon Anomaly and Dark Parity Violation". In: *Phys. Rev. Lett.* 109 (3 July 2012), p. 031802. DOI: 10.1103/PhysRevLett.109.031802. URL: https://link.aps.org/doi/10.1103/PhysRevLett.109.031802.

[230] H. Davoudiasl, H.S. Lee, and W. J. Marciano. ""Dark" Z implications for parity violation, rare meson decays, and Higgs physics". In: *Phys. Rev. D* 85 (11 June 2012), p. 115019. DOI: 10.1103/PhysRevD.85.115019. URL: https://link.aps.org/doi/10.1103/PhysRevD.85.115019.

[231] G. Hagen et al. "Neutron and weak-charge distributions of the ^{48}Ca nucleus". In: *Nature Phys.* 12.2 (2015), p. 186. arXiv: 1509.07169 [nucl-th]. URL: https://doi.org/10.1038/nphys3529.

[232] S. Tagami et al. "Neutron skin in ^{48}Ca determined from p+^{48}Ca and ^{48}Ca+^{12}C scattering". In: (Jan. 2022). arXiv: 2201.08541 [nucl-th].

[233] C. G. Payne et al. "Coherent elastic neutrino-nucleus scattering on ^{40}Ar from first principles". In: *Phys. Rev. C* 100.6 (2019), p. 061304. DOI: 10.1103/PhysRevC.100.061304. arXiv: 1908.09739 [nucl-th].

[234] M. Cadeddu et al. “Physics results from the first COHERENT observation of coherent elastic neutrino-nucleus scattering in argon and their combination with cesium-iodide data”. In: *Phys. Rev. D* 102.1 (2020), p. 015030. DOI: 10.1103/PhysRevD.102.015030. arXiv: 2005.01645 [hep-ph].

[235] S. Klein and J. Nystrand. “Exclusive vector meson production in relativistic heavy ion collisions”. In: *Phys. Rev. C* 60 (1999), p. 014903. DOI: 10.1103/PhysRevC.60.014903. arXiv: hep-ph/9902259.

[236] D. Aristizabal Sierra. “Extraction of neutron density distributions from high-statistics coherent elastic neutrino-nucleus scattering data”. In: (Jan. 2023). arXiv: 2301.13249 [hep-ph].

[237] G. P. Zeller et al. “A precise determination of electroweak parameters in neutrino nucleon scattering”. In: *Phys. Rev. Lett.* 88 (2002), p. 091802. eprint: hep-ex/0110059.

[238] V. De Romeri et al. “Physics implications of a combined analysis of COHERENT CsI and LAr data”. In: (Nov. 2022). arXiv: 2211.11905 [hep-ph].

[239] C. M. Lewis and J. I. Collar. “Response of undoped cryogenic CsI to low-energy nuclear recoils”. In: *Phys. Rev. C* 104.1 (2021), p. 014612. DOI: 10.1103/PhysRevC.104.014612. arXiv: 2101.03264 [physics.ins-det].

[240] M. Cadeddu et al. “Average CsI neutron density distribution from COHERENT data”. In: *Phys. Rev. Lett.* 120.7 (2018), p. 072501. DOI: 10.1103/PhysRevLett.120.072501. arXiv: 1710.02730 [hep-ph].

[241] H. Abele et al. “Particle Physics at the European Spallation Source”. In: (Nov. 2022). arXiv: 2211.10396 [physics.ins-det].

[242] D. Baxter et al. “Coherent Elastic Neutrino-Nucleus Scattering at the European Spallation Source”. In: *JHEP* 02 (2020), p. 123. DOI: 10.1007/JHEP02(2020)123. arXiv: 1911.00762 [physics.ins-det].

[243] C. Su, Q. Liu, and T. Liang. “CEνNS Experiment Proposal at CSNS”. In: (Mar. 2023). arXiv: 2303.13423 [physics.ins-det].

[244] M. Lindner, W. Rodejohann, and X.J. Xu. “Coherent Neutrino-Nucleus Scattering and new Neutrino Interactions”. In: *JHEP* 03 (2017), p. 097. DOI: 10.1007/JHEP03(2017)097. arXiv: 1612.04150 [hep-ph].

[245] H. T. Wong et al. “A Search of Neutrino Magnetic Moments with a High-Purity Germanium Detector at the Kuo-Sheng Nuclear Power Station”. In: *Phys. Rev. D* 75 (2007), p. 012001. DOI: 10.1103/PhysRevD.75.012001. arXiv: hep-ex/0605006.

[246] A. Aguilar-Arevalo et al. “Results of the Engineering Run of the Coherent Neutrino Nucleus Interaction Experiment (CONNIE)”. In: *JINST* 11.07 (2016), P07024. DOI: 10.1088/1748-0221/11/07/P07024. arXiv: 1604.01343 [physics.ins-det].

[247] G. Agnolet et al. “Background Studies for the MINER Coherent Neutrino Scattering Reactor Experiment”. In: *Nucl. Instrum. Meth. A* 853 (2017), p. 53. DOI: 10.1016/j.nima.2017.02.024. arXiv: 1609.02066 [physics.ins-det].

[248] B. C. Cañas et al. “Future perspectives for a weak mixing angle measurement in coherent elastic neutrino nucleus scattering experiments”. In: *Phys. Lett. B* 784 (2018), p. 159. DOI: 10.1016/j.physletb.2018.07.049. arXiv: 1806.01310 [hep-ph].

[249] A. Majumdar et al. “Physics implications of recent Dresden-II reactor data”. In: *Phys. Rev. D* 106.9 (2022), p. 093010. DOI: 10.1103/PhysRevD.106.093010. arXiv: 2208.13262 [hep-ph].

[250] T. Aoyama et al. “The anomalous magnetic moment of the muon in the Standard Model”. In: *Phys. Rept.* 887 (2020), p. 1. DOI: 10.1016/j.physrep.2020.07.006. arXiv: 2006.04822 [hep-ph].

[251] M. Davier et al. “A new evaluation of the hadronic vacuum polarisation contributions to the muon anomalous magnetic moment and to $\boldsymbol{\alpha(m_Z^2)}$”. In: *Eur. Phys. J. C* 80.3 (2020). [Erratum: Eur.Phys.J.C 80, 410 (2020)], p. 241. DOI: 10.1140/epjc/s10052-020-7792-2. arXiv: 1908.00921 [hep-ph].

[252] A. Keshavarzi, D. Nomura, and T. Teubner. “$g-2$ of charged leptons, $\alpha(M_Z^2)$, and the hyperfine splitting of muonium”. In: *Phys. Rev. D* 101.1 (2020), p. 014029. DOI: 10.1103/PhysRevD.101.014029. arXiv: 1911.00367 [hep-ph].

[253] K. Melnikov and A. Vainshtein. “Hadronic light-by-light scattering contribution to the muon anomalous magnetic moment revisited”. In: *Phys. Rev. D* 70 (2004), p. 113006. DOI: 10.1103/PhysRevD.70.113006. arXiv: hep-ph/0312226.

[254] P. Masjuan and P. Sanchez-Puertas. “Pseudoscalar-pole contribution to the $(g_\mu - 2)$: a rational approach”. In: *Phys. Rev. D* 95.5 (2017), p. 054026. DOI: 10.1103/PhysRevD.95.054026. arXiv: 1701.05829 [hep-ph].

[255] G. Colangelo et al. “Dispersion relation for hadronic light-by-light scattering: two-pion contributions”. In: *JHEP* 04 (2017), p. 161. DOI: 10.1007/JHEP04(2017)161. arXiv: 1702.07347 [hep-ph].

[256] M. Hoferichter et al. “Dispersion relation for hadronic light-by-light scattering: pion pole”. In: *JHEP* 10 (2018), p. 141. DOI: 10.1007/JHEP10(2018)141. arXiv: 1808.04823 [hep-ph].

[257] A. Gérardin, H. B. Meyer, and A. Nyffeler. “Lattice calculation of the pion transition form factor with $N_f = 2 + 1$ Wilson quarks”. In: *Phys. Rev. D* 100.3 (2019), p. 034520. DOI: 10.1103/PhysRevD.100.034520. arXiv: 1903.09471 [hep-lat].

[258] J. Bijnens, N. Hermansson-Truedsson, and A. Rodríguez-Sánchez. “Short-distance constraints for the HLbL contribution to the muon anomalous magnetic moment”. In: *Phys. Lett. B* 798 (2019), p. 134994. DOI: 10.1016/j.physletb.2019.134994. arXiv: 1908.03331 [hep-ph].

[259] G. Colangelo et al. “Longitudinal short-distance constraints for the hadronic light-by-light contribution to $(g-2)_\mu$ with large-N_c Regge models”. In: *JHEP* 03 (2020), p. 101. DOI: 10.1007/JHEP03(2020)101. arXiv: 1910.13432 [hep-ph].

[260] V. Pauk and M. Vanderhaeghen. “Single meson contributions to the muon‘s anomalous magnetic moment”. In: *Eur. Phys. J. C* 74.8 (2014), p. 3008. DOI: 10.1140/epjc/s10052-014-3008-y. arXiv: 1401.0832 [hep-ph].

[261] T. Aoyama et al. “Complete Tenth-Order QED Contribution to the Muon g-2”. In: *Phys. Rev. Lett.* 109 (2012), p. 111808. DOI: 10.1103/PhysRevLett.109.111808. arXiv: 1205.5370 [hep-ph].

[262] I. Danilkin and M. Vanderhaeghen. “Light-by-light scattering sum rules in light of new data”. In: *Phys. Rev. D* 95.1 (2017), p. 014019. DOI: 10.1103/PhysRevD.95.014019. arXiv: 1611.04646 [hep-ph].

[263] F. Jegerlehner. *The Anomalous Magnetic Moment of the Muon*. Vol. 274. Cham: Springer, 2017. DOI: 10.1007/978-3-319-63577-4.

[264] M. Knecht et al. “Scalar meson contributions to a μ from hadronic light-by-light scattering”. In: *Phys. Lett. B* 787 (2018), p. 111. DOI: 10.1016/j.physletb.2018.10.048. arXiv: 1808.03848 [hep-ph].

[265] G. Eichmann, C. S. Fischer, and R. Williams. “Kaon-box contribution to the anomalous magnetic moment of the muon”. In: *Phys. Rev. D* 101.5 (2020), p. 054015. DOI: 10.1103/PhysRevD.101.054015. arXiv: 1910.06795 [hep-ph].

[266] P. Roig and P. Sanchez-Puertas. “Axial-vector exchange contribution to the hadronic light-by-light piece of the muon anomalous magnetic moment”. In: *Phys. Rev. D* 101.7 (2020), p. 074019. DOI: 10.1103/PhysRevD.101.074019. arXiv: 1910.02881 [hep-ph].

[267] T. Blum et al. “Hadronic Light-by-Light Scattering Contribution to the Muon Anomalous Magnetic Moment from Lattice QCD”. In: *Phys. Rev. Lett.* 124.13 (2020), p. 132002. DOI: 10.1103/PhysRevLett.124.132002. arXiv: 1911.08123 [hep-lat].

[268] G. Colangelo et al. “Remarks on higher-order hadronic corrections to the muon g-2”. In: *Phys. Lett. B* 735 (2014), p. 90. DOI: 10.1016/j.physletb.2014.06.012. arXiv: 1403.7512 [hep-ph].

[269] T. Aoyama, Toichiro Kinoshita, and Makiko Nio. “Theory of the Anomalous Magnetic Moment of the Electron”. In: *Atoms* 7.1 (2019), p. 28. DOI: 10.3390/atoms7010028.

[270] A. Czarnecki, W. J. Marciano, and A. Vainshtein. “Refinements in electroweak contributions to the muon anomalous magnetic moment”. In: *Phys. Rev. D* 67 (2003). [Erratum: Phys.Rev.D 73, 119901 (2006)], p. 073006. DOI: 10.1103/PhysRevD.67.073006. arXiv: hep-ph/0212229.

[271] C. Gnendiger, D. Stöckinger, and H. Stöckinger-Kim. "The electroweak contributions to $(g-2)_\mu$ after the Higgs boson mass measurement". In: *Phys. Rev. D* 88 (2013), p. 053005. DOI: 10.1103/PhysRevD.88.053005. arXiv: 1306.5546 [hep-ph].

[272] M. Davier et al. "Reevaluation of the hadronic vacuum polarisation contributions to the Standard Model predictions of the muon $g-2$ and $\alpha(m_Z^2)$ using newest hadronic cross-section data". In: *Eur. Phys. J. C* 77.12 (2017), p. 827. DOI: 10.1140/epjc/s10052-017-5161-6. arXiv: 1706.09436 [hep-ph].

[273] A. Keshavarzi, D. Nomura, and T. Teubner. "Muon $g-2$ and $\alpha(M_Z^2)$: a new data-based analysis". In: *Phys. Rev. D* 97.11 (2018), p. 114025. DOI: 10.1103/PhysRevD.97.114025. arXiv: 1802.02995 [hep-ph].

[274] G. Colangelo, M. Hoferichter, and P. Stoffer. "Two-pion contribution to hadronic vacuum polarization". In: *JHEP* 02 (2019), p. 006. DOI: 10.1007/JHEP02(2019)006. arXiv: 1810.00007 [hep-ph].

[275] M. Hoferichter, B.L. Hoid, and B. Kubis. "Three-pion contribution to hadronic vacuum polarization". In: *JHEP* 08 (2019), p. 137. DOI: 10.1007/JHEP08(2019)137. arXiv: 1907.01556 [hep-ph].

[276] G. W. Bennett et al. "Final Report of the Muon E821 Anomalous Magnetic Moment Measurement at BNL". In: *Phys. Rev. D* 73 (2006), p. 072003. DOI: 10.1103/PhysRevD.73.072003. arXiv: hep-ex/0602035.

[277] B. Abi et al. "Measurement of the Positive Muon Anomalous Magnetic Moment to 0.46 ppm". In: *Phys. Rev. Lett.* 126.14 (2021), p. 141801. DOI: 10.1103/PhysRevLett.126.141801. arXiv: 2104.03281 [hep-ex].

[278] D. P. Aguillard et al. "Measurement of the Positive Muon Anomalous Magnetic Moment to 0.20 ppm". In: (Aug. 2023). arXiv: 2308.06230 [hep-ex].

[279] P. Athron et al. "New physics explanations of a_μ in light of the FNAL muon $g-2$ measurement". In: *JHEP* 09 (2021), p. 080. DOI: 10.1007/JHEP09(2021)080. arXiv: 2104.03691 [hep-ph].

[280] M. Lindner, M. Platscher, and F. S. Queiroz. "A Call for New Physics : The Muon Anomalous Magnetic Moment and Lepton Flavor Violation". In: *Phys. Rept.* 731 (2018), p. 1. DOI: 10.1016/j.physrep.2017.12.001. arXiv: 1610.06587 [hep-ph].

[281] S. Baek et al. "Muon anomalous g-2 and gauged L(muon) - L(tau) models". In: *Phys. Rev. D* 64 (2001), p. 055006. DOI: 10.1103/PhysRevD.64.055006. arXiv: hep-ph/0104141.

[282] E. Ma, D. P. Roy, and S. Roy. "Gauged L(mu) - L(tau) with large muon anomalous magnetic moment and the bimaximal mixing of neutrinos". In: *Phys. Lett. B* 525 (2002), p. 101. DOI: 10.1016/S0370-2693(01)01428-9. arXiv: hep-ph/0110146.

[283] W. Altmannshofer, M. Carena, and A. Crivellin. "$L_\mu - L_\tau$ theory of Higgs flavor violation and $(g-2)_\mu$". In: *Phys. Rev. D* 94.9 (2016), p. 095026. DOI: 10.1103/PhysRevD.94.095026. arXiv: 1604.08221 [hep-ph].

[284] D. W. P. Amaral et al. "Confirming $U(1)_{L_\mu - L_\tau}$ as a solution for $(g-2)_\mu$ with neutrinos". In: *Eur. Phys. J. C* 81.10 (2021), p. 861. DOI: 10.1140/epjc/s10052-021-09670-z. arXiv: 2104.03297 [hep-ph].

[285] S. Zhou. "Neutrino Masses, Leptonic Flavor Mixing and Muon $(g-2)$ in the Seesaw Model with the $U(1)_{L_\mu - L_\tau}$ Gauge Symmetry". In: (Apr. 2021). DOI: 10.1088/1674-1137/ac2a25. arXiv: 2104.06858 [hep-ph].

[286] P. Ko, T. Nomura, and H. Okada. "Muon $g-2$, $B \to K^{(*)}\mu^+\mu^-$ anomalies, and leptophilic dark matter in $U(1)_{\mu-\tau}$ gauge symmetry". In: (Oct. 2021). arXiv: 2110.10513 [hep-ph].

[287] T. Hapitas, D. Tuckler, and Y. Zhang. "General Kinetic Mixing in Gauged $U(1)_{L_\mu - L_\tau}$ Model for Muon $g-2$ and Dark Matter". In: (Aug. 2021). arXiv: 2108.12440 [hep-ph].

[288] Y. Cheng, X.G. He, and J. Sun. "Widening the $U(1)_{L_\mu - L_\tau}$ Z' mass range for resolving the muon $g-2$ anomaly". In: (Dec. 2021). arXiv: 2112.09920 [hep-ph].

[289] F. Jegerlehner and A. Nyffeler. "The Muon g-2". In: *Phys. Rept.* 477 (2009), p. 1. DOI: 10.1016/j.physrep.2009.04.003. arXiv: 0902.3360 [hep-ph].

[290] C. Giunti. "General COHERENT constraints on neutrino nonstandard interactions". In: *Phys. Rev. D* 101.3 (2020), p. 035039. DOI: 10.1103/PhysRevD.101.035039. arXiv: 1909.00466 [hep-ph].

[291] P. Langacker. "The Physics of Heavy Z' Gauge Bosons". In: *Rev. Mod. Phys.* 81 (2009), p. 1199. DOI: 10.1103/RevModPhys.81.1199. arXiv: 0801.1345 [hep-ph].

[292] J. Liao and D. Marfatia. "COHERENT constraints on nonstandard neutrino interactions". In: *Phys. Lett. B* 775 (2017), p. 54. DOI: 10.1016/j.physletb.2017.10.046. arXiv: 1708.04255 [hep-ph].

[293] D. K. Papoulias and T. S. Kosmas. "COHERENT constraints to conventional and exotic neutrino physics". In: *Phys. Rev. D* 97.3 (2018), p. 033003. DOI: 10.1103/PhysRevD.97.033003. arXiv: 1711.09773 [hep-ph].

[294] J. Billard, J. Johnston, and B. J. Kavanagh. "Prospects for exploring New Physics in Coherent Elastic Neutrino-Nucleus Scattering". In: *JCAP* 11 (2018), p. 016. DOI: 10.1088/1475-7516/2018/11/016. arXiv: 1805.01798 [hep-ph].

[295] D. K. Papoulias. "COHERENT constraints after the COHERENT-2020 quenching factor measurement". In: *Phys. Rev. D* 102.11 (2020), p. 113004. DOI: 10.1103/PhysRevD.102.113004. arXiv: 1907.11644 [hep-ph].

[296] A. N. Khan and W. Rodejohann. "New physics from COHERENT data with an improved quenching factor". In: *Phys. Rev. D* 100.11 (2019), p. 113003. DOI: 10.1103/PhysRevD.100.113003. arXiv: 1907.12444 [hep-ph].

[297] E. Bertuzzo, G. Grilli di Cortona, and L. Magno Dantas Ramos. "Probing light vector mediators with coherent scattering at future facilities". In: (Dec. 2021). arXiv: 2112.04020 [hep-ph].

[298] R. N. Mohapatra. "From Old Symmetries to New Symmetries: Quarks, Leptons and B-L". In: *Int. J. Mod. Phys. A* 29.29 (2014), p. 1430066. DOI: 10.1142/S0217751X1430066X. arXiv: 1409.7557 [hep-ph].

[299] S. Okada. "Z' Portal Dark Matter in the Minimal $B - L$ Model". In: *Adv. High Energy Phys.* 2018 (2018), p. 5340935. DOI: 10.1155/2018/5340935. arXiv: 1803.06793 [hep-ph].

[300] R. Foot. "New Physics From Electric Charge Quantization?" In: *Mod. Phys. Lett. A* 6 (1991), p. 527. DOI: 10.1142/S0217732391000543.

[301] R. Foot et al. "Charge quantization in the standard model and some of its extensions". In: *Mod. Phys. Lett. A* 5 (1990), p. 2721. DOI: 10.1142/S0217732390003176.

[302] X. G. He et al. "New-Z' phenomenology". In: *Phys. Rev. D* 43 (1991), R22. DOI: 10.1103/PhysRevD.43.R22.

[303] R. Foot, H. Lew, and R. R. Volkas. "Electric charge quantization". In: *J. Phys. G* 19 (1993). [Erratum: J.Phys.G 19, 1067 (1993)], p. 361. DOI: 10.1088/0954-3899/19/3/005. arXiv: hep-ph/9209259.

[304] W. Altmannshofer et al. "Neutrino Tridents at DUNE". In: *Phys. Rev. D* 100.11 (2019), p. 115029. DOI: 10.1103/PhysRevD.100.115029. arXiv: 1902.06765 [hep-ph].

[305] H. Banerjee and S. Roy. "Signatures of supersymmetry and $L_\mu - L_\tau$ gauge bosons at Belle-II". In: *Phys. Rev. D* 99.3 (2019), p. 035035. DOI: 10.1103/PhysRevD.99.035035. arXiv: 1811.00407 [hep-ph].

[306] H. Banerjee, B. Dutta, and S. Roy. "Probing Lμ-Lτ models with CEνNS: A new look at the combined COHERENT CsI and Ar data". In: *Phys. Rev. D* 104.1 (2021), p. 015015. DOI: 10.1103/PhysRevD.104.015015. arXiv: 2103.10196 [hep-ph].

[307] B. C. Allanach, J. Davighi, and S. Melville. "An Anomaly-free Atlas: charting the space of flavour-dependent gauged $U(1)$ extensions of the Standard Model". In: *JHEP* 02 (2019). [Erratum: JHEP 08, 064 (2019)], p. 082. DOI: 10.1007/JHEP02(2019)082. arXiv: 1812.04602 [hep-ph].

[308] H.S. Lee and E. Ma. "Gauged $B - x_i L$ origin of R Parity and its implications". In: *Phys. Lett. B* 688 (2010), p. 319. DOI: 10.1016/j.physletb.2010.04.032. arXiv: 1001.0768 [hep-ph].

[309] T. Araki, J. Heeck, and J. Kubo. "Vanishing Minors in the Neutrino Mass Matrix from Abelian Gauge Symmetries". In: *JHEP* 07 (2012), p. 083. DOI: 10.1007/JHEP07(2012)083. arXiv: 1203.4951 [hep-ph].

[310] O. G. Miranda et al. "Implications of the first detection of coherent elastic neutrino-nucleus scattering (CEvNS) with Liquid Argon". In: *JHEP* 05 (2020). [Erratum: JHEP 01, 067 (2021)], p. 130. DOI: 10.1007/JHEP05(2020)130. arXiv: 2003.12050 [hep-ph].

[311] P. Coloma, M. C. Gonzalez-Garcia, and M. Maltoni. "Neutrino oscillation constraints on U(1)' models: from non-standard interactions to long-range forces". In: *JHEP* 01 (2021), p. 114. DOI: 10.1007/JHEP01(2021)114. arXiv: 2009.14220 [hep-ph].

[312] L. M. G. de la Vega et al. "Complementarity between dark matter direct searches and CEνNS experiments in U(1)' models". In: *JHEP* 09 (2021), p. 146. DOI: 10.1007/JHEP09(2021)146. arXiv: 2107.04037 [hep-ph].

[313] T. Han et al. "Nonstandard neutrino interactions at COHERENT, DUNE, T2HK and LHC". In: *JHEP* 11 (2019), p. 028. DOI: 10.1007/JHEP11(2019)028. arXiv: 1910.03272 [hep-ph].

[314] Y. Farzan. "A model for large non-standard interactions of neutrinos leading to the LMA-Dark solution". In: *Phys. Lett. B* 748 (2015), p. 311. DOI: 10.1016/j.physletb.2015.07.015. arXiv: 1505.06906 [hep-ph].

[315] J. Heeck et al. "Non-Standard Neutrino Interactions and Neutral Gauge Bosons". In: *SciPost Phys.* 6.3 (2019), p. 038. DOI: 10.21468/SciPostPhys.6.3.038. arXiv: 1812.04067 [hep-ph].

[316] X.G. He et al. "Simplest Z' model". In: *Phys. Rev. D* 44 (1991), p. 2118. DOI: 10.1103/PhysRevD.44.2118.

[317] S. Gninenko and D. Gorbunov. "Refining constraints from Borexino measurements on a light Z'-boson coupled to Lμ-Lτ current". In: *Phys. Lett. B* 823 (2021), p. 136739. DOI: 10.1016/j.physletb.2021.136739. arXiv: 2007.16098 [hep-ph].

[318] P. Ilten et al. "Serendipity in dark photon searches". In: *JHEP* 06 (2018), p. 004. DOI: 10.1007/JHEP06(2018)004. arXiv: 1801.04847 [hep-ph].

[319] A. Aguilar-Arevalo et al. "Search for light mediators in the low-energy data of the CONNIE reactor neutrino experiment". In: *JHEP* 04 (2020), p. 054. DOI: 10.1007/JHEP04(2020)054. arXiv: 1910.04951 [hep-ex].

[320] S. R. Mishra et al. "Neutrino tridents and W Z interference". In: *Phys. Rev. Lett.* 66 (1991), p. 3117. DOI: 10.1103/PhysRevLett.66.3117.

[321] W. Altmannshofer et al. "Neutrino Trident Production: A Powerful Probe of New Physics with Neutrino Beams". In: *Phys. Rev. Lett.* 113 (2014), p. 091801. DOI: 10.1103/PhysRevLett.113.091801. arXiv: 1406.2332 [hep-ph].

[322] D. G. Cerdeño et al. "Physics from solar neutrinos in dark matter direct detection experiments". In: *JHEP* 05 (2016). [Erratum: JHEP 09, 048 (2016)], p. 118. DOI: 10.1007/JHEP09(2016)048. arXiv: 1604.01025 [hep-ph].

[323] Y. Farzan et al. "Probing neutrino coupling to a light scalar with coherent neutrino scattering". In: *JHEP* 05 (2018), p. 066. DOI: 10.1007/JHEP05(2018)066. arXiv: 1802.05171 [hep-ph].

[324] D. Aristizabal Sierra, V. De Romeri, and N. Rojas. "COHERENT analysis of neutrino generalized interactions". In: *Phys. Rev. D* 98 (2018), p. 075018. DOI: 10.1103/PhysRevD.98.075018. arXiv: 1806.07424 [hep-ph].

[325] D. Aristizabal Sierra et al. "Coherent elastic neutrino-nucleus scattering in multi-ton scale dark matter experiments: Classification of vector and scalar interactions new physics signals". In: *JHEP* 12 (2019), p. 124. DOI: 10.1007/JHEP12(2019)124. arXiv: 1910.12437 [hep-ph].

[326] M. Hoferichter et al. "High-Precision Determination of the Pion-Nucleon σ Term from Roy-Steiner Equations". In: *Phys. Rev. Lett.* 115 (2015), p. 092301. DOI: 10.1103/PhysRevLett.115.092301. arXiv: 1506.04142 [hep-ph].

[327] S. Durr et al. "Lattice computation of the nucleon scalar quark contents at the physical point". In: *Phys. Rev. Lett.* 116.17 (2016), p. 172001. DOI: 10.1103/PhysRevLett.116.172001. arXiv: 1510.08013 [hep-lat].

[328] J. Ellis, N. Nagata, and K. A. Olive. "Uncertainties in WIMP Dark Matter Scattering Revisited". In: *Eur. Phys. J. C* 78.7 (2018), p. 569. DOI: 10.1140/epjc/s10052-018-6047-y. arXiv: 1805.09795 [hep-ph].

[329] C. Alexandrou et al. "Nucleon axial, tensor, and scalar charges and σ-terms in lattice QCD". In: *Phys. Rev. D* 102.5 (2020), p. 054517. DOI: 10.1103/PhysRevD.102.054517. arXiv: 1909.00485 [hep-lat].

[330] J. M. Alarcón. "Brief history of the pion–nucleon sigma term". In: *Eur. Phys. J. ST* 230.6 (2021), p. 1609. DOI: 10.1140/epjs/s11734-021-00145-6.

[331] J. Ruiz de Elvira et al. "Extracting the σ-term from low-energy pion-nucleon scattering". In: *J. Phys. G* 45.2 (2018), p. 024001. DOI: 10.1088/1361-6471/aa9422. arXiv: 1706.01465 [hep-ph].

[332] E. Friedman and A. Gal. "The pion-nucleon σ term from pionic atoms". In: *Phys. Lett. B* 792 (2019), p. 340. DOI: 10.1016/j.physletb.2019.03.036. arXiv: 1901.03130 [nucl-th].

[333] A. M. Suliga and I. Tamborra. "Astrophysical constraints on nonstandard coherent neutrino-nucleus scattering". In: *Phys. Rev. D* 103.8 (2021), p. 083002. DOI: 10.1103/PhysRevD.103.083002. arXiv: 2010.14545 [hep-ph].

[334] M. Cirelli, E. Del Nobile, and P. Panci. "Tools for model-independent bounds in direct dark matter searches". In: *JCAP* 10 (2013), p. 019. DOI: 10.1088/1475-7516/2013/10/019. arXiv: 1307.5955 [hep-ph].

[335] H. Davoudiasl, H.S. Lee, and W. J. Marciano. ""Dark" Z implications for parity violation, rare meson decays, and Higgs physics". In: *Physical Review D* 85.11 (June 2012). ISSN: 1550-2368. DOI: 10.1103/physrevd.85.115019. URL: http://dx.doi.org/10.1103/PhysRevD.85.115019.

[336] H. Davoudiasl, H.S. Lee, and W. J. Marciano. "Muon Anomaly and Dark Parity Violation". In: *Physical Review Letters* 109.3 (July 2012). ISSN: 1079-7114. DOI: 10.1103/physrevlett.109.031802. URL: http://dx.doi.org/10.1103/PhysRevLett.109.031802.

[337] H. Davoudiasl, H.S. Lee, and W. J. Marciano. "Dark side of Higgs diphoton decays and muon g-2". In: *Physical Review D* 86.9 (Nov. 2012). ISSN: 1550-2368. DOI: 10.1103/physrevd.86.095009. URL: http://dx.doi.org/10.1103/PhysRevD.86.095009.

[338] H. Davoudiasl et al. “Higgs decays as a window into the dark sector”. In: *Physical Review D* 88.1 (July 2013). ISSN: 1550-2368. DOI: 10.1103/physrevd.88.015022. URL: http://dx.doi.org/10.1103/PhysRevD.88.015022.

[339] H. Davoudiasl, H.S. Lee, and W. J. Marciano. “LowQ2weak mixing angle measurements and rare Higgs decays”. In: *Physical Review D* 92.5 (Sept. 2015). ISSN: 1550-2368. DOI: 10.1103/physrevd.92.055005. URL: http://dx.doi.org/10.1103/PhysRevD.92.055005.

[340] H. Davoudiasl, H.S. Lee, and W. J. Marciano. “Muon $g-2$, rare kaon decays, and parity violation from dark bosons”. In: *Phys. Rev. D* 89.9 (2014), p. 095006. DOI: 10.1103/PhysRevD.89.095006. arXiv: 1402.3620 [hep-ph].

[341] C. Bouchiat and P. Fayet. “Constraints on the parity-violating couplings of a new gauge boson”. In: *Physics Letters B* 608.1-2 (Feb. 2005), p. 87. ISSN: 0370-2693. DOI: 10.1016/j.physletb.2004.12.065. URL: http://dx.doi.org/10.1016/j.physletb.2004.12.065.

[342] L. Morel et al. “Determination of the fine-structure constant with an accuracy of 81 parts per trillion”. In: *Nature* 588.7836 (2020), p. 61. DOI: 10.1038/s41586-020-2964-7.

[343] M. S. Safronova et al. “Search for New Physics with Atoms and Molecules”. In: *Rev. Mod. Phys.* 90.2 (2018), p. 025008. arXiv: 1710.01833 [physics.atom-ph]. URL: http://dx.doi.org/10.1103/RevModPhys.90.025008.

[344] J. Bernabeu et al. “On the charge radius of the neutrino”. In: *Phys. Rev. D* 62 (2000), p. 113012. DOI: 10.1103/PhysRevD.62.113012. arXiv: hep-ph/0008114.

[345] J. Bernabeu, J. Papavassiliou, and J. Vidal. “On the observability of the neutrino charge radius”. In: *Phys. Rev. Lett.* 89 (2002). [Erratum: Phys.Rev.Lett. 89, 229902 (2002)], p. 101802. DOI: 10.1103/PhysRevLett.89.101802. arXiv: hep-ph/0206015.

[346] J. Bernabeu, J. Papavassiliou, and J. Vidal. “The Neutrino charge radius is a physical observable”. In: *Nucl. Phys. B* 680 (2004), p. 450. DOI: 10.1016/j.nuclphysb.2003.12.025. arXiv: hep-ph/0210055.

[347] W. J. Marciano and Z. Parsa. “Neutrino electron scattering theory”. In: *J. Phys. G* 29 (2003), p. 2629. DOI: 10.1088/0954-3899/29/11/013. arXiv: hep-ph/0403168.

[348] M. Deniz et al. “Measurement of Neutrino-Electron Scattering Cross-Section with a CsI(Tl) Scintillating Crystal Array at the Kuo-Sheng Nuclear Power Reactor”. In: *Phys. Rev.* D81 (2010), p. 072001. eprint: arXiv:0911.1597 (hep-ex).

[349] L.A. Ahrens et al. “Determination of electroweak parameters from the elastic scattering of muon-neutrinos and anti-neutrinos on electrons”. In: *Phys. Rev.* D41 (1990), p. 3297. DOI: 10.1103/PhysRevD.41.3297.

[350] M. Cadeddu et al. “Neutrino Charge Radii From Coherent Elastic Neutrino-nucleus Scattering”. In: *Phys. Rev. D* 98.11 (2018). [Erratum: Phys.Rev.D 101, 059902 (2020)], p. 113010. DOI: 10.1142/9789811233913_0013. arXiv: 1810.05606 [hep-ph].

[351] G. S. Vidyakin et al. “Limitations on the magnetic moment and charge radius of the electron-anti-neutrino”. In: *JETP Lett.* 55 (1992), p. 206.

[352] R. C. Allen et al. “Study of electron-neutrino—electron elastic scattering at LAMPF”. In: *Phys. Rev. D* 47 (1 Jan. 1993), p. 11. DOI: 10.1103/PhysRevD.47.11. URL: https://link.aps.org/doi/10.1103/PhysRevD.47.11.

[353] L. B. Auerbach et al. “Measurement of electron-neutrino electron elastic scattering”. In: *Phys. Rev.* D63 (2001), p. 112001. eprint: hep-ex/0101039.

[354] P. Vilain et al. “Experimental study of electromagnetic properties of the muon-neutrino in neutrino - electron scattering”. In: *Phys. Lett. B* 345 (1995), p. 115. DOI: 10.1016/0370-2693(94)01678-6.

[355] M. Hirsch, E. Nardi, and D. Restrepo. “Bounds on the tau and muon neutrino vector and axial vector charge radius”. In: *Phys. Rev. D* 67 (2003), p. 033005. DOI: 10.1103/PhysRevD.67.033005. arXiv: hep-ph/0210137.

[356] O. Tomalak et al. “Flavor-dependent radiative corrections in coherent elastic neutrino-nucleus scattering”. In: *JHEP* 02 (2021), p. 097. DOI: 10.1007/JHEP02(2021)097. arXiv: 2011.05960 [hep-ph].

[357] C. Giunti et al. “Electromagnetic neutrinos in terrestrial experiments and astrophysics”. In: *Annalen Phys.* 528 (2016), p. 198. eprint: arXiv:1506.05387 (hep-ph).

[358] M. Aker et al. “Direct neutrino-mass measurement with sub-electronvolt sensitivity”. In: *Nature Phys.* 18.2 (2022), p. 160. DOI: 10.1038/s41567-021-01463-1. arXiv: 2105.08533 [hep-ex].

[359] Z. Daraktchieva et al. “Final results on the neutrino magnetic moment from the MUNU experiment”. In: *Phys. Lett. B* 615 (2005), p. 153. DOI: 10.1016/j.physletb.2005.04.030. arXiv: hep-ex/0502037.

[360] A.G. Beda et al. “The results of search for the neutrino magnetic moment in GEMMA experiment”. In: *Adv.High Energy Phys.* 2012 (2012), p. 350150. DOI: 10.1155/2012/350150.

[361] P. Coloma et al. “Bounds on new physics with data of the Dresden-II reactor experiment and COHERENT”. In: *JHEP* 05 (2022), p. 037. DOI: 10.1007/JHEP05(2022)037. arXiv: 2202.10829 [hep-ph].

[362] J. Liao, H. Liu, and D. Marfatia. *Implications of the first evidence for coherent elastic scattering of reactor neutrinos*. Feb. 2022. arXiv: 2202.10622 [hep-ph].

[363] M. Marinelli and Giacomo Morpurgo. “The Electric Neutrality of Matter: A Summary”. In: *Phys. Lett. B* 137 (1984), p. 439. DOI: 10.1016/0370-2693(84)91752-0.

[364] G. Bressi et al. “Testing the neutrality of matter by acoustic means in a spherical resonator”. In: *Phys. Rev. A* 83 (5 May 2011), p. 052101. DOI: 10.1103/PhysRevA.83.052101. URL: https://link.aps.org/doi/10.1103/PhysRevA.83.052101.

[365] S. N. Gninenko, N. V. Krasnikov, and A. Rubbia. “Search for millicharged particles in reactor neutrino experiments: A Probe of the PVLAS anomaly”. In: *Phys. Rev. D* 75 (2007), p. 075014. DOI: 10.1103/PhysRevD.75.075014. arXiv: hep-ph/0612203.

[366] H. B. Li et al. “Limit on the electron neutrino magnetic moment from the Kuo-Sheng reactor neutrino experiment”. In: *Phys. Rev. Lett.* 90 (2003), p. 131802. DOI: 10.1103/PhysRevLett.90.131802. arXiv: hep-ex/0212003.

[367] A. Studenikin. “New bounds on neutrino electric millicharge from limits on neutrino magnetic moment”. In: *Europhys.Lett.* 107 (2014), p. 21001. eprint: arXiv:1302.1168 (hep-ph).

[368] J.W. Chen et al. “Constraints on millicharged neutrinos via analysis of data from atomic ionizations with germanium detectors at sub-keV sensitivities”. In: *Phys. Rev.* D90.1 (2014), p. 011301. DOI: 10.1103/PhysRevD.90.011301. eprint: arXiv:1405.7168 (hep-ph).

[369] A. Das et al. “Neutrino charge constraints from scattering to the weak gravity conjecture to neutron stars”. In: *Phys. Rev. D* 102.11 (2020), p. 115009. DOI: 10.1103/PhysRevD.102.115009. arXiv: 2005.12304 [hep-ph].

[370] K. Abe et al. “Search for exotic neutrino-electron interactions using solar neutrinos in XMASS-I”. In: *Phys. Lett. B* 809 (2020), p. 135741. DOI: 10.1016/j.physletb.2020.135741. arXiv: 2005.11891 [hep-ex].

[371] J. Aalbers et al. “Search for new physics in low-energy electron recoils from the first LZ exposure”. In: *Phys. Rev. D* 108.7 (2023), p. 072006. DOI: 10.1103/PhysRevD.108.072006. arXiv: 2307.15753 [hep-ex].

[372] K. A. ShivaSankar et al. “Implications of first LZ and XENONnT results: A comparative study of neutrino properties and light mediators”. In: *Phys. Lett. B* 839 (2023), p. 137742. DOI: 10.1016/j.physletb.2023.137742. arXiv: 2208.06415 [hep-ph].

[373] A. N. Khan. “Light new physics and neutrino electromagnetic interactions in XENONnT”. In: *Phys. Lett. B* 837 (2023), p. 137650. DOI: 10.1016/j.physletb.2022.137650. arXiv: 2208.02144 [hep-ph].

[374] D. W. Liu et al. “Limits on the neutrino magnetic moment using 1496 days of Super-Kamiokande-I solar neutrino data”. In: *Phys. Rev. Lett.* 93 (2004), p. 021802. DOI: 10.1103/PhysRevLett.93.021802. arXiv: hep-ex/0402015.

[375] A. G. Beda et al. “Gemma experiment: The results of neutrino magnetic moment search”. In: *Phys. Part. Nucl. Lett.* 10 (2013), p. 139. DOI: 10.1134/S1547477113020027.

[376] S. Arceo-Díaz et al. “Constraint on the magnetic dipole moment of neutrinos by the tip-RGB luminosity in Centauri”. In: *Astroparticle Physics* 70 (2015), p. 1. ISSN: 0927-6505. DOI: https://doi.org/10.1016/j.astropartphys.2015.03.006. URL: https://www.sciencedirect.com/science/article/pii/S0927650515000468.

[377] S. Arceo-Díaz et al. “Constraint on the axion-electron coupling constant and the neutrino magnetic dipole moment by using the tip-RGB luminosity of fifty globular clusters”. In: (Oct. 2019). arXiv: 1910.10568 [astro-ph.SR].

[378] A. H. Córsico et al. “Constraining the neutrino magnetic dipole moment from white dwarf pulsations”. In: *JCAP* 08 (2014), p. 054. DOI: 10.1088/1475-7516/2014/08/054. arXiv: 1406.6034 [astro-ph.SR].

[379] L. Singh et al. “Constraints on millicharged particles with low threshold germanium detectors at Kuo-Sheng Reactor Neutrino Laboratory”. In: *Phys. Rev. D* 99.3 (2019), p. 032009. DOI: 10.1103/PhysRevD.99.032009. arXiv: 1808.02719 [hep-ph].

[380] L. B. Auerbach et al. “Measurement of electron - neutrino - electron elastic scattering”. In: *Phys. Rev. D* 63 (2001), p. 112001. DOI: 10.1103/PhysRevD.63.112001. arXiv: hep-ex/0101039.

[381] H. Bonet et al. “First upper limits on neutrino electromagnetic properties from the CONUS experiment”. In: *Eur. Phys. J. C* 82.9 (2022), p. 813. DOI: 10.1140/epjc/s10052-022-10722-1. arXiv: 2201.12257 [hep-ex].

[382] J. Alitti et al. “A Determination of the strong coupling constant alpha-s from W production at the CERN p anti-p collider”. In: *Phys. Lett. B* 263 (1991), p. 563. DOI: 10.1016/0370-2693(91)90505-K.

[383] W. J. Marciano and A. Sirlin. “Radiative corrections to atomic parity violation”. In: *Phys. Rev. D* 27 (3 Feb. 1983), p. 552. DOI: 10.1103/PhysRevD.27.552. URL: https://link.aps.org/doi/10.1103/PhysRevD.27.552.

[384] W. J. Marciano and A. Sirlin. “Some general properties of the $O(\alpha)$ corrections to parity violation in atoms”. In: *Phys. Rev. D* 29 (1 Jan. 1984), p. 75. DOI: 10.1103/PhysRevD.29.75. URL: https://link.aps.org/doi/10.1103/PhysRevD.29.75.

[385] P. Souder and K. D. Paschke. “Parity violation in electron scattering”. In: *Front. Phys. (Beijing)* 11.1 (2016), p. 111301. DOI: 10.1007/s11467-015-0482-0.

[386] M. Vorabbi. “Electron and proton scattering off nuclei with neutron and proton excess”. Other thesis. 2016.

[387] A. Keshavarzi, K. S. Khaw, and T. Yoshioka. “Muon g-2: A review”. In: *Nucl. Phys. B* 975 (2022), p. 115675. DOI: 10.1016/j.nuclphysb.2022.115675. arXiv: 2106.06723 [hep-ex].

[388] S. Li, Y. Xiao, and J. M. Yang. “A pedagogical review on muon $g-2$”. In: *Physics* 4 (2021), p. 40. arXiv: 2110.04673 [hep-ph].

[389] S. J. Brodsky and E. De Rafael. “SUGGESTED BOSON - LEPTON PAIR COUPLINGS AND THE ANOMALOUS MAGNETIC MOMENT OF THE MUON”. In: *Phys. Rev.* 168 (1968), p. 1620. DOI: 10.1103/PhysRev.168.1620.

[390] D. Hanneke, S. Fogwell, and G. Gabrielse. “New Measurement of the Electron Magnetic Moment and the Fine Structure Constant”. In: *Physical Review Letters* 100.12 (Mar. 2008). ISSN: 1079-7114. DOI: 10.1103/physrevlett.100.120801. URL: http://dx.doi.org/10.1103/PhysRevLett.100.120801.

[391] D. Hanneke, S. Fogwell Hoogerheide, and G. Gabrielse. “Cavity control of a single-electron quantum cyclotron: Measuring the electron magnetic moment”. In: *Physical Review A* 83.5 (May 2011). ISSN: 1094-1622. DOI: 10.1103/physreva.83.052122. URL: http://dx.doi.org/10.1103/PhysRevA.83.052122.

[392] R. H. Parker et al. “Measurement of the fine-structure constant as a test of the Standard Model”. In: *Science* 360.6385 (Apr. 2018), p. 191. ISSN: 1095-9203. DOI: 10.1126/science.aap7706. URL: http://dx.doi.org/10.1126/science.aap7706.

Appendix A

Radiative corrections for low energy weak neutral currents

In this appendix, we make a short summary of how to calculate the couplings accounting radiative corrections for CEνNS, νES and also electron scattering off nuclei.

NEUTRINO-FERMION COUPLING CONSTANTS

We implemented the radiative corrections following the formalism given in Ref. [147]. In particular, the ℓ flavor neutrino right and left couplings to a fermion $f = e,\, u\, d$, are given by

$$g_{LL}^{\nu_\ell f} = \rho\left[-\frac{1}{2} - Q_f \hat{s}_0^2 + \boxtimes_{ZZ}^{fL}\right] - Q_f \circledcirc_{\nu_\ell W} + \square_{WW} \quad \text{for } f = e,\, d\ , \tag{A.1}$$

$$g_{LL}^{\nu_\ell f} = \rho\left[\frac{1}{2} - Q_f \hat{s}_0^2 + \boxtimes_{ZZ}^{fL}\right] - Q_f \circledcirc_{\nu_\ell W} + \boxtimes_{WW} \quad \text{for } f = u\ , \tag{A.2}$$

$$g_{LR}^{\nu_\ell f} = -\rho\left[Q_f \hat{s}_0^2 + \boxtimes_{ZZ}^{fR}\right] - Q_f \circledcirc_{\nu_\ell W} \quad \text{for } f = e,\, u,\, d\ . \tag{A.3}$$

where $\rho = 1.00063$ represents a low-energy correction for neutral-current processes and Q_f is the fermion charge in units of the electron charge e_0. Here $\hat{s}_0^2 = \sin^2\theta_W^{\rm SM}$, which keeps the same value for $\mu < \mathcal{O}(0.1\ \text{GeV})$. The other corrections inserted come from different contributions, such as the neutrino charge radius, $\circledcirc_{\nu_\ell W}$ (see Sec. 7.1), and the EW box diagrams ($\boxtimes_{ZZ}^{fX}$, $\square_{WW}\boxtimes_{WW}$). They can be expressed as

$$\circledcirc_{\nu_\ell W} = -\frac{\alpha}{6\pi}\left(\ln\frac{m_W^2}{m_\ell^2} + \frac{3}{2}\right), \tag{A.4}$$

$$\square_{WW} = -\frac{\hat{\alpha}_Z}{2\pi\hat{s}_Z^2}\left[1 - \frac{\hat{\alpha}_s(m_W)}{2\pi}\right], \tag{A.5}$$

$$\boxtimes_{WW} = -\frac{\hat{\alpha}_Z}{8\pi\hat{s}_Z^2}\left[1 + \frac{\hat{\alpha}_s(m_W)}{\pi}\right], \tag{A.6}$$

$$\boxtimes_{ZZ}^{fX} = -\frac{3\hat{\alpha}_Z}{8\pi \hat{s}_Z^2 \hat{c}_Z^2}(g_{LX}^{\nu_\ell f})^2 \left[1 - \frac{\hat{\alpha}_s(m_Z)}{\pi}\right], \tag{A.7}$$

where $X \in \{L, R\}$ and $\hat{\alpha}_Z \equiv \alpha(m_Z)$. Note that in Eq. A.7 all the $(g_{LX})^{\nu_\ell f}$ are evaluated at lowest order but replacing $\hat{s}_0^2$ by $\hat{s}_Z^2$ and are given by

$$g_{LL}^{\nu_\ell e} = -\frac{1}{2} + \hat{s}_Z^2\,, \quad g_{LR}^{\nu_\ell e} = \hat{s}_Z^2\,, \tag{A.8}$$

$$g_{LL}^{\nu_\ell u} = \frac{1}{2} - \frac{2}{3}\hat{s}_Z^2\,, \quad g_{LR}^{\nu_\ell u} = -\frac{2}{3}\hat{s}_Z^2\,, \tag{A.9}$$

$$g_{LL}^{\nu_\ell d} = -\frac{1}{2} + \frac{1}{3}\hat{s}_Z^2\,, \quad g_{LR}^{\nu_\ell d} = \frac{1}{3}\hat{s}_Z^2\,. \tag{A.10}$$

Being the vector coupling defined as $g_V^{\nu_\ell f} = g_{LL}^{\nu_\ell f} + g_{LR}^{\nu_\ell f}$ and the axial one as $g_A^{\nu_\ell f} = g_{LL}^{\nu_\ell f} - g_{LR}^{\nu_\ell f}$, the resulting vector and axial couplings for neutrino-electron scattering are given by [7]

$$g_V^{\nu_\ell e} = \rho\left(-\frac{1}{2} + 2\hat{s}_0^2\right) + \square_{WW} + 2\varnothing_{\nu_\ell W} + \rho(\boxtimes_{ZZ}^{eL} - \boxtimes_{ZZ}^{eR}), \tag{A.11}$$

$$g_A^{\nu_\ell e} = \rho\left(-\frac{1}{2} + \boxtimes_{ZZ}^{eL} + \boxtimes_{ZZ}^{eR}\right) + \square_{WW}. \tag{A.12}$$

For the numerical SM evaluation, we assume the values from Refs. [7, 203, 382]. We obtain the couplings $g_V^{\nu_e e} = 0.9521$, $g_A^{\nu_e e} = 0.4938$, $g_V^{\nu_\mu e} = -0.0397$, $g_A^{\nu_{\mu,\tau} e} = -0.5062$, and $g_V^{\nu_\tau e} = -0.0353$ that take into account all radiative corrections [7]. We note that, for the ν_e coupling, a unity factor has been added to the result in order to take into account the charge current contribution.
Similarly, we can calculate the vector coupling of neutrinos with u and d quarks, namely

$$g_V^{\nu_\ell u} = \rho\left(\frac{1}{2} - \frac{4}{3}\hat{s}_0^2\right) + \boxtimes_{WW} - \frac{4}{3}\varnothing_{\nu_\ell W} + \rho(\boxtimes_{ZZ}^{uL} - \boxtimes_{ZZ}^{uR}), \tag{A.13}$$

$$g_V^{\nu_\ell d} = \rho\left(-\frac{1}{2} + \frac{2}{3}\hat{s}_0^2\right) + \square_{WW} + \frac{2}{3}\varnothing_{\nu_\ell W} + \rho(\boxtimes_{ZZ}^{dL} - \boxtimes_{ZZ}^{dR}). \tag{A.14}$$

From them we can obtain the vector coupling to protons and neutrinos, necessary for CEνNS, by considering the proper linear combination of u and d quarks, namely [8]

$$g_V^{\nu_\ell p} = 2g_V^{\nu_\ell u} + g_V^{\nu_\ell d} = \tag{A.15}$$
$$= \rho\left(\frac{1}{2} - 2\hat{s}_0^2\right) + 2\boxtimes_{WW} + \square_{WW} - 2\varnothing_{\nu_\ell W} + \rho(2\,\boxtimes_{ZZ}^{uL} + \boxtimes_{ZZ}^{dL} - 2\,\boxtimes_{ZZ}^{uR} - \boxtimes_{ZZ}^{dR})\,,$$

$$g_V^{\nu_\ell n} = g_V^{\nu_\ell u} + 2g_V^{\nu_\ell d} = \tag{A.16}$$
$$= -\frac{\rho}{2} + 2\,\square_{WW} + \boxtimes_{WW} + \rho(2\,\boxtimes_{ZZ}^{dL} + \boxtimes_{ZZ}^{uL} - 2\,\boxtimes_{ZZ}^{dR} - \boxtimes_{ZZ}^{uR}).$$

Numerically, the values of these couplings correspond to $g_V^p(\nu_e) = 0.0382$, $g_V^p(\nu_\mu) = 0.0300$, and $g_V^n = -0.5117$ [8].

ELECTRON-FERMION COUPLING CONSTANTS

For the case of atomic parity violations or parity violating electron scattering, we need to determine the couplings for electrons interacting with nucleons accounting for radiative corrections. Following Refs. [2, 147, 148, 383, 384] the lepton-fermion couplings are given by

$$g_{AV}^{\ell f} = \rho\Big[-\frac{1}{2} + 2Q_f\hat{s}_0^2 - 2Q_f\varkappa_{\ell Z} + \boxtimes_{ZZ}^{\ell f} + \boxtimes_{\gamma Z}^{\ell f}\Big] - 2Q_f\varkappa_{\ell W} + \square_{WW}, \quad \text{for } f = u, \tag{A.17}$$

$$g_{AV}^{\ell f} = \rho\Big[\frac{1}{2} + 2Q_f\hat{s}_0^2 - 2Q_f\varkappa_{\ell Z} + \boxtimes_{ZZ}^{\ell f} + \boxtimes_{\gamma Z}^{\ell f}\Big] - 2Q_f\varkappa_{\ell W} + \boxtimes_{WW}, \quad \text{for } f = d. \tag{A.18}$$

The radiative contributions in the case of electron-fermion scattering, introduced in Eq. A.17 and Eq. A.18, are the electron charge radii ($\varkappa_{eW}$,$\varkappa_{eZ}$), the EW box diagrams ($\boxtimes_{ZZ}^{\ell f}$, $\square_{WW}$,$\boxtimes_{WW}$) and the vacuum polarization of γZ diagrams ($\boxtimes_{\gamma Z}^{\ell f}$) [148]. They can be expressed as

$$\varkappa_{\ell W} = \frac{2\alpha}{9\pi}, \tag{A.19a}$$

$$\varkappa_{\ell Z} = \frac{\alpha}{6\pi}Q_\ell g_{VA}^{\ell\ell}\Big(\ln\frac{m_Z^2}{m_\ell^2} + \frac{1}{6}\Big), \tag{A.19b}$$

$$\boxtimes_{ZZ}^{\ell f} = -\frac{3\hat{\alpha}_Z}{16\pi\hat{s}_Z^2\hat{c}_Z^2}\Big(g_{VA}^{\ell f}g_{VV}^{\ell f} + g_{AV}^{\ell f}g_{AA}^{\ell f}\Big) \times \Big[1 - \frac{\hat{\alpha}_s(m_Z)}{\pi}\Big], \tag{A.19c}$$

$$\boxtimes_{\gamma Z}^{\ell f} = \frac{3\hat{\alpha}_{fZ}}{2\pi}Q_f g_{VA}^{\ell f}\Big(\ln\frac{m_Z^2}{m_f^2} + \frac{3}{2}\Big), \tag{A.19d}$$

$$\square_{WW} = -\frac{\hat{\alpha}_Z}{2\pi\hat{s}_Z^2}\Big[1 - \frac{\hat{\alpha}_s(m_W)}{2\pi}\Big], \tag{A.19e}$$

$$\boxtimes_{WW} = \frac{\hat{\alpha}_Z}{8\pi\hat{s}_Z^2}\Big[1 + \frac{\hat{\alpha}_s(m_W)}{\pi}\Big]. \tag{A.19f}$$

In the expressions above, ℓ indicates the lepton involved in the interaction (in our case $\ell = e$), while f indicates the quarks (in our case $f = u, d$). For the electromagnetic-running coupling we adopt the abbreviation $\hat{\alpha}_{ij} \equiv \hat{\alpha}(\sqrt{m_i M_j})$ and $\hat{\alpha}_Z \equiv \alpha(m_Z)$. In particular, $\hat{\alpha}_{fZ}$, that is present in the $\boxtimes_{\gamma Z}^{\ell f}$ contribution in Eq. A.19d, is evaluated considering the quark masses equal to the proton one, and inside the logarithmic term the same value ($m_q = m_p$) is used. For the strong coupling, we use the values $\hat{\alpha}_s(M_Z) = 0.1185$ [203] and $\hat{\alpha}_s(m_W) = 0.123$ [382]. Inside the correction diagrams in Eqs. A.19b, A.19c, A.19d, the neutral-current couplings enter at tree-level and can be written as [147]

$$g_V^f \equiv \sqrt{2}\frac{T_f^3 - 2Q_f\sin^2\vartheta_W(\mu)}{\cos\vartheta_W(\mu)}, \tag{A.20}$$

$$g_A^f \equiv \sqrt{2}\frac{T_f^3}{\cos\vartheta_W(\mu)}. \tag{A.21}$$

Their products are defined as

$$g_{\alpha\beta}^{\ell f} = \cos^2\vartheta_W(\mu) g_\alpha^\ell g_\beta^f \quad \text{for} \;\; \alpha,\beta = V,A. \tag{A.22}$$

It is important to remark, as reported in Ref. [148], that for the EW box corrections (Eqs. A.19c, A.19e, A.19f) the sine is evaluated at the value of the Z mass, $\hat{s}_Z^2 \equiv \sin^2\hat{\theta}_W(m_Z) = 0.23121$ [203], while in the $\boxtimes_{\gamma Z}^{\ell f}$ term (Eq. A.19d) the sine is evaluated at scale $\mu = \sqrt{m_p m_Z}$. Finally, inside the $\varnothing_{\ell Z}$ term (Eq. A.19b) the coupling $g_{VA}^{\ell\ell}$ is obtained using the value $\sin^2\theta_W(\sqrt{m_\ell m_Z})$ as discussed in Ref. [148]. In order to determine the couplings to the proton and to the neutron it is sufficient to use the fact that

$$g_{AV}^{ep} = 2g_{AV}^{eu} + g_{AV}^{ed}, \tag{A.23}$$
$$g_{AV}^{en} = g_{AV}^{eu} + 2g_{AV}^{ed}. \tag{A.24}$$

Numerically, we obtain $g_{AV}^{ep} = -0.0357$ and $g_{AV}^{en} = 0.495$ [2, 8].

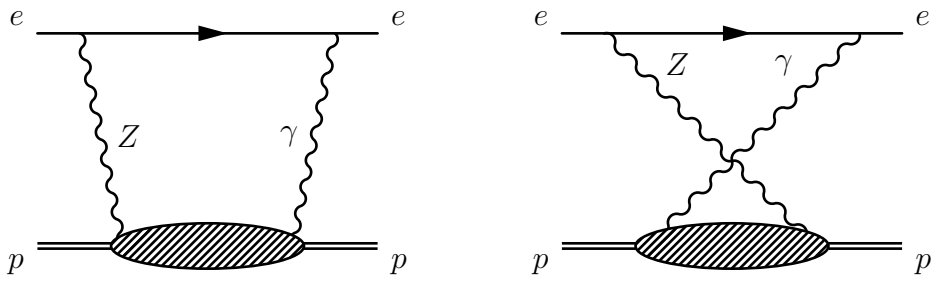

Figure A.1: The $\gamma - Z$ box diagrams for the electron-proton interaction. Not shown are the two remaining diagrams with the γ and Z interchanged [155–157].

However, as pointed out in Refs. [147, 148], it is necessary to take into account also a correction relative to the $\boxtimes_{\gamma Z}^{\ell f}$ and $\square_{\gamma Z}^{\ell f}$ contributions. Such corrections arise from the diagrams shown in Fig. A.1 (for the case of electron-proton interaction) [155–157]. Indeed, in the case of APV the contribution from the $\gamma - Z$ box is rather small and it is usually incorporated by adding to the proton and neutron couplings some small constants such that [2]

$$g_{AV}^{ep} \to g_{AV}^{ep} + 0.00005, \tag{A.25}$$
$$g_{AV}^{en} \to g_{AV}^{en} + 0.00006. \tag{A.26}$$

The contribution to PVES instead has to be calculated for every nuclear target considering the energy at which the experiment is performed [155–158]. Therefore, we can say that, in general, the contribution of the $\gamma - Z$ box radiative correction is different between APV and PVES experiments, making the nuclear weak charge entering the calculation slightly different in the two cases. In particular, the contribution is larger in PVES experiments, given the higher energy and momentum transfer at which the measurements are performed.

Appendix B

Momentum transfer in elastic electron scattering off nuclei

In this appendix, we report the determination of the momentum transfer expression employed in the case of elastic electron scattering off nuclei, as reported in Eq. 3.17.
We define $\mathbf{k}$, $\mathbf{k}'$ the quadrimomenta of the electron before and after the scattering, while $\mathbf{p}$, $\mathbf{p}'$ the nucleus ones.
The momentum transfer in the plane wave born approximation is well defined and is determined from the electron energy through the relation [385, 386]

$$q^2(\theta) = 4EE' \sin^2 \frac{\theta}{2}\,, \tag{B.1}$$

where E and E' are the electron energies prior to and after the scattering process, while θ is the scattering angle between the direction of the incoming electron and the outgoing one. The underlying assumption is that the process is fully elastic, so that no other particle is produced in the process. Moreover, the target nucleus in the initial state is assumed to be at rest, and generally, it is assumed to stay at rest after the scattering as well, given its heavy mass and the usually small energy exchange.

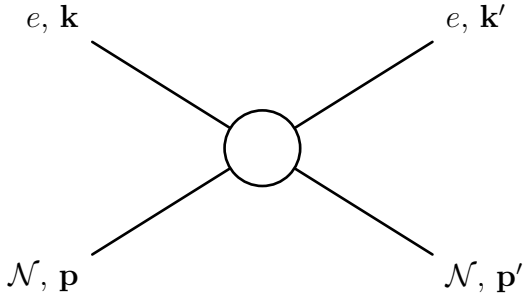

Figure B.1: Schematic representation of the elastic scattering of an electron off a nucleus, where we indicate the quadrimomentum corresponding to each particle before and after the scattering process.

We determine the energy of the outgoing electron by using kinematics within this framework and considering electrons as relativistic particles.

From quadrimomentum conservation, we can consider

$$\begin{aligned}\mathbf{p'}^2 = M_T^2 = (\mathbf{p} + \mathbf{k} - \mathbf{k'}) = \\ = \mathbf{p}^2 + \mathbf{k}^2 + \mathbf{k'}^2 + 2\mathbf{p}\cdot\mathbf{k} - 2\mathbf{p}\cdot\mathbf{k'} - 2\mathbf{k}\cdot\mathbf{k}\,. \end{aligned} \tag{B.2}$$

We can exploit that the quadrimomenta can be defined in the form

$$\mathbf{p} = \begin{pmatrix} M_T \\ 0 \end{pmatrix} \qquad \mathbf{k} = \begin{pmatrix} E_e \\ \vec{p} \end{pmatrix} \qquad \mathbf{k'} = \begin{pmatrix} E'_e \\ \vec{p'} \end{pmatrix}, \tag{B.3}$$

in which we can define the tri-momenta of the electrons in terms of their energies (given that the electrons are relativistic the mass can be neglected) so that $E_e = |\vec{p}|$ and $E'_e = |\vec{p'}|$, and we can consider that $\vec{p'} = \vec{p}\cos\theta$.
Considering the above definition and substituting inside Eq. B.2, we obtain

$$M_T^2 = M_T^2 + m_e^2 + m_e^2 + 2M_T\Big(E_e - E'_e\Big) - 2E_eE'_e + 2\vec{p}\cdot\vec{p'} = \tag{B.4}$$

$$= M_T^2 + 2M_T\Big(E_e - E'_e\Big) - 2E_eE'_e\Big(1 - \cos\theta\Big) \tag{B.5}$$

where we neglected the electron mass. From the above equation, we can obtain a relation between the incoming electron energy and the outgoing one, namely

$$2M_T\Big(E_e - E'_e\Big) = 2E_eE'_e\Big(1 - \cos\theta\Big) \tag{B.6}$$

$$2M_TE_e = 2M_TE'_e + 2E_eE'_e\Big(1 - \cos\theta\Big) \tag{B.7}$$

$$M_TE_e = E'_e\Big[M_T + E_e\Big(1 - \cos\theta\Big)\Big] \tag{B.8}$$

$$E'_e = \frac{E_e}{1 + \frac{E_e}{M}(1 - \cos\theta)} \tag{B.9}$$

$$E'_e = \frac{E_e}{1 + 2\frac{E_e}{M}\sin^2\frac{\theta}{2}}\,. \tag{B.10}$$

Substituing this expression for the outgoing electron energy inside Eq. B.1, we obtain the momentum trasfer definition in Eq. 3.17, namely

$$q^2(\theta) = \frac{4E_e^2\sin^2(\theta/2)}{1 + \frac{2E_e}{M_T}\sin^2(\theta/2)}\,. \tag{B.11}$$

Appendix C

Effective electron charge of the target atom, $Z_{\rm eff}^{\mathcal{A}}(T_e)$

In this appendix, we report the stepping functions $Z_{\rm eff}^{\mathcal{A}}(T_e)$ adopted in the analysis presented in the thesis. In particular, the stepping functions are reported for the case of Xenon, Cesium, Iodine, Germanium and Argon atoms [6, 7, 46, 47]. The $Z_{\rm eff}^{\mathcal{A}}(T_e)$ term, which quantifies the number of electrons that can be ionized by a certain energy deposit T_e. They have been obtained by using the edge energies extracted from photoabsorption data [48].

$$Z_{\rm eff}^{\rm Xe} = \begin{cases} 54, & T_e > 34.561 \text{ keV} \\ 52, & 34.561 \text{ keV} \geq T_e > 5.4528 \text{ keV} \\ 50, & 5.4528 \text{ keV} \geq T_e > 5.1037 \text{ keV} \\ 48, & 5.1037 \text{ keV} \geq T_e > 4.7822 \text{ keV} \\ 44, & 4.7822 \text{ keV} \geq T_e > 1.1487 \text{ keV} \\ 42, & 1.1487 \text{ keV} \geq T_e > 1.0021 \text{ keV} \\ 40, & 1.0021 \text{ keV} \geq T_e > 0.9406 \text{ keV} \\ 36, & 0.9406 \text{ keV} \geq T_e > 0.689 \text{ keV} \\ 32, & 0.689 \text{ keV} \geq T_e > 0.6764 \text{ keV} \\ 26, & 0.6764 \text{ keV} \geq T_e > 0.2132 \text{ keV} \\ 24, & 0.2132 \text{ keV} \geq T_e > 0.1467 \text{ keV} \\ 22, & 0.1467 \text{ keV} \geq T_e > 0.1455 \text{ keV} \\ 18, & 0.1455 \text{ keV} \geq T_e > 0.0695 \text{ keV} \\ 14, & 0.0695 \text{ keV} \geq T_e > 0.0675 \text{ keV} \\ 10, & 0.0675 \text{ keV} \geq T_e > 0.0233 \text{ keV} \\ 4, & 0.0233 \text{ keV} \geq T_e > 0.0134 \text{ keV} \\ 2, & 0.0134 \text{ keV} \geq T_e > 0.0121 \text{ keV} \\ 0, & T_e \leq 0.0121 \text{ keV} \end{cases}$$

Table C.1: The effective electron charge of the target atom, $Z_{\rm eff}^{\rm Xe}(T_e)$.

$$Z^{\text{Cs}}_{\text{eff}} = \begin{cases} 55, & T_e > 35.99 \text{ keV} \\ 53, & 35.99 \text{ keV} \geq T_e > 5.71 \text{ keV} \\ 51, & 5.71 \text{ keV} \geq T_e > 5.36 \text{ keV} \\ 49, & 5.36 \text{ keV} \geq T_e > 5.01 \text{ keV} \\ 45, & 5.01 \text{ keV} \geq T_e > 1.21 \text{ keV} \\ 43, & 1.21 \text{ keV} \geq T_e > 1.07 \text{ keV} \\ 41, & 1.07 \text{ keV} \geq T_e > 1 \text{ keV} \\ 37, & 1 \text{ keV} \geq T_e > 0.74 \text{ keV} \\ 33, & 0.74 \text{ keV} \geq T_e > 0.73 \text{ keV} \\ 27, & 0.73 \text{ keV} \geq T_e > 0.23 \text{ keV} \\ 25, & 0.23 \text{ keV} \geq T_e > 0.17 \text{ keV} \\ 23, & 0.17 \text{ keV} \geq T_e > 0.16 \text{ keV} \\ 19, & T_e < 0.16 \text{ keV} \end{cases} \qquad Z^{\text{I}}_{\text{eff}} = \begin{cases} 53, & T_e > 33.17 \text{ keV} \\ 51, & 33.17 \text{ keV} \geq T_e > 5.19 \text{ keV} \\ 49, & 5.19 \text{ keV} \geq T_e > 4.86 \text{ keV} \\ 47, & 4.86 \text{ keV} \geq T_e > 4.56 \text{ keV} \\ 43, & 4.56 \text{ keV} \geq T_e > 1.07 \text{ keV} \\ 41, & 1.07 \text{ keV} \geq T_e > 0.93 \text{ keV} \\ 39, & 0.93 \text{ keV} \geq T_e > 0.88 \text{ keV} \\ 35, & 0.88 \text{ keV} \geq T_e > 0.63 \text{ keV} \\ 31, & 0.63 \text{ keV} \geq T_e > 0.62 \text{ keV} \\ 25, & 0.62 \text{ keV} \geq T_e > 0.19 \text{ keV} \\ 23, & 0.19 \text{ keV} \geq T_e > 0.124 \text{ keV} \\ 21, & 0.124 \text{ keV} \geq T_e > 0.123 \text{ keV} \\ 17, & T_e < 0.123 \text{ keV} \end{cases}$$

Table C.2: The effective electron charge of the target atom, $Z^{\mathcal{A}}_{\text{eff}}(T_e)$, for Cs and I.

$$Z^{\text{Ge}}_{\text{eff}} = \begin{cases} 32, & T_e > 11.103 \text{ keV} \\ 30, & 11.103 \text{ keV} \geq T_e > 1.4146 \text{ keV} \\ 28, & 1.4146 \text{ keV} \geq T_e > 1.2481 \text{ keV} \\ 26, & 1.2481 \text{ keV} \geq T_e > 1.217 \text{ keV} \\ 22, & 1.217 \text{ keV} \geq T_e > 0.1801 \text{ keV} \\ 20, & 0.1801 \text{ keV} \geq T_e > 0.1249 \text{ keV} \\ 18, & 0.1249 \text{ keV} \geq T_e > 0.1208 \text{ keV} \\ 14, & 0.1208 \text{ keV} \geq T_e > 0.0298 \text{ keV} \\ 10, & 0.0298 \text{ keV} \geq T_e > 0.0292 \text{ keV} \\ 4, & T_e \leq 0.0292 \text{ keV} \end{cases}$$

Table C.3: The effective electron charge of the target atom, $Z^{\mathcal{A}}_{\text{eff}}(T_e)$, for Ge.

$$Z^{\text{Ar}}_{\text{eff}} = \begin{cases} 18, & T_e > 3.21 \text{ keV} \\ 16, & 3.21 \text{ keV} \geq T_e > 0.326 \text{ keV} \\ 14, & 0.326 \text{ keV} \geq T_e > 0.251 \text{ keV} \\ 12, & 0.251 \text{ keV} \geq T_e > 0.248 \text{ keV} \\ 8, & 0.248 \text{ keV} \geq T_e > 0.0293 \text{ keV} \\ 6, & 0.0293 \text{ keV} \geq T_e > 0.0159 \text{ keV} \\ 4, & 0.0159 \text{ keV} \geq T_e > 0.0157 \text{ keV} \\ 0, & T_e \leq 0.157 \text{ keV} \end{cases}$$

Table C.4: The effective electron charge of the target atom, $Z^{\mathcal{A}}_{\text{eff}}(T_e)$, for Ar.

Appendix D

Muon and Electron anomalous magnetic moment

A new measurement of the anomalous muon magnetic moment, referred to as $a_\mu \equiv (g_\mu - 2)/2$, has been largely awaited due to the presence of a long-standing deviation of the experimental determination of a_μ, performed at BNL [276] in 2004, from the theoretical expectation of about 3.7σ. In 2021, the Muon g-2 Collaboration at Fermilab (FNAL) released a new measurement [277], with a slightly better precision, about 15% less, than the BNL one, which is $a_\mu^{\mathrm{FNAL,\,exp}} = 116\ 592\ 040(54) \times 10^{-11}$. The combined experimental average between the FNAL and BNL results

$$a_\mu^{\mathrm{exp}} = 116\ 592\ 061(41) \times 10^{-11}, \tag{D.1}$$

can be compared with the standard model (SM) prediction $a_\mu^{\mathrm{SM}} = 116\ 591\ 810(43) \times 10^{-11}$ [250–275], showing an intriguing 4.2σ discrepancy

$$\Delta a_\mu = a_\mu^{\mathrm{exp}} - a_\mu^{\mathrm{SM}} = 251(59) \times 10^{-11}. \tag{D.2}$$

Recently, the Muon g-2 Collaboration released the new collected data [278], which resulted in a significantly improved experimental precision, a factor of 2 better than the previous measurement. The new experimental average is

$$a_\mu^{\mathrm{exp}} = 116\ 592\ 059(22) \times 10^{-11}, \tag{D.3}$$

so that, the discrepancy now is

$$\Delta a_\mu = a_\mu^{\mathrm{exp}} - a_\mu^{\mathrm{SM}} = 249(48) \times 10^{-11}, \tag{D.4}$$

which yields to a 5σ tension with respect to the theoretical value described above. However, there is a lot of discussion around the community about the theoretical prediction from the SM as it counts many contributions and the recent results from lattice calculations seem to be able to alleviate the tension. However, a significant amount of work needs still to be done to arrive at the final solution of this anomaly.

From the theoretical point of view, the SM prediction of the muon anomalous magnetic moment is often defined as a sum of three contributions: one coming

from QED, $a_\mu^{\rm QED}$, an electroweak contribution, $a_\mu^{\rm EW}$, and a hadronic contribution, $a_\mu^{\rm had}$, whose leading order diagrams are shown in Fig. D.1.

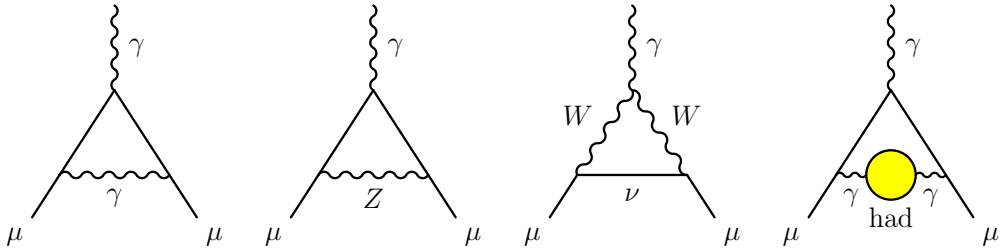

Figure D.1: Diagrams contributing the theoretical prediction of $a_\mu^{\rm th}$. Namely the first order QED contribution, the two electroweak contributions at the leading order and the hadronic contribution, going from left to right [25].

Indeed, this $(g-2)_\mu$ anomaly may represent a signature of new physics beyond the SM (see the reviews in Refs. [289, 387, 388]). In fact, in theories beyond the SM, an additional neutral boson B with mass M_B, which interacts with muons with coupling g_B, contributes to the muon anomalous magnetic moment with [389]

$$\Delta a_\mu^B = \frac{g_B^2}{8\pi^2}\int_0^1 dx\,\frac{Q(x)}{x^2+(1-x)\,M_B^2/m_\mu^2}, \tag{D.5}$$

where $Q(x)$ depends on the scalar or vector nature of the neutral boson B:

$$Q(x) = \begin{cases} x^2\,(2-x) & \text{(scalar)}, \\ 2x^2\,(1-x) & \text{(vector)}. \end{cases} \tag{D.6}$$

Depending on the specific light mediator model, the g_B coupling will assume a specific value, giving rise to a different contribution.
We show an example of fit of the discrepancy in terms of a generic vector Z' model in Fig. D.2, where in the left plot we compare the allowed region at 2σ C.L. considering the experimental average at 2021 [277] and the one updated at 2023 [278]. In the right one, we show the result from the latest experimental average at different confidence levels.
Instead, in the case of a dark Z boson, the one-loop vector contribution to the magnetic moment of the muon due to the new boson is [229]

$$\Delta a_{\mu,\,\text{vector}}^{Z_d} = \frac{\alpha}{2\pi}\Big(\epsilon + \frac{m_{Z_d}}{m_Z}\delta'\frac{1-4\sin^2\theta_W}{4\sin\theta_W\cos\theta_W}\Big)^2 F_V\Big(\frac{m_{Z_d}}{m_\mu}\Big), \tag{D.7}$$

where $\sin\theta_W$ is employed at the corresponding lepton mass scale, α is the fine-structure constant, and

$$F_V(x) \equiv \int_0^1 dz \frac{2z(1-z)^2}{(1-z)^2+x^2 z}. \tag{D.8}$$

The mass mixing characterizing the Z_d model introduces also an axial contribution, which is although negligible, given by [229]

$$\Delta a_{\mu,\,\text{axial}}^{Z_d} = -\frac{G_F m_\mu^2}{8\sqrt{2}\pi^2}\delta'^2 F_A\Big(\frac{m_{Z_d}}{m_\mu}\Big), \tag{D.9}$$

where

$$F_A(x) \equiv \int_0^1 dz \frac{2(1-z)^3 + x^2 z(1-z)(z+3)}{(1-z)^2 + x^2 z}. \tag{D.10}$$

Adding the two contributions in Eqs. (D.7) and (D.9), it is possible to retrieve the total Z_d induced magnetic momentum contribution $\Delta a_\mu^{Z_d}(\epsilon,\,\delta,\,m_{Z_d}) = \Delta a_{\mu,\,\text{vector}}^{Z_d} + \Delta a_{\mu,\,\text{axial}}^{Z_d}$.

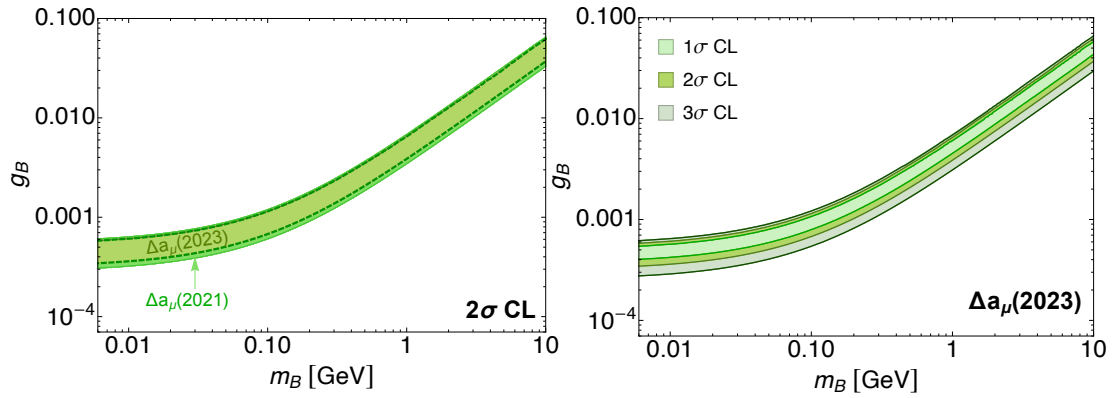

Figure D.2: (Left) Generic band representing the allowed parameter space at 2σ C.L. for the fit of a generic vector Z' coupling to muons. We compare the result considering the experimental average at 2021 [277] and the one updated at 2023 [278]. (Right) Favored contours at different confidence levels considering the latest experimental average [278].

The same discussion applies also to the case of the electron anomalous magnetic moment, considering the coupling of the new boson to electrons, so that we can simply modify the above expressions by substituting $\mu \to e$. Indeed, the experimental result on $a_e \equiv (g_e - 2)/2$ [390, 391] has shown a greater than 2σ discrepancy with the SM prediction [392], even if with an opposite sign with respect to the muon one. However, a different determination of the fine structure constant [342], obtained from the measurement of the recoil velocity on rubidium atoms, results in a reevaluation of the SM electron magnetic moment, bringing to a positive discrepancy of about 1.6σ. Namely

$$\Delta a_e = a_e^{\text{exp}} - a_e^{\text{SM, Rb}} = 0.48(30) \times 10^{-12}. \tag{D.11}$$

Interestingly, considering the latter result, the electron and muon magnetic moment discrepancies point in the same direction.

Appendix E

List of acronyms

—— PROCESSES ——

CEνNS: Coherent Elastic Neutrino Nucleus Scattering

νES: Elastic Neutrino Electron Scattering, sometimes ES

PVES: Parity Violating Electron Scattering

PWBA: Plane Wave Born Approximation

DWBA: Distorted Wave Born Approximation

$A_{\rm pv}$: parity-violating asymmetry measured in a PVES experiment

IBD: Inverse Beta Decay Process

NIN: Neutrino-Induced Neutron process

APV: Atomic Parity Violation process

PNC: Parity non-conservation process (same as APV)

—— GENERAL TERMINOLOGY ——

SM: Standard Model

BSM: Beyond the Standard Model

QED: Quantum Electro-Dynamics

QCD: Quantum Chromo-Dynamics

EM: electromagnetic

wk: weak

EW: electroweak

GSW model: Model of the electroweak unification developed by Glashow, Salam and Weinberg

θ_W: weak mixing angle

MSW effect: Mikheyev-Smirnov-Wolfenstein effect which describes the neutrino oscillation mechanism in matter

$\overline{MS}$ scheme: Modified Minimal Subtraction renormalization scheme

RGE: Renormalization Group Equation

EFT: Effective Field Theory

CC: weak charge current

NC: weak neutral current

SD: Spin-dependent

SI: Spin-independent

PDG: Particle Data Group

—— EXPERIMENTS AND MEASUREMENTS ——

E158: Experiment performed at SLAC which measured the electron weak charge

Q_{weak}: Experiment performed at JLab which measured the proton weak charge

PVDIS: Experiment performed at Jlab which measured parity violation in the deep inelastic scattering process

PREX: Lead ($^{208}\mathrm{Pb}$) Radius EXperiment

CREX: Calcium ($^{48}\mathrm{Ca}$) Radius EXperiment

MESA: Mainz Energy recovering Superconducting Accelerator facility under construction in Mainz

MAMi: Mainz Microtron campus accelerator facility

JGU: Johannes Gutenberg University in Mainz, Germany

MREX: Mainz Radius EXperiment on $^{208}\mathrm{Pb}$

P2 experiment: proton weak charge measurement planned at MESA

MOLLER experiment: electron weak charge measurement planned at JLab

NCC-1701: Name of the Germanium detector used in for the CEνNS observation at the Dresden-II nuclear power plant

CENNS-10: Name of the single-phase detector filled with liquid argon employed by the COHERENT Collaboration

COH LAr: detector filled with LAr employed by the COHERENT Collaboration, equivalent to CENNS-10

COH-LAr 750 kg: future ton-scale LAr detector foreseen by the COHERENT Collaboration

COH CsI: Cesium iodide crystal detector used by the COHERENT Collaboration

COH-CryoCsI-I: cryogenic undoped CsI detector foreseen by the COHERENT Collaboration, scheduled to be operational starting from 2025 with a mass of about 10 kg

COH-CryoCsI-II: updated version of the COH CryoCsI-I detector with a mass of about 700 kg foreseen by the COHERENT Collaboration from 2030

ORNL: Oak Ridge National Laboratory

APV PDG: APV measurements on cesium calculated considering the ingredients reported by the latest PDG

APV 2021: APV measurements on cesium calculated considering the theoretical calculation reported by Sahoo et al. in 2021

APV PDG + CsI: results from the combined analysis of APV PDG and COH CsI

APV 2021 + CsI: results from the combined analysis of APV 2021 and COH CsI

LZ Collaboration: Lux-Zeplin Collaboration

LNGS: Laboratori Nazionali del Gran Sasso

DS-50 Collaboration: DarkSide-50 Collaboration

DS-20k Collaboration: DarkSide-20k Collaboration

LHC: Large Hadron Collider at CERN, Geneva

—— MATERIALS ——

Ar: Argon

LAr: Liquid Argon

AAr: argon extracted from the atmosphere

UAr: argon extracted from the underground reservoirs

C: Carbon

Ca: Calcium

Cs: Cesium

Ge: Germanium

I: Iodine

CsI: Cesium Iodide

Xe: Xenon

LXe: Liquid Xenon

Pb: Lead

Pu: Plutonium

U: Uranium

—— NUCLEAR PARAMETERS AND MODELS ——

rms: root-mean-squared

M_T: target mass (usually nuclear mass)

R_p: Nuclear proton distribution rms radius

R_n: Nuclear neutron distribution rms radius

$\Delta R_{\rm np}$: Neutron skin, difference between the nuclear neutron and proton distribution radii

$R_{\rm ch}$: Nuclear charge distribution rms radius

$R_{\rm wk}$: Nuclear weak distribution rms radius

$\Delta R_{\rm wk,\,skin}$: Weak skin, difference between the nuclear weak and charge distribution radii

$\Delta R_{\rm np}^{\rm had}$: Neutron skin obtained from antiprotonic atom x-rays data (via hadronic probes)

F_p: Nuclear proton form factor

F_n: Nuclear neutron form factor

$F_{\rm ch}$: Nuclear charge form factor

$F_{\rm wk}$: Nuclear weak form factor

ρ_p: Nuclear proton density distribution

ρ_n: Nuclear neutron density distribution

$\rho_{\rm ch}$: Nuclear charge density distribution

$\rho_{\rm wk}$: Nuclear weak density distribution

SF model: Symmetrized two-parameter Fermi model for the nuclear form factor

2pF model: two-parameter Fermi model

SOG: Sum-of-Gaussians

FB: Fourier-Bessel

3pF model: three-parameter-Fermi model

EDFs: Energy density functionals

NSM: Nuclear Shell Models

$E_{\rm PNC}^{\rm w.n.s.}$: parity violating amplitude without the neutron skin correction

$E_{\rm PNC}^{\rm n.s.}$: parity violating amplitude with the neutron skin correction

—— NEUTRINO FLUXES ——

HM parametrization: parametrization of the reactor neutrino spectra by Hubert and Mueller

EF parametrization: parametrization of the reactor neutrino spectra by Estienne and Fallot

VE parametrization: parametrization of the reactor neutrino spectra by Vogel and Engel

K parametrization: parametrization of the reactor neutrino spectra by Kopeikin

HMVE parametrization: parametrization of the reactor neutrino spectrum obtained by combining the high energy part described in the HM description and the low energy part from VE

HMK parametrization: parametrization of the reactor neutrino spectrum obtained by combining the high energy part described in the HM description and the low energy part from K

EFK parametrization: parametrization of the reactor neutrino spectrum obtained by combining the high energy part described in the EF description and the low energy part from K

π-DAR: pion decay-at-rest

K-DAR: kaon decay-at-rest

SNS: Spallation Neutron Source

ESS: European Spallation Source

CSNS: China Spallation Neutron Source

—— EXPERIMENTAL DETAILS AND PARAMETERS ——

TPC: Time Projection Chamber

C.L.: Confidence Level

f_Q: Quenching factor

QF: Quenching factor (equivalent to f_Q)

ER: Electron Recoil

NR: Nuclear Recoil

T_e: Electron recoil energy

$T_{\rm nr}$: Nuclear recoil energy

L_Y: Light yield

PE: Photo-electron

F_{90}: fraction of light emitted in the first 90 ns after the recoil with respect to the total light collected

BRN: Beam Related Neutrons background component

PBRN: Prompt Beam Related Neutrons background component

DBRN: Delayed Beam Related Neutrons background component

POT: Proton-on-target

SS: Steady-State background

PDFs: Probability Distribution Functions

CV: Central-value

Fef: iron-filter Germanium quenching factor parametrization

YBe: photo-neutron Germanium quenching factor parametrization

Rx-ON: reactor operation period

S1 signal: scintillation signal in a dual-phase TPC

S2 signal: ionization signal in a dual-phase TPC

ROI: Region-of-interest

SEC: Single Electron Candidate

PMT: Photo-multipliers

ITO: indium tin oxide

HV cathode: High voltage cathode

PTFE reflector: polytetrafluoroethylene reflector

TPB wavelength shifter: tetraphenyl butadiene wavelength shifter

S2-echo: SEC events generated by the extraction of electrons from the cathode plane by S2 photons

S1-echo: SEC events generated by the extraction of electrons from the cathode plane by S1 photons

S2-bulk: SEC event generated by the extraction of electrons from the liquid with the SEC signal following the S2 one

S2-bulk: SEC event generated by the extraction of electrons from the liquid with the SEC signal happening between the S1 and the S2 ones

UV: Ultra-violet

VUV photons: vacuum ultra-violet photons

QE: Quantum efficiency

PEP: photoelectric extraction probability

—— BSM PROPERTIES AND MODELS ——

$B - L$: light mediator model based on the conservation of the difference between the baryon number B and the lepton number L

$L_\alpha - L_\beta$: class of light mediator models based on the conservation of the difference between the lepton number of flavor α and the one of flavor β

$(g-2)_\mu$: muon anomalous magnetic moment

$(g-2)_e$: electron anomalous magnetic moment

NCR: Neutrino Charge Radius, sometimes also CR

MM: Neutrino Magnetic Moment

EC: Neutrino Electric Charge, sometimes called neutrino millicharge

FEA: Free Electron Approximation

MCRRPA: Multiconfiguration Relativistic Random Phase Approximation, sometimes RRPA

EPA: Equivalent Photon Approximation

Acknowledgements

I want to thank the referees of this thesis work, Dott. Valentina De Romeri and Prof. Giampaolo Cò, for carefully reading the work and providing me with very useful comments.
I am very thankful to Dott. Matteo Cadeddu for the huge amount of information he has taught me during my PhD. You have been an amazing supervisor, both from the human and scientific points of view.
I am equally thankful to my close collaborators, namely Dott. Francesca Dordei, Dott. Carlo Giunti, Dott. Walter Bonivento and Dott. Mattia Atzori Corona. Collaborating is surely the best way to produce a profitable research outcome. I have learned a lot from each of you and I hope I will be able to keep learning from you. Particular thanks to Mattia, who has shared with me this experience, sometimes rewarding sometimes not, but that I have never regretted.
I would like to thank warmly Dott. Mikhail Gorchtein, who has supervised me during my PhD period abroad. I enjoyed working with you and having the chance to discover a different working environment. I am sure this will be the beginning of a nice collaboration. Moreover, I am thankful to Prof. Jens Erler and Prof. Hubert Spiesberger for all the things I have learned from you and the warm welcoming me into your working group.